



NAM

V7 Ground-Motion Model for Induced Seismicity in the Groningen Gas Field (Update)

With Assurance Letter

Julian J Bommer¹, Benjamin Edwards¹, Pauline P Kruiver², Adrian Rodriguez-Marek¹, Peter J Stafford¹, Bernard Dost³, Michail Ntinalexis¹, Elmer Ruigrok³ and Jesper Spetzler³

1. Independent consultant,

2. Deltares,

3. Royal Netherlands Meteorological Institute (KNMI)

Datum February 2022

Editors Jan van Elk & Jeroen Uilenreef

General Introduction

The seismic hazard in Groningen, due to earthquakes induced by the production of gas, is primarily presented by the ground motions to which buildings and people are subjected. The forecasting of these ground motions is therefore critical for hazard and risk assessment.

This research was started in 2012 and has continued with ever more ground motion data from Groningen earthquakes being acquired. The Ground Motion Prediction Model (GMM) was therefore updated and progress documented regularly. In the Technical Addendum to Winningsplan 2013, a Ground Motion Prediction Methodology based on a catalogue of tectonic earthquakes in southern Europe, was presented (Ref. 1). This methodology was inherently conservative, in the sense that it predicted ground motions, which in future with more data available would more likely be adjusted downwards than upwards.

In the report “Development of GMPEs for Response Spectral Accelerations and for Strong-Motion Durations (Version 1)” the status in May 2015 was documented (Ref. 2). An update of this document was issued in November 2015 which presented version 2 of the GMPE methodology (Ref. 3). This version of the Ground Motion Prediction Model was tailored to the Groningen situation (Ref. 4 to 7). In general, this update led to a downward adjustment of assessed ground motions for larger earthquakes, resulting in a reduction of the assessed hazard. After incorporating some adjustments, this version of the GMM was used for the hazard and risk assessment supporting Winningsplan 2016, issued in April 2016 (Ref. 8).

Originally, an update of the GMM (version 3) was planned for July 2016, in support of the hazard and risk assessment for Winningsplan 2016. However, when early 2016 the deadline of submission for the Winningsplan was brought forward from July 2016 to April 2016, version 3 of the GMM could not be ready in time to be implemented in the hazard and risk assessment for this winningsplan.

Version 4 of the Ground Motion Model (GMM) was completed mid-2017 and shared with experts for an assurance review (Ref. 9). Based on the comments of the assurance panel, version 5 of the Ground Motion Model was developed and documented in a report issued in November 2017 (Ref. 10). This version was used in Hazard, Building Damage and Risk Assessment of November 2017 (Ref. 12), the Hazard and Risk Assessment for production forecast Basispad Kabinet of August 2018 (Ref. 13) and the Hazard and Risk Assessment for the production forecast prepared by GTS (GTS-raming) of March 2019 (Ref. 14). The report on GMM V5 was later re-issued (Ref. 11) with the addition of the Assurance Letter and short resumes of the Assurance Panel members (Appendix I), and the full set of written comments on the first versions of the V4 and V5 GMM reports (Ref. 9 and 10), together with the detailed responses from the GMM development team (Appendices IX and X).

A number of improvements were incorporated in the development of version 6 of the Ground Motion Model (Ref. 15). The most important change is the switch from using the G4 geophones recordings acquired at 200 m depth to the G0-station accelerograms acquired at surface. This change was made possible by expansion of the database of ground motion recordings.

This current version of the Ground Motion Model (version 7) was first documented in a report issued in October 2021. This also included the impact on ground motions of anthropogenic dwelling mounds (wierden or terpen) (Ref. 16 to 19).

This report is a revision of the report issued in October 2021. In this revision some minor inconsistencies in the presentation have been corrected. These do not impact the model, which is unchanged from the October 2021 versions. The electronic supplements have also not been affected and are unchanged.

References:

- 1 Technical Addendum to the Winningsplan Groningen 2013; Subsidence, Induced Earthquakes and Seismic Hazard Analysis in the Groningen Field, Nederlandse Aardolie Maatschappij BV (Jan van Elk and Dirk Doornhof, eds), November 2013.
- 2 Development of Version 1 GMPEs for Response Spectral Accelerations and for Strong-Motion Durations, Julian J Bommer, Peter J Stafford, Benjamin Edwards, Michail Ntinalexis, Bernard Dost and Dirk Kraaijpoel, March 2015.
- 3 Development of Version 2 GMPEs for Response Spectral Accelerations and Significant Durations for Induced Earthquakes in the Groningen field, Julian J Bommer, Bernard Dost, Benjamin Edwards, Adrian Rodriguez-Marek, Pauline P Kruiver, Piet Meijers, Michail Ntinalexis & Peter J Stafford, October 2015
- 4 Geological schematisation of the shallow subsurface of Groningen (For site response to earthquakes for the Groningen gas field) – Part I, Deltares, Pauline Kruiver and Ger de Lange.
- 5 Geological schematisation of the shallow subsurface of Groningen (For site response to earthquakes for the Groningen gas field) – Part II, Deltares, Pauline Kruiver and Ger de Lange.
- 6 Geological schematisation of the shallow subsurface of Groningen (For site response to earthquakes for the Groningen gas field) – Part III, Deltares, Pauline Kruiver and Ger de Lange.
- 7 Modifications of the Geological model for Site response at the Groningen field, Deltares, Pauline Kruiver, Ger de Lange, Ane Wiersma, Piet Meijers, Mandy Korff, Jan Peeters, Jan Stafleu, Ronald Harting, Roula Dambrink, Freek Busschers, Jan Gunnink
- 8 Winningsplan Groningen 2016, NAM, April 2016.
- 9 V4 Ground-motion Model (GMM) for Response Spectral Accelerations, Peak Ground Velocity and Significant Duration in the Groningen field, Julian Bommer, Bernard Dost, Benjamin Edwards, Pauline Kruiver, Pier Meijers, Michail Ntinalexis, Adrian Rodriguez-Marek, Elmer Ruigrok, Jesper Spetzler and Peter Stafford, Independent Consultants, Deltares and KNMI, June 2017 with Parameter files - V4 Ground-Motion Model (GMM) for Response Spectral Accelerations, Peak Ground Velocity, and Significant Durations in the Groningen Field, Supplement to V4 GMM, Julian Bommer and Peter Stafford, Independent Consultants, June 2017
- 10 V5 Ground-Motion Model (GMM) for the Groningen Field, Julian J Bommer, Benjamin Edwards, Pauline P Kruiver, Adrian Rodriguez-Marek, Peter J Stafford, Bernard Dost, Michail Ntinalexis, Elmer Ruigrok and Jesper Spetzler, October 2017
- 11 V5 Ground-Motion Model (GMM) for the Groningen Field re-issued with assurance letter, Julian J Bommer, Benjamin Edwards, Pauline P Kruiver, Adrian Rodriguez-Marek, Peter J Stafford, Bernard Dost, Michail Ntinalexis, Elmer Ruigrok and Jesper Spetzler, March 2018
- 12 Hazard, Building Damage and Risk Assessment, NAM (Jan van Elk and Dirk Doornhof), November 2017.
- 13 Hazard and Risk Assessment for production forecast Basispad Kabinet, NAM, Jan van Elk and Dirk Doornhof, July 2018.
- 14 Hazard and Risk Assessment for production forecast GTS-raming 2019, NAM, Jan van Elk and Dirk Doornhof, March 2019.
- 15 V6 Ground-Motion Model (GMM) for Induced Seismicity in the Groningen Field - with Assurance Letter, Julian J Bommer, Benjamin Edwards, Pauline P Kruiver, Adrian Rodriguez-Marek, Peter J Stafford, Bernard Dost, Michail Ntinalexis, Elmer Ruigrok and Jesper Spetzler, December 2019
- 16 Terp composition in respect to earthquake risk in Groningen, Dr. ir. E.W. Meijles, Dr. G. Aalbersberg, and Prof. dr. H.A. Groenendijk, RUG, Mar 2016.
- 17 Archeologisch en seismisch onderzoek naar de lithologie en opbouw van acht wierden in de provincie Groningen - Gemeente Hogeland, Delfzijl en Westerkwartier, Dr. G. Aaldersberg en drs H.W. Veenstra, RAAP Archeologisch Adviesbureau, Feb 2021.

- 18 Lithoclass and shear wave velocity characterisation of terps: an assessment in relation to earthquake risks , Dr. G. Aaldersberg and dr. E.W. Meijles , Salisburt Archäologie GmbH and Faculty of Spatial Sciences, Rijksuniversiteit Groningen , Feb 2021.
- 19 V7 Ground-Motion Model (GMM) for Induced Seismicity in the Groningen Field - with Assurance Letter, Julian J Bommer, Benjamin Edwards, Pauline P Kruiver, Adrian Rodriguez-Marek, Peter J Stafford, Bernard Dost, Michail Ntinalexis, Elmer Ruigrok and Jesper Spetzler, October 2021

These reports are also available at the study reports page of the website www.nam.nl.



NAM

| | | | |
|---|--|---------------------|--------------------------------|
| Title | V7 Ground-Motion Model for Induced Seismicity in the Groningen Field (Update) - With Assurance Letter | Date | February 2022 |
| | | Initiator | NAM |
| Author(s) | Julian J Bommer ¹ , Benjamin Edwards ¹ , Pauline P Kruiver ² , Adrian Rodriguez-Marek ¹ , Peter J Stafford ¹ , Bernard Dost ³ , Michail Ntinalexis ¹ , Elmer Ruigrok ³ and Jesper Spetzler ³ | Editors | Jan van Elk & Jeroen Uilenreef |
| Organisation | 1. Independent consultant, 2. Deltares, 3. Royal Netherlands Meteorological Institute (KNMI) | Organisation | NAM |
| Place in the Study and Data Acquisition Plan | <p><u>Study Theme:</u> Ground Motion Prediction</p> <p><u>Comment:</u></p> <p>The hazard in Groningen, due to earthquakes induced by the production of gas, is primarily presented by the ground motions to which buildings and people are subjected. The forecasting of these ground motions is therefore critical for hazard and risk assessment.</p> <p>This research was started in 2012 and is continuing with ever more ground motion data from Groningen earthquakes being acquired. The Ground Motion Prediction Model (GMM) was therefore updated and progress documented regularly. In the Technical Addendum to Winningsplan 2013, a Ground Motion Prediction methodology based on a catalogue of tectonic earthquakes in southern Europe, was presented. This methodology was inherently conservative, in the sense that it predicted ground motions, which in future with more data available would more likely to be adjusted downwards than upwards.</p> <p>In the report “Development of GMPEs for Response Spectral Accelerations and for Strong-Motion Durations (Version 1)” the status in May 2015 was documented. An update of this document was issued in November 2015 which presented version 2 of the GMPE methodology. This version of the Ground Motion Prediction Model was tailored to the Groningen situation. In general, this update led to downward adjustment of assessed ground motions for larger earthquakes, resulting in a reduction of the assessed hazard. After incorporating some adjustments, this version of the GMM was used for the hazard and risk assessment supporting Winningsplan 2016, issued in April 2016.</p> <p>Originally, an update of the GMM (version 3) was planned for July 2016, in support of the hazard and risk assessment for Winningsplan 2016. However, when early 2016 the deadline of submission for the Winningsplan was brought forward from July 2016 to April 2016, version 3 of the GMM could not be ready in time to be implemented in the hazard and risk assessment for this winningsplan.</p> | | |

| | |
|---------------------------------|--|
| | <p>Version 4 of the Ground Motion Model (GMM) was completed mid-2017 and shared with experts for an assurance review. Based on the comments of the assurance panel, version 5 of the Ground Motion Model was developed and documented in a report issued in November 2017. This version was used in Hazard, Building Damage and Risk Assessment of November 2017, the Hazard and Risk Assessment for production forecast Basispad Kabinet of August 2018 and the Hazard and Risk Assessment for the production forecast prepared by GTS (GTS-raming) of March 2019. The report on GMM V5 was later re-issued with the addition of the Assurance Letter and short resumes of the Assurance Panel members (Appendix I), and the full set of written comments on the first versions of the V4 and V5 GMM reports, together with the detailed responses from the GMM development team (Appendices IX and X).</p> <p>A number of improvements were incorporated in the development of version 6 of the Ground Motion Model. The most important change is the switch from using the G4 geophones recordings acquired at 200 m depth to the G0-station accelerograms acquired at surface. This change was made possible by expansion of the database of ground motion recordings.</p> <p>This current version of the Ground Motion Model (version 7) was first documented in a report issued in October 2021. This also included the impact on ground motions of anthropogenic dwelling mounts (wierden or terpen).</p> <p>This report is a revision of the report issued in October 2021. In this revision some minor inconsistencies in the presentation have been corrected. These do not impact the model, which is unchanged from the October 2021 versions. The electronic supplements have also not been affected and are unchanged.</p> |
| Directly linked research | <p>(1) Hazard Assessment.</p> <p>(2) Fragility assessment of buildings in the Groningen region.</p> |
| Used data | <p>Accelerograms from the accelerometers placed in the Groningen field.</p> <p>P- and S-wave velocity model sub-surface Groningen.</p> <p>Description of the shallow geology of Groningen.</p> |
| Associated organisation | KNMI |
| Assurance | External assurance team has reviewed the report for GMM version 4, 5, 6 and 7. Comments from the assurance team on GMM version 4, 5 and 6 are included in these reports as appendices. |

V7 Ground-Motion Model for Induced Seismicity in the Groningen Gas Field

A report prepared for NAM

**Julian J Bommer¹, Benjamin Edwards¹, Pauline P Kruiver², Adrian Rodriguez-Marek¹,
Peter J Stafford¹, Michail Ntinalexis¹, Elmer Ruigrok², and Bernard Dost²**

1. Independent consultant, 2. Royal Netherlands Meteorological Institute (KNMI),

Revision 1.1

26 February 2022

TABLE of CONTENTS

| | |
|---|-----|
| Closure letter from the International Expert Review Panel | iii |
| Significant changes to V7 GMM report relative to first issue | v |
| Acknowledgements | vi |
| | |
| 1. INTRODUCTION | 1 |
| 2. EVOLUTION of the GRONINGEN GMMs | 3 |
| 2.1. Model development from V0 to V7 | 3 |
| 2.2. Milestones in the model development process | 10 |
| 2.3. Overview of the V7 GMM | 15 |
| 3. V7 GROUND-MOTION DATABASE | 19 |
| 3.1. Groningen recording networks and record selection | 19 |
| 3.2. Record processing and usable period ranges | 41 |
| 3.3. Database characteristics | 49 |
| 4. SITE CHARACTERISATION MODEL | 53 |
| 4.1. Shear-wave velocity model for the field | 53 |
| 4.2. Site profiles at recording stations | 57 |
| 4.3. Soil damping model | 59 |
| 4.4. Recording station transfer functions and amplification factors | 66 |
| 5. INVERSION and SIMULATION of REFERENCE ROCK MOTIONS | 71 |
| 5.1. FAS and response spectra at NS_B | 71 |
| 5.2. Inversions for source, path and site parameters | 74 |
| 5.3. Calibration of central model parameters for simulations | 87 |
| 5.4. Logic-tree and parameters for forward simulations | 89 |
| 6. PARAMETRIC MODEL for REFERENCE ROCK MOTIONS | 94 |
| 6.1. Simulated motions at NS_B horizon | 94 |
| 6.2. Regressions on simulated motions | 99 |
| 6.3. Variability of reference rock predictions | 118 |
| 6.4. Influence of instrument type on model bias | 127 |
| 7. FIELD-WIDE SITE RESPONSE ANALYSES | 131 |
| 7.1. Input motions | 131 |
| 7.2. Site response profiles and soil properties | 133 |
| 7.3. Linear and equivalent linear analyses | 140 |
| 7.4. Site response analyses for <i>wierden</i> | 141 |
| 8. FIELD ZONATION and AMPLIFICATION FACTORS | 147 |
| 8.1. Field zonation model | 147 |
| 8.2. Amplification factors | 150 |
| 8.3. Logic-tree for site amplification factors | 160 |
| 8.4. Amplification penalty function for <i>wierden</i> | 166 |

| | |
|--|-----|
| 9. MODEL SUMMARY and INSTRUCTIONS for IMPLEMENTATION | 168 |
| 9.1. Complete V7 GMM logic-tree | 168 |
| 9.2. Sampling of variance components and correlations | 178 |
| 9.3. Including <i>wierden</i> in seismic risk calculations | 183 |
| 10. V7 GMM PERFORMANCE | 185 |
| 10.1. Residuals with respect to V7 GMM | 185 |
| 10.2. Comparison with V6 GMM | 200 |
| 10.3. Epistemic uncertainty and comparison with other GMMs | 210 |
| 11. CONCLUDING REMARKS | 224 |
| 12. REFERENCES | 227 |
| APPENDIX I Geomechanical look-up tables for soil properties | 236 |
| APPENDIX II Surface residuals from the V5 and V6 GMMs | 257 |

October 9, 2021

Mr Jan van Elk
Nederlandse Aardolie Maatschappij B.V. (NAM)
Schepersmaat 2,
9405 TA Assen, The Netherlands

Dear Mr. van Elk:

The undersigned are members of an international panel of experts in earthquake ground motion modelling (hereafter referred to as the *Panel*), which was engaged at various time intervals since July 2015 to review the development of ground motion models for the Groningen Gas Field. Panel reports presenting our assessments have been submitted following reviews of reports for the Version 4 model (May 2017), the Version 5 model (January 2018), the Version 6 model (our report on this model also included comments on the planning for Version 7 model development; September 2019), and Version 7 model (August 2021). The previously reviewed draft of the Version 7 report included an appendix presenting a ground motion model for peak ground velocity (PGV). Our August 2021 report also provided comments on the PGV model. We previously issued a letter endorsing the Version 5 model in January 2018, which was later re-affirmed for the Version 6 model (September 2019).

Panel membership through the various stages has remained the same, with the exception that Dr. Fabrice Cotton left the Panel following the Version 6 review due to another engagement with an agency involved with the Groningen Field hazard assessment that may have created a perceived conflict of interest.

Since our review of the draft Version 7 report, the Version 7 model report and PGV document (now issued as a separate report¹) have been finalized in consideration of our comments. The revised reports and a response document were provided to the Panel by Dr. Julian J. Bommer on 29 September 2021. Our comments on both reports have been satisfactorily addressed in the revised versions.

¹ Bommer, J.J., P.J. Stafford & M. Ntinalexis (2021). Empirical Equations for the Prediction of Peak Ground Velocity due to Induced Earthquakes in the Groningen Gas Field. A report for NAM, October 2021, 33 pp.

In consideration of all the work that has been completed by the ground motion modeling team and reviewed by this Panel, our principal finding is that the Version 7 model is suitable for its intended purpose, which is to conduct hazard and risk analyses in the Groningen Field. Likewise, we consider the PGV model to provide a suitable basis for estimating PGV for earthquakes within the model's recommended magnitude and distance range.

The Panel appreciates the opportunity to have been of service over the course of the Groningen Field ground motion model development work. Our interactions with NAM and the modeling team were intellectually stimulating and productive throughout this project.

Respectfully submitted,



Jonathan P. Stewart (Chair)

Norman A. Abrahamson

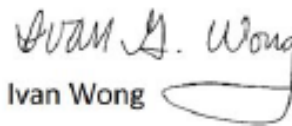
Gail M. Atkinson



Hilmar Bungum



John Douglas



Ivan Wong



Robert R. Youngs

Significant Changes to V7 GMM Report Relative to First Issue

The V7 GMM report was originally issued on 2 July 2021 for review by the International Expert Panel. Based on the Expert Panel feedback, the report was revised and issued publicly on 10 October 2021. During the implementation of the model in the hazard codes of NAM and KNMI, a number of issues were identified with regards to presentation, prompting the issue of this Revision 1 of the report. The model has not been changed in any way – all the modifications relate to presentation. The most significant changes are listed in the table below. Some of these are corrections to glitches that have been spotted in the October 2021 version of the report, others are related to the fact that the model is now presented strictly and exclusively for the oscillator periods from 0.01 to 1.0 second, which are used in the risk calculations. In the model derivation, coefficients were obtained for a few periods above 1.0 second and while these are shown in some of the plots, they do not form part of the model and have been eliminated from the electronic supplements.

| Location | Change and Motivation |
|---|--|
| Figure 4.5 | Map with ground-motion recording stations, distinguishing those with <i>in situ</i> V_s measurements; this figure, which was very cluttered and difficult to read, was removed, and the information conveyed in the text |
| Figure 5.12 | Residuals of database with respect to central model, modified to make confidence intervals more clearly visible |
| Figures 8.18 and 9.5 | Modified to display consistent branch weights (in terms of numbers of decimal places) |
| Figure 8.8 | The AFs for 0.01 s were plotted incorrectly and the figure has been replaced |
| Equations (9.13) and (9.14) | Small corrections to match the corresponding equations in Chapter 8 |
| Figures 10.1, 10.11, 10.15, and 10.25-10.68 | Figures updated to reflect small change to AFs at 0.01 s that was made just before completing the report, after the original plots had been generated |
| Missing references | A small number of references cited in the text but excluded from the list of references at the end have been added |

Acknowledgements

In the report for each ground-motion model (GMM) that has been produced over the last several years, we have included expressions of appreciation and gratitude to the individuals and organisations that contributed, in one way or another, to that stage of the model development (in the V4 GMM report, the acknowledgements filled almost three pages). Since this is the final version of the GMM and this report will represent the legacy of this work stream, it is tempting to include acknowledgements to everyone who played a role along the way, but this would be a very long list. Instead, we limit ourselves to expressions of thanks to the individuals who made specific contributions during this final stage of the model development.

We start by thanking Rui Pinho and his colleagues Francesco Cavaliere and António Correia for their excellent work on exploring dynamic soil-structure interaction effects at the strong-motion recording stations and applying corrections to the recordings from accelerographs installed in basements.

We are also grateful to Helen Crowley for liaising with us regarding the fragility model and the interfaces with the ground-motion predictions and the risk calculations.

Our thanks are also due to Jesper Spetzler of KNMI for providing valuable information regarding earthquake source parameters. Jesper also identified many of the inconsistencies in presentation of the model in the original version of this report through his implementation of the model in the KNMI hazard calculation code. We are very grateful to Jesper for highlighting these issues. Similarly pertinent questions were raised by Pablo Castellanos-Nash, who implemented the model in the NAM hazard and risk engine, and we also gratefully acknowledge these insightful observations.

Special mention is due to Onno Dijkstra and colleagues at Fugro for the rapid deployment of seismic CPT measurements at the G-stations and for being so accommodating with regards to order of priority for these *in situ* tests.

We also wish to thank Edwin Obando-Hernández and Manos Pefkos from Deltares for continuing the coordination of the site response analysis work after Pauline Kruiver transferred to KNMI. The efforts of all the Deltares staff involved in the site response calculations are greatly appreciated.

Our greatest debt is to the international GMM review panel, chaired by Jonathan Stewart and comprising Norm Abrahamson, Gail Atkinson, Hilmar Bungum, Fabrice Cotton, John Douglas, Ivan Wong and Bob Youngs. The panel members have continued to provide insightful and constructive input throughout the latest stage of model development, giving us feedback that has been both challenging and encouraging in appropriate measure. The value and quality of the Groningen ground-motion modelling work have been greatly enhanced through the engagement of this panel of renowned experts in this field. The reader will note that Fabrice Cotton is not a signatory to the closure letter from the panel, which is the result of his resigning from the panel in March 2021 in order to accept an invitation from SodM to serve on the KEM Expert Panel; however, Fabrice did participate actively until that time and his contributions to the review panel's work are greatly appreciated.

Finally, we express our debt to Jan van Elk for continuing to provide the space and conditions to undertake this work, as well as for the wisdom of knowing that people produce their best work when they are enjoying themselves.

1. Introduction

This report presents the final ground-motion model (GMM) to be developed by this team for application to induced and triggered earthquake scenarios in the Groningen gas field. The model presented herein is the seventh iteration of a bespoke ground-motion prediction model for acceleration response spectral ordinates in Groningen and marks the culmination of an evolutionary process that began with the work that led to the publication of the first (V1) GMM in 2015. The process of model development is now considered complete, not because the current model is considered perfect and incapable of being improved, but rather because the model has evolved to a state such that any further refinements are likely to produce modest changes. The V7 GMM is considered to be a stable representation of the centre, body, and range of technically defensible interpretations of the available data, methods, and models. Throughout its development the model has undergone extensive peer review by both an appointed panel of international experts and reviewers of many journal papers that have been published from this work.

This report is intended to serve as a standalone document that explains and presents the V7 GMM and the reader should not need to refer to the reports on earlier versions of the model. However, we do cite extensively the large number of journal papers that have been published on different elements of the model development, and the interested reader will be able to find additional details and background in these papers, all of which are available in the mainstream scientific literature.

Following this introduction, Chapter 2 presents an overview of the GMM evolution both in terms of technical development and the process of review and revision, ending with an overview of the framework of the V7 model. Chapters 3 and 4 then present the basic building blocks of the model in terms of databases, the former presenting the ground-motion database, including the record processing procedures that have been applied and the characteristics—and possible influence on the ground motions—of the recording stations. Chapter 4 presents the site characterisation model in terms of shear-wave velocity profiles from the ground surface to the reference rock horizon at ~800 m depth, including the measured profiles now available for most of the recording stations.

The GMM consists of two basic elements, a model for prediction of spectral accelerations at the reference rock horizon and a model for the dynamic response of the overlying soil layers to these rock motions. At this point, we make a note on our adopted nomenclature in this report. For many years, equations for the prediction of ground-motion parameters as a function of variables such as magnitude and distance were referred to as attenuation relationships (or even attenuation laws). Subsequently, it was pointed out that this was an inappropriate name given that the equations describe both attenuation with distance and scaling with magnitude (and other variables such as style-of-faulting, site classification, etc.). The title of GMPEs was

proposed and became widely adopted. However, in recent years there has been a trend to using GMM to refer to these models, in the recognition of the fact that they have often evolved beyond simple equations. In the context of the work presented herein to develop predictions of surface motions due to induced earthquakes in the Groningen field, we have adopted the title GMPE to refer to the parametric equations that predict motions at a buried reference rock horizon as a function of magnitude and distance. The complete prediction of surface motions, which involves a logic-tree of multiple GMPEs, a zonation for site amplification factors, and additional logic-tree branches for those amplification factors, is referred to as a GMM. Chapter 5 and 6 present the reference rock model, Chapters 7 and 8 the site amplification model. Chapter 5 describes the inversion of recorded motions to estimate source, path, and site parameters, and the use of these parameters in forward simulations, as well as the capture of epistemic uncertainty associated with this extrapolation far beyond the bounds of the Groningen database. Chapter 6 presents the development of parametric ground-motion prediction equations (GMPEs) derived from the simulated motions at the rock horizon, and the parallel development of a model for the associated aleatory variability. Chapter 7 provides an overview of the site response analyses performed to characterise the dynamic response of the layers of geomaterials overlying the reference rock horizon. Chapter 8 presents the zonation of the field and the parameterised amplification factors developed for each zone based on the results from the site response analyses.

Chapter 9 presents a summary of the complete model without explanation or justification for any of the model elements or their associated weights (all of which is discussed in detail in the previous chapters). For anyone wishing to implement the V7 GMM, Chapter 9 is intended as a standalone summary of the model and the only part of the report to which it is necessary to refer. The chapter refers to several electronic files containing the model parameters, which form digital annexes to the written report.

Chapter 10 presents an evaluation of the model performance in terms of residual analyses. The model predictions are also compared with those from the previous version of the GMM as well as with predictions from GMPEs derived for natural (tectonic earthquakes); these latter comparisons are intended primarily to explore the range of epistemic uncertainty that has been captured in the V7 GMM logic tree. The report ends with some Closing Remarks in Chapter 11.

2. Evolution of the Groningen GMMs

The work of developing a GMM to be applied to induced earthquakes in the Groningen gas field began in early 2013, in order to provide this critical input to the seismic hazard and risk models that were being developed to inform choices regarding risk mitigation strategies. The model presented in this report therefore represents the culmination of almost eight years of work and multiple iterations through a process of review and revision. This chapter briefly summarises how the model evolved through this process.

The chapter begins in Section 2.1 with a chronology of the GMM development up to the V6 model, with a focus on the process followed to arrive at this final model. Section 2.2 then focuses the evolution of the models from a purely scientific perspective, highlighting the main technical enhancements and improvements that marked the progress towards the model that is presented in this report. Section 2.3 briefly explains the motivation for producing a V7 model and provides an overview of the model in terms of the predicted ground-motion parameters and the general structure of the model.

2.1. Model Development from V0 to V7

The work to produce a GMM for the induced earthquakes in the Groningen field began in early 2013. At that time, NAM was beginning to develop a comprehensive seismic hazard and risk model as part of the response to the August 2012 Huizinge earthquake, and the lead author of this report was engaged to work with Shell seismologists Stephen Bourne and Steve Oates on the hazard model. As has been the case throughout the development of this work, the GMM was required as input to hazard calculations at a fairly early stage and therefore had to be generated in a very short time frame.

The first approach was to review existing GMPEs and consider their suitability for application to the shallow induced earthquakes in the field while also being able to estimate ground-motion amplitudes for potential larger induced and triggered events. Among the candidate GMPEs considered were the equations for PGA (peak ground acceleration) and PGV of Dost *et al.* (2004), which had been derived using recordings of induced earthquakes in the Roswinkel gas field and were specifically intended for application to induced seismicity. Using the small database of Groningen ground-motion recordings available at the time, the Dost *et al.* (2004) equations were checked for their applicability and found to overpredict, by a significant margin, the Groningen motions (Figure 2.1). This was interpreted as being primarily the result of the effect of the high-velocity Zechstein salt layer overlying the Rotliegend sandstone that contains the gas reservoir on the propagation of seismic waves, as discussed by Kraaijpoel &

Dost (2013); in the Roswinkel field, the gas reservoir is located above the Zechstein formation.

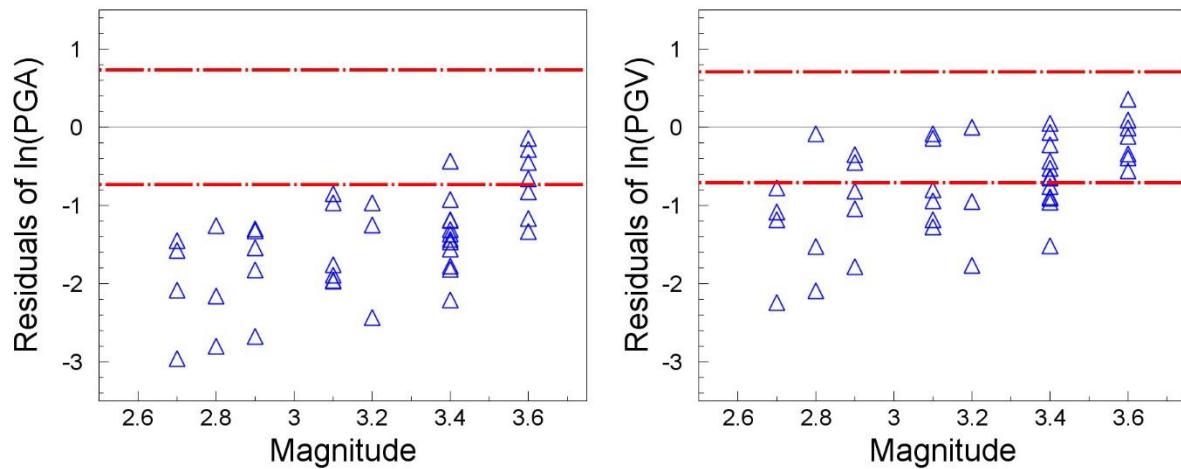


Figure 2.1. Residuals of PGA (*left*) and PGV (*right*) of Groningen motions with respect to the Dost *et al.* (2004) GMPEs (Bourne *et al.*, 2015).

The observation that a GMPE derived specifically for application to shallow-focus, low-magnitude induced earthquakes in the Netherlands performed so poorly in the Groningen field led to the inevitable conclusion that a bespoke model for the field was required. For the very first hazard calculations, a crudely simple approach was adopted to obtain a model that was consistent with the observed motions in Groningen at small magnitudes and would mimic ground motions from tectonic earthquakes at the upper limit of 6.5, which was the M_{max} value used at the time. The European GMPEs of Akkar *et al.* (2014) were modified by introducing a hinge point at around magnitude M_L 4 and then adjusting the predictions at smaller magnitudes to match the Groningen PGA and PGV values. This was considered to be consistent with the findings of Bommer *et al.* (2007) that extrapolation of empirical GMPEs to magnitudes below the lower bound of the dataset generally leads to overestimation, but it was also acknowledged to be a rather crude approach. One of the many shortcomings of this preliminary model—subsequently named as the V0 GMM—was that it did not include any epistemic uncertainty, including only a single predictive model even at the largest magnitudes (although the Euro-Mediterranean model was viewed as a possible upper branch).

The subsequent derivation of more complete GMMs calibrated to the local conditions in the Groningen field has been undertaken through a series of iterations, each time involving the generation of a complete model within a logic-tree framework to capture the epistemic uncertainty and comprehensive documentation. The average time between each successive version of the GMM has been about one year, with the gap often being much shorter. The primary driver for this mode of operation were the

demands of the regulatory body, SodM (State Supervision of Mines), which did not create an optimal approach for the execution of this scientific work. The full process of developing each GMM involves several weeks of consecutive calculations and the timescale imposed on the process allowed very few opportunities for iterations and sensitivity calculations within each stage of model development. The cyclic process of the GMM development did allow for thorough review of each version of the model but it also meant a great deal of effort was expended on documentation—reports of several hundred pages in length, which were superseded within less than a year in most cases—as well as on presentations and meetings, which could otherwise have been invested in refinement of the models.

In setting out to develop a GMM for the Groningen field, several key objectives were identified. The first was the need to use small-magnitude earthquake recordings to develop predictions of motions from larger earthquakes, which led to the decision to use stochastic simulations, for which reason a specialist in this area (Ben Edwards from Liverpool University) was recruited to the team. The GMM team also began to work very closely with seismologists from KNMI (initially Bernard Dost and later on Elmer Ruigrok and Jesper Spetzler as well) as the operators of the recording networks and custodians of the primary earthquake catalogue for the region. To correctly capture the influence of the upper crustal structure on wave propagation in the Groningen field, the team also worked closely with Remco Romijn of NAM, who was the primary developer of the deep velocity model for the field, and with geophysicists at Shell (Ewoud van Dedem and colleagues) and ExxonMobil (Brian Zurek and Brian deMartin) who performed finite difference wave propagation analyses (Edwards *et al.*, 2019). Another important objective of the model was to capture the variation in site response effects across the field, including non-linear response in the very soft soils encountered particularly in the northern part of the field. To this end, Deltares was engaged to develop a field-wide model of the near-surface layers and their dynamic properties, with the work led by Pauline Kruiver (who has recently moved to KNMI), and Adrian Rodriguez-Marek (Virginia Tech) was brought into the team to lead the development of the site response model. The team was also expanded to include a ground-motion database manager, responsible for the processing and compilation of the motions for analysis (Michail Ntinalexis) and an engineering seismologist skilled in statistical analyses and the interface with structural engineering and risk analyses (Peter Stafford of Imperial College London).

The first complete GMM (V1) was reviewed through the submission and publication of a paper in the *Bulletin of the Seismological Society of America* (Bommer *et al.*, 2016a), which highlighted the Groningen-specific features of the model as well as its limitations. The V2 GMM addressed the key limitation (consideration of only linear site response, see Section 2.2) and defined the basic framework for the GMMs that has been refined and improved in the subsequent stages of development.

At this stage, the GMM development team also decided that it would be very helpful to form a panel of experts to review the model and provide constructive feedback towards its ongoing evolution. We were fortunate to be able to assemble a panel comprised of Gail Atkinson (Canada), Hilmar Bungum (Norway), Fabrice Cotton (France/Germany), John Douglas (UK), Jon Stewart (USA), Ivan Wong (USA) and Bob Youngs (USA). A two-day workshop with the review panel was held in London in October 2015 and the feedback was incorporated into the V3 GMM, which fixed all of the key features of the GMMs that have followed (Bommer *et al.*, 2017).

Another development came in March 2016, with the organisation of a workshop in Amsterdam on M_{max} in the Groningen field (Bommer & van Elk, 2017), with an expert panel charged with developing a distribution for the maximum magnitude to be used in the seismic hazard and risk analyses. Although this yielded a distribution centred on values considerably smaller than the M_{max} of 6.5 that had been used up until that time, the upper tail extended to above magnitude 7. Even though the weight assigned to this upper tail was very small, the GMM had to accommodate scenarios of magnitude up to about 7.25. For the V1 to V3 GMMs, we had used point-source stochastic simulations in generating the models, which is not really appropriate even at magnitude 6 and became indefensible when these larger magnitudes needed to be accommodated. In July 2016, a workshop was held in London to discuss options for introducing finite fault rupture simulations into the GMM development, with the participation of geophysicists from Shell and ExxonMobil and four invited experts with extensive experience and expertise in the development, validation and/or application of finite rupture simulations: Norm Abrahamson, Luis Angel Dalguer, Christine Goulet, and Bob Youngs. The outcome of the workshop was the decision to adopt EXSIM rather than SMSIM for the V4 GMM, and this has been used in all subsequent models.

The V4 GMM was the first attempt to incorporate finite rupture simulations and review comments from the international expert panel identified several features that could be refined or improved. Additionally, the V4 GMM development adopted a preliminary version of a new conversion between local magnitudes, M_L , and moment magnitudes, M : $M = M_L - 0.2$. The relationship between the two magnitude scales is important in this work since the inversions of the reference rock FAS requires treats the magnitudes as moment magnitudes and the global GMPEs used to calibrate the upper branch of the logic tree are expressed in term of moment magnitude, yet the recurrence statistics in the seismological model are based on the KNMI catalogue magnitudes which are M_L . Subsequent work revealed that the relationship adopted for the V4 GMM was incorrect, and that in the range of interest to the risk calculations ($M_L \geq 2.5$), the two scales can be considered broadly equivalent (Dost *et al.*, 2018).

In another rapid iteration, work on the V5 GMM began shortly after the V4 GMM had been finalised, in an attempt to refine some of the new features related to the use of finite rupture simulations as well as incorporating some new recordings into the ground motion database. The V5 GMM was issued in late 2017 and then reviewed by the

international expert panel; the final report was issued in January 2018, together with an endorsement letter from the panel. At this stage, Norm Abrahamson had been incorporated into the review panel and Jon Stewart appointed the panel chair to coordinate the review process.

At that point, it was considered that the GMM development had reached a stable plateau and future work will only involve checking the model performance against recordings obtained in future earthquakes. However, a request was made to produce a V6 model for the 2019 hazard and risk calculations, taking advantage of recordings of new earthquakes that had become available, including the January 2018 M_L 3.4 Zeerijp earthquake that generated a large number of records. At the same time, as the database was being updated, it came to light that an error had been made in the processing of the recordings from the M_L 2.6 Slochteren earthquake when incorporating those records into the V5 database. The Slochteren event occurred on 27 May 2017, just as the database for the V5 model was being finalised. The V1 model had been developed from a database of 58 recordings from 12 earthquakes, and the V3 GMM was derived using a database that had grown to include 178 recordings from 22 earthquakes, but no additional records had been generated when the V4 GMM was developed. The 68 records from the Slochteren earthquake were therefore viewed as an essential addition to the database (Figure 2.2). However, in order to meet the strict schedule imposed for delivery of the model, the records were processed very swiftly, and consequently an error was made that led to significant underestimation of the longer-period response spectral ordinates (Figure 2.3). The discovery of this error provided additional impetus for the generation of a new model to replace the V5 GMM.

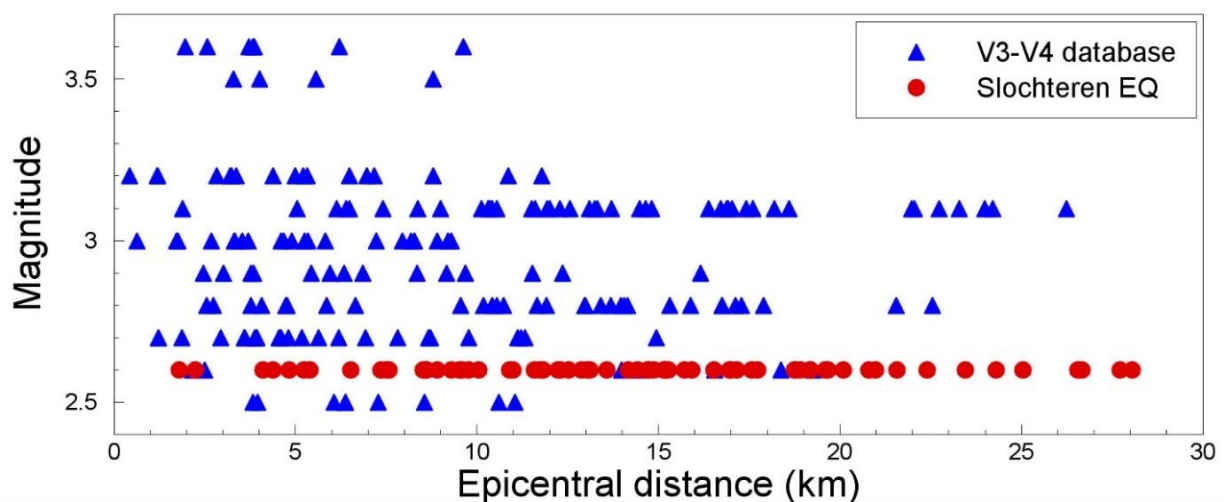


Figure 2.2. Magnitude-distance distribution of the database used to derive the V5 GMM, highlighting the records from the May 2017 Slochteren earthquake.

As the work on the V6 GMM was beginning, another issue came to light, which was a calibration error in the surface accelerographs of the G-network (see Section 3.1 for a

description of the Groningen recording networks), which had been set to record half of the real amplitude. This error, which was studied and documented in detail by KNMI and the GMM development team (Dost *et al.*, 2019), had no impact at all on the derivation of the GMMs since the decisions had been taken to use the recordings from the 200-m geophones at the G-network stations (called G4-stations). The motivation behind that choice was the lack of *in situ* measured shear-wave velocity, V_s , profiles at the G-stations, whereas such measurements had been made at the B-stations (Noorlandt *et al.*, 2018).

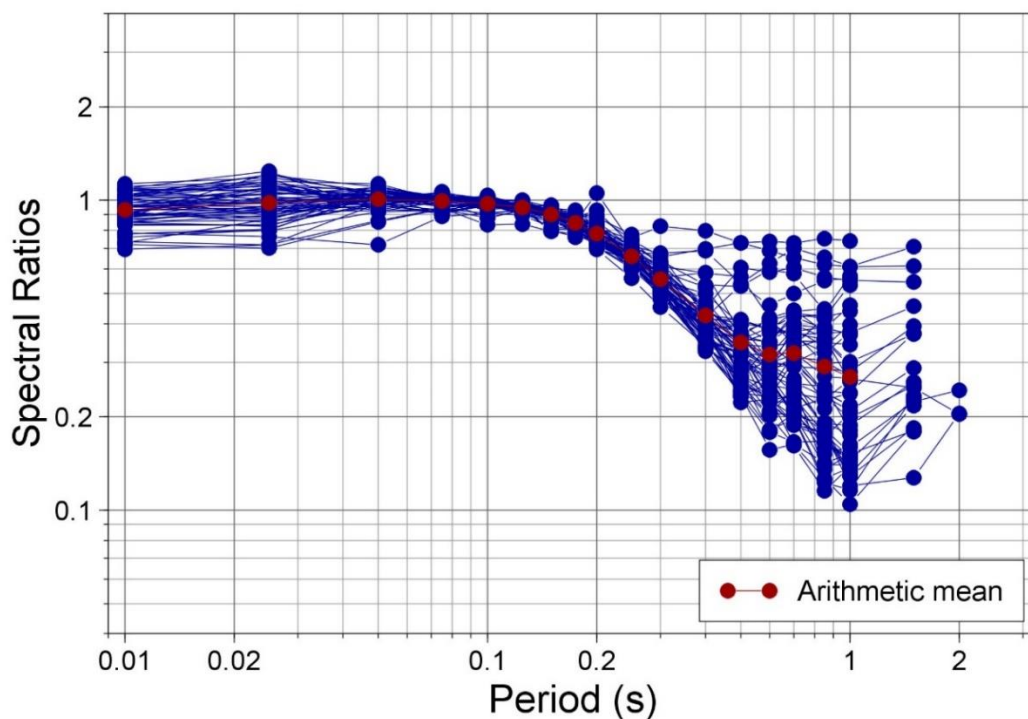


Figure 2.3. Ratios of erroneous to corrected response spectra of the records of the 200-m G-station geophone recordings obtained during the Slochteren earthquake.

Following discussions within the GMM development team, it was concluded that with the error corrected and now having total confidence in the G0-station records, the GMM development should use only surface accelerograph recordings, especially since no test of the reliability of the G4-stations was possible at the time. Using only surface recordings meant that all data were from the same model of accelerograph (other than the earliest recordings at the B-stations, up to and including the Huizinge earthquake) and, more importantly, the site adjustments to deconvolve surface motions to the NS_B horizon and the site amplification factors used in the forward modelling were both referenced to the same stratigraphic columns.

The V6 GMM report was issued in March 2019 and shared with the international expert panel for review. A new workshop was held in Amsterdam in 2019 to discuss the development of the final V7 GMM and agree a path forward that would extend the

foreseen period to allow for a less rushed process: in the view of the panel members, to conduct one more sprint through the model production process with minor refinements and improvements, would have been “*irresponsible*”. Instead, the model was developed in stages, starting with the database, the inversions of the NS_B motions, and the development of the final site response model (including a new assessment of the soil damping). Each of these elements was presented to the review panel, discussed, revised and agreed, through written reviews and online meetings (by this time, physical meetings had become impossible due to the Covid-19 pandemic). In this way, for the first time, all the model elements and their individual impacts were evaluated before commencing the process of the final model generation.

In closing this overview of the model evolution, we can also note that another influence on the GMM development process has been the changing needs of end users, and specifically the NAM risk engine. The inputs for the risk model are controlled mainly by the parameters used to characterise the fragility functions for buildings in the Groningen region. For the V1 GMM, the outputs were selected as response spectral accelerations at five periods between 0.01 and 2.0 seconds, the first ordinate being equivalent to PGA (Figure 2.4).

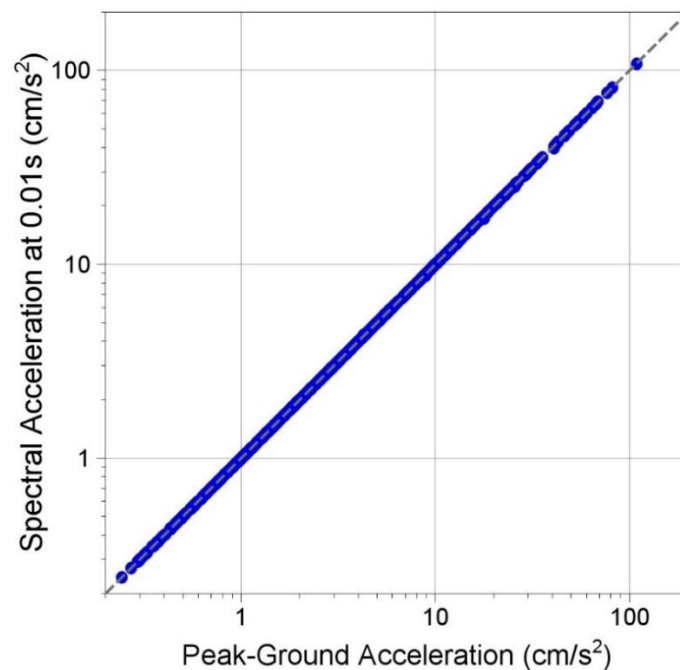


Figure 2.4. Correlation between PGA and spectral accelerations at 0.01 s for the Groningen ground-motion data

The limited outputs for the V1 GMM were determined in part by the need to reduce the calculations required in order to allow the model to be developed on schedule. With the basic approach established, the V2 GMM was able to predict spectral

accelerations at 16 oscillators up to 5 seconds, the longer periods being included to cover the possibility of applications to lifelines, infrastructure and tall buildings. In the V3 GMM, the number of target periods was increased to 23, all of the additional periods being at the short-period range; these were added solely to facilitate the generation of reliable vertical response spectra through the application of vertical-to-horizontal spectral ratios. The V4 GMM predicted spectral accelerations at the same 23 periods, and also included the prediction of PGV, a parameter for which potential applications were emerging. The same suite of ground-motion parameters was predicted by the V5 and V6 GMMs.

The first five versions of the GMM also included predictions of significant duration, which was considered to be potentially of importance in the assessment of liquefaction hazard and at one stage was included in the fragility functions for some building typologies. More recently, the need to provide predictions for so many ground-motion parameters was re-evaluated. Duration was dropped in V6 GMM since it was no longer included as a parameter in any of the fragility functions and the question of liquefaction hazard has been comprehensively addressed in parallel studies (Green *et al.*, 2020). Furthermore, it became clear that there is no particular call for vertical response spectra, obviating the need for closely spaced spectral accelerations at short periods, and the only applications requiring predictions of PGV are focused on small-magnitude earthquakes, for which an empirical GMPE is more appropriate (Bommer *et al.*, 2021b). The current fragility models are defined in terms of the horizontal spectral acceleration averaged over 10 periods (0.01, 0.1, 0.2, 0.3, 0.4, 0.5, 0.6, 0.7, 0.85 and 1.0 second) and therefore the focus has moved exclusively to providing these inputs required for the risk calculations.

2.2. Milestones in the Model Development Process

Leaving aside the tortuous path that has been followed to arrive at this final GMM for Groningen, it may be useful to highlight the key advances during the evolution of the model. The primary objective was to capture the very specific local conditions in terms of the geological structure from the Rotliegend sandstone—where the earthquake ruptures originate—to the ground surface (Figure 2.5). The second objective was to develop a model constrained by the available ground motion data but also capturing the unavoidable epistemic uncertainty associated with extrapolating from recordings of earthquakes with magnitudes from 2.5 to 3.6 to make predictions for earthquakes of magnitude 6.5 or even greater (Figure 2.6). The first objective was addressed by analysis of the recordings and gathering of data to characterise the field; the latter objective by using simulations based on source, path and site parameters determined by inversions of the recorded motions and embedded within a logic-tree framework that captures the broader distribution of predicted motions as the degree of extrapolation increases.

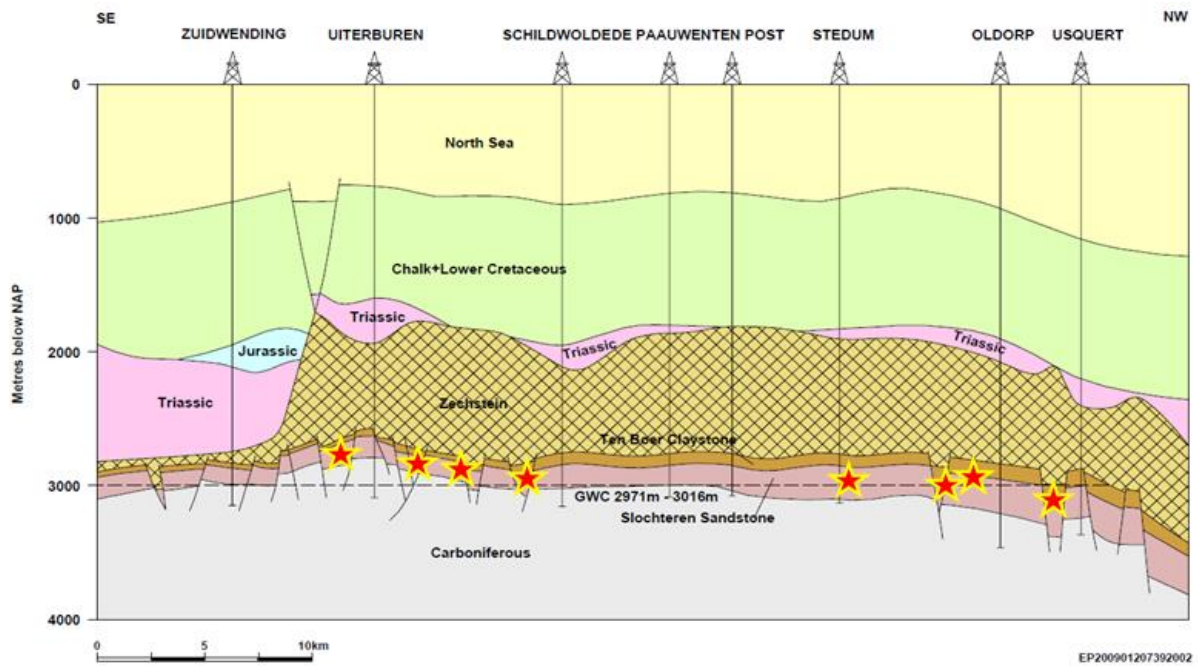


Figure 2.5. Cross-section of the Groningen field; the red stars schematically illustrate the locations of earthquake hypocentres in the Rotliegend sandstone.

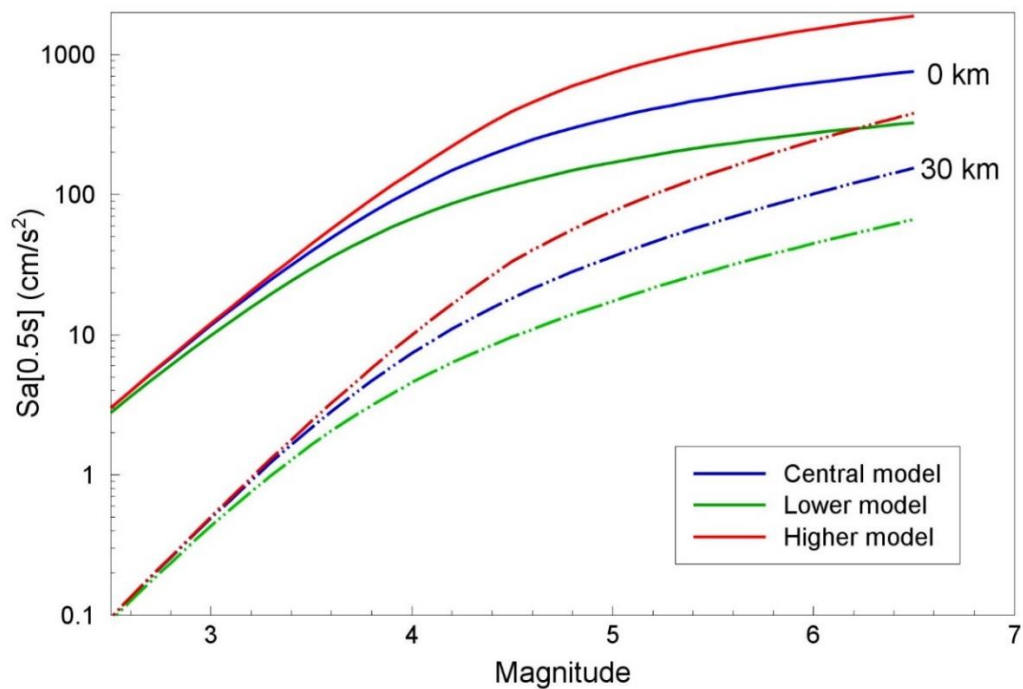


Figure 2.6. Median predictions from the three branches of the V1 GMM logic-tree as a function of magnitude for two epicentral distances (Bommer *et al.*, 2016).

For the V1 GMM, the Fourier amplitude spectra (FAS) of the surface recordings were inverted to estimate source (stress drop) and path (geometric spreading and Q)

parameters, as well as a field-wide site amplification factor and kappa (damping); the distances corresponding to the hinge points for changes in the geometric spreading were separately determined from finite difference wave propagation models. These parameters were then used in forward simulations but with branches for alternative values of stress drop at larger magnitudes (Figure 2.7). The model had the advantage of being calibrated to Groningen data but also two significant shortcomings in terms of the site response: the amplification factors were a network average that ignored spatial differences in the near-surface geology and dynamic amplification effects, and included only linear site amplification, regardless of the strength of the shaking.

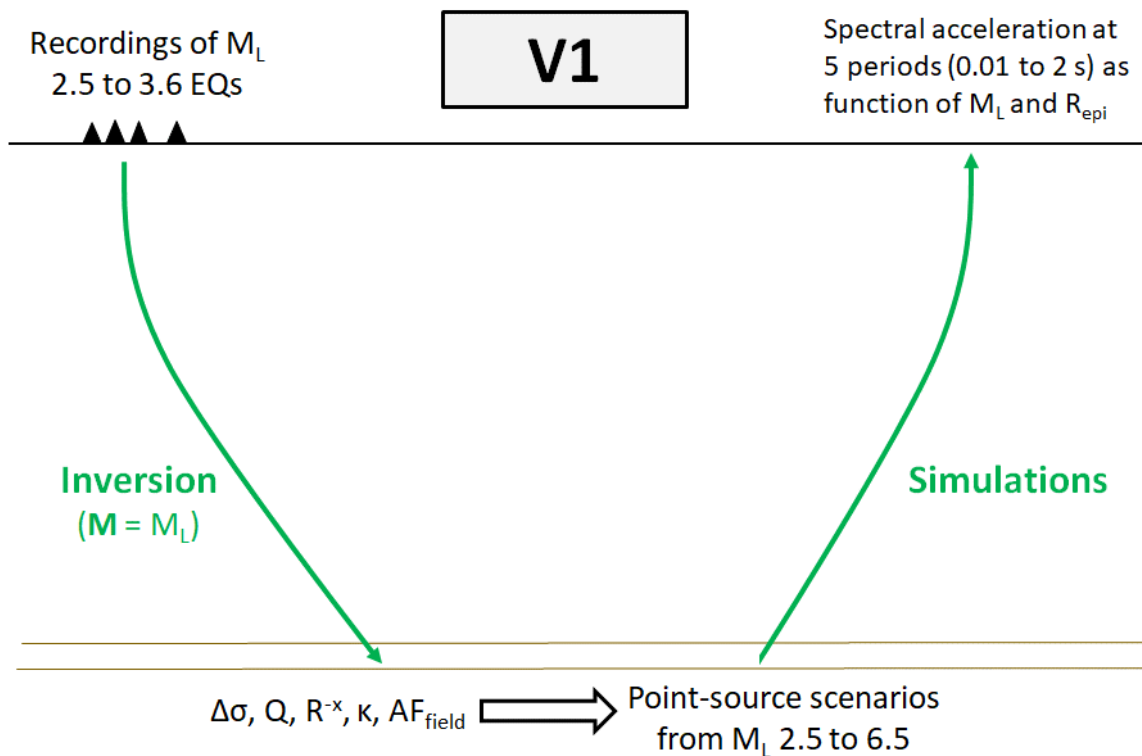


Figure 2.7. Schematic illustration of the scheme followed in the derivation of the V1 GMM.

These two site response issues were both addressed in the V2 GMM, which in many ways could be regarded as the most significant evolutionary step for the model. To derive this model, the surface motions were first deconvolved, using linear transfer functions, to a reference 'rock' horizon, which was the base of the Upper North Sea formation (NU_B), located at about 350 m depth. The inversions were then performed on the NU_B motions and the forward simulations predicted spectral accelerations at the same buried horizon. Non-linear, frequency-dependent site amplification factors defined for ~160 zones defined across the field, were then used to transform the rock motions to the ground surface (Figure 2.8). The V2 GMM was made possible by the development of a field-wide V_s model (Kruiver *et al.*, 2017a) and field-wide site response analyses (Rodriguez-Marek *et al.*, 2017).

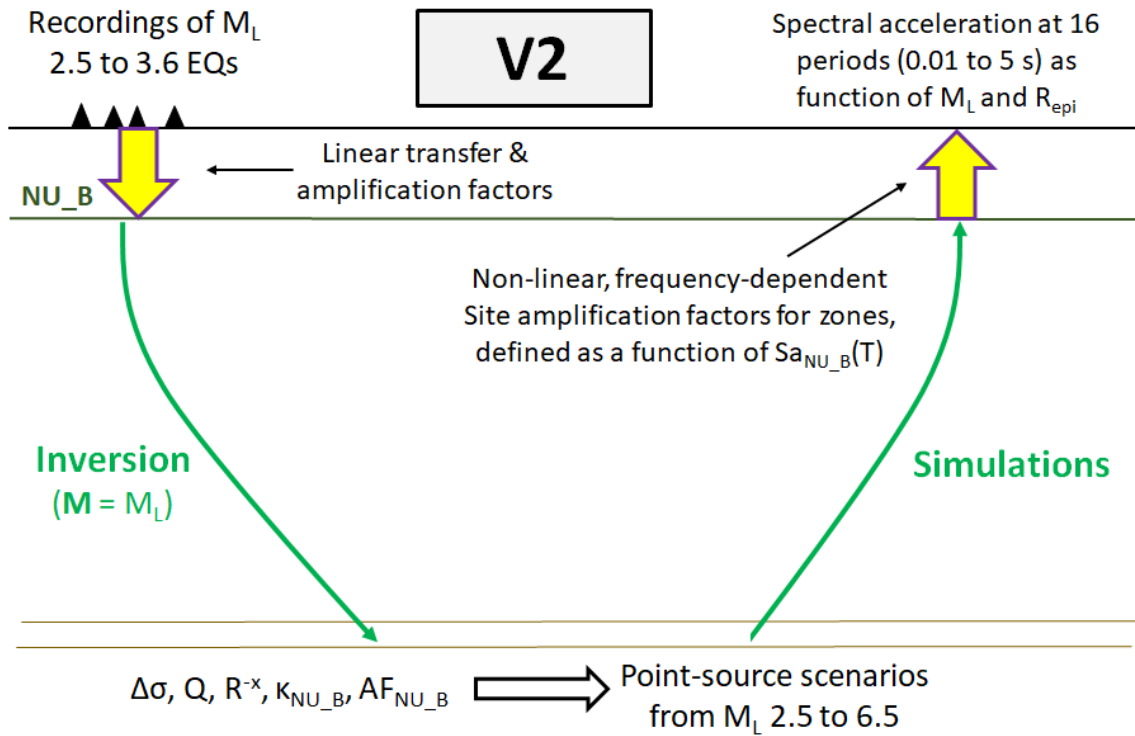


Figure 2.8. Schematic illustration of the scheme followed in the derivation of the V2 GMM.

The framework established for the V2 GMM defined how all the subsequent models would be derived, all further changes being adjustments or refinements of the scheme illustrated in Figure 2.8. The only notable modification to this scheme in the V3 GMM derivation was to change the reference rock horizon from the base of the Upper North Sea formation to the base of the North Sea formation (NS_B), which is located at about 800 m depth (see Figure 2.5). The NS_B represents a more pronounced and laterally more consistent impedance contrast than the NU_B horizon and it has remained as the reference rock horizon for all subsequent GMMs. The scheme for the V3 GMM, which is very similar to that for the V2 GMM, is illustrated in Figure 2.9. The only significant differences from the V2 GMM framework, other than the change from NU_B to NS_B as the reference rock horizon, was the inclusion of additional spectral ordinates at short oscillator periods.

The jump from V3 to V4 was the second most significant evolutionary step after the incorporation of the site response model in the V2 GMM and defined the framework that has remained essentially unchanged for all subsequent models. The scheme for the V4 GMM derivation is shown in Figure 2.10. The key change was the move from point source (SMSIM) to finite rupture (EXSIM) stochastic simulations, which was accompanied by a necessary change of the distance metric from epicentral distance, R_{epi} , to the rupture distance, R_{rup} . As mentioned in Section 2.1, the upper value of the M_{max} distribution also increased to 7.25 at this stage. Another change was the introduction of scenario-dependence in the linear site amplification factors at short

periods, reflecting a discovery that arose from the Groningen ground-motion modelling work, but which has far broader implications (Stafford *et al.*, 2017).

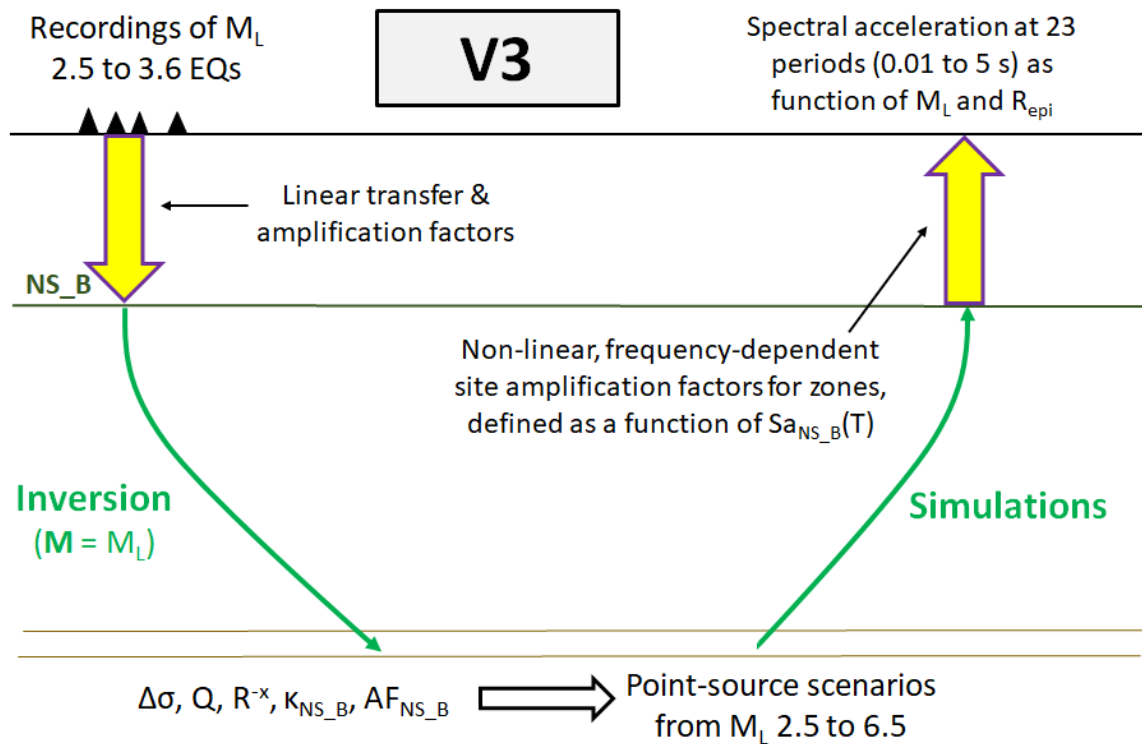


Figure 2.9. Schematic illustration of the scheme followed in the derivation of the V3 GMM.

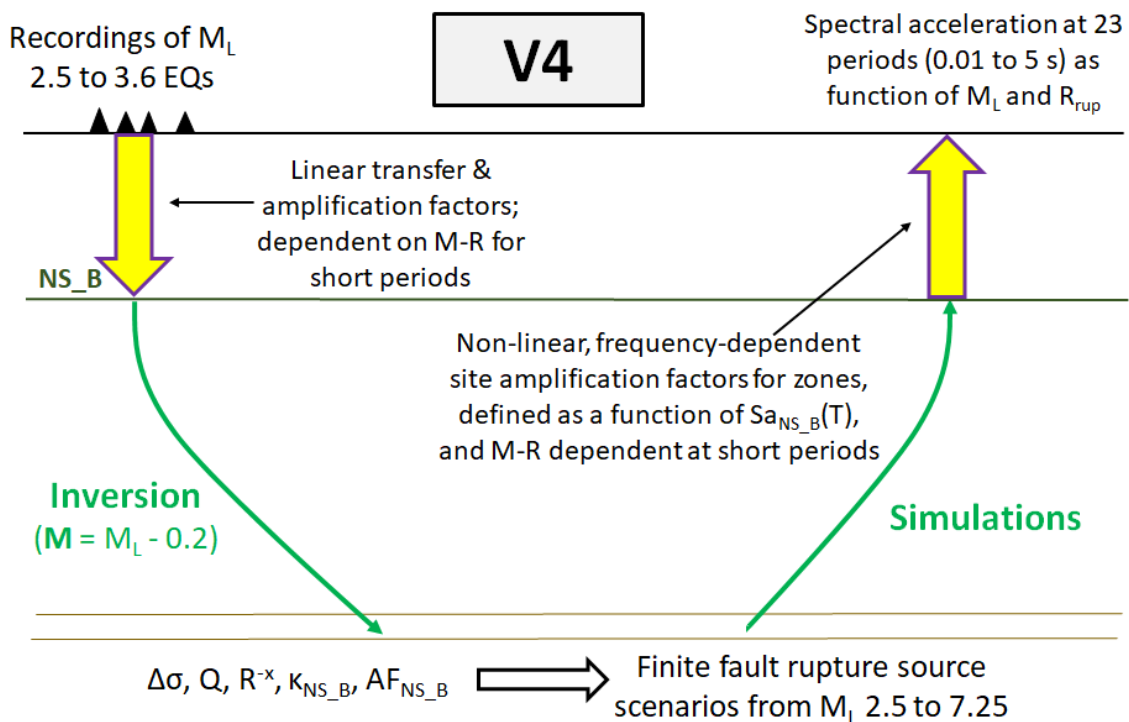


Figure 2.10. Schematic illustration of the scheme followed in the derivation of the V4 GMM.

As already mentioned in Section 2.1, the derivation of the V4 GMM included the adoption of an incorrect relationship between M and M_L (another fruit of having to use immature research due to the rushed schedule of model development). The magnitude conversion was corrected in the V5 GMM development, which reverted to equivalence of the two magnitude scales (now demonstrated rather than assumed). As indicated in Figure 2.11, the V5 GMM scheme has been retained for all subsequent versions of the model. All three of the most recent models included predictions of PGV, which is now addressed separately through empirical GMPEs (Bommer et al., 2021b); the V4 and V5 models included duration as a predicted variable, but this was dropped in the V6 model since at that stage it was no longer required for the risk calculations.

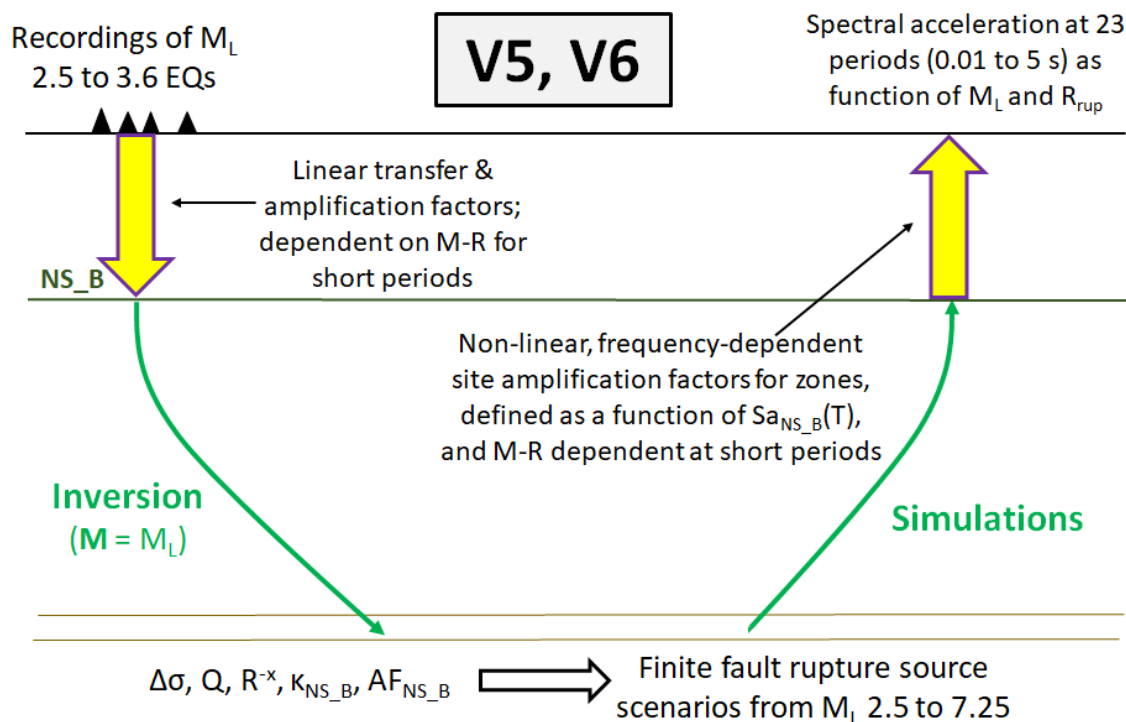


Figure 2.11. Schematic illustration of the scheme followed in the derivation of the V5 and V6 GMMs.

2.3. Overview of the V7 GMM

The V7 GMM is the final refinement in terms of implementing the framework that was established at the V4 and V5 stages of the model development (which were identical apart from the M - M_L relationship). Several important improvements have been incorporated with respect to the V6 GMM and earlier models, including all of the following:

1. An expanded database with additional new recordings
2. Correction for soil-structure interaction effects at B-stations with basements

3. New record processing procedures applied to the complete database
4. A stricter criterion to determine the maximum usable period
5. Measured V_s profiles at nearly all the G-network stations
6. A refined field-wide site model including a new model for soil damping
7. Refinements to the FAS inversions including a layered Q model
8. New criteria for constraining the upper branch simulations to match predictions from tectonic GMPEs, which reflect the fact that the parameter used in the fragility functions is the average spectral acceleration over a range of periods
9. A modified functional form for the parametric GMPEs for reference rock motions (although these equations remain functions of only magnitude and distance)
10. Logic-tree branches for between-event ground-motion variability
11. Exclusion of site response analyses results with excessive ($>1\%$) strains
12. Explicit representation of epistemic uncertainty in site amplification factors through a logic-tree formulation
13. The inclusion of a penalty function to be applied to the amplification factors for buildings that are located on dwelling mounds (*wierden*)

Points 1-4 are described in Chapter 3, points 5 and 6 in Chapter 4, points 7 and 8 in Chapter 5, points 9 and 10 in Chapter 6, point 11 in Chapter 7, and point 12 in Chapter 8. Point 12 is developed in Chapter 8 and the final model presented in Chapter 9. We also note that during the course of the V7 GMM development, new journal papers have been published that address some of these innovations (points 3, 6 and 13), and these are cited within the corresponding discussions.

The scheme for deriving the V7 GMM is illustrated schematically in Figure 2.12. One modification from this general scheme in terms of the implementation of the V7 GMM is that the site-to-site variability illustrated in the upper right-hand corner is no longer treated as an aleatory distribution to be sampled in the ground-motion realisations but is now represented by discrete branches in the GMM logic-tree.

The model derivation described in detail in the ensuing chapters is for the geometric mean horizontal component of the 5%-damped response spectral pseudo-acceleration at oscillator periods of 0.01, 0.1, 0.2, 0.3, 0.4, 0.5, 0.6, 0.7, 0.85, and 1.0 seconds; periods of 1.15, 1.3 and 1.5 seconds were also included in the derivation and are shown in some plots, but results are only provided for the 10 shorter periods since the focus is primarily on the period ≤ 1 second since only these are used in the fragility functions.

For the risk calculations, the arbitrary horizontal component of motion, rather than the geometric mean component, is required to define the input to the fragility functions. To transform the predictions to the arbitrary component, an adjustment is needed to the variability term to account for the component-to-component variability. This additional variability is defined using the model of Stafford et al. (2019), which is dependent on both magnitude and distance, as illustrated in Figure 2.13.

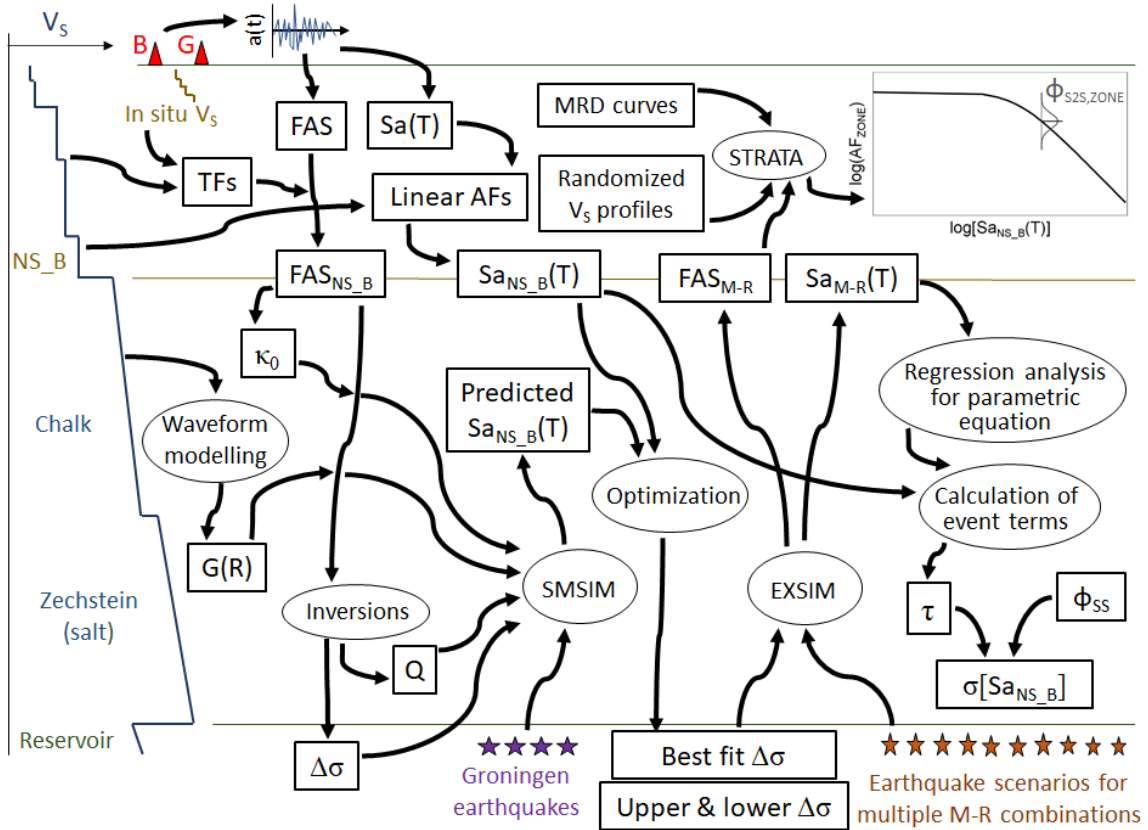


Figure 2.12. Schematic illustration of the derivation of the V7 GMM, adapted from Bommer *et al.* (2017).

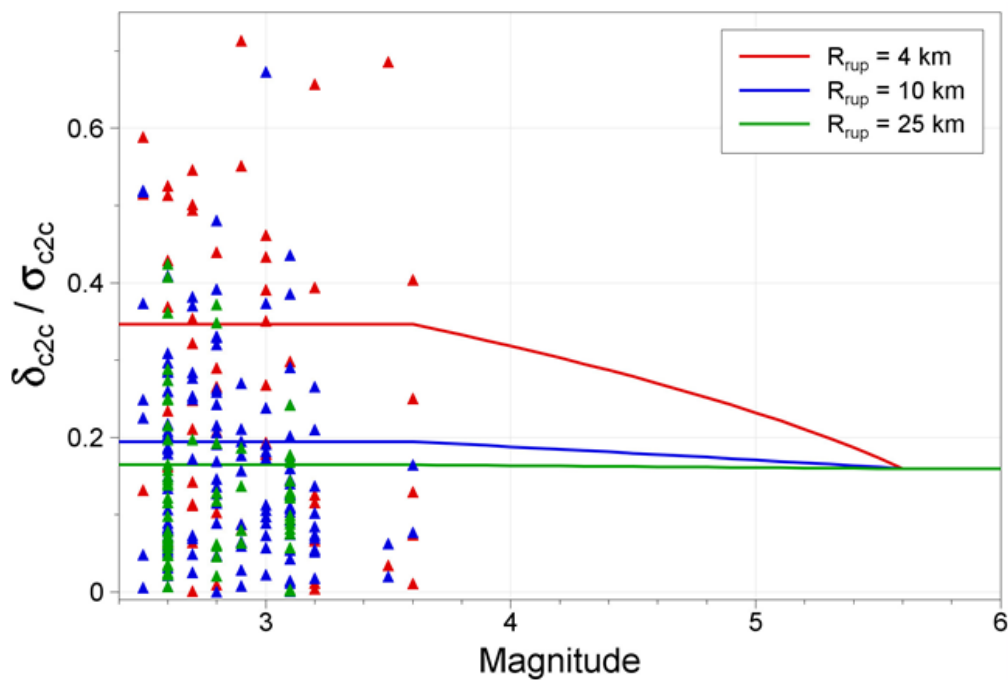


Figure 2.13. Magnitude- and distance-dependent model for component-to-component variability of Groningen ground motions (Stafford *et al.*, 2019). The y-axis label refers to the component-to-component residuals (the data points in the plot) and the component-to-component variability (the lines).

This component-to-component variability model was derived using ground-motion recordings from Groningen, which often display strong polarisation at very short distances. However, the model is also formulated calibrated to converge to the levels of component-to-component variability predicted by a model derived from tectonic ground-motion recordings at larger magnitudes ($M_L \geq 5.6$). The rationale for this extension of the model is that the pronounced polarisation observed in the small-magnitude recordings is directly related to the radiation pattern from these shallow-focus events. Once the fault rupture dimensions grow so that the seismic waves are emanating from several locations along an extended source, it is assumed that the radiation pattern will become less distinct through the interaction of the waves from different parts of the rupture, and consequently the degree of polarisation will drop to the levels commonly observed in recordings of tectonic earthquakes.

3. V7 Ground-Motion Database

This chapter summarises the database of ground-motion recordings from the Groningen field that have been used to derive the V7 model. The chapter begins in Section 3.1 with a brief description of the different ground-motion recording networks and the selection of stations for inclusion in the final database. Section 3.2 then describes the record processing techniques applied, including the criteria for excluding records with excessively low signal-to-noise ratios and the definition of the maximum and minimum periods at which the response spectral ordinates are deemed to be reliably usable. Finally, Section 3.3 discusses the determination of the associated metadata and presents an overview of the database characteristics in terms of recorded amplitudes and distribution with respect to independent variables.

3.1. Groningen Recording Networks and Record Selection

The database consists of recordings obtained from the KNMI's B-station and G-station networks during all events of magnitude equal to or greater than M_L 2.5, having occurred between 2006 and 20 July 2020, at which point the database was finalised. A total of 835 recordings from 29 events, recorded at epicentral distances ranging from 0.4 to 34 km, are available under those criteria. Their magnitude-distance distribution and as-recorded horizontal PGA values against distance are shown in Figure 3.1.

The B- and G- networks are described by Dost *et al.* (2017). The B-network consists of 19 stations, only 14 of which are currently operational, installed in private residences and other small structures in the villages of the Groningen area. All stations are installed on the ground floors of the buildings in which they are located, except three which were installed in basements. To account for this, a correction has been applied to the records of these three stations before use (see Section 3.2). The G-network consists of 79 stations, installed in metal cabinets in remote locations throughout the gas field in order to avoid noise from nearby activity as much as possible. All G-stations contain an accelerograph at surface level, while 69 stations also contain four geophones placed at 50 metre depth intervals, down to a depth of 200 metres. The locations of the stations are shown in Figure 3.2, from which the good coverage of the Groningen field can be appreciated. Both networks currently operate EpiSensor accelerographs and Kinematics recorders, which transmit continuous data-streams publicly available via the KNMI website (KNMI, 1993; <https://doi.org/10.21944/e970fd34-23b9-3411-b366-e4f72877d2c5>). The G-network was installed between 2014 and 2017 while the first stations of the B-network were installed in 1995. Until 2014, different types of accelerographs were periodically used in the B-network (including the GeoSig AC-23 and AC-63 models), which operated on a triggering basis, only generating records when motion was fulfilling certain requirements that ensured detection of an earthquake signal.

In late 2020, the manufacturer of the AC-23 instrument updated the information provided for those sensors, with small changes to the transfer functions used to deconvolve the instrument response, however the records corresponding to those sensors were not reprocessed as the changes were small and only noticeably affecting FAS frequencies smaller than 0.5Hz, a value typically outside the usable range of the records of this database.

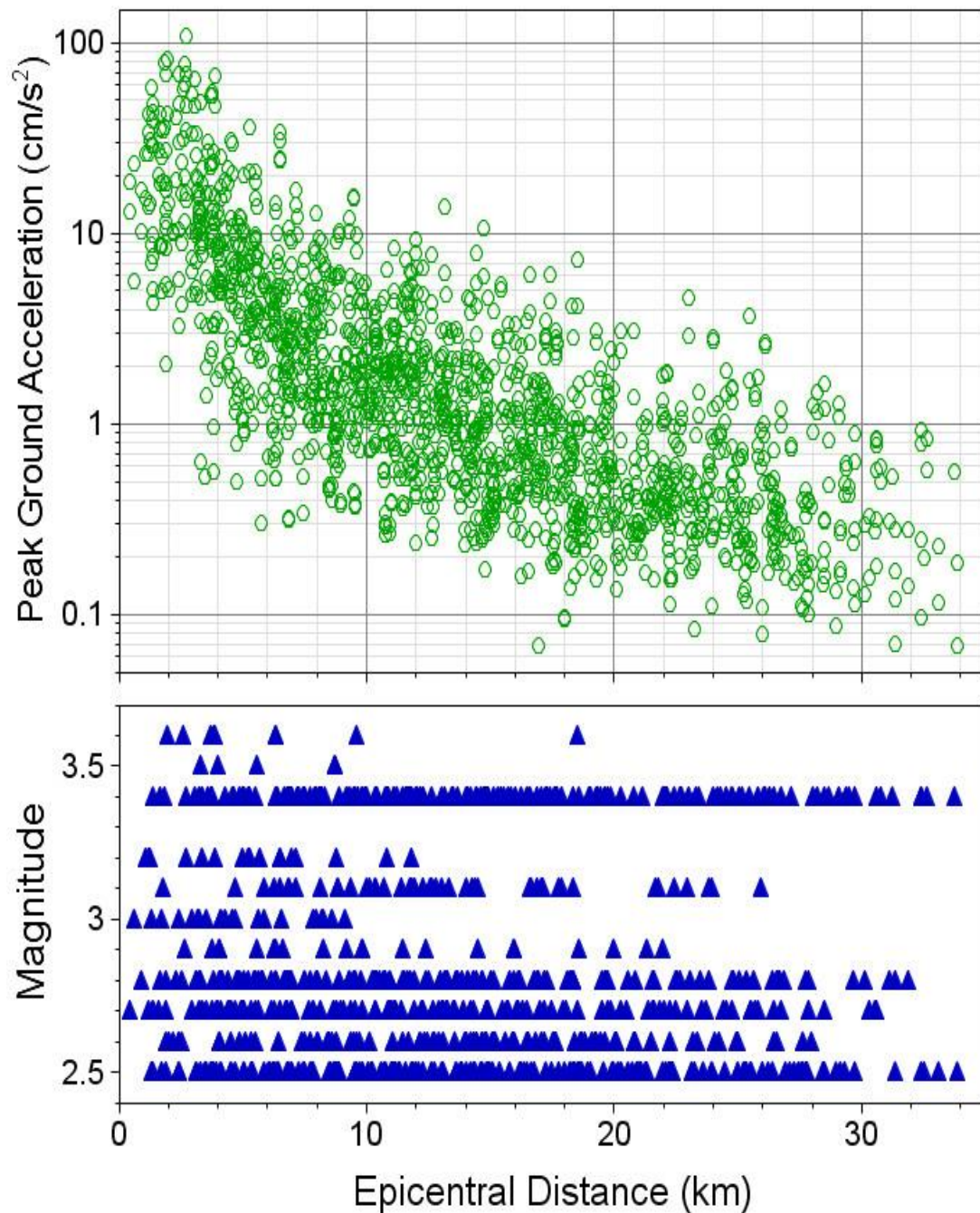


Figure 3.1. Peak ground acceleration of the Groningen horizontal component records plotted against distance (*upper*) and magnitude-distance distribution of the Groningen database (*lower*).

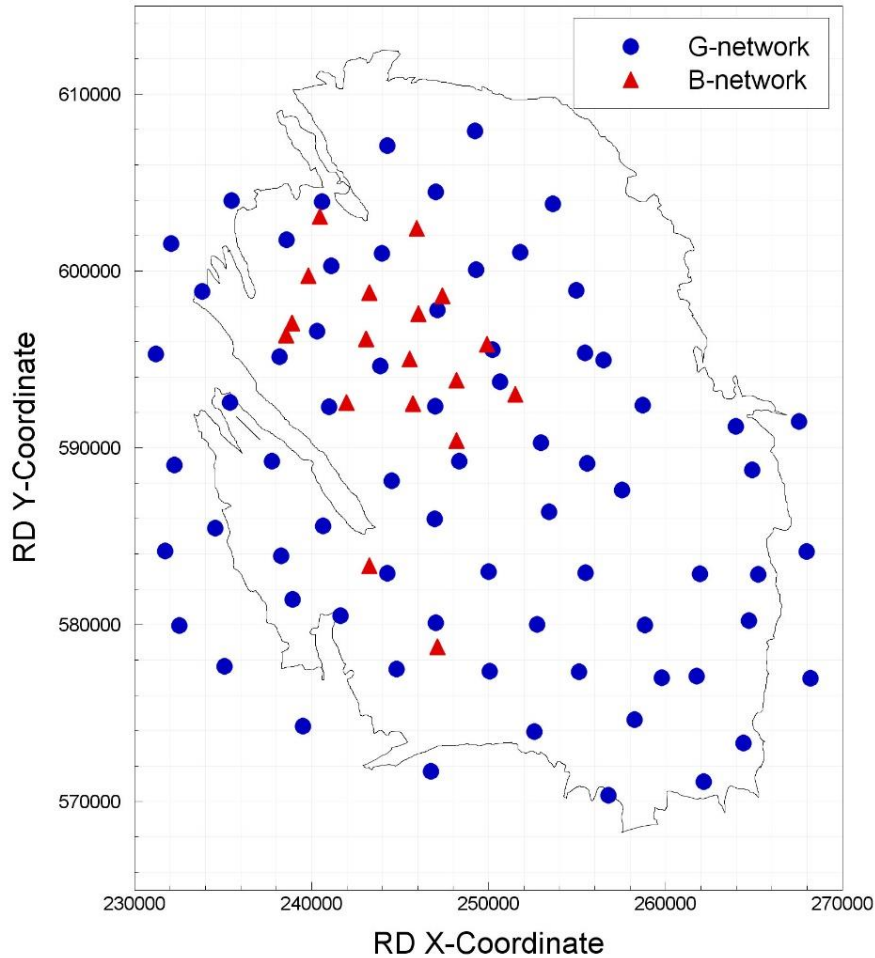


Figure 3.2. Instrument locations of the B- and G-station networks with respect to the Groningen gas field.

Records from three additional networks are also available (Ntinalaxis *et al.*, 2019), namely the NAM Facilities Network, the NAM Flexible Geophone Array, and the Household Network, which was installed by TNO on behalf of NAM. These records were not used, however, for the following reasons:

1. The location metadata of the Household Network cannot be shared publicly as they describe the location of private residences and are protected by privacy laws. Using these data would thus create a model that other researchers could not replicate, and the data could not be fully vetted, which is contrary to the policy of openness that has been adopted by the GMM Team.
2. Records of the NAM Facilities Network are heavily contaminated by high-frequency noise due to the heavy machinery operating in the facilities, leading to a low potential for use.
3. Due to their large number and close spacing, incorporation of records from the flexible network can lead to issues in the calculation of event-terms and inter-event variability, as discussed in Stafford *et al.* (2019).

Another reason for not using records from the three networks is that there are no measured shear-wave velocity profiles available at the locations of their stations (see Section 3.2).

Identification of stations with issues in recording

A thorough quality assessment and review of the B- and G-networks has been carried out between 2017 and 2019. This involved two parallel lines of work, (a) visits to the stations and (b) analyses of the data produced by the stations. This assessment included investigations presented in Ntinalexis *et al.* (2019) as well as work led by Elmer Ruigrok of the KNMI involving power spectral density (PSD) analyses (e.g., Figure 3.3) and probabilistic PSD plots. Two site visits took place (not counting the numerous visits by KNMI technicians over the years), one in September 2018, by Elmer Ruigrok (KNMI), Gert-Jan van der Hazel (KNMI) and Michail Ntinalexis (GMM Team), and another in November 2019, by the same group except Gert-Jan, joined by Mira Vasic (SodM) and Rui Pinho (Fragility/HRA Team).

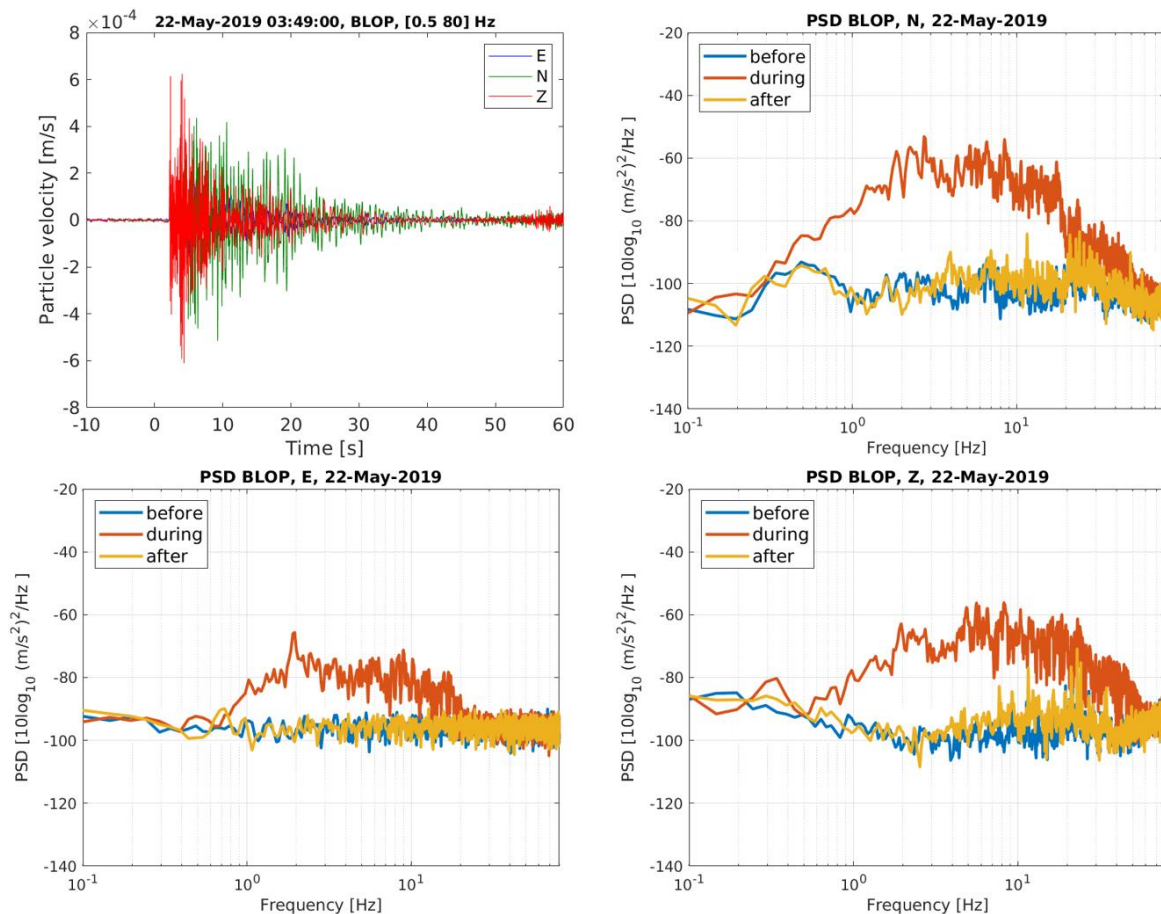


Figure 3.3. Power spectral density of acceleration time-series at station BLOP (*top left*) for the North-South (*top right*), East-West (*bottom left*) and vertical components (*bottom right*), before, during and after the $M_{L}3.4$ Westerwijtwerd earthquake of 22 May 2019.

The first visit resulted in the confirmation of a suspected calibration problem with the surface accelerographs at the G-stations, which was subsequently resolved (as discussed in Dost *et al.*, 2019). During the second field visit, station BSTD was discovered to be unanchored to the floor of the structure in which it is located. The GMM Team initially considered removing the records of this station from the database but ultimately decided to retain them. There are three reasons which led to this decision. First of all, it is very unlikely that the small-amplitude motions recorded in Groningen have caused either sliding or rocking of the sensor; secondly, the station has produced a number of important recordings, including near-source records from three out of the four largest Groningen earthquakes (Figure 3.4); and finally, an examination of BSTD records showed no apparent irregularities (*e.g.*, Figure 3.5).

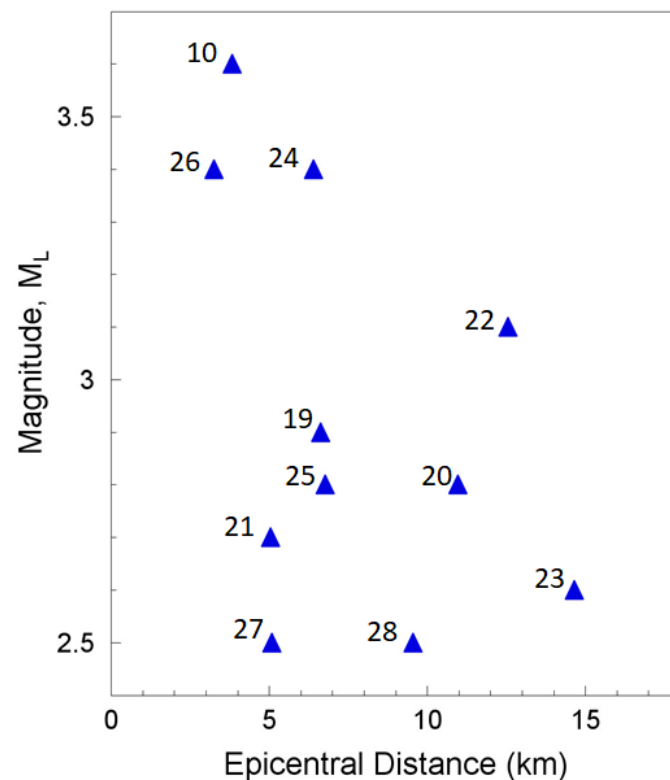


Figure 3.4. Magnitude-distance distribution of usable records obtained from station BSTD (EQ10 was recorded at the former STDM station)

On the other hand, a total of 27 records from stations G050, G530, G680, station BLOP (for a specific time period between the end of 2017 and 2019) and a single recording from station G640, have been removed because of problems with the instrument performance, which were identified by PSD analyses (such as the one shown in Figure 3.3) as well as probabilistic PSD analyses. The magnitude-distance distribution of these records is shown in Figure 3.6. A list of the stations discussed in this section as well as a summary of the issues identified, and the decisions taken, is provided in Table 3.1.

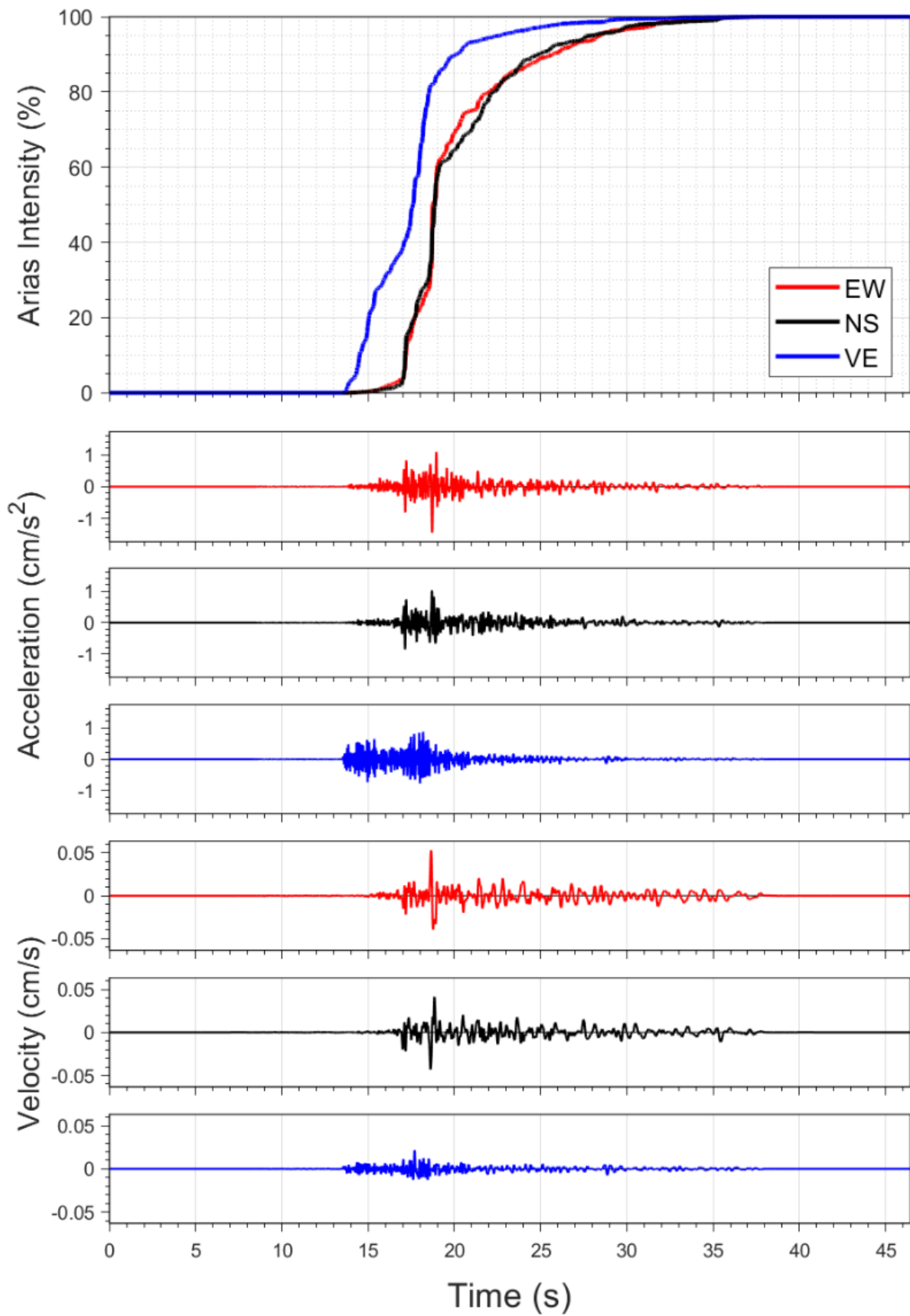


Figure 3.5. Acceleration and velocity time-histories, and Husid plot, of record BSTD from the 30 September 2015 M_L 3.0 Hellum earthquake

Table 3.1. Stations with issues with recording

| EQ-ID | Issue | Decision |
|-------|--------------------------------|-----------------------------------|
| G050 | Malfunction | Removal of records |
| G530 | Malfunction | Removal of records |
| G680 | Malfunction | Removal of records |
| BLOP | Malfunction (end of 2017-2019) | Removal of records in time period |
| BSTD | Unanchored (until Dec. 2019) | Retain records |

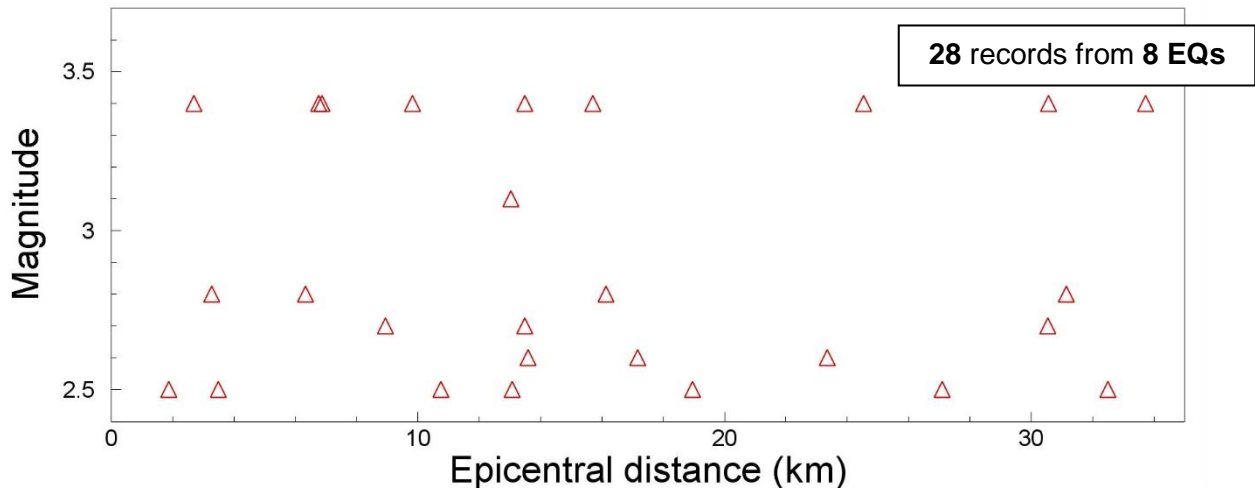


Figure 3.6. Magnitude-distance distribution of records removed due to malfunctioning stations

Exclusion of records from stations outside the zonation area

A total of seven G-stations (G720, G730, G740, G760, G770, G790 and G800) and one B-station (BKMZ), are not located inside the study area of the risk model, which is defined by the gas field plus a 5 km buffer onshore. The records from these stations are still processed as they are used in other work, such as the derivation of the empirical PGV models (Bommer *et al.*, 2019a) and reporting on earthquake amplitudes (e.g., Bommer & Ntinalexis, 2020), but are not relevant to the development of the GMM. A total of 62 records from six events are removed for this reason, and their magnitude-distance distribution is shown in Figure 3.7.

Investigation of short-period attenuation at B-stations

Work conducted by researchers in the KEM projects, based mainly on comparisons of records from pairs of B-stations and the closest G-station, identified a general tendency for the short-period spectral ordinates from the B-stations to be lower. This was interpreted by the KEM researchers as being the result of dynamic soil-structure interaction (SSI). For the work being undertaken by the KEM researchers—which, it has been emphasised many times, is not to develop a complete GMM—the decision was taken to simply drop all the B-station recordings. For the GMM development team,

this was not considered a viable option given how many important events have been recorded only on this network and how many of the recordings at short epicentral distances come from B-stations. As shown in Figure 3.8, recordings from the B-stations are a vital component of the Groningen ground-motion database, comprising more than one third of the records. Additionally, for the first 18 earthquakes in the database, there are no G-station recordings, and the two largest horizontal PGA values obtained to date— $0.08g$ and $0.11g$ —were both obtained at B-stations.

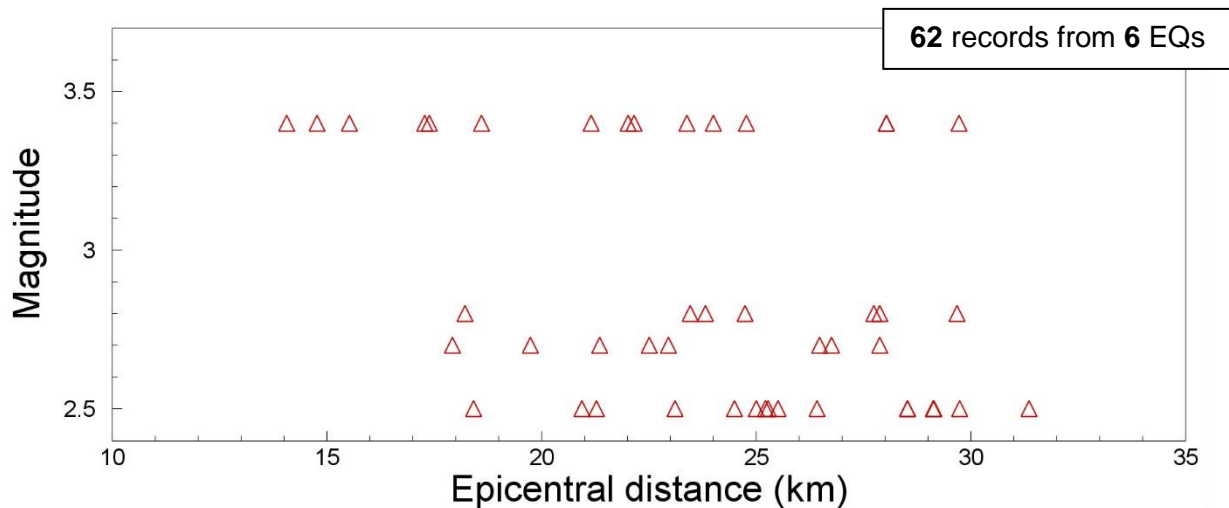


Figure 3.7. Magnitude-distance distribution of records from stations outside the study area

An investigation on the potential systematic differences between the B-network and G-network recordings was also carried out during the development of the updated empirical PGV GMPEs that were published earlier in June 2021 (Bommer *et al.*, 2021a). More specifically event- and station-corrected residuals with respect to the network-independent GMPEs (ESV model) were grouped by recording network, as shown in Figure 3.8, with the B-network separated in “old” and “new”, to separate records obtained before and after the 2014 upgrade. For the residuals of recordings from each of the networks, the box indicates the range from the 25-percentile to the 75-percentile, while the line in the middle of the box indicates the median residual; the whiskers indicate the range from the minimum to maximum value. There is a clear tendency towards lower PGV values—as revealed by the negative median residual—from the B_new network. The lower frame shows the same residuals adjusted for the station terms found as part of the mixed effects regression, which confirms that the offset of the B_new residuals is a station effect.

This immediately raises the question of why there should be a difference between the B_old and B_new recordings in terms of their amplitudes and residuals, given that they correspond to instruments installed in the same buildings. The possible explanation might be as follows: there is a systematic average effect of B-network records being lower at short periods—and note that for the Groningen data, PGV correlates well with

spectral accelerations at periods in the range of 0.2-0.3 seconds (Bommer et al., 2017c)—than those from the free-field stations of the G-network, even if not manifested at all of the B-stations. However, because the “old” B-network was operating under a triggering protocol, it recorded weaker motions poorly, with only the relatively stronger records retained, leading to higher average amplitudes recorded.

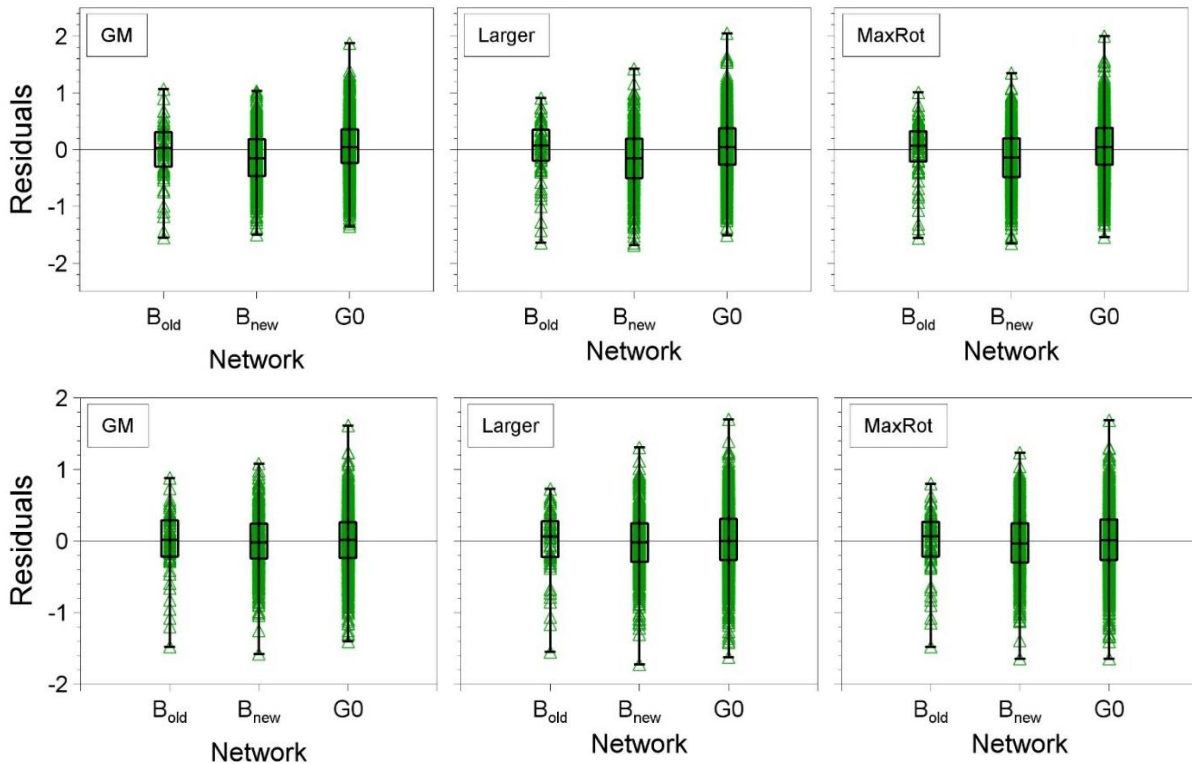


Figure 3.8. Within-event residuals (*upper*) and after adjustment for station terms (*lower*), with respect to the ESV model of Bommer *et al.* (2021a), grouped by recording network and instrument type.

This observation prompted further regressions with a functional form including an additional term identifying the contributing network. Figure 3.9 compares the predictions from this model, with the network-independent model. As would be expected, the network-independent model predicts median PGV values that always lie between those corresponding to the predictions for B_new stations and for all other stations, although it is interesting to note that the network-independent predictions are very close to those for all stations other than those of the B_new network.

The KEM researchers followed another line of investigation, by comparing the records of nearby B- and G- stations. Table 3.2 lists the B-stations as well as the closest and second-closest G-stations, together with the separation distances and the number of events for which the stations produced usable records. Stations KANT, BONL and BMD1 have been decommissioned and have not produced any records during the

same events as the closest G-station; station BHAR is known to have a site profile which results in very specific amplification effects and thus is ill-suited to comparisons. The remaining pairs, with the exception of BOWW-G190, are at least one kilometre apart, too large for these simple comparisons to provide anything other than very general indications.

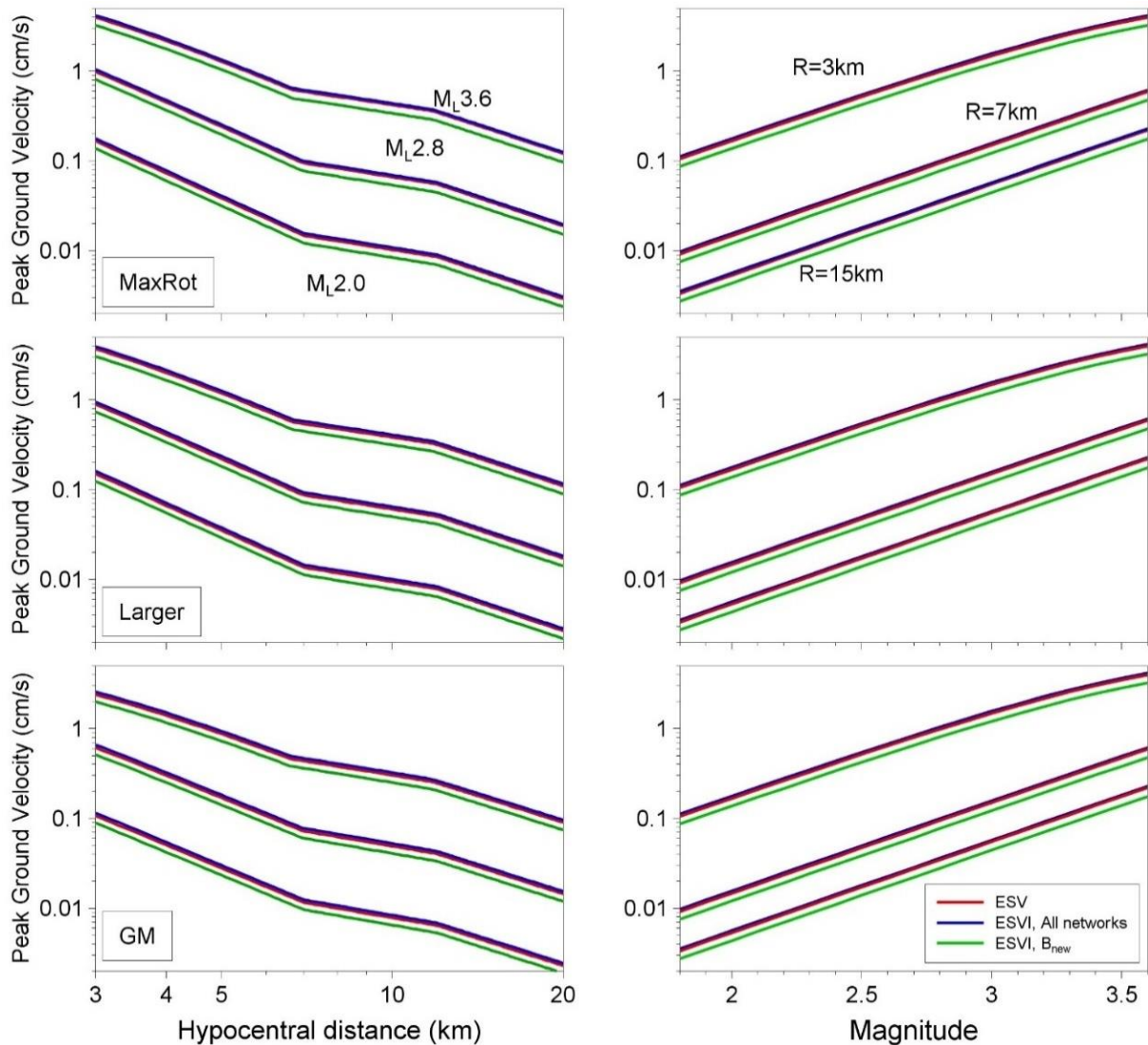


Figure 3.9. Comparison of median predictions for $V_{S30} = 200$ m/s for different combinations of magnitude and distance, using the network-independent model (ESV) and the network-dependent (ESVI) model of Bommer *et al.* (2021a)

The records of BOWW and G190, where the separation distance is 430 metres (the closest spaced pair), are very similar (Figure 3.11). At the same time, the spectral accelerations of the three stations located in basements (BUHZ, BWIN and BZN1), are consistently lower than those of the closest G-station at periods <0.2 seconds, due to embedment effects (Figure 3.12). However, there is no consistent pattern in the remaining 10 stations; weak short-period attenuation can be observed in the ratios of

some of the stations (Figure 3.13), while, in others, there is no clear indication of this effect (Figure 3.14).

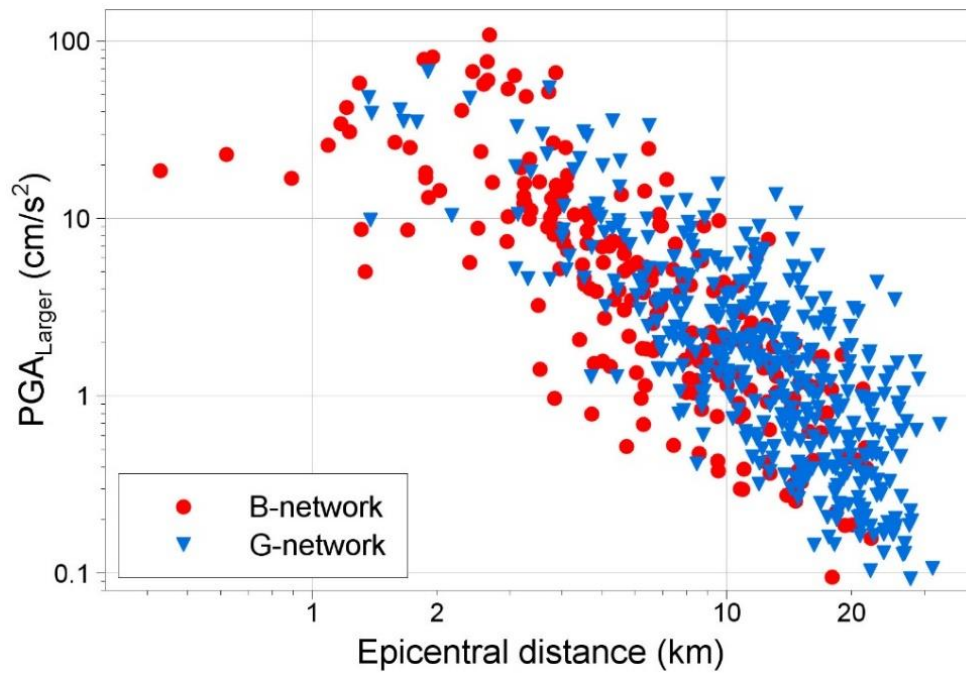


Figure 3.10. Larger as-recorded horizontal PGA plotted against epicentral distance

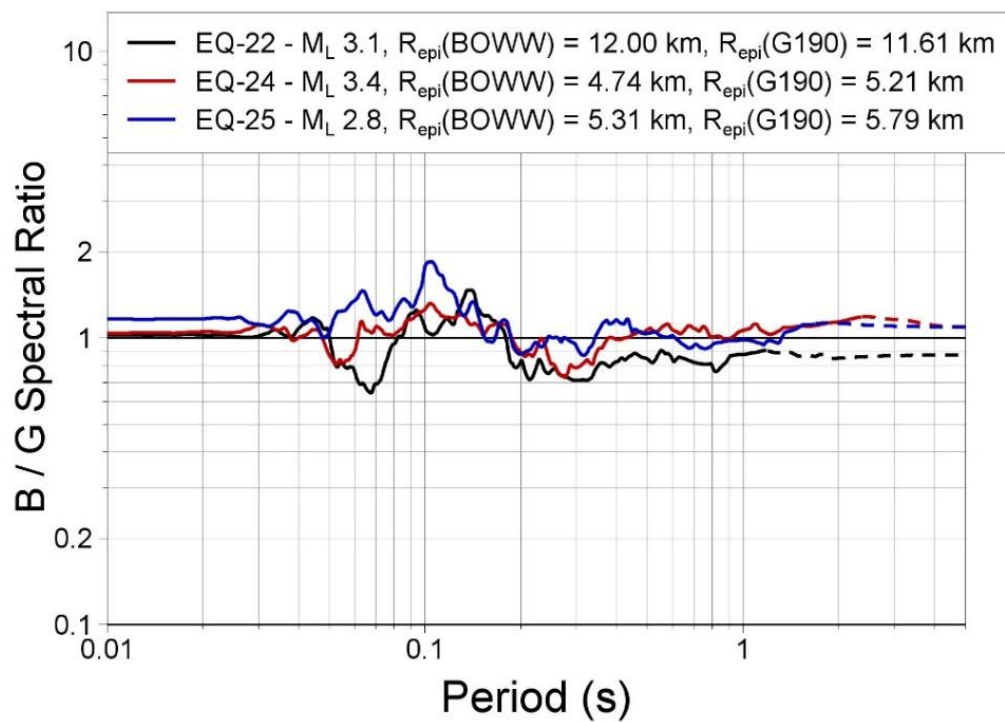


Figure 3.11. Ratios of B- to G-station recordings at BOWW and G190. Dashed lines denote parts of the spectra outside the usable period limits of the records.

Table 3.2. List of the B-stations and the closest G-stations

| STAT ID | Closest G-station | Distance (km) | No. of EQs | Second Closest G-station | Distance (km) | No. of EQs | | | | | | | | | | | |
|---------|-------------------|---------------|--|--------------------------|---------------|------------|---|------|------|---|------|------|------|---|------|------|---|
| BAPP | G670 | 1.11 | 4 | G190 | 2.84 | 3 | | | | | | | | | | | |
| BFB2 | G450 | 1.34 | 8 | G490 | 2.64 | 9 | | | | | | | | | | | |
| BGAR | G090 | 2.33 | 6 | G610 | 2.65 | 5 | | | | | | | | | | | |
| BHAR | G390 | 1.10 | 6 | G440 | 3.24 | 7 | | | | | | | | | | | |
| KANT | G610 | 1.38 | 0 | G080 | 2.36 | 0 | | | | | | | | | | | |
| BHKS | G290 | 1.18 | 3 | G230 | 2.27 | 6 | | | | | | | | | | | |
| BLOP | G180 | 1.70 | 3 | G230 | 3.05 | 2 | | | | | | | | | | | |
| BMD1 | G170 | 1.29 | 0 | G130 | 1.76 | 0 | | | | | | | | | | | |
| BMD2 | G130 | 1.5 | 3 | G170 | 2.03 | 5 | | | | | | | | | | | |
| BONL | G090 | 2.44 | 0 | G100 | 4.09 | 0 | | | | | | | | | | | |
| BOWW | G190 | 0.43 | 3 | G670 | 2.24 | 4 | | | | | | | | | | | |
| BSTD | G220 | 0.99 | 4 | G180 | 2.84 | 7 | | | | | | | | | | | |
| BUHZ | G040 | 0.86 | 4 | G080 | 2.3 | 2 | | | | | | | | | | | |
| BWIN | G230 | 1.29 | 5 | G180 | 2.80 | 6 | | | | | | | | | | | |
| BWIR | G230 | 1.91 | 6 | G670 | 2.45 | 6 | | | | | | | | | | | |
| BWSE | G180 | 1.72 | 6 </tr <tr> <td>BZN1</td> <td>G140</td> <td>0.84</td> <td>2</td> <td>G100</td> <td>2.42</td> <td>2</td> </tr> <tr> <td>BZN2</td> <td>G140</td> <td>1.09</td> <td>2</td> <td>G180</td> <td>3.65</td> <td>2</td> </tr> | BZN1 | G140 | 0.84 | 2 | G100 | 2.42 | 2 | BZN2 | G140 | 1.09 | 2 | G180 | 3.65 | 2 |
| BZN1 | G140 | 0.84 | 2 | G100 | 2.42 | 2 | | | | | | | | | | | |
| BZN2 | G140 | 1.09 | 2 | G180 | 3.65 | 2 | | | | | | | | | | | |

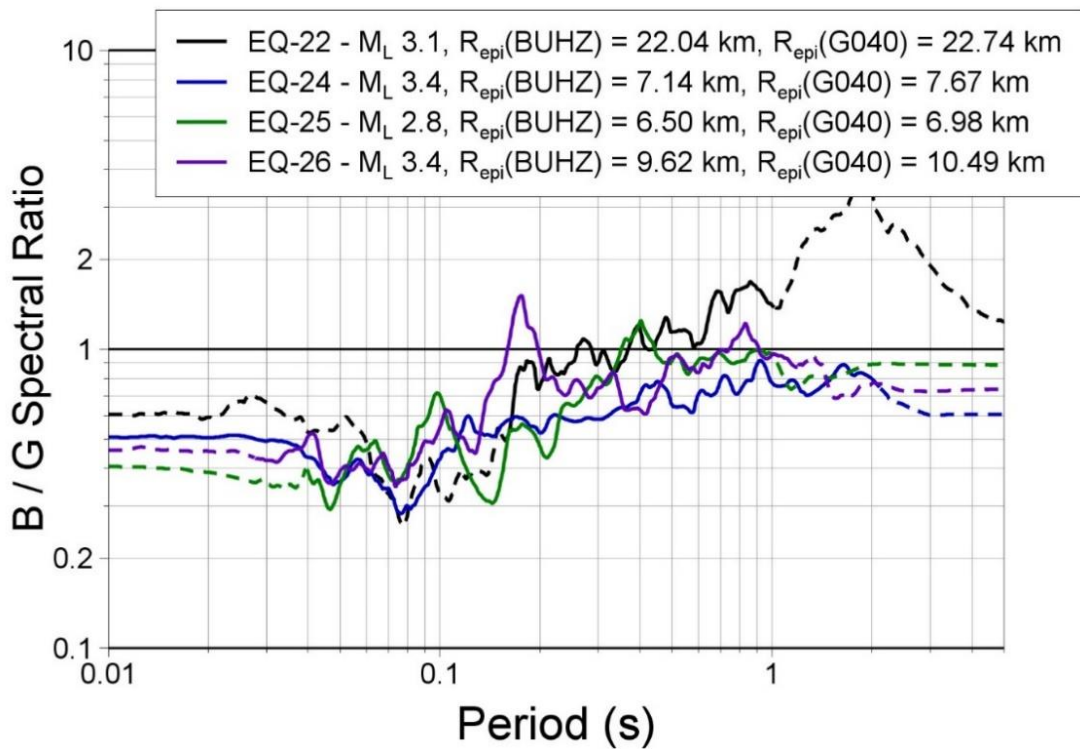


Figure 3.12. Ratios of B- to G-station recordings at BUHZ and G140. Dashed lines denote parts of the spectra outside the usable period limits of the records.

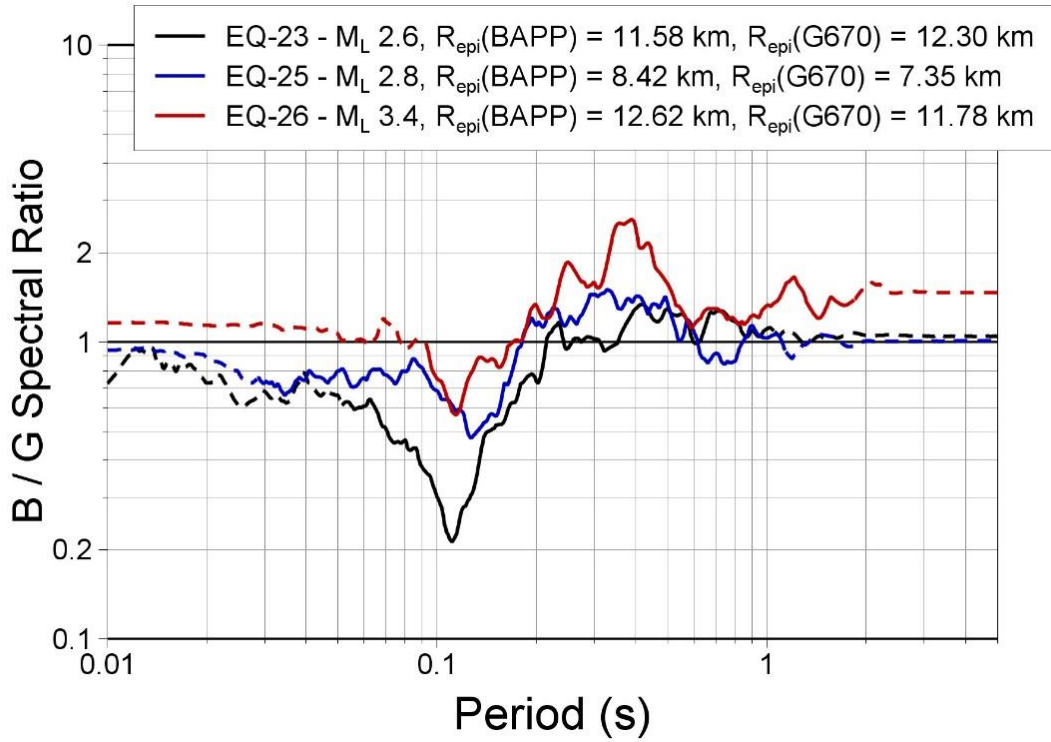


Figure 3.13. Ratios of B- to G-station recordings at BAPP and G670. *Dashed* lines denote parts of the spectra outside the usable period limits of the records.

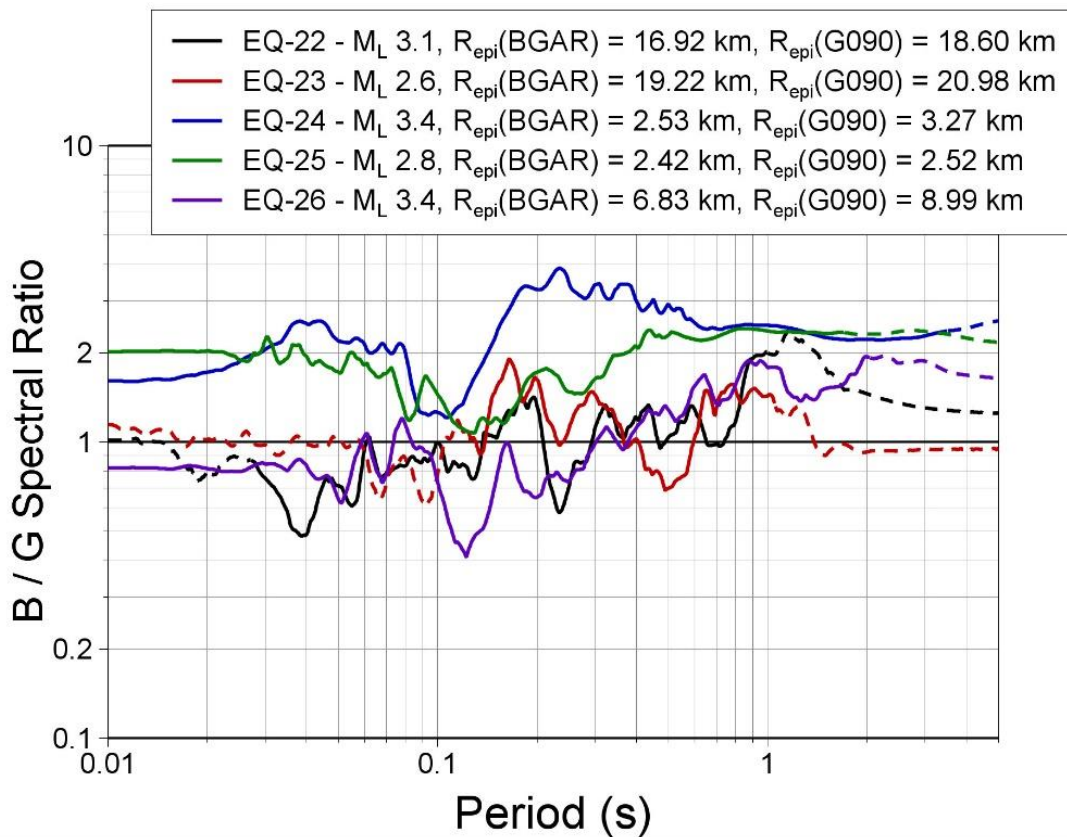


Figure 3.14. Ratios of B- to G-station recordings at BGAR and G090. *Dashed* lines denote parts of the spectra outside the usable period limits of the records.

Normalised offsets (after removal of mean residual with respect to the V6 GMM) of spectral accelerations at all of the B-stations and G-stations are shown in Figure 3.15 for selected periods. These are plotted only for eight events that were recorded by both the B-stations and the G-stations, in order to facilitate direct comparisons across the stations. Inspection of the offsets plotted in Figure 3.15 does not show a systematic and consistent difference in the motions from the B-stations and the G-stations, even at short periods (apart from BUHZ and BWIN, where the instruments are in basements). However, some of the B-stations do seem to display negative offsets at shorter periods (e.g., WIR), which would be consistent with inference of suppressed high-frequency motions at these stations. Station BHAR also stands out but this is known to be a station where the difference between the location-specific amplification function and that of the site response zone in which the station is located (and therefore used for the GMM prediction) is very large. Station BHKS also displays strongly negative offsets at short periods.

Following the field visit in November 2019, Rui Pinho coordinated an extensive set of soil-structure interaction (SSI) analyses for representative structures and soil profiles from the B-stations (Cavalieri *et al.*, 2020). These analyses did confirm that for the BUHZ instrument (located in the basement of municipal offices in one of the small towns) there was clear evidence for SSI affecting the recorded motions. This is consistent with findings of many previous studies of the effect of sensor placement within basements (e.g., Abrahamson *et al.*, 1991) and also, for the case of this rather massive 3-storey building, likely to be also influenced by kinematic interaction effects (e.g., Stewart, 2000). Instead of removing the records from the three basement stations, which would result in the complete removal of EQ-14 from the database, it was decided to apply the correction/conversion that is proposed by NIST (2012) for basement recordings (Figures 3.16 and 3.17).

For the remaining 15 stations, which are located in lightweight sheds and barns, the SSI analyses conducted by Cavalieri *et al.* (2020) clearly demonstrate that there are no strong dynamic soil-structure interaction effects that could influence the nature of recordings obtained at ground level inside these buildings (which was the speculative conclusion of the KEM researchers). However, additional work undertaken by Cavalieri *et al.* (2020) did identify a likely cause of the apparent suppression of short-period spectral ordinates at the B-stations. It is known that prior to construction of houses in the region, at least for the case of buildings with shallow foundations, it is common practice to improve the ground, usually through consolidation under the weight of a layer of sand that is subsequently removed. This process is likely to create a surface layer with increased V_s and thus creates a velocity reversal close to the surface.

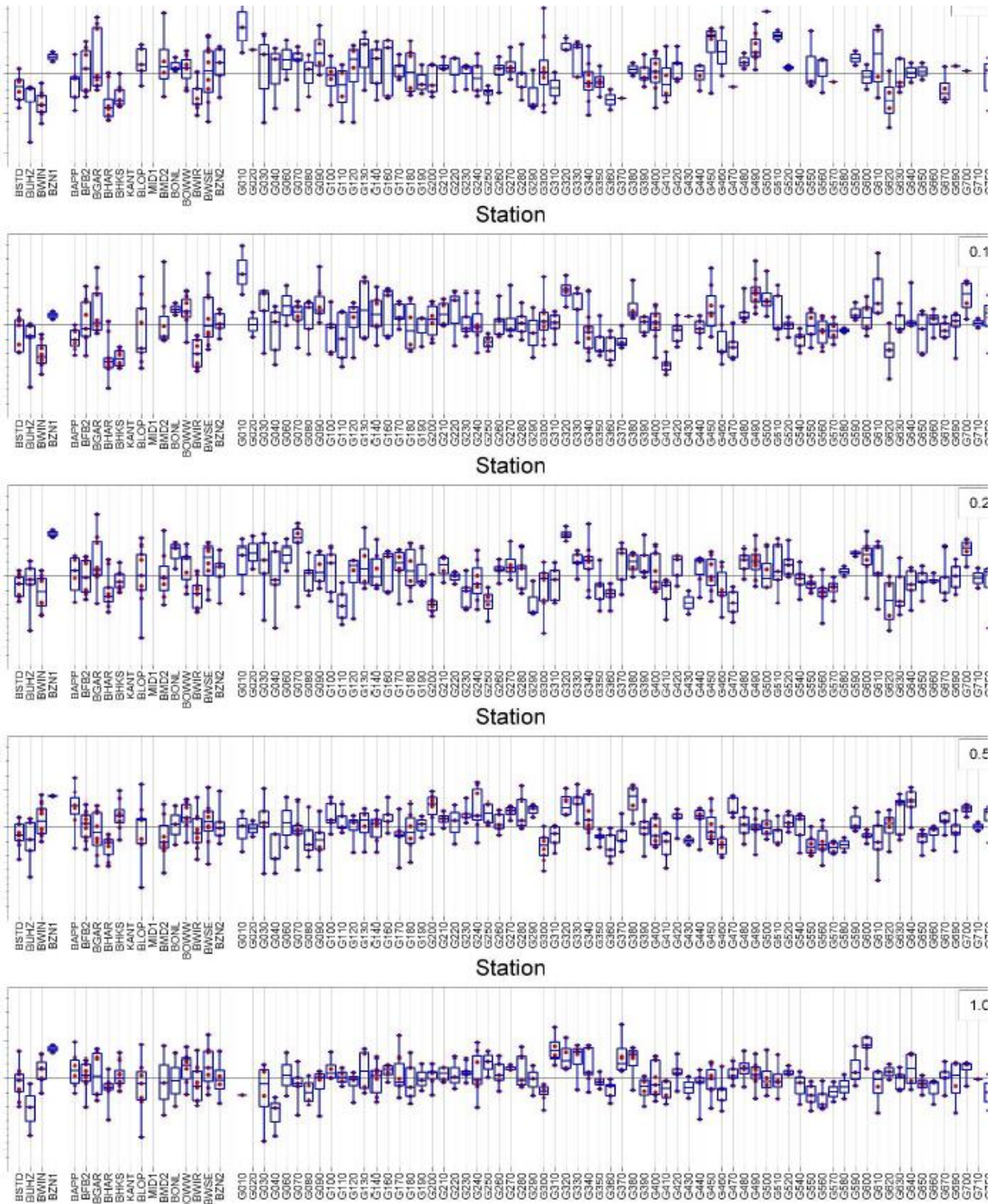


Figure 3.15. Relative offsets (mean-centered total residuals, *red dots*) of eight earthquakes common to both networks plotted against the station ID for five oscillator periods (top to bottom: 0.01, 0.1, 0.2, 0.5, 1.0 second). The blue lines indicate maximum and minimum values, the boxes the 25th and 75th percentiles, with blue lines showing the medians.

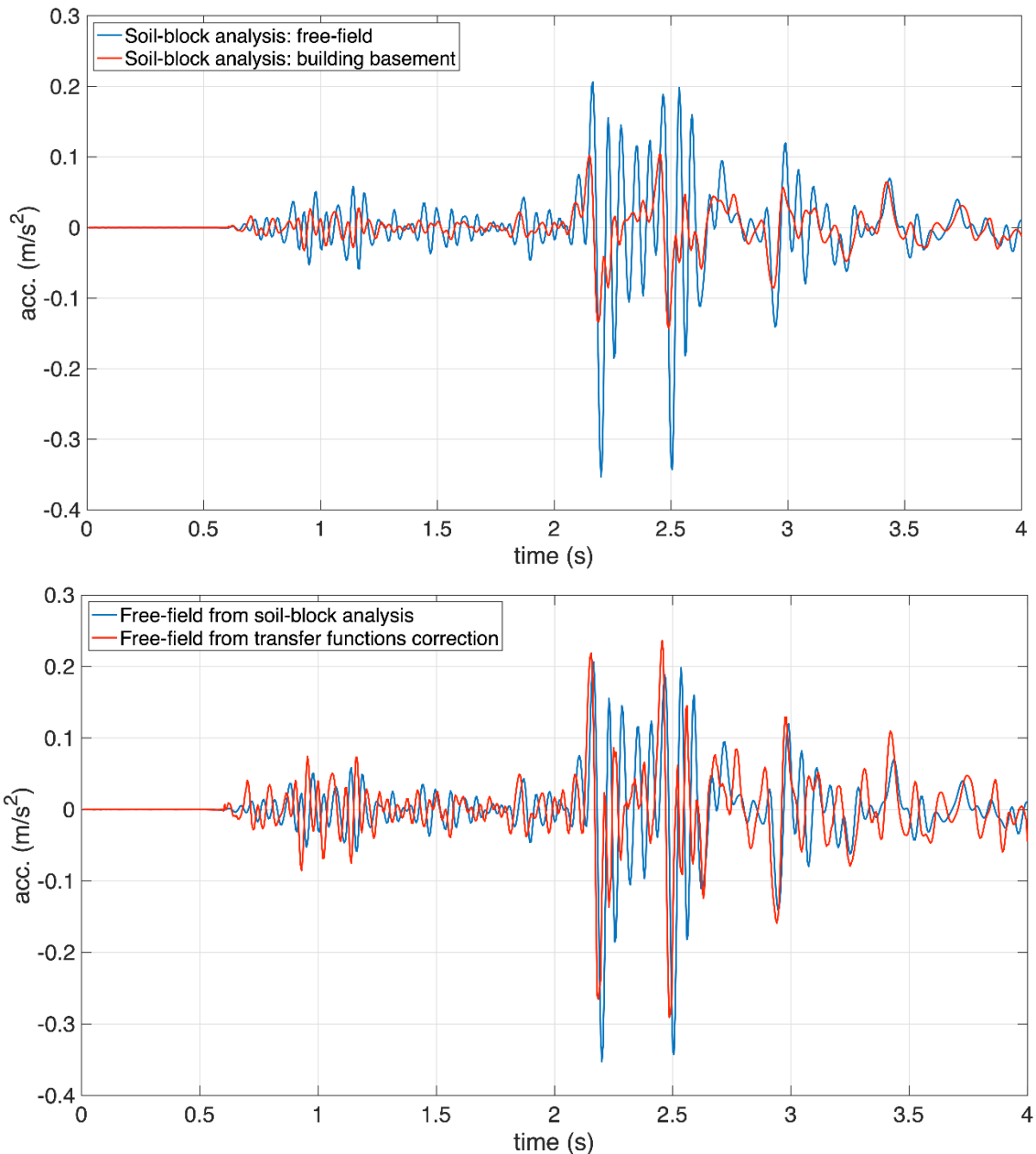


Figure 3.16. Example of the application of the correction proposed by NIST (2012) on a time-history in order to match free-field ground-motion. The *red* trace represents the time-history before (*upper*) and after (*lower*) the correction. The time-histories all come from numerical simulations: the ‘free-field’ time-history is obtained at the surface of a soil block analysed without any structure; ‘inside structure’ is a time-history obtained at basement level from a soil-block analysis that featured the presence of a building with a basement; and ‘estimated free-field’ is obtained by applying to the ‘inside structure’ time-history the embedment and base-slab average correction transfer functions from NIST (2012).

The analyses conducted show that this would result in the reduction of short-period response spectral ordinates that has been inferred to occur at several of the B-stations. It is reasonable to assume that such ground improvement measures have been carried out at many of the B-stations and this would not have been revealed by the *in situ* V_s measurements conducted for the network because access issues meant

that those measurements were always conducted at some distance away from the buildings (Noorlandt *et al.*, 2018). Such higher velocity surface layers will clearly not be encountered at the G-stations, which are installed in open fields.

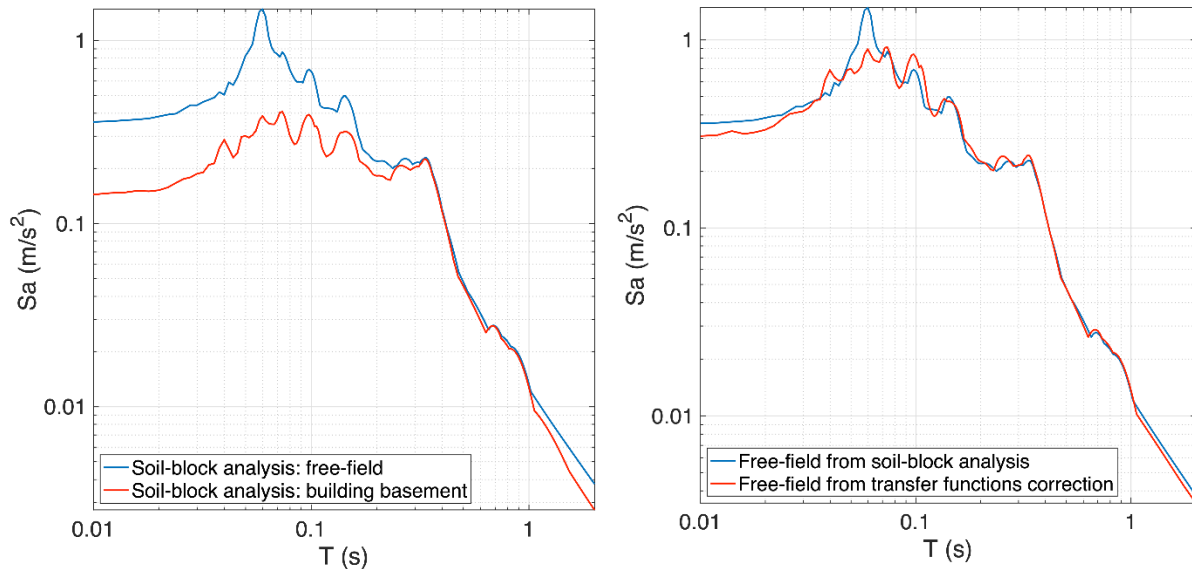


Figure 3.17. Example of the effect of the application of the correction proposed by NIST (2012) on the response spectra of the record presented in Figure 3.16. The red spectrum represents the record before (*left*) and after (*right*) the correction.

Although this line of reasoning is perfectly plausible, it cannot be easily proven. Furthermore, comparisons of the spectral accelerations demonstrate that the source of the differences, where they are observed, is more complicated. Figures 3.18 and 3.19 show spectral accelerations plotted against distance for the M_L 2.6 Slochteren and M_L 3.4 Zeerijp events, respectively. While the effect can be observed in Figure 3.18, where the B-stations recorded weaker motions, it is not clear in Figure 3.19, where the motions are higher.

One line of investigation that was proposed and planned was to install geophones (from the flexible network) at several B-stations, both within the buildings housing the accelerographs and at intervals in the adjacent gardens (plan shown in Figure 3.20). The purpose of this exercise would be to obtain in-building and free-field recordings from the same location (of earthquakes and/or artificially generated vibrations) in order to empirically explore the extent of the influence of the structure housing the instrument. Candidate B-stations were identified and three were selected for the exercise, ensuring that the building stock of the B-network was well-represented: BHAR (braced-steel-frame barn/warehouse), BLOP (small shed) and BMD2 (masonry-wall, timber-roof barn). The agreement of the owners was secured for the installation of the geophones but regrettably work was just about to commence as the restrictions on movement to combat the spread of Covid-19 were implemented.

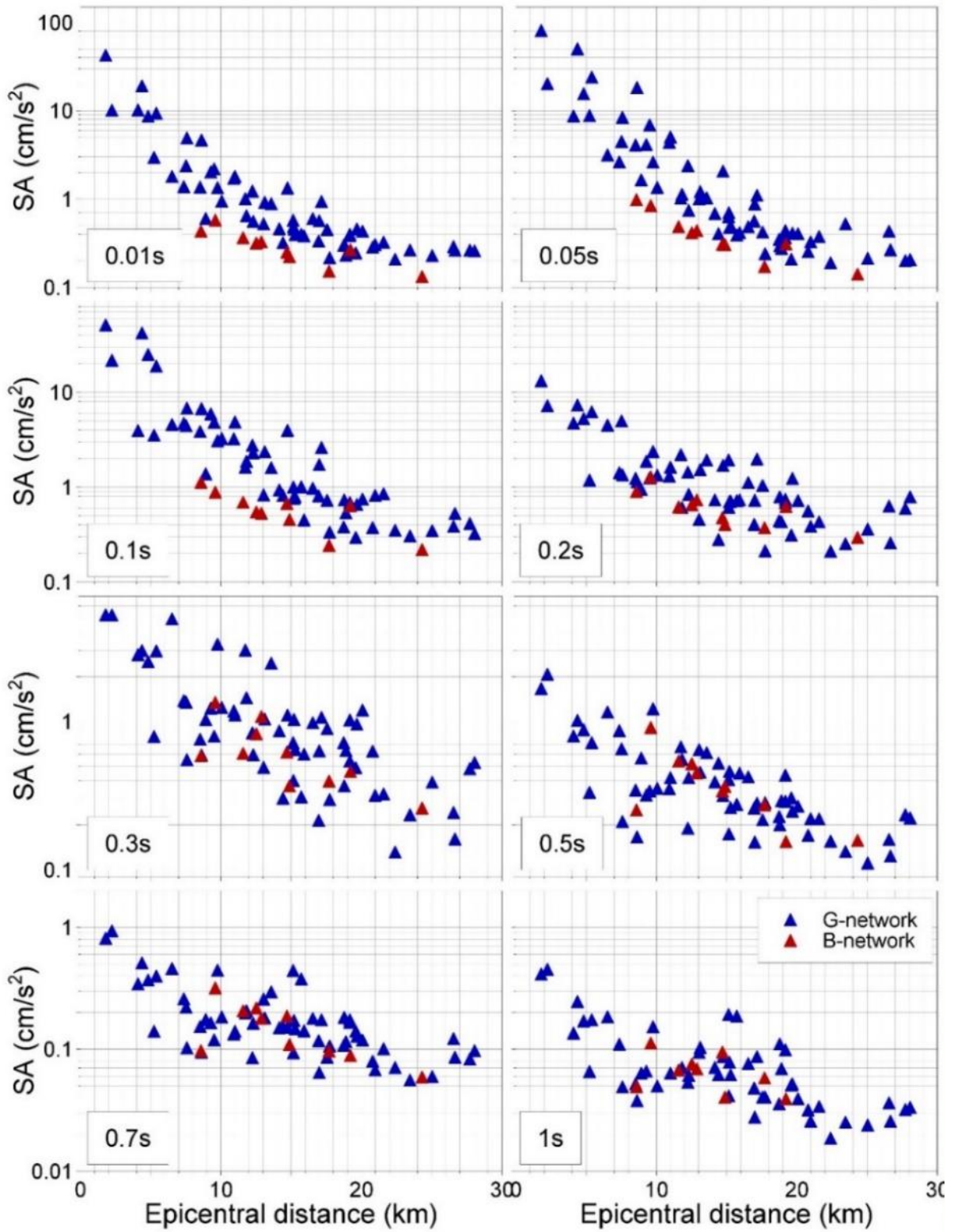


Figure 3.18. Spectral accelerations recorded during the 27 May 2017 $M_L2.6$ Slochteren event, plotted against epicentral distance

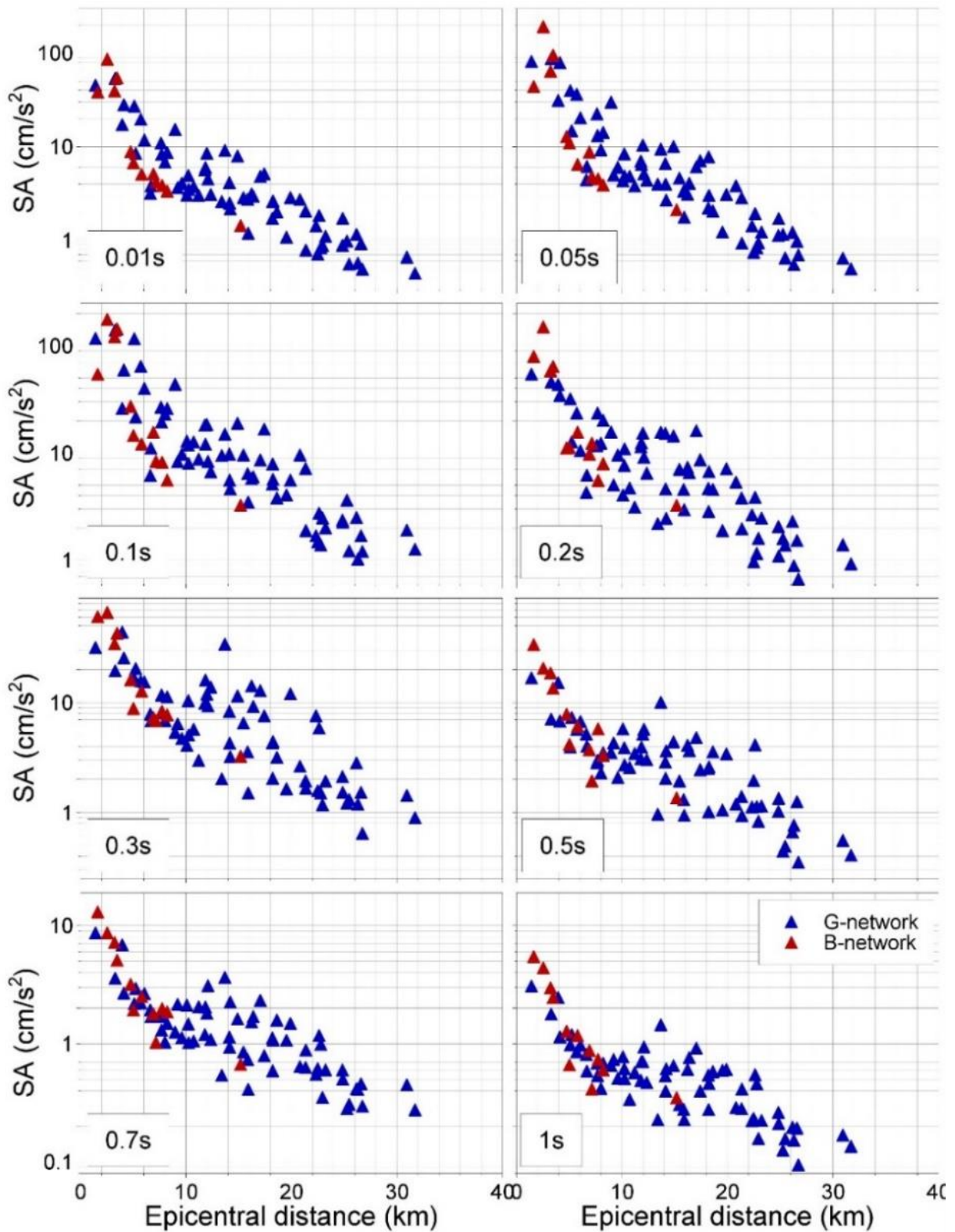


Figure 3.19. Spectral accelerations recorded during the 8 January 2018 M_L 3.4 Zeerijp event, plotted against epicentral distance

The identification of the cause or exact impact of the apparent issues regarding high-frequency attenuation at some of the B-stations is, as demonstrated, not

straightforward. It should be noted that this effect likely occurs in many locations around the world where strong-motion stations are installed on soft soils, but it is evident in Groningen because of the existence of multiple strong-motion networks. Three options were considered:

1. Eliminate the affected short periods ($T < 0.2s$) from the GMM and the fragility functions.
2. Formulate and apply a correction to the affected periods.
3. Use the data without correction.

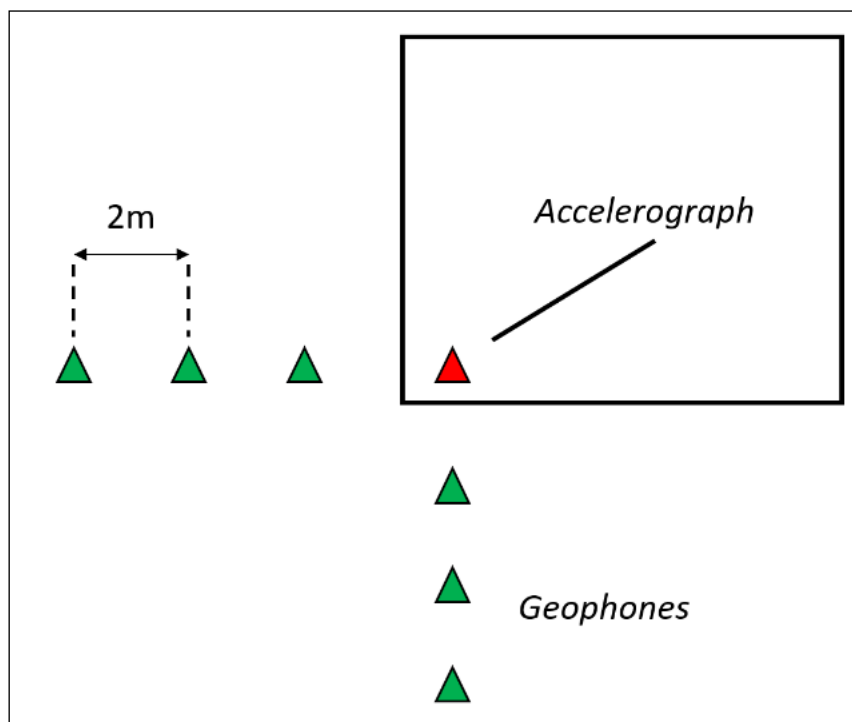


Figure 3.20. Layout plan of the installations of geophones in the B-stations. The *black rectangle* which contains the accelerograph represents the house walls.

The first option, to eliminate the short periods would circumvent the issue with the short-period response spectral ordinates and could be accommodated by a change in the intensity measure used by the fragility functions (although this could reduce their efficiency for some structural typologies). However, this position was rejected because the issue would remain in the high frequencies of the FAS, which are critical for the inversions that are carried out to obtain source parameters and cannot be ignored in a similar manner as the short periods of the response spectra.

The second option, to formulate and apply a correction similar to the correction proposed by NIST (2012) for basement instruments, was suggested by the review panel. However, it is impossible to yield an unambiguous identification of the frequency

range and amplitude of the effect at all B-stations, even when carrying out comparisons of the B- and G- records (Figures 3.11-14). A possible solution could be based on a concept of typical free-field response spectral shapes and include an attempt to identify and correct any short-period deviations from these shapes in B-station recordings. However, this would require many assumptions and would be even more limited in terms of the insights it could provide regarding the stations affected as well as the period ranges requiring correction at each station.

Therefore, and noting that the B-station recordings do represent motions experienced in buildings of the same type as those being analysed in the risk calculations, decided to proceed with the third option: using the full database of B-station and G station recordings. The derivation of the V7 GMM will track the trends with regards to the two networks and, where possible, individual stations as well. We also note that the within-event variability (currently imported ϕ_{ss} models) will need to be modified to capture the increased variability at short periods due to this decision.

Exclusion of records from stations with no measured V_s profiles

One additional criterion has been instituted for the removal of a small subset of the data, imposed not on the quality of the data or the characteristics of the recording stations but on the information available and, more specifically, the information on the V_s profile of the sites.

The V_s profiles are used to inform the calculation of the site transfer and amplification functions (TFs and AFs, respectively). These are used in the model development to deconvolve, respectively, the Fourier and response spectra of the records to the baserock horizon. Following the upgrade of the B-network, in 2014, a campaign of seismic cone-penetration tests (SCPTs) was carried out by Deltares on behalf of NAM in the 18 locations of the B-network inside the field. This allowed V_s profiles for these sites to be determined (see Noorlandt *et al.*, 2018). The development of the Groningen GMMs has since benefitted from these measurements, which have been used to calculate the TFs and AFs for those stations. At the same time, the geological models of the Groningen field were used to infer the V_s profiles for the sites of the G-stations, in which no *in situ* measurements had been carried out, and for the field in general (Kruiver *et al.*, 2017b). A comparison of the AFs calculated using the measured profiles of the B-stations with the AFs calculated using inferred profiles for the same locations, carried out during the development of the V6 GMM and discussed in Bommer *et al.* (2019b), showed that the use of inferred profiles introduces a bias in the deconvolutions of the ground-motions to the baserock horizon (Figures 3.21 and 3.22).

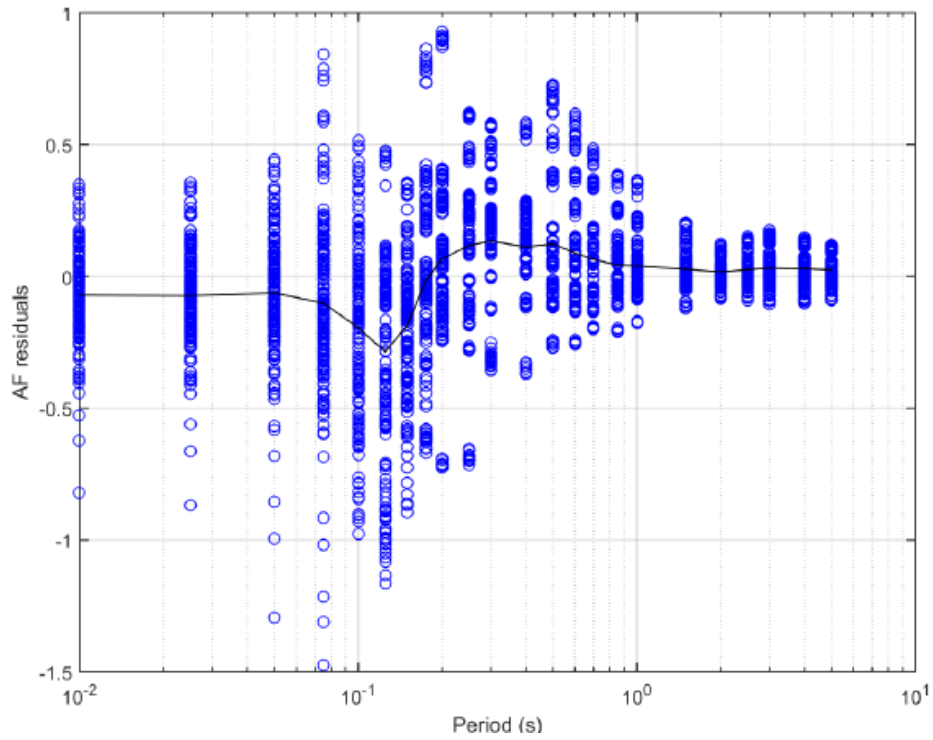


Figure 3.21. Residuals of AFs (in natural logarithms) obtained from inferred V_s profiles relative to the AFs obtained from the measured V_s profiles at the B-stations (Bommer *et al.*, 2019b).

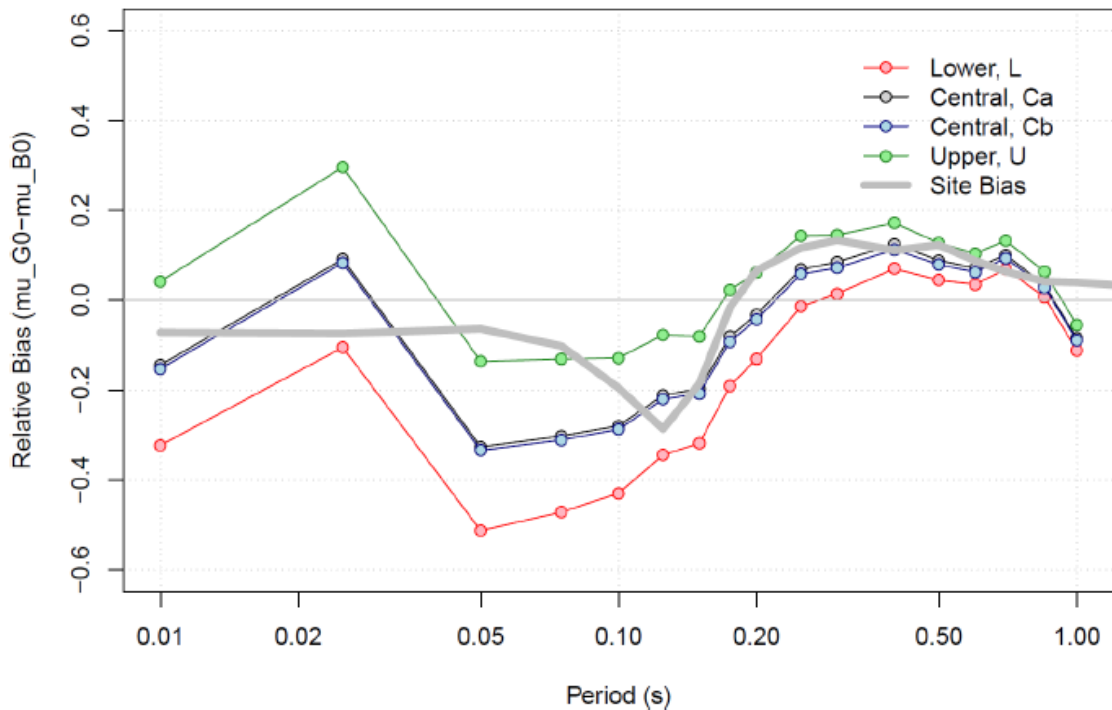


Figure 3.22. Comparison of the average trend of the ratios of AFs calculated using measured and modelled profiles at the B-stations (grey curve) with the relative bias of the model for NS_B motions computed with recordings from B-stations and G0-stations (Bommer *et al.*, 2019b).

In April 2019, Fugro carried out Seismic Code Penetration Test (SCPTs) at 14 G-stations for the purposes of the KEM projects. Following a request from NAM, an additional 38 SCPTs were carried out between October and December of the same year and another 12 in July 2020. As a result of these three recent measurement campaigns, and the preceding measurements at the B-stations, there are now a total of 72 B- and G-stations with measured V_s profiles and only 15 G-stations and one B-station (BKMZ) without. As explained previously (Table 3.1), three of those 15 G-stations are malfunctioning while seven are located outside the GMM study area, as is station BKMZ. Furthermore, the SCPT results from four stations only became available after the finalisation of the V7 database (which could not be delayed further due to constraints posed by the timetable of the V7 model development). Thus, a total of only nine G-stations which produce records potentially usable in the development of the GMM, did not have measured V_s profiles at the time of the finalisation of the database. The total number of records contributed by these stations is 40 (6.3% of the records considered usable at this stage) and their magnitude and distance (M-R) distribution is shown in Figure 3.23. Removing these records would not significantly impoverish the database in size or terms of M-R distribution but it should lead to better estimates of the NS_B motions and therefore reduce the uncertainty in the inversions. Thus, it has been decided not to retain these records in the final dataset that will be used in the GMM development.

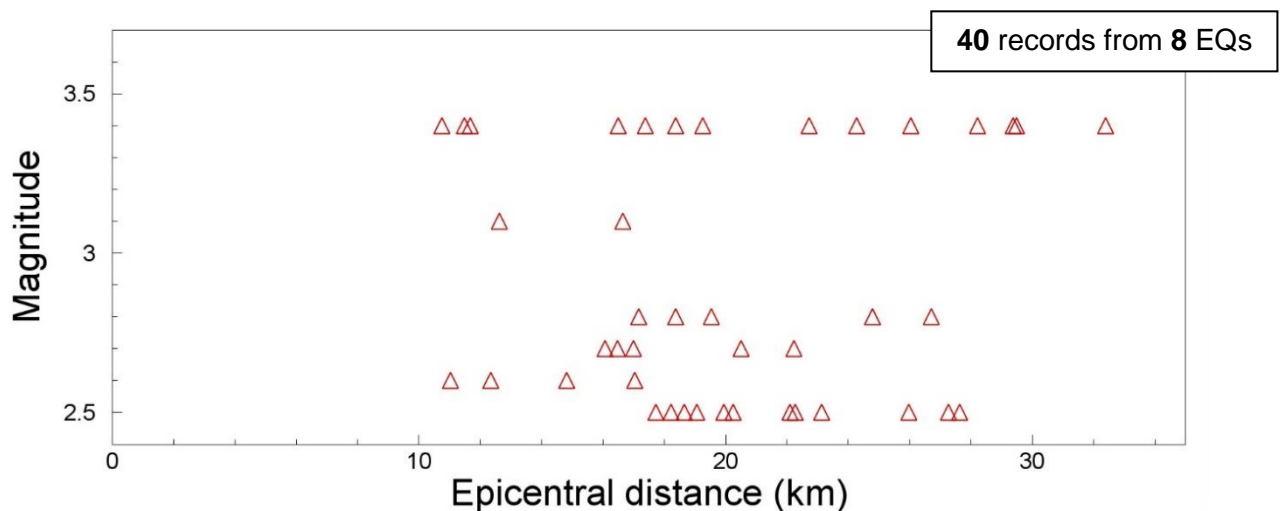


Figure 3.23. Magnitude-distance distribution of the records from G-stations with no measured V_s profiles.

3.2. Record Processing and Usable Period Ranges

The processing procedure applied to the V7 database is described in detail in Edwards & Ntinalexis (2021), including the development of an innovative prediction model for the minimum usable period of the pseudo-acceleration response spectra of a record. The main workflow for selecting the usable period and frequency ranges of the

pseudo-acceleration response spectra and Fourier amplitude spectra (FAS), respectively, is summarised here.

Usable Frequencies of a Record's FAS

We select a record's maximum usable frequency, f_u , as the maximum frequency of the continuous frequency window with FAS signal-to-noise ratio (SNR) above 3. This is the simplest method to select the maximum usable frequency and is also widely employed in engineering and seismology work globally.

To conduct an SNR analysis, it is first necessary to obtain a noise model representative of the noise in the record. This is routinely determined as the FAS of the pre-event memory. In most modern recording networks, continuous data-streams are available via online services and data-portals, which allows the user to select a time-window of their choice around the event. In these cases, it suffices for the user to select a time-window with a long pre-event memory and select the first 5-10 seconds of that window to sample noise without contamination by the earthquake signal itself.

However, in networks operating on a triggering-only basis, such as the KNMI B-network in Groningen prior to 2014 (see Ntinalexis *et al.*, 2019), limited time lengths of pre-event memory may be available. Furthermore, in small-amplitude records such as those included in the Groningen database, the SNR above 20 Hz can be very sensitive to the selection of the noise window, and hence it is important to make sure that the noise window is carefully selected.

To do this, we have developed a technique of dynamic noise-window selection. We use the vertical component motion to determine the noise window to ensure we avoid P-wave energy. While small in amplitude on the horizontal components, the P-wave has non-negligible high-frequency energy that may bias the noise estimate (and therefore SNR and ultimately f_u). We begin by locating the time window from the beginning of the record to the point where the Arias Intensity is 0.5% of the total. We then calculate two types of moving averages of the absolute acceleration of the time-history, for each point of the time-history. The first includes one second preceding and 0.5 seconds following each point (short-term average) and the second includes three seconds preceding and 0.5 seconds following (long-term average). A ratio of the short- to the long-term moving average above 1.2 signifies a significant amplitude change that can be associated with the first arrivals of the earthquake signal. Therefore, we choose the end of the noise window to be the shortest time between the earliest moment that this ratio is achieved and the time of 0.5% Arias Intensity. The noise window, as defined on the vertical component, is then used for the horizontal components. An example is shown in Figure 3.24.

If the sensor is close to a circuit board of an electricity mains network, then it is very likely that the records generated will be contaminated with noise at the frequency of the electric network, which, for most electrical systems is at 50 Hz. For small-amplitude records, this may result in a peak in the FAS (Figure 3.25) and affect the calculation

of f_u as well as the response spectra of the record (Figure 3.25). Douglas & Boore (2011) recommend the removal of this peak at 50 Hz with a notch filter.

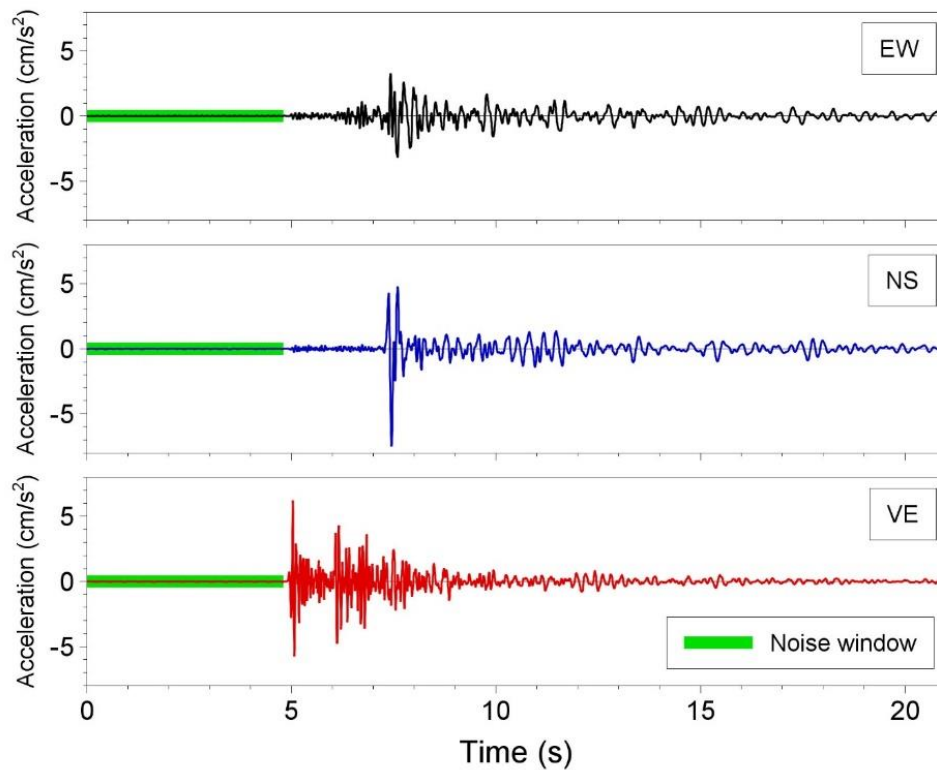


Figure 3.24. Time-histories and selected noise window of the MID1 recording of the M_L 3.2 Westeremden event on 30 October 2008.

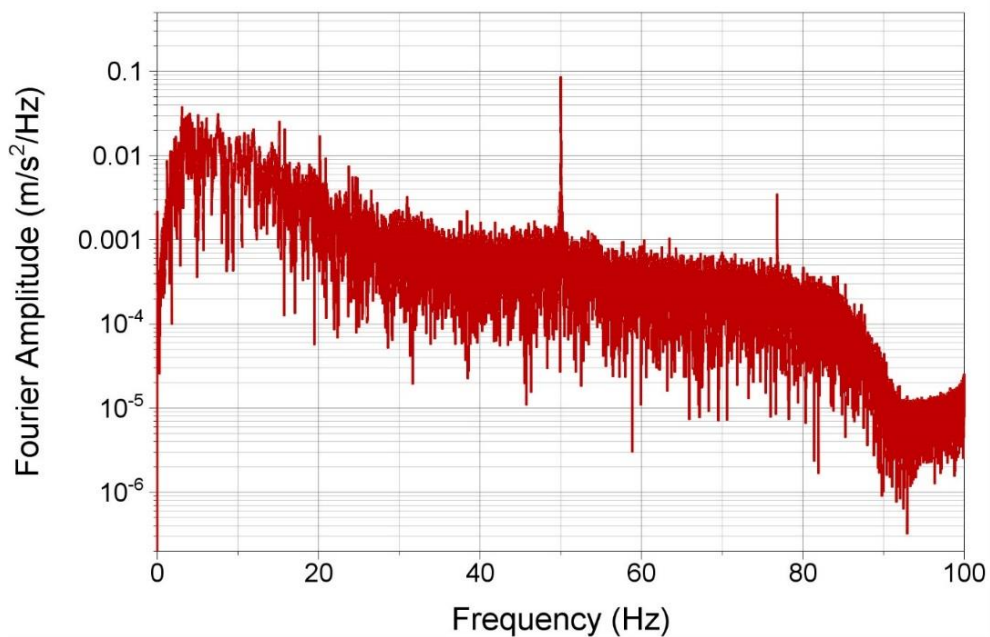


Figure 3.25. Example of the presence and amplitude of the 50 Hz electricity mains noise in a record's FAS.

At the KNMI G-stations in the Groningen field, the circuit board of the mains of the station is within half-a-metre of the accelerograph (see Ntinalexis *et al.*, 2019). As a result, the small-amplitude records of those stations are typically contaminated with this form of noise. In this case, it is necessary to remove the peak at 50 Hz to obtain correct estimates of pseudospectral acceleration (Figure 3.26). This was carried out with a notch filter between 49 and 51 Hz

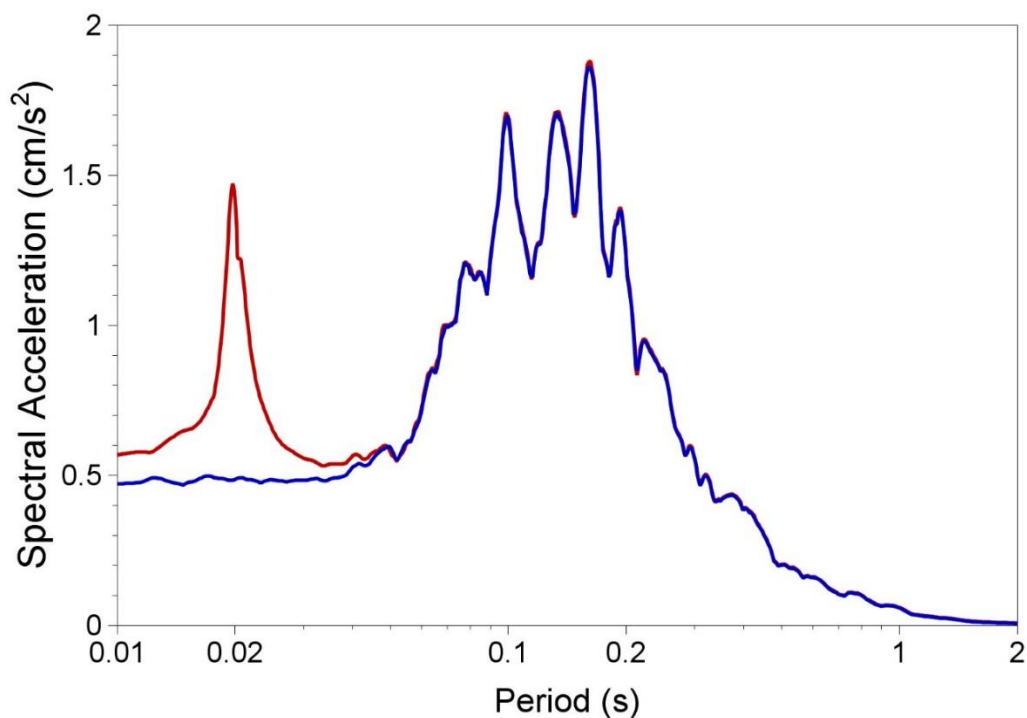


Figure 3.26. Response spectra of record G040 from the $M_L3.1$ Hellum earthquake in Groningen (30 September 2015), with (*blue*) and without (*red*) removing the 50 Hz noise peak.

Determining the lower usable frequency (f_l) by employing the same $SNR < 3$ criterion is a choice that is also often employed. However, because the SNRs of small-amplitude records are smaller and the resulting bandwidth can be very limited, it is desirable to use a method that results in more forgiving estimates. We have developed such a method which is summarized in the following.

The first step is to obtain an initial estimate of f_l ; this is defined as the first point that the FAS of the recording is observed to decay more slowly than the theoretical Brune (1970) spectrum at low frequency. The Brune model suggests that the FAS of acceleration should decay proportional to $-\omega$ at low frequency, any additional amplitude in those frequencies can be concluded to originate from noise present in the record. Hence, the largest frequency where this behaviour is observed can be considered as the first estimate of f_l .

The next step is to low-cut filter the record using f_l as the filter frequency and then compute the displacement trace. Any low-frequency noise can then be easily observed in the time-series. If the total displacement is zero and long-period noise cannot be readily observed in the displacement trace, then this frequency is selected as the final f_l value. If the user judges the displacement trace to still be unacceptably contaminated with noise, a higher frequency is selected, and the process is repeated until a frequency is found such that a noise-free displacement trace is achieved.

An example of the application of this procedure is shown in Figures 3.27-3.28. Figure 3.27 displays the FAS of record KANT of EQ-07 where the identification of different possible low-cut filter frequencies from the FAS of the record is illustrated. The displacement traces obtained after the application of the different filters are compared in Figure 3.25. It is obvious that applying a filter of 0.342 Hz (the lowest possible f_l) is not sufficient in the case of this record, as long-period waves are still clearly observable in the displacement trace. At the same time, we can observe that a frequency of 1.611 Hz is excessive, as it results in a reduction in the amplitude of the record. Low-cut frequencies of 0.635 Hz and 0.732 Hz both produce acceptable results, hence the lowest, 0.635 Hz, is selected.

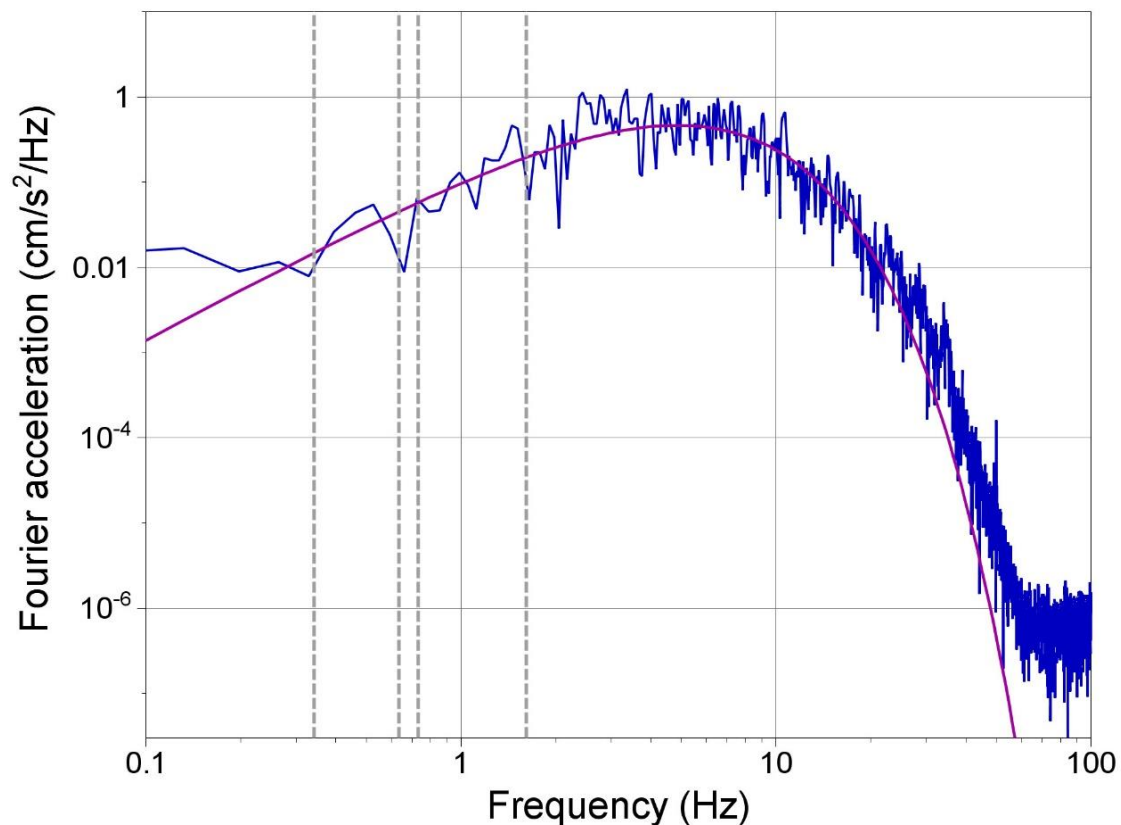


Figure 3.27. The Fourier amplitude spectra of raw acceleration recording 07KANT_NS (*blue*) and the Brune (noise-free) model for the same record (*red*). Possible lower usable frequencies (f_l) are indicated (*grey dashed*)

A record is removed by the database when any of the following is true for at least one of its horizontal components:

1. The lower usable frequency is above 2 Hz
2. The upper usable frequency is below 10 Hz
3. The SNR is below 3 throughout the FAS frequency range.

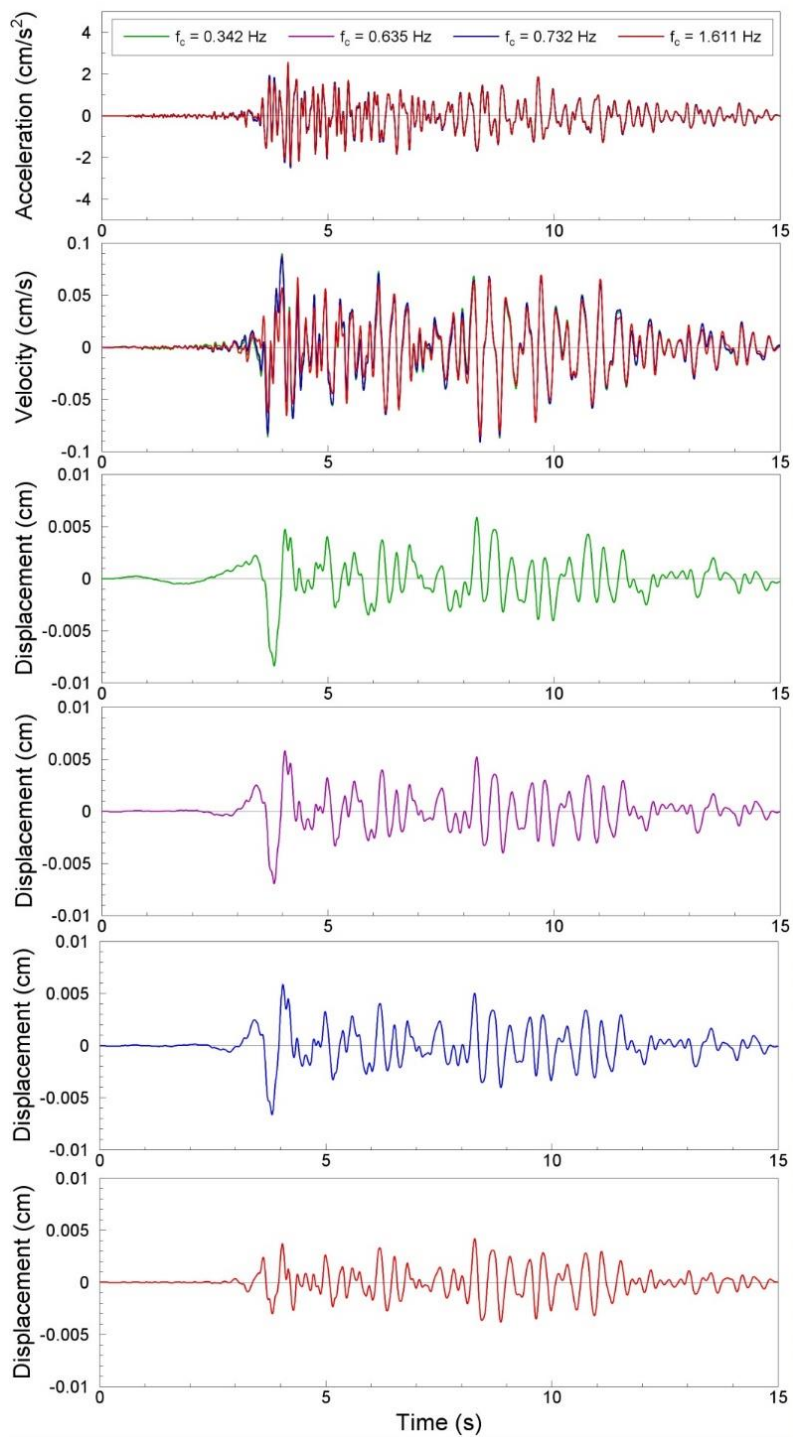


Figure 3.28. Acceleration, velocity and displacement traces of recording 07KANT_NS after the application of different low-cut filters.

A total of 96 records have been removed based on these criteria. Their magnitude-distance distribution is shown in Figure 3.29. Unsurprisingly, the records that are removed by this step are predominantly weaker signals from smaller earthquakes. Only three out of the 57 records removed were obtained by the older B-stations before 2014. This is mainly due to the vast expansion of the KNMI networks after 2014, which allows them to now capture a larger number of lower-amplitude records with smaller SNR. Another reason is the fact that the older B-stations operated on a record-triggering basis, generating records only once ground-motion was clearly detected, which resulted in signals with small SNRs not being identified as earthquake signals and generating records (see Dost *et al.*, 2017; Ntinalexis *et al.*, 2019).

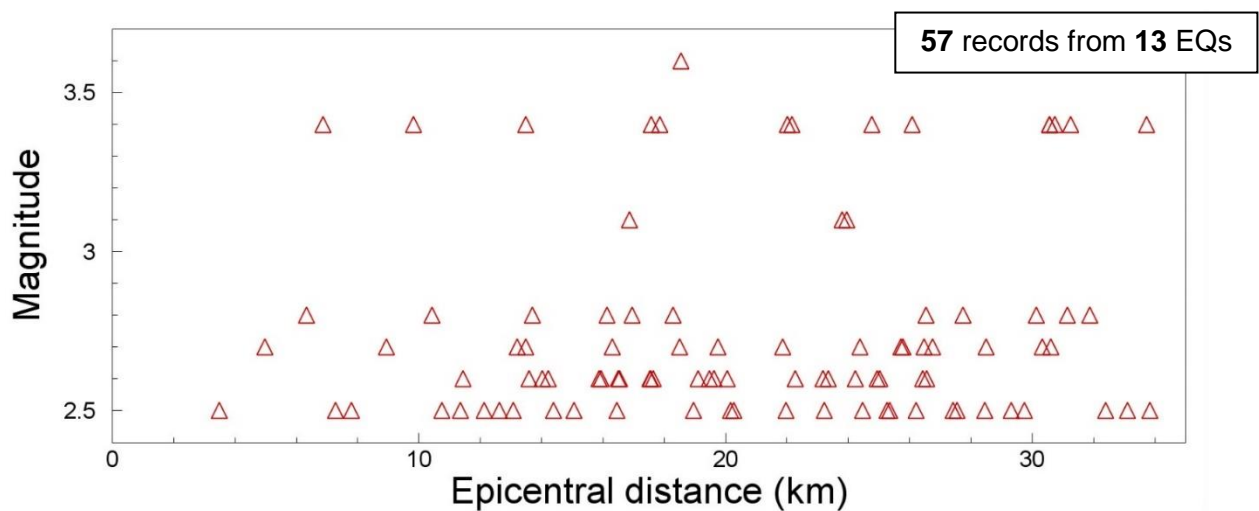


Figure 3.29 Magnitude-distance distribution of records removed due to limited usability of FAS

Usable Periods of PSA

In the absence of high-frequency artefacts introduced by deconvolution of the instrument response, such as may arise from the correction/restitution of anti-alias filters, further filtering of the high-frequencies is not recommended as it may have a knock-on effect on a wide range of spectral periods. In the Groningen records, the instrument response, as deconvolved from the record, is broadly flat at high frequencies, up to the Nyquist. As a result, no such artefacts are introduced. Filtering of high-frequency amplitudes was therefore not undertaken. However, as shown by Edwards & Ntinalexis (2021), it is still necessary to define a minimum usable period in the short period range in order to exclude noise-contaminated periods from use.

The result of the parametric prediction model presented by Edwards & Ntinalexis (2021) for the ratio threshold of 5% is adopted as a first estimate of T_{\min} . However, as Edwards & Ntinalexis (2021) recommend, we create two semi-synthetic records using the FAS of each recording examined, to better constrain the final T_{\min} value selected and better assess the relationship between noise and signal and its effect on the spectra.

To create the first synthetic, we fit the idealized Brune spectrum to the FAS of each record (Figure 3.30) and use the FAS of the record within its usable frequency range and the Brune spectrum in the unusable frequencies. Thus, we create an idealized noise-free version of the same record. To create the second synthetic, we use again the FAS of the record but double it for frequencies higher than f_{upper} . In this way we obtain a noisier version of the same record.

By comparing the response spectra of the original raw record to the idealized noise-free version, we can obtain an estimate of the periods that are affected by noise. At the same time, by comparing them with the response spectra of the noisier version, we can observe which periods are more sensitive to a further increase in the noise present. From these comparisons we can define two additional estimates of T_{min} , one where the spectrum of the real record diverges more than 5% from the spectrum of the idealized synthetic and one where spectrum of the noisier synthetic diverges more than 5% from the spectrum of the real record.

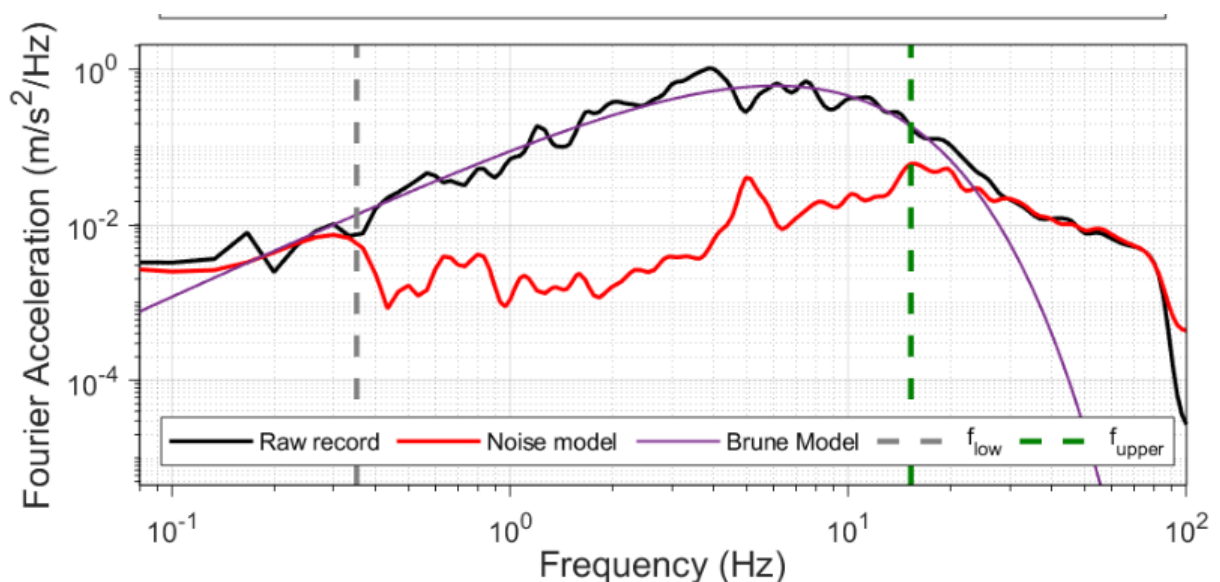


Figure 3.30 FAS of the record obtained at station G780 from the $M_L3.4$ Zeerijp event of 8 January 2018 in Groningen.

Finally, we select T_{min} using the following logic (illustrated in Figure 3.31):

- If the parametric model result is 0.01s (the shortest period defined), we retain that value
- If two of the three estimates are within 10% of each other, and the third is more than 10% different, we retain the largest value of the two that agree
- If the result of the parametric model is between the two estimates, we retain that value
- Otherwise, we use the largest value of the three

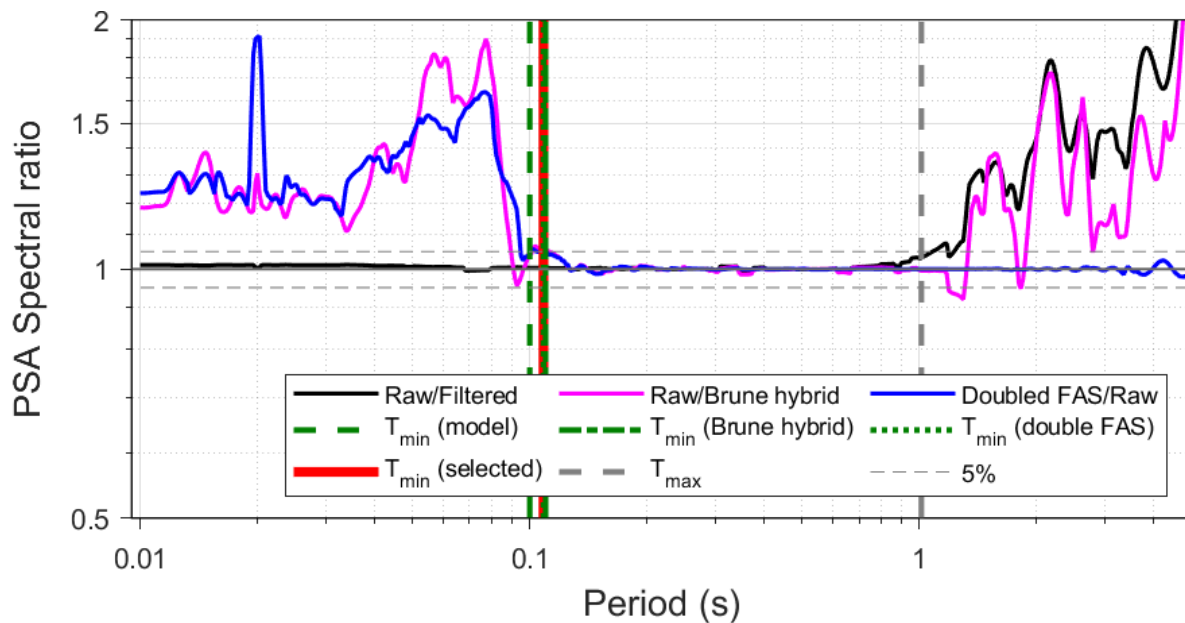


Figure 3.31 Spectral ratios and selection of T_{\min} for the H2 component of record G310 of the 2 May 2020 $M_L 2.5$ Zijldijk earthquake in Groningen

3.3. Database Characteristics

The final dataset comprises of 648 records obtained at 81 locations during 29 earthquakes of local magnitude from $M_L 2.5$ to 3.6. Figure 3.32 shows the magnitude-distance distribution of the records, with different symbols for records generated by the two KNMI networks. In Figure 3.33, the breakdown of the contribution of each station is displayed, with different colours used for records obtained during events of magnitude greater than $M_L 3.0$ and records obtained during events of magnitude equal to $M_L 3.0$ and smaller. The basic metadata of the 29 events and the number of records included in the dataset from each event are presented in Table 3.3, with coordinates given in the Dutch RD (Rijks-Driehoek) system. The hypocentral locations were provided by the KNMI; they were determined by the Equal Differential Time (EDT) method described by Spetzler & Dost (2017) for events 16 and 18-29 and using the automatic solutions of the SeisComp software for all other events. The SeisComp solutions are publicly available in the KNMI website (KNMI, 1993).

As can be observed in Figures 3.32 and 3.33, while, as a whole, the G-network has contributed more records to the database than the B-network, the individual contribution of each B-station is significantly greater than that of the G-stations, with the exceptions of course to the now-decommissioned stations (KANT, BMD1 and BONL) and station BLOP (as discussed in Section 3.1).

Table 3.3 Basic metadata of the events included in the V7 database

| EQ-ID | M_L | Date | Time (UTC) | RD-X (m) | RD-Y (m) | No. Recs | Location |
|--------------|----------------------|-------------|-------------------|-----------------|-----------------|-----------------|-----------------|
| 1 | 3.5 | 2006-08-08 | 05:04:00 | 242159 | 596659 | 4 | Westeremden |
| 2 | 2.5 | 2006-08-08 | 09:49:23 | 242826 | 596579 | 1 | Westeremden |
| 3 | 3.2 | 2008-10-30 | 05:54:29 | 243740 | 595168 | 6 | Westeremden |
| 4 | 2.6 | 2009-04-14 | 21:05:25 | 241060 | 596009 | 3 | Huizinge |
| 5 | 3.0 | 2009-05-08 | 05:23:11 | 246479 | 597129 | 5 | Zeerjip |
| 6 | 2.5 | 2010-08-14 | 07:43:20 | 242496 | 602509 | 4 | Uithuizermeeden |
| 7 | 3.2 | 2011-06-27 | 15:48:09 | 248253 | 591487 | 8 | Garrelsweer |
| 8 | 2.5 | 2011-08-31 | 06:23:57 | 241305 | 607070 | 3 | Uithuizen |
| 9 | 2.5 | 2011-09-06 | 21:48:10 | 249399 | 595368 | 1 | Oosterwijtwerd |
| 10 | 3.6 | 2012-08-16 | 20:30:33 | 240504 | 596073 | 7 | Huizinge |
| 11 | 2.7 | 2013-02-07 | 22:31:58 | 240112 | 599405 | 3 | Zandweer |
| 12 | 3.2 | 2013-02-07 | 23:19:08 | 240085 | 600945 | 3 | Zandweer |
| 13 | 2.7 | 2013-02-09 | 05:26:10 | 246230 | 598516 | 2 | t Zandt' |
| 14 | 3.0 | 2013-07-02 | 23:03:55 | 248163 | 590446 | 2 | Garrelsweer |
| 15 | 2.8 | 2013-09-04 | 01:33:32 | 247166 | 596048 | 5 | Zeerjip |
| 16 | 3.0 | 2014-02-13 | 02:13:14 | 247144 | 596870 | 14 | Leermens |
| 17 | 2.6 | 2014-09-01 | 07:17:42 | 248489 | 579359 | 5 | Froombosch |
| 18 | 2.8 | 2014-09-30 | 11:42:03 | 239566 | 586336 | 12 | Garmerwolde |
| 19 | 2.9 | 2014-11-05 | 01:12:34 | 240652 | 599029 | 19 | Zandweer |
| 20 | 2.8 | 2014-12-30 | 02:37:36 | 244481 | 581878 | 20 | Woudbloem |
| 21 | 2.7 | 2015-01-06 | 06:55:28 | 246882 | 593646 | 20 | Wirdum |
| 22 | 3.1 | 2015-09-30 | 18:05:37 | 251326 | 584194 | 40 | Hellum |
| 23 | 2.6 | 2017-05-27 | 15:29:00 | 251675 | 581586 | 52 | Slochteren |
| 24 | 3.4 | 2018-01-08 | 14:00:52. | 245748 | 597703 | 69 | Zeerjip |
| 25 | 2.8 | 2018-04-13 | 21:31:35 | 245534 | 598304 | 70 | Garrelsweer |
| 26 | 3.4 | 2019-05-22 | 03:49:00 | 238928 | 593678 | 65 | Westerwijtwerd |
| 27 | 2.5 | 2019-06-09 | 05:00:15 | 246911 | 593706 | 64 | Garsthuizen |
| 28 | 2.5 | 2020-05-02 | 03:13:15 | 246371 | 601025 | 56 | Zijldijk |
| 29 | 2.7 | 2020-07-14 | 15:18:47 | 244288 | 595960 | 62 | Loppersum |

The pseudo-spectral accelerations calculated using each record are usable at a particular response period only if it lies between the maximum and minimum usable periods defined for that record (T_{\min} and T_{\max}). As a result, the total number of available data varies from period to period. The V7 GMM was designed to predict geometric-mean horizontal spectral accelerations at 10 response periods (0.01, 0.1, 0.2, 0.3, 0.4, 0.5, 0.6, 0.7, 0.85, and 1.0 seconds). These were chosen because the intensity measure currently used in the fragility functions is the geometric mean of the spectral accelerations at these periods; moreover, there is a significant drop-off in the number of usable records at oscillator periods beyond 1.0 second (Figure 3.34).

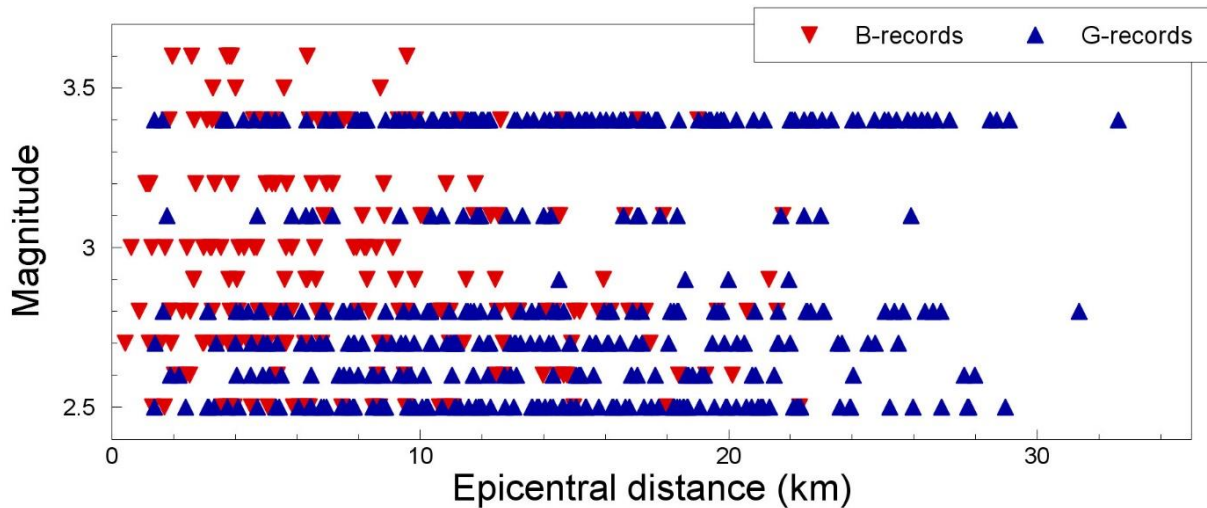


Figure 3.32. Magnitude-distance distribution of the final V7 GMM ground-motion database.

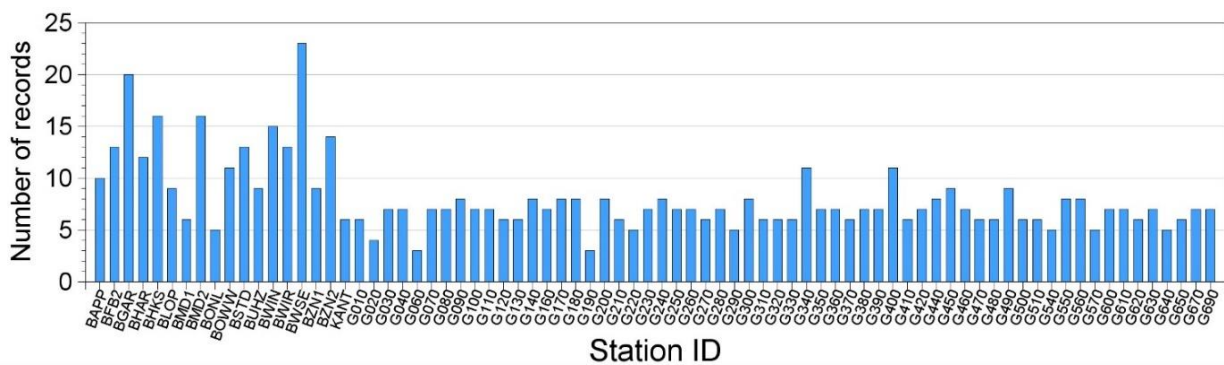


Figure 3.33. Number of records from each recording station in the final V7 GMM ground-motion database.

Previous GMMs provided predictions also for the oscillation periods of 2, 2.5, 3, 4 and 5 seconds, which are not included in the V7 GMM because they are not relevant to the buildings of the Groningen field as well as because there are not sufficient data available for those periods. Additionally, seven periods < 0.2 s that were introduced in the V3 GMM (Bommer *et al.*, 2016) to provide better short-period resolution to facilitate application of V/H ratios to obtain vertical response spectra are no longer included since vertical motions have not been found to be important in the risk calculations.

As shown in Figure 3.34, a larger number of usable spectral accelerations correspond to the intermediate periods (0.1 – 0.7 seconds), a smaller number (475) are available at 0.01 seconds and a rapid decay can be observed with increasing period from 0.85 seconds. At 1.5 seconds, the number of usable spectral accelerations is 168, which can still be considered sufficient for the limited distance and magnitude range covered by the database.

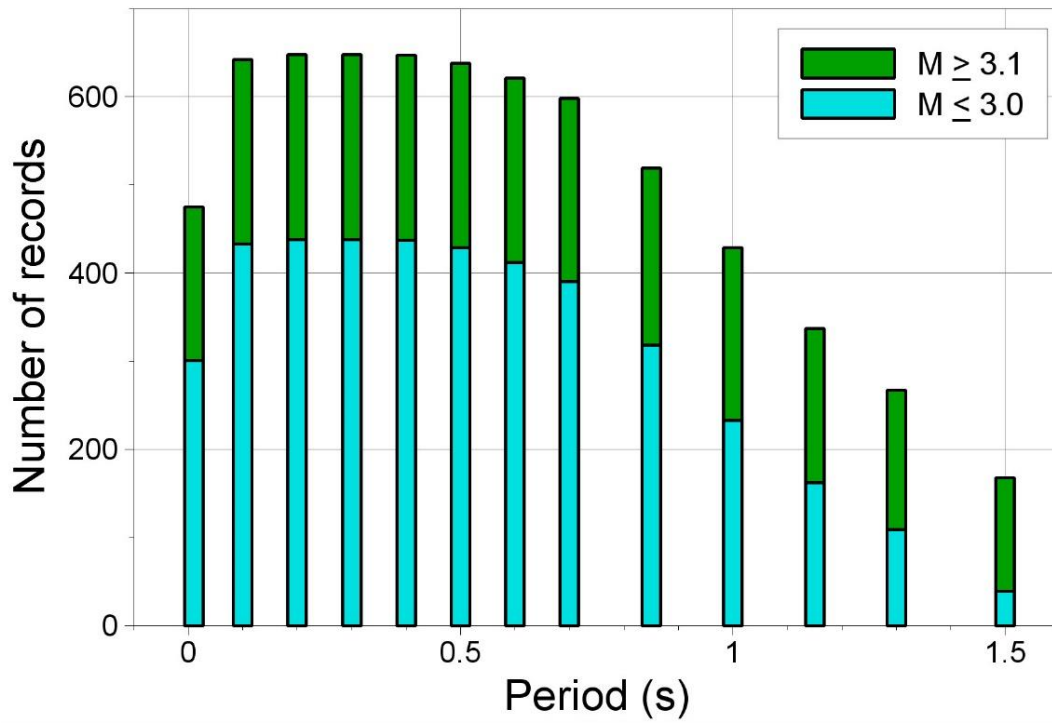


Figure 3.34. Number of usable records as a function of oscillator period, showing the total number and those corresponding to different earthquake magnitude ranges.

4. Site Characterisation Model

A key feature of the ground-motion model for the Groningen field is that it both captures the unique structure of the 3km of crust overlying the Rotliegend sandstone that houses the gas reservoir, while also capturing the lateral variations of the near-surface geology. Section 4.1 summarises the construction of a field-wide model for the shear-wave velocity (V_s) profiles from the selected NS_B reference rock horizon to the ground surface. Section 4.2 presents the work undertaken to derive a Groningen-specific model for soil damping. Section 4.3 describes the construction of the site response profiles at the recording stations, combining the field-wide model presented in Section 4.1 with *in situ* measurements at the individual ground-motion recording locations. The chapter closes in Section 4.4 with the calculation of factors to transfer FAS and response spectra of the surface recordings to the NS_B horizon.

4.1. Shear-Wave Velocity Model for the Field

The shear-wave velocity (V_s) model of the field was developed during the early versions of the GMM. The approach has been stable since V2, but updated with new information, such as the final GeoTOP version, the randomisation of V_s since V3, as well as the update from the NAM velocity model (Romijn, 2017) in V6.

The starting point for the Groningen V_s model is the GeoTOP model, that is being developed and updated at regular intervals by TNO. The GeoTOP model discretizes the sub-surface of the Netherlands to voxels (volume pixels) of 100m x 100m width and length and 0.5 m thickness, and assigns to each a stratigraphy, a lithoclass distribution and the most likely lithoclass. The Groningen V_s model consists of a V_s profile for each of the 100m x 100m grid cells in the GMM study area (which is defined by the outline of the gas field plus a 5 km buffer). The profiles range from the ground surface to the reference rock horizon of the GMM—the base of the North Sea formation, NS_B, at ~800m of depth.

The construction of the V_s profiles is described in detail by Kruiver *et al.* (2017a) and summarised here. The V_s profile for each grid cell is constructed by combining data from three sources of information, each valid over a different depth range (note that NAP is *Normaal Amsterdams Peil* or Amsterdam Ordnance Datum):

- a. the GeoTOP model, with a range from the surface to 50m below the NAP (50m-NAP)
- b. data inferred from recordings of surface waves surveys carried out in the 1980s using the Modal Elastic Inversion method (MEI), valid for the depth range of 20m-NAP to ~ 120m-NAP, but used only from 50m-NAP and below

- c. data obtained from a conversion of the Pre-Stack Depth Migration (PSDM) compressional wave velocity (V_P) model to V_S using relationships established from sonic logs of deep boreholes at the Groningen field, used for the range of ~ 70 m-NAP to ~ 800 m-NAP (NS_B)

A summary of each V_S depth range is described below.

GeoTOP V_S

For the shallow subsurface, from surface to 50m depth, the V_S model is based on the GeoTOP model, which provides stratigraphy and lithoclass, and has been combined with V_S distributions defining the V_S values for stratigraphy-lithology combinations with depth. These distributions are based on a Groningen SCPT dataset. An example of a V_S distribution based on SCPT's is given in Figure 4.1 for Naaldwijk clay and Peelo clay. These distributions were used to define the parameters V_{S1} and n in the empirical relation between V_S and confining stress σ'_o :

$$\ln V_S = \ln V_{S1} + n \ln \left(\frac{\sigma'_o}{p_a} \right) \quad (4.1)$$

where σ'_o is the confining stress, p_a is atmospheric pressure, V_S is a parameter that represents the shear-wave velocity at a confining stress equal to one atmosphere, and n is the slope that defines confining stress dependence. The parameters V_{S1} , n and the standard deviation of $\ln(V_S)$ were determined for all combinations of stratigraphy and lithoclass present in the top 50 m in the Groningen field. The tables listing the parameters are given in Kruiver *et al.* (2017a).

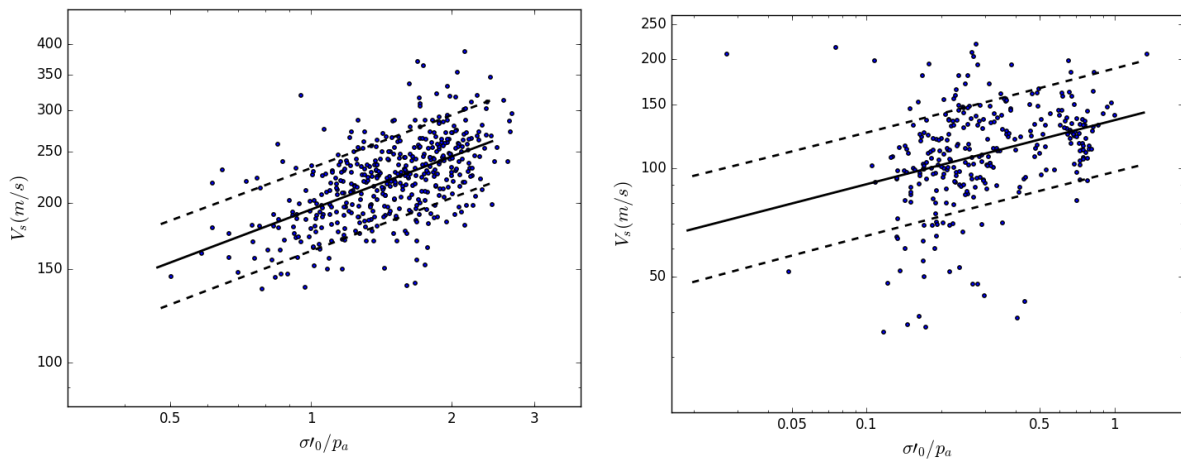


Figure 4.1. Example of V_S observations from the SCPT data set, for clays from the Peelo Formation (*left*) and Naaldwijk Formation (*right*). The solid line describes the median and the dotted lines indicate 95% confidence intervals. From Kruiver *et al.* (2017a).

The empirical V_s relation with parameters V_{S1} and n were used for construct mean V_s profiles based on the GeoTOP voxels. In addition to the mean V_s profiles, randomised V_s profiles were constructed using the standard deviation of $\ln(V_s)$ and a sampling scheme (Figure 15 from Kruiver *et al.*, 2017a) assuming a correlation coefficient of 0.5 between layers of different stratigraphy-lithoclass. Because of the large amount of grid cells (~140,000) only one randomised V_s profile was constructed for each GeoTOP grid cell. The number of grid cells varies between 58 and 7500 among the geological zones, resulting in a representative sample of V_s profiles using one randomisation per grid cell. Three examples of mean and randomised V_s profiles are shown in Figure 4.2.

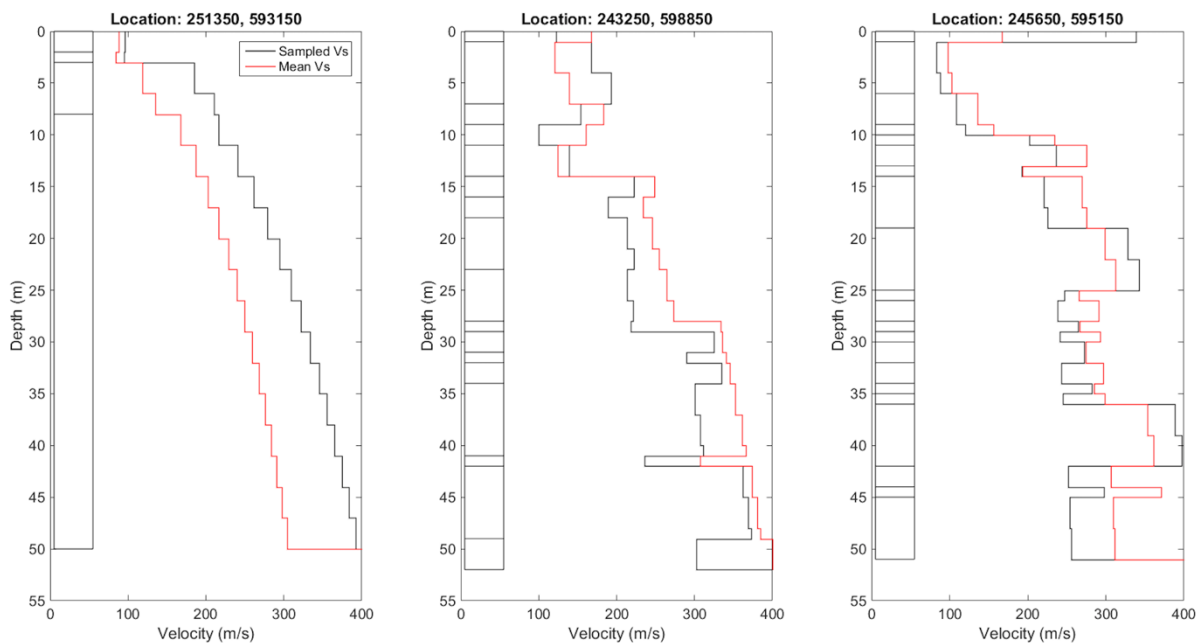


Figure 4.2. Three examples of randomised V_s profiles (*black line*) and mean V_s profiles (*red lines*). The column at the left of each graph indicates the units in the voxel-stack. *Left*: example of homogeneous voxel-stack with only four units of stratigraphy-lithology; *middle and right*: examples of more heterogeneous voxel-stacks. From Kruiver *et al.* (2017a).

MEI V_s

The next depth interval, from 50 m depth to maximum 120 m depth, consists of V_s inferred from inversion of ground-roll (surface waves) from the legacy seismic data from the 1980's. Although the seismic survey design for imaging the reservoir was designed to suppress the generation of surface waves, some ground roll energy was preserved in the seismic data in the frequency band between 1 and 3 Hz. The Modal Elastic Inversion method (MEI) was used for the elastic near-surface model building. The depth sensitivity kernel for the fundamental mode of the Rayleigh wave showed that maximum penetration depth is ~120 m and there is a limited resolving power of velocities in the shallow layers of the model (0 – 20 m). Because of the limited resolution in the shallow layers and the good quality of the GeoTOP V_s model, the MEI

V_s model is used from a depth of 50 m-NAP. An example of a depth slice through the MEI V_s model is shown in Figure 4.3. Distinct zones of relatively low and relatively high V_s values are visible, forming patterns that resemble geological features, such as buried valleys.

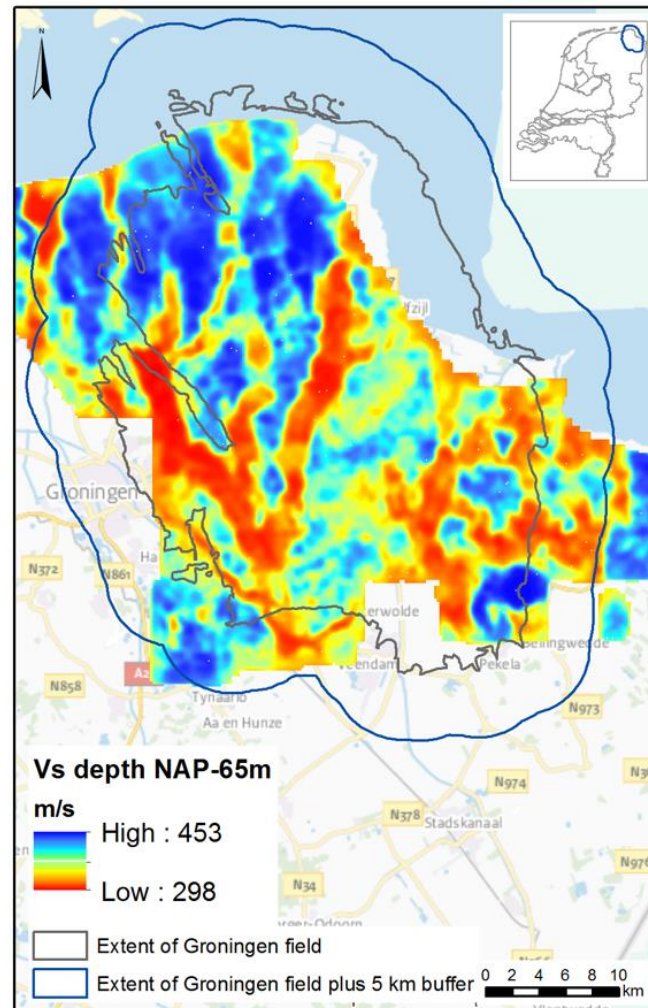


Figure 4.3. Depth slice through the MEIDAS V_s model at a depth of NAP-65 m. From Kruiver *et al.* (2017a).

Sonic V_s

The deepest part, starting from ~70 m to the depth of the reference baserock at ~800 m, consists of the Pre-Stack Depth Migration (PSDM) V_P model that was converted to V_s using V_P/V_s relations derived from two deep well logs in the field. The PSDM V_P model was updated by Romijn (2017) and this updated model has been used since the V6 GMM. The conversion between V_P and V_s is based on the sonic logs at wells BRW-5 and ZRP-2. The conversion is different for the upper and for the lower North Sea Group, using a depth-dependent conversion in the upper and a constant V_P/V_s factor in the lower North Sea Group (see Kruiver *et al.*, 2017a).

In the spliced V_S profile, the transition between the MEI and the sonic V_S profile occurs at a depth where the MEI part would be larger in value than the sonic part. This ensures that the V_S profile is monotonically increasing with depth at the transition. No randomisation of the V_S profile was applied to the MEI and sonic depth range.

4.2. Site Profiles at Recording Stations

In situ shear-wave velocity measurements have been carried out for 80 out of the 99 station locations. The measurements at the B-stations (with the exception of BKMZ, which was installed later and outside the GMM study area), are described by Noorlandt *et al.* (2018). During pilot measurements at three stations, four techniques were tested: SCPT, Multi-channel Analysis of Surface Waves (MASW), cross-hole tomography between three boreholes of 30 m depth and PS suspension logging. The combination of SCPT's and MASW was found most effective in the Groningen setting. These two techniques were applied at the remainder of the B stations. Examples of measured V_S profiles are shown in Figure 4.4 for the locations of four stations, where they are also compared with the *predictions* of the field-wide V_S model discussed in the previous section for those locations. As can be observed, the two sets of V_S profiles are generally in good agreement. The V_{S30} values resulting from the two sets of V_S profiles were also compared for all stations, with the values of the measured profiles being, on average, slightly lower, particularly for the stations with V_{S30} values lower than the network average.

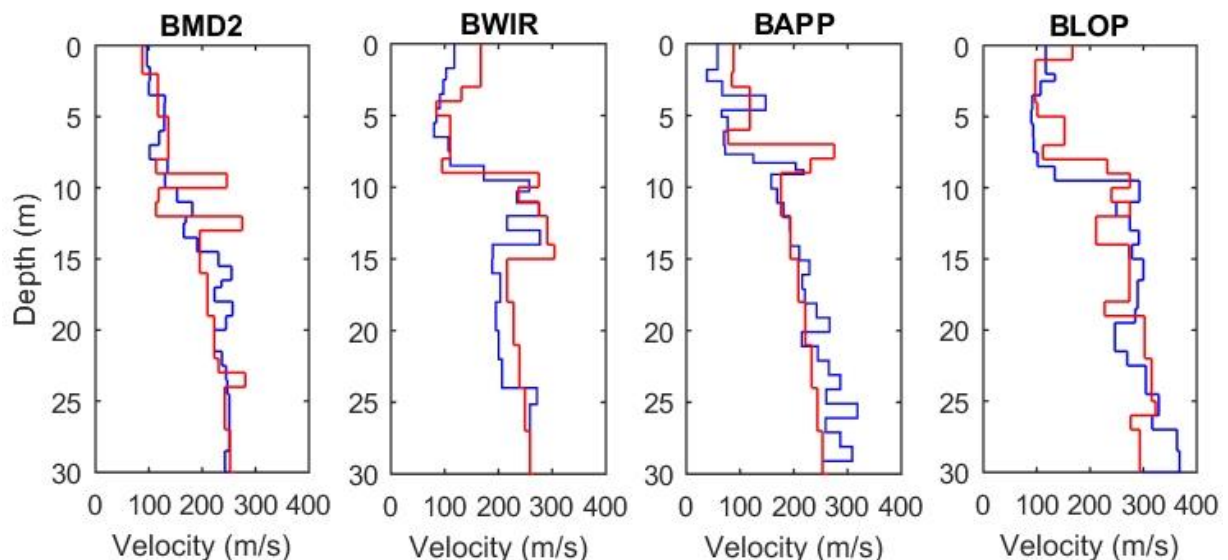


Figure 4.4. V_S profiles at selected B stations. Measured V_S in blue and modelled mean V_S in red. From Noorlandt *et al.* (2018).

During three more rounds of field measurements, Fugro performed CPT's and SCPT's at 64 out of the 80 G stations (Fugro, 2020a, 2020b). The CPT and SCPT data were used to determine the local lithology and V_s . Stations included in the campaigns were prioritized on the basis of the number of usable records they had generated by the time the campaigns took place. The 16 stations that were not covered by the measurement campaigns are: G43, G52, G58, G59, G71, G72, G73, G74, G76, G77, G78, G79, G80, as well as the three G-stations (G150, G530 and G680) which do not produce usable surface records due to malfunctions.

The local V_s and stratigraphy-lithoclass data from the SCPTs were further improved using measured transfer functions (TFs) between 50 and 0 m depth and the lithological description of the top 5 meters. The V_s profile from the SCPT is not reliable over the top part of the soil column (Noorlandt *et al.*, 2018) due to overlapping P- and S-waves, short travel times and noisy records. Nonetheless, the top 1 to 5 metres of the model have a large effect on the TF, both with respect to correct timing of the direct wave as in explaining free-surface reverberations. The top part of the soil column is adjusted with velocity values that match the timing of the measured TF and that are consistent with the lithological description as obtained from the CPT.

The TF is obtained by applying seismic interferometry to borehole records of local seismicity (Ruigrok *et al.*, 2022). Transverse component recordings of local seismicity contain primarily SH waves that propagate nearly vertically over the top 50 meters of the soil column. By deconvolving recordings at 0 m depth by the ones at 50 m depth, S-waves are isolated that have propagated between these two depth levels. Using only a single earthquake, a direct pulse can be obtained whose travel time is close to the actual travel time between 50 and 0 m depth. By stacking deconvolutions over many events, the stationary contributions interfere constructively, and both the direct wave and the main reverberations are correctly retrieved (Wapenaar *et al.*, 2010). In a similar setup, Nakata & Snieder (2012) applied seismic interferometry by deconvolution to boreholes of Japan's KiK-net.

Figure 4.5 shows the updating sequence for station G14 as an example. Before the update, the modeled TF (blue line in Figure 4.5b) is slower than the measured direct wave in the TF (black line in Figure 4.5b). The lithological description shows a sandy clay for the top 3.5 meters. Choosing a uniform velocity of 90 m/s improves the timing of the modeled direct wave. In addition, the timing of free surface multiple over the Holocene sequence, at about 0.5 seconds in Figure 4.5c, is improved. The V_s profile update also improves the match between the modeled and measured amplitude spectra (Figure 4.5d,e).

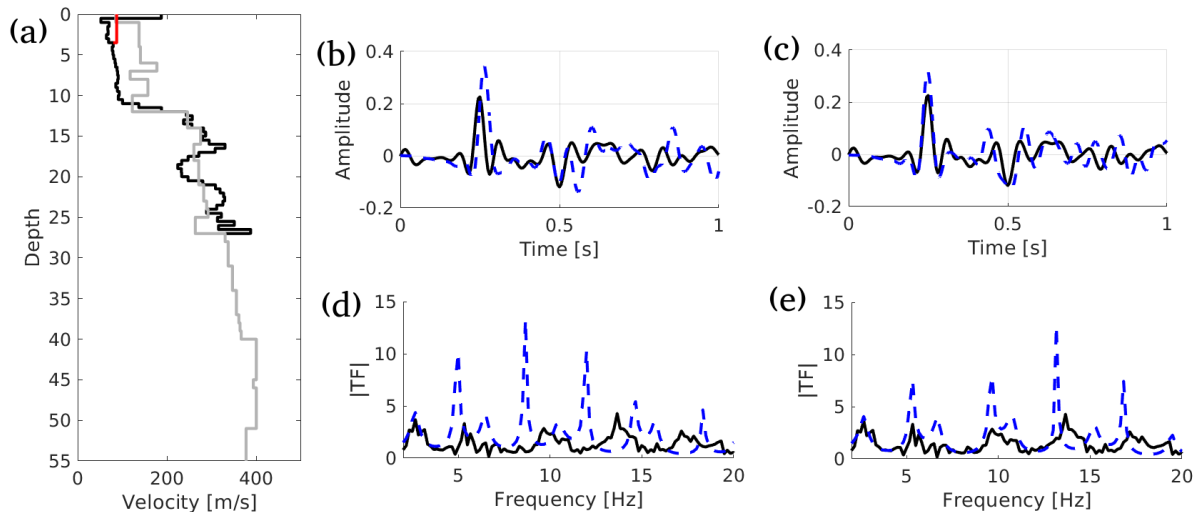


Figure 4.5. Example of using the locally estimated transfer function (TF) for updating the top part of the V_s profile. (a) the Version 6 velocity profile at G14 (*grey line*) with the upper part replaced with the SCPT measurement (black line) from which the top 3.5 meters is replaced by a model (*red line*) consistent with the measured TF between 50 and 0 m depth. (b) and (c) show the measured (black line) and modeled (*blue dashed line*) TF (b) before and (c) after updating the top 3 meters of the model. (d) and (e) show the corresponding amplitude spectra (d) before and (e) after updating the model. The SH-wave TF is modeled without losses. Hence, the modeled amplitudes are somewhat higher than the observed amplitudes, especially for the higher frequencies.

The final V_s profiles at the G stations are used in the linear transfer functions (Section 4.4).

4.3. Soil Damping Model

Damping at G-stations

In Ruigrok *et al.* (2022) different methods are tested to derive damping values from G-station recordings. He *et al.* (2021) apply an adaptation of the spectral-ratio method to boreholes in Groningen. The method we found to be most robust is the so-called up-down method as worked out in Ruigrok *et al.* (2022). With this method, earthquake records at depth are deconvolved by records at the Earth's surface. This results in a response in which the direct up- and down-going waves stand out. In Fukushima *et al.* (2016) the spectral ratio of this up- and down-going wave is used to estimate damping. In our study area, at many stations, strong reverberations in the near surface perturb the spectra of the direct waves. For this reason, we use the maximum method instead (Tonn, 1991).

In Figure 4.6 two examples are shown for the results after applying seismic interferometry to transverse-component recordings. The local SH-wave TFs are

estimated by first deconvolving waveforms measured at depth with waveforms measured at the Earth's surface and then stacking the deconvolutions over local events. The upper trace shows the stacked deconvolution of the recording at the Earth's surface with itself, yielding a band-limited delta pulse. At all other depth levels, the estimated TFs are shown, which show an up-going direct wave at negative times, and a down-going wave at positive times. The damping is then estimated with the maximum method (Tonn, 1991). With this method, the attenuation is extracted from the decay of the instantaneous amplitude and frequency of the up- and down-going wave. This results in an estimate of the attenuation parameter Q or damping ($d=1/2Q$) over the 0-50, 0-100, 0-150 and 0-200 m trajectories. Subsequently, Q values over 50 m depth intervals are obtained with harmonically de-averaging.

The examples in Figure 4.6 show that there is quite strong near-surface scattering and losses at site G20, which is reflected in the character of the estimated TF. In contrast, there is less near-surface scattering and damping at site G30. The mean damping over both sites (over the 200 m depth interval) is 1.71 and 0.94%, respectively.

There are different reasons why the up-down method is attractive. One important aspect is that no correction needs to be made for elastic propagation effects. Although the Groningen subsurface is well characterized, such corrections remain imperfect. Another reason is that small geophone differences between depth levels are not relevant, because up- and down-going waves are compared at the same depth level, thus using the same geophone. The *in situ* geophone response likely varies somewhat from depth level to depth level and station to station, whereas the nominal geophone response is assumed in the processing. Finally, by using a broadband method (the maximum method) the damping estimation is less sensitive to spectral perturbations due to scattered waves.

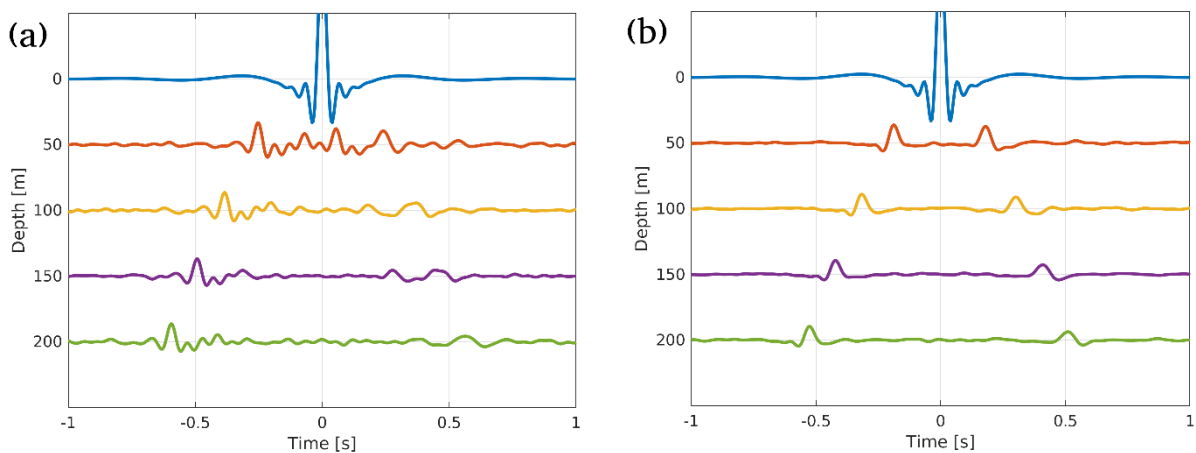


Figure 4.6. The results of applying seismic interferometry by deconvolution at (a) station G20 and (b) station G30, with a virtual source constructed at the 0 m depth level. The transverse-component result is shown in the frequency band [2 20] Hz. At station G20 52 local events are used, for station G30 there are 67 local events.

In Ruigrok *et al.* (2022) damping estimates are made for each depth interval (0 to 50, 50 to 100 m, etc.) For the GMM, however, only the damping estimates over the top 200 m are relevant. For these estimates, only the sensors at 200 and 0 m depth are used. From the 69 G-network stations, the damping estimates of four stations are disregarded, because of known issues with one of the horizontal channels (G050, G454, G494, G634). Damping estimates of stations G35 and G33 are disregarded as well, because of suspicious amplitude behaviour. G354 has a down-going wave that is larger than the up-going wave. G334 has a weak up-going wave. The estimated damping at the remaining 63 sites is shown in Figure 4.7. Figure 4.7a shows that all sites with high velocities in the top 10 m have low damping. Sites with velocities lower than 180 m/s show a large scatter in damping, ranging from 0.5 to 2.7%. Figure 4.7b shows the spatial distribution of the estimated damping values over the top 200 m. There is no obvious spatial pattern, but for a few higher values in the east and, in general, lower damping values in the south. The lower damping values in the south correspond to locations with Pleistocene sands (instead of Holocene peats or clays) in the near surface. The high damping values in the east correspond to locations with a presence of peat.

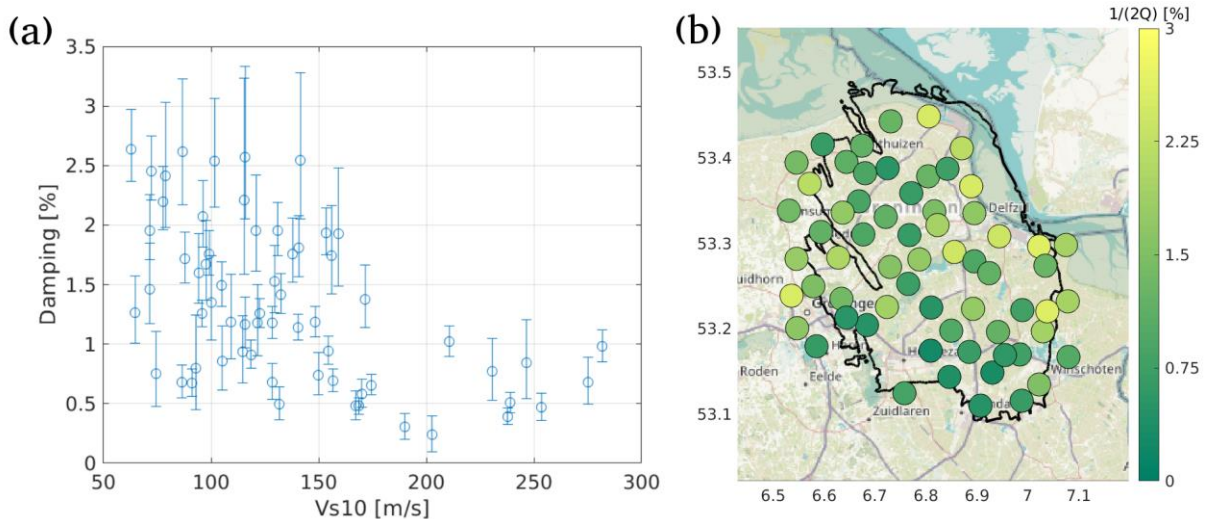


Figure 4.7. (a) Estimated damping over the top 200 m plotted as function of V_{S10} (V_S averaged over the top 10 m). The circles represent the mean damping values for 63 sites. The error bars show the 68% confidence interval. The implemented error propagation is described in Ruigrok *et al.* (2022). (b) Spatial distribution of the mean damping ($1/(2Q)$) values. The black line denotes the outline of the Groningen gas field. Background map is from openstreetmap.org.

Fieldwide damping model

The estimates of the quality factor Q at the stations from the G network correspond to an estimate of the average effect of attenuation from 200 m depth to the surface at the location of these stations. These values are used to develop a field-wide low-strain damping model that can be applied to stations of the B network as well as to all other

locations across the field for the site response analyses described in Chapter 7. The field-wide damping model is a hybrid model that uses the Q values estimated at each of the stations to scale low-strain damping values estimated from published models for the soils underlying each of the stations. The scaling factor (D_{fact}) is obtained for each station using the following steps:

- For each of the G-network stations where Q was estimated, the average effect of damping from the deeper instrument (-200 m) to the surface is estimated using the kappa parameter:

$$(\Delta\kappa)_Q = \int_{z=-200}^{z=0} \frac{1}{QV_S} dz \quad (4.2)$$

- Low-strain damping ($D_{min,lab}$) profiles for each station are constructed using the laboratory-based models of Menq (2003) for sands, Darendeli (2001) for clays, and a model for peats presented in Section 7.2 of this report. The index parameters that are input to these models are obtained either from correlations to the CPT tip resistances measured at the stations, or from parameters associated with each soil type, as described in Section 7.2.
- The D_{min} profiles are integrated to obtain the equivalent effect of damping over the entire column using:

$$(\Delta\kappa)_{D^*} = \int_{z=-200}^{z=0} \frac{2D^*}{V_S} dz \quad (4.3)$$

where $D^* = D_{fact} \times D_{min} < 0.05$ and D_{fact} is a factor that scales the laboratory-based D_{min} values. The values of low-strain damping are limited to 5% of critical damping to prevent unreasonably large damping values.

- The values of $(\Delta\kappa)_Q$ are plotted against the V_{S30} value for each station (Figure 4.8) and a linear model is fitted to the data.
- For each station, the value of D_{fact} is obtained by equating the $\Delta\kappa$ values from Eq. (4.1) with the $\Delta\kappa$ from the linear model in Figure 4.8, using the V_{S30} of each station. The resulting D_{fact} values are plotted in Figure 4.9.

In order to extrapolate the station-specific D_{fact} values to the entire field, the computed factor is plotted versus the V_{S30} value for each station (Figure 4.9). Observe that the D_{fact} is strongly correlated with V_{S30} . Therefore, a linear model [D_{fact} vs. $\ln(V_{S30})$] is fitted to the data in Figure 4.8. Constraints are placed to limit the maximum values of D_{fact} to not exceed the value predicted for the lowest V_{S30} for all the stations considered, and a lower bound of 1.0 is placed to avoid reducing the laboratory estimates of damping. The lower limit is a conservative choice based on the fact that field estimates of damping have been often observed to exceed laboratory estimates due to effects not captured in a laboratory sample (*i.e.*, scattering due to small-scale heterogeneities

in the field, see for example Cabas *et al.*, 2017); on the other hand, there is scant evidence that field damping should be lower than laboratory estimates.

The final model for field-wide low-strain damping is given by:

$$D_{min} = D_{min,lab} \times D_{fact} < 0.05 \quad (4.4)$$

where D_{min} is given in decimal units and

$$D_{fact} = \begin{cases} 1.7 & \text{for } V_{S30} \leq 119.6 \text{ m/s} \\ \exp(5.2874 - 0.9942 \ln(V_{S30})) & \text{for } 119.6 \text{ m/s} < V_{S30} \leq 204.0 \text{ m/s} \\ 1 & \text{for } V_{S30} > 204.0 \text{ m/s} \end{cases} \quad (4.5)$$

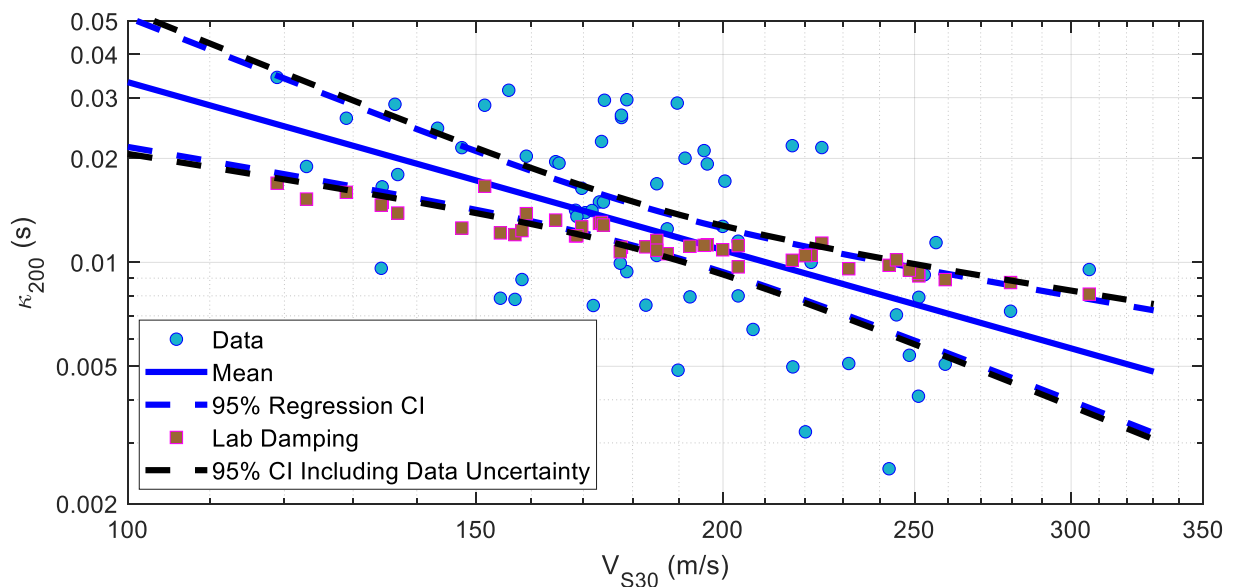


Figure 4.8. Estimates of $\Delta\kappa$ for each station plotted against the V_{S30} for the station. The blue dots (labelled as “Data”) correspond to $(\Delta\kappa)_Q$ (Eq. 4.2); the red squares correspond to estimates of $\Delta\kappa$ using laboratory-based estimates of D_{min} (these are obtained from Eq. (4.3) using unity for the D_{fact}). The dotted lines are 95% Confidence Intervals.

The damping model in Eq. (4.5) and Figure 4.8 corresponds to a best-estimate model for the field. To obtain uncertainty bounds on this model, two uncertainties were considered: the uncertainty in Q estimates, which were propagated to uncertainties in the estimated D_{fact} , and uncertainties in the regression of the $\Delta\kappa$ values for each station versus V_{S30} (Figure 4.8). The latter dominate the uncertainty, as can be seen in Figure 4.9. An upper and lower model for the D_{fact} is obtained using the same approach as for the central value but using the upper- and lower-bound of the 95% Confidence Intervals shown in Figure 4.9. the resulting upper- and lower-bound models are shown

in Figure 4.9. The upper and lower limits on D_{fact} were developed based on the judgment of the authors.

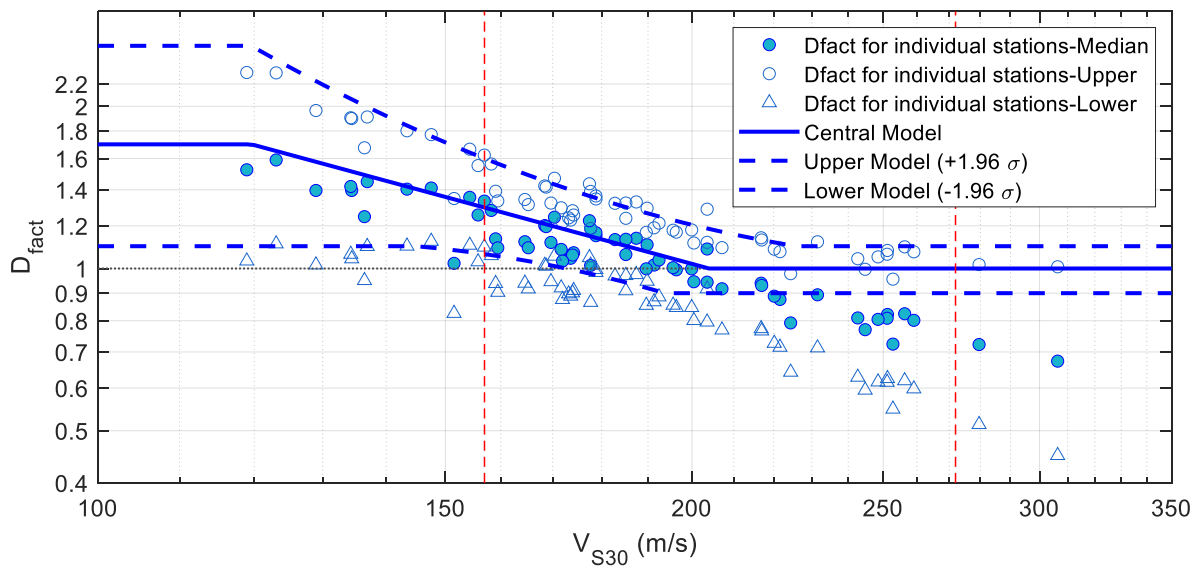


Figure 4.9. Estimates of D_{fact} for each station plotted against the V_{S30} for the station. The central, upper, and lower models correspond to the 95% confidence intervals of the models shown in Figure 4.9. The red dotted lines bound the range of V_{S30} for the zones in the Groningen field (Section 8.1).

A check on the validity of the transfer functions (Section 4.4) and the damping model in particular is to deconvolve separately records from the surface instrument (G0) to the NS_B horizon, and from the borehole instrument (G4) to the NS_B horizon. If the site response model, including the damping profile, are broadly correct over the upper 200m then the deconvolved motions from the surface and borehole instruments would be similar. Ratios of the two sets of deconvolved motions are shown for the V6 model in Figure 4.10. These ratios were similar to those obtained from the V4 and V5 models. Observe that these ratios have a frequency-independent value of around 2. These ratios were recomputed using the proposed damping model and the resulting ratios are reduced to 1.30 (Figure 4.11). This implies that the lower damping values in the V7 model have largely addressed the inconsistency observed in previous versions of the model. If a stricter selection criterion is applied, such as selecting only those stations with a match of empirical and analytical transfer function, the average ratio drops to 1.19.

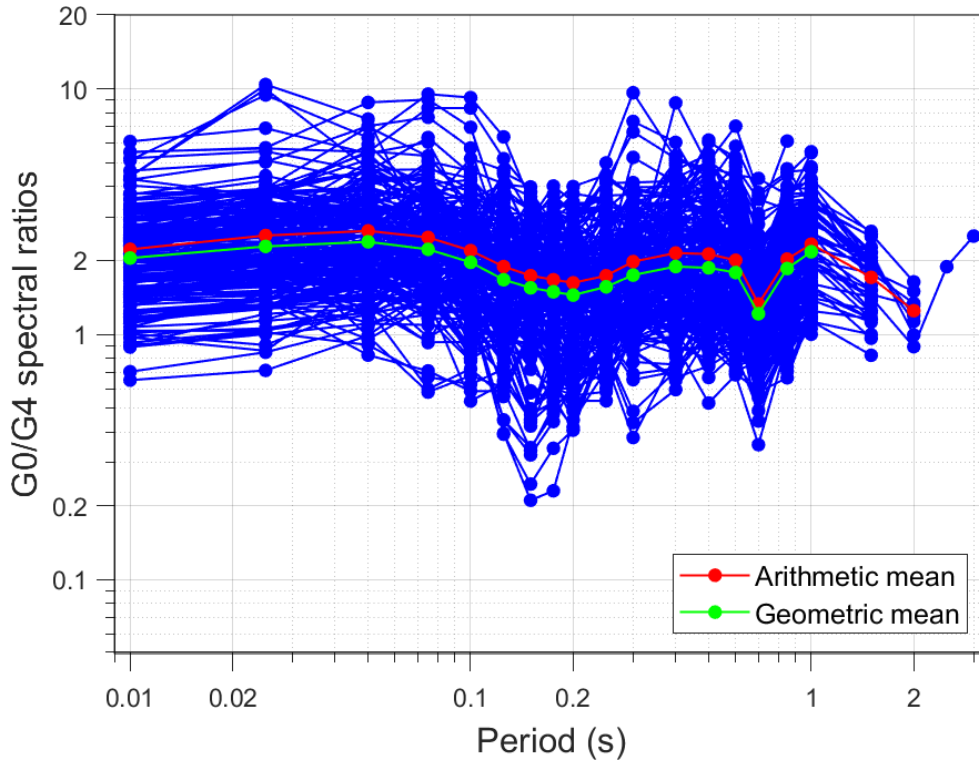


Figure 4.10. Ratios of $Sa(T)$ at NS_B from G0 recordings to those from G4 records using the GMM V6 site response model and the V6 ground-motion database

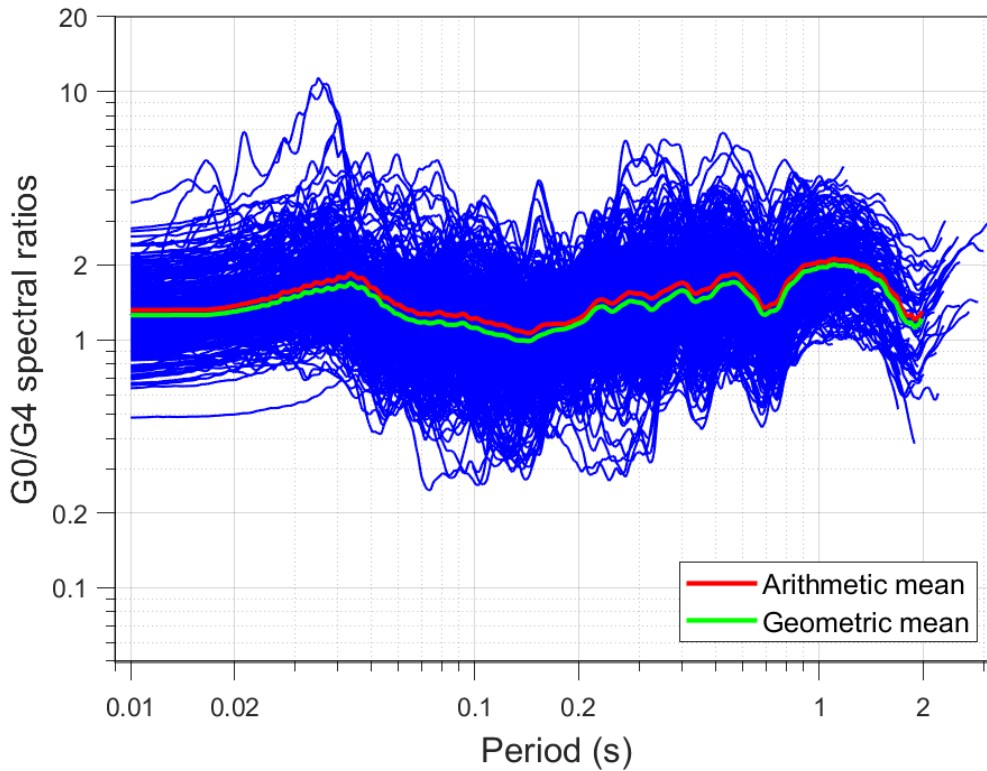


Figure 4.11. Ratios of $Sa(T)$ at NS_B from G0 recordings to those from G4 records using the GMM V7 site response model and V7 ground-motion database. The average G0/G4 ratio between $T = 0.1$ s and $T = 1.0$ s is 1.30.

4.4. Recording Station Transfer Functions and Amplification Factors

In order to develop the GMPE for rock motions at the NS_B horizon, as outlined in Section 2.3, it is necessary to transform the surface recordings to the NS_B horizon. For different elements of the model-building process, both the Fourier amplitude spectra (FAS) of acceleration and acceleration response spectra are required at the NS_B horizon, so factors to convert surface motions to the NS_B are defined in both domains. We refer to Fourier domain factors as the TF, and the spectral domain factors as AF. The methodology applied to calculate these amplification factors is 1D linear analysis using the random vibration theory (RVT) approach as implemented in the program STRATA (see Section 7.4). Due to the low amplitudes of the recorded motions only linear response is expected. Therefore, the inputs needed for computing site response are the V_s and D_{min} profiles described in the previous sections (and unit weight), together with the properties of the elastic half-space starting at the NS_B horizon (*i.e.*, $V_s = 1400$ m/s, unit weight = 21 kN/m³).

Linear TFs are independent of the input motions; however, the linear spectral-domain AFs are a function of the shape of the input motion FAS. This dependence results from the interaction of the corner frequency of the input motions with the effects of the small-strain damping in the soil column. This phenomenon is explained in detail in Stafford *et al.* (2017). The input motions at the NS_B horizon are obtained from the seismological model described in Chapter 5. Since the seismological model is calibrated using response spectra at the surface, linear AFs are needed for its derivation. This implies that an iterative process is required, where preliminary amplification factors are developed first and used to develop an initial version of the seismological model which is then in turn used to develop a new set of input motions. Changes in the amplification functions after one iteration were small thus no additional iterations were deemed necessary. The motions are generated for a range of scenarios reflecting the ranges covered by the recordings: M_L 2.5 to 3.6, and distances from 0 to 20 km.

The analytical TFs computed with STRATA are smoothed using a Konno-Ohmachi filter (Konno & Ohmachi, 1998) with the b -parameter set equal to 40. This value of the b -parameter of the Konno-Ohmachi filter was selected by trial and error. The objective of the smoothing was to eliminate oscillations in the TF that were observed at high frequencies (> 10 Hz), and the selected value eliminated these oscillations without affecting the value of the TF at lower frequencies. The computed and smoothed TFs are shown for selected stations in Figure 4.12.

As indicated before, the AFs are function of the shape of the input motion FAS, thus are scenario-dependent, particularly for short oscillator periods. The AFs for selected stations are shown in Figure 4.13 for all the scenarios considered. Observe that the degree to which the AFs vary from scenario to scenario varies from station to station.

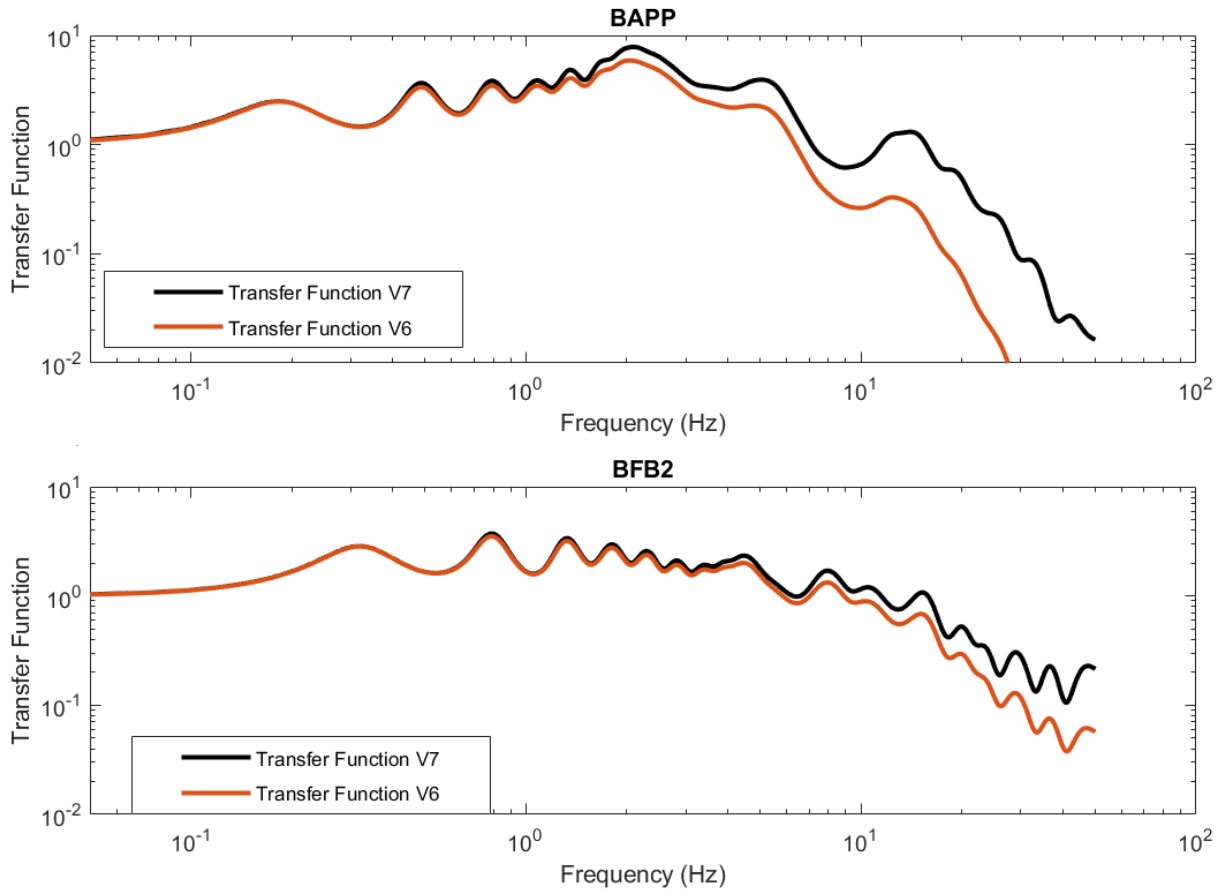


Figure 4.12. Transfer function for the BAPP and BFB2 stations. The TFs for the V6 GMM are shown for comparison.

For magnitudes in the range of the recorded earthquakes at Groningen ($M_L \leq 3.6$), the magnitude dependence of the AFs follows a quadratic trend. The computed AFs were fitted to the following model:

$$\ln AF = [a_0 + a_1 \ln(R)] + [b_0 + b_1 \ln(R)][\min(M, M_{ref1}) - M_{ref1}] + a_2[\ln(R) - \ln(R_{ref})]^2 + b_2[M - M_{ref2}]^2 \quad (4.6)$$

where AF is the amplification factor; M is magnitude; R is closest distance; a_0 , a_1 , a_2 , b_0 , b_1 , and b_2 are period dependent parameters and $M_{ref1} = 4.5$, $M_{ref2} = 3.2$, and $R_{ref} = 10.25 \text{ km}$ are period independent parameters. The model only applies for $3 \text{ km} \leq R \leq 35 \text{ km}$ and for $2.5 \leq M \leq 3.8$.

For distances and magnitudes outside these bounds, the nearest bounding value should be used (e.g., to apply the model to $R=40 \text{ km}$, R should be replaced by 35 km). The magnitude and distance range cover all the recordings used in the development of the V7 model. The parameters of the model were obtained using maximum

likelihood regression. Multiple regressions were conducted, and one parameter was smoothed after each iteration using a Konno-Ohmachi filter (Konno & Ohmachi, 1998; the order was $b_2, b_1, a_2; a_0, a_1$ and a_2 were not smoothed). A sample of the smoothed and unsmoothed coefficients is shown in Figure 4.14 for station BAPP, and a sample of the model fit to the data is shown in Figure 4.15 for stations BAPP and BFB2. The scenario-dependence of the AFs is clearly visible in in Figure 4.15 for selected periods, from which it can be observed that the AFs are dependent both on magnitude and distance. Although the AFs shown are only for two selected stations, the same trends are observed at all stations.

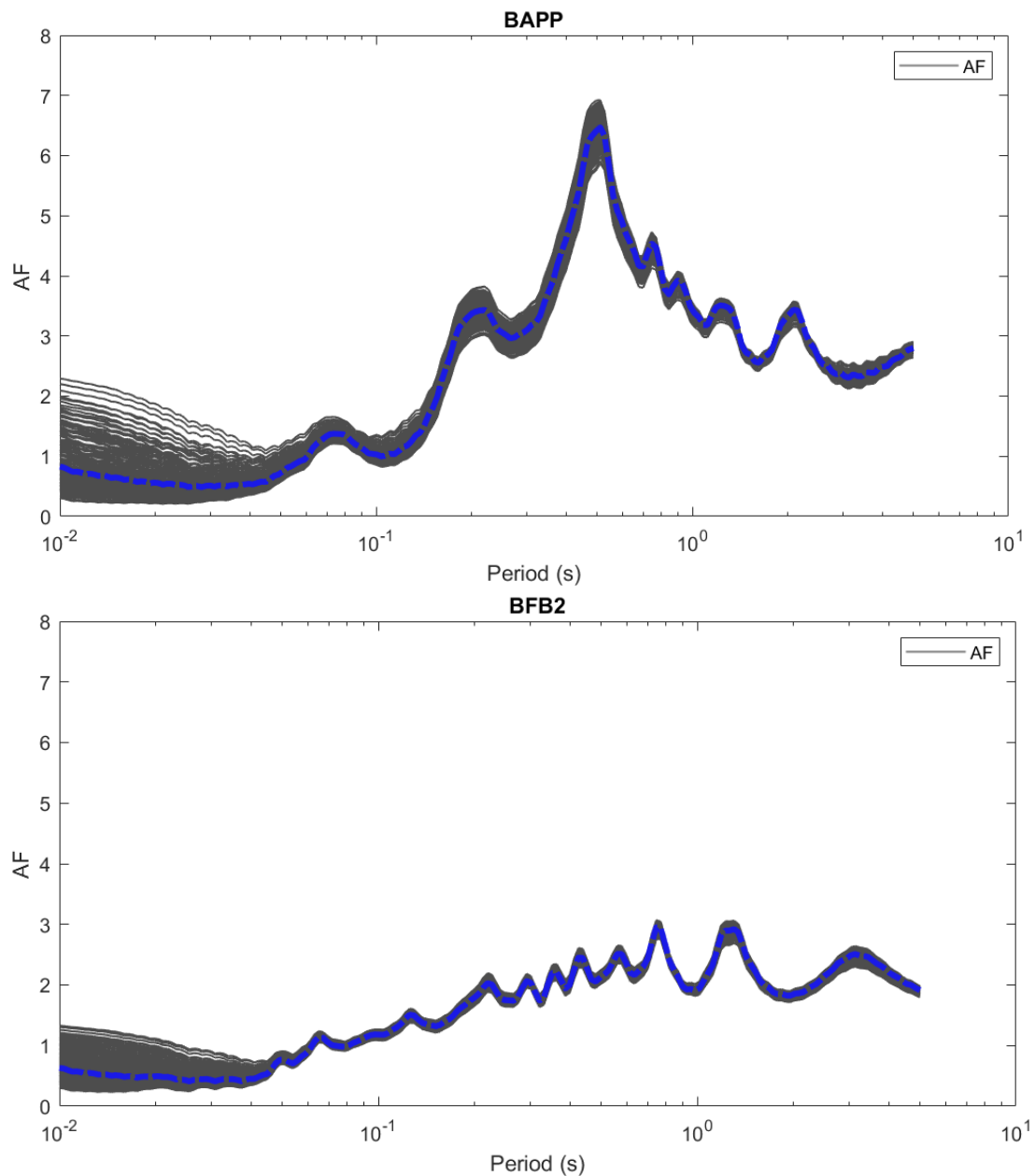


Figure 4.13. Spectral AFs for stations BAPP and BFB2. The thin black lines are for all scenarios considered in the derivation of the station AFs (M 2.5 to 3.6, $R < 20$ km). The dashed blue line is the average of all the scenarios.

BAPP

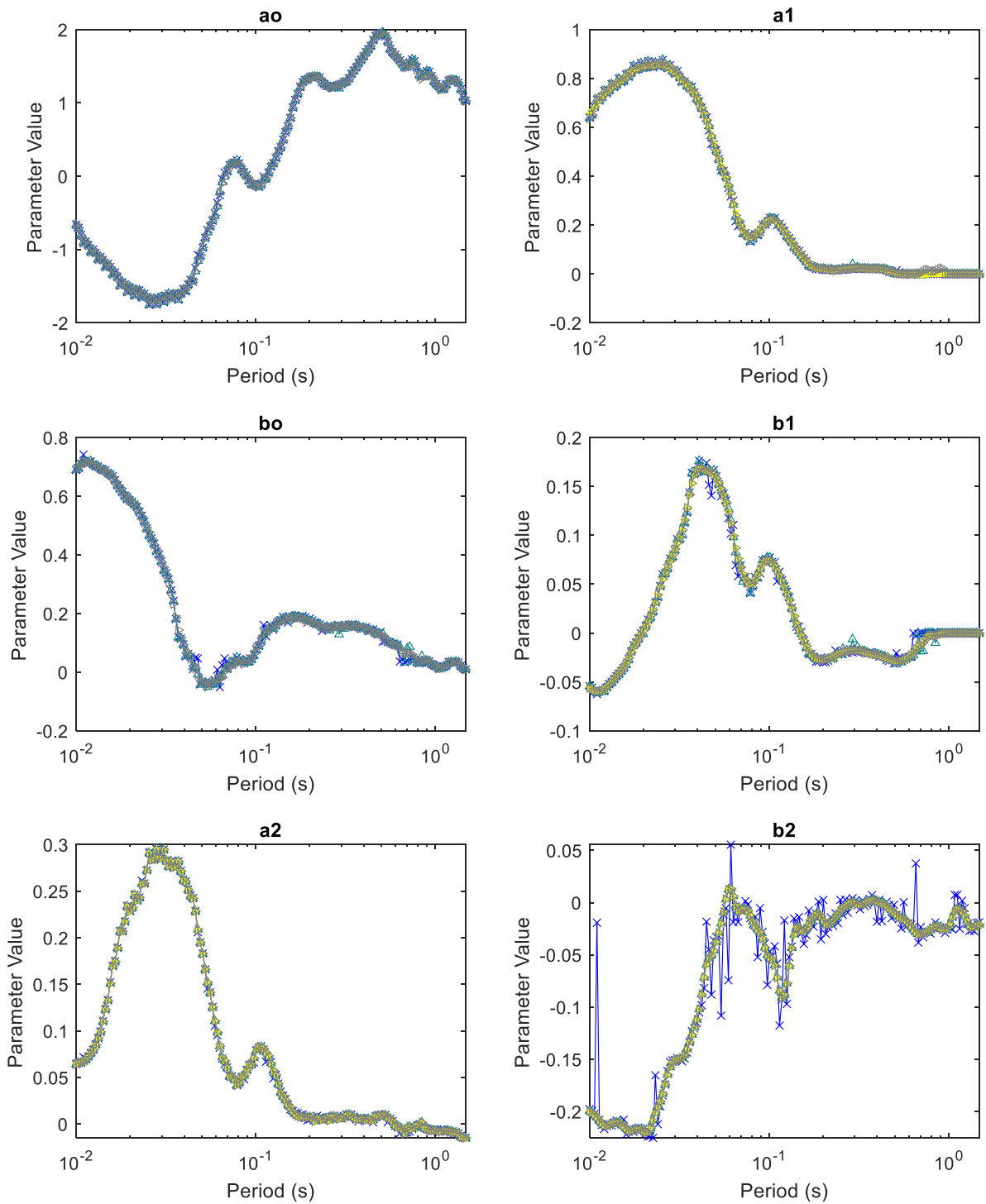


Figure 4.14. Coefficients of the model for the linear AF (Eq. 4.5) for station BAPP. The different symbols represent coefficients for different regression steps.

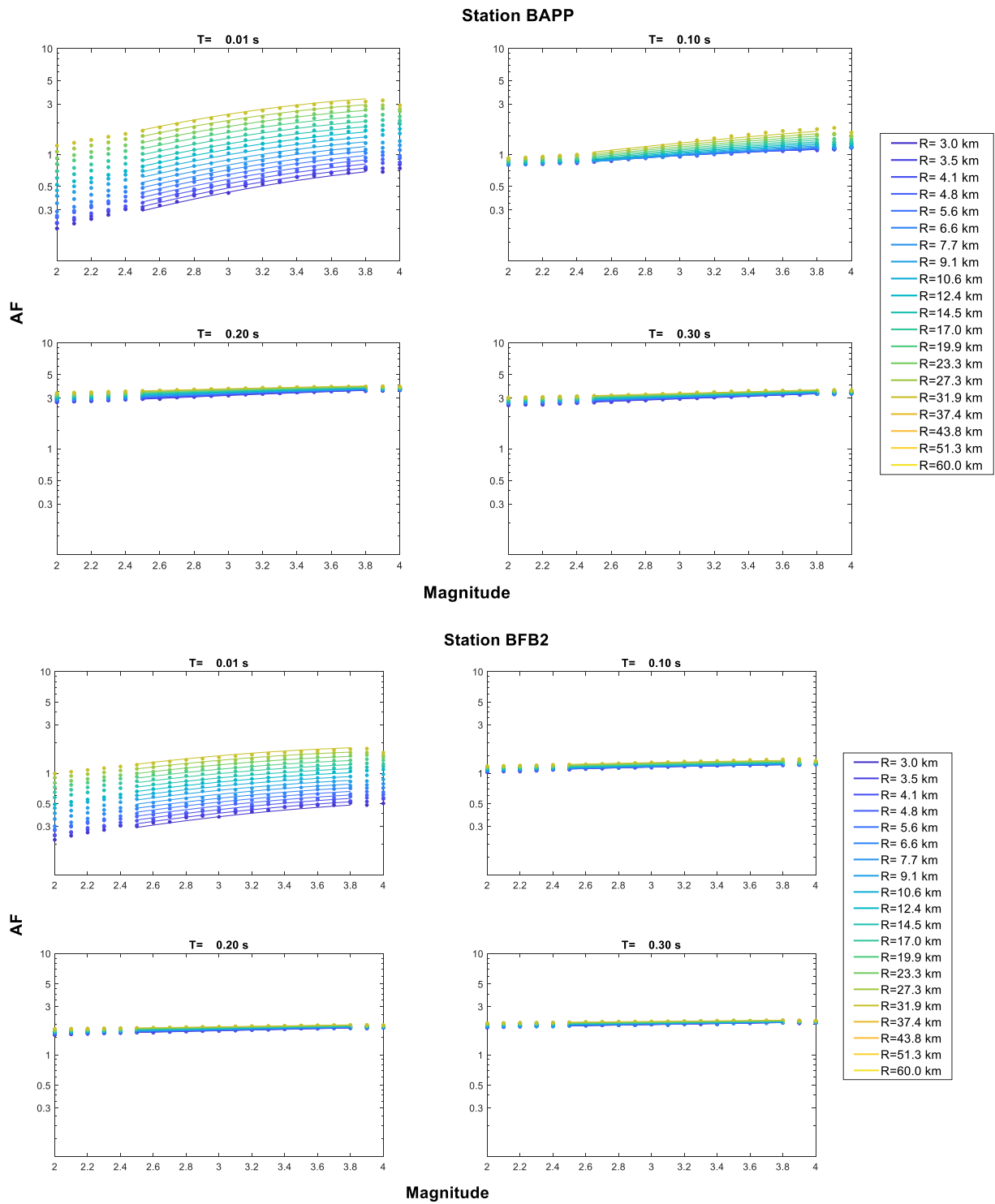


Figure 4.15. Computed AFs (small circles) and the predictive model for selected stations and periods. The AFs are plotted versus magnitude and are colour coded for distance. Models for different distances are plotted.

5. Inversion and Simulation of Reference Rock Motions

As explained in Section 2.3, the GMM is fundamentally composed of two basic elements: a model for the prediction of spectral accelerations at a buried reference rock horizon (the base of the North Sea formation, NS_B), and a model for the non-linear dynamic response of the overlying layers. This chapter focuses on the development of the model for the motions at the NS_B horizon. Since the data available for the Groningen field are limited to magnitudes up to M_L 3.6 and that predictions are currently required up to magnitudes in excess of 7, the model development relies on simulations. The basic parameters for the simulations are first determined from inversions of Fourier amplitude spectra (FAS) of motions deconvolved from the surface to the NS_B horizon. The NS_B motions are discussed in Section 5.1 and this is then followed by a description of the inversions for source, path and site parameters in Section 5.2. Section 5.3 presents the forward simulations for the central model, based on the optimal parameters determined from the inversions. The chapter closes with a discussion of the full logic-tree developed to capture the uncertainty in the forward simulations and the extrapolations to several magnitude units above the upper limit of the database (Section 5.4).

5.1. FAS and Response Spectra at NS_B

Low-strain outcrop motions at a reference horizon are typically determined by removing linear 1D propagation effects (amplification and damping), which occur during wave propagation through overlying strata. In our case, the reference horizon is the NS_B, lying at a depth of approximately 800 m (Sections 2 and 4). Following this approach, the deconvolved acceleration FAS and pseudo-spectral acceleration, $FAS_{NSB'}$ and $PSA_{NSB'}$, respectively, are defined as:

$$FAS_{NSB'}(f) = FAS(f)/|TF(f)|, \quad (5.1)$$

and: $PSA_{NSB'}(T) = PSA(T)/AF(T)$. (5.2)

$FAS(f)$ and $PSA(T)$, which are the 'as-recorded' (surface) spectra, are described in Section 3.2. The site-specific 1D SH transfer functions, $|TF(f)|$, and amplification factors, $AF(T)$, defining linear amplification and damping (in terms of FAS and PSA , respectively) between the NS_B and surface, are described in Section 4.4.

A notable omission in the deconvolution approach defined by Equations (5.1) and (5.2), is the consideration of geometrical and duration effects between the NS_B and surface. These are not accounted for in the derivation of linear site TFs or AFs, nor during non-linear site response analyses (Chapter 7). This is a feature common to site response analyses, rather than their implementation in this project. Typically, this has

negligible impact, as site response analysis is considered over a depth much smaller than the source-site distance. However, in the case of induced earthquakes in Groningen the approximately 800 m over which site response analysis is performed is not substantially shorter than the total path length (approximately 3 to 25 km). This is particularly relevant when considering data recorded at short epicentral distances, where the NS_B to surface distance may comprise of up to a quarter of the complete travel-path.

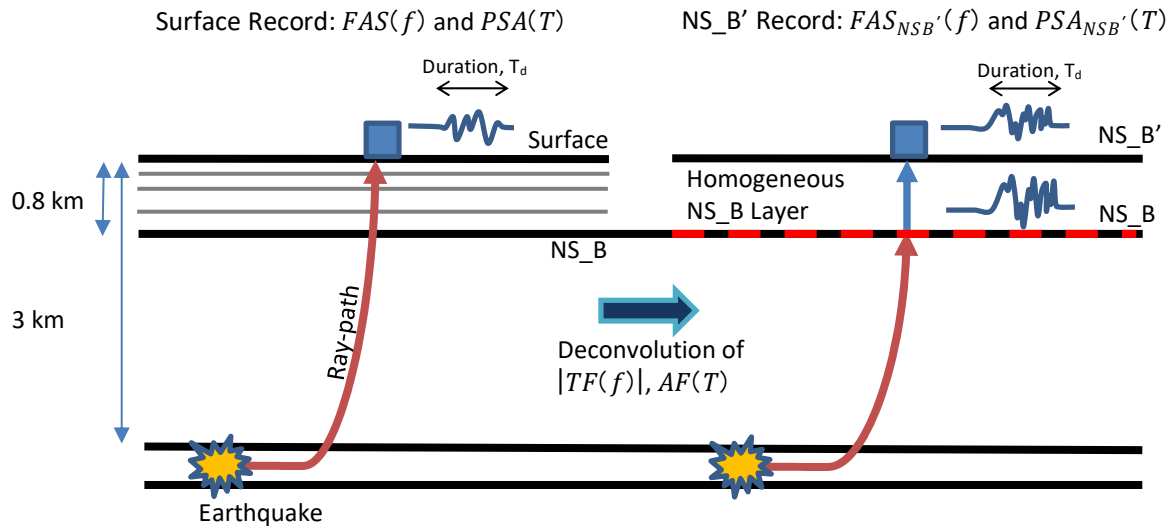


Figure 5.1. Schematic diagram showing the effect of deconvolving $|TF(f)|$ and $AF(T)$ from $FAS(f)$ and $PSA(T)$ to obtain $FAS_{NSB'}(f)$ and $PSA_{NSB'}(T)$, respectively. Duration, T_d , is unaffected by the deconvolution. After deconvolution, only geometrical spreading remains unaccounted for, and can be considered as propagation through an elastic homogeneous layer above the NS_B.

Rather than further modifying the deconvolved spectra, $FAS_{NSB'}(f)$ and $PSA_{NSB'}(T)$, to account for unknown geometrical effects in an attempt to approximate $FAS_{NSB}(f)$ and $PSA_{NSB}(T)$, we instead defer this to the subsequent inversion stage (Section 5.2). Similarly, no modification of $PSA_{NSB'}(T)$ is made to account for the fact that $AF(T)$ does not consider differences in the duration of motion.

$FAS_{NSB'}(f)$ and $PSA_{NSB'}(T)$, as defined in Equations (5.1) and (5.2), can therefore be considered as surface outcrop motions, with the strata between the NS_B horizon and the surface having been replaced with a homogeneous elastic layer that only results in a geometrical effect on the ground motion (Figure 5.1). Note that this consideration is consistent with the forward modelling approach later adopted: (1) anelastic effects are considered up to the NS_B; (2) geometric effects up to the surface, and duration is always modelled as 'at surface', such that final simulated surface motions, after convolution with the relevant NS_B-to-surface site response functions, are consistent with observations thereof.

Figures 5.2 and 5.3 show examples of $FAS_{NSB'}(f)$ and $PSA_{NSB'}(T)$ along with the original surface spectra. The deconvolution typically results in a reduction of low to mid-frequency amplitude in the FAS due to the reduction of NS_B to surface amplification, along with an increase in the high frequency ($f > \sim 10$ Hz) amplitudes due to removal of damping (Figure 5.2). In the response spectra a decrease in the peak period is typically observed, with reduction in mid- to long-period amplitudes and an increase in PGA (Figure 5.3).

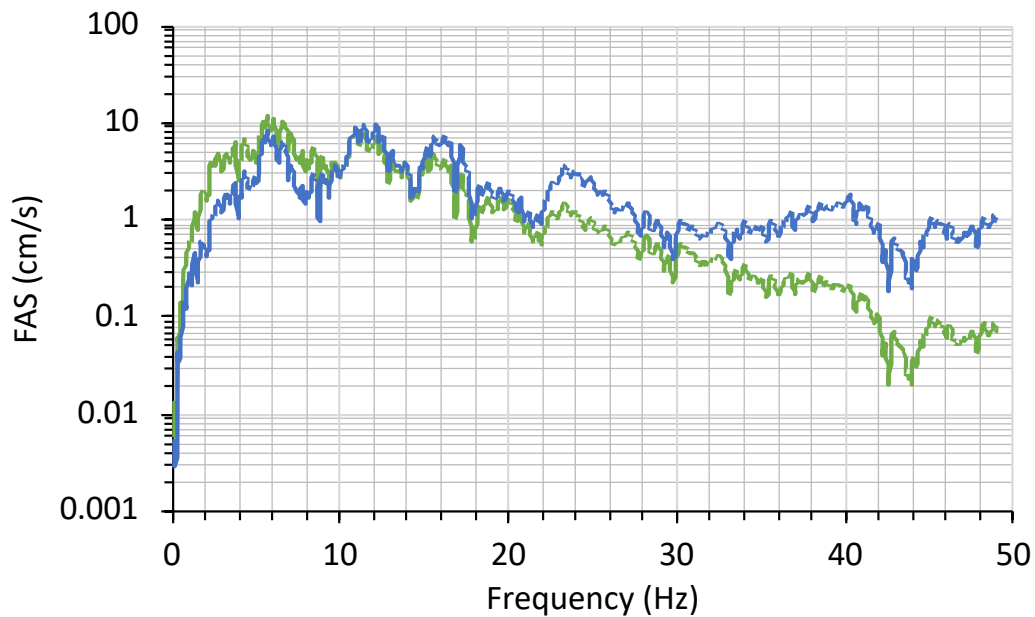


Figure 5.2. Example of surface acceleration $FAS(f)$ (green) and deconvolved $FAS_{NSB'}(f)$ (blue) for recording at site BGAR of earthquake 24 (M_L 3.4).

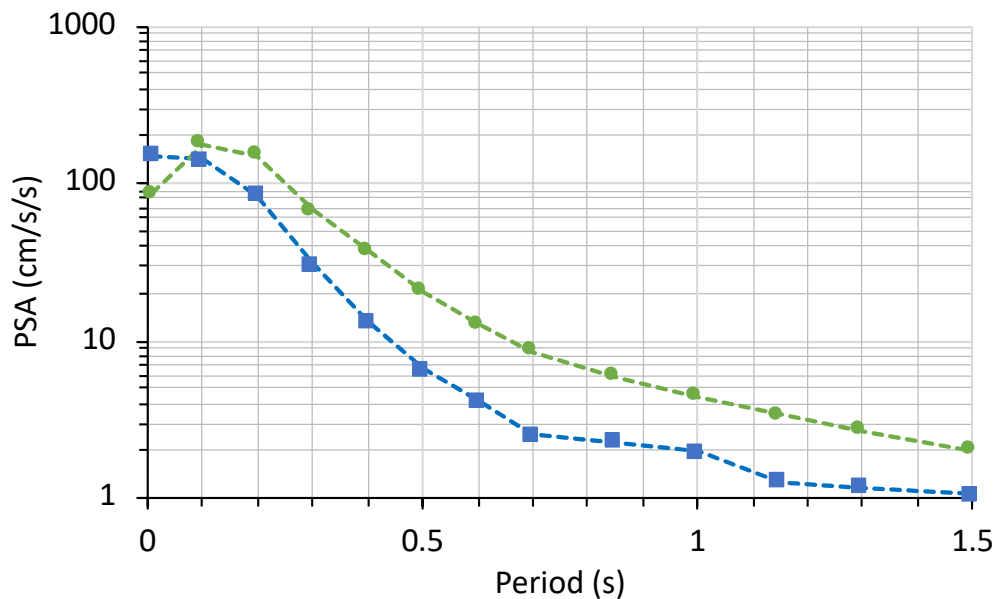


Figure 5.3. Example of surface $PSA(T)$ (green) and deconvolved $PSA_{NSB'}(T)$ (blue) for recording at site BGAR of earthquake 24 (M_L 3.4).

5.2. Inversion for Source, Path and Site Parameters

Root-mean-square (RMS) horizontal component NS_B horizon FAS ($FAS_{NSB'}$) from the 29 $M_L \geq 2.5$ Groningen earthquakes (Sections 3, 5.1), are used in a multi-step inversion framework to determine Groningen-specific source-, path- and reference rock amplification and damping. The RMS horizontal component is an orientation-independent metric, which is consistent with the geometric-mean subsequently used for PSA. All $FAS_{NSB'}$ are used only within their SNR-based usable bandwidth (*i.e.*, between their lower and upper usable frequencies, f_l to f_u , respectively, as detailed in Section 3.2)

Site Specific High-frequency Decay, κ_0

Initially, we determine site-specific high frequency decay (κ_0), following Anderson & Hough (1984). This involves fitting the linear, high-frequency portion of $FAS_{NSB'}$ when plotted as log-acceleration versus linear-frequency. The Anderson & Hough (1984) approach assumes an ω^2 -type source model with the acceleration FAS plateauing above the source corner-frequency, f_c (Brune, 1970) and defines the gradient of the recorded FAS (in log spectral-acceleration) as $-\pi\kappa$ for $f \gg f_c$. The frequency range over which the slope of the FAS is measured is from f_1 (with $f_1 > f_c$) to f_2 , which is below the frequency at which the noise floor begins (Figure 5.4). Note that at this point we are specifically determining the record- (or equivalently, path-) specific parameter κ , not the site-specific κ_0 .

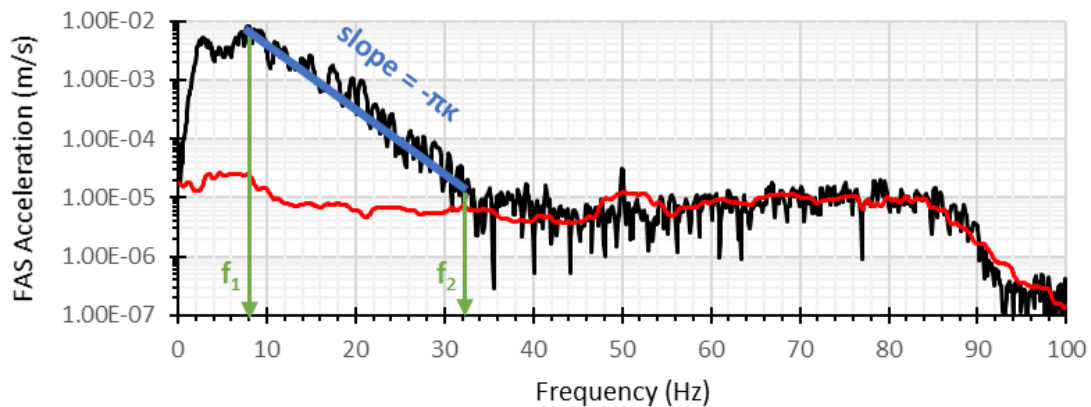


Figure 5.4. Example of κ measured from FAS recorded in the Groningen gas field. The black line indicates the earthquake signal FAS, red is the noise and blue the fitted slope between frequency range f_1 and f_2 .

The decay of the high frequency FAS, as characterised by κ , has, in the past, been attributed to site-, path- and, less typically, source-effects. The majority of studies find that the dominant components of κ are related to the path and site, with measured κ increasing with distance from the source. This has been interpreted as being related to Q , where attenuation, acting along the propagation path, contributes to the loss of high frequency energy, such that:

$$\kappa = t^* = \int_{r=0}^R \frac{1}{\beta(r)Q(r)} dr \quad (5.3)$$

where $\beta(r)$ and $Q(r)$ are the shear wave velocity and Q at given points along the propagation path, respectively. t^* is often used to denote attenuation due to Q , but can be used interchangeably with κ on the assumption that it is caused only by frequency independent Q (and in the absence of source-effects). This interpretation is due to the fact that κ represents a linear decay (in log-FAS versus frequency); frequency-dependent Q would instead manifest as a non-linear decay. From borehole analyses (e.g., Abercrombie & Leary, 1993) it is apparent that the bulk of the observed high-frequency decay is due to attenuation (characterized by low Q) in the uppermost layers of rock and soil. Since the near surface is (i) significantly more heterogeneous than the deeper layers and (ii) the time spent in the near surface is, typically, significantly shorter, it is common, therefore, to separate path and site components of κ in Eq. 5.3:

$$\kappa = \kappa_R R + \kappa_0 = \frac{R_{hyp}}{\bar{\beta} Q_\kappa} + \kappa_0 \quad (5.4)$$

where $\bar{\beta}$ and Q_κ are the average shear wave velocity and average (frequency independent) quality factor, respectively. $\bar{\beta} = 2.2$ is determined for a travel-path in the Groningen field with $R_{hyp} = 9.1$ km, from the arithmetic-average epicentral distance of the data used. κ_0 , is a path-independent site-specific attenuation parameter, attributed to damping in the uppermost layers. The choice of $\bar{\beta}$ is not crucial (as long as consistency in inverse and forward modelling is ensured), since Q_κ will simply increase or decrease proportionally to any changes in $\bar{\beta}$ ($\bar{\beta} Q_\kappa = const$). The resulting path contribution to κ will therefore remain the same.

Conceptually, Eq. (5.4) defines a layer-over-half-space, with the layer depth not explicitly defined. The component of κ that increases with distance from the source is attributed to Q_κ (and $\bar{\beta}$) in the half-space, while the ‘zero-distance’ component, κ_0 , is a repeatable site-effect attributed to propagation in the upper layers (where body wave paths are almost vertical). Consistent with its implementation in forward simulations used in Chapter 7 and Eq. (5.3) for short path lengths, the distance used in Eq. (5.4) is hypocentral distance (between the source and the NS_B horizon). This is in contrast to the epicentral distance used in some studies, which is a more appropriate choice for regional data ($R_{epi} > 30$ km).

The minimum frequency used to measure the slope of the $FAS_{NSB'}$ (f_1) was calculated based on the expected source-corner frequency for a $\Delta\sigma = 5$ MPa earthquake according to the model of Brune (1970). The value of f_1 is therefore set to 10 Hz for earthquakes with $\mathbf{M} \geq 2.7$, and 15 Hz for events with $2.5 \leq \mathbf{M} < 2.7$. The upper frequency ($f_2 = f_u$) is the record-specific usability limit, as defined in Section 3.2. A minimum bandwidth ($f_2 - f_1$) of 10 Hz is required to use each $FAS_{NSB'}$ in the inversion.

After measuring κ for all records with suitable bandwidth (417 out of 648 records, Figure 5.5), κ_0 values for each station are determined by separating the path-average (Q_κ) and site-specific components (κ_0) in Eq. (5.4). Different approaches can be used to decouple the path and site components. In Anderson & Hough (1984) this was performed individually for each station, j , providing a unique, station-specific slope of measured κ versus distance [$\kappa_{r,j}$, equivalent to $1/\bar{\beta}Q_{\kappa,j}$, in Eq. (5.4)]. However, since a field-wide average Q_κ will subsequently be used in the simulations for response spectral ordinates at the NS_B, we require damping, and therefore κ_0 , values consistent with a single field-wide average.

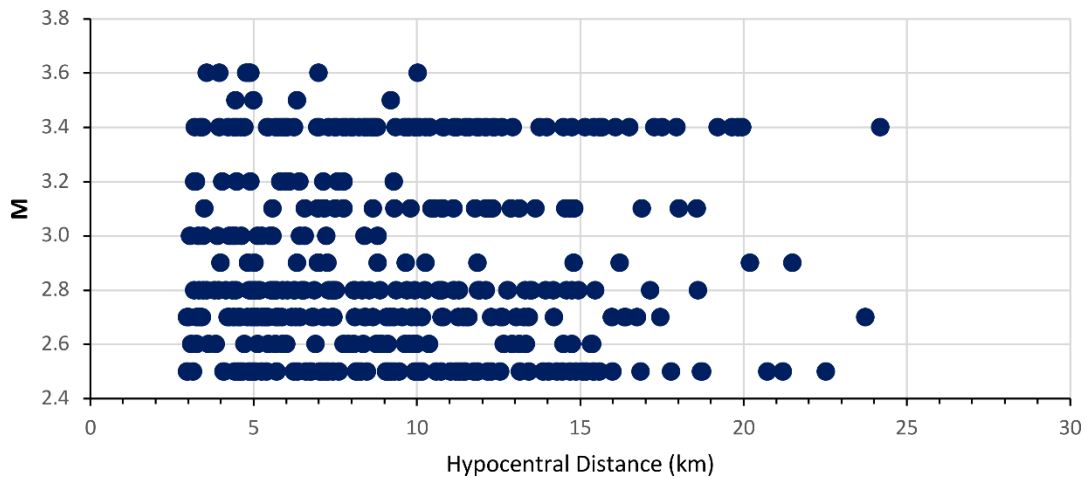


Figure 5.5. Magnitude-distance distribution of data used in inversions.

Two approaches are used to determine the field average Q_κ and site-specific κ_0 parameters: the first is to use an iterative approach—where we can take advantage of an outlier-resistant technique (minimisation of the misfit modulus, L1)—with an initial regression using all stations for a common Q_κ and record-average κ_0 . Subsequent station-by-station regressions are performed using this Q as *a priori*, searching only for the best fitting site-specific κ_0 . The second approach is to solve simultaneously for Q_κ and site specific κ_0 using a least-squares (L2) minimisation. The latter approach avoids issues related to uneven data sampling but is more sensitive to outliers.

Using all available data, the L1 solution for $Q_{\kappa,NSB}$ was 667 using an average shear-wave velocity of $\bar{\beta} = 2.2$ km/s. A bootstrapping procedure was used to estimate the uncertainty, resampling the data 1000 times with random selection (with repetition) in each sub-sample. The resulting $Q_{\kappa,NSB}$ values have a mean value of 658 (with unit standard error limits 651 – 666). Lower and upper limits of the standard-deviation of the bootstrap distribution were 481 and 1042 respectively. In this case, 0.017 s is contributed by the path to κ for the most distant (~ 25 km) records.

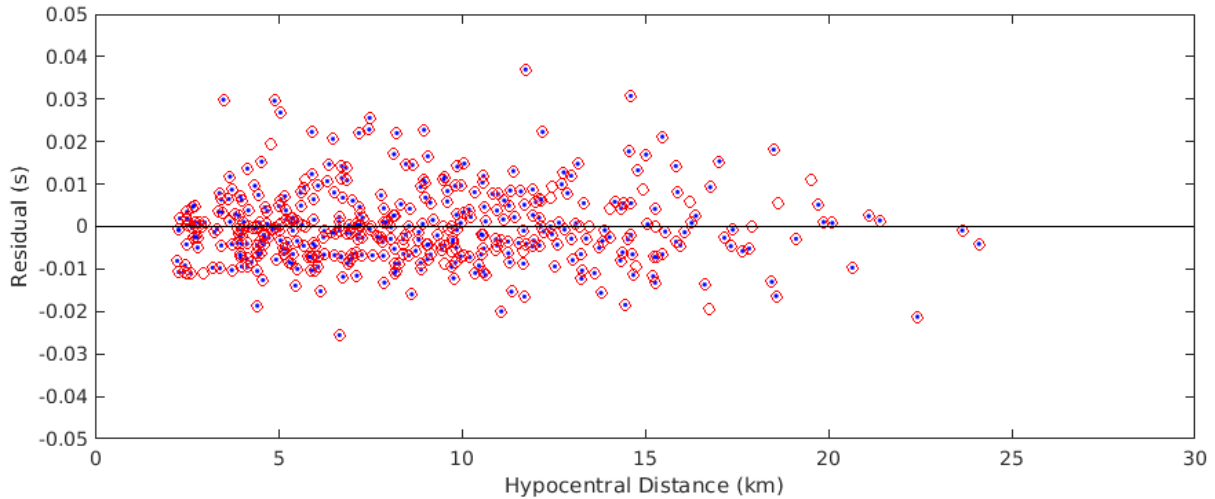


Figure 5.6. Residual κ (measured-modelled) versus distance for the matrix solution. Circles with blue dots are included in the determination of $Q_{\kappa,NSB}$.

Using the matrix approach, a $Q_{\kappa,NSB}$ value of 415 was obtained (Figure 5.6), with unit standard-error spanning 369 to 475. A minimum threshold of 3 records was required for computing Q_{κ} , then in a second step κ_0 values were obtained for all 85 stations (irrespective of record count), with $Q_{\kappa,NSB}$ fixed. The difference between the matrix and iterative bootstrap solutions (667 and 415, respectively) highlights the uncertainty in determining $Q_{\kappa,NSB}$ using records spanning a limited range of distance. However, the differences in $\kappa_{0,NSB}$ are small (0.004 s) when using either $Q_{\kappa,NSB} = 415$ or 658 (iterative and matrix solutions, respectively). Given its reduced sensitivity to station distribution we implement $\kappa_{0,NSB}$ determined by the matrix approach, as listed in Table 5.1. The average $\kappa_{0,NSB}$ is very low, at 0.002 s. In fact, several stations exhibit negative $\kappa_{0,NSB}$, which may be due to over correction for damping during the deconvolution process, or simply statistical uncertainty owing to a limited sample size and low median values.

Table 5.1. Summary of $\kappa_{0,NSB}$

| Station | Matrix, $Q_{\kappa,NSB} = 415$ | | Iterative $Q_{\kappa,NSB} = 658$ | | Difference $\Delta\kappa_{0,NSB}$ (s) | No. Records |
|---------|--------------------------------|----------------|----------------------------------|----------------|--|----------------|
| | $\kappa_{0,NSB}$ (s) | Std. Error (s) | $\kappa_{0,NSB}$ (s) | Std. Error (s) | | |
| BAPP | -0.0058 | 0.0036 | -0.0023 | 0.0039 | -0.0034 | 6 |
| BFB2 | -0.0033 | 0.0029 | 0.0022 | 0.0032 | -0.0055 | 9 |
| BGAR | 0.0236 | 0.0028 | 0.0265 | 0.0030 | -0.0029 | 10 |
| BHAR | 0.0014 | 0.0029 | 0.0055 | 0.0032 | -0.0041 | 9 |
| BHKS | 0.0147 | 0.0029 | 0.0180 | 0.0032 | -0.0033 | 9 |
| BLOP | 0.0049 | 0.0040 | 0.0072 | 0.0043 | -0.0023 | 5 |
| BMD2 | -0.0011 | 0.0031 | 0.0018 | 0.0034 | -0.0029 | 8 |
| BONL | 0.0028 | 0.0051 | 0.0057 | 0.0055 | -0.0029 | 3 |

| Station | Matrix, $Q_{k,NSB} = 415$ | | Iterative $Q_{k,NSB} = 658$ | | Difference | |
|---------|---------------------------|----------------|-----------------------------|----------------|------------------------|-------------|
| | $K_{0,NSB}$ (s) | Std. Error (s) | $K_{0,NSB}$ (s) | Std. Error (s) | $\Delta K_{0,NSB}$ (s) | No. Records |
| BOWW | 0.0082 | 0.0029 | 0.0108 | 0.0032 | -0.0026 | 9 |
| BSTD | 0.0068 | 0.0027 | 0.0098 | 0.0029 | -0.0030 | 11 |
| BUHZ | -0.0007 | 0.0051 | 0.0022 | 0.0055 | -0.0030 | 3 |
| BWIN | -0.0043 | 0.0033 | -0.0013 | 0.0036 | -0.0031 | 7 |
| BWIR | -0.0017 | 0.0025 | 0.0015 | 0.0027 | -0.0032 | 13 |
| BWSE | 0.0222 | 0.0026 | 0.0247 | 0.0028 | -0.0025 | 12 |
| BZN1 | -0.0031 | 0.0062 | -0.0020 | 0.0068 | -0.0012 | 2 |
| BZN2 | 0.0081 | 0.0036 | 0.0110 | 0.0039 | -0.0029 | 6 |
| G010 | 0.0029 | 0.0040 | 0.0071 | 0.0043 | -0.0042 | 5 |
| G020 | -0.0097 | 0.0051 | -0.0054 | 0.0055 | -0.0042 | 3 |
| G030 | -0.0088 | 0.0036 | -0.0038 | 0.0039 | -0.0050 | 6 |
| G040 | 0.0062 | 0.0036 | 0.0099 | 0.0039 | -0.0037 | 6 |
| G060 | 0.0075 | 0.0062 | 0.0121 | 0.0068 | -0.0045 | 2 |
| G070 | -0.0129 | 0.0044 | -0.0075 | 0.0048 | -0.0054 | 4 |
| G080 | 0.0055 | 0.0040 | 0.0091 | 0.0043 | -0.0036 | 5 |
| G090 | -0.0072 | 0.0036 | -0.0039 | 0.0039 | -0.0033 | 6 |
| G100 | -0.0025 | 0.0044 | -0.0002 | 0.0048 | -0.0023 | 4 |
| G110 | 0.0020 | 0.0044 | 0.0059 | 0.0048 | -0.0039 | 4 |
| G120 | 0.0107 | 0.0036 | 0.0154 | 0.0039 | -0.0047 | 6 |
| G130 | 0.0054 | 0.0044 | 0.0079 | 0.0048 | -0.0025 | 4 |
| G140 | -0.0005 | 0.0033 | 0.0019 | 0.0036 | -0.0024 | 7 |
| G160 | 0.0021 | 0.0044 | 0.0074 | 0.0048 | -0.0053 | 4 |
| G170 | -0.0004 | 0.0036 | 0.0026 | 0.0039 | -0.0030 | 6 |
| G180 | -0.0026 | 0.0031 | 0.0002 | 0.0034 | -0.0028 | 8 |
| G190 | 0.0057 | 0.0051 | 0.0088 | 0.0055 | -0.0031 | 3 |
| G200 | 0.0073 | 0.0033 | 0.0118 | 0.0036 | -0.0045 | 7 |
| G210 | 0.0037 | 0.0044 | 0.0075 | 0.0048 | -0.0038 | 4 |
| G220 | -0.0050 | 0.0040 | -0.0012 | 0.0043 | -0.0038 | 5 |
| G230 | -0.0023 | 0.0036 | 0.0003 | 0.0039 | -0.0025 | 6 |
| G240 | 0.0185 | 0.0040 | 0.0218 | 0.0043 | -0.0033 | 5 |
| G250 | -0.0063 | 0.0044 | -0.0008 | 0.0048 | -0.0055 | 4 |
| G260 | 0.0057 | 0.0062 | 0.0103 | 0.0068 | -0.0045 | 2 |
| G270 | 0.0117 | 0.0062 | 0.0146 | 0.0068 | -0.0030 | 2 |
| G280 | -0.0023 | 0.0033 | 0.0016 | 0.0036 | -0.0038 | 7 |
| G290 | -0.0002 | 0.0044 | 0.0028 | 0.0048 | -0.0030 | 4 |
| G300 | 0.0167 | 0.0033 | 0.0213 | 0.0036 | -0.0046 | 7 |
| G320 | 0.0091 | 0.0062 | 0.0141 | 0.0068 | -0.0049 | 2 |
| G330 | -0.0051 | 0.0088 | -0.0016 | 0.0096 | -0.0035 | 1 |
| G340 | -0.0095 | 0.0027 | -0.0055 | 0.0029 | -0.0040 | 11 |
| G350 | 0.0032 | 0.0044 | 0.0078 | 0.0048 | -0.0046 | 4 |

| Station | Matrix, $Q_{k,NSB} = 415$ | | Iterative $Q_{k,NSB} = 658$ | | Difference | |
|----------------|---------------------------|----------------|-----------------------------|----------------|------------------------|-------------|
| | $K_{0,NSB}$ (s) | Std. Error (s) | $K_{0,NSB}$ (s) | Std. Error (s) | $\Delta K_{0,NSB}$ (s) | No. Records |
| G360 | -0.0136 | 0.0040 | -0.0076 | 0.0043 | -0.0060 | 5 |
| G380 | 0.0108 | 0.0088 | 0.0170 | 0.0096 | -0.0062 | 1 |
| G390 | -0.0060 | 0.0036 | -0.0015 | 0.0039 | -0.0045 | 6 |
| G400 | -0.0040 | 0.0031 | 0.0002 | 0.0034 | -0.0042 | 8 |
| G410 | -0.0144 | 0.0040 | -0.0084 | 0.0043 | -0.0059 | 5 |
| G420 | 0.0035 | 0.0062 | 0.0095 | 0.0068 | -0.0060 | 2 |
| G440 | -0.0040 | 0.0040 | 0.0012 | 0.0043 | -0.0052 | 5 |
| G450 | 0.0048 | 0.0033 | 0.0104 | 0.0036 | -0.0055 | 7 |
| G460 | 0.0083 | 0.0062 | 0.0128 | 0.0068 | -0.0045 | 2 |
| G470 | -0.0083 | 0.0088 | -0.0052 | 0.0096 | -0.0030 | 1 |
| G480 | -0.0145 | 0.0088 | -0.0091 | 0.0096 | -0.0053 | 1 |
| G490 | 0.0064 | 0.0051 | 0.0094 | 0.0055 | -0.0030 | 3 |
| G500 | 0.0010 | 0.0062 | 0.0053 | 0.0068 | -0.0044 | 2 |
| G510 | -0.0063 | 0.0088 | -0.0040 | 0.0096 | -0.0023 | 1 |
| G540 | -0.0100 | 0.0088 | -0.0045 | 0.0096 | -0.0054 | 1 |
| G550 | -0.0129 | 0.0040 | -0.0059 | 0.0043 | -0.0070 | 5 |
| G560 | -0.0035 | 0.0062 | 0.0009 | 0.0068 | -0.0044 | 2 |
| G600 | 0.0146 | 0.0088 | 0.0218 | 0.0096 | -0.0072 | 1 |
| G610 | 0.0008 | 0.0036 | 0.0034 | 0.0039 | -0.0026 | 6 |
| G620 | -0.0081 | 0.0044 | -0.0051 | 0.0048 | -0.0030 | 4 |
| G630 | 0.0171 | 0.0044 | 0.0218 | 0.0048 | -0.0047 | 4 |
| G650 | -0.0104 | 0.0088 | -0.0065 | 0.0096 | -0.0038 | 1 |
| G670 | -0.0084 | 0.0036 | -0.0053 | 0.0039 | -0.0031 | 6 |
| G690 | 0.0016 | 0.0062 | 0.0071 | 0.0068 | -0.0055 | 2 |
| G750 | -0.0045 | 0.0051 | 0.0017 | 0.0055 | -0.0062 | 3 |
| G780 | 0.0018 | 0.0062 | 0.0075 | 0.0068 | -0.0056 | 2 |
| GART | 0.0265 | 0.0029 | 0.0287 | 0.0032 | -0.0022 | 9 |
| HOEK | 0.0105 | 0.0040 | 0.0133 | 0.0043 | -0.0028 | 5 |
| KANT | 0.0056 | 0.0040 | 0.0074 | 0.0043 | -0.0017 | 5 |
| MID1 | 0.0170 | 0.0062 | 0.0187 | 0.0068 | -0.0018 | 2 |
| MID3 | 0.0012 | 0.0044 | 0.0030 | 0.0048 | -0.0018 | 4 |
| STDM | -0.0048 | 0.0088 | -0.0030 | 0.0096 | -0.0018 | 1 |
| WINN | -0.0004 | 0.0033 | 0.0015 | 0.0036 | -0.0019 | 7 |
| WSER | 0.0197 | 0.0027 | 0.0220 | 0.0029 | -0.0022 | 11 |
| ZAN1 | 0.0079 | 0.0040 | 0.0100 | 0.0043 | -0.0020 | 5 |
| ZAN2 | 0.0082 | 0.0040 | 0.0233 | 0.0039 | -0.0151 | 5 |
| Average | 0.0018 | ±0.0091 | 0.0058 | ±0.0091 | -0.0039 | |

Frequency Dependent Q

Anelastic path attenuation is usually modelled with a frequency dependent Q . We retain the $\kappa_{0,NSB}$ values from the matrix solution (Table 5.1) and, using the same high-frequency data, search for the best fitting attenuation function of the form:

$$Q(f) = Q_0 f^\alpha, \quad (5.5)$$

with Q_0 the reference Q at 1 Hz. The anelastic attenuation model, describing the decay of the high frequency FAS, $B(f)$, therefore becomes a combination of frequency-dependent path- $Q(f)$ and κ_0 :

$$\begin{aligned} B_{ij}(f) &= \exp\left(-\frac{\pi f R_{ij}}{\bar{\beta} Q(f)} - \pi f \kappa_{0j,NSB}\right) = \exp\left(-\frac{\pi f^{1-\alpha} R_{ij}}{\bar{\beta} Q_0} - \pi f \kappa_{0j,NSB}\right) \\ &= \exp(-\pi f^{1-\alpha} t_{ij}^* - \pi f \kappa_{0j,NSB}), \end{aligned} \quad (5.6)$$

where α is determined through a grid-search with step interval 0.1, decreasing to 0.01 around the misfit minima. The value of $\alpha = 0.42$ is found to best fit the data, with a 2.4 % improvement in misfit with respect to frequency independent model Q ($\alpha = 0$).

Depth-Dependent Q_0

Once site-specific $\kappa_{0,NSB}$ and path $Q(f)$ had been determined, record-specific κ values at the NS_B were re-estimated for all RMS horizontal FAS_{NSB} using a broadband method that extends the inverted frequency range to lower frequencies (*i.e.* to the lowest usable frequency, as defined in Section 3, rather than $f_1 > f_c$). The approach we are using is detailed in Edwards *et al.* (2011) and fits FAS_{NSB} with an earthquake far-field point-source model [*e.g.*, Brune (1970)], defined by a source-corner frequency (f_c) and long-period far-field spectral displacement plateau ($\hat{\Omega}$), along with the t^* parameter to account for anelastic path-attenuation. The FAS for an acceleration time-history is given by:

$$\Omega_{ij}(f) = 4\pi^2 f^2 \hat{\Omega}_{ij} E_i(f, f_{ci}) B_{ij}(f, t_{ij}^*, \alpha) |T_j(f)| \quad (5.7)$$

where f is the frequency and i and j represent the i^{th} source and j^{th} station, respectively; B is the anelastic attenuation along the path, given by Eq. (5.6) [with $\alpha = 0.42$ and $\kappa_{0j,NSB}$ based on the high-frequency (Anderson & Hough, 1984) analyses in Table 5.1]. $\hat{\Omega}$ is a frequency independent parameter that is dependent on the seismic moment (M_0), average amplification, geometrical spreading, shear wave velocity and density at the source, and radiation pattern effects. E is the normalised (*i.e.*, unit amplitude at long-periods) Brune (1970) source model with a defining corner-frequency, f_c :

$$E_i(f, f_c) = \frac{1}{1 + \left(\frac{f}{f_c}\right)^2} \quad (5.8)$$

The site transfer function, T , reflects the amplification between the source and, in this case, the NS_B horizon. In addition, T will accommodate any effects not fully accounted for through the deconvolution to the NS_B, such as resonances.

Frequencies up to 49 Hz (or f_u , whichever is lower) are considered in the inversion. This avoids any potential issue of mains electricity noise (see Section 3). The bandwidth of individual spectra is defined as in Section 3.2. A least-squares minimisation is performed to find the best fitting parameters to Eq. (5.7): a grid-search at 5% resolution is used to determine event-specific f_c , while a guided Powell's conjugate direction method is implemented (at each f_c) to determine corresponding best-fitting record-specific $\hat{\Omega}$ and path-specific t^* . The broadband minimisation is performed on $FAS_{NSB'}$ in the log-amplitude, linear-frequency space in order to focus the fit on high-frequencies [similar to the Anderson & Hough (1984) approach].

Using t^* from the best fitting parameter combinations for each record ($f_{ci}, \hat{\Omega}_{ij}, t_{ij}^*$), we next reconstruct a 1D- $Q_0(z)$ model, based on Eq. (5.3). A 3D Q_0 model is considered unresolvable given the ray-path coverage and, more importantly would be incompatible with the hazard model, which does not account for spatially variable attenuation. The inversion code SIMUL2000 (Thurber & Eberhart-Phillips, 1999; modified by Haberland & Rietbrock, 2001), which performs ray-tracing and non-linear inversion for velocity or Q_0 is used to determine $Q_0(z)$. As shown in Eq. (5.3), measured t^* are dependent on both Q_0 and the velocity along the path. SIMUL2000 cannot account for sharp changes in velocity or fine-scale features. For the 1D velocity model, we therefore implement a 1D simplification of the NAM field model (Figure 5.7), that reproduces the main features, but does not include the high velocity layers bounding the reservoir. Values of V_S are determined through visual inspection of the ZRP-2 and BRW-5 logs (Figure 5.7, *left*; Table 5.2). For the velocity below the V_S log, at 4 km depth and corresponding to the Dinantian Carboniferous group (denoted DC in Figure 5.7), we define V_S and V_P of 2.83 and 5.04 km/s, respectively, based on analyses by Jagt *et al.* (2017). Jagt *et al.* (2017) also show that that waves propagate along the upper DC as critically-refracted head-waves, a feature which is implemented in our ray-tracing model

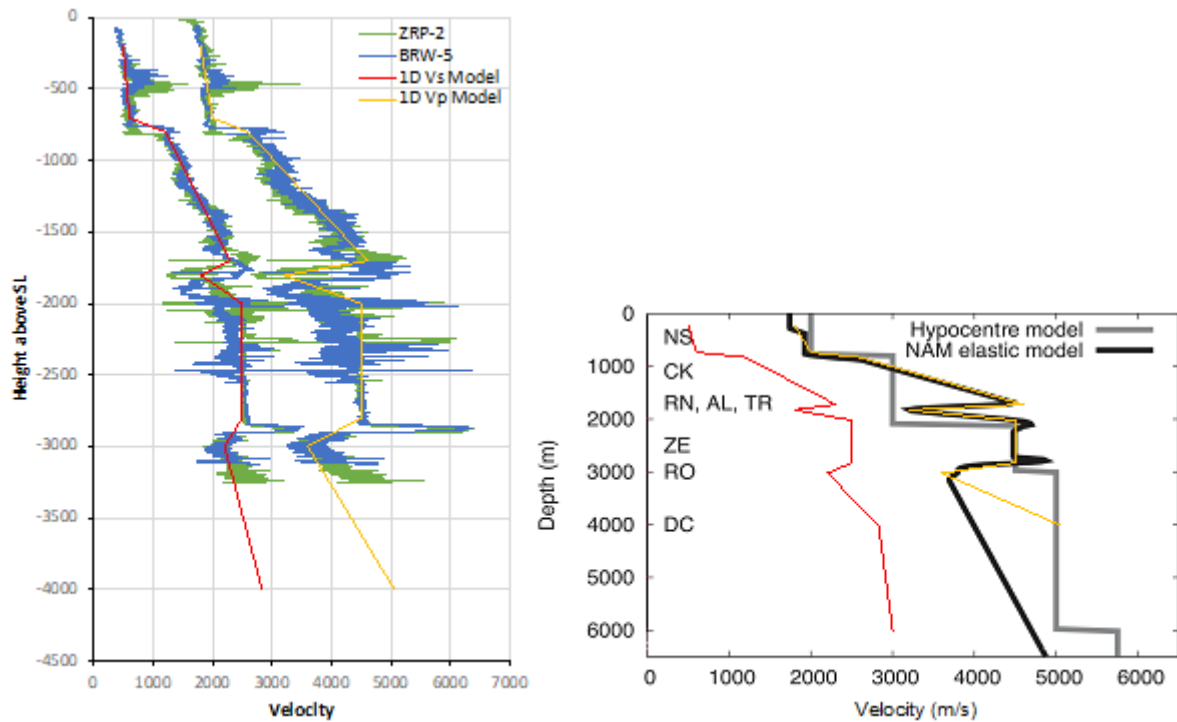


Figure 5.7. 1D V_P (yellow) and V_S (red) models overlaying ZRP-2 and BRW-5 borehole velocity logs (left) and the NAM elastic V_P model (black) and KNMI minimum 1D hypocentre V_P model (grey) [modified after Spetzler and Dost (2017)] (right).

Table 5.2. V_S model.

| Depth (km) | V_S (km/s) |
|------------|--------------|
| 0.2 | 0.5 |
| 0.7 | 0.6 |
| 0.8 | 1.2 |
| 1.7 | 2.3 |
| 1.8 | 1.8 |
| 2 | 2.5 |
| 2.8 | 2.5 |
| 3 | 2.2 |
| 4 | 2.83 |

Table 5.3. Q_0 model.

| Depth (km) | Q_0 (start) | Q_0 (inverted) |
|------------|---------------|------------------|
| 0.2 | -- | -- |
| 0.7 | -- | -- |
| 0.8 | 100 | 63 |
| 1.7 | 100 | 81 |
| 1.8 | 100 | 75 |
| 2 | 100 | 52 |
| 2.8 | 100 | 52 |
| 3 | 100 | 45 |
| 4 | 150 | 61 |

The inversion for Q_0 (at depths corresponding to those in the V_S model, Table 5.2), is non-linear, and is therefore determined through an iterative damped least-squares approach. To determine the degree of damping, we construct a plot of misfit versus model variance. Damping (0.010) is chosen as the knee of this hyperbola: providing low misfit, while limiting model complexity. To constrain the inversion, we link nodes at 0.8, 1.7 and 1.8 km and at 2, 2.8 and 3 km (such that $\Delta Q V_S = const$). Furthermore, for an event of $M = 5.5$, at a depth of 10 km and a distance of 80 km, we force the

path-average $Q(1 \text{ Hz})$ to be consistent with the model of Bindi et al. (2020), who found $Q(f) = 348f^{0.26}$. The model converges after two iterations, and results in an RMS misfit of 0.052 s (without site terms), or 0.043 s (allowing for site terms). The 1D model results in a 6.3 % reduction, compared to the RMS when using a least-squares estimate for a homogeneous half-space ($Q_0 = 58$ and $\bar{\beta} = 2.2 \text{ km/s}$). A rough comparison can be made with the high-frequency analyses (Section 5.2.1) by extrapolation of the $Q(f)$ model: $Q(10 \text{ Hz}) \sim 118$ to 213 and $Q(50 \text{ Hz}) \sim 233$ to 419. The broadband analyses therefore indicate slightly higher damping compared to the high-frequency analyses previously undertaken ($Q_{\kappa,NSB} = 415$), particularly at lower frequencies. Note that t^* , and therefore RMS misfit values are higher for increasingly frequency-dependent $Q(f)$. As a result, direct comparison of misfit with the results of the frequency independent $Q_{\kappa,NSB}$ analyses (e.g., Figure 5.6) is not possible.

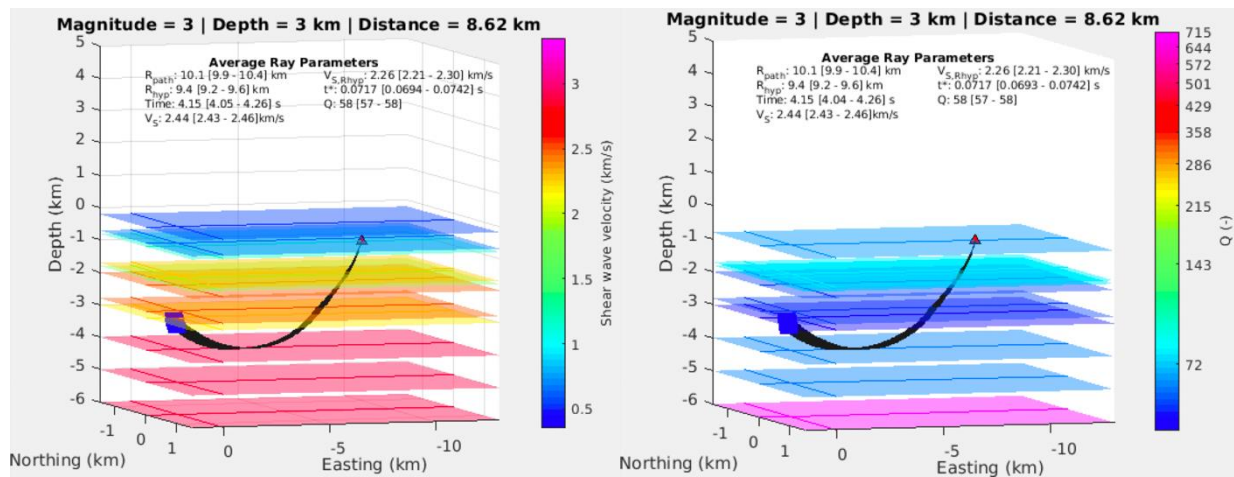


Figure 5.8. Example ray tracing through 1D V_S and Q_0 model between the reservoir and NS_B horizon (-0.8 km). Layer values are shown, with V_S on the left and Q_0 on the right. Path-average and hypocentre-equivalent values of Q_0 and V_S are also shown.

Broadband Model of FAS

Using the V_S and newly derived Q_0 models (Tables 5.2 and 5.3), we forward-model t^* for each of the records in the dataset using SIMUL2000 (Figure 5.8). Then, using these path-specific t^* , the FAS are refit in log-log space to robustly determine the record-specific $\hat{\Omega}$ and the event-specific f_c .

A Bayesian inversion approach was implemented to reduce the strong trade-off between the event stress-parameter (or, equivalently, f_c) and other modelled and unmodelled features. A prior distribution for the stress-parameter was defined using a log-space median and standard-deviation ($\mu_{\log_{10} \Delta\sigma}$ and $\sigma_{\log_{10}(\Delta\sigma)}$). Alternative priors for the stress-parameter distribution were tested with the aim being to reduce strong trade-offs and minimise the overall misfit between recorded FAS_{NSB} (Ω_d) and model

(Ω_m) over all frequencies in the record's usable passband f_l to f_u (see Section 3.2). A wide prior allows for a data-driven solution, while a narrow prior results in a user-controlled solution. The misfit, χ , is minimised after selecting appropriate values for the prior:

$$\chi = -2 \log_e \left\{ \frac{1}{2\pi\sigma_{\log_{10}(\Delta\sigma)}^2} \exp \left[-\frac{\log_{10}\left(\frac{\Delta\sigma}{\mu_{\Delta\sigma}}\right)^2}{2\sigma_{\log_{10}(\Delta\sigma)}^2} \right] \right\} \sum_{f_l}^{f_h} \left\{ \frac{\log_e[\Omega_d(f)] - \log_e[\Omega_m(f)]}{f} \right\} \quad (5.9)$$

Note that the $1/f$ normalisation within the sum of residuals provides a log-based weighting, which, in turn, gives increased weight to the fitting of the source corner frequency and spectral displacement plateau. The stress parameter, $\Delta\sigma$, is related to the source corner frequency and the seismic moment using the Brune (1970) and Eshelby (1957) models:

$$\Delta\sigma = f_0^3 M_0 / (0.4906 \beta_r)^3 \quad (5.10)$$

where M_0 (in SI units) is given by (Hanks & Kanamori, 1979):

$$M_0 = 10^{1.5M+9.05}. \quad (5.11)$$

The shear wave velocity in the reservoir, $\beta_r = 2.29$ km/s (Romijn, 2017), while the moment magnitudes are based on local magnitudes provided by KNMI, given the equivalence $\mathbf{M} = M_L$ (Dost *et al.*, 2018).

For the prior on $\Delta\sigma$, the median was set to 1.5 MPa. This value was the median $\Delta\sigma$ determined in the absence of any prior and resulted in negligible difference between prior and posterior median values when implementing Eq. 5.9 (*i.e.*, we avoid influencing the median $\Delta\sigma$, aiming only to reduce its variability). A wide standard deviation 0.65 \log_{10} unit was used. This is much higher than the values inferred by Cotton *et al.* (2013) from analysis of GMPEs for PGA (0.11 – 0.26), and consistent with the standard deviations observed from spectral fitting (which are assumed to overestimate the variability of $\Delta\sigma$, Cotton *et al.*, 2013). This choice was made to avoid overcontrolling the posterior, preferring, on balance, a data-controlled result. The Brune (1970) stress drops calculated for the events are shown in Figure 5.9. The mean value was 1.47 MPa (median 1.48 MPa) with a \log_{10} standard deviation of 0.15.

In a final step, the far-field spectral displacement plateau, $\widehat{\Omega}$, is split into average site amplification and geometrical decay as a function of distance. The far-field long period spectral amplitude is defined as:

$$\widehat{\Omega}_{ij} = \Omega_{0i} A_j S_{ij}(R, R_{0..n-1}, \lambda_{1..n}) \quad (5.12)$$

where $S_{ij}(R, R_{0..n-1}, \lambda_{1..n})$ is the amplitude decay with distance or ‘apparent geometrical spreading’, given by:

$$S_{ij}(R, R_{0..n-1}, \lambda_{1..n}) = \begin{cases} \left(\frac{R_0}{R}\right)^{\lambda_1} & R \leq R_1 \\ S(R = R_1) \left(\frac{R_1}{R}\right)^{\lambda_2} & R_1 \leq R \leq R_2 \\ \vdots & \vdots \\ S(R = R_n) \left(\frac{R_n}{R}\right)^{\lambda_n} & R \geq R_n \end{cases} \quad (5.13)$$

with R the hypocentral distance, R_n are distances at which the rate of decay changes from λ_n to λ_{n+1} , and R_0 is the rupture radius. A_j is the frequency-independent average site amplification, and Ω_0 is the long period plateau value at the source (Brune, 1970):

$$\Omega_{0i} = \frac{M_{0i} F \theta}{4\pi\beta^3 \rho R_0} \quad (5.14)$$

where F is the free surface amplification ($F = 2.0$ for normally incident SH waves and a good approximation for SV) and ρ is the crustal density ($\rho = 2600 \text{ kgm}^{-3}$). Due to the definition of Equations (5.12) to (5.14), the rupture radius (R_0) cancels out and does not need to be explicitly determined. Furthermore, since \mathbf{M} , and therefore M_0 are pre-defined, and we assume a constant radiation pattern coefficient of $\theta = 0.55$ (Boore & Boatwright, 1984), the only remaining terms to determine are (i) site average amplification, A_j , and (ii) variables related to the geometrical decay (Eq. 5.13).

Using the long-period displacement plateau ($\hat{\Omega}$) of $FAS_{NSB'}$, the geometrical decay function, S , along with average site amplification was inverted for using singular value decomposition, fixing the moment magnitudes by assuming equivalence $\mathbf{M} = \mathbf{M}_L$. The hinge points of the geometrical spreading function ($R_{1..n}$) were selected to coincide with the distances observed during the full waveform simulations undertaken at Shell: 7 km and 12 km, as detailed in Edwards *et al.* (2018). An additional hinge point is located at 2 km (just below the minimum observed hypocentral distance), such that the decay rate ~3 to 7 km is data controlled. The shape of the decay observed is similar (although less pronounced) to that seen during full waveform simulations (Edwards *et al.*, 2018), confirming that the velocity structure has a strong impact on the recorded amplitudes as a function of distance. The decay rates observed were: $R^{-0.49}$ up to 2 km, $R^{-1.53 \pm 0.11}$ from 2 to 7 km, $R^{-0.67 \pm 0.11}$ from 7 to 12 km and $R^{-0.69 \pm 0.10}$ from 12 to 25 km. There is no uncertainty assigned to the first rate of decay, as it is defined by the selected \mathbf{M} values (and segmentation distances). Although there are no data beyond around 25 km, we assume R^{-1} , as determined by full waveform analyses. The results show that decay between 7 and 25 km is similar, with exponents of $R^{-0.67}$ and $R^{-0.69}$ before and after 12 km.

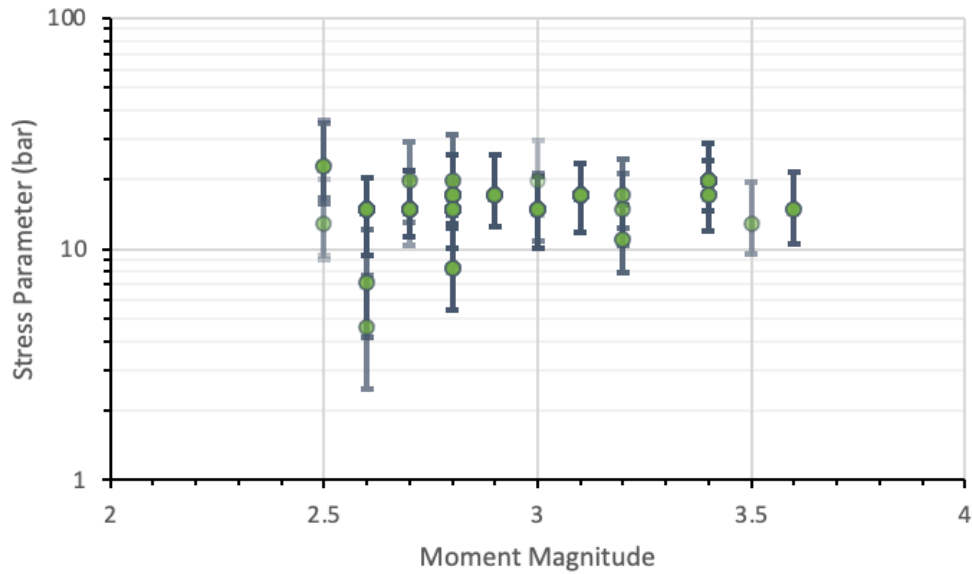


Figure 5.9. Inverted stress parameters plotted against moment magnitude. Symbol transparency indicates the number of recordings used (darker indicates more records; refer to Section 3). Note that 1 bar = 0.1 MPa.

In order to define a field average transfer function, $|T(f)|$, at the NS_B, the (geometric) average amplification (source to NS_B) of all sites was computed (Figure 5.10). Amplification was found to be almost negligible (compared to near-surface amplification) and broadly frequency-independent between ~ 0.8 and 30 Hz. This suggests that the effect of the velocity structure between the source (the reservoir) and the NS_B interface results, overall, in no significant resonance at the periods of engineering interest. At high frequency (> 10 Hz), amplification increases slightly, and plateaus at ~ 1.2 . The overall amplification (from low to high frequency) is consistent with expectations from quarter-wavelength modelling of the velocity profile.

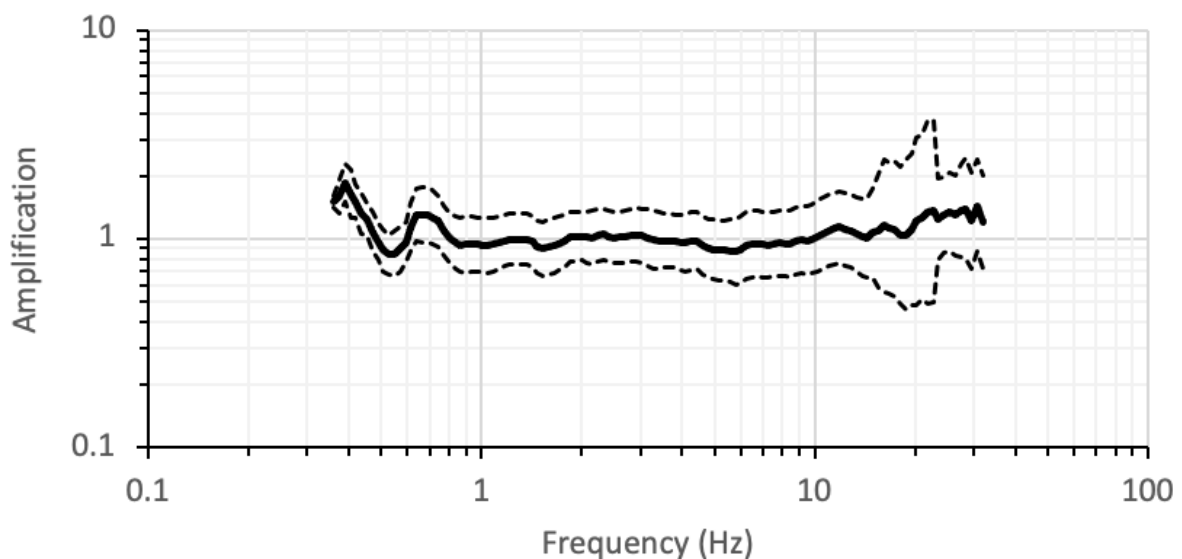


Figure 5.10. Inverted NS_B transfer function, $|T(f)|$.

5.3. Calibration of Central Model Parameters for Simulations

The inversions described in Section 5.2 yield a suite of source-, path- and site-specific parameters that can be used to predict record-specific $FAS_{NSB'}$. Simulations for $PSA_{NSB'}$ are, at a later stage in the GMM development, undertaken using finite-fault, stochastic simulations (see Section 6.1). The method implemented is based on a discretised rupture model with dynamic corner-frequency (EXSIM: Motazedian & Atkinson, 2005; EXSIM_dmb: Boore, 2009). Each of the distributed sub-faults in this technique is assumed to be a point source, the FAS of which can be characterised using the previously derived seismological parameters (Eq. 5.7, Section 5.2). However, for the purposes of the GMM, a unique combination of event- and site-specific terms, namely $\Delta\sigma$ and κ_0 , is sought that yield $PSA_{NSB'}$ that best reproduce the recordings over the *entire* field (as opposed to event- and site-specific predictions). We term this ‘best estimate’ model the *central model*. In the following, we therefore seek to calibrate the simulation model to produce unbiased measures of $PSA_{NSB'}$ with respect to the field data, using single pairs of $\Delta\sigma$ and κ_0 .

As noted above, simulations, described subsequently, were performed using EXSIM, which performs time-domain calculations, and is significantly slower than the point-source code SMSIM (Boore, 2005). SMSIM can make use of random-vibration theory to speed up the simulation when only peak-amplitude ordinates (e.g., PSA) are required. For small magnitude events, EXSIM_dmb has been shown to produce consistent results to SMSIM (Boore, 2005, 2009), which was verified during development of the earlier V4 GMM. We therefore implement SMSIM for calibration of the simulations with field data.

Based on initial observations and broadly spanning the model space, we defined a range of candidate $\Delta\sigma$ and κ_0 values for use in the simulations of $PSA_{NSB'}$. A grid-search was undertaken covering this range: κ_0 equal to 0.0001, 0.001, 0.0015, 0.002, 0.0025, 0.003, 0.005 and 0.008 s; $\Delta\sigma$ equal to 0.5, 1.0, 1.5, 1.8, 2.0, 2.2, 2.5, 3.0, 3.5, 4.0, 5.0 and 7.0 MPa. All simulations used the $Q(f, z)$ model (including ray-tracing), the geometrical spreading model, S (Eq. 5.13), and the source to NS_B transfer function, $|T(f)|$ (Figure 5.10), as determined in Section 5.2. Below 0.5 Hz it was considered that insufficient data were available to constrain the transfer function and therefore amplification is assumed to be equal to unity.

In the simulation, the following choices are made regarding the propagation paths: path lengths are considered as reservoir-to-NS_B for anelastic propagation (beyond which, site response accounts for all damping and amplification effects); while the full reservoir-to-surface path length must be used to account for geometric spreading. Simulated $PSA_{NSB'}$ were compared to the geometric mean horizontal component response spectra at the NS_B horizon for all 13 spectral periods for which recorded data were available (0.01 to 1.5 s).

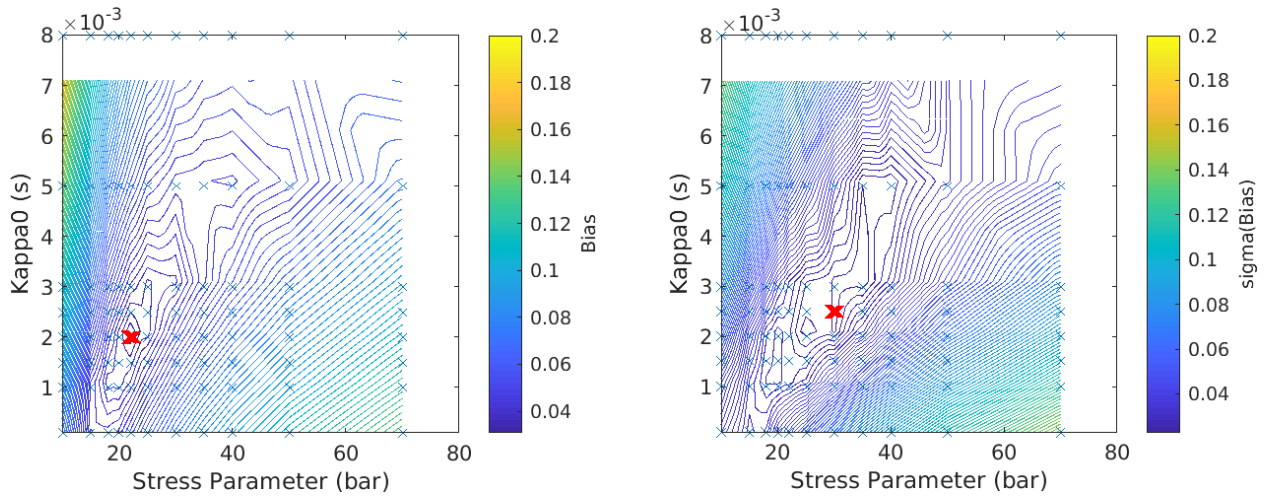


Figure 5.11. Mean bias (*left*) and the standard deviation across all periods (*right*) plotted against stress parameter and κ_0 . The red cross indicates the minimum value of bias or standard deviation.

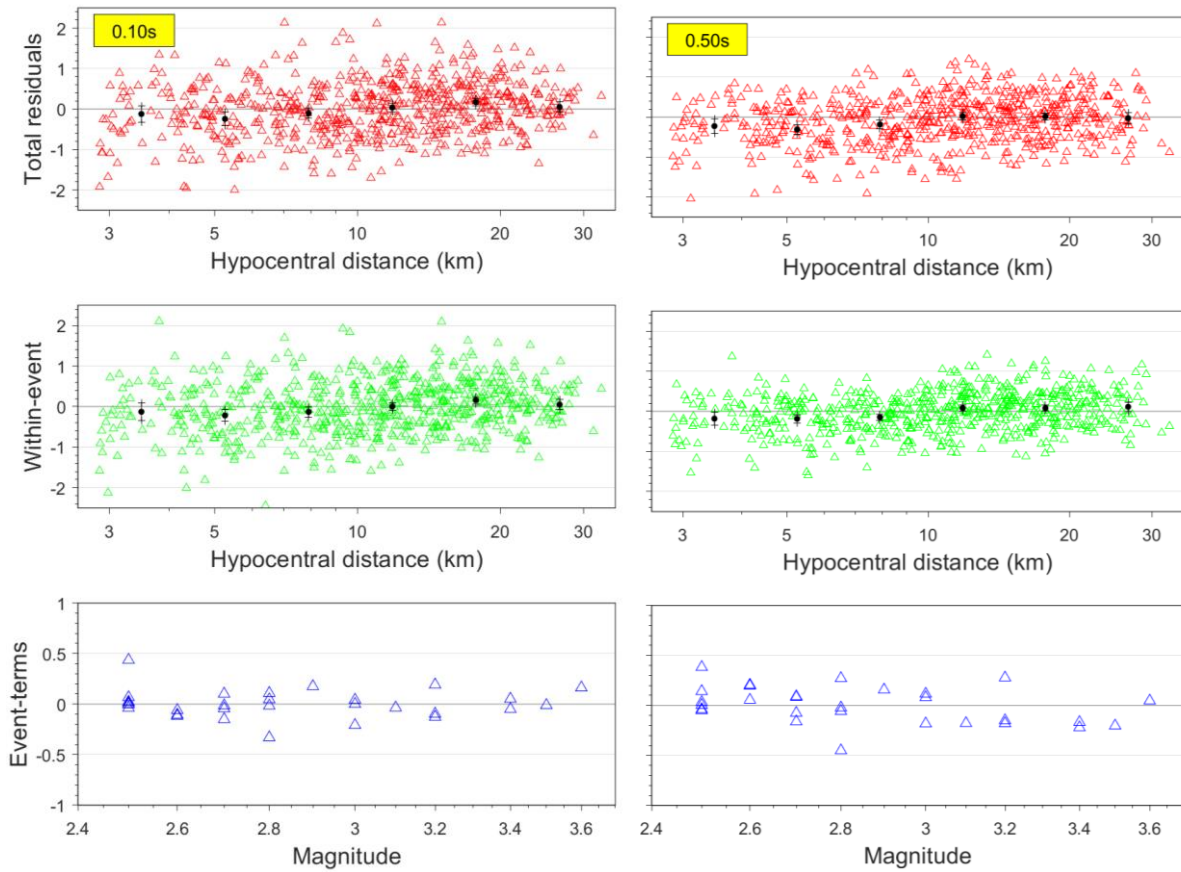


Figure 5.12. Residuals (natural log) between the central model simulations and field data; black circles and bars in the upper frames indicate the binned mean and 95% confidence intervals.

To assess the fit of each combination of $\Delta\sigma$ and κ_0 , model bias terms are calculated (i) at each period and (ii) for $SA_{avg} = [\prod_{T=0.01}^1 PSA(T)]^{\frac{1}{N}}$ computed over $N = 10$ periods between 0.01 and 1.0 s. A random effects regression is used to determine model bias and also accounts for event- and site-specific random effects (Abrahamson & Youngs, 1992). For each combination of $\Delta\sigma$ and κ_0 , we therefore obtain two quantitative measures of model fit: (i) mean and standard deviation of the period-specific bias terms, and (ii) bias of SA_{avg} . Bias for the various simulations is shown in Figure 5.11 versus $\Delta\sigma$ and κ_0 . After inspecting the bias and the associated misfit residuals, the models with: $\Delta\sigma = 2.2$ MPa; $\kappa_0 = 0.002$ s were deemed to best represent the field-recorded motions. As a final step in the calibration, in order to reduce any remaining bias, which may result from the use of a field-average amplification function, we modify the NS_B transfer function, $|T(f)|$, by multiplying it with the reciprocal of the model bias at each period, with log-linear interpolation between. Examples of the residual misfit of the central model are shown in Figure 5.12.

5.4. Logic-Tree and Parameters for Forward Simulations

The previous sections have dealt with the derivation of record specific seismological parameters (Section 5.2) used to model $FAS_{NSB'}$, followed by the calibration of a field-wide simulation model that estimates minimum-bias $PSA_{NSB'}$ for the central model. One of the key challenges in developing the GMM for the hazard and risk models has been the extrapolation from M_L 3.6 (the largest event that has occurred) to the largest magnitude considered in the hazard calculation, currently M 7.25. In the following, we therefore present a logic tree for possible alternative model formulations that allows us to account for epistemic uncertainty in the extrapolation above the maximum observed magnitude of 3.6.

The logic-tree for the Groningen GMM, predicting spectral accelerations at the NS_B horizon, consists of a single node with four branches carrying models that are distinguished by the pairs of values for $\Delta\sigma$ and κ_0 . The general framework is based on a best estimate (central) model, with upper and lower alternatives, in the magnitude range of the Groningen ground-motion recordings. However, for larger magnitudes ($M > 5$) it is assumed that any earthquakes would be triggered tectonic events, which would then be represented more favourably by the upper branch (and the central branch bifurcates into two alternative models). A key step in the model development, therefore, was to calibrate the upper branch to match, in a defined manner and in the larger magnitude range, predictions from global GMPEs for tectonic earthquakes.

Upper Branch – Calibration to Global GMPEs

The aim of the *upper* branch of the Groningen ground-motion model is to reflect ground motions observed for small-magnitude events in the gas field, while producing ground

motions comparable with global tectonic seismicity when extrapolating to larger magnitudes. In order to calibrate the model at large magnitude, we have performed a similar process to that described in Section 5.3 for matching models with locally recorded data. However, we now set the target as the PSA consistent with that expected from tectonic events. Target PSA are determined at the 13 GMM spectral periods 0.01 to 1.5 s at magnitudes $M = 5, 5.5, \text{ and } 6$, for logarithmically spaced distances of 0, 2.5, 5, 10 and 20 km and with $V_{S30} = 1400$ m/s (consistent with NS_B rock velocities). In all cases we use normal faulting mechanisms, consistent with the typical mechanism observed in the field. Six GMPEs were used: four NGA-W2 models (BSSA14: Boore *et al.*, 2014; CY14: Chiou & Youngs, 2014; CB14: Campbell & Bozognia, 2014; and ASK14: Abrahamson *et al.*, 2014) in addition to the European (RESORCE) models Aetal14: Akkar *et al.* (2014) and Beta14: Bindi *et al.* (2014). This results in 90 values of PSA at each period, or 1170 in total.

Due to the larger $\Delta\sigma$ expected for tectonic events, the simulation grid-search was expanded to include 11 values between 1.0 and 20 MPa. Based on the work of Boore (2009), who compared SMSIM against EXSIM_dmb, and the comparisons undertaken in previous versions of the GMM, SMSIM (with the R_{EFF} distance metric used for finite-fault approximation) was again used for the calibration stage rather than the full EXSIM simulations.

Assessing the fit of the simulations to the GMPE predictions was somewhat subjective due to the low κ_0 at the NS_B reference, which is inconsistent with the spectral shape predicted by the GMPEs. The low κ_0 leads to much higher simulated short-period motions than typically observed in tectonic GMPEs (which, even at high V_{S30} as used here, are based on outcrop motions). Due to the incompatibility of spectral shapes, a target of SA_{avg} is used (Figure 5.13), as this is consistent with the risk model (which uses SA_{avg} to predict losses). This comparison showed that $\Delta\sigma$ between 4 to 6 MPa produced broadly unbiased SA_{avg} . There was very little sensitivity to κ_0 .

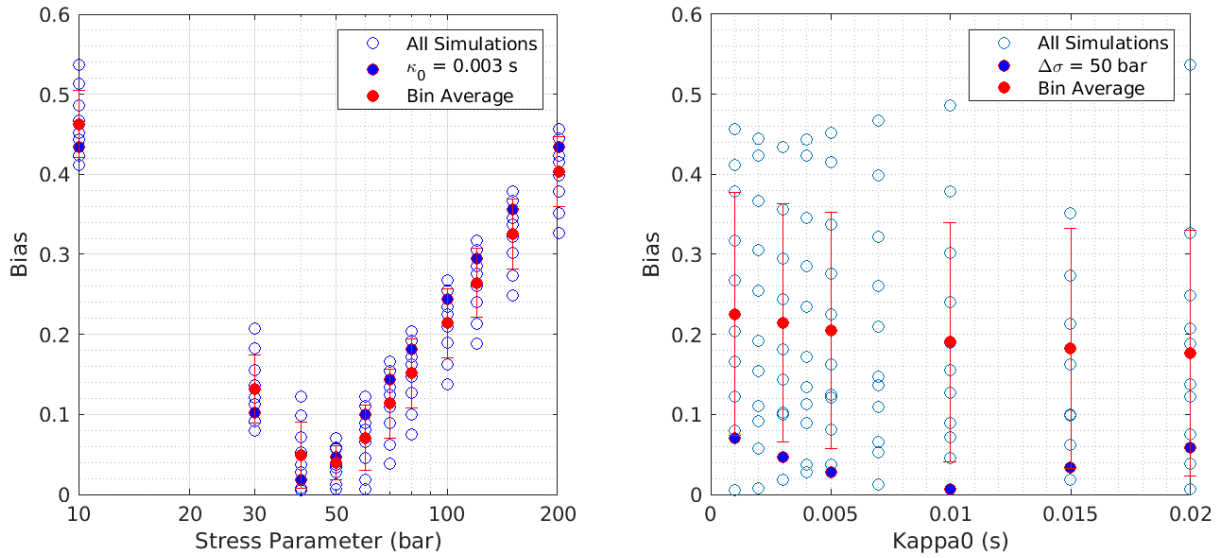


Figure 5.13. Bias in SA_{avg} for alternative $\Delta\sigma$ and κ_0 .

Definition of Logic Tree

We use the model bias from both local data (Section 5.3) and tectonic GMPE calibrations to inform the logic tree development. We first define the lower branch. In this case, we take the $\Delta\sigma$ and κ_0 combinations that lead to slight under-prediction (< 20 %) of field data ($\mathbf{M} \leq 3.6$), and underprediction of tectonic motions at $4.5 \leq \mathbf{M} \leq 6$. Taking into account the possibility of self-similarity (even if unlikely given the geology and geomechanics of reservoir-initiated ruptures), the lower model therefore has constant $\Delta\sigma = 1.5$ MPa and $\kappa_0 = 0.001$ s. The $\Delta\sigma = 1.5$ MPa is consistent with the spectral analyses undertaken on FAS (Section 5.3), while the reduction of κ_0 (with respect to the *central model*), reduces the degree of underprediction at short periods that would otherwise occur.

The remaining branches of the logic tree all have elements that have been directly calibrated (to minimise bias) to (i) local data ($\mathbf{M} \leq 3.6$), in the case of the *central model* and (ii) tectonic GMPEs ($4.5 \leq \mathbf{M} \leq 6$) in the case of the *upper model*.

The two central branches of the logic tree, at low magnitude ($\mathbf{M} \leq 3.6$), are explicitly defined by the *central model*: $\Delta\sigma = 2.2$ MPa and $\kappa_0 = 0.002$ s (the ‘best-fit’ to local data). The lower-central branch maintains a constant (self-similar) $\Delta\sigma = 2.2$ MPa over all \mathbf{M} . The upper-central branch considers the likelihood that $\Delta\sigma$ increases as faults propagate down into the Carboniferous, rising to 3.3 MPa (mid-way between the lower-central and upper models at $\mathbf{M} > 5$).

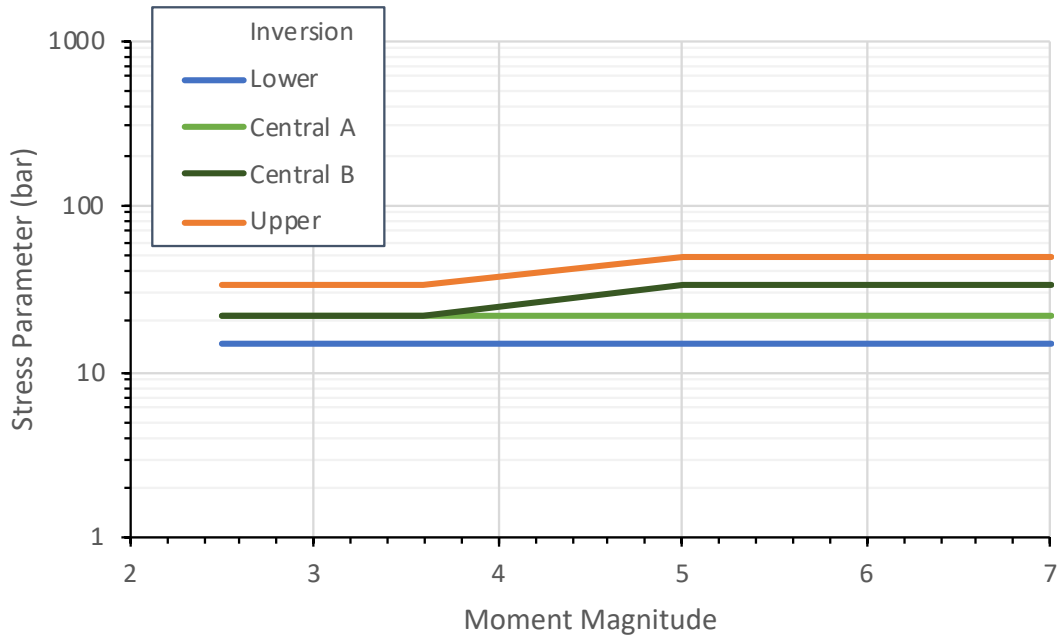


Figure 5.14. Magnitude dependent $\Delta\sigma$ for the alternative models. Note 1 bar = 0.1 MPa. Inversion results from Section 5.3 are provided for reference.

At $M > 5$, the upper branch is defined, based on the calibration against GMPEs, as $\Delta\sigma = 5$ MPa and $\kappa_0 = 0.003$ s. At low M , $\Delta\sigma$ is reduced, such that we limit the over-prediction of the field data (equivalent in magnitude to the under-prediction of the lower branch, *i.e.*, $< \sim 20\%$ overprediction). The magnitude-dependent $\Delta\sigma$ are shown in Figure 5.14.

To reflect the required shift to the upper branches for the triggered earthquakes corresponding to higher magnitudes, we assign magnitude dependent weights to the logic tree (Table 5.4, Figure 5.15). The weights assigned for magnitudes $M \leq 3.6$, within the range of the data from the Groningen field, are symmetrical and reflect the assumption of an approximately normal distribution and a well-constrained central model (the central-upper and central-lower branches are identical in this range, so the central model effectively has a weight of 0.6).

Table 5.4. Weights assigned to the four branches of the NS_B ground motion logic tree.

| Branch | Branch Weights | | |
|---------------|------------------------|---|---------------------|
| | $M \leq 3.6$ (w_L) | $3.6 < M \leq 5.0$ | $M > 5.0$ (w_H) |
| Upper | 0.2 | $w(M) = w_L + (w_H - w_L) \left(\frac{M - 3.6}{5.0 - 3.6} \right)$ | 0.4 |
| Central-upper | 0.3 | | 0.3 |
| Central-lower | 0.3 | | 0.2 |
| Lower | 0.2 | | 0.1 |

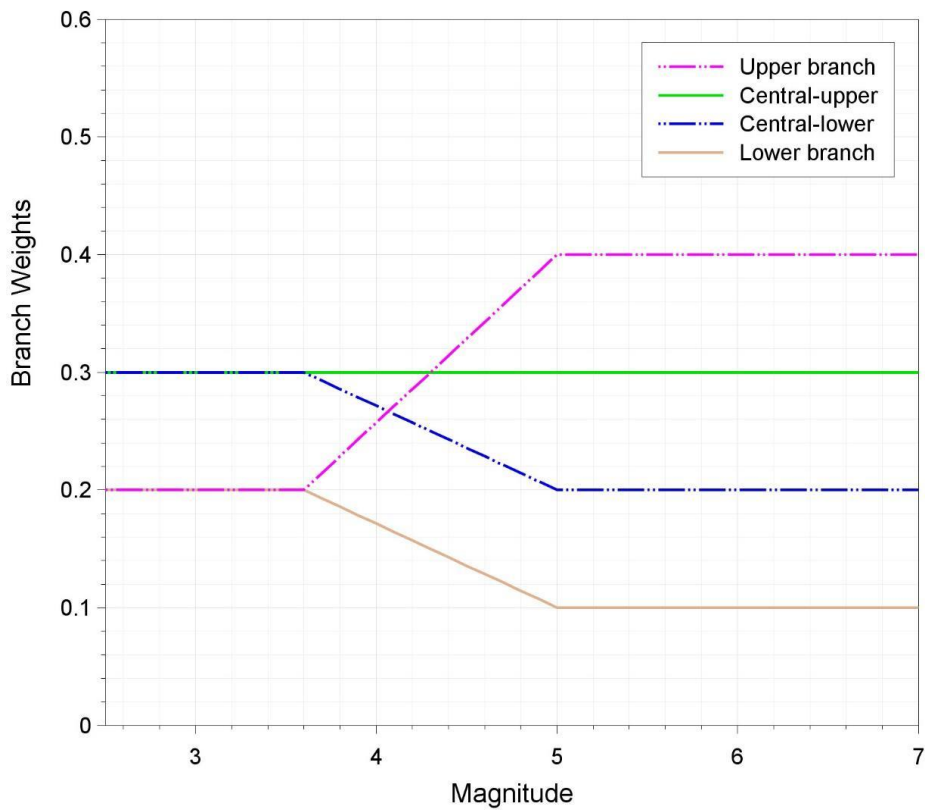


Figure 5.15. Magnitude dependent weights assigned to the four branches of the NS_B ground motion logic tree.

At larger magnitudes ($M \geq 5.0$), it is assumed that the earthquakes are triggered tectonic events that will rupture out of the gas reservoir into the Carboniferous. Since the Upper branch is calibrated to mimic predictions from GMPEs for tectonic earthquakes, this branch should have a much higher weight in the larger magnitude range. At the same time, the weights should also reflect the fact that these triggered earthquakes, associated with ruptures initiating at ~ 3 km depth and propagating downwards, would be different from the typical tectonic earthquakes that generated the data used to derive the GMPEs deployed for the calibration of this branch. The final decision of the GMM development team is that over the transition from small to large magnitudes, the weight on the upper branch should double, while the weight on the lower branches is halved.

6. Parametric Model for Reference Rock Motions

For implementation of the NS_B predictions in the hazard and risk calculations, parametric equations are derived using the simulations discussed in Chapter 5. Section 6.1 summarises the specific simulations performed for the regressions and Section 6.2 describes the selection of the functional form and the regressions. Section 6.3 then discusses the residuals with respect to the actual recorded motions transformed to the NS_B horizon and the development of the variability model. The chapter closes with a brief exploration of the influence of the different recording networks on the model bias.

6.1. Simulated Motions at NS_B

Response spectra were simulated using the code EXSIM (specifically, EXSIM_dmb version 05/17/15; Boore, 2009). EXSIM is based on a discretised rupture model with dynamic corner-frequency (EXSIM: Motazedian & Atkinson, 2005; EXSIM_dmb: Boore, 2009). Each of the distributed sub-faults in this model is assumed to be a point source that generates a stochastic ground-motion acceleration time-series. The FAS of these point-sources can be characterised by $\Delta\sigma$, as defined in the logic-tree branches (Section 5.4, Table 6.1). The combination of stochastic waveforms from numerous point-sources comprising the finite fault then generates the full rupture time-series, from which we compute PSA. A minor update was made to the source code 'exsim_dmb.for' to address a source code error in the Q -model: the source velocity 'beta' was being used rather than the average velocity 'c_q' to calculate path attenuation. This was reported to the author and subsequently acknowledged and corrected.

Simulations are performed for each of the four model branches defined in Section 5.4 (*i.e.*, the *lower*, *central-lower*, *central-upper*, and *upper branches*). A total of 3300 scenario events covering the range $M = 2.0$ to 7.25 in steps of 0.25 with random fault dimensions and hypocentre location are simulated for each branch. For each event two random epsilon values are drawn to define (i) the hypocentre location along strike and (ii) the length and width of the rupture, according to Wells & Coppersmith (1994). Recording locations were placed radially above the centre of the fault's top edge at 0 km and then 30 distances approximately logarithmically spaced between 1.0 and 79.5 km. Additional recording sites were located around the 'hinge points' of the geometrical decay function, at 7 and 12 km to aid the GMPE derivation. Each station had κ_0 defined based on the respective branch of the logic tree (see Section 5.4, Table 6.1). For each distance, six sites were located around the finite fault, at 45 , 90 , 135 , 225 , 270 and 315 degrees. Note that the strike parallel directions were omitted to avoid distances that are measured from the end of the rupture and therefore resulting in records at

significant distance from the epicentres of the larger faults. Overall, 613,800 simulations were computed per branch, for a total of almost 2.5 million waveforms.

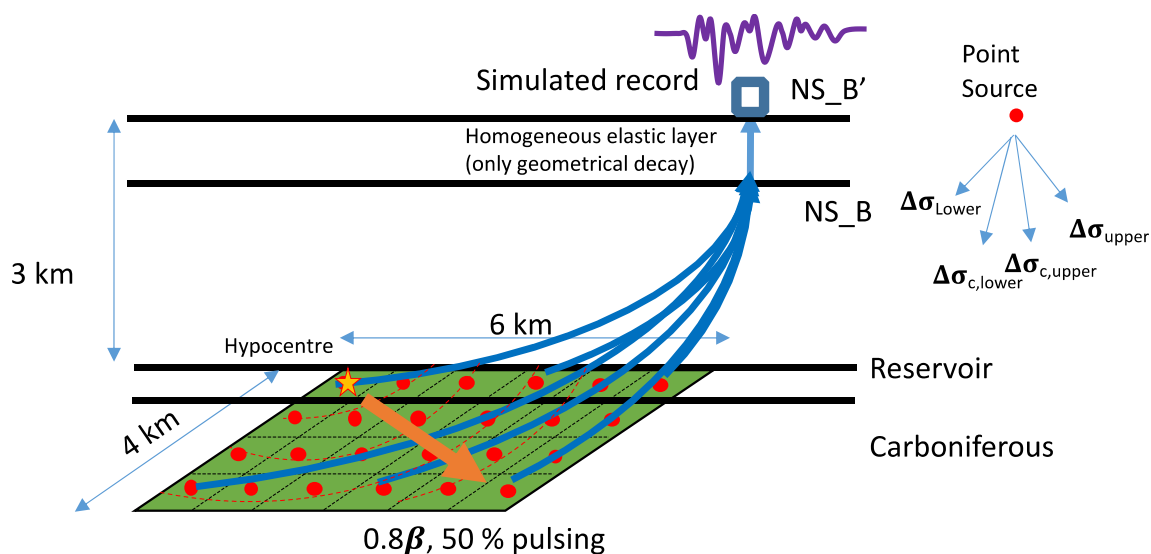


Figure 6.1. Schematic of model set up. Ruptures originate in the reservoir (at a random point along strike) and propagate downward. Q is accounted for up to the NS_B. Geometrical spreading is accounted for up to the surface. Each sub-fault (point source) is characterized by one of four $\Delta\sigma$, with the site (*lower, central-lower, central-upper* and *upper*: see Section 5.4) and the empirical duration model developed for field observations earlier in the GMMs evolution.

During the simulations it is necessary to account for the full path geometric effect, since it is not applied elsewhere (Figure 6.1). This means that the rock motion level ($SA_{rock} = PSA_{NSB'}$) used to determine the degree of non-linearity (Section 7) is somewhat lower than the true motion would be (*i.e.*, $PSA_{NSB'} < PSA_{NSB}$). This will lead to lower non-linearity—and potentially higher surface motions for limited high-strain scenarios—than would otherwise be expected. However, in this way the final surface motions, after convolution with non-linear site amplification factors, will include the appropriate full-path attenuation effects.

Figures 6.2 to 6.5 show simulated response spectral ordinates at (i) the NS_B rock horizon and (ii) the surface (using the field-average *linear* transfer function) for M 3.5 and 6.5 at 3 and 9 km distance. A significant caveat, of course, is that the surface motions estimated here do not account for the non-linearity expected for large magnitude events at short distances. Nevertheless, it facilitates a first order comparison. When comparing the GMPEs and the GMM, recall that only the upper branch is designed to be consistent (and only then in terms of SA_{avg}) with those tectonic predictions. The change in spectral shape (increase of the peak period) is clear when moving between the NS_B and surface motions, as can be seen

comparing the left- and right-hand panels of Figure 6.2. The comparison between GMPEs and the GMM only shows similar spectral shapes for the surface motions, despite using appropriate V_{S30} for the NS_B and surface (200 m/s). This suggests that the GMPEs are inappropriate in terms of spectral shape for prediction of motions at the NS_B horizon. This is not surprising as even the high V_{S30} motions used in the development of GMPEs are rock ‘outcrop’ motions, rather than buried horizons, and the NGA-West2 database is very limited in terms of recordings from very hard rock sites. The lower panels in Figures 6.2 to 6.5 show the model-to-model variability for both the GMM and the NGA-West2 GMPEs. At low M (within the data coverage), we obtain lower variability in the GMM than in the NGA-West2 GMPEs, while when extrapolating to the larger events, such as M 6.5 presented in Figure 6.4 and 6.5, the GMM predicts a significantly greater spread, as expected.

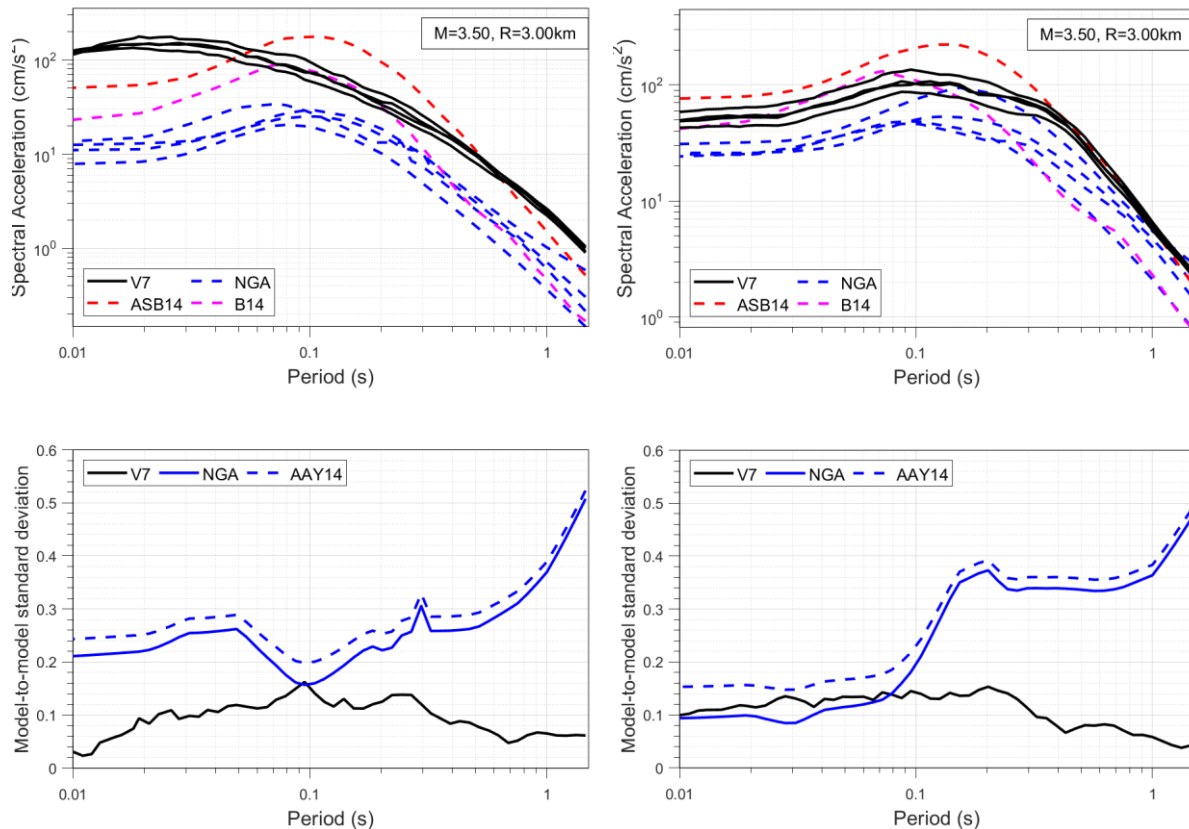


Figure 6.2. Example simulations for $M = 3.5$, $R_{rup} = 3$ km at the NS_B (left) and surface (without non-linear effects) (right). Black lines show the four logic-tree branch simulations compared to the NGA-West2, ASB14 (Akkar *et al.*, 2014) and B14 (Bindi *et al.*, 2014) models (*top*). Model-to-model variability is presented as a function of oscillator period for the four V7 GMM branches compared to the NGA models and NGA models plus the Al Atik & Youngs (2014; AAY14) adjustment (*bottom*). Periods beyond 1s are shown in the figure but do not form part of the deliverable.

Table 6.1. EXSIM_dmb parameter values used in simulations for NS_B motions

| Parameter | Symbol (units) | Value(s) | Notes |
|---|---|--|---|
| Density | ρ (g/cm ³) | 2.6 | |
| Shear-wave velocity | β (km/s) | V_s Profile | See Figure 5.7 |
| Horizontal partition | | 0.77 | Empirically derived |
| Radiation coefficient | θ | 0.55 | |
| Free surface | F | 2 | |
| Sub-fault source type | | Brune (1970) ω^{-2} | |
| Top of rupture depth | Z_{top} (km) | 3 | |
| Seismogenic depth | Z_{seis} (km) | 13 | |
| Fault dip | Dip (degrees) | 80 | |
| Fault mechanism | | Normal | |
| Fault width | W (km) | $\min(W_{WC94}, [Z_{seis}-3]/\sin(\text{dip})]$ | W_{WC94} : Width from Wells & Coppersmith (1994) |
| Fault length | L (km) | $L_{WC94} * W / W_{WC94}$ | L_{WC94} : Length from Wells & Coppersmith (1994) Conserve area of fault A given by $L \times W$ in case limited by Z_{seis} |
| Hypocentre location | $\Delta L, \Delta W$ (km, km) | Random, 0 | Located randomly along strike, at 3 km depth (top of fault). |
| Slip velocity | V_{slip} (km/s) | 0.8β | |
| Stress parameter (Lower, Central, Upper) | $\Delta\sigma$ [M ≤ 3.6] (bars) lower, central-lower, central-upper, upper | 15, 22, 22, 33 | Linear interpolation of $\log(\Delta\sigma)$ with M |
| | $\Delta\sigma$ [M ≥ 5.0] (bars) lower, central-lower, central-upper, upper | 15, 22, 33, 50 | |
| Geometrical spreading distances (R_{hyp}) | R_1, R_2, R_3, R_4 (km) | 2, 7, 12, 25 | |
| Geometrical decay rates | $\lambda_1, \lambda_2, \lambda_3, \lambda_4$ | 0.49, 1.53, 0.67, 0.69, 1.0 | |
| Path attenuation | $Q(f,z)$ | $Q(f) = Q_{0ij} f^{0.42}$ with SIMUL2000-based lookup table for path Q_{0ij} | |
| Site attenuation | κ_0 (s) lower, central-lower, central-upper, upper | 0.001, 0.002, 0.002, 0.003 | |
| Source duration | T_s (s) | $1/0.4906\beta(\Delta\sigma/M_0)^{1/3}$ | SI units |
| Path duration for sub-fault signals | T_P [R (km)] | $T_{5,75}/0.383$ | V3 Groningen $T_{5,75}$ model for M = 3.0, V_{s30} =1500. |
| Rise time | T_s (s) | $1/f_0$ | |
| Site amplification | A(f) | Network average NS_B TF | |
| Dynamic, pulsing percentage | | 50% | |
| Sub-fault averaging | | RMS | |
| Scaling | | (Acceleration FAS) ² | |

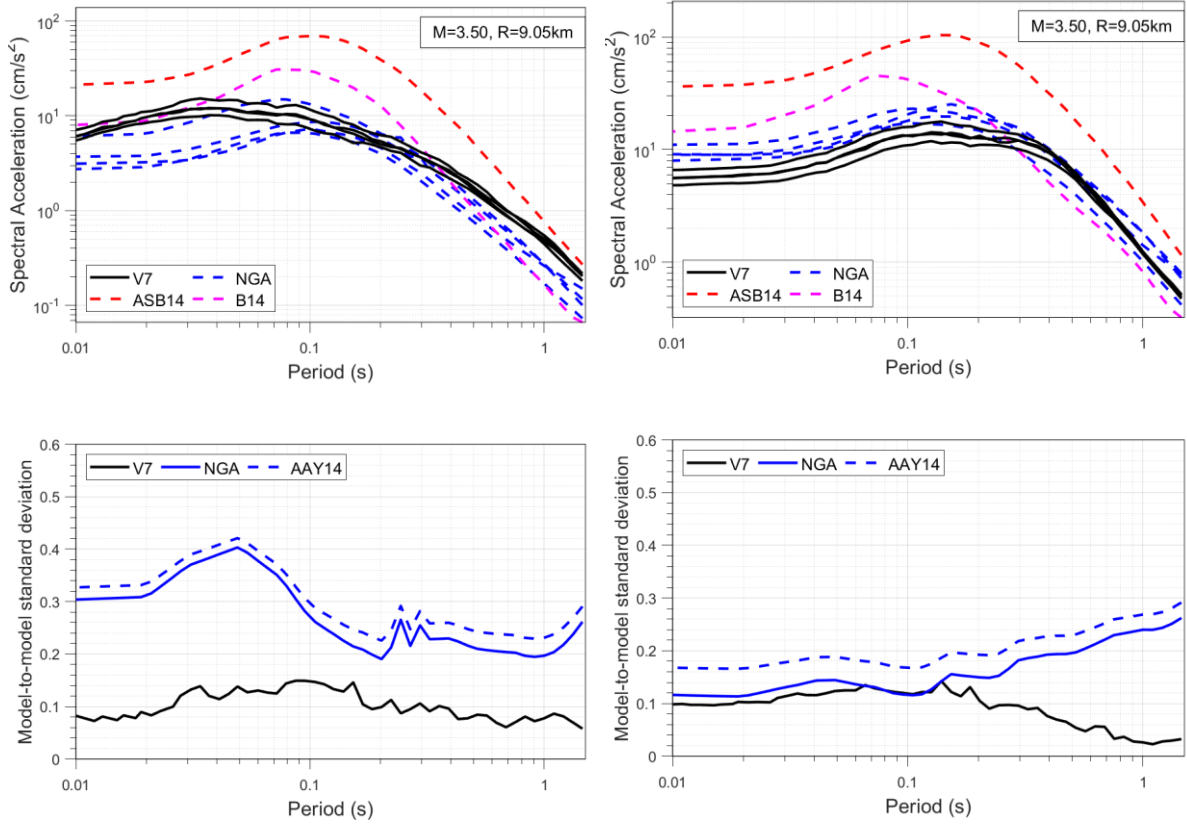


Figure 6.3. Same as Figure 6.2, but for $M = 3.5$, $R_{\text{rup}} = 9$ km.

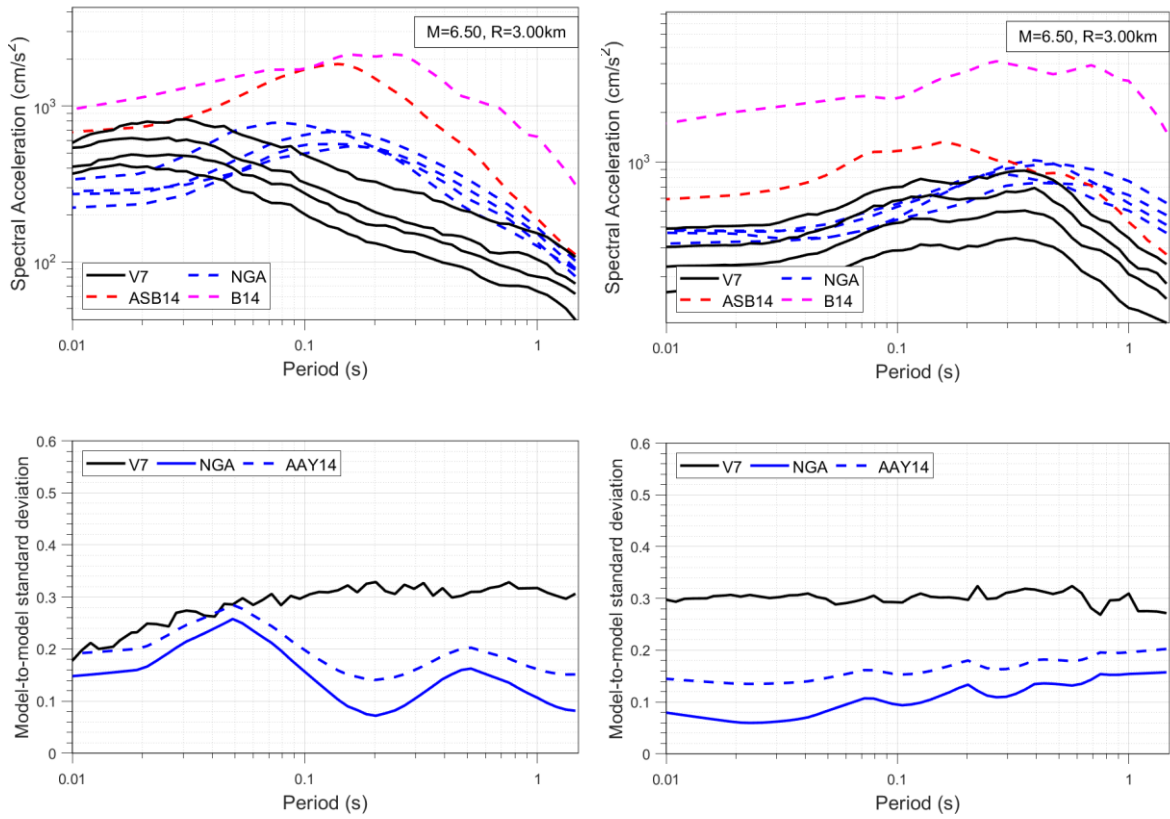


Figure 6.4. Same as Figure 6.2, but for $M = 6.5$, $R_{\text{rup}} = 3$ km.

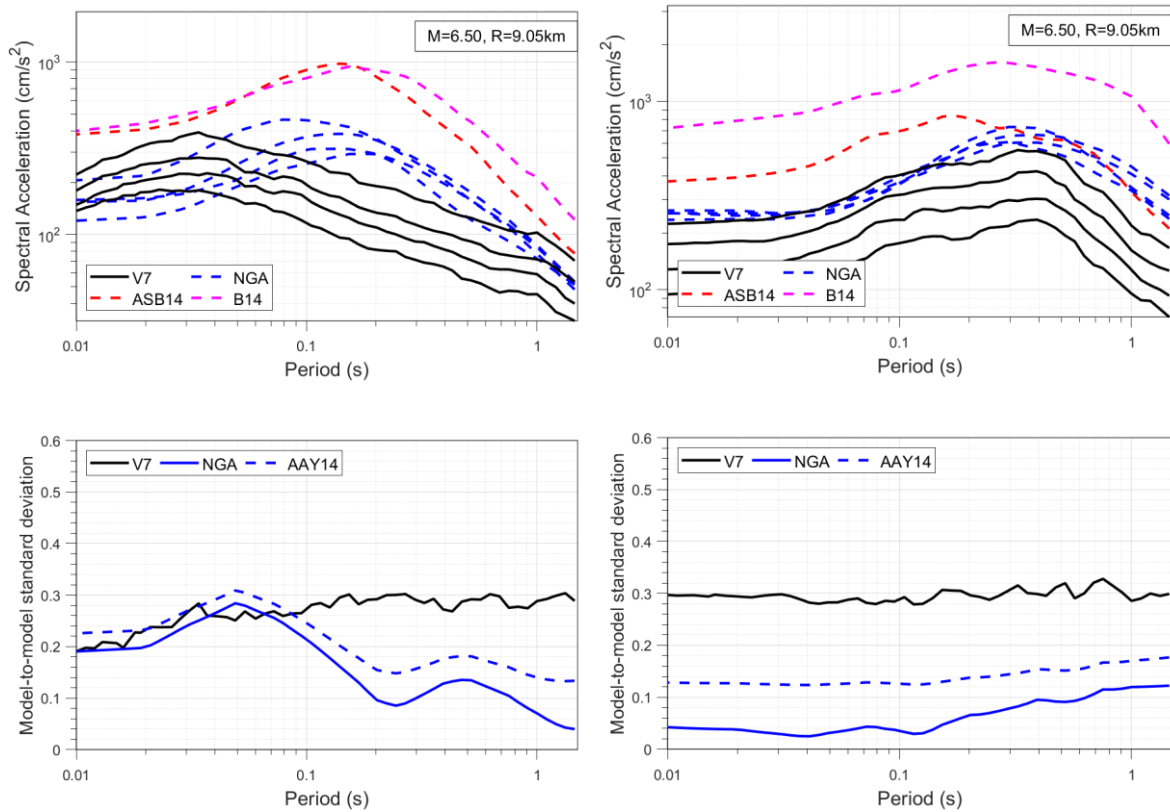


Figure 6.5. As Figure 6.2, but for $M = 6.5$, $R_{rup} = 9$ km.

6.2. Regression on Simulated Motions

The simulated spectral ordinates from EXSIM described in Section 6.1 are provided for particular rupture scenarios (magnitude-distance combinations). For each of these rupture scenarios, it is possible to compute a mean level of logarithmic spectral amplitude, and to then define the ‘ground-motion model’ in the form of tabulated amplitudes that can then be interpolated to find the expected level of logarithmic spectral acceleration for any arbitrary rupture scenario. There is precedent for this type of approach in practice, *e.g.*, Goulet *et al.* (2018). However, there are advantages of deriving a set of parametric equations that collectively represent the expected values of the logarithmic spectral acceleration. This circumvents the need for any interpolation within the hazard calculations, imposes a degree of smoothing upon the stochastic simulations arising from EXSIM, and permits derivatives of the parametric model to be computed with relative ease. This parametric approach has been adopted in all previous versions of the Groningen GMM and is again adopted here for the V7 model.

Although the Fourier spectral inversions have been performed in a slightly different manner for the V7 model, and slightly different Fourier parameters have arisen as a consequence, the impact upon the general scaling of spectral ordinates with respect to magnitude and distance is rather subtle. The parametric equations used for the V6

model have a good deal of flexibility (many degrees of freedom) and this functional expression proved to be a very robust starting point for the calibration of the V7 model.

Functional forms that have been used within ground-motion development in other regions have a strong influence upon the functional terms adopted within the present project. However, the unusual transition from reservoir-contained shallow events over the small-magnitude range to the larger events hypothesised to rupture down into the carboniferous dictates that functional expressions from published ground-motion models cannot be adopted directly. The development process therefore follows a series of steps, each of which is described in the following paragraphs.

Numerical waveform modelling conducted in the Groningen field, *e.g.*, Edwards *et al.* (2019), has suggested that distinct breaks in geometric spreading should arise for point-source ruptures. Finite-source simulations have additionally shown that these distinct changes in geometric spreading rates do not persist for larger magnitudes – which is to be expected from consideration of the effects of extended ruptures. We therefore seek to define a flexible parametric form for distance scaling that is informed by the numerical waveform modelling, but that is sufficiently flexible to represent distance scaling over the full magnitude range required by the hazard and risk calculations. The parametric form considered is defined by Equation (6.1):

$$\ln Sa(R_{rup}|\mathbf{M}) = \begin{cases} r_0 + r_1 \ln\left(\frac{R_{rup}}{3}\right) & \text{for } R_{rup} < 7 \text{ km} \\ r_0 + r_1 \ln\left(\frac{7}{3}\right) + r_2 \ln\left(\frac{R_{rup}}{7}\right) & \text{for } 7 \leq R_{rup} < 12 \text{ km} \\ r_0 + r_1 \ln\left(\frac{7}{3}\right) + r_2 \ln\left(\frac{12}{7}\right) + r_3 \ln\left(\frac{R_{rup}}{12}\right) & \text{for } 12 \leq R_{rup} < 25 \text{ km} \\ r_0 + r_1 \ln\left(\frac{7}{3}\right) + r_2 \ln\left(\frac{12}{7}\right) + r_3 \ln\left(\frac{25}{12}\right) + r_4 \ln\left(\frac{R_{rup}}{25}\right) & \text{for } R_{rup} > 25 \text{ km} \end{cases} \quad (6.1)$$

This functional form defines a piecewise linear function in $\ln Sa - \ln R_{rup}$ space, with four distinct slopes defined by the coefficients r_1, r_2, r_3, r_4 , and a source amplitude of r_0 . The ‘hinge’ distances, where the piecewise linear segments connect, are set to values of $R_{rup} = \{7, 12, 25\}$ to mimic the results of the numerical waveform modelling (Edwards *et al.*, 2019). Note that while the numerical waveform modelling is used to impose these hinge distances, no constraint is imposed upon the geometric spreading rates or the source amplitudes.

The functional expression in Equation (6.1) is used in conjunction with the simulated data for each considered magnitude. As explained in the previous section, simulations are provided for magnitudes spanning the range 2.0 to 7.25 in 0.25-unit increments, for a total of 22 magnitude values. For each magnitude, a grid of receivers (fictitious station locations; Figure 6.6) ‘observes’ the simulated ground motions. This grid is

defined using 31 approximately logarithmically spaced distances at six different source-to-site azimuth angles. Furthermore, for each magnitude, 150 stochastic simulations are performed. As a result, for each of the 22 considered magnitudes, 27,900 spectral ordinates are simulated for each response period. This relatively large dataset readily allows for the five free coefficients of Equation (6.1) to be constrained through a regression analysis. Examples of these magnitude-specific regressions are shown in Figure 6.6. One can readily appreciate from Figure 6.6 that the geometric spreading rates for each piecewise linear segment vary quite significantly as a function of magnitude.

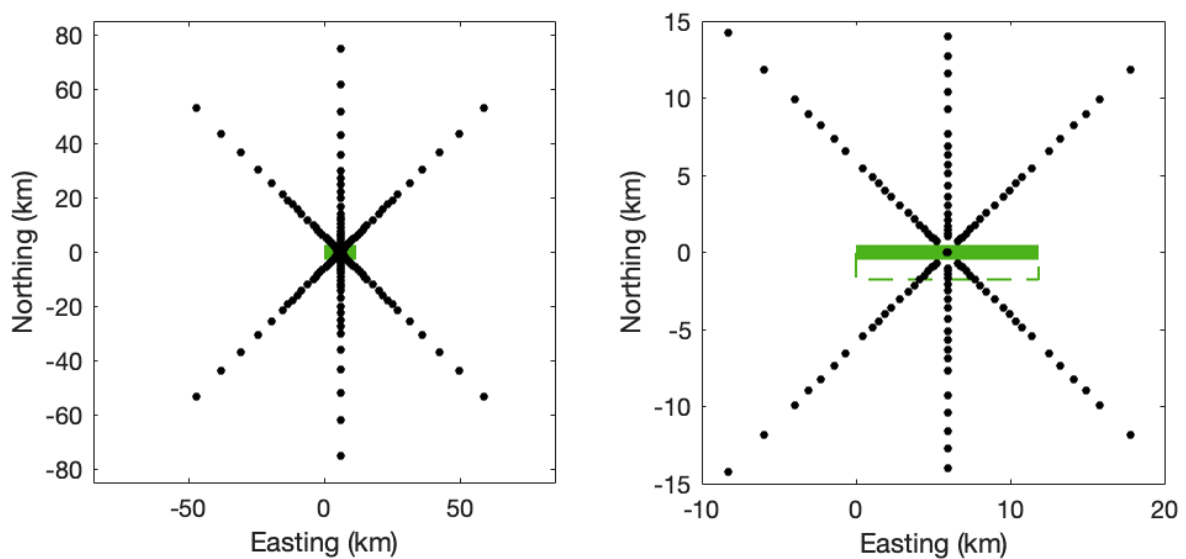


Figure 6.6. Receiver distribution used for simulations. *Left*: all receivers; *right*: zoom-in on the fault surface project of an M 6 event (green, with dashed line indicating dipping plane of the fault rupture).

Regression analyses, like those shown in Figure 6.7, are performed for all four stress parameter branches, for each of the 22 magnitude values, and for all response periods. Prior to adopting the expression of Equation (6.1), preliminary analyses were conducted to ensure that this functional form would be sufficiently flexible for all model branches and response periods. This was proven to be the case, but the magnitude dependence of the geometric spreading rates varies quite significantly with response period. This is discussed in more detail shortly.

The values of the coefficient r_0 for each magnitude can be plotted against magnitude in order to inform a suitable functional form for the source scaling. Alternatively, the simulation results for the shortest distance considered can also be inspected in order to observe how these near source amplitudes scale with magnitude. Both of these approaches lead to very similar results. Figures 6.8 and 6.9 show examples of these near-source simulation results against magnitude for response periods of 0.01 second

and 1.0 seconds, respectively. In both cases, the results are shown for the lower central stress parameter branch, but the behaviour for all other branches is similar in terms of how well the fitted model can capture the mean variation of spectral amplitudes.

Equation (6.2) defines the parametric equation shown in Figures 6.8 and 6.9. The source amplitudes scale differently for the small and large magnitude ranges, and this is seen most clearly at short periods (Figure 6.7). To capture this scaling, we adopt a function that makes use of two quadratic expressions, that connect at a value of m_0 at a magnitude of M_m . For magnitudes smaller than M_m the coefficients m_1 and m_2 control the scaling, while for larger magnitude the relevant coefficients are m_3 and m_4 .

$$r_0(\mathbf{M}) = \begin{cases} m_0 + m_1(\mathbf{M} - M_m) + m_2(\mathbf{M} - M_m)^2 & \text{for } \mathbf{M} < M_m \\ m_0 + m_3(\mathbf{M} - M_m) + m_4(\mathbf{M} - M_m)^2 & \text{for } \mathbf{M} \geq M_m \end{cases} \quad (6.2)$$

Equation (6.2) is sufficiently flexible to be used to model the source amplitudes for all response periods and stress parameter branches. The magnitude dependence of the geometric spreading coefficients is a little more complex. Figure 6.10 shows the variation of the geometric spreading coefficients with respect to magnitude at a period of $T = 0.01$ seconds. Figure 6.10 shows that for small magnitudes the dependence differs from that for large magnitudes – and that this break is most pronounced for the greatest distances. Estimates of the spreading rates are obtained in 0.25-unit magnitude increments, starting from 2.0. The change in scaling appears to occur just under a magnitude of 4.0, so the break point is set at 3.875 (half-way between 3.75 and 4.0).

The magnitude dependence of the geometric spreading rates reflects the near-source saturation effects that are embedded within the EXSIM simulations. This is partly seen in the magnitude dependence of the source amplitudes shown in Figure 6.8, where the gradient of the fitted curve decreases with increasing magnitude. However, saturation effects are also seen in Figure 6.10a where the large-magnitude spreading rates are much weaker than those for the smaller magnitudes. For the small-magnitude range, the geometric spreading rates at all distances appear to follow a linear trend with magnitude, as often seen in response spectral ground-motion models. However, from magnitudes of around 4.0, the linear scaling changes as the ruptures grow into the carboniferous and the ray paths of the waves take on significantly different routes and thus pass through propagation media with different quality factors. A hyperbolic tangent function was seen to replicate this general scaling relatively well and required the specification of a small number of parameters. Therefore, the red curves in Figures 6.10 to 6.12 combine a linear model for the small magnitude range (for three different periods) with a hyperbolic tangent function at larger magnitudes, as shown in Equation (6.3).

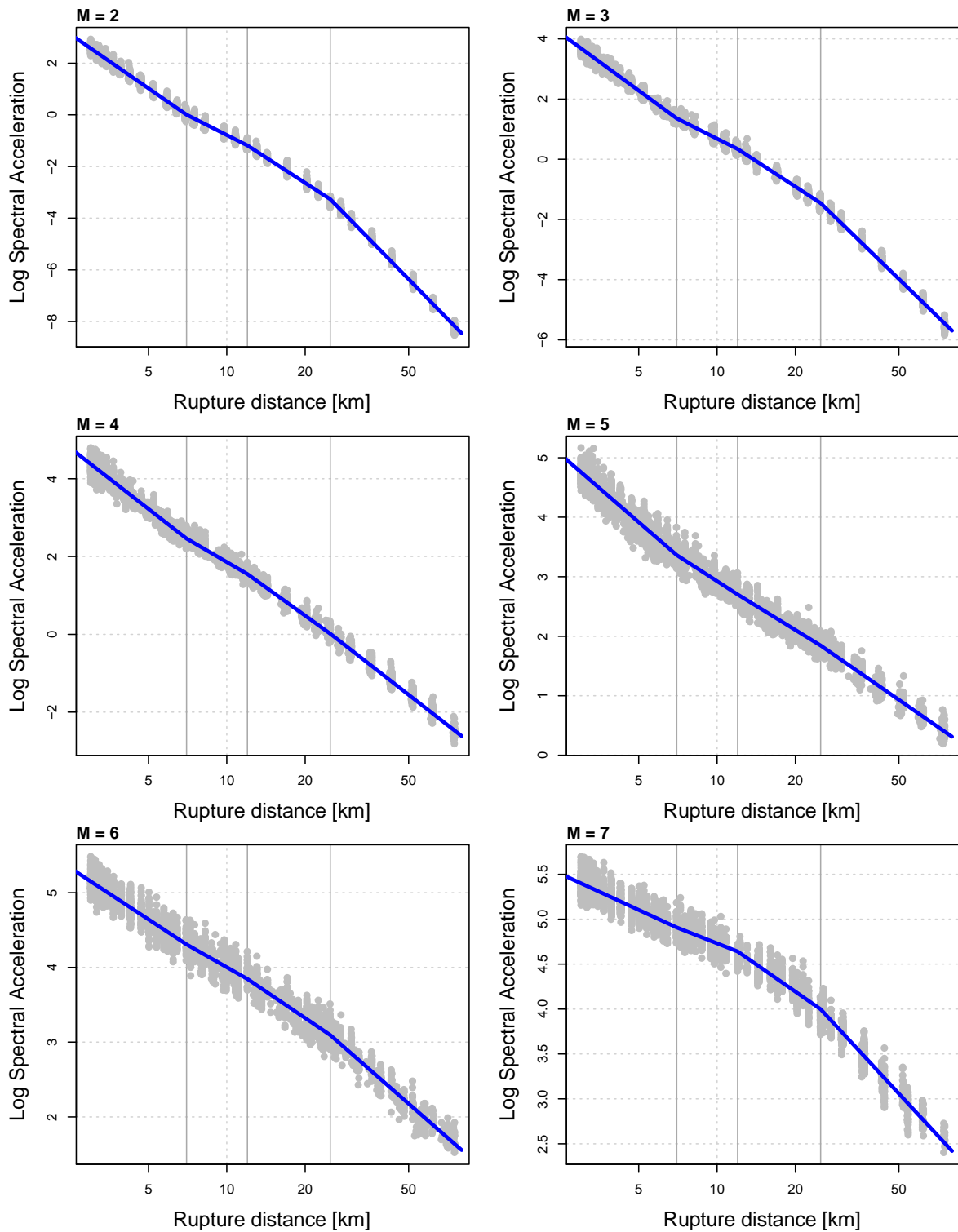


Figure 6.7. Examples of the initial fits to magnitude-specific simulations using Equation (6.1). Grey markers show the 27,900 simulations for each magnitude value and the blue lines show the fit to these markers. The relevant magnitude is shown in the upper left of each panel. Thin vertical grey lines mark the locations of the distance hinges from Equation (6.1). The example shown is for the central lower stress parameter branch, and for a response period of 0.01 seconds.

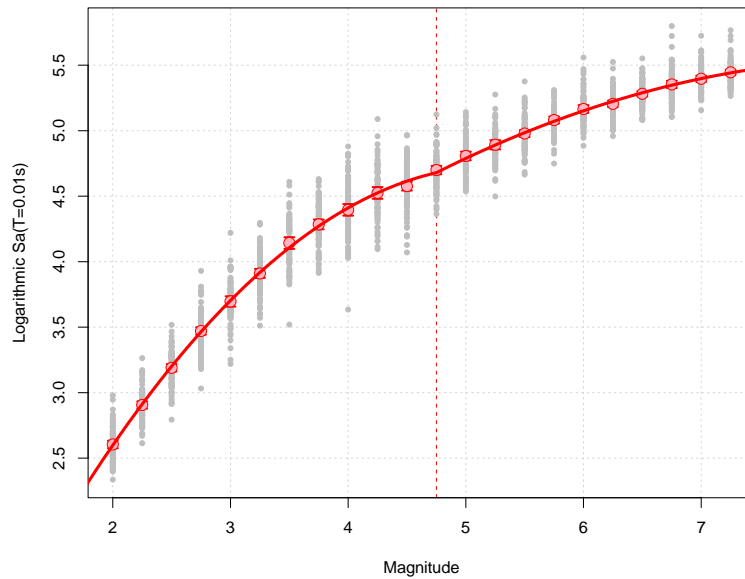


Figure 6.8. Scaling of the near-source spectral amplitude at short periods (the example shown is for $T = 0.01$ seconds) with respect to magnitude. The grey markers are the simulated response spectral ordinates at each magnitude at the shortest distance available (there are $6 \times 150 = 900$ simulations for each magnitude). The red markers show the mean and standard errors in each bin (the error bars representing the standard errors are largely masked by the mean markers, given the mean is so well constrained), while the solid red line shows the fit of the expression in Equation (6.2) to these data. The vertical dashed line shows the location of the transition magnitude, M_m , where the two quadratic portions of the magnitude scaling function join.

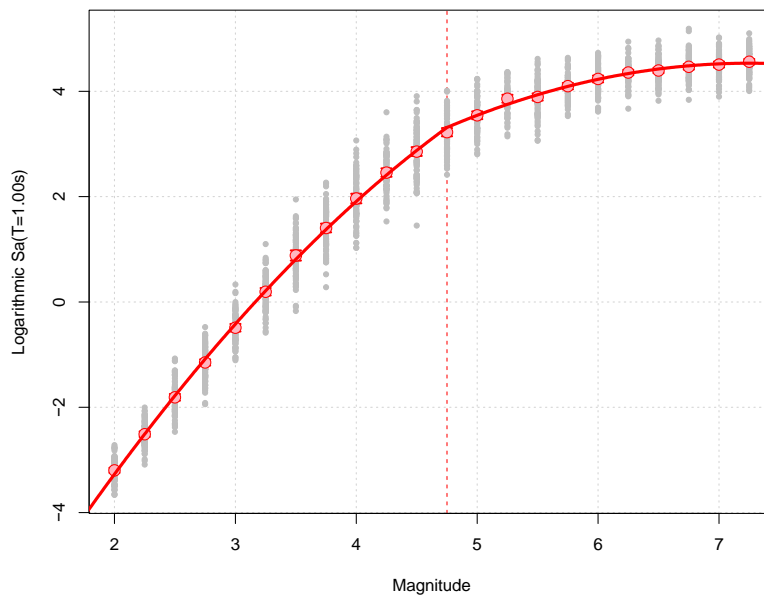


Figure 6.9. Scaling of the near-source spectral amplitude at short periods (the example shown is for $T = 1.0$ seconds) with respect to magnitude. The grey markers are the simulated response spectral ordinates at each magnitude at the shortest distance available (there are $6 \times 150 = 900$ simulations for each magnitude). The red markers show the mean and standard errors in each bin (the error bars representing the standard errors are largely masked by the mean markers, given the mean is so well constrained), while the solid red line shows the fit of the expression in Equation (6.2) to these data.

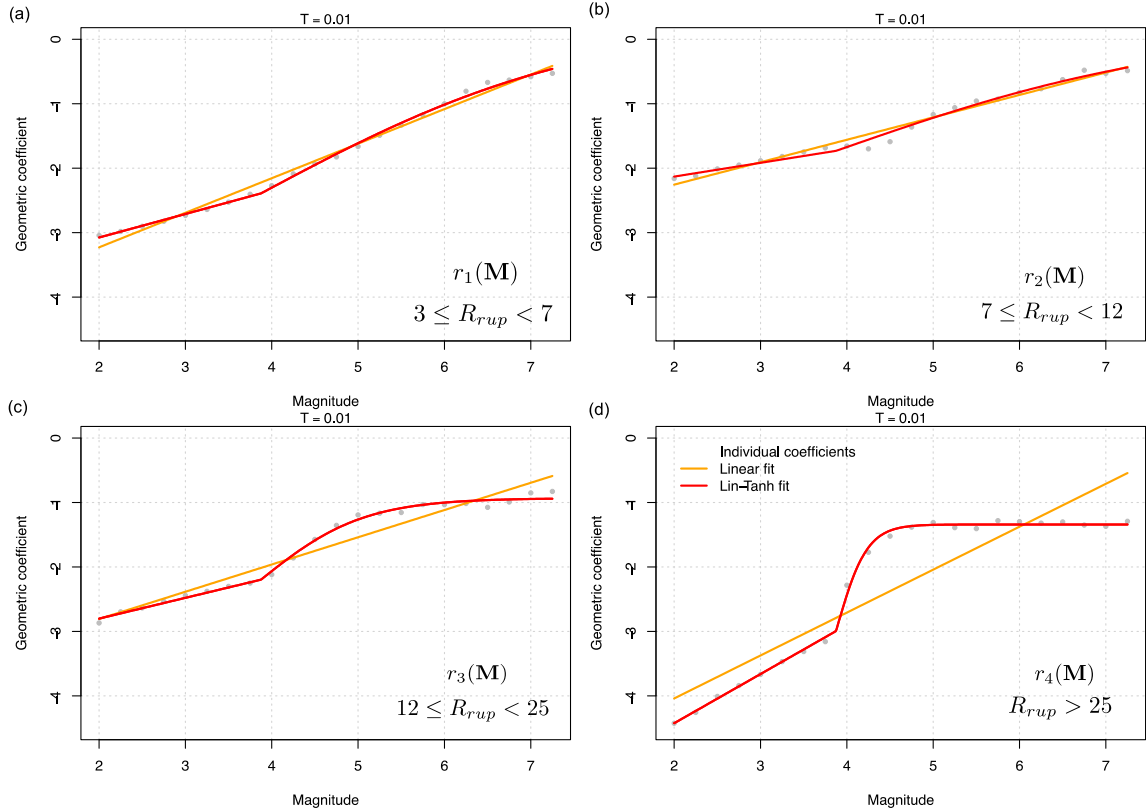


Figure 6.10. Magnitude dependence of the geometric spreading coefficients for a period of 0.01 seconds and the lower central stress parameter branch. Grey markers show the magnitude-specific estimates of the geometric spreading rates from the regression using Equation 6.2.1. The orange lines show linear fits to these grey markers, while the red line combines linear scaling at small magnitudes (below 3.875) with hyperbolic tangent scaling at larger magnitudes.

$$r_i(\mathbf{M}) = \begin{cases} r_{i,a} + r_{i,b}(\mathbf{M} - M_r) & \text{for } \mathbf{M} \leq M_r \\ r_{i,a} + r_{i,c} \tanh[r_{i,d}(\mathbf{M} - M_r)] & \text{for } \mathbf{M} > M_r \end{cases} \quad (6.3)$$

where the magnitude breakpoint is $M_r = 3.875$, and the coefficients $r_{i,a}, r_{i,b}, r_{i,c}, r_{i,d}$ with $i \in \{1,2,3,4\}$ are defined for the four distance ranges in Figures 6.10 to 6.12.

However, the appropriateness of the two-part scaling shown in Equation (6.3) varies with response period. For the shortest periods, such as the case of 0.01 seconds shown in Figure 6.9, these two scaling regimes can be seen at all distances (but the effect is clearly strongest at the largest distances). However, as the response period increases, we start to have difficulty in identifying any systematic departure from linearity in some distance ranges. Specifically, for periods longer than 0.2 seconds, the geometric spreading rate r_2 appears to vary linearly over the full magnitude range. Similarly, for periods longer than 0.5 seconds, the spreading rate r_3 also appears to vary linearly over the full magnitude range. These cases are exemplified in Figures

6.11b and 6.12b where only the linear model is fit to the r_2 spreading rates, and in Figure 6.12c where only a linear model is shown for r_3 .

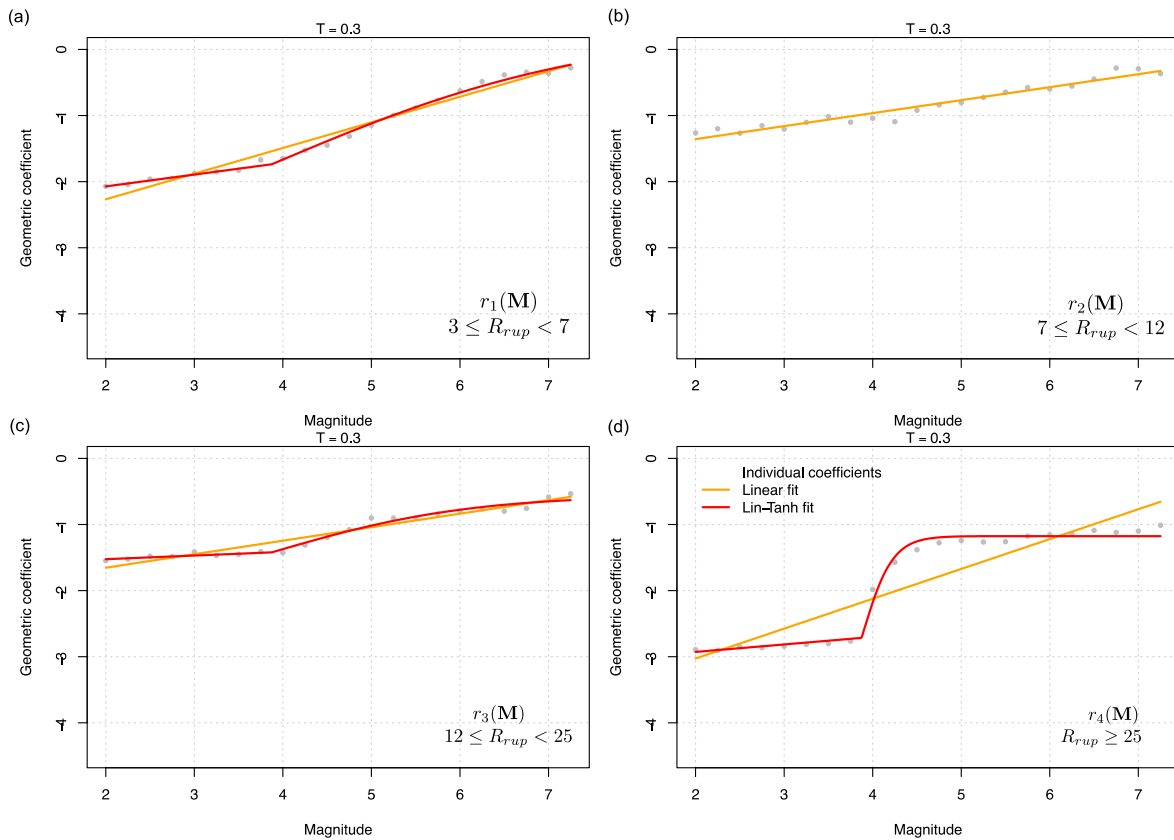


Figure 6.11. Magnitude dependence of the geometric spreading coefficients for a period of 0.3 seconds and the lower central stress parameter branch. Grey markers show the magnitude-specific estimates of the geometric spreading rates from the regression using Equation (6.1). The orange lines show linear fits to these grey markers, while the red line combines linear scaling at small magnitudes (below 3.875) with hyperbolic tangent scaling at larger magnitudes. In panel b, only the linear fit is computed and shown.

This behaviour, and the period ranges where changes take place, was examined across all four stress drop branches and the period ranges were chosen to be appropriate for all branches. This is helpful from a practical implementation standpoint as it means that the functional form does not change with the stress parameter branch, only the coefficient sets change.

The steps undertaken thus far are performed using a sample of the full dataset (10% of the total available data). This is done simply to facilitate rapid evaluation of alternative functional forms, and to ensure the regression analyses run swiftly. However, the calibration of the complete model is performed using the complete database of EXSIM simulated spectral ordinates, as well as the empirical data available from the Groningen field.

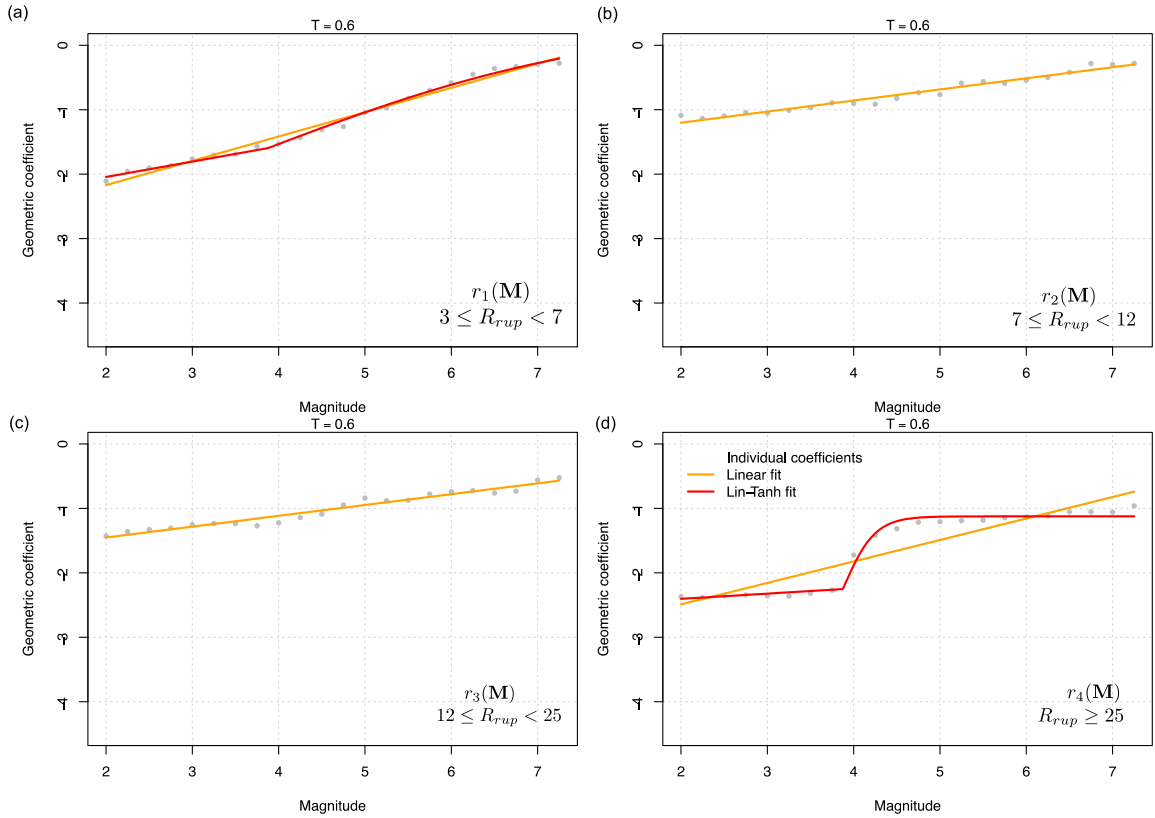


Figure 6.12. Magnitude dependence of the geometric spreading coefficients for a period of 0.6 seconds and the lower central stress parameter branch. Grey markers show the magnitude-specific estimates of the geometric spreading rates from the regression using Equation (6.1). The orange lines show linear fits to these grey markers, while the red line combines linear scaling at small magnitudes (below 3.875) with hyperbolic tangent scaling at larger magnitudes. In panels b and c, only the linear fits are computed and shown.

The overall functional form of the parametric model for the median accelerations at the NS-B horizon is defined using the following set of equations:

$$\ln Sa(\mathbf{M}, R_{rup}; T) = g_{src}(\mathbf{M}; T) + g_{path}(R_{rup}, \mathbf{M}; T) \quad (6.4)$$

In Equation (6.4), the term g_{src} represents the source scaling and g_{path} represents the path scaling. The source scaling term is a function of magnitude, and has period-dependent coefficients, as shown in Equation (6.5).

$$g_{src}(\mathbf{M}; T) = \begin{cases} m_0(T) + m_1(T)(\mathbf{M} - M_m) + m_2(T)(\mathbf{M} - M_m)^2 & \text{for } \mathbf{M} < M_m \\ m_0(T) + m_3(T)(\mathbf{M} - M_m) + m_4(T)(\mathbf{M} - M_m)^2 & \text{for } \mathbf{M} \geq M_m \end{cases} \quad (6.5)$$

That is, the functional form from Equation (6.2) is retained. The magnitude joining the two quadratic scaling functions is $M_m = 4.75$. The path scaling function combines the functional elements of Equations (6.1) and (6.3) such that:

$$\begin{aligned}
g_{path}(R_{rup}, \mathbf{M}; T) &= r_0(\mathbf{M}; T) \ln \left(\frac{\max[\min(R_{rup}, R_{h,1}), R_{h,0}]}{R_{h,0}} \right) \\
&+ r_1(\mathbf{M}; T) \ln \left(\frac{\max[\min(R_{rup}, R_{h,2}), R_{h,1}]}{R_{h,1}} \right) \\
&+ r_2(\mathbf{M}; T) \ln \left(\frac{\max[\min(R_{rup}, R_{h,3}), R_{h,2}]}{R_{h,2}} \right) \\
&+ r_3(\mathbf{M}; T) \ln \left[\frac{\max(R_{rup}, R_{h,3})}{R_{h,3}} \right]
\end{aligned} \tag{6.6}$$

The hinge distances are defined as $R_{h,0} = 3$ km, $R_{h,1} = 7$ km, $R_{h,2} = 12$ km, and $R_{h,3} = 25$ km, while the rates r_0, r_1, r_2, r_3 are defined by the expressions in Equations (6.7) to (6.10).

$$r_0(\mathbf{M}; T) = \begin{cases} r_{0,a}(T) + r_{0,b}(T)(\mathbf{M} - M_r) & \text{for } \mathbf{M} \leq M_r \\ r_{0,a}(T) + r_{0,c}(T) \tanh[r_{0,d}(\mathbf{M} - M_r)] & \text{for } \mathbf{M} > M_r \end{cases} \tag{6.7}$$

$$r_1(\mathbf{M}; T) = \begin{cases} r_{1,a}(T) + r_{1,b}(T)(\mathbf{M} - M_r) & \text{for } T \leq 0.2 \text{ s, and } \mathbf{M} \leq M_r \\ r_{1,a}(T) + r_{1,c}(T) \tanh[r_{1,d}(\mathbf{M} - M_r)] & \text{for } T \leq 0.2 \text{ s, and } \mathbf{M} > M_r \\ r_{1,a}(T) + r_{1,b}(T)(\mathbf{M} - M_r) & \text{for } T > 0.2 \text{ s} \end{cases} \tag{6.8}$$

$$r_2(\mathbf{M}; T) = \begin{cases} r_{2,a}(T) + r_{2,b}(T)(\mathbf{M} - M_r) & \text{for } T \leq 0.5 \text{ s, and } \mathbf{M} \leq M_r \\ r_{2,a}(T) + r_{2,c}(T) \tanh[r_{2,d}(\mathbf{M} - M_r)] & \text{for } T \leq 0.5 \text{ s, and } \mathbf{M} > M_r \\ r_{2,a}(T) + r_{2,b}(T)(\mathbf{M} - M_r) & \text{for } T > 0.5 \text{ s} \end{cases} \tag{6.9}$$

$$r_3(\mathbf{M}; T) = \begin{cases} r_{3,a}(T) + r_{3,b}(T)(\mathbf{M} - M_r) & \text{for } \mathbf{M} \leq M_r \\ r_{3,a}(T) + r_{3,c}(T) \tanh[r_{3,d}(\mathbf{M} - M_r)] & \text{for } \mathbf{M} > M_r \end{cases} \tag{6.10}$$

This set of equations requires the determination of up to 21 coefficients at the shortest periods, with slightly fewer being required at longer periods. Although this is a relatively large number, we also have a very large dataset of EXSIM simulations and empirical observations, and a very sound basis for developing initial estimates for all these coefficients.

The initial parameter estimates are determined through two stages. Firstly, the magnitude-specific regressions using Equation (6.1) provide estimates of the r_0, r_1, r_2, r_3 terms of Equation (6.6) for each magnitude, and the preliminary estimates of the $r_{i,a}, r_{i,b}, r_{i,c}, r_{i,d}$ are found from performing regressions on the r_0, r_1, r_2, r_3 terms with magnitude (examples of which were shown in Figures 6.10 to 6.12). Similarly, preliminary estimates of the source scaling coefficients come from the regressions shown in Figures 6.8 and 6.9 (and corresponding results for other periods not shown). In the second stage, these preliminary coefficient estimates are used as initial estimates of the parameters for a regression using the full functional form but using just 10% of the complete dataset of EXSIM simulations (the 10% is a random sample

from the full dataset). This regression still makes use of sufficient data to constrain the necessary coefficients but can be run relatively quickly. The coefficient values obtained from the regression on the data subset are then used as the starting estimates of the parameters for the final regressions on the complete dataset. Note that two alternative regressions are also performed, one using only the EXSIM simulation results, and another that also includes the empirical data from the Groningen field. The latter option is used to help guide the model towards the empirical data where this exists. However, the overall model fit is very heavily dominated by the EXSIM ordinates, which are more abundant and cover the full magnitude range.

The above procedure is followed on a period-by-period basis for each of the four stress parameter branches. No smoothing of the coefficients is subsequently applied across the response periods. This is not necessary given that the generating model of EXSIM creates spectra that are relatively smooth (once multiple stochastic realisations are obtained), and because the parametric functional form does an excellent job of replicating the simulated amplitudes.

The performance of the fitted models can be assessed by comparing the predicted amplitudes with the target data. As the dataset is so large, consideration of traditional residual plots is not particularly instructive. To circumvent this to some extent, the target amplitudes and predictions are compared for discrete magnitude bins, and metrics representing the mean residuals in each magnitude bin are computed.

Figures 6.13 to 6.15 show examples of these comparisons for example periods that span the full range considered. These three examples cover the three possible cases represented by the path scaling terms in Equations (6.8) and (6.9). The examples are all shown for the lower central stress parameter branch, but similar figures for any other branch and response period show a very similar performance. In particular, the four stress parameter branches give similar predictions over the magnitude range where the empirical data exists, and the metrics reported in Figures 6.13 to 6.15 are therefore representative.

The metrics presented in the upper right corners of each panel in Figures 6.13 to 6.15 show that the parametric models all represent the target data very well. There are no clear systematic patterns that would be of concern, and the most extreme of the mean residuals correspond to a ~3-5% maximum bias in any given magnitude bin. For many magnitude bins, the mean residual corresponds to a bias of around 1% or less.

Figures 6.13 to 6.15 show that the EXSIM simulations include increasing levels of variability as the magnitude increases. This increase primarily reflects the influence of randomizing the source parameters within the finite-fault simulations (the rupture aspect ratios and the hypocentral locations). The observed variability is not used as part of the model development but does serve to demonstrate the need to consider large numbers of simulations in order to obtain smoothly varying ground-motion

amplitudes. In the small-magnitude range, where empirical data exists, the empirical data has significantly more variability than the essentially point-source simulations that are performed in this magnitude range. This is to be expected as the purpose of the EXSIM parameter calibration is to help identify the appropriate median model, not to constrain any elements of the variability. The issue earthquake-to-earthquake variability is discussed in detail in the following section.

The final step in deriving the parametric models is to compare the model predictions directly to the small-magnitude empirical data from the Groningen field (after accounting for site response effects). At this point, a relatively sophisticated regression analysis (to be explained in Section 6.3) is conducted to account for systematic earthquake effects, systematic recording station effects, influence of the recording network, and magnitude uncertainties. This analysis allows for an estimate of the bias of the parametric models with respect to the observed Groningen data. Any bias encountered is then removed from the parametric ground-motion models to ensure that the final set of models are unbiased with respect to the intensity measures of interest for the hazard and risk calculations.

Figures 6.16 to 6.18 demonstrate the behaviour of the final fitted models. Figure 6.16 shows the magnitude scaling for the four stress parameter branches at four selected distances, and for all periods considered within the model development. For the shortest distances, the general magnitude scaling exhibits trends commonly encountered in ground-motion models. The magnitude scaling at these distances transitions from having a relatively steep gradient at small magnitudes, to a flatter gradient at larger magnitudes. The transition between these scaling regimes is related to the scaling of the source corner frequency, and so varies with response period. However, as one moves away from the source, the complexity of the path scaling model plays a stronger role and we observe the influence of the different geometric spreading rates at small and large magnitudes, as shown previously in Figures 6.10 to 6.12. Figure 6.16 also clearly shows that the range of model predictions at the NS-B horizon over the four stress parameter branches varies considerably with magnitude. This behaviour is discussed in greater detail later in Chapter 10.

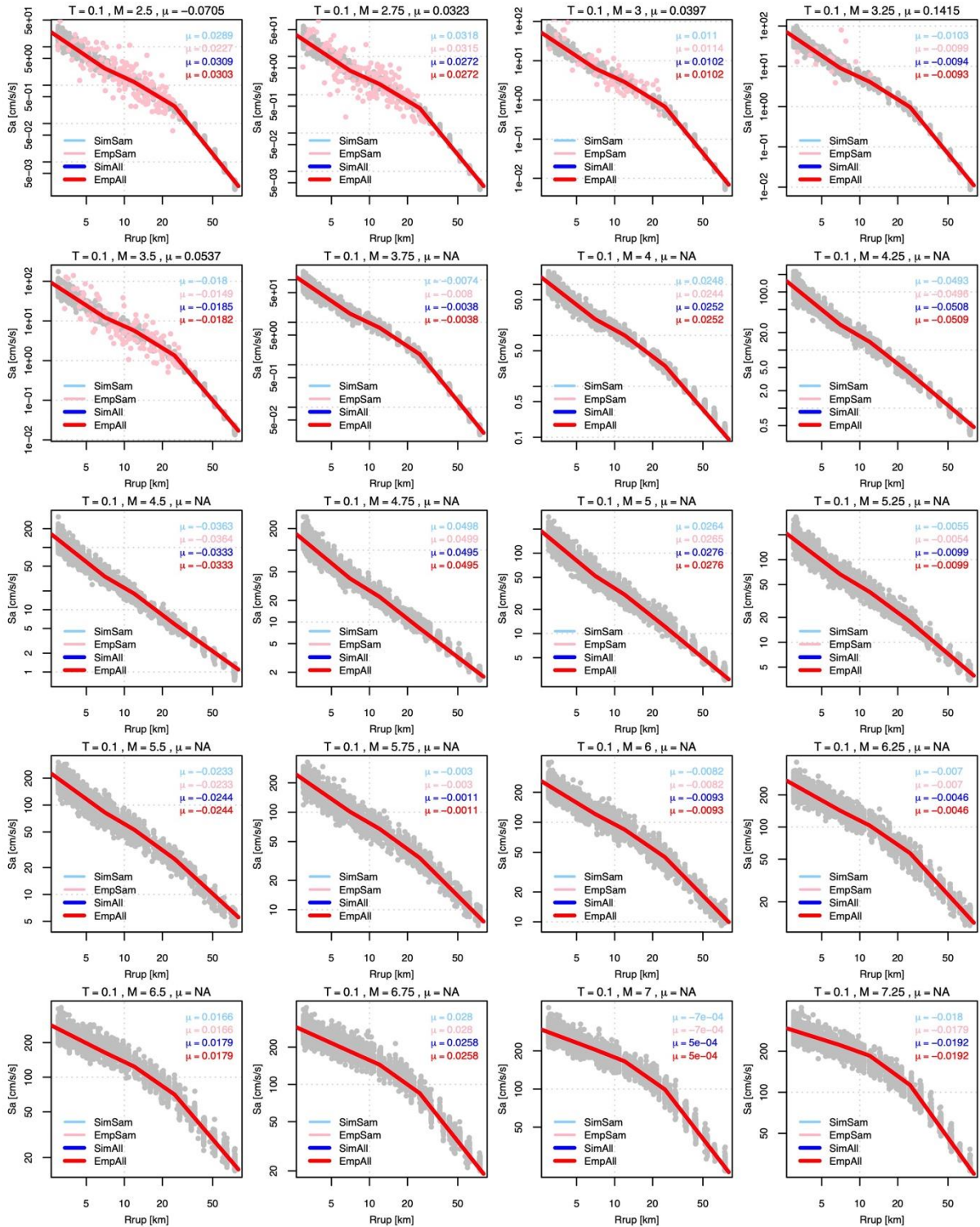


Figure 6.13. Comparison of the fitted model to the target NS-B data for the central lower model, and $T = 0.1$ s. Grey markers show EXSIM simulated spectral ordinates, pink markers show empirical Groningen ordinates (in bins of 0.25 units width, where applicable). Four fitted models are shown, but only the ‘EmpAll’ is visibly discernible. The legend key consists of a compound string, the first three letters are ‘Sim’ if the data is solely simulated and ‘Emp’ if the empirical data is included, the final three letters are ‘Sam’ if the model is fit to the 10% dataset sample, and ‘All’ if the complete dataset is used. Numerical values in the upper right of each panel are the mean residuals for the corresponding model (by colour) in that magnitude bin. Metrics in the panel headers show the period, magnitude, and the mean of the empirical residuals in this magnitude bin, where applicable.

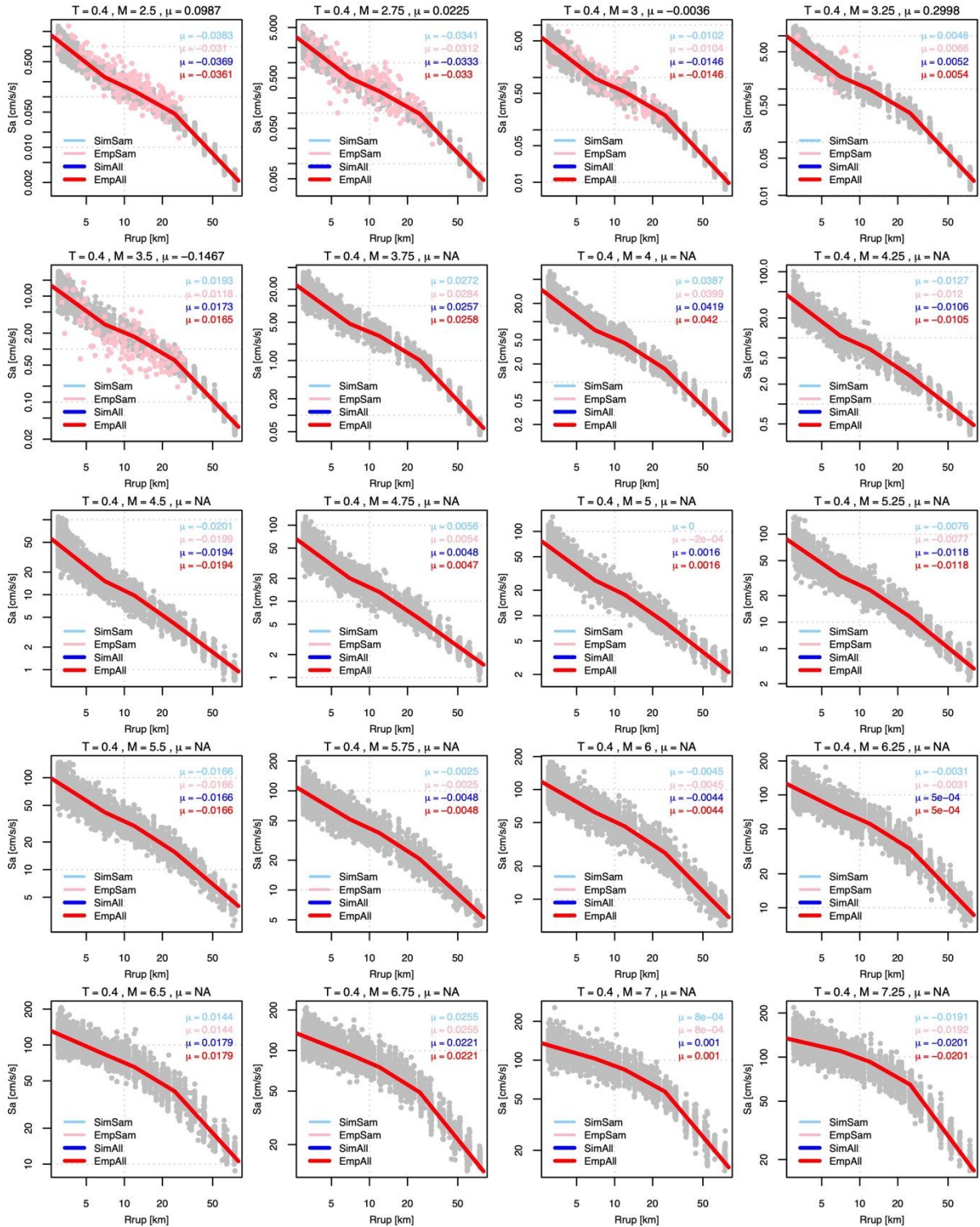


Figure 6.14. Comparison of the fitted model to the target NS-B data for the central lower model, and $T = 0.4$ s. Grey markers show EXSIM simulated spectral ordinates, pink markers show empirical Groningen ordinates (in bins of 0.25 units width, where applicable). Four fitted models are shown, but only the ‘EmpAll’ is visibly discernible. The legend key consists of a compound string, the first three letters are ‘Sim’ if the data is solely simulated and ‘Emp’ if the empirical data is included, the final three letters are ‘Sam’ if the model is fit to the 10% dataset sample, and ‘All’ if the complete dataset is used. Numerical values in the upper right of each panel are the mean residuals for the corresponding model (by colour) in that magnitude bin. Metrics in the panel headers show the period, magnitude, and the mean of the empirical residuals in this magnitude bin, where applicable.

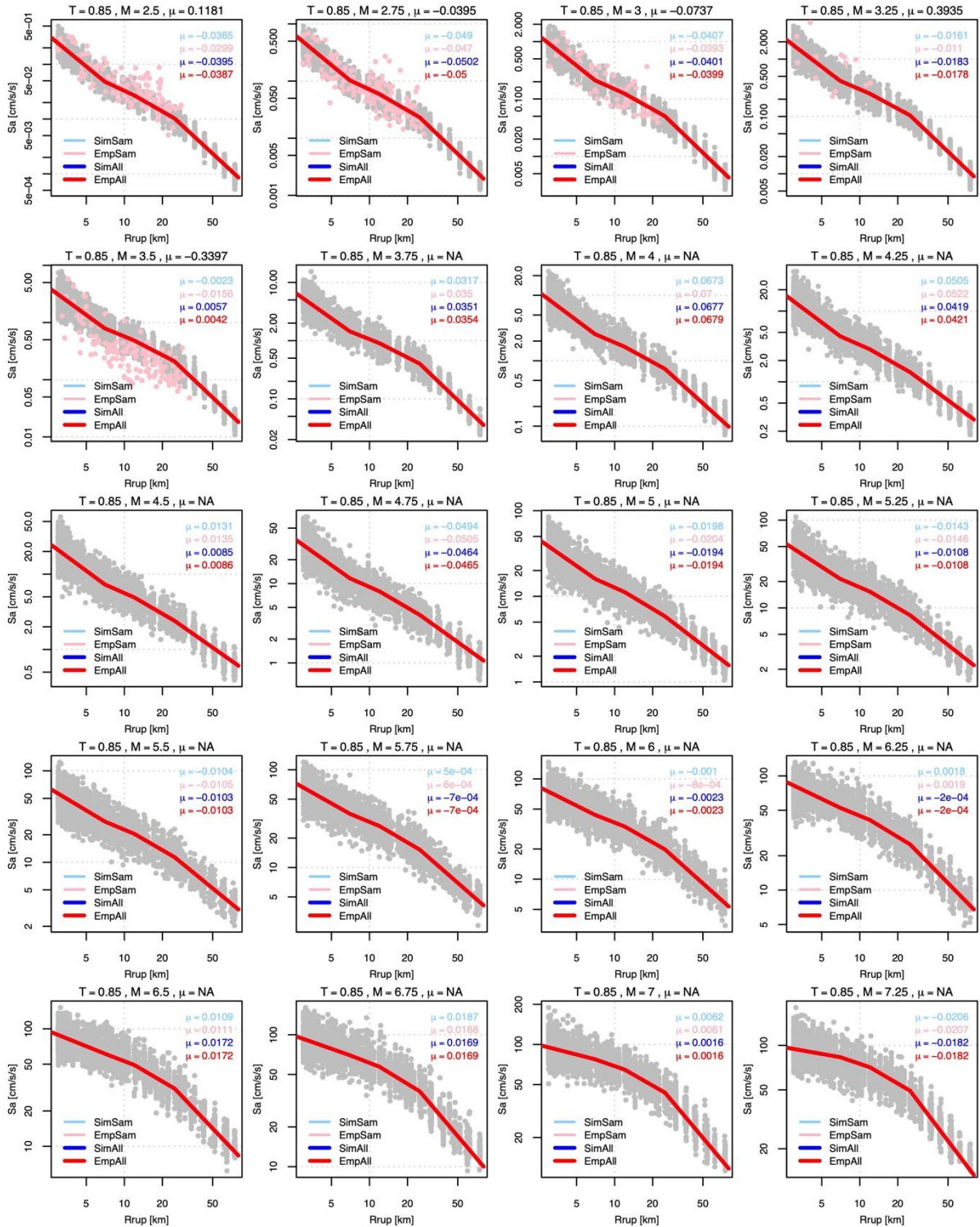


Figure 6.15. Comparison of the fitted model to the target NS-B data for the central lower model, and $T = 0.85$ s. Grey markers show EXSIM simulated spectral ordinates, pink markers show empirical Groningen ordinates (in bins of 0.25s unit width, where applicable). Four fitted models are shown, but only the ‘EmpAll’ is visibly discernible. The legend key consists of a compound string, the first three letters are ‘Sim’ if the data is solely simulated and ‘Emp’ if the empirical data is included, the final three letters are ‘Sam’ if the model is fit to the 10% dataset sample, and ‘All’ if the complete dataset is used. Numerical values in the upper right of each panel are the mean residuals for the corresponding model (by colour) in that magnitude bin. Metrics in the panel headers show the period, magnitude, and the mean of the empirical residuals in this magnitude bin, where applicable.

The distance scaling of the models is shown in Figure 6.17 for all response periods, stress parameter branches, and a selection of magnitudes that span the full range of interest. This figure demonstrates that response spectral amplitudes from small magnitude events decay rapidly with distance in the near field. The finite-rupture effects within EXSIM cause this scaling to flatten considerably at larger magnitudes, and we also see the distance hinges playing a far more limited role for these larger events. Again, the range of model predictions over the four stress parameter branches widens as the magnitude increases, as was previously emphasised with respect to Figure 6.16.

Finally, Figure 6.18 shows response spectral ordinates plotted against period for particular magnitude and distance combinations. Again, all four stress parameter models are shown on the same figure. In Figure 6.18, only markers are shown in order to avoid suggesting any spectral scaling between the ordinates of 0.01 and 0.1 seconds. However, it is clear from the ordinates that are plotted that the spectral peak is located at short periods, somewhere between 0.01 and 0.1 seconds – consistent with the low levels of kappa used from the EXSIM simulations at NS-B.

The spectra in Figure 6.18 again show the increasing spread of model predictions with magnitude – as previously seen in Figures 6.16 and 6.17. However, it is clearer from Figure 6.18 that this spread also varies with response period, as should be expected. Both stress parameter and kappa have their strongest influence at short periods and the larger spread of model predictions at these periods is associated with this.

The overall scaling seen across Figures 6.16 to 6.17 shows that the model at NS-B is well-behaved in the sense that the order of branches is always consistent (from low stress parameter to high, *etc.*), and that the models converge or diverge as intended. For the largest magnitudes we also see that the general scaling is similar to what would be expected from tectonic events (focussing purely upon the general features of the magnitude and distance scaling). However, it is also clear that some complexities are associated with the transition from the reservoir-hosted events to the larger events assumed to rupture down into the Carboniferous material below the reservoir.

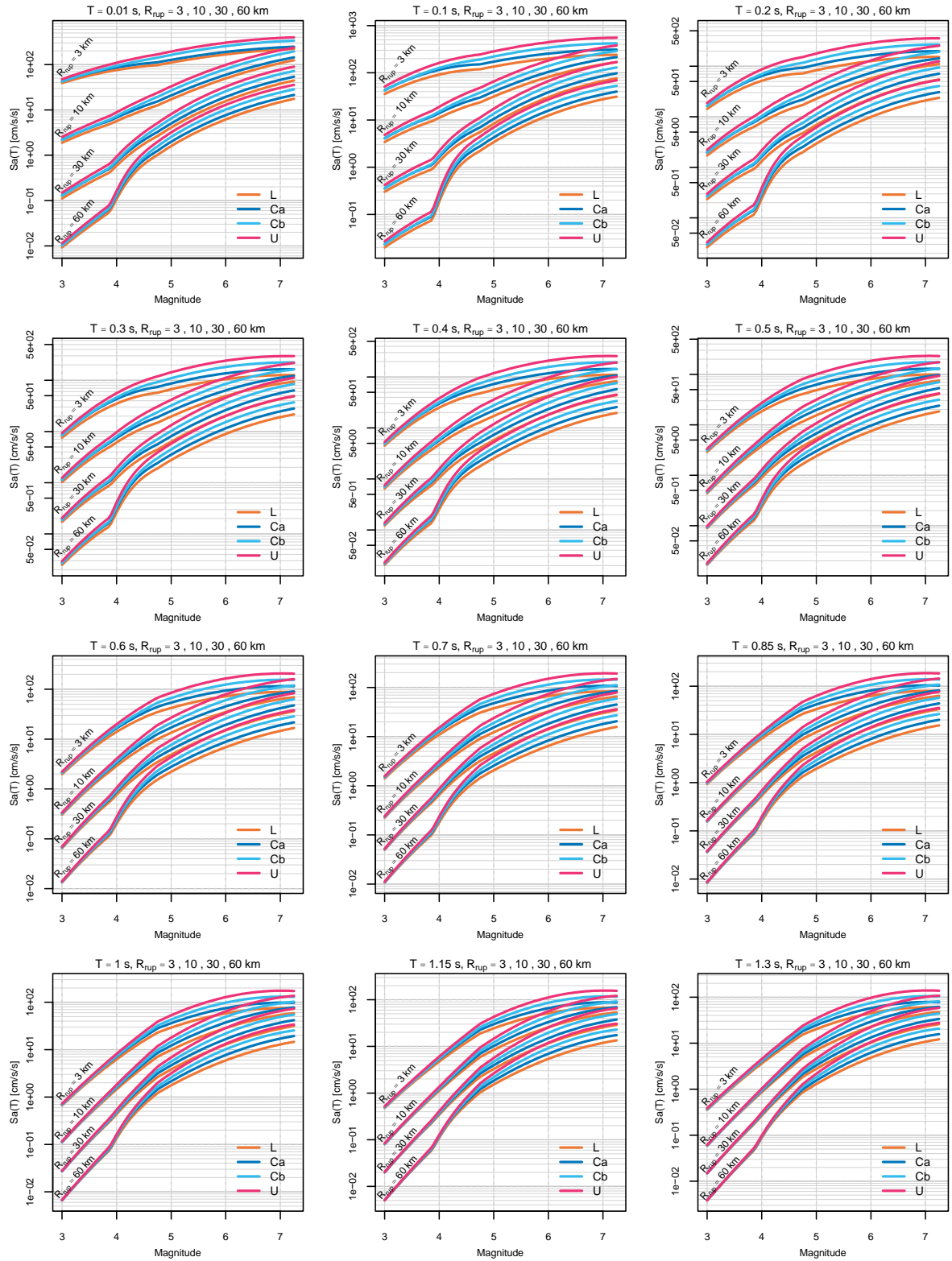


Figure 6.16. Magnitude scaling of the four stress parameter branches of the NS-B model. The four stress parameter branches are shown using the colours indicated in the legend, while the response period and distances are included in the panel titles. Rupture distances are also annotated within the individual panels. Periods beyond 1 second are shown but do not form part of the deliverable.

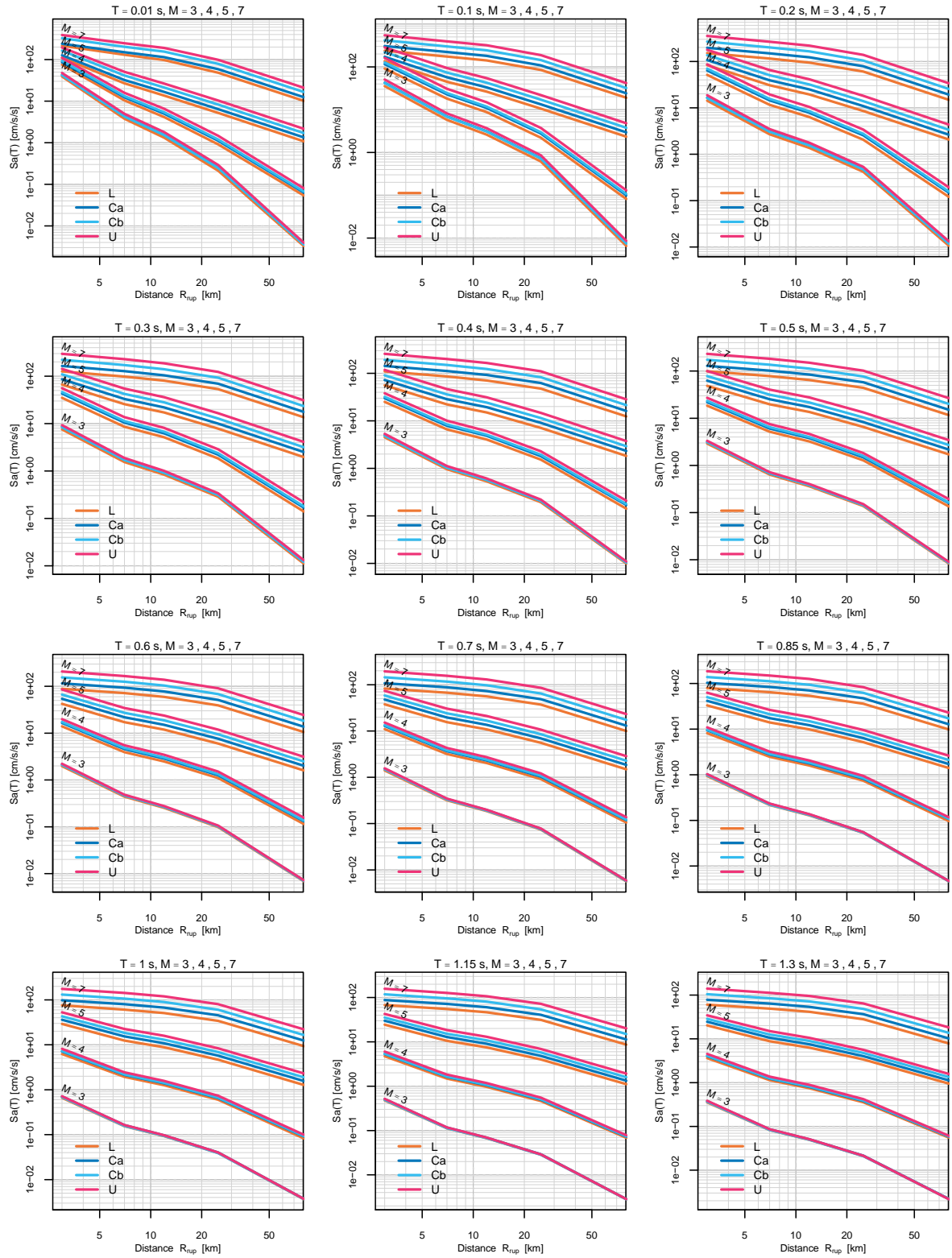


Figure 6.17. Distance scaling of the four stress parameter branches of the NS-B model. The four stress parameter branches are shown using the colours indicated in the legend, while the response period and magnitudes are included in the panel titles. Magnitudes are also annotated within the individual panels. Periods beyond 1 second are shown but do not form part of the deliverable.

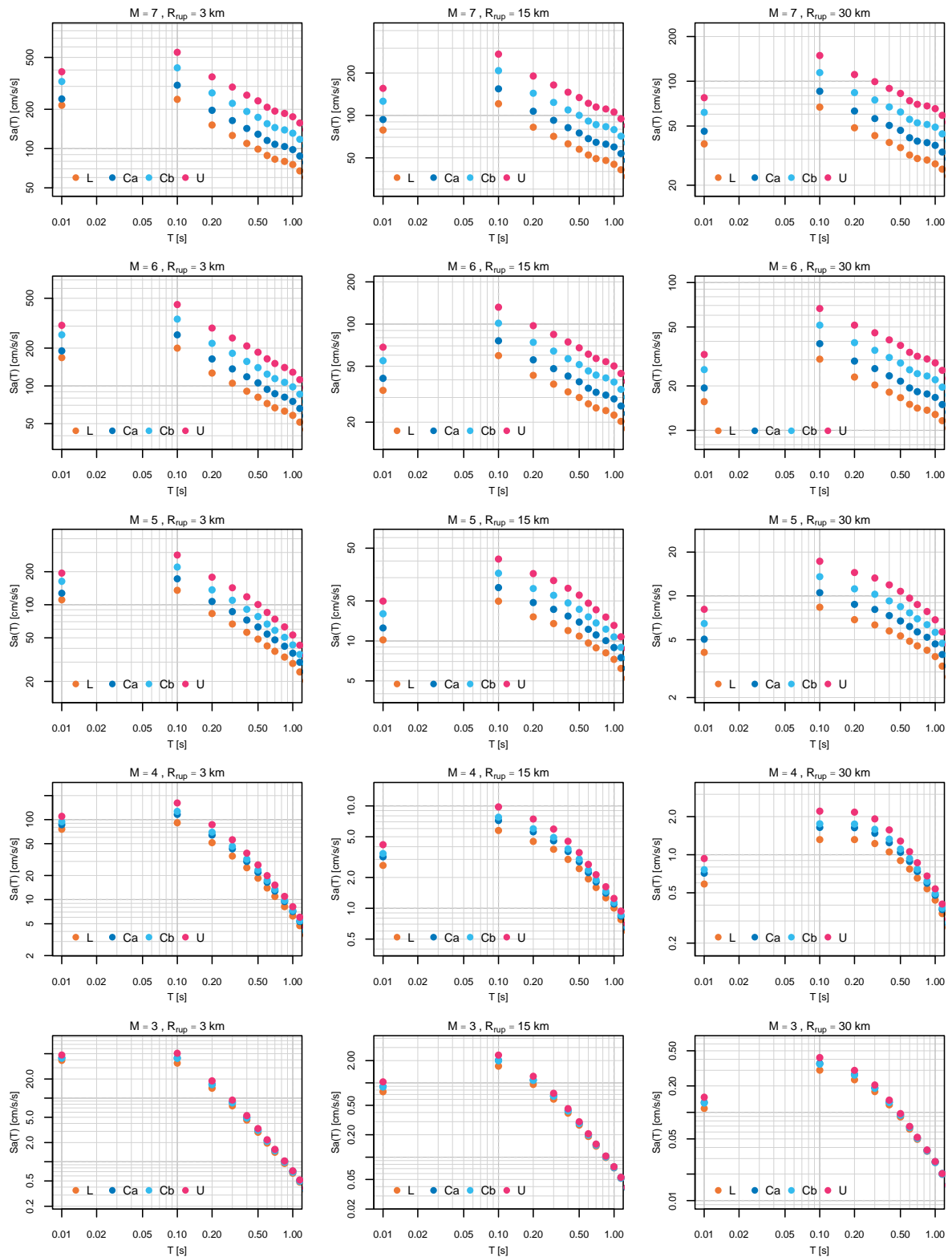


Figure 6.18. Spectral scaling of the four stress parameter branches of the NS-B model. The four stress parameter branches are shown using the marker colours indicated in the legend, while the magnitudes and distances associated with each panel are noted in the panel titles. Periods beyond 1 second are shown but do not form part of the deliverable.

6.3. Variability of Reference Rock Predictions

The variability of spectral amplitudes at the NS-B horizon is comprised of two key components, the model for the between-event variability, τ^2 , and the model for the within-event variability (after removing systematic site effects), ϕ_{SS}^2 . These terms collectively describe the degree of variability of geometric mean amplitudes entering the near-surface strata above NS-B. They are assumed independent of one another (which has also been shown by analyses of empirical data) and are combined as:

$$\sigma_{SS} = \sqrt{\tau^2 + \phi_{SS}^2} \quad (6.11)$$

to define a single-station 'sigma' value (e.g., Atkinson, 2006). This single-station sigma is the degree of variability that one should expect to observe in geometric mean response spectral ordinates when the systematic components of site response are accounted for (which is the assumption being made within the current modelling framework).

As in previous versions of the Groningen ground-motion model, the between-event variability model is developed from analysis of the empirical data recorded in the Groningen field, while the model for ϕ_{SS}^2 is imported from independent studies. The rationale for this approach is that the earthquake ruptures expected to be encountered within Groningen are atypical in comparison with ruptures contained in empirical databases of natural earthquakes. At the same time, numerous studies have looked at developing models for ϕ_{SS}^2 using different approaches and datasets from various parts of the world, and the results are very similar in all cases. For this reason, generic models for ϕ_{SS}^2 were considered and ultimately adopted. The present section first explains the selected model for ϕ_{SS}^2 and then provides the details regarding the derivation of the field-specific model for the between-event variance τ^2 .

The model for ϕ_{SS}^2 is based upon work originally conducted by Rodriguez-Marek *et al.* (2013) for the PEGASOS Refinement Project, that was subsequently updated by Al Atik (2015) within the NGA-East project. No magnitude or distance dependence is included within the model, but the ϕ_{SS} values do vary with response period. The basis of the method is to assume that the variance ϕ_{SS}^2 is χ^2 -distributed, and to select quantiles of this χ^2 distribution as discrete logic tree nodes. Two equally-weighted branches are adopted and the quantiles chosen correspond to the 16th and 84th percentiles of the distribution. The equations for these quantiles are defined as:

$$\phi_{SS,low} = \sqrt{c\chi_{2,k}^{-1}(0.159)} \quad (6.12)$$

and

$$\phi_{SS,high} = \sqrt{c\chi_{2,k}^{-1}(0.841)} \quad (6.13)$$

where c is a scaling parameter that maps the actual distribution of ϕ_{SS}^2 to the χ^2 distribution, and k is an equivalent number of degrees of freedom for the χ^2 distribution. The parameters c and k are both functions of the standard deviation of ϕ_{SS}^2 as defined in Equations (6.14) and (6.15):

$$c = \frac{[SD(\phi_{SS}^2)]^2}{2\phi_{SS}^2} \quad (6.14)$$

$$k = \frac{2\phi_{SS}^4}{[SD(\phi_{SS}^2)]^2} \quad (6.15)$$

The key parameter to determine is therefore $SD(\phi_{SS}^2)$ and this is obtained from the coefficient of variation of ϕ_{SS}^2 found in comprehensive analyses of empirical datasets of natural ground-motions. In particular, within the SWUS project (GeoPentech, 2015), a coefficient of variation of $COV(\phi_{SS}^2) = 0.12$ was obtained, and the standard deviation of ϕ_{SS}^2 is then obtained as $SD(\phi_{SS}^2) = 2COV(\phi_{SS}^2)$. This same value is adopted by Al Atik (2015) and is assumed here also. Note that previous versions of the Groningen ϕ_{SS} model have used this same formulation and values.

Figure 6.19 shows the model for ϕ_{SS} as a function of response period. As can be seen, the levels of ϕ_{SS} are higher for short periods than they are for longer periods. Due to the particular response periods being considered within the computation of average spectral acceleration, we effectively have equal values of ϕ_{SS} for 0.01 and 0.1 seconds, with a linear dependence upon $\ln T$ for periods between 0.1 and 1.0 seconds.

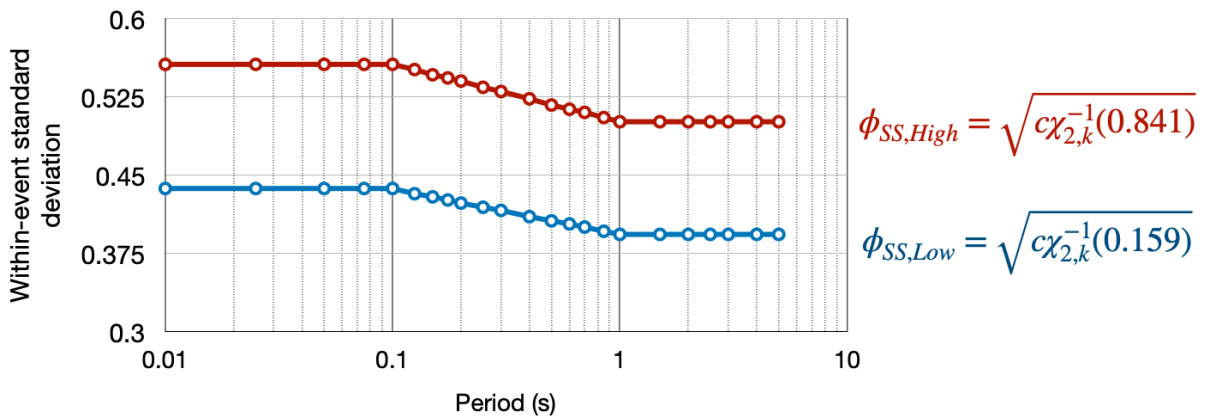


Figure 6.19. Model for ϕ_{SS} in the V7 GMM. The two branches are given equal weighting and are based upon the model of Al Atik (2015).

The development of the model for the between-event variability makes use of the parametric ground-motion model presented in the previous section. The conceptual framework is shown in Figure 6.20 where the parametric ground-motion model is represented as $\mu_{\ln Sa_{nsb}}$. The surface spectral amplitudes depend upon this expected level of amplitude at the NS-B horizon, plus any components of the variability that exist at this horizon. In Figure 6.19 these are represented as systematic earthquake, $\eta_{E,nsb}$, and ‘site’ effects, $\eta_{S,nsb}$, as well as apparent variability, ϵ_{nsb} . As noted in the figure, these station effects at NS-B, $\eta_{S,nsb}$, are not the same as random effects for stations that are sometimes considered within mixed effects regression analyses, but rather represent average systematic path effects at these locations.

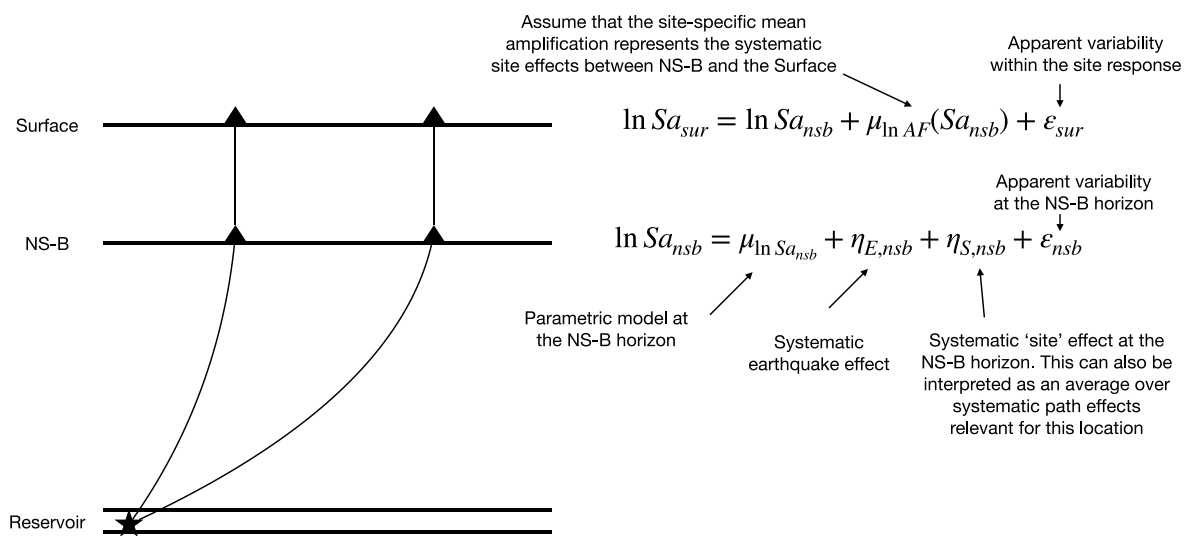


Figure 6.20. Conceptual framework used to develop the τ^2 variance model. ‘Observed’ amplitudes at the NS-B horizon have systematic earthquake effects $\eta_{E,nsb}$ that have a variance of τ^2 . Components of variability arise from processes at the source (indicated by the star located within the reservoir), through the travel path from the reservoir to the NS-B horizon, and from this horizon to the surface. The cross section on the left is highly idealised, and the mathematical expressions on the right represent the treatment when deriving the between-event variability model – there are some subtle differences between this framework and the generation of spectral amplitudes within the hazard and risk calculations.

The surface amplitudes then depend upon the level of Sa_{nsb} at the NS-B horizon, the site amplification/response between the NS-B horizon and the surface, and any apparently random components of this site response, ϵ_{sur} . The reason why this overall framework needs to be considered at this point is that the approach to constraining the between-event variance considers the uncertainty estimates in the magnitude for each event. If this uncertainty is not considered, it is passed through to τ^2 leading to an artificial inflation. To assess the impact of the magnitude uncertainties, the sensitivity of the surface amplitudes with respect to magnitude needs to be determined. However, as can be appreciated from Figure 6.20, the surface amplitudes depend upon magnitude due to the magnitude dependence of the parametric model

at NS-B (presented in the previous section), and the magnitude dependence within the site amplification model (to be discussed in Section 8.2).

When comparing the parametric model of Section 6.2 with the empirical data from the Groningen field, we expect to observe small differences. In principle, the FAS model is developed with the hope of giving rise to completely unbiased predictions of response spectral ordinates. However, there are good reasons why this will not be achieved. For a start, the upper and lower stress parameter branches are defined to deliberately bound the mean of the empirical data. On a more subtle level, the variance framework shown in Figure 6.20 is not replicated practically within the development of the FAS model. For example, station-specific kappa estimates are obtained, but these do not map directly to the systematic site terms represented within Figure 6.20. Additionally, the step-wise nature of the FAS model development can lead to conditional dependencies among the parameters that mean the final model may not be perfectly centred. For this reason, the process of computing the optimal value of τ^2 also looks to identify any residual bias that may exist between the parametric model of the previous section and the empirical Groningen data.

The regression model that is used to identify any biases and the τ^2 model can be expressed as:

$$\Delta_T \sim N(\beta, \tau^2 + \phi_{S2S}^2 + \phi_{SS}^2) \quad (6.16)$$

where β is the parametric model bias, τ^2 is the between-event variance, ϕ_{S2S}^2 is the site-to-site variance, and ϕ_{SS}^2 is the residual variance (event and site-corrected variance). These parameters are assumed to describe the distribution of the total residuals, Δ_T , defined by Equation (6.17):

$$\Delta_T = \ln Sa_{sur} - \mu_{\ln Sa_{nsb}}(\mathbf{M}, R_{rup}) - \mu_{\ln AF}(\mathbf{M}, R_{rup}; site) \quad (6.17)$$

in which $\mu_{\ln Sa_{nsb}}$ is the parametric model at NS-B and $\mu_{\ln AF}$ is the mean amplification function. Following the conceptual framework of Figure 6.20, the systematic event and site effects, as well as the apparent aleatory components are distributed according to the following set of expressions:

$$\eta_{E,nsb}^{(i)} \sim N \left[0, \tau^2 + \left(\frac{\partial \mu_{\ln Sa_{sur}}(\mathbf{M})}{\partial \mathbf{M}} \right)^2 \sigma_{\mathbf{M},i}^2 \right] \quad (6.18)$$

$$\eta_{S,nsb} \sim N(0, \phi_{S2S}^2) \quad (6.19)$$

$$\varepsilon_{nsb} + \varepsilon_{sur} \sim N(0, \phi_{SS}^2) \quad (6.20)$$

Of particular note is Equation (6.18) where the effects of individual magnitude uncertainties, $\sigma_{M,i}$, are accounted for. This approach assumes that the apparent between-event variance that would be observed if one ignored the effects of magnitude uncertainties is equal to the real between-event variance and the variance associated with propagating (in a first-order manner) the magnitude uncertainty through the overall ground-motion model.

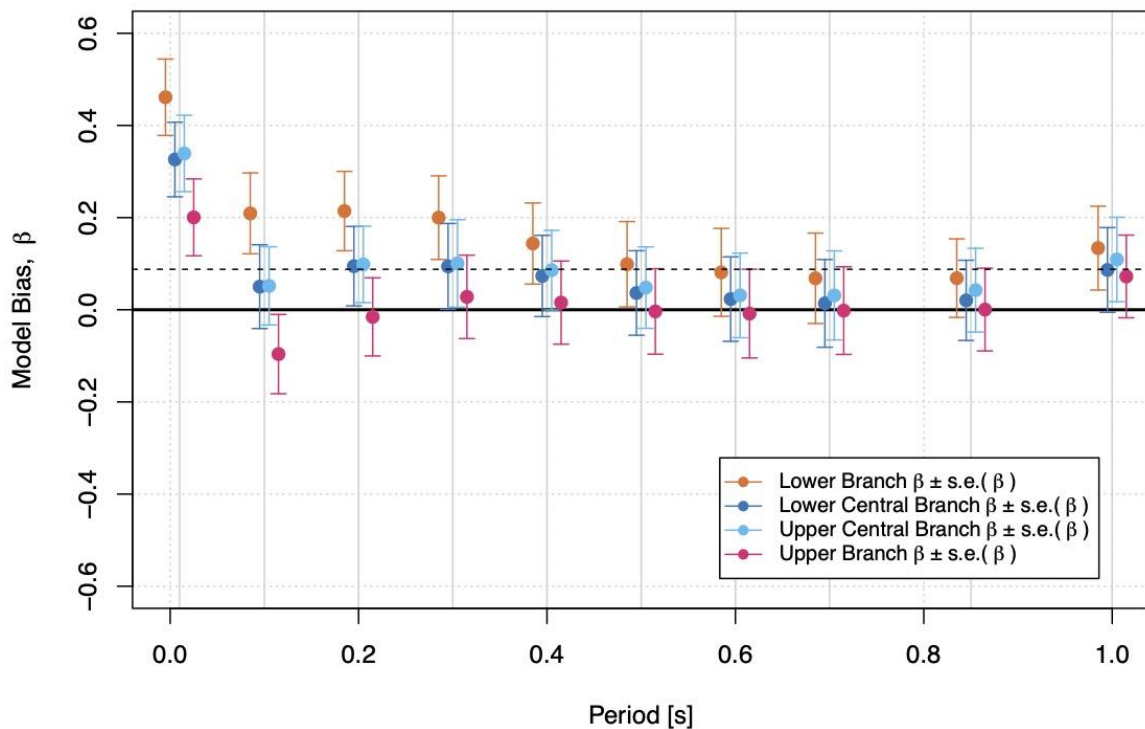


Figure 6.21. Bias of the original parametric model, β of Equation (6.16), against period for the four stress parameter branches (individual branch estimates are horizontally offset from the actual periods shown using the vertical grey lines to avoid overlap). The dashed horizontal line shows the average of the two central branch biases over the period range shown.

Figure 6.21 shows the biases at individual periods plotted against period. The average of these period-dependent biases, computed across all periods, is then removed from the results in Figure 6.21 to obtain the final period-dependent biases shown in Figure 6.22. Removing this average bias ensures that the model is unbiased with respect to the average spectral acceleration. This property could also have been achieved by making adjustments on a period-by-period basis to the results in Figure 6.21 (essentially centring each set of biases at each period so that the central branches fall on zero bias). However, that approach would lead to the predicted response spectra at NS-B being non-smooth. This final parametric model, as noted in the previous section, is obtained from the regressions against the EXSIM simulations, and this final bias adjustment step. The average level of bias found and shown by the horizontal dashed line in Figure 6.21, is added to the original parametric model predictions (the

same adjustment is made to all four stress parameter branches) to ensure that the final model is centered with respect to the empirical data. Note that this centering applies to the overall average spectral acceleration level, not to individual periods, as can be appreciated from Figure 6.22, where each period displays some offset from the ideal target level of zero. In particular, it is clear that the spectral ordinate at 0.01 seconds is systematically underpredicted, while the spectral ordinates at intermediate periods are over-predicted in order to compensate for this.

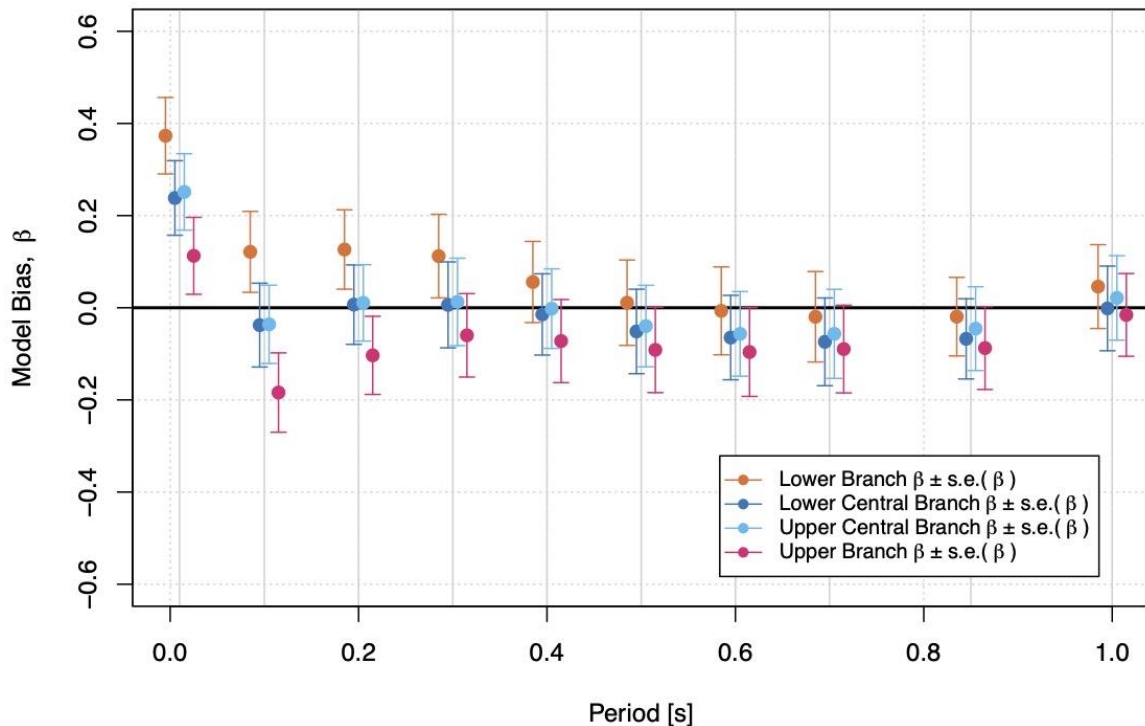


Figure 6.22. Period-dependent bias after removal of the overall bias in Figure 6.21. As in Figure 6.21, the individual markers are offset slightly from the actual periods shown by the vertical grey lines.

The corresponding estimates, and standard errors, of the between-event standard deviation τ are shown in Figure 6.23. This figure suggests a degree of period dependence of the between-event variability. Previous versions of the Groningen model have sought to model this period dependence, using the argument that there are physical reasons why the between event variability should be slightly lower at short periods. However, the same arguments underpinning that period dependence also suggest that the location of the dip should also depend upon the stress parameter and magnitude (it is related to the location of the source corner frequency). As we are seeking to develop a single model for the between-event variability to apply to all magnitudes, and that there is no way of testing whether the stress drop dependence of this effect scales to larger magnitudes in Groningen, the final model proposed averages through the period-dependent estimates shown here.

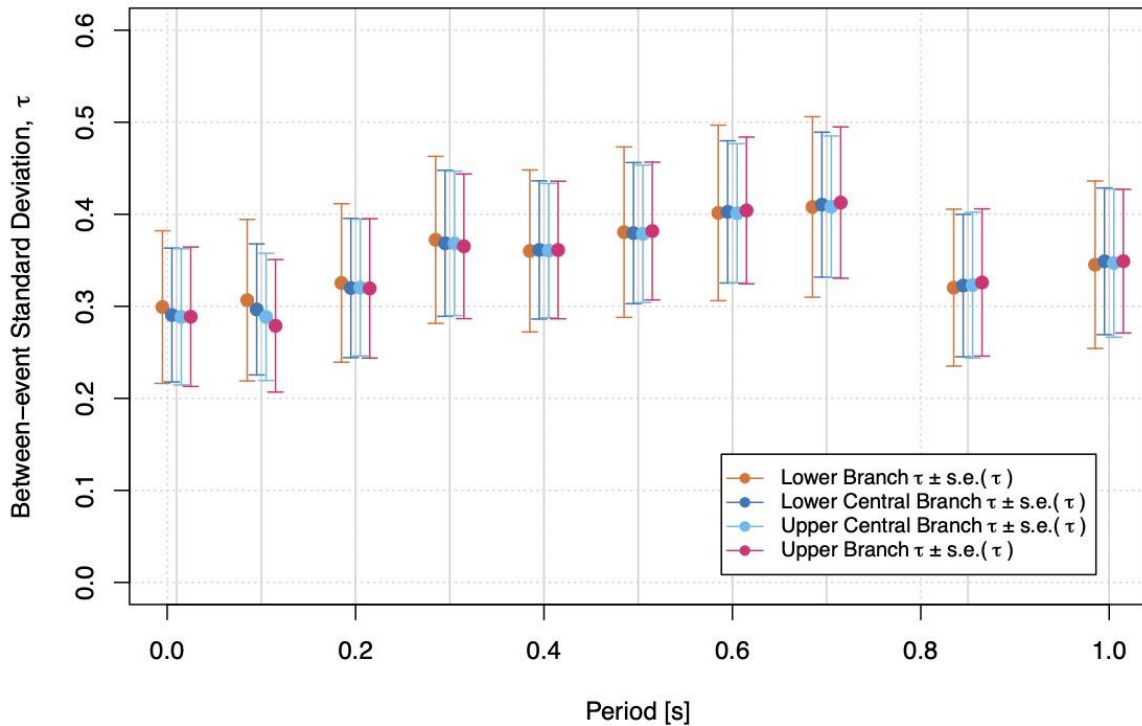


Figure 6.23. Raw estimates of the between-event standard deviation, τ , against response period, for each of the four stress parameter branches. Individual branch estimates are horizontally offset from the true period value to avoid visual overlap. The error bars represent the standard errors in the estimates of τ .

As noted earlier with respect to the model for ϕ_{SS}^2 , it is common to assume that the variance is χ^2 distributed (and theoretically, this is a consistent assumption). However, the regression analysis conducted herein is performed within a Bayesian framework where such assumptions are not enforced. As a result, we can gauge the uncertainty in the estimates of τ by looking directly at the posterior distribution of this parameter from our regression analysis. Figure 6.24 compares the theoretical 5th and 95th quantiles of the χ^2 distribution (the heavy black lines) with the corresponding quantiles of the posterior distribution at each period. This comparison shows that the posterior distribution has heavier tails than suggested by the theoretical distribution (the thin vertical lines for each branch represent the range from the 5th to 95th quantile of the posterior distribution – and these extend beyond the limits from the χ^2 distribution in all cases). Given the current sample size of empirical data (here we are concerned with the number of events, rather than records) there are good reasons to anticipate deviations from the expected theoretical behaviour. As such, we prefer to define the quantiles of the τ^2 model directly from the posterior distributions obtained in the regression analysis.

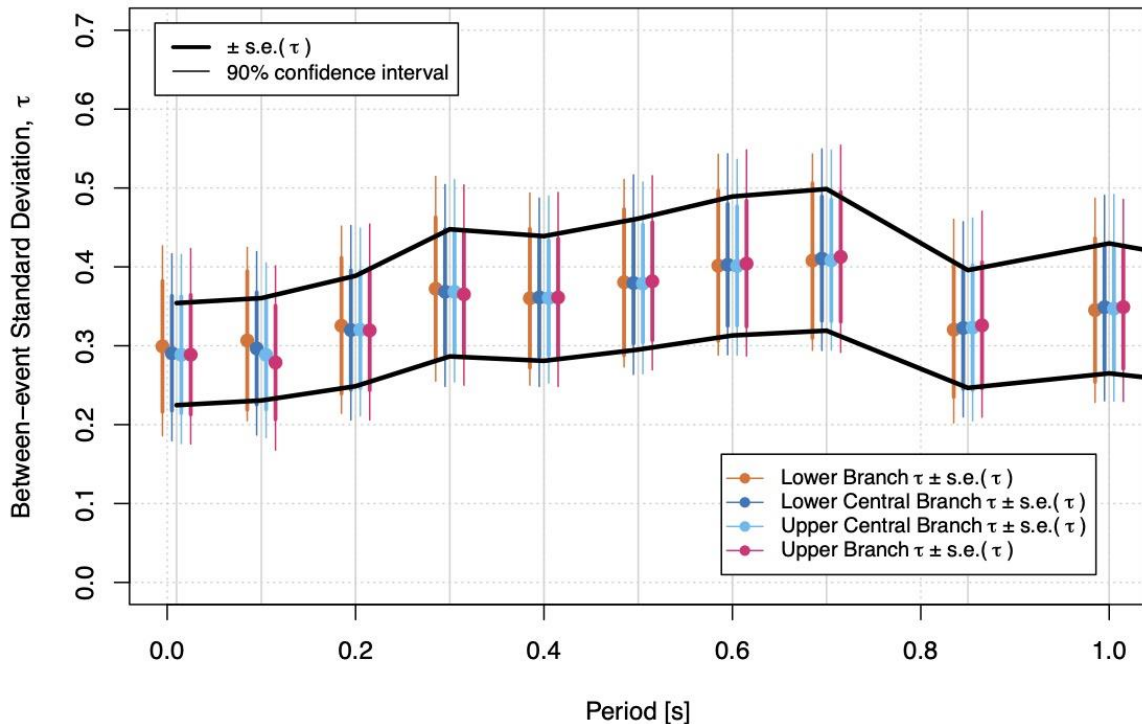


Figure 6.24. Comparison of the 5th and 95th quantiles of the posterior distributions of τ from the Bayesian regression analysis with the theoretical quantiles from the χ^2 distribution (the heavy black lines). Results for each branch are offset slightly from the true period value to avoid visual overlap. The coloured lines are explained in the figure legend.

Figure 6.25 shows the final adopted model. This model consists of three branches, the mean and the 5th and 95th quantiles. To define these values, we simply pool the quantile estimates across all periods and branches and take the mean of these. As can be appreciated from Figure 6.25, this leads to a slight increase in τ at very short periods (with respect to the period-specific values) and a slight reduction at intermediate periods. The 5th and 95th quantiles are shown by the dashed horizontal lines in the figure.

To gauge the extent to which the spread of τ model branches is reasonable, the final model was compared to equivalent models from the NGA-East and NGA-West2 Projects (as discussed in Al Atik, 2015). The central estimates of between-event standard deviation for NGA-East and for the small magnitude range in NGA-West2 are higher than those of the final Groningen model. This is to be expected due to the very large spatial extent of the NGA-East Project, and the ergodic nature of the NGA-West2 Project (even if the small magnitude data is dominated by Californian events). However, a comparison with the model for larger magnitudes for NGA-West2 shows a remarkably close agreement with the final Groningen model (in Figure 6.26, the horizontal line for the NGA-West2 models plots directly beneath that for Groningen—the two cannot be visually distinguished). Given that we have essentially a non-ergodic estimate over the small magnitude range (and quite a large effective sample size in

the magnitude range where we have data), we should expect lower estimates of τ than in NGA-West2.

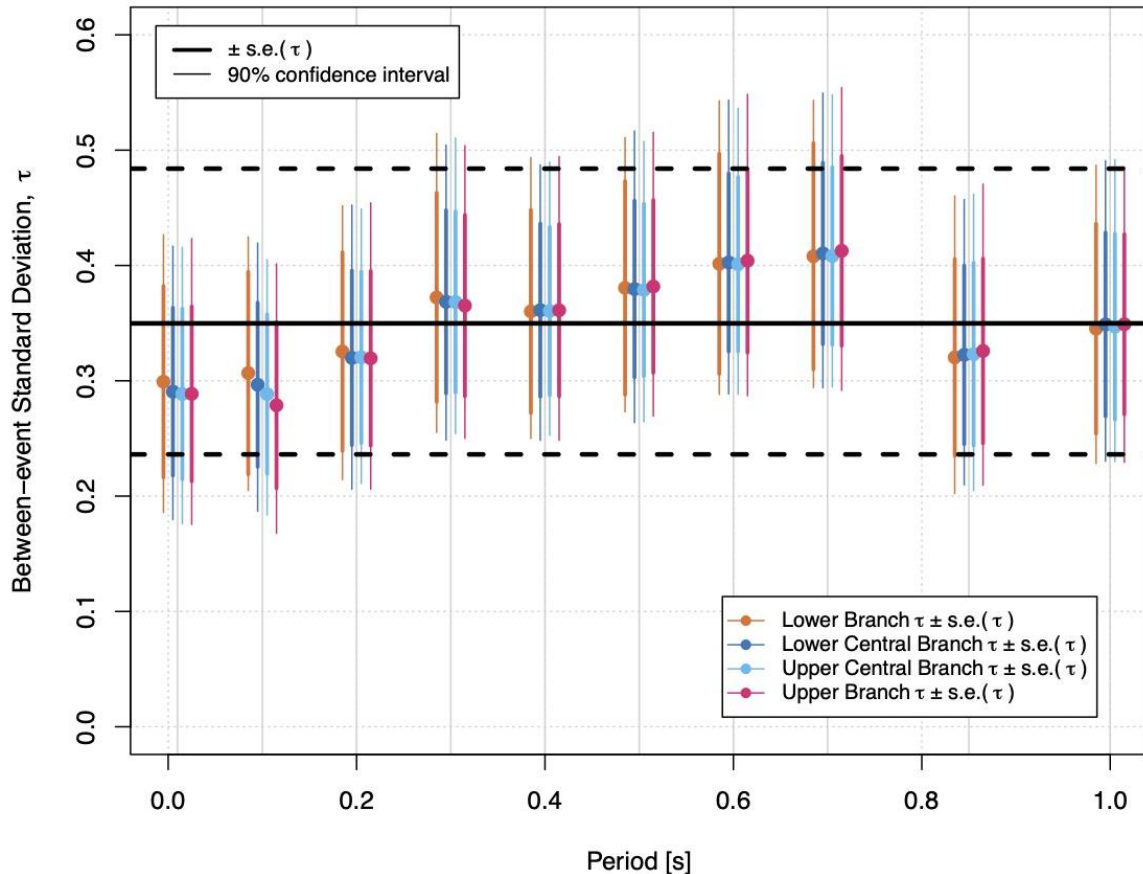


Figure 6.25. Final model for τ (the horizontal black lines) smoothing through the period-dependent results for each branch. The solid black horizontal line shows the mean of the median tau values across period, while the upper and lower horizontal black dashed lines show the mean of the 5th and 95th percentiles.

At the same time, we seek to use this model over the full magnitude range and so the final τ model should be comparable to estimates associated with large tectonic earthquakes. The agreement with the NGA-West2 model for large magnitudes, as shown in Figure 6.26 therefore suggests that the final τ model adopted is reasonable. Note that in Figure 6.26 it is not possible to see differences in the mean estimates of τ as they are numerically extremely similar. However, the Groningen quantiles are slightly lower and higher than the corresponding NGA-West2 values.

The components τ^2 and ϕ_{SS}^2 are key elements of the variance model within the Groningen GMM, but the risk calculations require the full specification of the covariance matrix of spectral ordinates rather than just variances at independent periods. The inter-period correlations presented in Section 9.2 must be used in conjunction with the variance components of this section within the risk calculations.

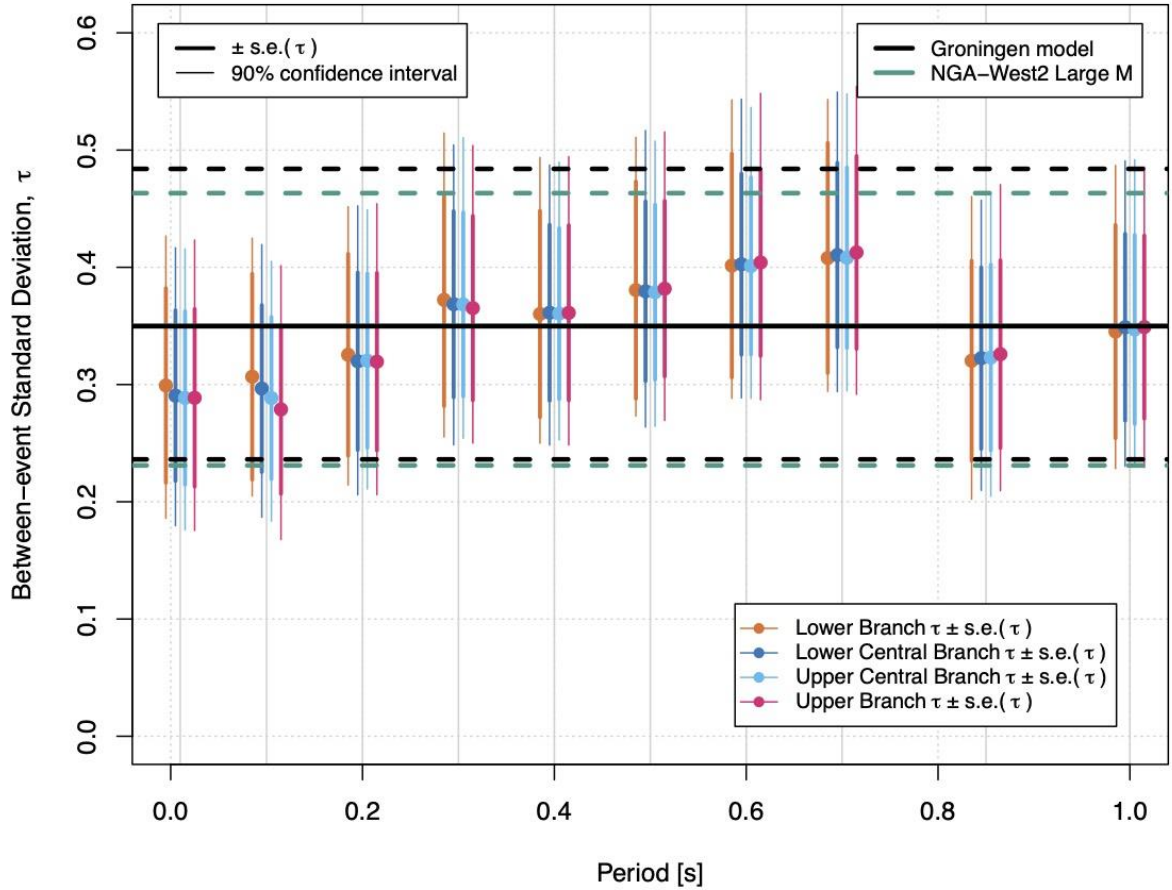


Figure 6.26. Comparison of the final model for τ with the equivalent model for the NGA-West2 project (Al Atik, 2015). The solid black horizontal line shows the mean of the median tau values across period, while the upper and lower horizontal black dashed lines show the mean of the 5th and 95th percentiles. Note that the NGA-West2 and Groningen models at the 50th percentile are almost identical. The horizontal line for the NGA-West2 model is plotted beneath that for the Groningen model, but they cannot be visually distinguished.

6.4. Influence of Instrument Type on Model Bias

At several points throughout this project, apparent differences in the levels of ground-motion amplitude recorded on instruments of differing types have been observed. It remains very challenging to identify instrument effects from other potential sources of apparent differences, but the present section extends the regression approach of Section 6.3 to identify any systematic differences arising from instrument effects.

The approach adopted is to modify the regression framework to allow for fixed effects associated with instrument type. This requires the model for the distribution of the total residuals to be expressed as:

$$\Delta_T \sim N(\beta_G F_G + \beta_{B0} F_{B0} + \beta_{Bn} F_{Bn}, \tau^2 + \phi_{S2S}^2 + \phi_{SS}^2) \quad (6.21)$$

In Equation (6.21), the single bias coefficient, β , from Equation 6.3.6 is replaced by a linear combination of three mutually exclusive terms that represent the potential bias with respect to individual instrument types. The F_G , F_{Bo} and F_{Bn} terms are binary variables that are defined as:

- $F_G = 1$ for a G station, and is 0 otherwise;
- $F_{Bo} = 1$ for an ‘old’ B station, and is 0 otherwise; and,
- $F_{Bn} = 1$ for a ‘new’ B station, and is 0 otherwise.

The coefficients β_G , β_{Bo} and β_{Bn} are then the apparent biases related to each of these instrument/station types.

One of the challenges in isolating the instrument effects is that systematic station effects are already modelled through the zone-specific site amplification functions, and through the consideration of systematic ‘site’ effects within the regression framework. While it was previously noted that the systematic ‘site’ effects at the NS-B horizon can conceptually be thought of as representing some average systematic path effects, in practice any bias in the assumed site response models will also manifest as contributions to these site terms. Therefore, if some of this bias arises from an attribute of the instrument type, then the site terms will partly accommodate this. Similarly, earlier events were recorded primarily on B stations, while more recent (and more comprehensively recorded) events are dominated by recordings from G stations. There is consequently a potential trade-off between average instrument-type effects and the random effects for earthquakes. That said, the regression approach adopted herein attempts to balance these trade-offs in order to find the most likely values of the elements in Equation (6.21).

Figure 6.27 shows the results from the regression analyses using this framework. Each panel shows the results from a different stress parameter branch, while within each panel we show the bias coefficients (and their standard errors) by instrument type. It can be appreciated that there are significant degrees of overlap between the error bar ranges shown, which suggests that the observed differences are not significant in a statistical sense. However, there is clearly a very systematic offset between the G stations and the B stations (old and new). For all stress parameter branches, the β_G coefficients are systematically higher than the β_{Bo} and β_{Bn} values.

Figure 6.28 quantifies the degree of difference between the G and B station effects. As Figure 6.27 showed that the recordings from the B stations were broadly consistent, irrespective of whether they are old or new stations, the average bias over these B stations was computed. Figure 6.28 then shows the implied ratio of spectral acceleration levels that would be recorded on G versus B station instruments. The error bars show the standard errors associated with these ratios, and we can

appreciate that there are non-trivial departures from unity (which would correspond to no difference in amplitudes over the G and B stations).

Figures 6.27 and 6.28 collectively indicate that G stations tend to record higher amplitudes than B stations, and that the difference is most pronounced at short periods. For the average spectral acceleration intensity measure used for the risk calculations, the amplitudes from the G stations will be more than 10% higher than those from B stations.

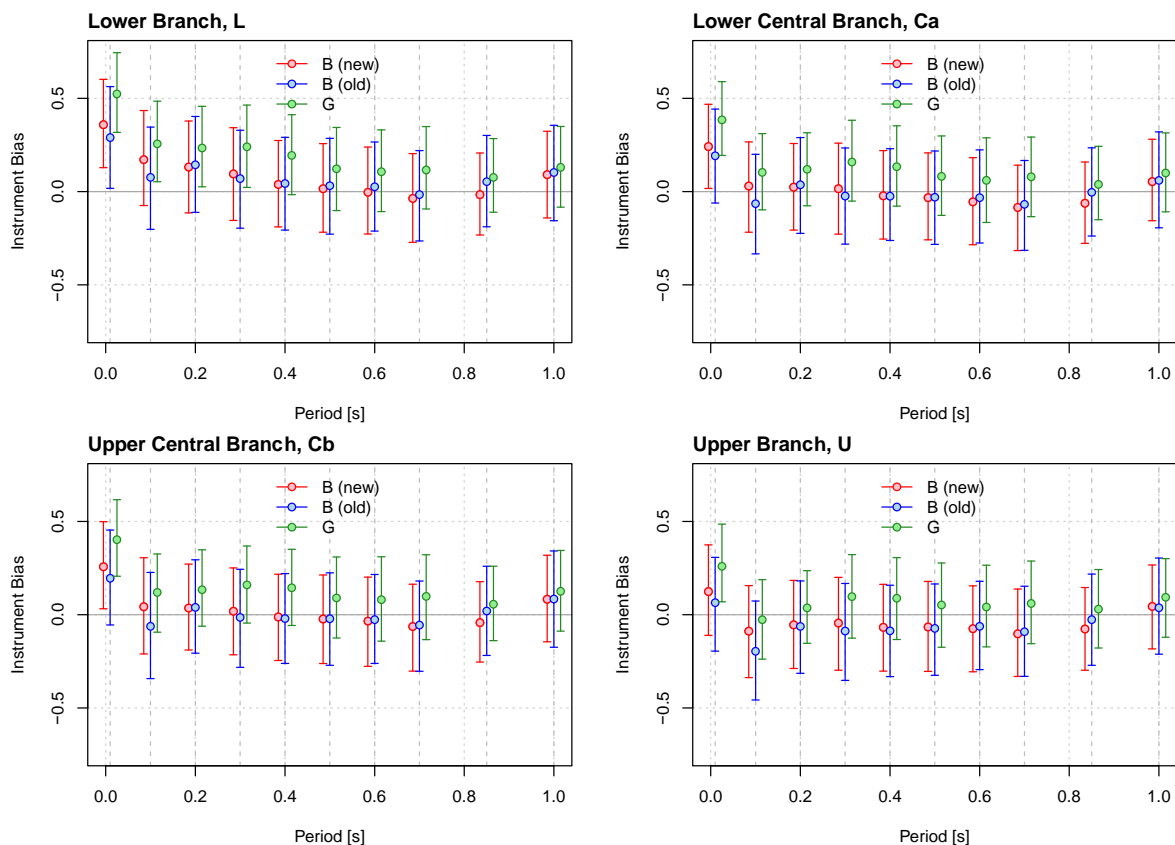


Figure 6.27. Period dependence of the potential instrument effects for each instrument type. Markers are horizontally shifted from their true periods (shown with vertical dashed lines) to avoid visual overlap. Error bars show the standard errors in these instrument effects.

As noted previously, it is very difficult to fully decouple instrument effects from other systematic effects, like station random effects, event random effects, magnitude uncertainties, and spatial patterns in within-event residuals. However, the figures presented in this section demonstrate a systematic difference between the station types, and indicate that the raw NS-B parametric model (prior to being adjusted for bias) is mostly unbiased with respect to the B station recordings. The observed bias is primarily related with the G station offset.

In both Sections 6.2 and 6.3 the adjustment to the parametric equation obtained from the EXSIM regressions was discussed. This adjustment does not discriminate between the instrument types considered in the present section. Therefore, the average bias of around 8% that was seen in Figure 6.22 is effectively a weighted average of the instrument bias terms observed in Figure 6.27. The final bias adjusted model for NS-B spectral ordinates will consequently provide predictions that are slightly below those for the G stations and slightly above those for the B stations.

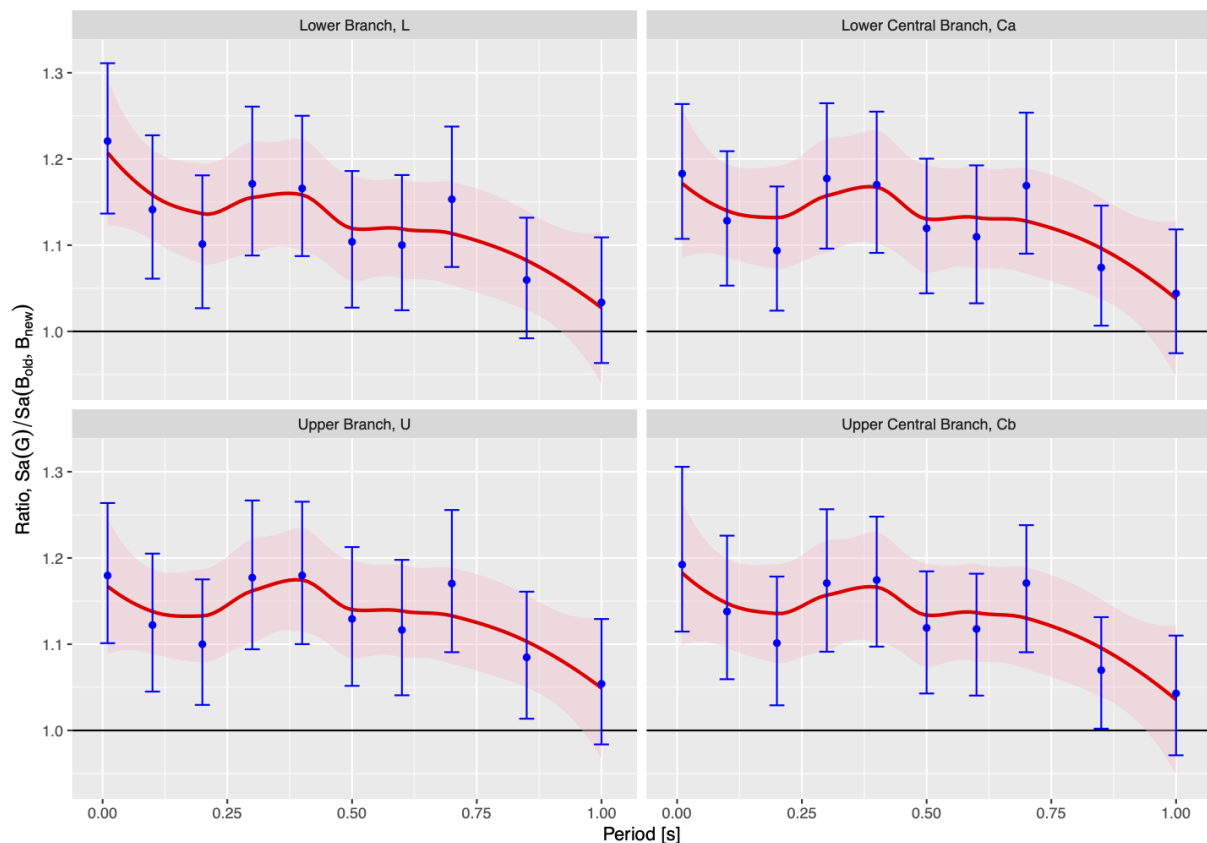


Figure 6.28. Ratios of spectral accelerations between G and B stations implied by the bias coefficients shown in Figure 6.4.1. Error bars show standard errors in the ratios. The heavy red line shows a LOESS (locally estimated scatterplot smoothing) fit to the ratios, while the pink ribbon shows the 95% confidence interval around these loess fits.

Lacking a rational means by which to remove systematic network effects in the establishment of bias terms, we accept the merged bias from Figure 6.22 for subsequent applications to hazard and risk analysis.

7. Field-Wide Site Response Analyses

The model presented in the previous chapter enables the prediction of distributions of response spectral accelerations at the NS_B horizon for any combination of earthquake magnitude and rupture distance. The surface motions are then calculated by multiplication of the reference rock motions by non-linear, frequency-dependent site amplification factors representing the dynamic response of the overlying layers. This chapter presents the site response analyses conducted to determine the site amplification factors, including the additional adjustment to be applied to structures located on dwelling mounds (*wierden*).

7.1. Input Motions

A set of 3,360 input motions, simulated for various magnitude-distance scenarios at the NS_B horizon, was used as input for the STRATA (Kottke & Rathje, 2008) site response calculations. Since site response analyses are conducted using Random Vibration Theory (RVT), the input motions are defined by their Fourier Amplitude Spectra (FAS) and duration. The motions span a magnitude range **M** 1.5 to 7.25. Intervals of 0.25-unit magnitude are used from **M** 1.5 to 2.5, 0.1-unit from **M** 2.5 to 5.5, and 0.25-unit from **M** 5.5 to 7.25, resulting in a total of 42 scenario magnitudes. The rupture distances simulated for each event range from 3.0 to 60 km in 20 log-spaced steps. These ranges enable the derivation of the magnitude and distance dependence of the AFs (Section 8.2). The derivation of the model for V7 FAS motions and the simulation configuration is described in Chapter 5.

The ground motion durations used in the STRATA analyses were based on the measured duration of the simulated signals from EXSIM (D75-5) and corrected using Parseval's Theorem (see Atkinson, 1993, for more detail). This theorem described the physical basis for the equivalence in PGV from time and frequency (Fourier) domain measures, the latter through random vibration theory. The corrected duration for the input signals, D_{corr} , was derived for the Version 5 GMM (Bommer *et al.*, 2018) and is given by:

$$D_{corr} = \frac{D_{75-5}}{0.64} \quad (7.1)$$

As for previous versions of the ground motion model, the motions were ranked according to their PGA and subsequently divided into groups of a maximum of 360 motions. The first nine groups contained 360 motions, while group 10 includes 120 motions. The FAS motions per group are shown in Figure 7.1. One motion per group of ranked motions was randomly selected as input motion for each voxel stack, corresponding to 10 STRATA calculations per voxel stack. Examples of the sampling of motions for two small and two large zones are included in Figure 7.2.

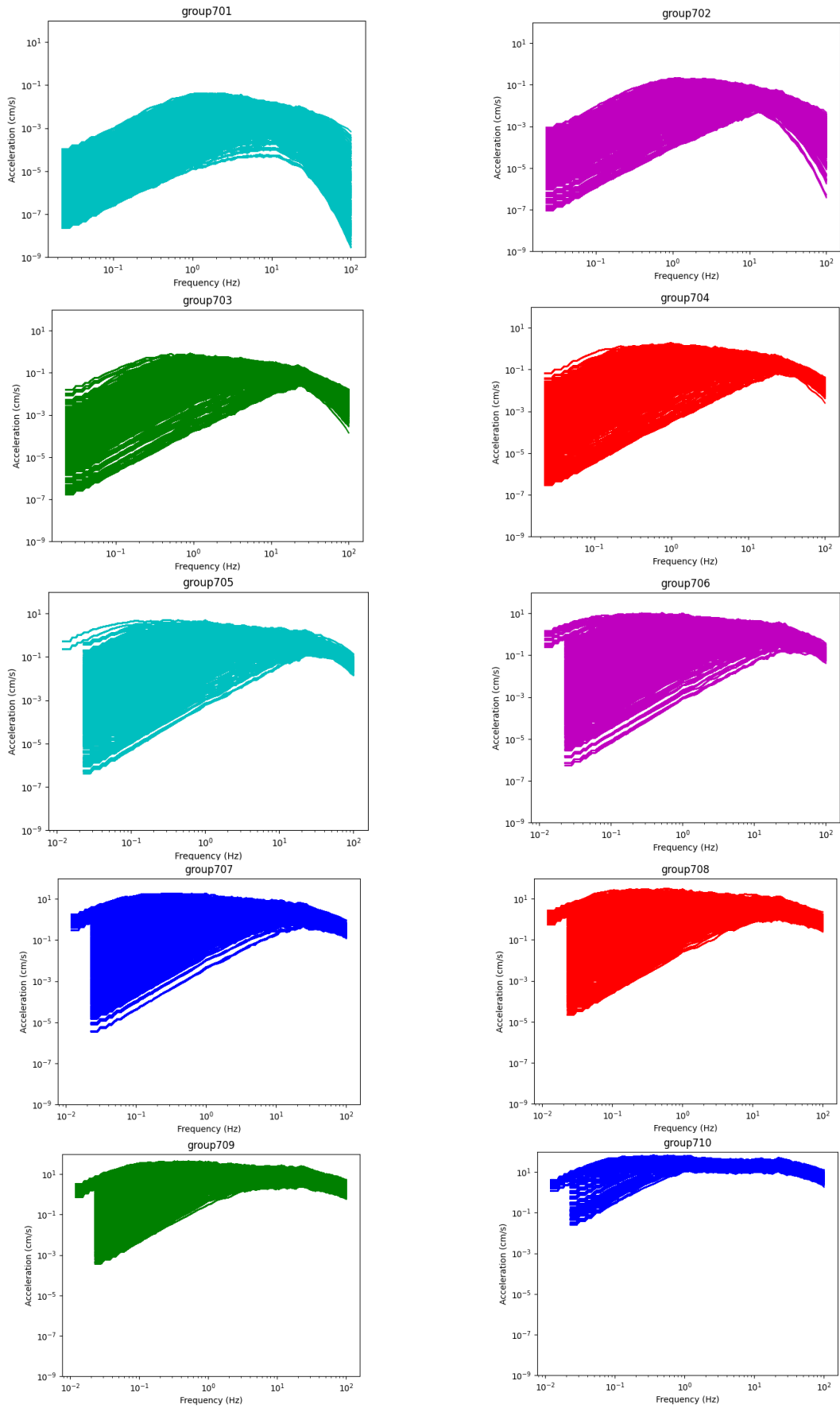


Figure 7.1. FAS generated at the NS_B horizon for use in RVT-based site response analyses.

Over the full analysis, each motion has been sampled 391 ± 24 times on average for groups 701-709; while for group 710 motions are sampled 1167 ± 83 times, owing to the smaller number of motions in this group.

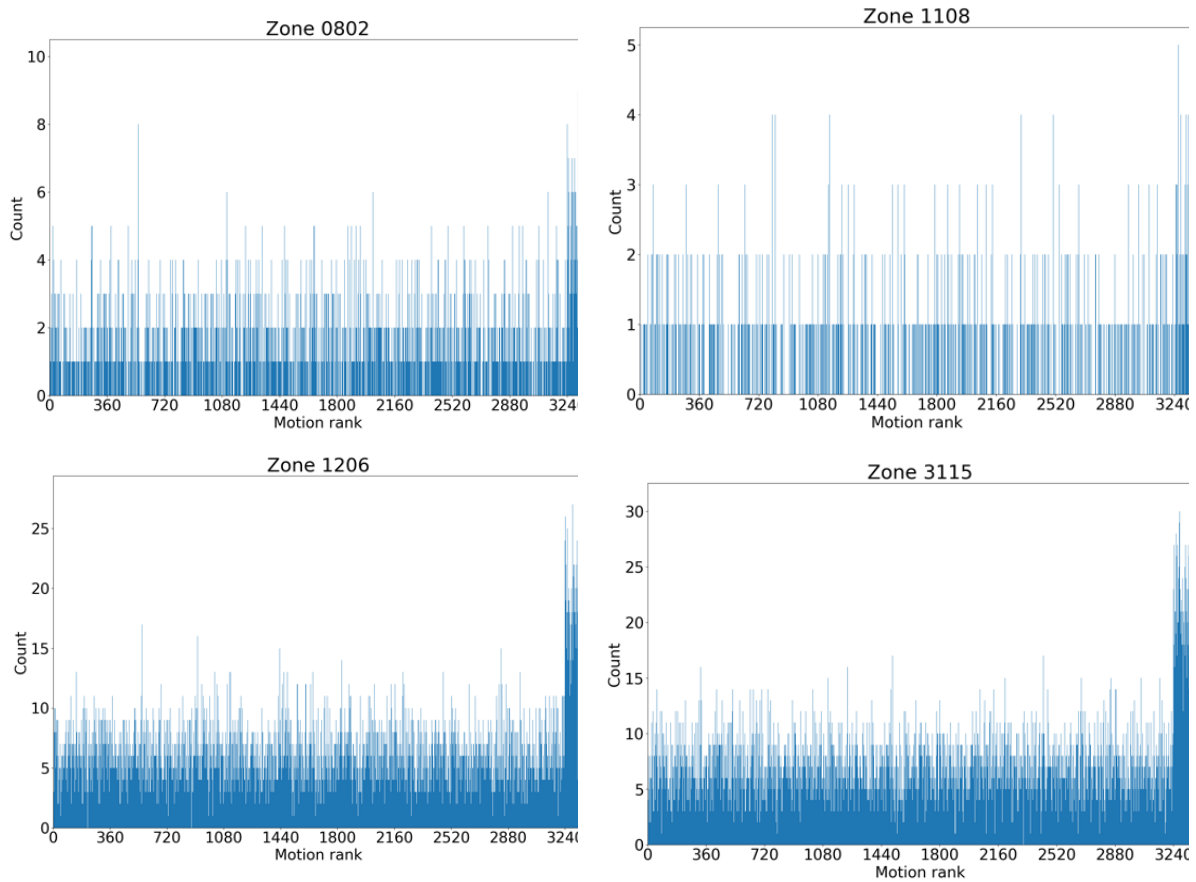


Figure 7.2. Sampling of the 3,360 NS_B FAS in the site response analyses for four of the geological zones. Top panels show the sampling for two small zones, bottom panels the sampling for two large zones.

7.2. Site Response Profiles and Soil Properties

Layer model

The soil stratigraphy and associated properties defining the MRD curves are described in Kruiver et al (2017b). The soil stratigraphy is a combination of the detailed GeoTOP model between the surface and 50 m-NAP and scenarios of lithostratigraphy between 50 m-NAP and the base of the Upper North Sea Group at ~ 350 m (Figure 7.3). The Lower North Sea Group forms a separate type of stratigraphy, present between ~ 350 m and ~ 800 m.

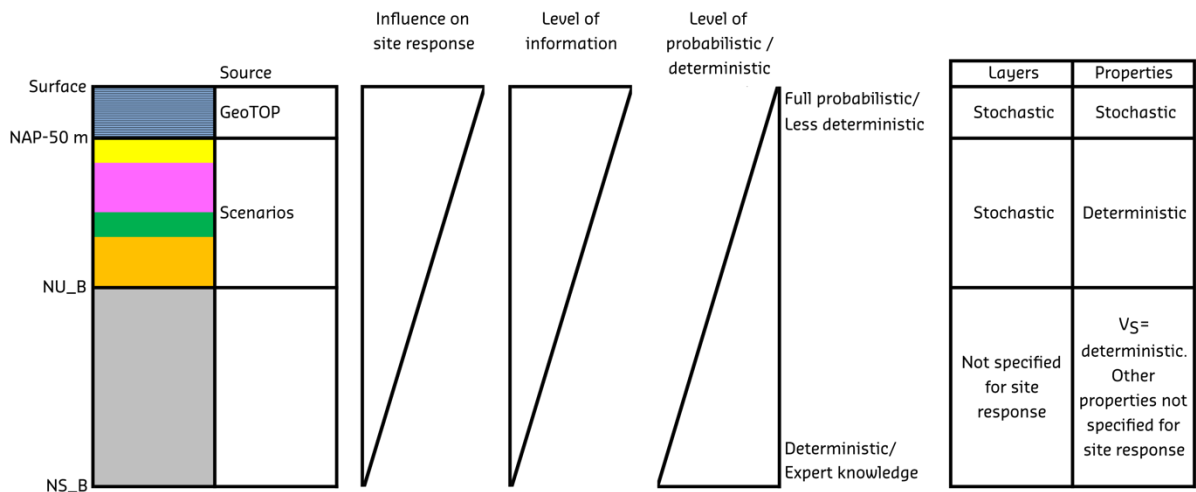


Figure 7.3. Visualisation of the coupling of depth ranges in the geological model and the relation between the level of information, the influence of the depth range on site response and the adopted probabilistic or deterministic approach. NU_B is the base of the Upper North Sea Group; NS_B is the base of the North Sea Supergroup (Kruiver *et al.*, 2017b).

Vs profiles

The site response profiles consist of 1D profiles of V_S and soil properties that define the MRD curves. The generation of mean and randomized V_S profiles is described in Kruiver *et al* (2017a) and summarized in Section 4.1. The randomized V_S profiles are input for the site response calculations. Randomization of V_S is limited to the GeoTOP depth range, from surface to 50 m-NAP.

MRD curves

The soil properties defining the modulus reduction and damping (MRD) curves are based on laboratory-derived relationships. The basic assumptions for the Groningen MRD curves are described in Kruiver *et al.* (2017b) and Rodriguez-Marek *et al.* (2017), and these are summarized here. For sands, Menq's (2003) model is used. The parameters defining the MRD curves for sand are the median grain size (D_{50}), the coefficient of uniformity (C_u) and the mean effective stress. To compute the mean effective stress, the total unit weight of all the soil units in a profile as well as the depth of the ground water table are needed. For clays, sandy clay and clayey sand, the formulae from Darendeli (2001) are used. The parameters defining the MRD curves for clays are overconsolidation ratio (OCR), plasticity index (I_p), undrained shear strength (S_u), and mean effective stress. The Darendeli and Menq models depend on frequency and number of loading cycles. The default values recommended by the authors (frequency of 1 Hz and 10 loading cycles) are used.

Peats are abundantly present in Groningen. There are two types of peats: the younger Holland peat and the older Basal Peat. The Basal Peats behave different to Holland peats due to the recent sediment load. Because of the absence of MRD curves for

Groningen peat at the earlier stages of the GMM development, a set of MRD curves were derived based on literature from worldwide cases. The literature-derived curves were applied to both Holland peat and Basal peat in earlier versions of the GMM. In the meantime, Groningen specific MRD curves were derived for Holland peat from laboratory tests conducted on local samples from the field. The results became available in 2017 and have been used since the V5 GMM. The laboratory MRD curves apply to Holland peat only, because only this type of peat is present near the surface and could be sampled undisturbed for testing. The literature based MRD curves developed earlier continue to be applied to Basal peat.

The MRD behaviour of peat described in literature is very diverse (Seed & Idriss, 1970; Kramer, 1996, 2000; Stokoe *et al.*, 1994; Boulanger *et al.*, 1997; Wehling *et al.*, 2001; Kishida *et al.*, 2009a,b; Zwanenburg, 2005; Tokimatsu and Sekiguchi, 2006a, b, 2007; Kallioglou *et al.*, 2009; Den Haan and Kruse, 2007). In order to be consistent with the sand and clay curves, we adopt a formulation similar to the Darendeli (2001) model. In this formulation, four parameters describe the curves: (γ_r , a , b , and D_{min}). The average values for these parameters were derived for Basal Peats from the plots of these values from data obtained in the literature. Outliers were discarded based on expert judgement. The modifications to the Darendeli (2001) model for Basal Peat are:

- $a = 0.776$
- $l_p = 100$
- $OCR = 1$
- $\gamma_r = 0.995 \left(\frac{\sigma'}{p_a} \right)^{0.694}$, where γ_r is reference shear strain amplitude, σ' is the mean effective stress and p_a is atmospheric pressure, both in the same sets of units
- $K_o = 0.35$, where K_o is the coefficient of lateral earth pressure at rest and is used to compute the mean effective stresses.

As an example, the literature based MRD curves for Basal peat are compared with curves for peats in the Sacramento River delta (Kishida *et al.*, 2009b) in Figure 7.4. Our literature-based curves have a stronger dependence on confining stress. This dependence was also noted by various other studies (e.g., Kramer, 2000).

In addition, Groningen-specific MRD curves for Holland peat have been derived using laboratory measurements on samples from three locations (Zwanenburg *et al.*, 2020). Examples from the laboratory curves are shown in Figure 7.5 and 7.6. Based on these laboratory measurements and adopting the functional form of Darendeli (2001), the values for coefficients were adjusted. For the modulus reduction and damping curves for Holland peat, three of the parameters of the Darendeli (2001) model are modified:

- $\gamma_{ref} = 2\%$, independent of the consolidation stress
- $a = 0.8$
- $b = 0.712$

In addition, the small strain damping model was re-evaluated and is given by:

$$D_{min} = 2.512 \left(\frac{\sigma'_o}{p_a} \right)^{-0.2889} \quad (7.2)$$

where σ'_o is the initial confining stress and p_a is atmospheric pressure, both in the same sets of units.

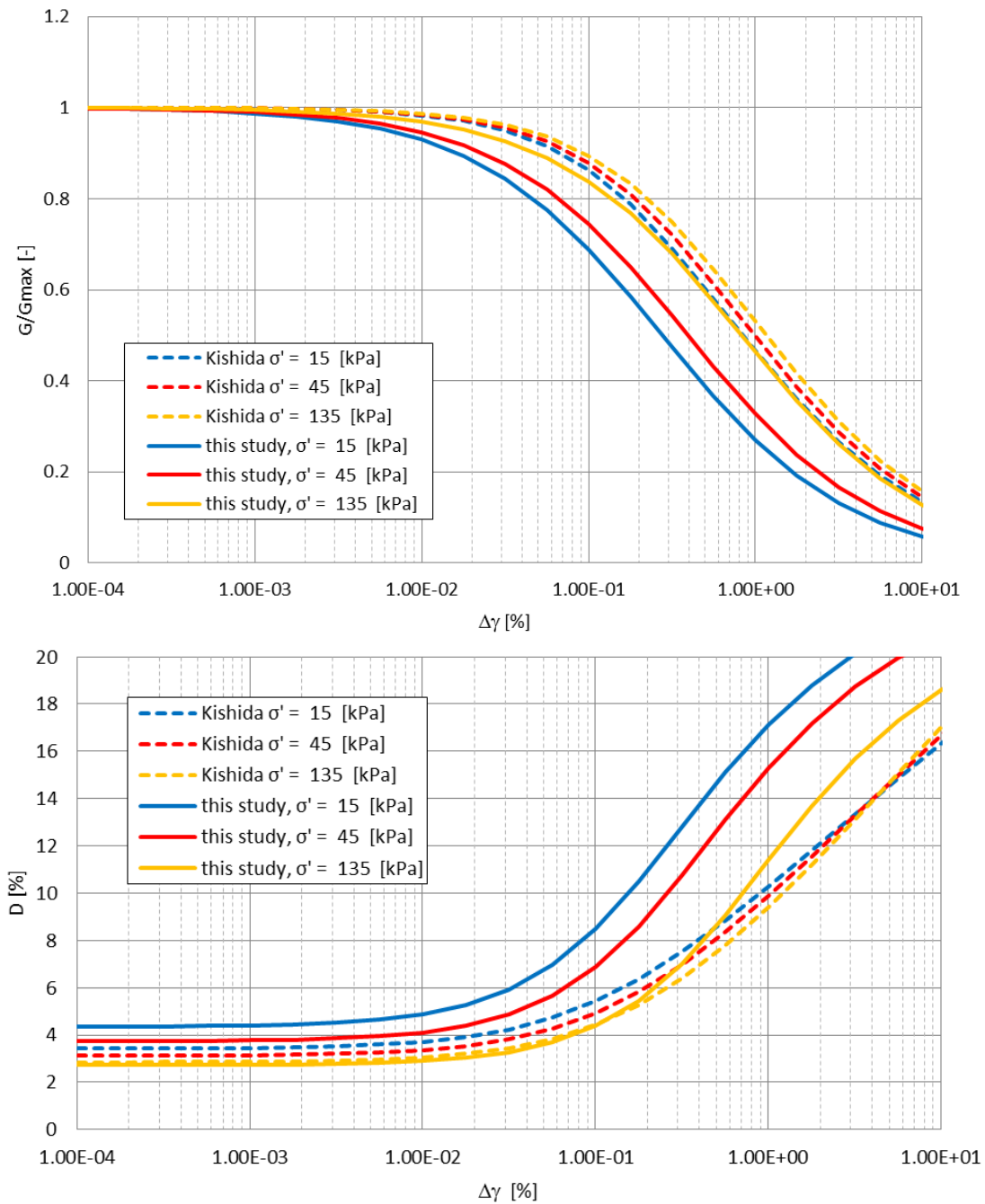


Figure 7.4. Comparison of MRD curves obtained from the parameters used for Groningen Basal Peat and the model by Kishida *et al.* (2009b) for different vertical effective stresses. Curves for Kishida *et al.* (2009b) are shown for an organic content of 50%.

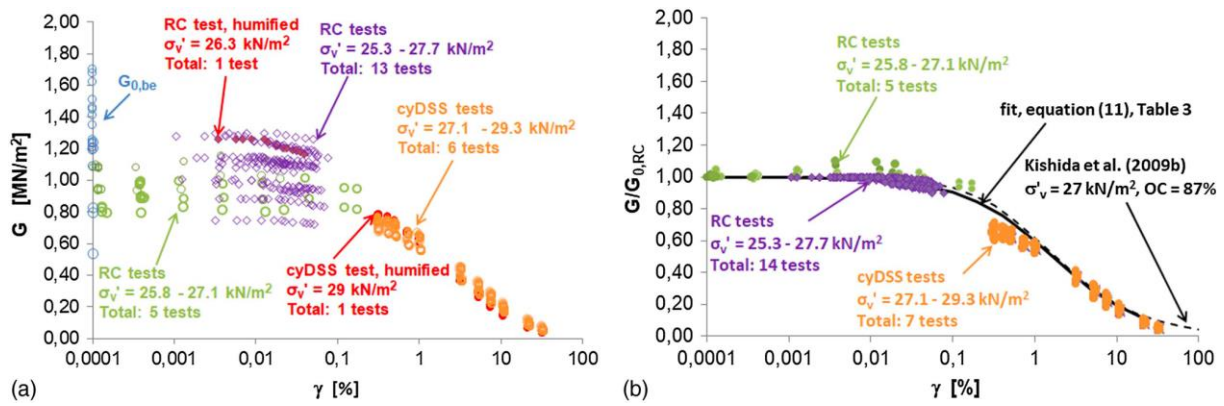


Figure 7.5. Shear modulus degradation curve for Holland Peat from Nieuwolda: (a) measured data; and (b) data normalized by $G_{0,RC}$ compared to the relation given by Kishida et al. (2009b). From Zwanenburg *et al.* (2020).

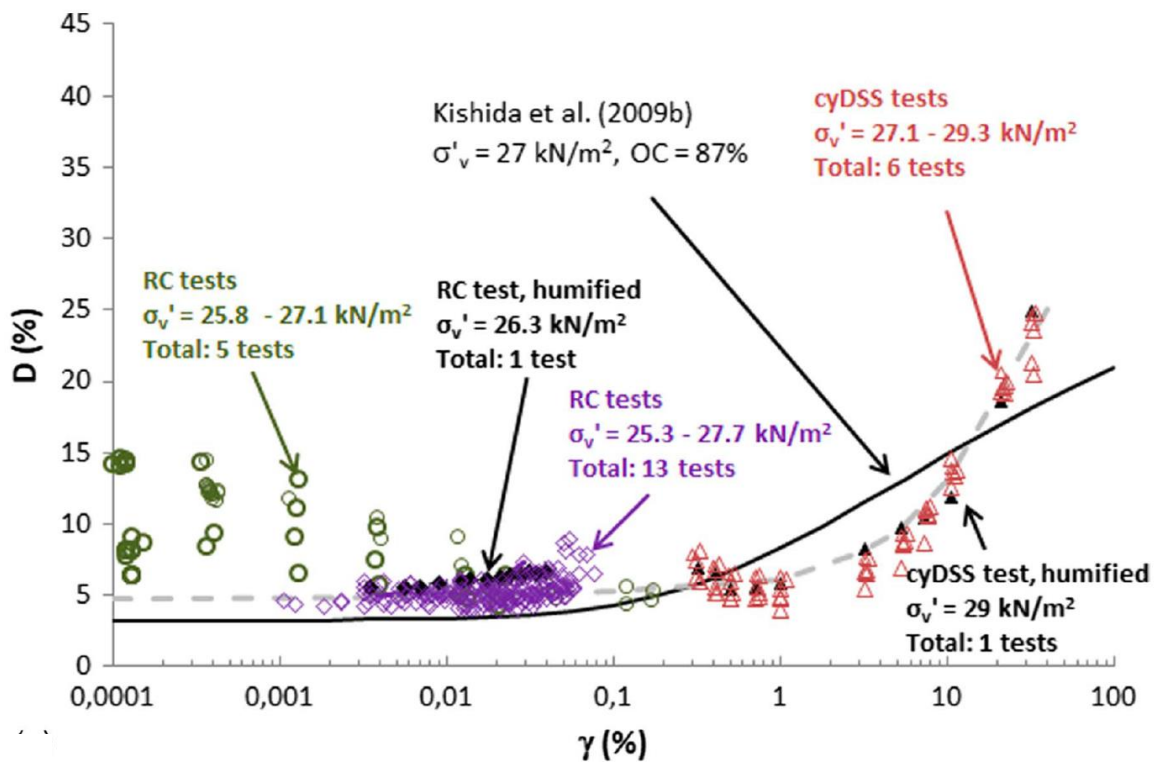


Figure 7.6. Damping curves for Holland peat from Nieuwolda. The grey dotted line represents a general trend line, drawn manually through the data. From Zwanenburg *et al.* (2020).

All parameters defining MRD curves for all soil types present in the Groningen region were listed in a geomechanical look-up table. The parameter values were derived from literature and expert judgement. OCR , S_u and total unit weight were estimated for soil types using empirical relations with cone resistance (Kulhawy & Mayne, 1990; Robertson, 1990; Lunne *et al.*, 1997). The Plasticity Index (I_p) was estimated from CPT data using Skempton & Henkel (1953), from scarce site investigation data from Rijkers

et al. (1998) and Sorensen & Okkels (2013), and from expert judgement. An extensive inventory of grain size distributions from TNO Geological Survey of the Netherlands (Bosch *et al.*, 2014) provided information on D_{50} and C_u for sand. The most recent update of the geomechanical look-up table was implemented for GMM Version 5 using laboratory results from Groningen field samples (e.g., van Essen, 2017), adjusting undrained shear strength values for various soil types. The geomechanical look-up tables are included in Appendix I.

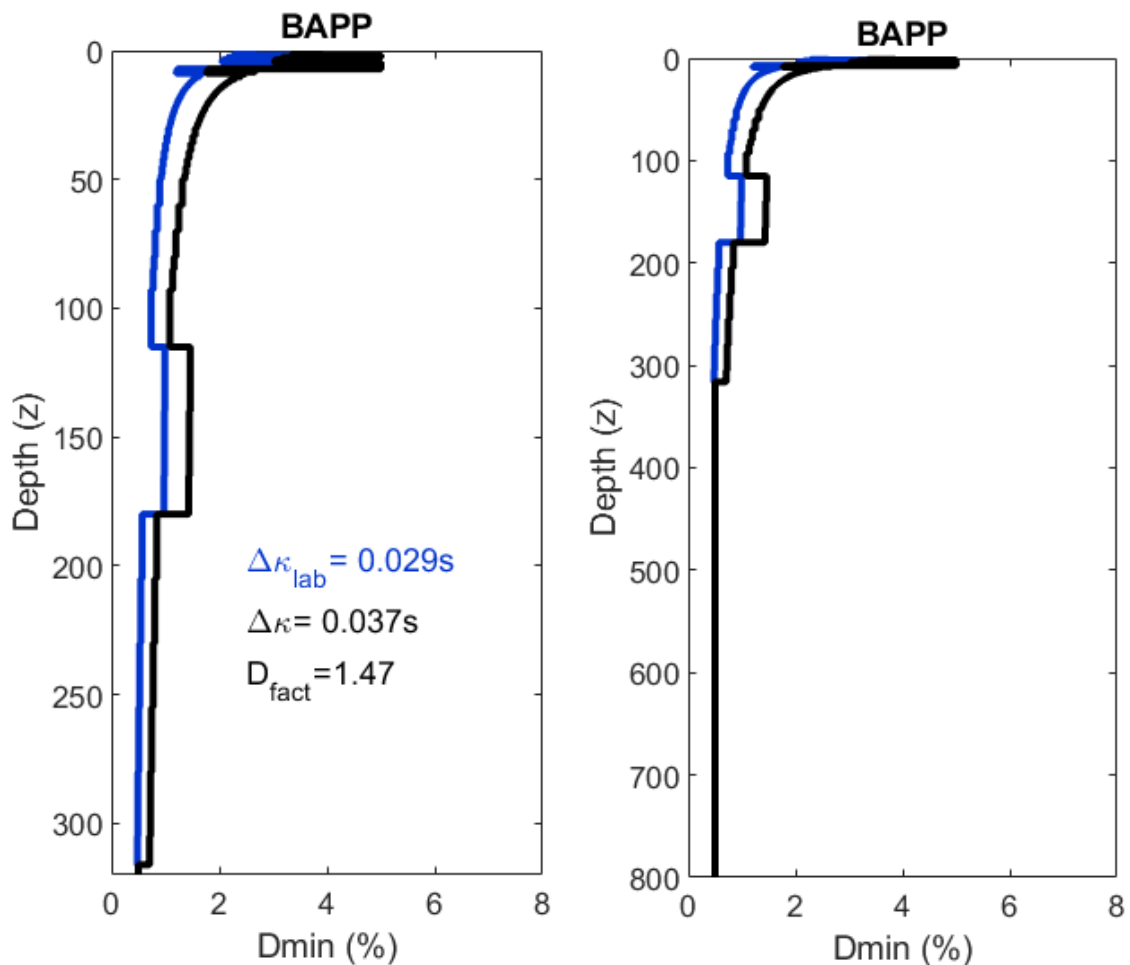


Figure 7.7 Low strain damping (D_{min}) profile with depth showing laboratory estimates in blue along with the field-wide damping model applied to the profile for the BAPP station. The linear factor to scale the laboratory-based damping is shown in the figure.

The damping versus strain curves of the selected MRD models have a small strain component (D_{min}) and a strain-dependent component. The small-strain component of these curves was adjusted for all soils based on the field-wide model presented in Section 4.3. The factor used for the adjustment (D_{fact}) was applied for each of the zones in the field using the median V_{s30} for the zones (the zonation model is discussed in Section 8.1). The adjustment is applied for all soils above the Lower North Sea Group (including peats), which is encountered at depths larger than about 350 m.

Damping for this unit was set to 0.5%. The Lower North Sea Group mainly consists of unconsolidated sediments consisting of sands, marls and clays. The consistency is mainly dense glauconitic sand, and hard clay. In the upper part cementation is present in the form of thin sandstone layers. A sample of a D_{min} profile is shown in Figure 7.7 for the site of the BAPP accelerometer. The geographical distribution of D_{fact} is shown in Figure 7.8.

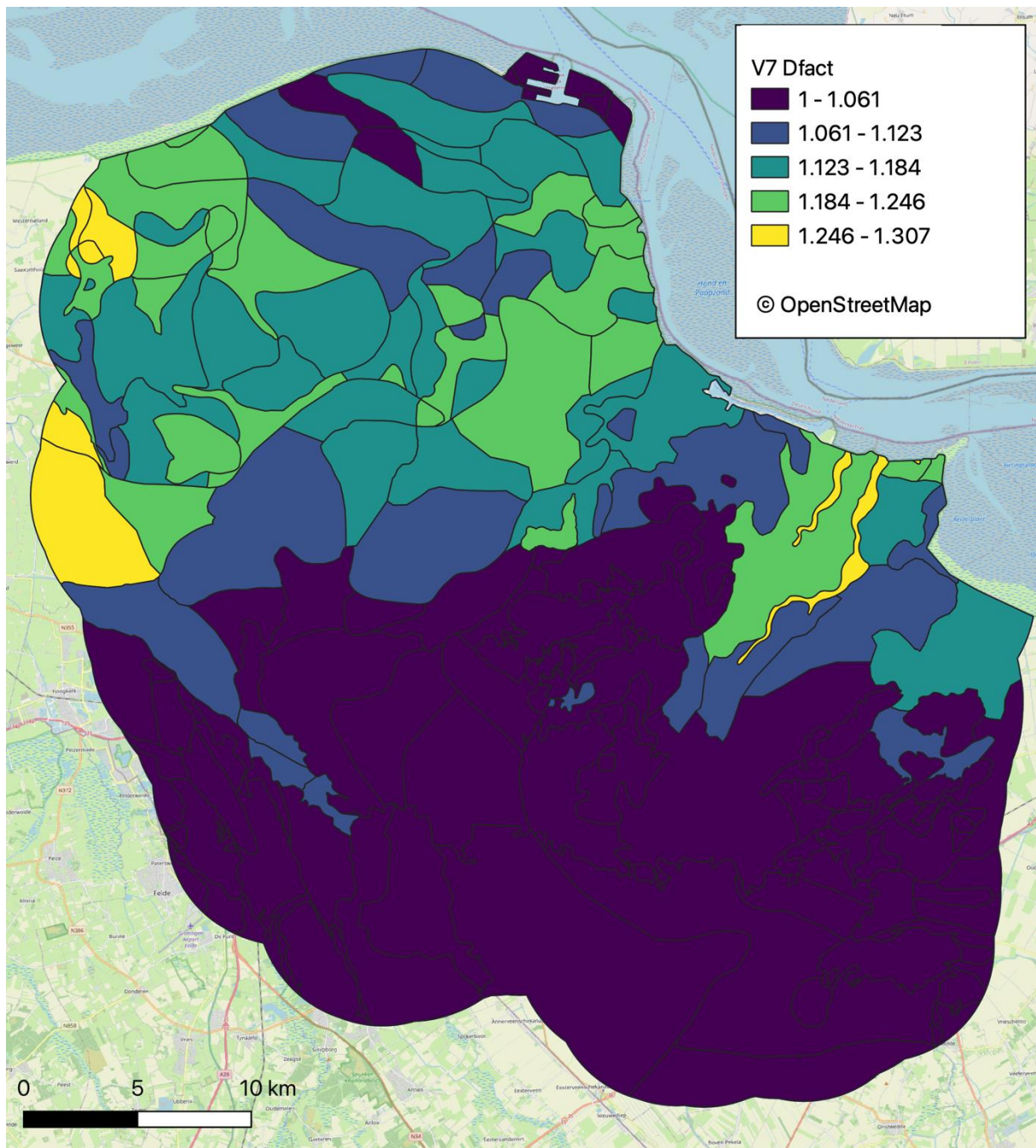


Figure 7.8 Map of D_{fact} for the geological zones

The hyperbolic model used by the Darendeli (2001) and Menq (2003) models implies a large stress-strain behaviour that is not necessarily compatible with the shear strength of the soil. For this reason, a model to impose a limiting shear strength at large strains was implemented for clays using the undrained strength (S_u). We used the Yee *et al.* (2013) model with a parameter γ equal to 0.3% to modify the G/G_{\max} curves such that they are compatible with the undrained strength. Additionally, the undrained shear strength S_u was increased by 30% to account for rate effects (Lefebvre & LeBoeuf, 1987; Stewart *et al.* 2014). Limiting shear strengths were implemented for clay, clayey sand and sandy clay and for peat. No limiting strength was used for sand layers because of the higher strengths for sand and the lower strains typically observed in the analyses.

7.3. Linear and Equivalent Linear Analyses

The site response analyses were conducted assuming 1D wave propagation and using an Equivalent Linear (EQL) approach as implemented in STRATA. The Random Vibration Theory (RVT) option in STRATA was used (Rathje & Ozbey, 2006) to estimate the maximum strains and to compute response spectra from FAS. Kottke & Rathje (2013) also point out that RVT analyses tend to result in higher amplifications than time-domain analyses (i.e., the choice of the RVT approach is slightly conservative). The choice of EQL analyses was dictated by its prevalence in practice. Numerous studies have indicated that the EQL approach should be limited to strains below about 0.4%, especially for oscillator periods lower than 0.4 seconds (Kaklamanos *et al.*, 2013; Kim *et al.*, 2013). For larger strains, both EQL and fully nonlinear (NL) analyses fare poorly when compared with empirical data (Zalachoris & Rathje, 2015). Kim *et al.* (2013) also show that the differences between EQL and NL analyses at high frequencies are less evident in the response spectral domain than in the Fourier domain, even for large amplitudes. Zalachoris & Rathje (2015) compared predictions of EQL analyses with empirical observations from downhole arrays and concluded that if a strength correction approach is used, the errors in EQL analyses at short oscillator periods decrease. On the other hand, Afacan *et al.* (2019) concluded that NL models perform well provided the 1D assumption is satisfied and the strength of the soil is properly accounted for. To compensate for the limitations of EQL analyses, the results of EQL analyses along with recordings from the Groningen field are used to develop a field-specific model error that is applicable for small strains. In addition, the strains for which the EQL model results are applicable are limited to 1%. Moreover, the model error is increased at large strains, where the field-specific model error is not applicable. These elements are described in Chapter 8.

Site response analyses were conducted for all the voxel stacks in the field, using v0.8.0 (<https://github.com/arkottke/strata/releases>). To aid in the derivation of the amplification model for the zones (Section 8.2), both linear (LIN) and EQL analyses were conducted. Input motions, defined in terms of the Fourier Amplitude Spectra and

ground motion duration, were randomly selected from the motions described in Section 7.1. The same set of motions were used for the EQL and the linear analyses.

7.4. Site Response Analyses for *Wierden*

Several old and densely populated village centres are located on dwelling mounds, which were constructed several centuries ago. The mounds, called *terps* in Dutch and *wierden* in the Groningen dialect, were constructed to raise building foundations as a defence against flooding. They are typically 2 to 3 m high and were constructed with whatever material was available at the time, for example animal dung and clay or sand from the surroundings. The GeoTOP model includes an “anthropogenic” lithoclass. This is a container, which includes foundation layers, rubble layers, infills and *wierden*. There is no separate lithoclass for *wierden*. Moreover, not all of them are included in the anthropogenic lithoclass in GeoTOP. Until GMM Version 6, hazard and risk on *wierden* were not separately assessed. While only a very small proportion of the exposed buildings in the Groningen region are founded on these dwelling mounds, it has been a long-term objective to include the *wierden* into the risk modelling for completeness. Although the total number of buildings located on *wierden* is small, these include many structures considered to be part of the cultural heritage of the region. This section summarises the site response analyses for *wierden* and the soil-structure interaction. The Penalty Factor for structures on *wierden* is included in Section 8.4. The work has been published in Kruiver *et al.* (2021).

The *wierden* Penalty Factor is the result of a multidisciplinary approach, combining information from archaeology and geography (dwelling mound occurrence), field work (descriptive drillings and in situ shear-wave velocity), geology (subsurface structure), geo-engineering (subsurface properties) and earthquake engineering (site response and soil-structure interaction). Each of these component parts is summarized below.

The physical geography study led to the selection of eight *wierden* in the northern part of the Netherlands (Figure 7.9). They form a well-balanced mix of the major physical geographical regions within the coastal zone, size, age and expected composition. Three of them are situated inside the GMM area and five outside of the GMM area. A detailed drilling program with hand augers to ~ 5 m depth and archaeological core description resulted in a general lithoclass description for the *wierden* (Figure 7.10). Most of the *wierden* have comparable proportions of soft material, predominantly organic and clayey material. Exceptions are Groot Maarslag, with a relatively large proportion of fine sand, and Grote Houw, which consists of 70% fine sand.

Rossingh Geophysics conducted MASW surveys on the eight *wierden* on survey lines of ~ 110 m length on top of the *wierden*. Geovision processed the data and delivered 2D V_S profiles to a depth of 16 to 19 m. An example of a cross-section showing the V_S distribution and the hand auger descriptions is included in Figure 7.11. For this *wierde*,

V_s varies between 50 and 230 m/s, with a general increase with depth. The drillings indicate the presence of a zone of peat in the natural soil at the right side of the figure. This corresponds well with the very low V_s zone, which is typical of peat.

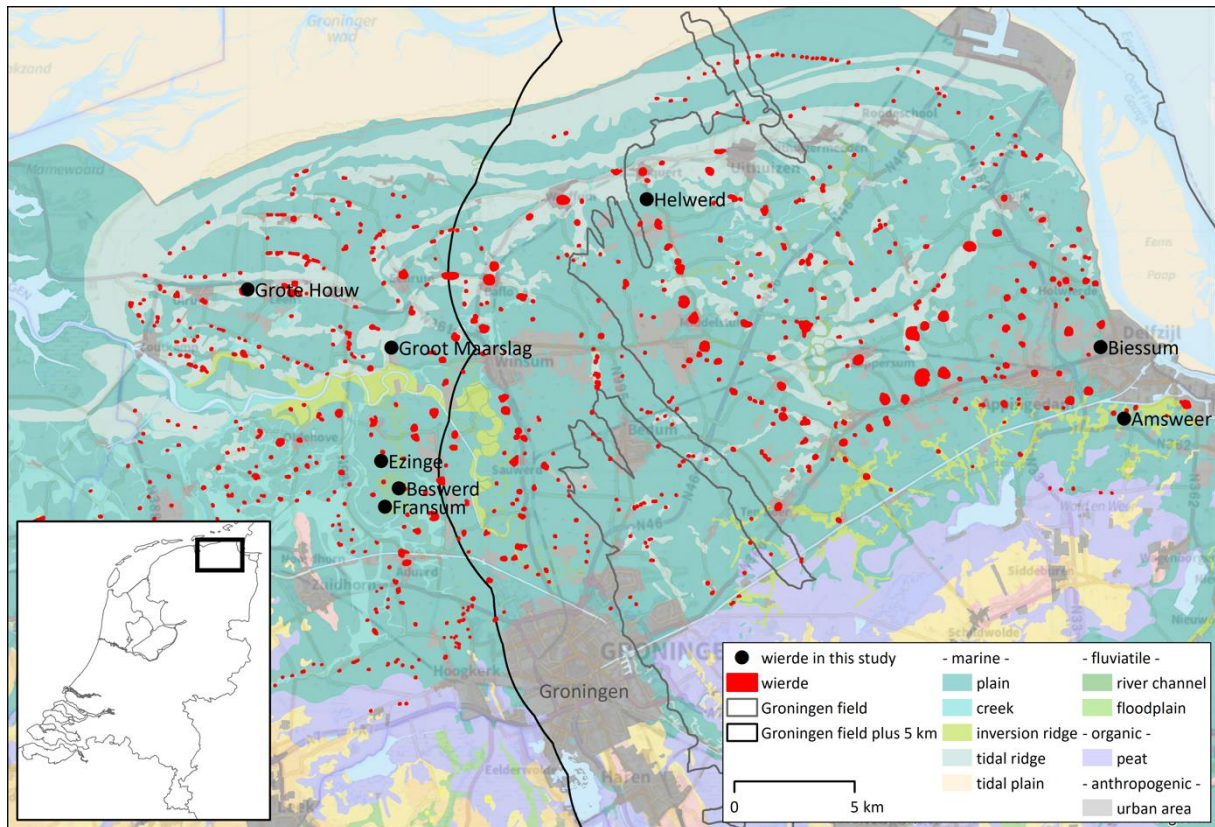


Figure 7.9 Map showing the locations of the eight *wierden* analysed in this study on a physical geographical background. From Kruiver *et al* (2021).

Site response analyses were performed using either the local data (stratigraphy from drillings and V_s from MASW measurements) or the GMM site response model. The results were compared to assess the influence of the *wierde*. This was first done for all eight *wierden* using soil columns of 16 m thickness (Figure 7.12), because there is no V_s information below the measured V_s depth range for the *wierden* outside the GMM area. All *wierden*, except for Grote Houw, show similar AF behaviour among the periods relevant for risk (0.1-1.0 s). Grote Houw shows substantially lower AF compared to the other *wierden*, probably because this *wierde* is much sandier (Figure 7.10). Based on the fact that seven out of eight *wierden* show similar AF behaviour we concluded that one average *wierde* response is sufficient.

Next, the site response analysis was repeated using the new V7 motions and the full soil columns for the three *wierden* in the GMM area. The full column either consisted of the GMM V_s and stratigraphy model (Section 7.2) or the model column with the top 18-19 m replaced by the field data. The residuals in AF are shown in Figure 7.13. The

GMM already incorporates a strong degree of epistemic uncertainty. The 95% confidence interval (CI) of the epistemic uncertainty (shown in Figure 7.13 as thin dotted lines) generally envelopes the residuals. Therefore, we define a simple modification, consisting of a unique Penalty Factor (that modifies the site amplification when a *wierde* is present) for all *wierden*. The *wierden* Penalty Factor is included in Section 8.4.

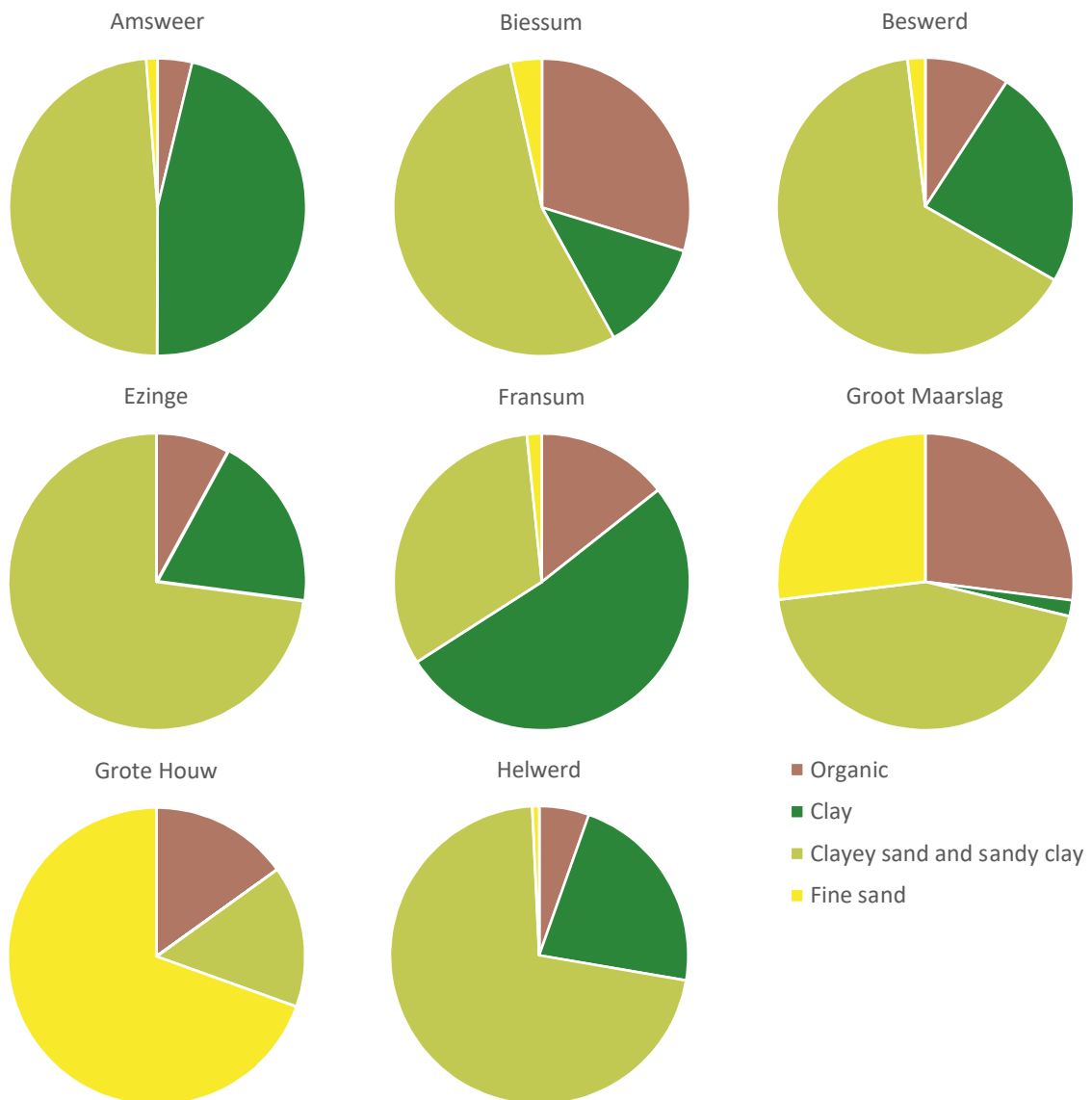


Figure 7.10. Lithoclass distribution of the *wierden* material according to the GeoTOP lithoclass definition. Animal dung is included in the “organic” lithoclass. From Kruiver *et al* (2021).

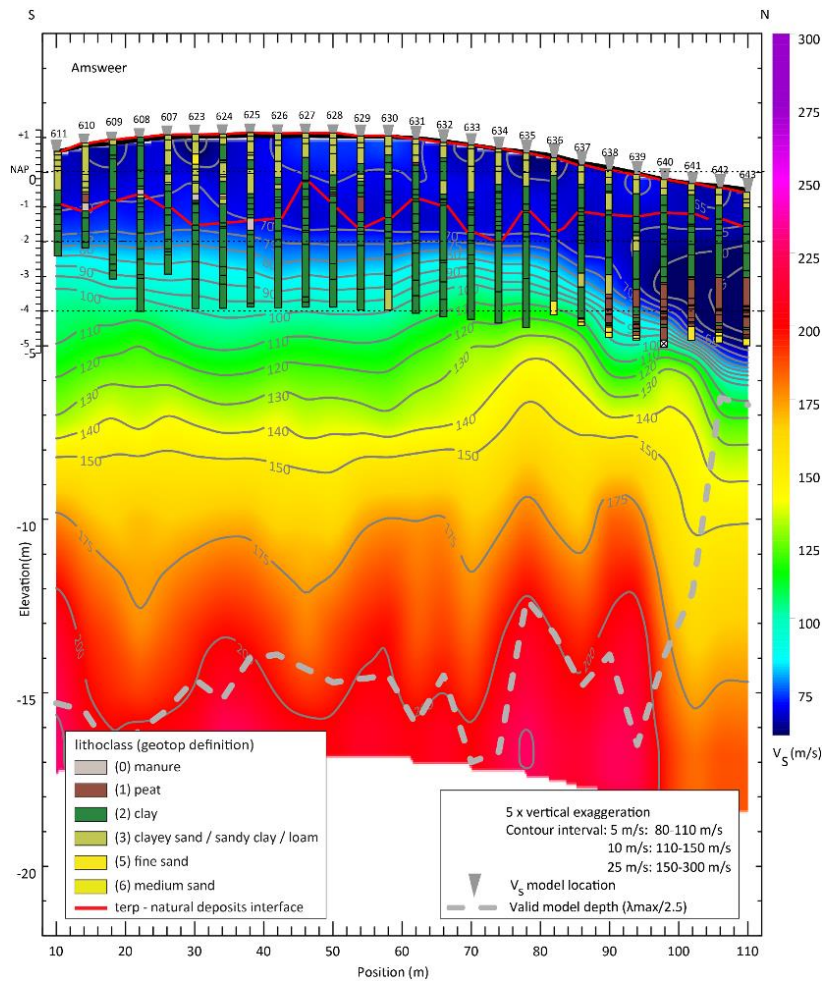


Figure 7.11. Example of field measurements results at Amsweer, showing the results from the MASW data of Rayleigh waves and the GeoTOP lithoclasses of the drillings. The grey dotted line denotes the maximum reliable depth of the MASW result. From Kruiver *et al.* (2021).

The approach described above concerns issues related to including *wierden* in the hazard analyses. A study has also been made about possible adjustments required in the risk analyses. To this end, the fragility of buildings on *wierden* has been assessed. Nine vulnerability classes characterize the seismic response of the majority (>88%) of the buildings founded on *wierden* (sorted from high to low absolute numbers): URM6L, URM8L, URM1F_B, URM7L, URM1F_HA, URM1F_HC, URM3L, URM5L, URM4L. Apart from URM1F_B (farmhouse barn), these are all unreinforced masonry (URM) structures founded on shallow foundations, mainly of a detached/terraced houses type. Soil-structure interaction on *wierden* was modelled using a single, representative *wierde* soil profile for all building types (except URM1F_B). Soil-structure interaction for buildings not situated on *wierden* was taken from Mosayk (2019) considering field-wide average soil properties. The resulting curves of Figure 7.14 show that there is little difference between the fragility considering *wierden* or not. A very modest change (decrease) in fragility is observed for terraced house vulnerability classes (URM3L, URM4L). However, only 0.35% of such buildings are founded on *wierden* soil and

consequently the impact of this reduction in the fragility for this particular building class when located on *wierden* on the computed risk estimates over the whole field would be very minor. We conclude that the fragility for buildings on *wierden* does not have to be adjusted. A simple flag in the exposure database for buildings on *wierden* is sufficient. For the flagged buildings, only the hazard is adjusted using the Penalty Factor defined in Section 8.4.

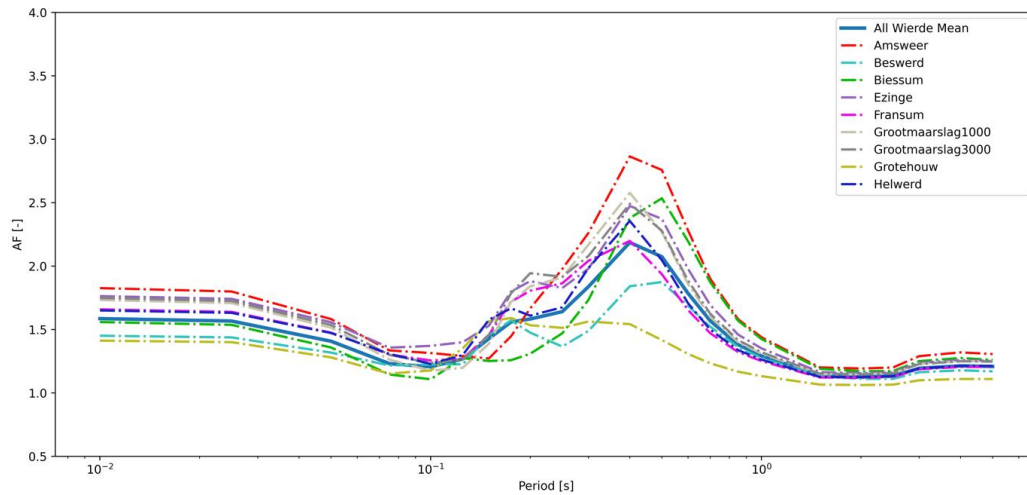


Figure 7.12. Mean AFs for the 16 m-thick soil columns of all *wierden*. The mean amplification is calculated for the ~ 24 soil columns per *wierde* and four GMM V5 motions with M and R values which were dominant for the risk. From Kruiver *et al.* (2021). Periods above 1 second are shown but do not form part of the deliverable.

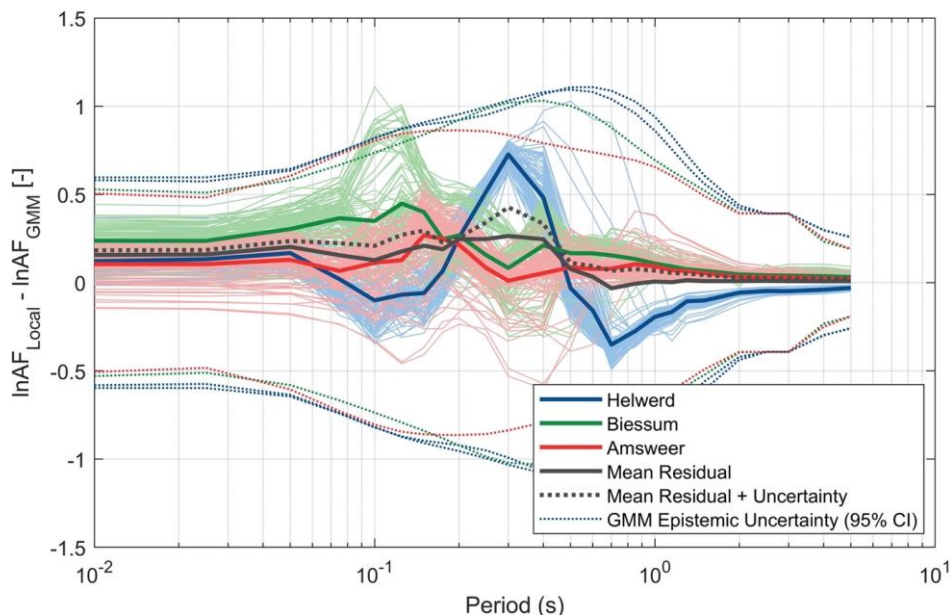


Figure 7.13. Residuals $[\ln(AF_{local}) - \ln(AF_{GMM})]$ for the three *wierden* in the GMM area. The solid line is the mean residual for the three *wierden* and the dotted line is the 75th percentile considering the uncertainty in the mean. The thin dotted line represents the 95% confidence interval of epistemic uncertainty for the zones where the *wierden* situated. From Kruiver *et al.* (2021). Periods above 1 second are shown but do not form part of the deliverable.

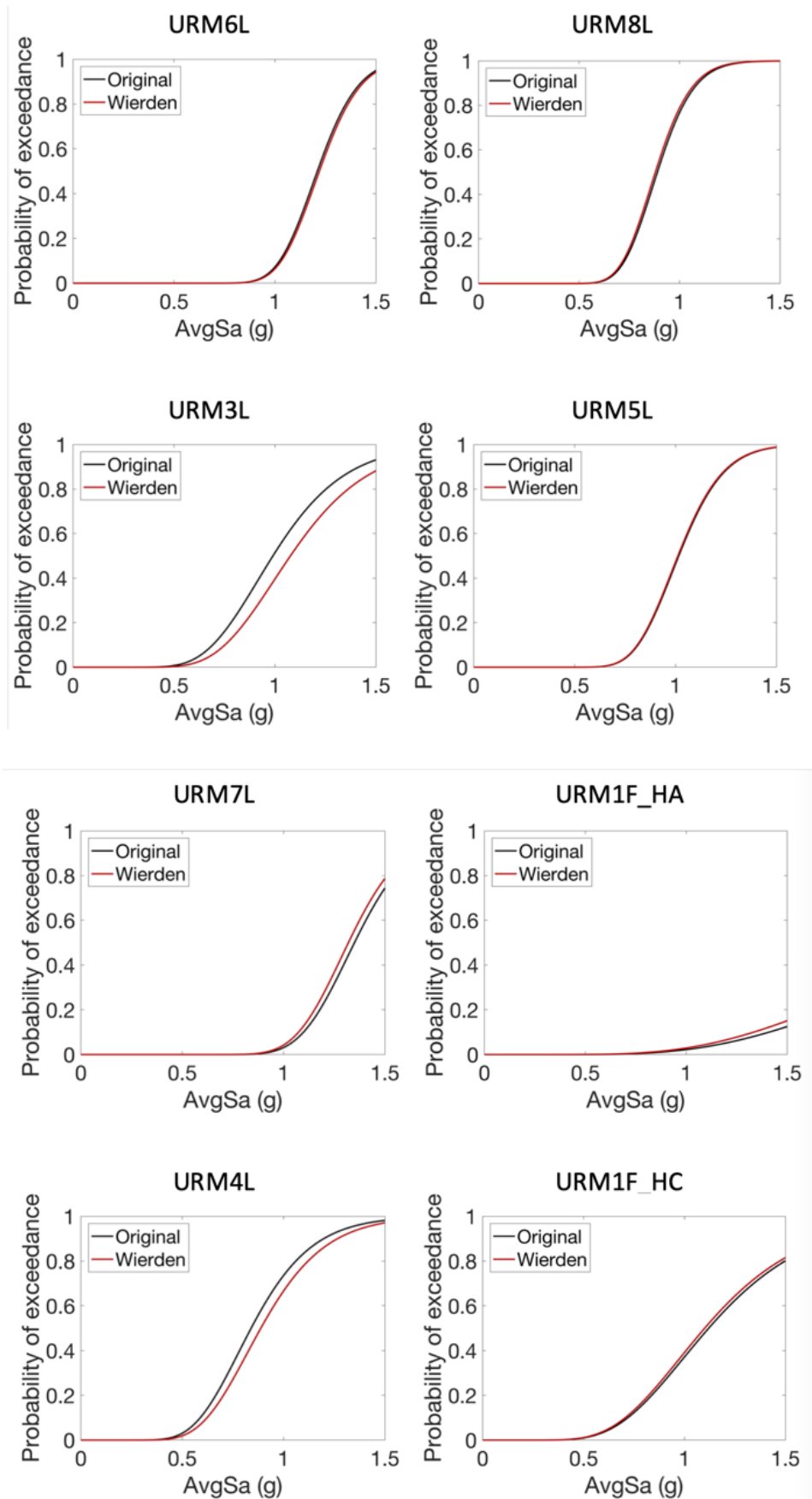


Figure 7.14. Fragility functions developed considering SSI with and without *wierden* layers. From Kruiver *et al.* (2021).

8. Field Zonation and Amplification Factors

Using the results from the site response analyses presented in the previous chapter, a site amplification model has been developed to transform the predictions of spectral accelerations at the NS_B horizon (Chapter 6) into surface motions.

The field zonation is presented first, and this is then followed by an explanation of the associated non-linear amplification factors applied to each zone and for each target oscillator period. The third section then presents the development of a logic-tree to capture the epistemic uncertainty in the site amplifications.

The chapter closes with a brief discussion of the additional adjustments applied for sites location on *wierden* using the results of the investigations summarised in Section 7.4.

8.1. Field Zonation Model

The field zonation was developed based on the geological model (Kruiver et al, 2017b). Because of the dominance of the shallow sediments in site response, the zonation is based on characteristic profile types in the top 20 m according to the GeoTOP model. The zonation has been stable with only minor changes since the V3 GMM, with approximately 160 geological zones. For each new GMM version, the zonation has been checked by plotting the weak motion AF results (for mean V_s) on the map. In some cases, a zone was split in two or two zones were combined based on the AF patterns. Only 2 to 4 zones were adjusted per GMM version. Between V6 and V7, no further adjustments were needed: the V7 AF pattern is consistent with the V6 zonation among the spectral periods (Figure 8.1 for $T = 0.2$ s). Therefore, the zonation of the V6 GMM (Figure 8.2) has been retained for V7.

The zonation of the field has remained fairly stable over several versions of the GMM. In earlier versions, some minor changes were made by adjusting some boundaries and by splitting or merging a few zones, but the total number of zones has always been on the same order and the changes have always been limited in both number and extent. The fact that the V7 GMM uses the same zonation as the V6 model is consistent with stability of the original zonation and confirms that the original geological zonation was a remarkably good proxy of the spatial variation of the dynamic response characteristics of the soil profiles across the Groningen field.

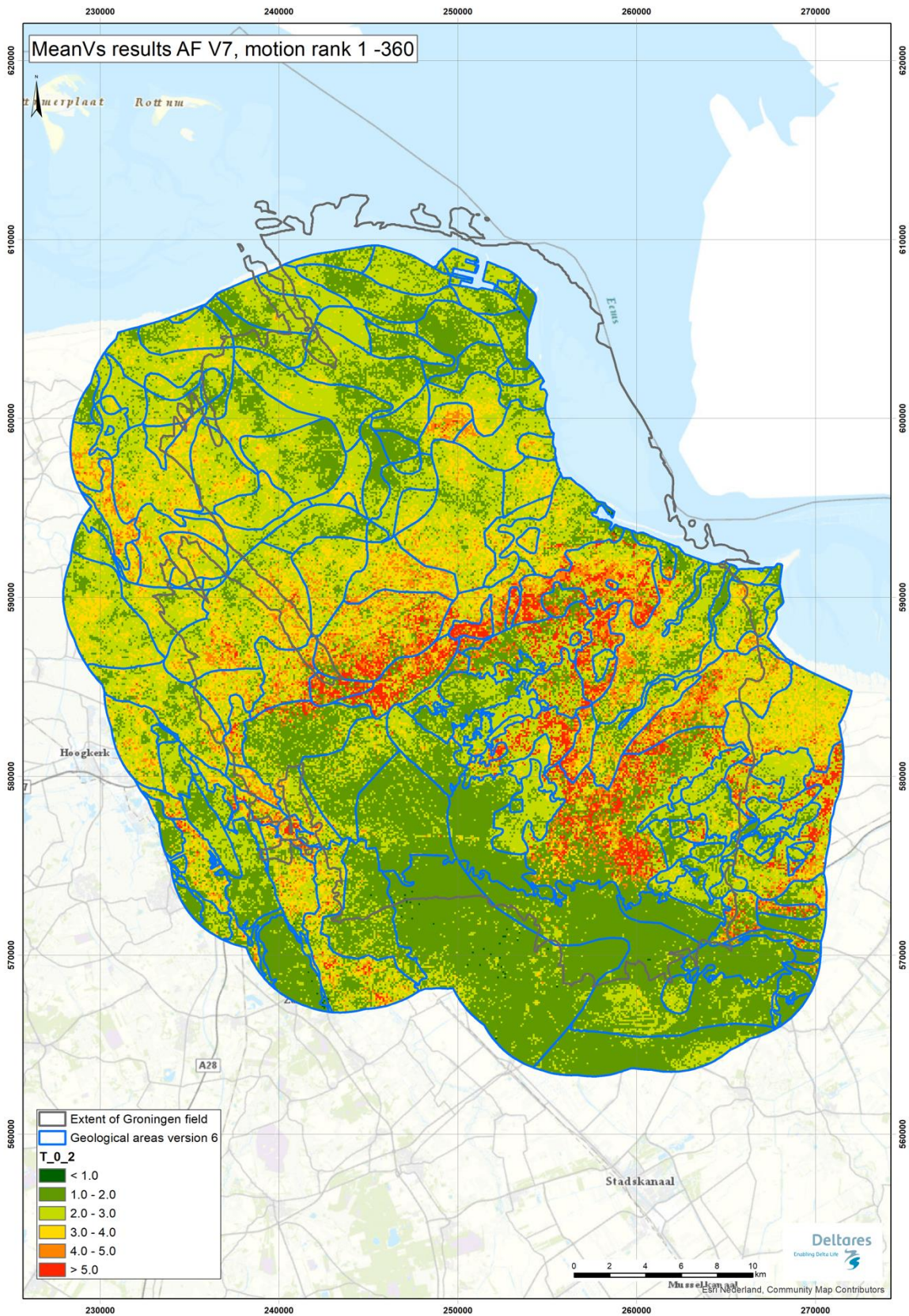


Figure 8.1. AF from the STRATA calculations, plotted for each voxel stack for the weak motions (rank 1-360) for spectral period $T = 0.2$ s. The V6 zonation is shown in blue. No adjustments were required.

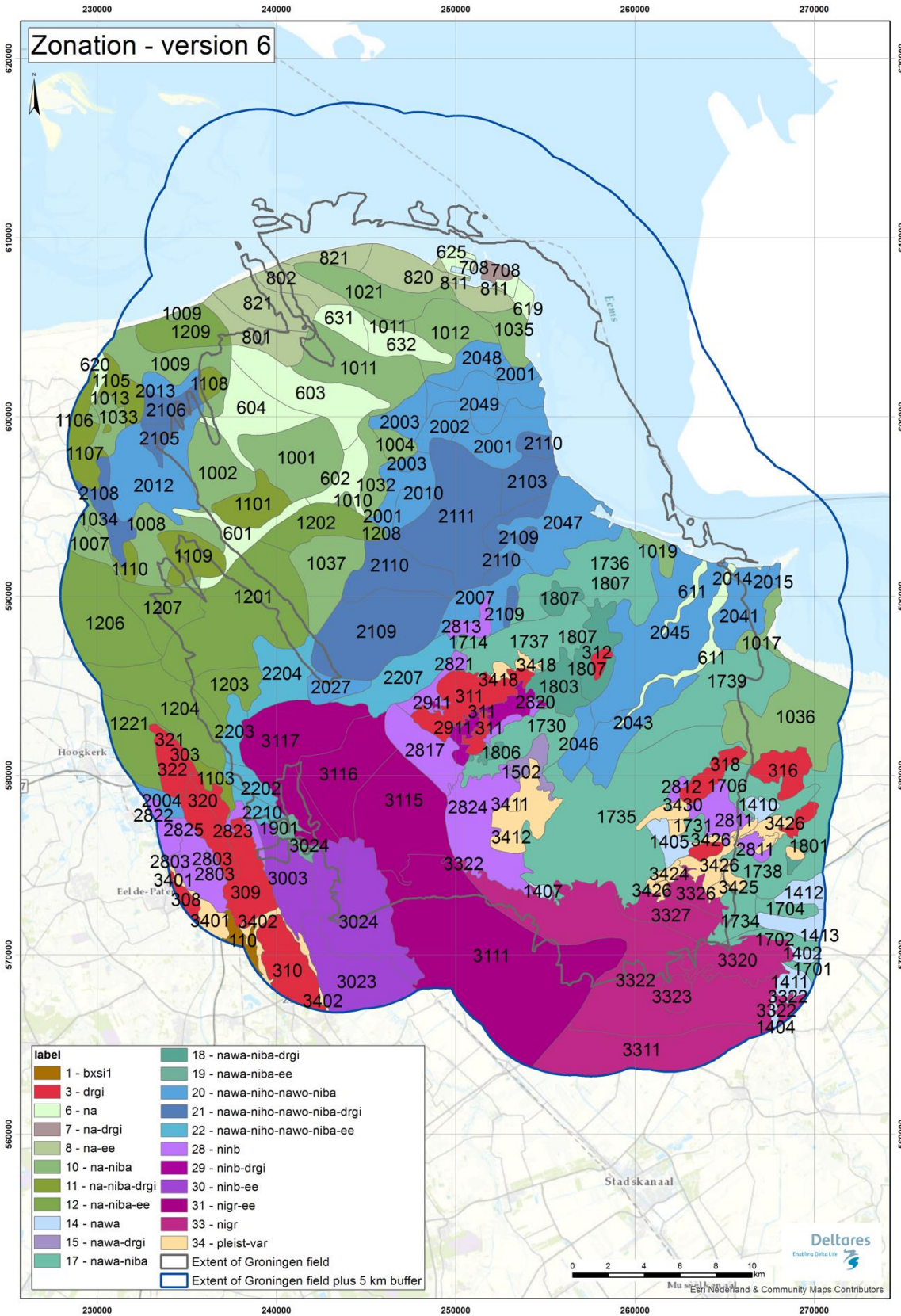


Figure 8.2. V7 zonation used for the Amplification Factors, identical to V6 zonation.

8.2. Amplification Factors

As discussed in Chapter 7, the spectral amplification factors (AF) were calculated using STRATA with the RVT option. The motions at the NS_B horizon are defined as outcrop motions. Ten input motions with different intensities are randomly selected for each voxel stack, as described in Section 7.1. The Vs profile for each voxel stack is a randomized profile; the randomization accounts for the uncertainties in the shear-wave velocity profile for each voxel stack. The AFs are grouped into zones using the zonation model described in Section 8.2. The resulting AFs are strongly nonlinear. In addition, for short oscillator periods the AFs are scenario dependent. A sample of the Afs from EQL for Zone 1801 and selected oscillator periods is shown in Figure 8.3.

The computed AFs are used to derive an intensity and scenario (magnitude and distance) dependent model. The selected model is given by (Stewart *et al.*, 2014):

$$\ln(AF) = f_1^* + f_2 \ln\left(\frac{Sa_{NS_B,g} + f_3}{f_3}\right) + \varepsilon \sigma_{\ln AF} \quad (8.1)$$

where $Sa_{NS_B,g}$ is the spectral acceleration at the NS_B horizon and is given in units of g (the acceleration of gravity), f_2 and f_3 are model parameters, ε is a standard normal random variable, $\sigma_{\ln AF}$ is a parameter that represents the standard deviation of the data with respect to the median prediction of the model, and f_1^* is a variable that depends on magnitude and distance as is explained below. The standard deviation $\sigma_{\ln AF}$ is allowed to vary with the input spectral acceleration (*i.e.*, a heteroskedastic model) in a manner that will be described later in this section. The parameter f_1^* is magnitude-and distance-dependent and is given by:

$$\begin{aligned} f_1^* = & [a_0 + a_1 \ln(R)] + [b_0 + b_1 \ln(R)][\min(M, M_{ref1}) - M_{ref1}] + \\ & a_2 [\ln(R) - \ln(R_{ref})]^2 + b_2 [\min(M, M_{ref1}) - M_{ref2}]^2 + \\ & a_3 [\max(M, M_{ref1}) - M_{ref1}] \end{aligned} \quad (8.2)$$

where M is magnitude, R is closest distance, a_i , b_i , M_{ref2} , and R_{ref} are model parameters, and M_{ref1} is given by:

$$M_{ref1} = \begin{cases} M_a & \text{for } R < 3km \\ M_a + \frac{\ln(R) - \ln(3)}{\ln(60) - \ln(3)} (M_b - M_a) & \text{for } 3km \leq R \leq 60km \\ M_b & \text{for } R > 60km \end{cases} \quad (8.3)$$

where M_a and M_b are model parameters. Eq. (8.1) captures a quadratic dependence of the linear Afs with respect to magnitude and distance for magnitudes lower than M_{ref1} . For magnitudes greater than M_{ref1} , the model has a linear magnitude dependence. The model is applicable for magnitudes up to 7.25 and distances up to 60 km. The standard deviation is fitted using a trilinear function given by

$$\sigma_{\ln AF} = \begin{cases} \sigma_{\ln AF, low} & \text{for } Sa_{NS_B, g} < x_l \\ \sigma_{\ln AF, low} + (\sigma_{\ln AF, high} - \sigma_{\ln AF, low}) \frac{\ln(Sa_{NS_B, g}) - \ln(x_l)}{\ln(x_h) - \ln(x_l)} & \text{for } x_l \leq Sa_{NS_B, g} \leq x_h \\ \sigma_{\ln AF, high} & \text{for } Sa_{NS_B, g} > x_h \end{cases} \quad (8.4)$$

where σ_{low} , σ_{high} , x_l and x_h are model parameters.

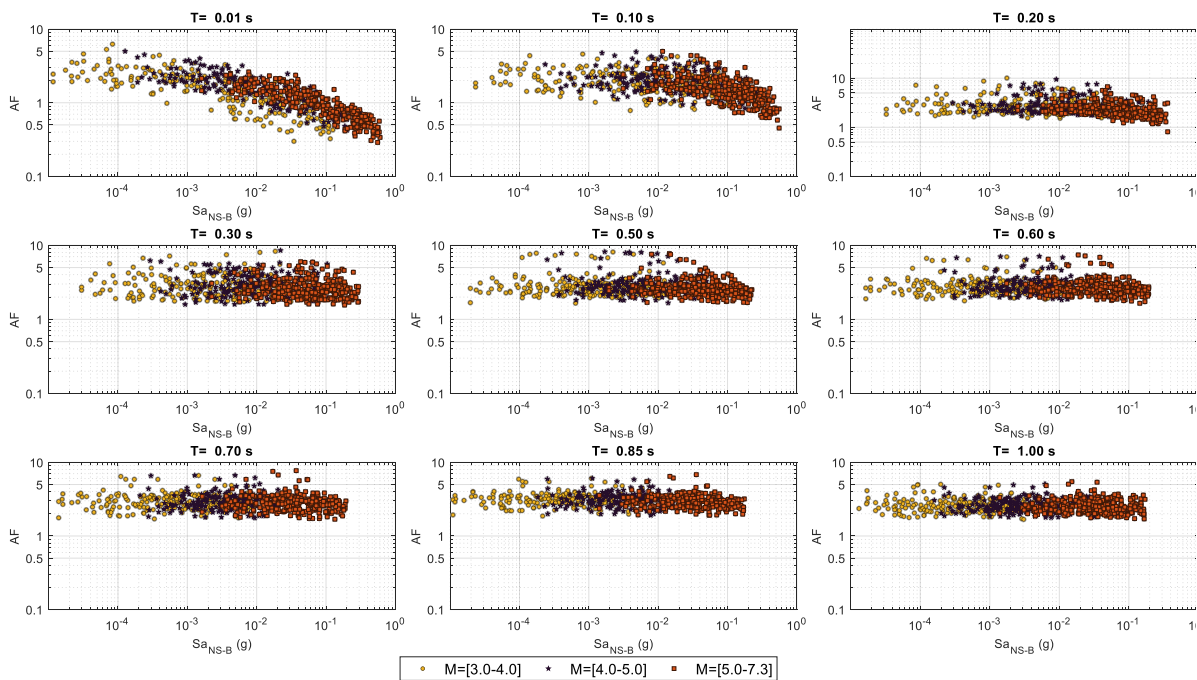


Figure 8.3. Amplification Factors plotted versus spectral acceleration at NS_B for Zone 1801 (average $V_{S30}=201.7$ m/s). Different symbols are used to indicate magnitude bins.

The model parameters for Eqs. (8.1) to (8.4) are obtained using the following approach. First, the AF computed from the linear site amplification runs are used to compute the parameters from Eq. (8.2). Parameters M_{ref2} and R_{ref} are only used to center the regression model and are fixed to period-independent values. An initial regression step using maximum likelihood is conducted by fixing M_{ref1} to 4.5. After this step, a grid search is conducted to obtain the parameters M_a and M_b for the M_{ref1} model (Eq. 8.3). The parameters selected are those that minimize the likelihood function. Once the reference magnitudes and reference distances are set, multiple

regressions are run by sequentially smoothing one or two parameters at a time; the smoothed parameters are fixed in subsequent iteration steps (the order for smoothing is b_2 and a_3 first, then b_1 , followed by b_0 ; a_2 and a_0 are not smoothed).

In order to fix the parameters that control the nonlinear behaviour of the AFs (i.e., f_2 and f_3 in Eq. 8.1), we normalize the AFs from the nonlinear runs (AF_{NL}) to those of the linear runs (AF_{LIN}). Using Eq. (8.1) and ignoring the uncertainty term, this ratio is written as:

$$\ln\left(\frac{AF_{NL}}{AF_{LIN}}\right) = f_2 \ln\left(\frac{S_{a,NS,B,g} + f_3}{f_3}\right) \quad (8.5)$$

In this equation, f_2 controls the degree of nonlinearity and f_3 controls the intensity at which nonlinearity becomes significant. Note that for negative values of f_2 AF decreases with input motion intensity, the opposite occurs for positive f_2 values. Decrease of AF with increase in input motion intensity occurs as a result of the increase in damping and the increase in the site period due to softening of the soil as a result of large strains. This increase implies that the resonant frequency shifts to lower frequencies and away from the frequency bandwidth where the input motion has significant energy. For longer periods, the shift in resonance may lead to amplifications as the site period moves closer to the oscillator period. The parameters of Eq. (8.5) were derived using maximum likelihood regression. Site response analyses for which the maximum strain anywhere along the profile was higher than 1% were not considered in the regression. Maximum strains have been used in the past to identify cases where EQL analyses result in large errors (Kaklamanos *et al.*, 2013; Zalachoris & Rathje, 2015), and the level of 1% has been associated with large deviations from observed site response in downhole arrays (Zalachoris & Rathje, 2015). Large strains typically occur in a single layer, producing an apparent base isolation effect for the layers above. This isolation effect was considered unrealistic because it is unlikely to occur in the presence of site heterogeneities. An initial regression was used to fix both f_3 and f_2 . Subsequently, f_3 was smoothed and the value of f_2 was recomputed via regression. Figure 8.4 illustrates the resulting model fits for a selected zone and selected periods.

The final step is to determine the parameters of the uncertainty model (Eq. 8.4). The parameter x_l is meant to determine the initiation of nonlinearity. This parameter was set to the value for which AF_{NL}/AF_{LIN} became 0.95. The parameter x_h is meant to capture the value of $S_{a,NS,B}$ for which the nonlinearity is strong. This parameter was set equal to f_3 , since the model has strong nonlinearity beyond this value. The other model parameters (σ_{low} and σ_{high}) were obtained via maximum likelihood regression of the full model (Eq. 8.1). At this last regression stage, the only free parameters were those of the uncertainty model ($\sigma_{lnAF,low}$ and $\sigma_{lnAF,high}$) and a_0 . A final smoothing was performed for the f_2 , σ_{low} , and σ_{high} .

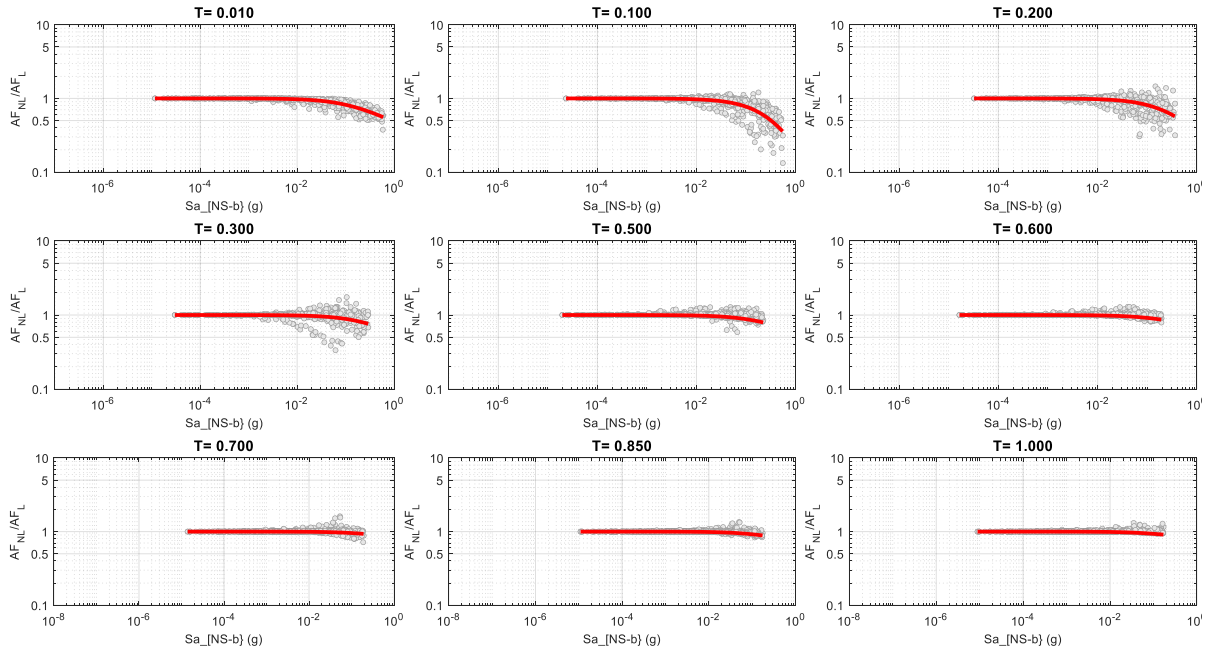


Figure 8.4. Ratio of nonlinear to linear AF for Zone 1801 and selected periods. The red line is the model fit to the data (Eq. 8.5)

The residuals ($AF_{computed} - AF_{predicted}$) of the model are shown in Figures 8.5 to 8.7 for selected zones and periods. Note that the model is unbiased and the uncertainty model is consistent with the data. The zones correspond to zones that sample the range of V_{S30} values of the Groningen field.

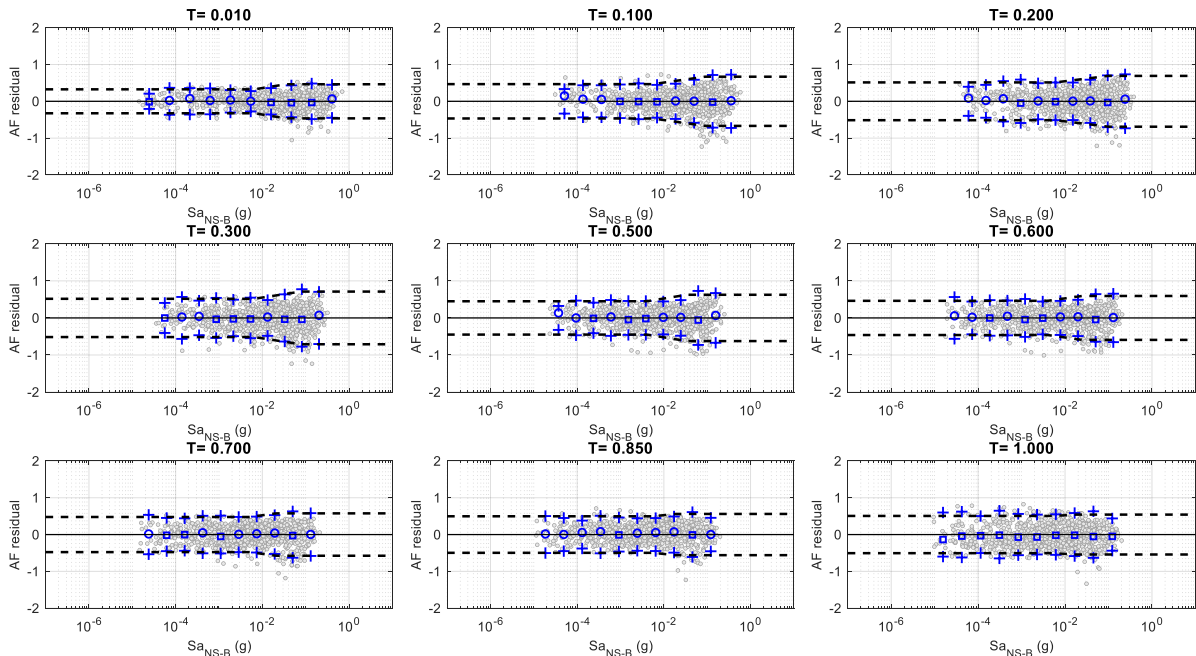


Figure 8.5. AF residuals for Zone 1013 (average $V_{S30} = 155.9$ m/s). The dashed black lines are plotted at a value of \pm two standard deviations. The blue circles are the sample mean of data within Sa_{NS-B} bins. The blue crosses are plotted at the \pm 2 sample standard deviations from the sample mean for the same selected bins.

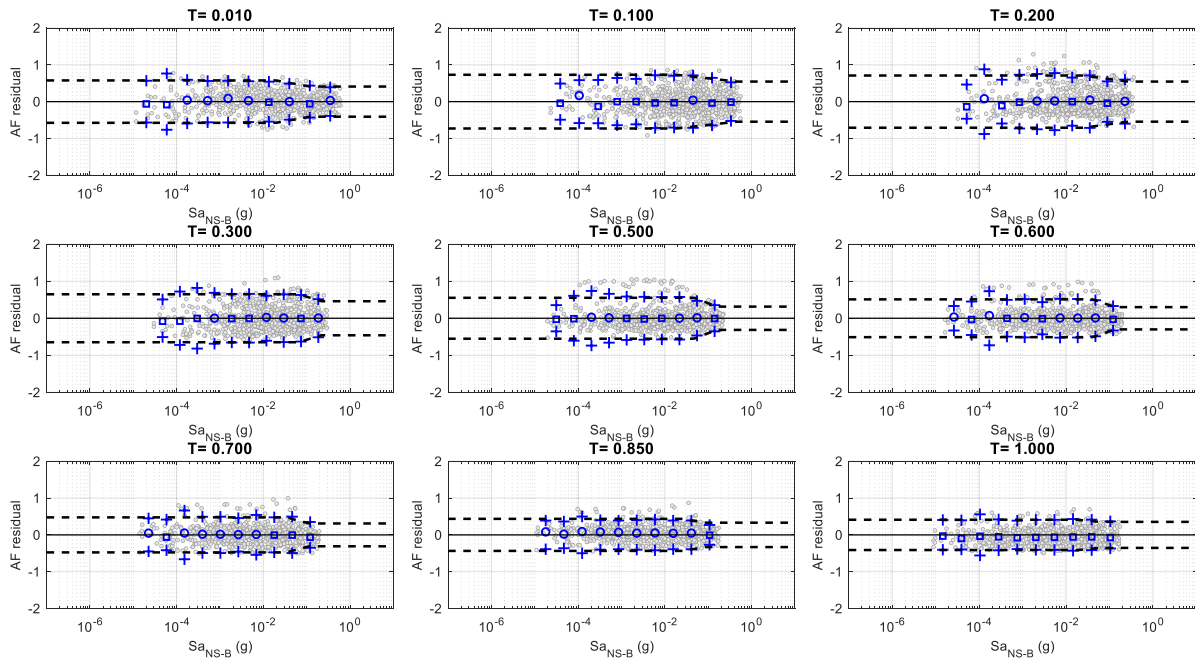


Figure 8.6. AF residuals for Zone 1801 (average $V_{S30} = 201.7$ m/s). The dashed black lines are plotted at a value of \pm two standard deviations. The blue circles are the sample mean of data within Sa_{NS-B} bins. The blue crosses are plotted at the \pm 2 sample standard deviations from the sample mean for the same selected bins.

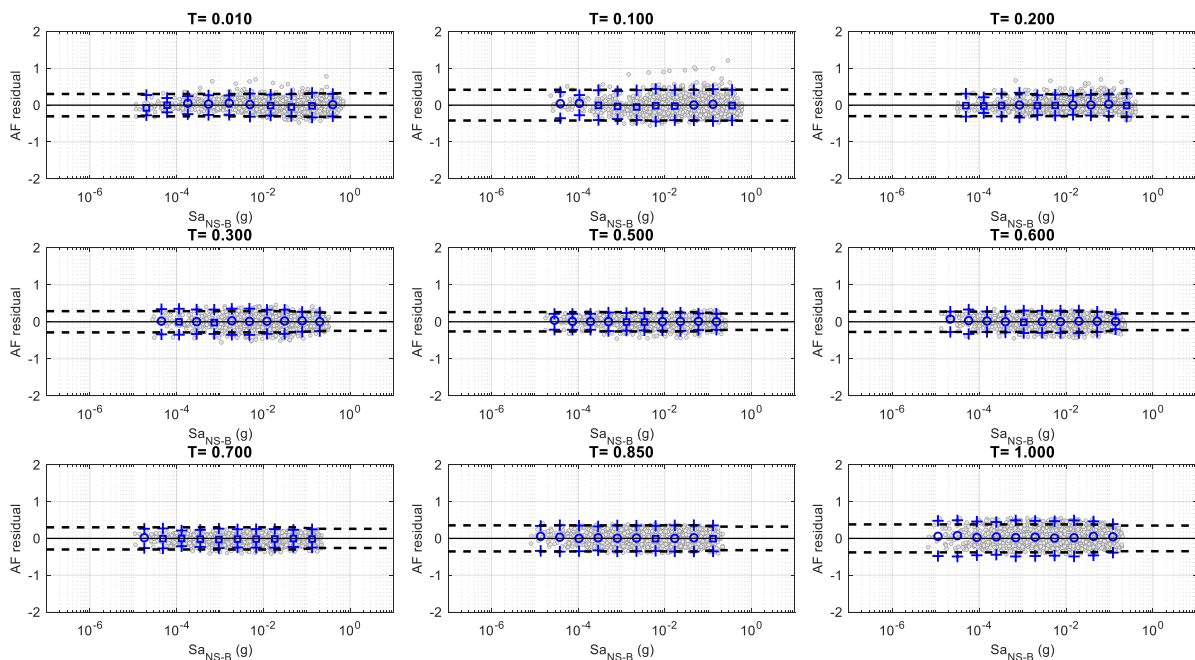


Figure 8.7. AF residuals for Zone 308 (average $V_{S30} = 258.2$ m/s). The dashed black lines are plotted at a value of \pm two standard deviations. The blue circles are the sample mean of data within Sa_{NS-B} bins. The blue crosses are plotted at the \pm 2 sample standard deviations from the sample mean for the same selected bins.

In order to avoid unrealistic AF values outside the range of S_{aNS_B} represented by the input motions, for each zone and each period a minimum and a maximum median AF is imposed. The minimum AF is equal to 0.25. This value is a conservative choice that limits the reduction in ground motions resulting from the extrapolation of the model. The minimum AF is relevant for periods less than 1.0 s, and only comes into play if the model is extrapolated beyond the range of NS_B motions considered in this study. The maximum AF is set to the predicted median AF at the maximum S_{aNS_B} according to Eq. (8.1). This upper limit only comes into play if the model is extrapolated to large input motions and if parameter f_2 is greater than 0. The amplification factors for all zones and periods, including the imposed lower and upper limits, are shown in Figure 8.8.

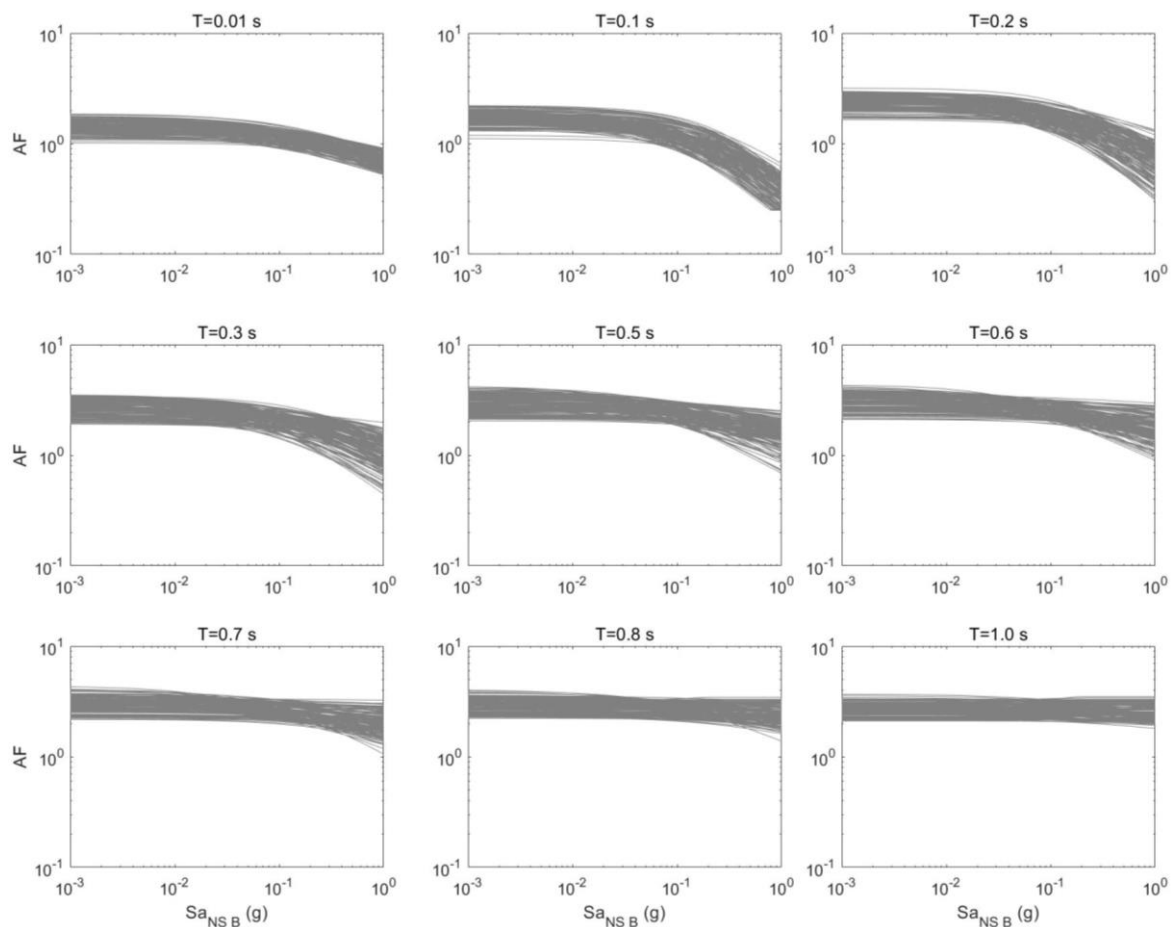


Figure 8.8. Fitted AF functions for all zones for select periods (for $M=4.5$, $R=15$ km).

The spatial distributions of weak motion amplification factors (i.e., e^{f1^*}) is plotted in Figure 8.9 for selected periods and one combination of M and R . The AFs show a clear geographical variability, that is different for each period. The geology is reflected in the AF maps, especially for periods of 0.6 and 1.0 s. The distinction between the northern part with Holocene dominance and the southern part (Pleistocene at surface)

is very clear. Details of channel structures (east) and the Hondsrug (southwest) can also be recognized.

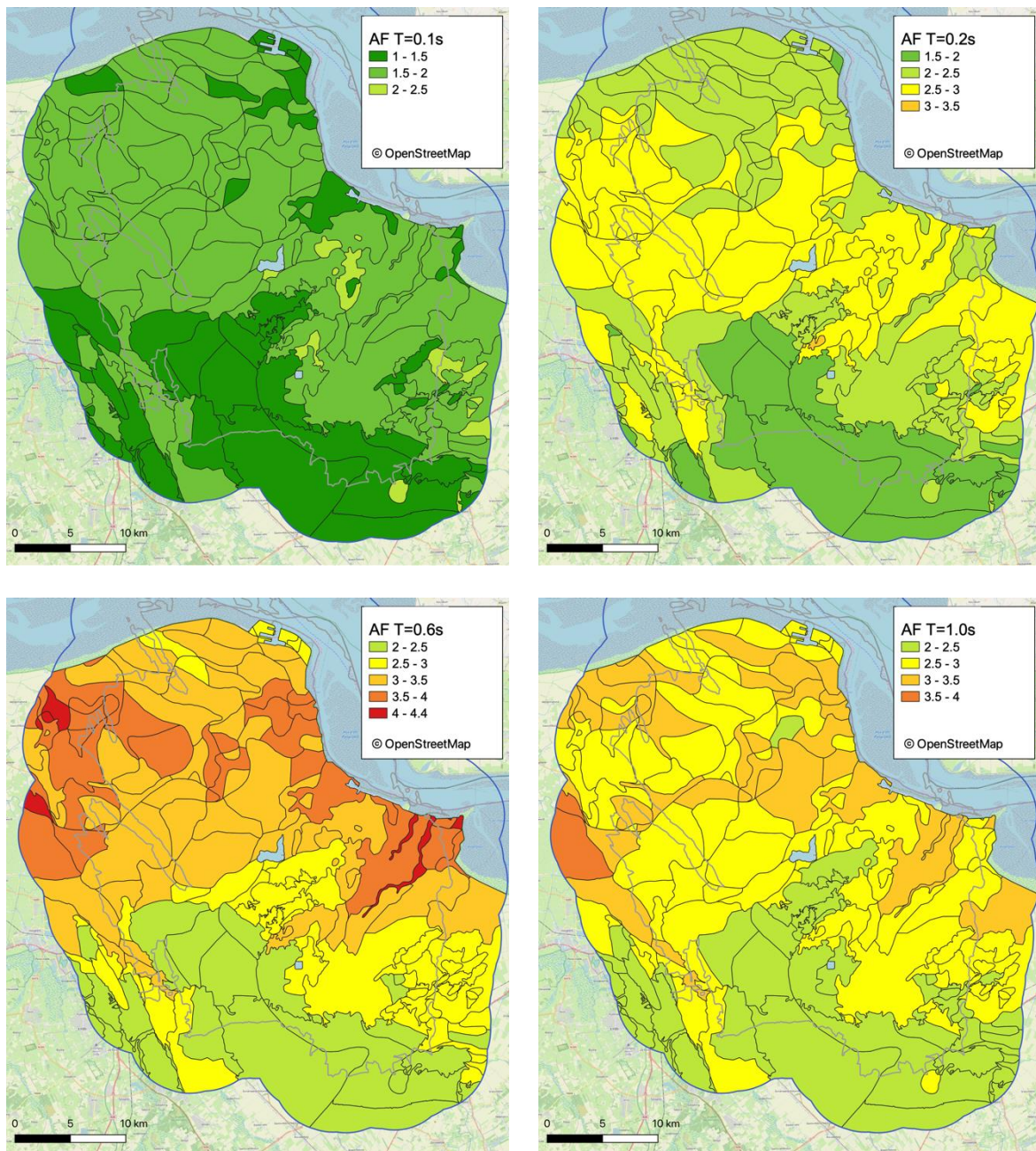


Figure 8.9. Weak motion AFs (e^{f1^*}) for the zones in the Groningen region. The AFs are shown for an M 4.5, R 5 km scenario and selected periods (0.1, 0.2, 0.6 and 1.0 s).

The predictions of the AF model for all the zones in the Groningen field are shown in Figure 8.10, where they are plotted versus the average V_{S30} of each zone. Note that for most oscillator periods larger than 0.5 s, the AFs reduce with increasing V_{S30} , as is expected. For shorter oscillator periods, there is an initial increase in amplification as the V_{S30} increases, followed by a decrease (e.g., see T=0.2 s in Figure 8.10). This

behaviour reflects the larger damping for softer sites, which affects high-frequency motions, as well as possible resonance effects.

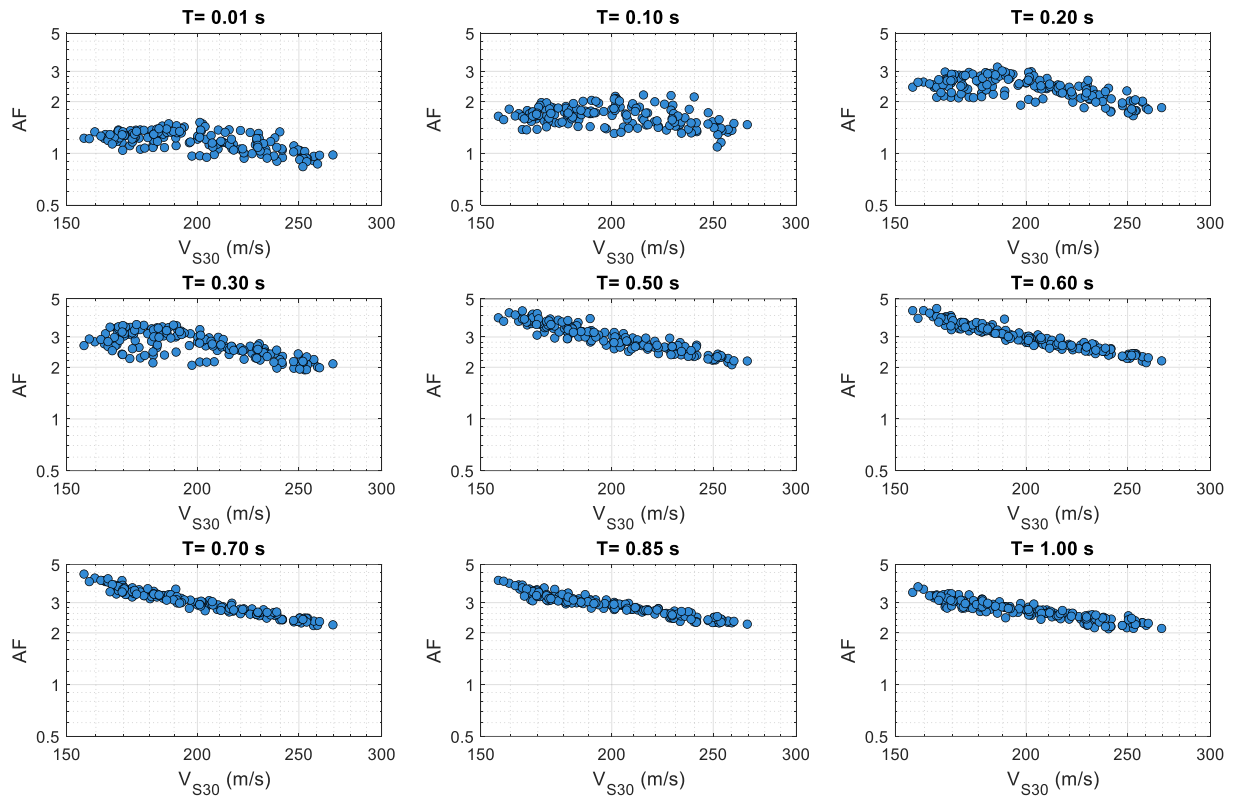


Figure 8.10. Predictions of the AF model for all zones in the Groningen field plotted versus the average V_{S30} of each zone. Predictions are for $M=5$ and $R=10$ km.

The parameters of Eq. (8.5) that control the nonlinearity in the AFs are plotted for all the zones in Figure 8.11. Observe that the nonlinearity is strongest (more negative f_2 value) for an oscillator period of 0.1 s. Also note that the parameter f_2 becomes positive for oscillator periods greater than about 1.0 s, indicating that for these periods AF values increase as the intensity of shaking increases. For comparison purposes, the values of the parameters for two NGA West2 models (Chiou & Youngs, 2014 and Boore *et al.*, 2014) are also shown. The Groningen model parameters follow the same trends as those of the NGA West2 models, although the degree of nonlinearity for $T=0.1$ s is much stronger for the Groningen field (*i.e.*, more negative f_2). Since the nonlinear behavior is dependent both on f_2 and f_3 , a more direct comparison of the nonlinearity in the Groningen field with existing models is obtained by first constraining f_3 to be equal to the NGA W2 models, and then recomputing f_2 . This is done for the Chiou & Youngs (2014) model in Figure 8.12. Note that the trends of f_2 with V_{S30} are similar for both models. The degree of nonlinearity is stronger for the CY model for $T=0.1$ s and for zones with low V_{S30} for $T=0.2$ s and 0.3 s but is milder for other periods. This is consistent with the very soft soils present near the surface in the Groningen gas field.

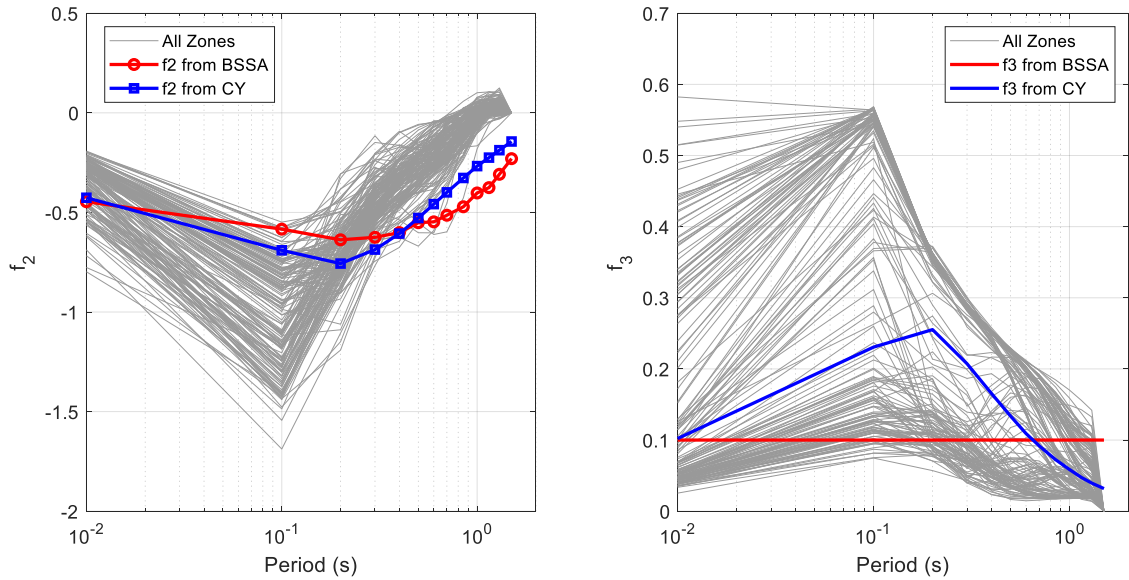


Figure 8.11. Parameters f_2 and f_3 (Eqs. 8. 1 and 8.5) for all the zones in the Groningen field. For comparison purposes, the parameters for the Chiou & Youngs (2014; CY) and Boore *et al.* (2014; BSSA) models are also shown. Periods beyond 1 second are shown but do not form part of the deliverable.

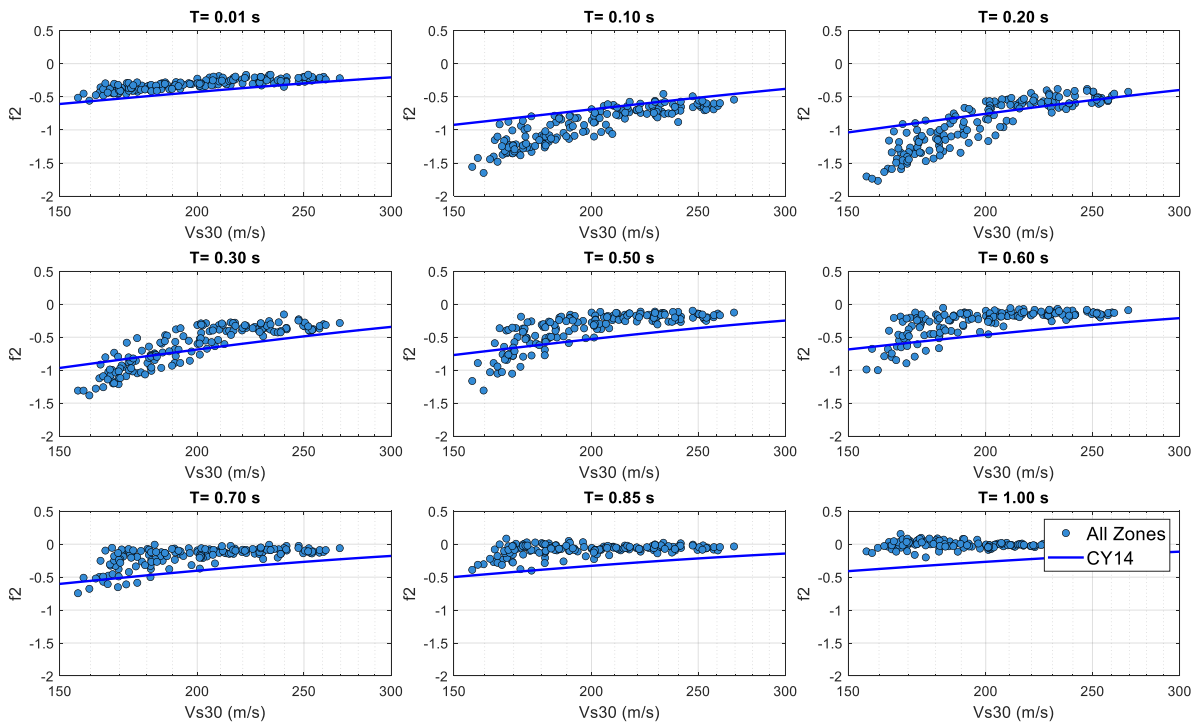


Figure 8.12. Parameter f_2 for the Groningen model, but derived by constraining the model to have the same value of parameter f_3 as the Chiou & Youngs (2014; CY) model. For comparison, the f_2 parameter from Chiou & Youngs (2014) is also shown.

An additional check for the model validity is that the AFs computed for a station (Section 4.4) should fall within the range of variability of the AFs computed for the zone

where the station lies. This check is shown in Figure 8.13, which plots the difference between zone and station AFs for the set of magnitudes and distances that were recorded at these stations. The trends seen in Figure 8.13 are typical of the entire field. In general, the AFs for the zones plot within a +/- two standard deviations of the Zone factors, with larger differences seen for $T=0.01$ s and $T=0.1$ s. The larger differences for short periods are due to differences in magnitude- and distance-dependence between the zone and the station model.

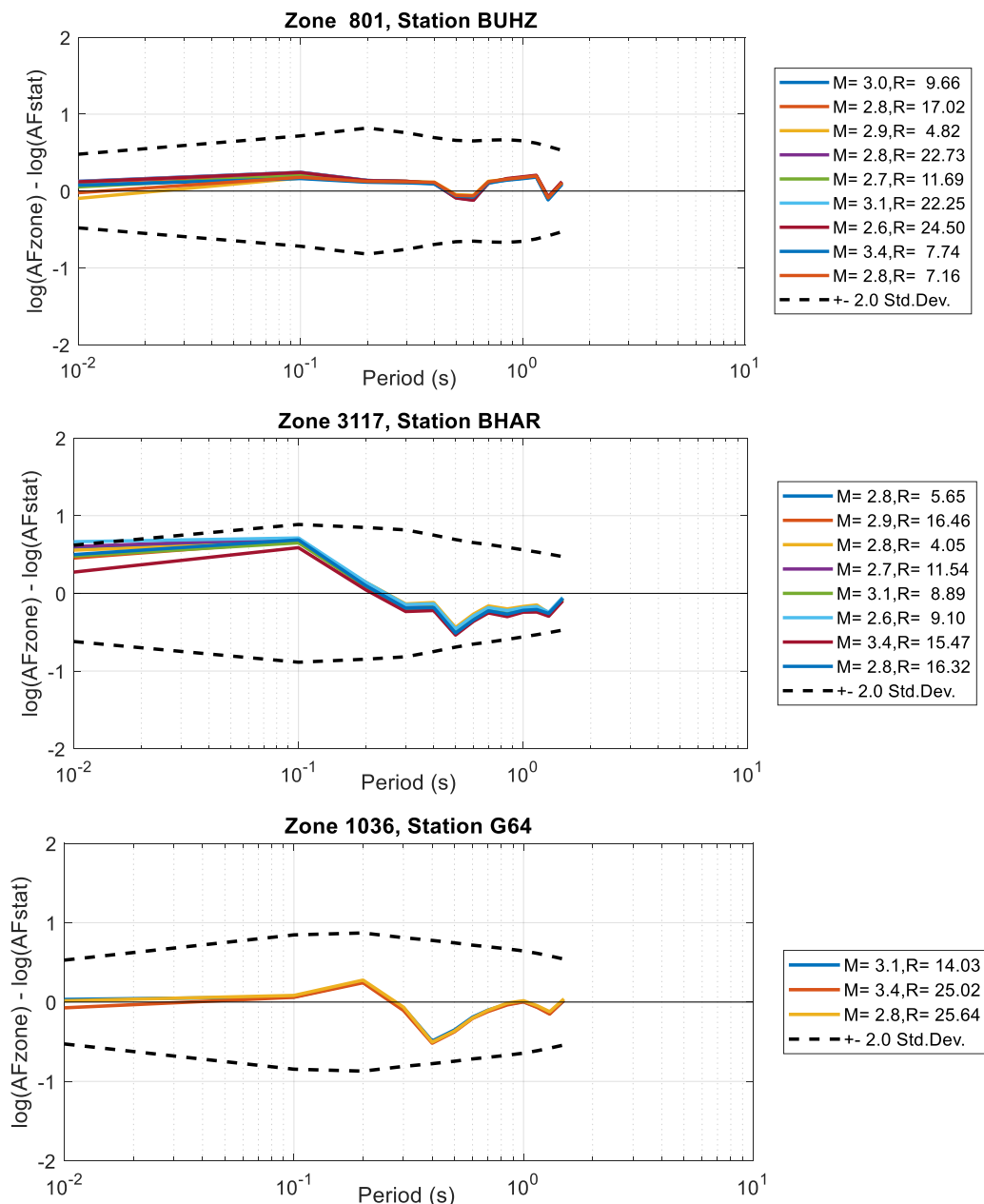


Figure 8.13. Comparison of linear AF for selected stations and the corresponding zone where the station is located. AFs are shown for magnitude and distance pairs that correspond to the recordings at the station. The dashed lines are the +/- two standard deviation bounds of the Zone AF model. Periods beyond 1 second are shown but do not form part of the deliverable.

8.3. Logic-Tree for Site Amplification Factors

The AF model presented in Section 8.2 is used to develop the logic tree for the site amplification factors. The central branch of the proposed model is obtained directly from the model in Section 8.2. However, the uncertainty model in Eq. (8.4) needs to be modified to account for additional sources of uncertainty. More specifically, the AF model was developed by grouping the AFs from all voxel stacks within a zone, where the AFs for each voxel stack were obtained using a randomized V_S profile. Therefore, the uncertainty model captures both the uncertainty in V_S and the spatial variability across a zone. An alternative approach would have been to include multiple randomized profiles for each voxel stack. However, preliminary calculations indicated that thanks to the large number of voxel stacks in each zone, the adopted approach correctly captured the total uncertainty in each zone. In addition, the model in Eq. (8.4) captures motion-to-motion variability thanks to the use of randomly selected input motions in the analyses.

However, there are sources of uncertainty that are not captured in the model presented in the previous section. Namely, the contribution to uncertainty in AF due to uncertainty in MRD curves and epistemic uncertainty due to potential errors in the model adopted for conducting site response analyses. The parameter that captures the full uncertainty of the AFs for the Groningen site is labelled ϕ_{S2S} . The subscript “S2S” implies that this uncertainty component represents the “site-to-site” variability for all sites within a given zone; albeit this model also captures other sources of uncertainty.

The additional uncertainty in AFs that results from uncertainty in MRD curves is obtained using the approach in Bahrampouri *et al.* (2019). This approach was adopted for the development of the V4 GMM and remains unchanged. Details of the model development are given in Bahrampouri *et al.* (2019) and only a summary is presented herein. The model is parameterized by the maximum value of the linear site amplification across all oscillator periods. We label this parameter $f_{1,max}$, where f_1 is the linear amplification parameter from Eq. (8.2). The model is developed separately for low-intensity motions (*i.e.*, $Sa_{NS_B} < x_l$) and high intensity motions (*i.e.*, $Sa_{NS_B} \geq x_h$). Figure 8.14 shows the resulting model. For the V7 GMM, the model was updated using the model for uncertainty in low-strain damping presented in Chapter 4. In addition to the uncertainties obtained from the field-estimates of damping (Figure 4.7), model error uncertainties were added. The values for model error were taken as 0.3 in natural log units for damping, and 0.15 for modulus reduction. These values are commonly used for the uncertainty in MRD for sites when no site-specific MRD curves are available in site response analyses for nuclear power plants (Walt Silva, *personal communication*, 2015). These values are lower than the values reported by Darendeli (2001) and used in the V4 GMM model. The lower values are justified because the Darendeli model is developed using soils of different origins within a common soil

class, whereas the Groningen soils (for a given soil type) are more uniform. The uncertainties in damping and modulus reduction are assumed to be negatively correlated with a correlation coefficient of -0.5. Moreover, the undrained shear strength is assumed to have a standard deviation of 0.5 in natural log units (e.g., Phoon & Kulhawy, 1999).

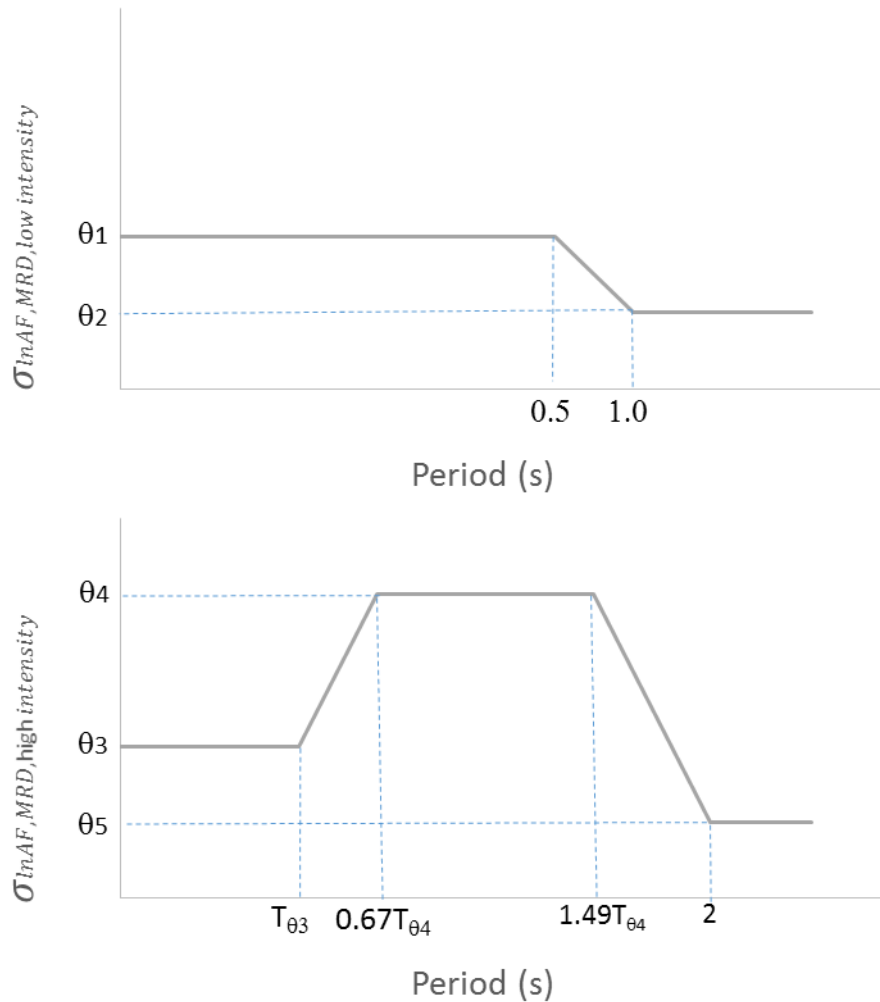


Figure 8.14. Model for the contribution of MRD uncertainty to the total uncertainty in AF. Top: low-intensity model. Bottom: high-intensity model.

The updated model parameters for the Bahrapouri *et al.* (2019) model are:

$$\theta_1 = \begin{cases} -0.106 + 0.2235 f_{1,max} & \text{for } f_{1,max} < 1.2 \\ -0.106 + 0.2235 * 1.2 & \text{for } f_{1,max} \geq 1.2 \end{cases} \quad (8.6a)$$

$$\theta_2 = \begin{cases} -0.0375 + 0.0778 f_{1,max} & \text{for } f_{1,max} < 1.2 \\ -0.0375 + 0.0778 * 1.2 & \text{for } f_{1,max} \geq 1.2 \end{cases} \quad (8.6b)$$

$$\theta_3 = -0.1778 + 0.3315 f_{1,max} \quad (8.6c)$$

$$\theta_4 = \begin{cases} -0.6183 + 0.8446 & \text{for } f_{1,max} < 1 \\ -0.6183 + 0.8446f_{1,max} & \text{for } 1 \leq f_{1,max} \leq 1.324 \\ 0.5 & \text{for } f_{1,max} > 1.324 \end{cases} \quad (8.6d)$$

$$\theta_5 = \begin{cases} -0.4048 + 0.4345 & \text{for } f_{1,max} < 1 \\ -0.4048 + 0.4345f_{1,max} & \text{for } f_{1,max} \geq 1 \end{cases} \quad (8.6e)$$

$$T_{\theta_4} = \begin{cases} -0.7703 + 0.8507 & \text{for } f_{1,max} < 1 \\ -0.7703 + 0.8507f_{1,max} & \text{for } f_{1,max} \geq 1 \end{cases} \quad (8.6f)$$

Finally, T_{θ_3} is defined as 0.05 s if $0.67T_{\theta_4}$ is bigger than 0.08 s and 0.025 s otherwise.

The model error was developed using the recordings of the G-network stations by comparing theoretical and empirical transfer functions. Theoretical transfer functions are computed using linear site response analyses for the full profiles at the station and computing the ratio of surface-outcrop to within-motions at the level of the G4 instruments (-200 m). Empirical transfer functions are obtained by taking the average ratios of surface to borehole (G4) recordings for all records at each station. A Bayesian approach is used to separate model error from parametric error, as described in Bahrapouri (2021). The resulting estimate of model error is shown in Figure 8.15 and is labelled “Bayesian”. The model error has peaks at intermediate periods that are likely the results of pseudo-resonances that are observed in empirical surface-to-borehole transfer functions (Tao & Rathje, 2020). For this reason, these resonances were smoothed for the proposed model to capture model error. For comparison, the model used in the V6 GMM and the model by Stewart & Afshari (2021) are also included in Figure 8.15. The model error proposed in this study is lower than the Stewart & Afshari (2021) estimate because of the generally more favourable conditions for 1D site response in the Groningen field versus the California sites used in the aforementioned study. Moreover, the separation of parametric and model uncertainty that is achieved via the Bayesian regression approach also leads to smaller estimates of uncertainty compared with the model used in the V6 GMM.

In previous versions of the Groningen ground motion model the model error was imposed as a minimum epistemic uncertainty on the site term. The reason for this choice was that the model error estimates also contained an unquantified degree of parametric uncertainty, which was already accounted for via the randomization approach and the additional MRD uncertainty. However, the model error estimates obtained using the Bayesian approach (Figure 8.15) decouple model error and parametric uncertainty, hence they are applied as additional uncertainty to the model (*i.e.*, added as square root of sum of squares). The final uncertainty model for the AF for the Groningen field is thus given as:

$$\phi_{S2S} = \begin{cases} \phi_{S2S,1} & \text{for } Sa_{NS,B} < Sa_{rock,low} \\ \phi_{S2S,1} + (\phi_{S2S,2} - \phi_{S2S,1}) \frac{\log\left(\frac{Sa_{NS,B}}{Sa_{rock,low}}\right)}{\log\left(\frac{Sa_{rock,high}}{Sa_{rock,low}}\right)} & \text{for } Sa_{rock,low} \leq Sa_{NS,B} \leq Sa_{rock,high} \\ \phi_{S2S,2} & \text{for } Sa_{NS,B} > Sa_{rock,high} \end{cases} \quad (8.7)$$

where $Sa_{rock,low}$ and $Sa_{rock,high}$ are model parameters and

$$\phi_{S2S,1} = \sqrt{(\sigma_{lnAF,low})^2 + (\sigma_{lnAF,MRD,low\ intensity})^2 + (\sigma_{model})^2} \quad (8.8)$$

$$\phi_{S2S,2} = \sqrt{(\sigma_{lnAF,high})^2 + (\sigma_{lnAF,MRD,high\ intensity})^2 + (\sigma_{model})^2}$$

where $\sigma_{lnAF,MRD}$ is the additional uncertainty due to MRD for low and high intensity given by Figure 8.14 and Eq. (8.6), $\sigma_{lnAF,high}$ and $\sigma_{lnAF,low}$ are the parameters of the model in Eq.(8.4), and σ_{model} is the model error given in Figure 8.15. The geographical distribution of site-to-site variability $\phi_{S2S,1}$ is shown in Figure 8.15 for the selected periods.

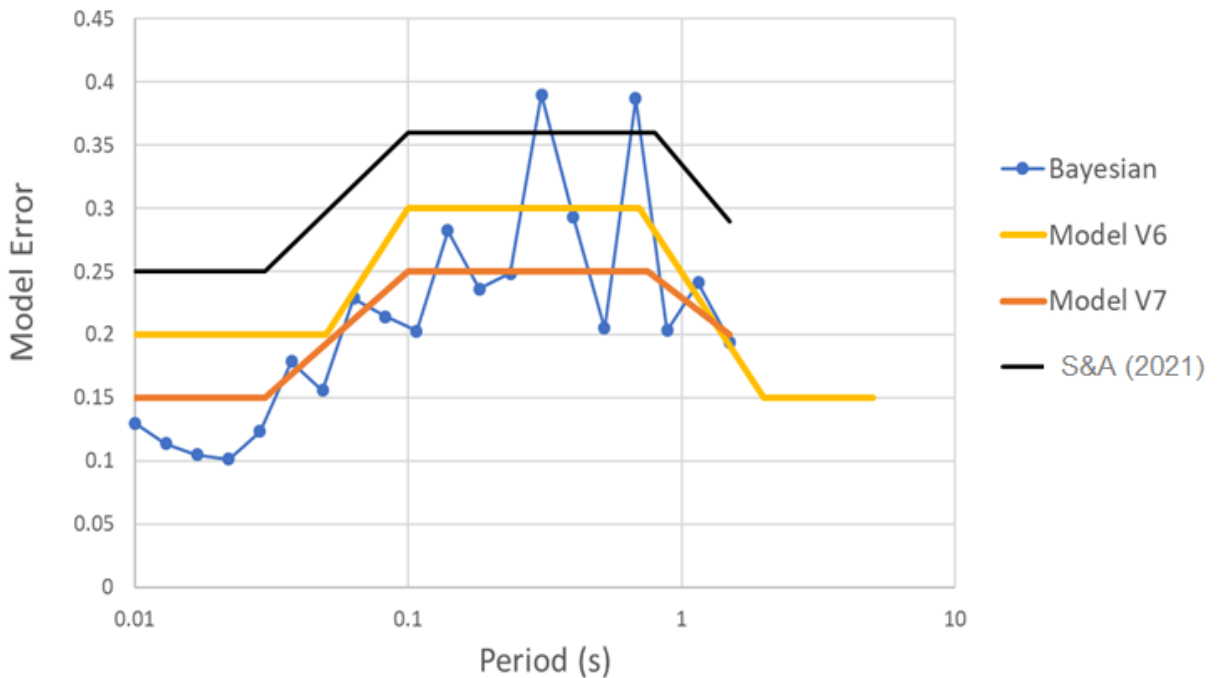


Figure 8.15. Model error (in ln units) estimates computed using a Bayesian approach for recordings at the G-network stations, and the proposed model for the V7 GMM (labelled Model V7). For comparison, the model error used in the V6 GMM and the model error proposed by Stewart & Afshari (2021) are also included. Periods beyond 1 second are shown but do not form part of the deliverable.

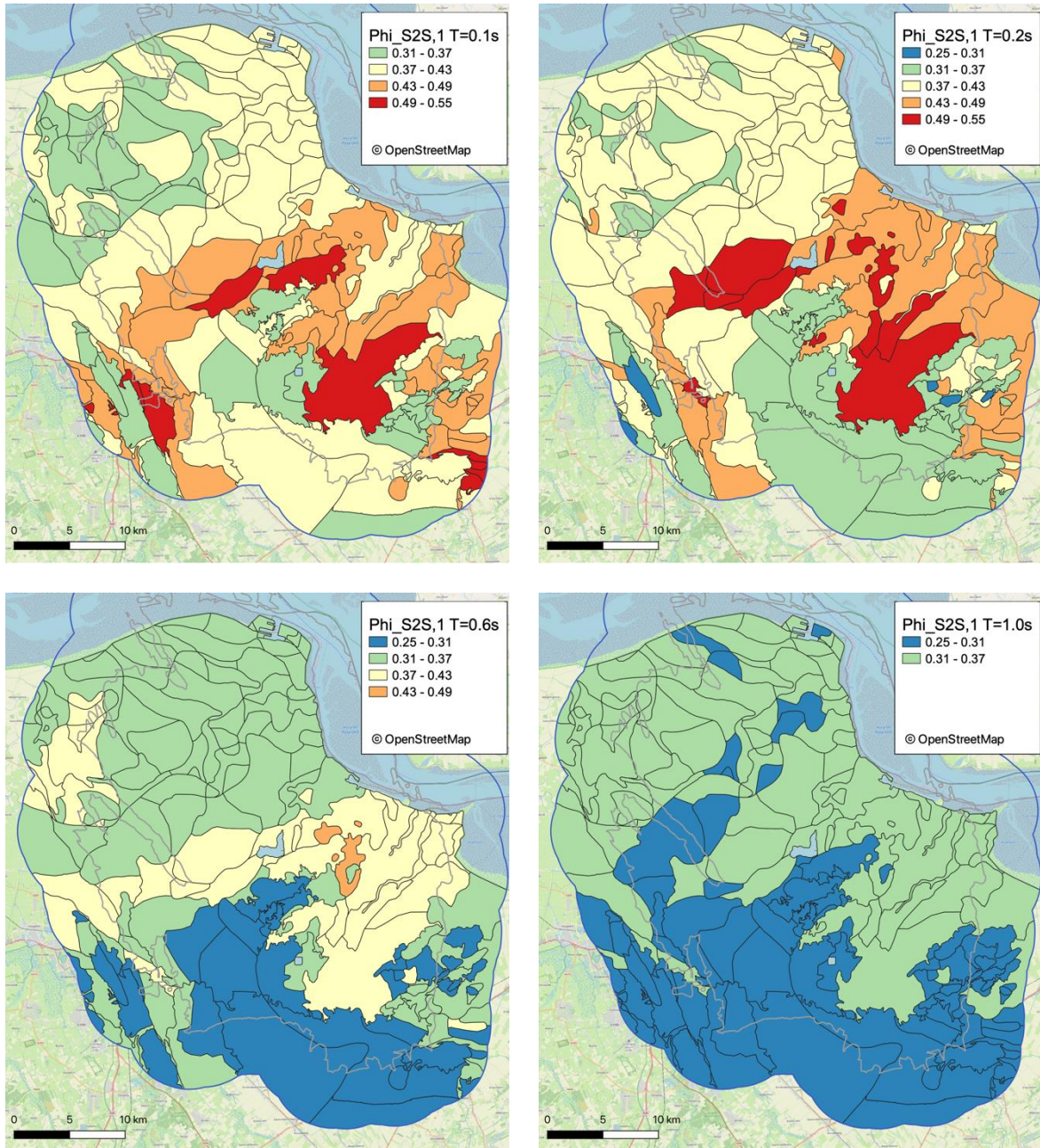


Figure. 8.16. $\phi_{S2S,1}$ values for selected periods (0.1, 0.2, 0.6 and 1.0 s) and for all zones in the Groningen region.

An additional consideration prior to the final development of the amplification factor logic tree was an evaluation of the shape of the distribution for the AF residuals. The maximum likelihood regression approach used to obtain the uncertainty model in Eq. (8.4) assumes a log-normal distribution of the AF residuals. However, in some cases, the empirical CDF deviated from the CDF of the assumed log-normal distribution. The deviations from log-normality, however, were not systematic. For example, if we considered the 95th quantile (*i.e.*, the level for which the probability of exceedance is only 0.05), for a given zone at some periods the empirical quantile would be lower than

the theoretical quantile assuming a log-normal distribution, while for others it would be larger. This is illustrated for Zone 308 in Figure 8.17.

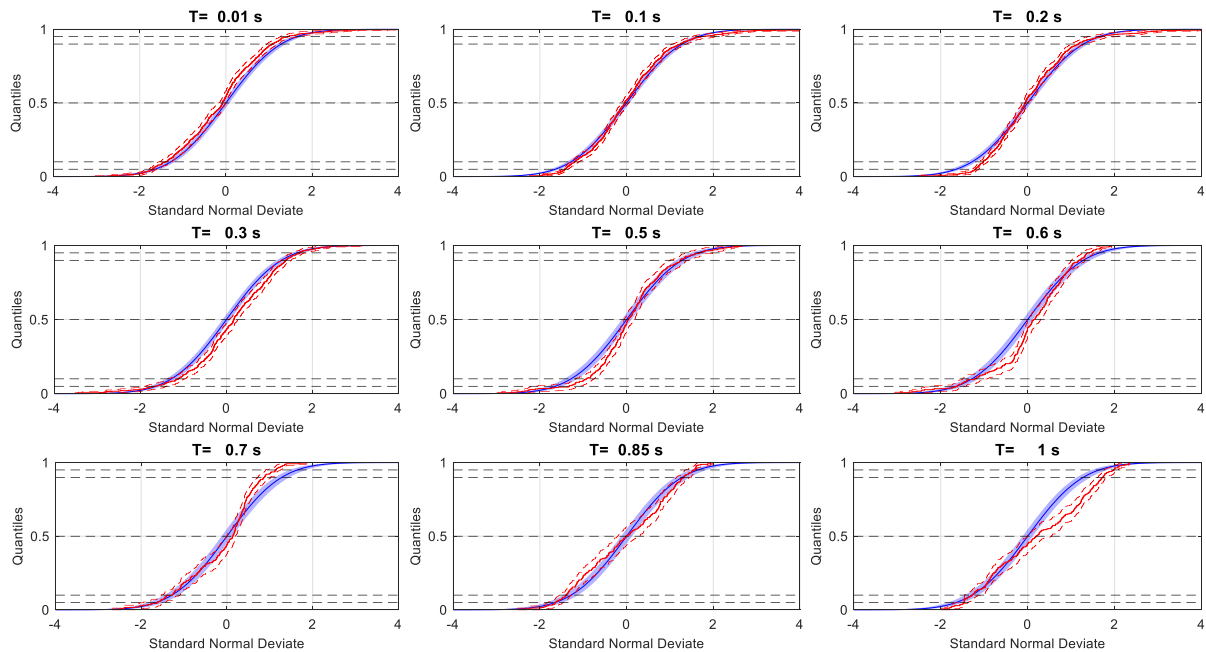


Figure 8.17. Theoretical quantiles (blue) and empirical quantiles (red) for the AF predicted for low-intensity motions for Zone 308. The shaded region around the theoretical quantiles represents a 95% confidence interval computed from the uncertainty in the sample mean and sample standard deviation. The dashed lines around the empirical quantiles correspond to the 95% Confidence Interval. Horizontal dashed lines identify the 5th, 10th, 50th, 90th and 95th quantiles.

Overall, the team’s assessment is that the assumption of log-normality did not introduce errors in the predictions of the model. The final amplification factor logic tree is built by sampling the normal distribution on the natural logarithm of AF given by Equations (8.7) and (8.8) into a three-branch discrete distribution. The weights of the distribution are computed using Keefer & Bodily (1983) for 5th, 50th and 95th quantiles. The final logic tree is illustrated in Figure 8.18.

The explicit representation of the AF uncertainty as an epistemic uncertainty rather than a variability term is one of the more substantial changes in the V7 GMM relative to earlier versions of the model. In reality, the uncertainty in AF is likely to consist of both epistemic uncertainty and aleatory variability, but the pervading view is that the former dominates, hence the introduction of this additional node to the logic tree.

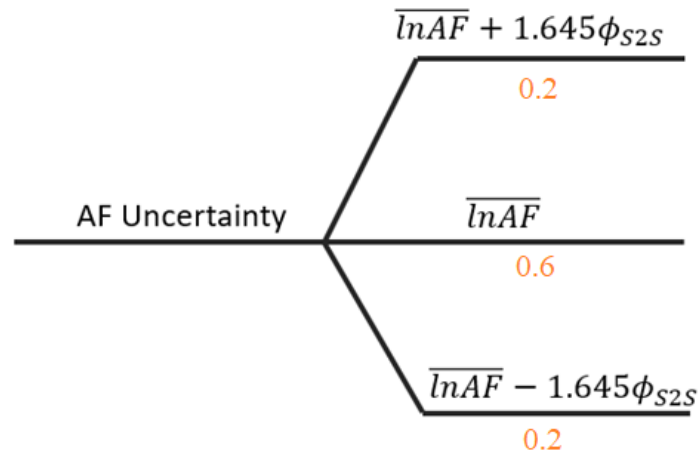


Figure 8.18. Logic tree for the Amplification Factors. The mean values for AF ($\overline{\ln AF}$) are obtained from Eqs. (8.1) to (8.3), and the uncertainty (ϕ_{S2S}) is obtained from Eqs. (8.7) and (8.8).

8.4. Amplification Penalty Function for *Wierden*

The site response analysis on *wierden* has been described in Kruiver et al (2021) and summarized in Section 7.4. Several considerations were considered during the derivation of the Penalty Function. First, the GMM already incorporates a strong degree of epistemic uncertainty. The 95% confidence interval (CI) of the epistemic uncertainty generally envelopes the residuals (Figure 7.13). Therefore, a simple modification, consisting of a unique Penalty Factor for all *wierden*, is sufficient. The Penalty Factor is based on the average of the mean residuals of the three GMM *wierden*. To account for the fact that only three *wierden* are used, the standard error of the mean is used to compute the 75th percentile of the mean residual (as a suitably conservative estimate). Finally, the Penalty Factor is defined via a piecewise log-linear function that envelopes the 75th percentile (Figure 8.19). The corrected amplification factor $AF_{\text{building on wierden}}$ is given by:

$$\ln(AF_{\text{building on wierde}}) = \ln(AF_{\text{GMM zone}}) + \text{Penalty Factor} \quad (8.9)$$

with the Penalty Factor in *ln* units. The Penalty Factor is tabulated for the hinge point periods in Table 8.1. For periods between the hinge points, the Penalty factor can be obtained using log-linear interpolation.

Table 8.1 Penalty Factor (in *ln* units) at hinge point periods (Figure 8.19).

| Period (s) | Penalty Factor (<i>ln</i> units) |
|------------|-----------------------------------|
| 0.01 | 0.20 |
| 0.1 | 0.25 |
| 0.2 | 0.35 |
| 0.5 | 0.35 |
| 1.0 | 0.10 |

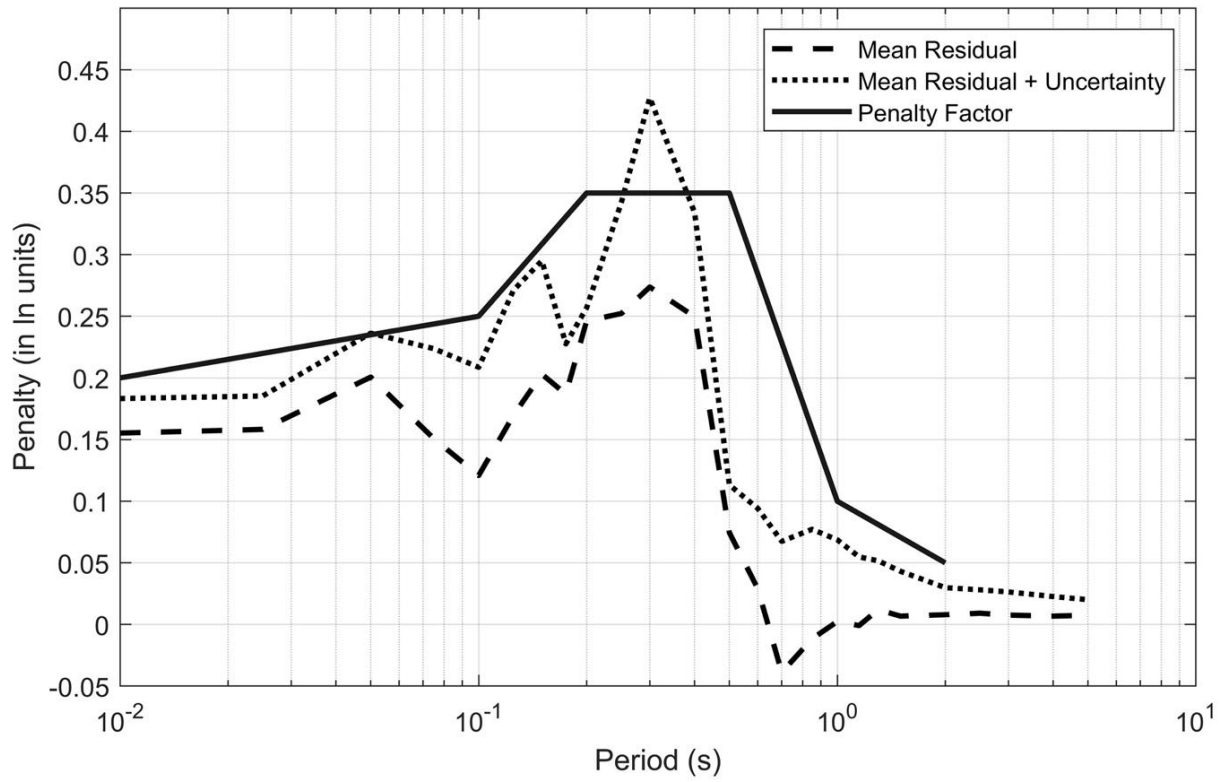


Figure 8.19. Penalty Function (solid black line) for buildings on *wierden*. Periods beyond 1 second are shown but do not form part of the deliverable.

9. MODEL SUMMARY and INSTRUCTIONS for IMPLEMENTATION

As noted in Chapter 1, this chapter provides a concise summary of the complete model for those interested in its implementation. This means that some information is repeated from previous chapters but for the convenience of the user, the complete model is presented here in its entirety. Section 9.1 presents the basic model elements, including the equations and their coefficients, as well as identifying all of the electronic supplements where the model parameters are listed. Section 9.2 provides instructions for the sampling of the variance components. Section 9.3 provides the guidance for how to implement the model in risk calculations for structures that are located on *wierden*.

9.1. Complete GMM Logic-Tree

The V7 Groningen GMM has the same basic structure as the V5 model: equations for the prediction of response spectral ordinates at the NS_B rock horizon combined with period-dependent non-linear site AFs assigned to zones defined throughout the study area (onshore gas field plus 5 km buffer). As for the V6 model, the V7 GMM provides predictions of 5%-damped spectral accelerations, $S_a(T)$. However, whereas the V6 model covered 23 periods and peak ground velocity (PGV), the V7 model covers 10 periods up to 1.0 seconds and does not provide PGV predictions, which are provided separately for small-magnitude earthquakes (Bommer *et al.*, 2021b). The 10 periods for which the V7 GMM is defined are precisely those required to compute the average spectral acceleration (AvgSA), which is the intensity measure against which the fragility curves are calibrated within the risk model. This intensity measure is ultimately the only measure of ground-shaking intensity that is relevant for the risk computations.

The prediction of expected amplitudes of response spectral ordinates at the NS_B horizon is defined in terms of the geometric mean of the horizontal components (these amplitudes are subsequently converted to an arbitrary horizontal component definition for the purposes of the risk calculations). Like in the V6 GMM, the predictions at the NS_B horizon for the V7 GMM are solely a function of local magnitude (M_L) and rupture distance (R_{rup}). As has been explained previously, in the range of magnitudes over which the GMM is applicable, M_L and moment magnitude, M , can be considered equivalent for the Groningen field (Dost *et al.*, 2018, 2019). However, the GMM is derived using M_L values, which is consistent with the use of local magnitudes in the derivation of the seismological model.

Both the functional form of the predictive equations and the logic-tree structure have changed from the V6 GMM, with three branches for inter-event variability and three branches for the site Amplification Functions added to the existing structure of four branches for the median predictions and two branches for the within-event variability,

which has been carried over from V6. The field zonation is unchanged from the V6 GMM, with the study area divided in 162 geological zones – each of which has its own amplification function defined for it.

This section summarises the basic elements of the V7 model as required for its implementation in hazard and risk calculations. The coefficients and additional values (such as the site amplification zonation) are included in supplementary CSV files identified in the text.

Equations for Median Motions at NS_B Rock Horizon

The equations for predicting the median ground-motion parameters at the NS_B rock horizon are a function of only magnitude (M_L) and distance (R_{rup}); hereafter, these are specified simply as M and R , the latter measured in km. At each period (T), the model can be represented at the NS_B horizon as comprising a source component (g_{src}) and a path component (g_{path}), the latter being a function of magnitude and distance:

$$\ln Y(\mathbf{M}, R_{rup}; T) = g_{src}(\mathbf{M}; T) + g_{path}(R_{rup}, \mathbf{M}; T) \quad (9.1)$$

where Y is $Sa(T)$ in cm/s^2 . The source-scaling term is defined by two quadratic functions that operate above and below a particular magnitude M_m (with $M_m = 4.75$), where the source term will equal $m_0(T)$:

$$g_{src}(\mathbf{M}; T) = \begin{cases} m_0(T) + m_1(T)(\mathbf{M} - M_m) + m_2(T)(\mathbf{M} - M_m)^2 & \text{for } \mathbf{M} < M_m \\ m_0(T) + m_3(T)(\mathbf{M} - M_m) + m_4(T)(\mathbf{M} - M_m)^2 & \text{for } \mathbf{M} \geq M_m \end{cases} \quad (9.2)$$

Similarly, the path terms are also segmented into ranges of rupture distance:

$$\begin{aligned} g_{path}(R_{rup}, \mathbf{M}; T) &= r_0(\mathbf{M}; T) \ln \left(\frac{\max[\min(R_{rup}, R_{h,1}), R_{h,0}]}{R_{h,0}} \right) \\ &+ r_1(\mathbf{M}; T) \ln \left(\frac{\max[\min(R_{rup}, R_{h,2}), R_{h,1}]}{R_{h,1}} \right) \\ &+ r_2(\mathbf{M}; T) \ln \left(\frac{\max[\min(R_{rup}, R_{h,3}), R_{h,2}]}{R_{h,2}} \right) \\ &+ r_3(\mathbf{M}; T) \ln \left[\frac{\max(R_{rup}, R_{h,3})}{R_{h,3}} \right] \end{aligned} \quad (9.3)$$

with the hinge distances are defined as $R_{h,0} = 3$ km, $R_{h,1} = 7$ km, $R_{h,2} = 12$ km, and $R_{h,3} = 25$ km. The slopes of these distance scaling segments (in $\ln Y - g_{path}$ space), r_0, r_1, r_2, r_3 , are functions of magnitude and period and are defined by the expressions in Equations 9.4 to 9.7 in which $M_r = 3.875$.

$$r_0(\mathbf{M}; T) = \begin{cases} r_{0,a}(T) + r_{0,b}(T)(\mathbf{M} - M_r) & \text{for } \mathbf{M} \leq M_r \\ r_{0,a}(T) + r_{0,c}(T) \tanh[r_{0,d}(\mathbf{M} - M_r)] & \text{for } \mathbf{M} > M_r \end{cases} \quad (9.4)$$

$$r_1(\mathbf{M}; T) = \begin{cases} r_{1,a}(T) + r_{1,b}(T)(\mathbf{M} - M_r) & \text{for } T \leq 0.2 \text{ s, and } \mathbf{M} \leq M_r \\ r_{1,a}(T) + r_{1,c}(T) \tanh[r_{1,d}(\mathbf{M} - M_r)] & \text{for } T \leq 0.2 \text{ s, and } \mathbf{M} > M_r \\ r_{1,a}(T) + r_{1,b}(T)(\mathbf{M} - M_r) & \text{for } T > 0.2 \text{ s} \end{cases} \quad (9.5)$$

$$r_2(\mathbf{M}; T) = \begin{cases} r_{2,a}(T) + r_{2,b}(T)(\mathbf{M} - M_r) & \text{for } T \leq 0.5 \text{ s, and } \mathbf{M} \leq M_r \\ r_{2,a}(T) + r_{2,c}(T) \tanh[r_{2,d}(\mathbf{M} - M_r)] & \text{for } T \leq 0.5 \text{ s, and } \mathbf{M} > M_r \\ r_{2,a}(T) + r_{2,b}(T)(\mathbf{M} - M_r) & \text{for } T > 0.5 \text{ s} \end{cases} \quad (9.6)$$

$$r_3(\mathbf{M}; T) = \begin{cases} r_{3,a}(T) + r_{3,b}(T)(\mathbf{M} - M_r) & \text{for } \mathbf{M} \leq M_r \\ r_{3,a}(T) + r_{3,c}(T) \tanh[r_{3,d}(\mathbf{M} - M_r)] & \text{for } \mathbf{M} > M_r \end{cases} \quad (9.7)$$

The logic-tree for the GMM predicting spectral accelerations at the NS_B horizon consists of a single node with four branches carrying models that are distinguished by the pairs of values for $\Delta\sigma$ and κ .

The weights assigned for magnitudes $M \leq 3.6$, which is the range of the data from the Groningen field, are symmetrical and reflect the assumption of an approximately normal distribution of logarithmic amplitudes and a well-constrained central model (the Central-upper and Central-lower branches are identical in this range, so the central model effectively has a weight of 0.6).

At larger magnitudes ($M \geq 5.0$), it is assumed that the earthquakes are triggered tectonic events that will rupture out of the gas reservoir down into the Carboniferous. Since the Upper branch is calibrated to mimic predictions from GMPEs for tectonic earthquakes, this branch should have a much higher weight in the larger magnitude range. At the same time, the weights should also reflect the fact that these triggered earthquakes, associated with ruptures initiating at ~ 3 km depth and propagating downwards, could be different from the typical tectonic earthquakes that generated the data used to derive the GMPEs deployed for the calibration of this branch. Over the transition from small to large magnitudes, the weight on the Upper branch is doubled, while the weight on the Lower branches is halved.

The branch weights at each magnitude are shown in Figure 9.1 and can be calculated using Eq. (9.8), whose coefficients are listed in Table 9.1 for each branch. The coefficients of equations (9.2) to (9.7) for the four individual models are presented in the file [gmpe_medians_NS_B_20211010_v7.csv](#).

$$w(M) = w_L + (w_H - w_L) \left(\frac{M - 3.6}{5.0 - 3.6} \right) \quad (9.8)$$

Table 9.1. Coefficients of Eq.(9.8).

| Model | w _L | w _H |
|-----------------|----------------|----------------|
| Upper | 0.2 | 0.4 |
| Central – upper | 0.3 | 0.3 |
| Central – lower | 0.3 | 0.2 |
| Lower | 0.2 | 0.1 |

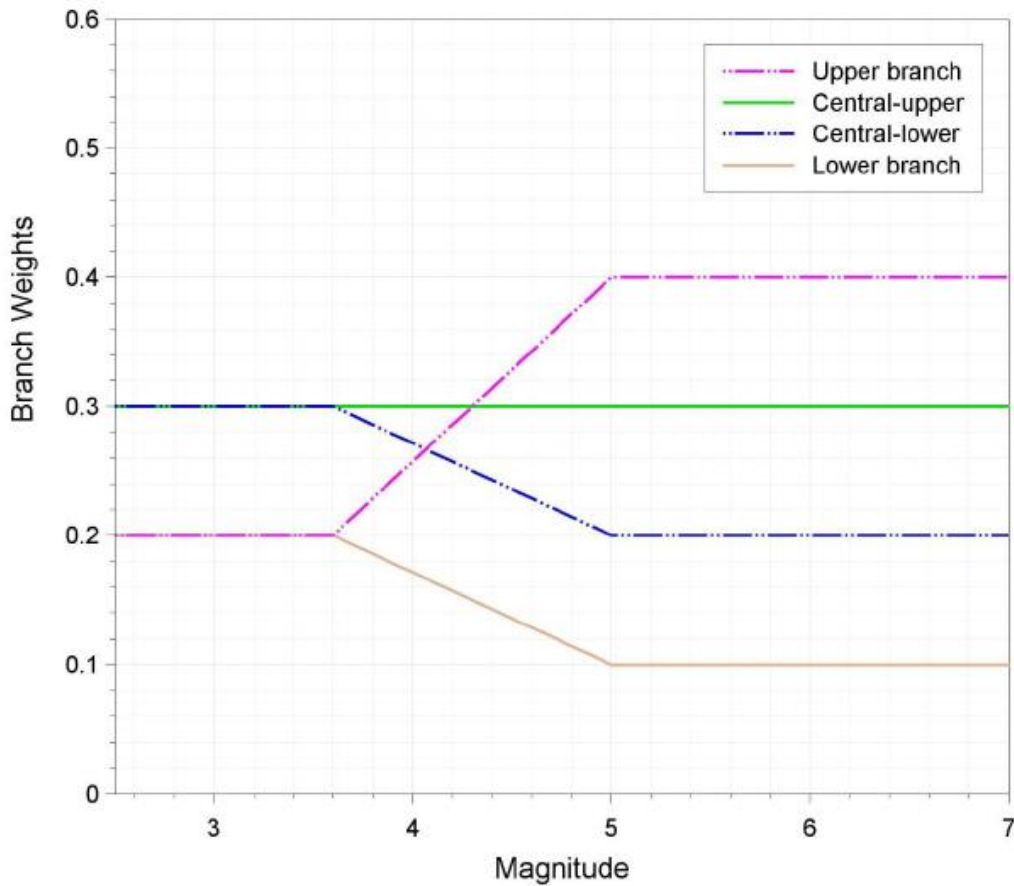


Figure 9.1 Weights on the four branches for median predictions at NS_B.

Sigma Model for NS_B Rock Horizon GMPEs

The sigma model representing the aleatory variability in the values of $\ln(Y)$ from Eq.(9.1) includes a between-earthquake component, τ , and a within-earthquake component, ϕ_{SS} . If Y_μ is the median value obtained from Equation 9.1, then two different quantities may be predicted by sampling from the components of variability: Y_{GM} , the geometric mean component (to be used for hazard mapping and shown in Eq.9.9a), and Y_{arb} , the arbitrary component (to be used in risk calculations and defined in Eq.9.9b):

$$\ln(Y_{GM}) = \ln(Y_\mu) + \varepsilon_E \tau + \varepsilon_S \phi_{SS} \quad (9.9a)$$

$$\ln(Y_{arb}) = \ln(Y_{\mu}) + \varepsilon_E \tau + \varepsilon_S \phi_{SS} + \varepsilon_C \sigma_{C2C} \quad (9.9b)$$

In Eq.(9.9b), σ_{C2C} is the component-to-component variability. The differences between $\ln Y_{GM}$ and $\ln Y_{arb}$ and the mean $\ln Y_{\mu}$ are represented by different residuals (or deviations) associated with the components of variability mentioned previously. Each of these deviations is represented as the product of an ε value and the standard deviation for that component of variability. Therefore, the actual deviations are characterised by the product of ε values (which are standard normal variates) and the standard deviations from each variability component. These deviations are all assumed to arise as samples from zero-centred normal distributions.

The component-to-component variability model has not changed from the V5 model and includes dependence on both magnitude and distance. The component-to-component variance is defined by the following equations for the value at different periods, T:

$$\sigma_{c2c}^2(M, R) = 0.026 + 1.03[5.6 - \min(5.6, \max[M, 3.6])]R^{-2.22} \quad T \leq 0.1s \quad (9.10a)$$

$$\sigma_{c2c}^2(M, R) = 0.045 + 5.315[5.6 - \min(5.6, \max[M, 3.6])]R^{-2.92} \quad T \geq 0.85s \quad (9.10b)$$

For periods in between 0.1 and 0.85 seconds, the following interpolation is used:

$$\sigma_{c2c}^2(T, M, R) = \sigma_{c2c}^2(0.1, R) + \left[\frac{\log(T) - \log(0.1)}{\log(0.85) - \log(0.1)} \right] [\sigma_{c2c}^2(0.85, R) - \sigma_{c2c}^2(0.1, R)] \quad (9.11)$$

There are three branches of period-independent values for the between-event standard deviation, τ , and two equally-weighted branches for the within-event standard deviation, ϕ_{SS} . The values of the within-event standard deviation are identical to those used in the V6 model. The complete logic-tree for motions at the NS_B horizon is illustrated in Figure 9.2.

The values of the sigma components are presented in the electronic comma-separated variables file: [gmpe_sigmas_NS_B_20211010_v7.csv](#).

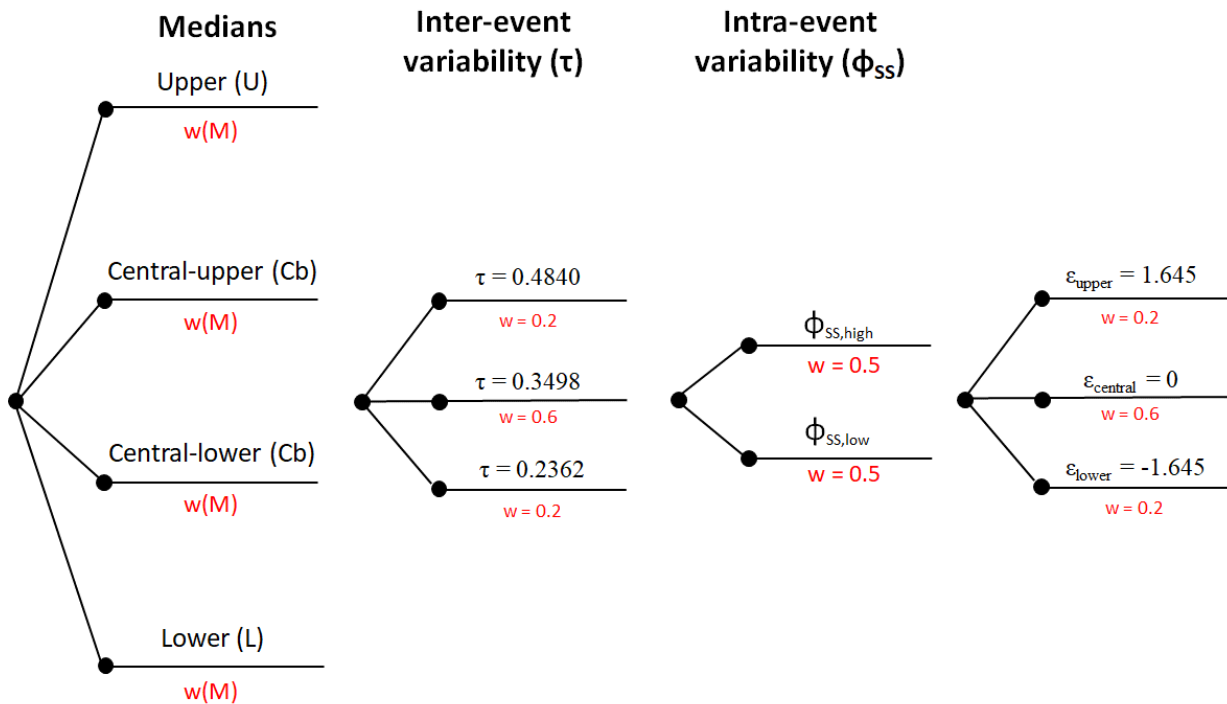


Figure 9.2. Logic-tree structure for model for motions at the NS_B horizon

Field Zonation

The study area is divided into **162** zones (Figure 9.3), with each zone having its own AFs for translating levels of $S_a(T)$ at NS_B to the surface. The zones are defined by a numerical code; the zones and their geographical limits are identical to those defined for the V4 and V5 models, except four zones which have resulted from the division of two previous zones, a change made for the V6 GMM.

A list of 140,862 voxel squares of 100 x 100 m—each identified by the RD coordinates of their centre—and the zone to which each voxel is identified is provided in the following file: [gmpeSurfaceZonation_20211010_v7.csv](#).

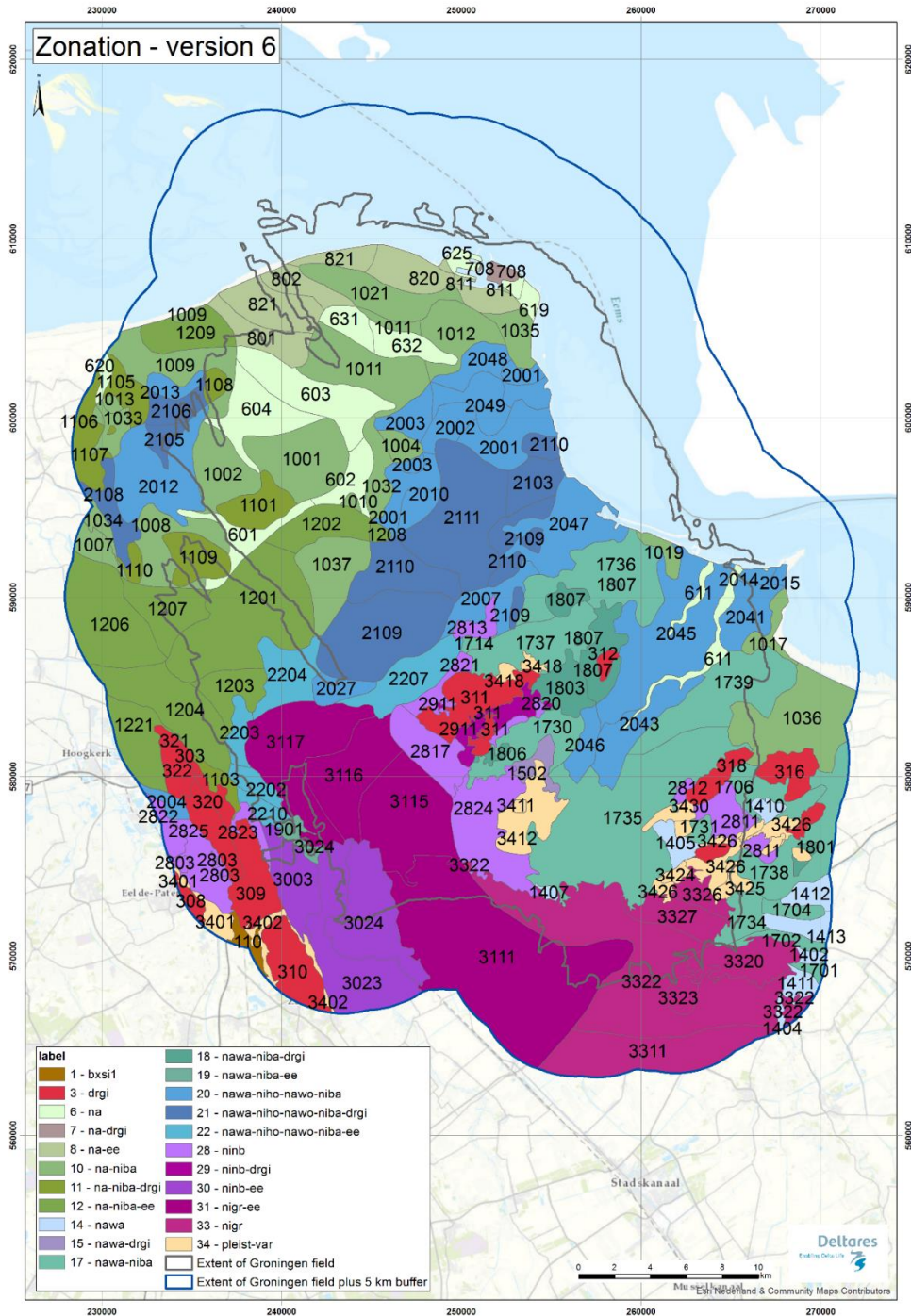


Figure 9.3. V6 zonation of the Groningen field for site AFs

Median Non-Linear Soil Amplification Factors

For each of the 162 zones and each ground-motion parameter [spectral acceleration, $Sa(T)$, at 10 periods], the amplification factors, AF, are defined as follows:

$$\ln[AF(Sa)] = f_1^* + f_2 \ln\left(\frac{Sa_{NS_B,g} + f_3}{f_3}\right) \quad (9.12)$$

In Eq.(9.12), $Sa_{NS_B,g}$ is $Sa(T)$ at the NS_B horizon, expressed in units of g (981 cm/s²). This general formulation is unchanged from previous models.

The first term on the right-hand side of Eq.(9.12), f_1^* , is the exponent of the linear part of the AFs. The term is magnitude- and distance-dependent and this dependence is defined by the following equation:

$$f_1^* = [a_0 + a_1 \ln(R)] + [b_0 + b_1 \ln(R)][\min(M, M_{ref1}) - M_{ref1}] + a_2[\ln(R) - \ln(R_{ref})]^2 + b_2[\min(M, M_{ref1}) - M_{ref1}]^2 + a_3[\max(M, M_{ref1}) - M_{ref1}] \quad (9.13)$$

where M_{ref} is given by:

$$M_{ref1} = \begin{cases} M_a & \text{for } R < 3km \\ M_a + \frac{\ln(R) - \ln(3)}{\ln(60) - \ln(3)} (M_b - M_a) & \text{for } 3km \leq R \leq 60km \\ M_b & \text{for } R > 60km \end{cases} \quad (9.14)$$

and M_a and M_b are model parameters.

The model parameters f_2 , f_3 , a_0 , a_1 , a_2 , a_3 , b_0 , b_1 , b_2 , M_a and M_b are given for all periods and all zones (except zones 2813 and 3411 which are entirely covered by water) in the file [gmpeSurfaceAmplificationModel_20211010_v7.csv](#). In addition, the values of AF in Eq.(9.12) are subject to upper and lower limits of AF_{max} and AF_{min} , which are also included in the same file. It should be noted that the model for AF is only applicable for $2.6 \leq M \leq 7.5$ and $3km \leq R \leq 60km$.

The alternative branches of the site amplification logic-tree are constructed using the variability in the site AFs as given by the standard deviation ϕ_{S2S} , which is defined as a tri-linear function as defined in the following equations (and illustrated in Figure 9.4). The site-to-site standard deviation model, ϕ_{S2S} , is given by:

$$\phi_{S2S} = \begin{cases} s_1 & \text{for } Sa_{NSB,g} < x_l \\ s_1 + (s_2 - s_1) \frac{\ln(Sa_{NSB,g}) - \ln(x_l)}{\ln(x_h) - \ln(x_l)} & \text{for } x_l \leq Sa_{NSB,g} \leq x_h \\ s_2 & \text{for } Sa_{NSB,g} > x_h \end{cases} \quad (9.15)$$

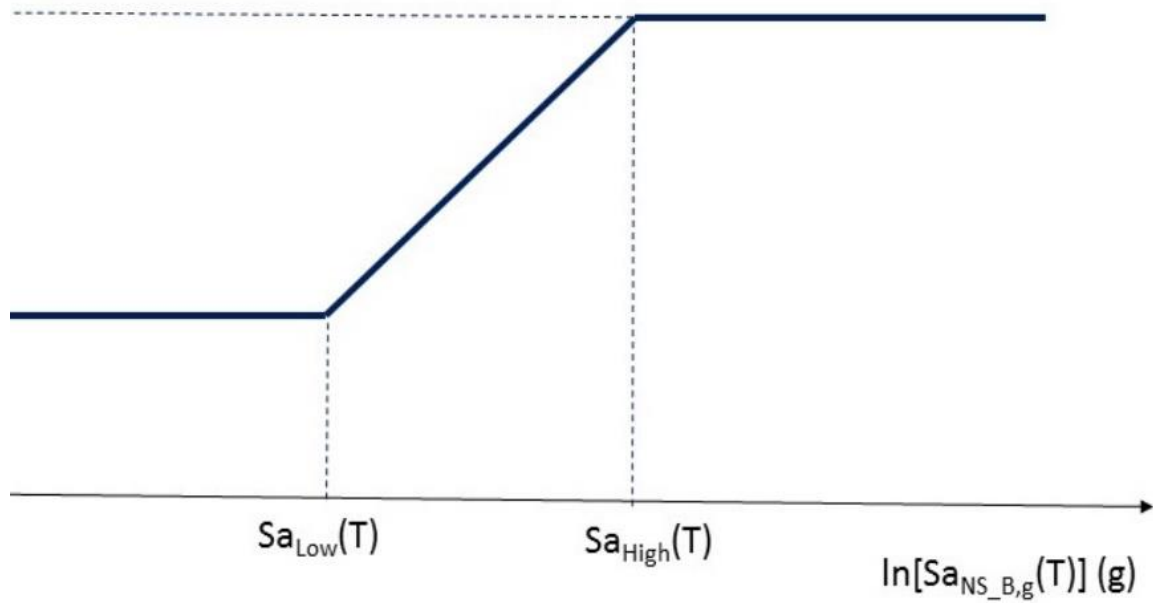


Figure 9.4. Schematic illustration of the site-to-site variability model. The values on the x-axis is the $Sa(T)$ at the NS_B, expressed in units of g . In either case, the value is obtained by application of Eqs.(9.1) to (9.7)

The four parameters defining the site-to-site variability model for $Sa(T)$ at all 10 periods in each of the 162 site amplification zones are listed in the electronic supplement file [gmpeSurfaceAmplificationModel_20211010_v7.csv](#). Three branches of AFs are defined, built from the assumption of a lognormal distribution of amplification functions. The AF of branch i is given by Eq.(9.16):

$$\ln(AF_i) = \ln(AF) + \varepsilon_i \phi_{S2S} \quad (9.16)$$

and has a weight of w_i associated with it. The values of the branch weights w_i and the deviation from the mean $\ln(AF)$, $\varepsilon_i \phi_{S2S}$ (defined in terms of ε_i) are given in Table 9.2; the format of the logic-tree is illustrated in Figure 9.5.

Table 9.2. Branches, weights, and coefficients of Eq.(9.16).

| Branch, i | Weight, w_i | ε_i |
|-------------|---------------|-----------------|
| Upper | 0.2 | 1.645 |
| Central | 0.6 | 0 |
| Lower | 0.2 | -1.645 |

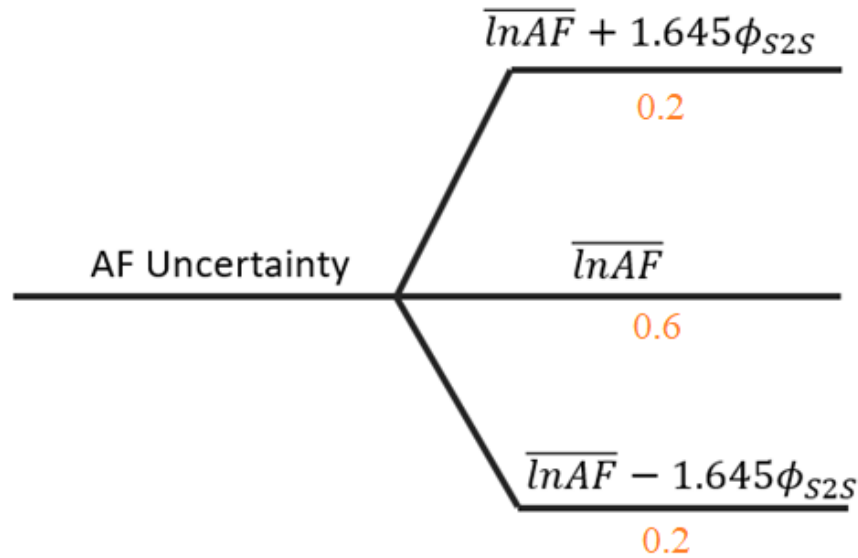


Figure 9.5. Logic tree for the Amplification Factors. The mean values for AF ($\overline{\ln AF}$) are obtained from Eqs. (9.12) to (9.14), and the uncertainty (ϕ_{S2S}) is obtained from Eq. (9.16).

The values of ε_i are used across all 10 periods simultaneously. Therefore, the logic tree for the amplification functions shown in Figure 9.5 depicts an expected level of amplification on the central branch (where the amplification itself is period dependent), and then deviations away from this expected amplification. These deviations shift the overall level of amplification up or down across all periods. The actual extent of the shift varies with period, as the values of ϕ_{S2S} are period-dependent, but the ε_i values are treated as independent of period.

Period-to-Period Correlation of Residuals of Sa(T)

For the risk calculations, values of Sa(T) calculated at a given location for different periods, T, must account for the period-to-period correlations of the residuals. The correlation coefficients necessary for specifying this period-to-period correlation are provided in the CSV file: [gmpe_period2period_correlations_20211010_v7.csv](#).

Summary List of Electronic Supplements

1. gmpe_medians_NS_B_20211010_v7.csv
2. gmpe_sigmas_NS_B_20211010_v7.csv
3. gmpeSurfaceZonation_20211010_v7.csv
4. gmpeSurfaceAmplificationModel_20211010_v7.csv
5. gmpe_period2period_correlations_20211010_v7.csv

9.2. Sampling of Variance Components

The prediction of the median values of SA is relatively straightforward, simply applying the relevant values of M and R for each earthquake-site combination, and then applying the relevant AF depending on the zone within which the site is located. However, the models predict distributions of values rather than unique estimates of SA. In all cases, the intensity measures, $S_a(T)$, are log-normally distributed and their joint distribution is assumed to be multivariate log-normal (which leads to lognormality of the AvgSA). For both model development and sampling it is convenient to work with the log-transformed intensity measures such that variation about the median motion for a given scenario is defined by a symmetric normal distribution (or multivariate normal). The scale of the variation in this transformed space is defined by a standard deviation. The total standard deviation in ground-motion prediction models is usually represented by the symbol σ and the total residuals are then defined by the product of σ and a standard normal variate ϵ , the number of standard deviations that a particular level of an intensity measure lies away from the mean.

The purpose of this section is to define the procedures for sampling the aleatory variability in the prediction of the ground-motion parameters. The NAM hazard and risk model for the Groningen field uses Monte Carlo simulations and therefore the focus herein is on the random sampling of ϵ values in each ground-motion realisation; the steps outlined below also assume a MC implementation and clearly some adaptation would be needed for other approaches to the hazard and risk calculations. The process is schematically illustrated in Figure 9.6, which depicts the estimation of $S_a(T)$ for a single value of T at three locations (over two zones) as a result of a single earthquake.

In practice, however, the implementation is somewhat more complicated because the sampling of variance components must also respect correlations between parameters. In the following, the first sub-section defines the different components of variability. After that, the sampling is discussed for different applications of increasing complexity with regards to the variability.

The V7 GMM is intended for the calculation of seismic hazard across the Groningen field, in terms of response spectral accelerations at 10 oscillator periods, and also for field-wide risk analyses in terms of Local Personal Risk (LPR). Previous GMMs have provided guidelines for approximating the effects of spatial correlation of ground motions, which is important when calculating aggregated measures of seismic risk. However, for a risk metric such as LPR, which is calculated independently for each building in the exposure database, spatial correlation is not required. The guidelines below discuss how spatial correlation could be included in the risk modelling, in an approximate manner, but no specific recommendations are made in this regard.

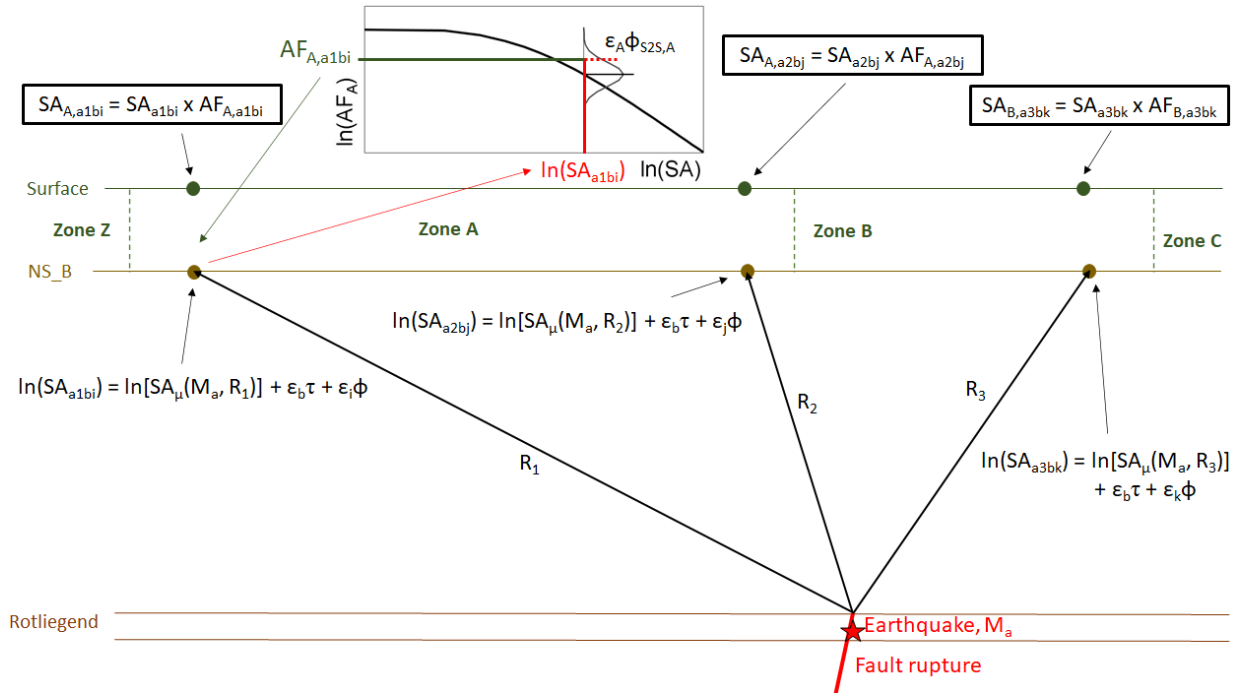


Figure 9.6. Schematic illustration of the calculation of SA at three surface points, in two zones, for an earthquake of magnitude M_a and an event-term of $\epsilon_b\tau$; in this simple example, the within-event variability is sampled without considering spatial correlation.

Components of Variability in the Groningen GMM

The components of variability defined in the Groningen GMM are listed in Table 9.3, indicating also which ground-motion parameters they are related to and where they are applied both in terms of a reference horizon and in the calculation of hazard or risk.

The total variability on the geometric mean ground-motion amplitudes is given by:

$$\sigma_{GM} = \sqrt{\tau^2 + \phi_{SS}^2} \quad (9.17)$$

whereas the total variability of the arbitrary component of motion is given by:

$$\sigma_{arb} = \sqrt{\tau^2 + \phi_{SS}^2 + \sigma_{c2c}^2} \quad (9.18)$$

One correlation model is defined for inter-period correlations, and its characteristics are summarised in Table 9.4. This correlation model is used to construct the full correlation matrix that is required for the sampling process within the risk calculations.

Table 9.3. Elements of ground-motion variability in the Groningen GMM

| Symbol | Description | Horizon ¹ | H or R ² | Epsilon ³ |
|----------------|---|----------------------|---------------------|----------------------|
| σ_{GM} | Standard deviation of geometric mean of ground-motion parameters | NS_B | Hazard | ε_{GM} |
| σ_{arb} | Standard deviation of arbitrary component of ground-motion parameters | NS_B | Risk | ε_{arb} |
| τ | Between-event standard deviation of ground-motion parameters | NS_B | H & R | ε_E |
| ϕ_{SS} | Within-event non-ergodic standard deviation of amplitude-based parameters | NS_B | H & R | ε_S |
| σ_{c2c} | Component-to-component variability of spectral accelerations | NS_B | Risk | ε_c |

Notes: 1 – Reference elevation at which applied; 2 – Whether used in hazard or risk calculations; 3 – Symbol for normalised residual used to sample distribution.

Table 9.4. Correlations of residuals in the Groningen GMM

| Symbol | Description | GM Parameter ¹ | Horizon ² |
|--------------|--|---------------------------|----------------------|
| ρ_{T2T} | Period-to-period correlation of spectral accelerations | Sa at multiple T | NS_B |

Notes: 1 – The ground-motion parameters to which it applies; 2 – Reference elevation where implemented.

Sampling Variability in Hazard Calculations for SA(T)

When hazard maps are generated in terms of spectral accelerations at the 10 response periods, they are treated completely independently; we assume that hazard will not be calculated in terms of AvgSa (it is were a required hazard output, then period-to-period correlation would need to be considered in the calculations). The uniform hazard response spectra (UHRS) at specified locations are obtained from individual location-specific hazard curves for Sa at the 10 response periods. The hazard is calculated at grid points defined across the field, usually with several grid points located within each site response zone.

The sequence of sampling of variability to be followed in generating the hazard estimates is therefore as follows:

1. For each earthquake and ground-motion parameter, a value of ε_E is randomly sampled. This value of ε_E is used for all grid points.
2. For each grid point, the NS_B motion is calculated randomly sampling ε_S and adding the resulting deviation ($\varepsilon_S\phi_{SS}$) to the event-specific deviation from step #1 ($\varepsilon_E\tau$). The NS_B amplitude is therefore $\ln Sa_{NS-B} + \varepsilon_E\tau + \varepsilon_S\phi_{SS}$.

3. For each grid point, the surface motion is estimated by applying the AF value conditioned on the realisation of the NS_B motion (including the two components of variability sampled in steps #1 and #2).

Sampling Variability in Ground-motion Values for Risk Calculations

When ground motions at the surface are predicted for the purpose of providing inputs to risk calculations, a number of differences arise when compared to the same predictions within the hazard calculations. One of these is that the component-to-component variability needs to be added in order to obtain estimates of the arbitrary component of motion rather than the geometric mean. And, since the fragility calculations make use of the AvgSa intensity measure, the period-to-period correlations of $\ln Sa(T)$ also need to be sampled. The sampling sequence now becomes as follows:

1. For each earthquake, a sample is generated from the between-event correlation matrix in order to obtain a vector ε_E that contains between-event epsilon values for all n spectral ordinates. This $n \times 1$ vector can be expressed mathematically as $\varepsilon_E = \{\varepsilon_E(T_1), \varepsilon_E(T_2), \dots, \varepsilon_E(T_n)\}$. The correlation matrix can be defined as:

$$\boldsymbol{\rho} = [\boldsymbol{\rho}_{\ln Sa(T), \ln Sa(T)}] = \begin{bmatrix} \rho_{\ln Sa(T_1), \ln Sa(T_1)} & \rho_{\ln Sa(T_1), \ln Sa(T_2)} & \dots & \rho_{\ln Sa(T_1), \ln Sa(T_n)} \\ \rho_{\ln Sa(T_2), \ln Sa(T_1)} & \rho_{\ln Sa(T_2), \ln Sa(T_2)} & \dots & \rho_{\ln Sa(T_2), \ln Sa(T_n)} \\ \vdots & \vdots & \ddots & \vdots \\ \rho_{\ln Sa(T_n), \ln Sa(T_1)} & \rho_{\ln Sa(T_n), \ln Sa(T_2)} & \dots & \rho_{\ln Sa(T_n), \ln Sa(T_n)} \end{bmatrix} \quad (9.19)$$

2. For each zone, the NS_B motion for the arbitrary component needs to reflect both the variability suggested by ϕ_{SS} as well as the component-to-component variability associated with σ_{c2c} . Rather than sample separate sets of epsilon values for each of these components individually, a vector of epsilon values $\varepsilon_A = \{\varepsilon_A(T_1), \varepsilon_A(T_2), \dots, \varepsilon_A(T_n)\}$ is generated. For each spectral ordinate, the residual of the arbitrary component is given by $\varepsilon_A \sqrt{\phi_{SS}^2 + \sigma_{c2c}^2} \equiv \varepsilon_S \phi_{SS} + \varepsilon_C \sigma_{c2c}$. That is, the covariance matrix from which ε_A is ultimately obtained has diagonal elements that are defined by $\phi_{SS}^2(T) + \sigma_{c2c}^2(T)$ (for all spectral ordinates). The off-diagonal elements of the covariance matrix make use of the same correlation matrix elements as used for the sampling of the between-event residuals.
3. For each grid point, the surface motion is estimated by applying the AF(T) value conditioned on the realisation of the NS_B motion (including the two components of variability ε_E and ε_A sampled in steps #1 and #2). The same AF branch is used across all periods in a given site zone.

Spatial Correlation of Ground Motions

The sampling procedure defined in the previous section includes period-to-period correlation among the spectral ordinates – which is necessary for the appropriate calculation of AvgSa and its variability. This correlation must be considered even when dealing with a single building type at a single location given that fragility curves are defined in terms of AvgSa.

For the calculation of Individual Local Personal Risk (ILPR), the procedures of the preceding sections are sufficient. However, for the calculation of Group Risk or any other aggregate measure of the seismic risk, the spatial correlation of ground motions should additionally be considered. Incorporation of spatial correlation in such applications is important since it leads to pockets of higher-than-average and lower-than-average ground motions rather than simply random spatial variation of the amplitudes. The coincidence of a pocket of higher-than-average ground motions with a group of seismically vulnerable structures will result in higher estimates of Group Risk than when spatial correlation of the ground motions is ignored. Although the primary focus of the risk modelling is Individual Local Personal Risk (ILPR, which is a location-specific measure), Group Risk estimates may be needed and for this reason the current section outlines options for accounting for spatial correlation in an approximate manner.

The reasons why the options below can only be regarded as approximate is that the components necessary to undertake a more precise treatment of spatial correlation are not currently available for the Groningen field. In particular, a complete treatment of this problem would consider the systematic spatial correlation of site amplification factors within a zone (as well as between zones). This information simply cannot be retrieved from the 1D site response calculations that have been used to derive the AFs.

With model components currently available, the effects of spatial correlation can be reasonably approximated by assuming that within-event variates within a given site zone are perfectly correlated and also using the same site amplification branch across all locations within a site zone simultaneously. Stafford *et al.* (2019) showed that this approach will over-estimate more realistic levels of correlation over very short spatial distances and will under-estimate more realistic levels over longer spatial distances. The degree of over- or under-estimation varies over the field as it depends upon the size of the spatial zone. Between site zones, no spatial correlation is considered.

Note that perfect correlation of within-event variates does not mean that the same level of ground-motion is applied to the AFs at all grid points within a zone. The NS_B motion at each grid point will still vary spatially to capture differences in source-to-site distance. As the mean NS_B motions, the AFs and σ_{c2c} all depend on M and R, and the value of R will vary for different grid points within a zone, the actual ground-motion

amplitudes over the zone will vary spatially, despite the correlation of the within-event residuals being perfect.

In terms of explicit modifications to the sampling procedure outlined in the previous section, the only change to accommodate these approximate spatial correlations is within Step 2 of the risk sampling where the sampled values of ε_A are used at all grid points within a zone. Additionally, and as noted previously, the same AF branch is used for all grid points within a zone, but those branches should vary from zone to zone for any individual ground-motion field.

An alternative, but more elaborate, approach to consider spatial correlation is to impose a spatial correlation structure upon the NS_B amplitudes directly. The study of Stafford *et al.* (2019) presented estimates of the spatial correlation length as a function of period and compared those to the unclustered model of Jayaram & Baker (2009). As discussed by Stafford (2021), the approach adopted in Stafford *et al.* (2019) does not explicitly consider the within-zone spatial correlation as distinct from spatial correlations that may exist at the NS_B level. However, to first order, a typical correlation length on the order of 5 km (in the context of a homogeneous isotropic exponential correlation model) provides a reasonable approximation to the spatial correlations observed over the Groningen field.

To implement this alternative approach, the covariance matrices considered previously for the period-to-period correlations need to be expanded very significantly to also include the appropriate inter-period and inter-position correlations. These mixed correlations of spectral ordinates at different periods and locations can be computed using the Markovian approximation specified in Stafford (2021). The within-event residuals are then obtained by sampling a vector $\varepsilon(x, \mathbf{T})$, where x denote spatial locations, and \mathbf{T} is the period vector. Under this approach, the motions at NS_B would have an appropriate spatial correlation structure and those motions are then passed through the zone-specific AFs. Note that the AF branch would still be held constant across a zone. This would lead to a degree of overestimation of the spatial correlation within a zone. However, the alternative of allowing different AF branches at different grid points within a zone (potentially with some assumed degree of correlation of these epistemic branches) would have an extremely severe computational cost.

It is again worth emphasizing that neither of these proposals for incorporating spatial correlations are ideal, and the degree of over- or under-estimation of the spatial correlation is both zone-dependent and very difficult to quantify.

9.3. Including *Wierden* in Seismic Risk Calculations

For hazard calculations, the target horizon is the natural ground surface and in generating hazard maps the presence of *wierden* is ignored. For risk calculations, the

effect of the *wierden* is included. The exposure database file is a simple table listing building ID codes and their X-Y coordinates in the RD system. A fourth column is now included in the table with a flag that takes a value of 1 if the building is located on a *wierde* (2,862 buildings) or 0 otherwise (155,094). For the buildings located on *wierde*, the amplification factor for $AF_{\text{building on wierden}}$ is given by:

$$\ln(AF_{\text{building on wierde}}) = \ln(AF_{GMM \text{ zone}}) + \text{Penalty Factor} \quad (9.20)$$

with the Penalty Factor in *ln* units. The Penalty Factor is tabulated for the hinge point periods in Table 9.5. For periods between the hinge points, the Penalty factor can be obtained using log-linear interpolation.

Table 9.5. Penalty Factor (in *ln* units) at hinge point periods.

| Period (s) | Penalty Factor (<i>ln</i> units) |
|-------------------|---|
| 0.01 | 0.20 |
| 0.1 | 0.25 |
| 0.2 | 0.35 |
| 0.5 | 0.35 |
| 1.0 | 0.10 |

10. V7 GMM Performance

In this chapter, the performance of the V7 GMM is assessed through residual analyses using different datasets of ground-motion recordings. The predictions from the V7 model are also compared with those from the V6 GMM and from ground-motion models developed for tectonic earthquakes. The range of epistemic uncertainty captured by the V7 GMM is evaluated by comparison of the branch-to-branch variability with the model-to-model variability of the NGA-West2 models.

10.1. Residuals of Recorded Motions with respect to V7 GMM

Figures 10.1 to 10.10 display residuals of the spectral accelerations of the V7 database (described in Section 3) with respect to the median surface predictions of the central-lower model (which in the range of the data is identical to central-upper model). In Figure 10.1, which corresponds to the period of 0.01s, the residuals shown are on average positive, which indicates an underestimation of the recorded spectral accelerations by the model. This apparent underestimation varies with distance, being more prominent in rupture distances < 6 km and less so at longer distances.

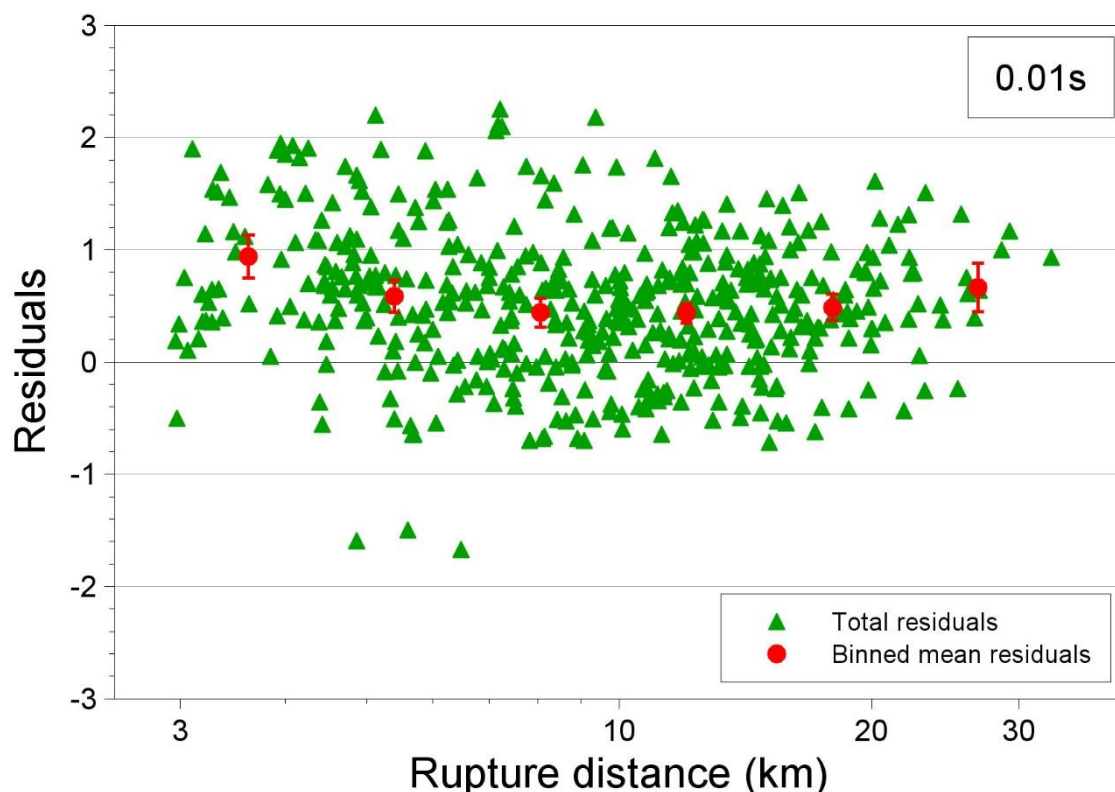


Figure 10.1. Total residuals of the spectral accelerations of the V7 database with respect to the median surface predictions of the central-lower model for the period of 0.01s; the red dots are bin means and the bars their associated 90 percentile confidence intervals.

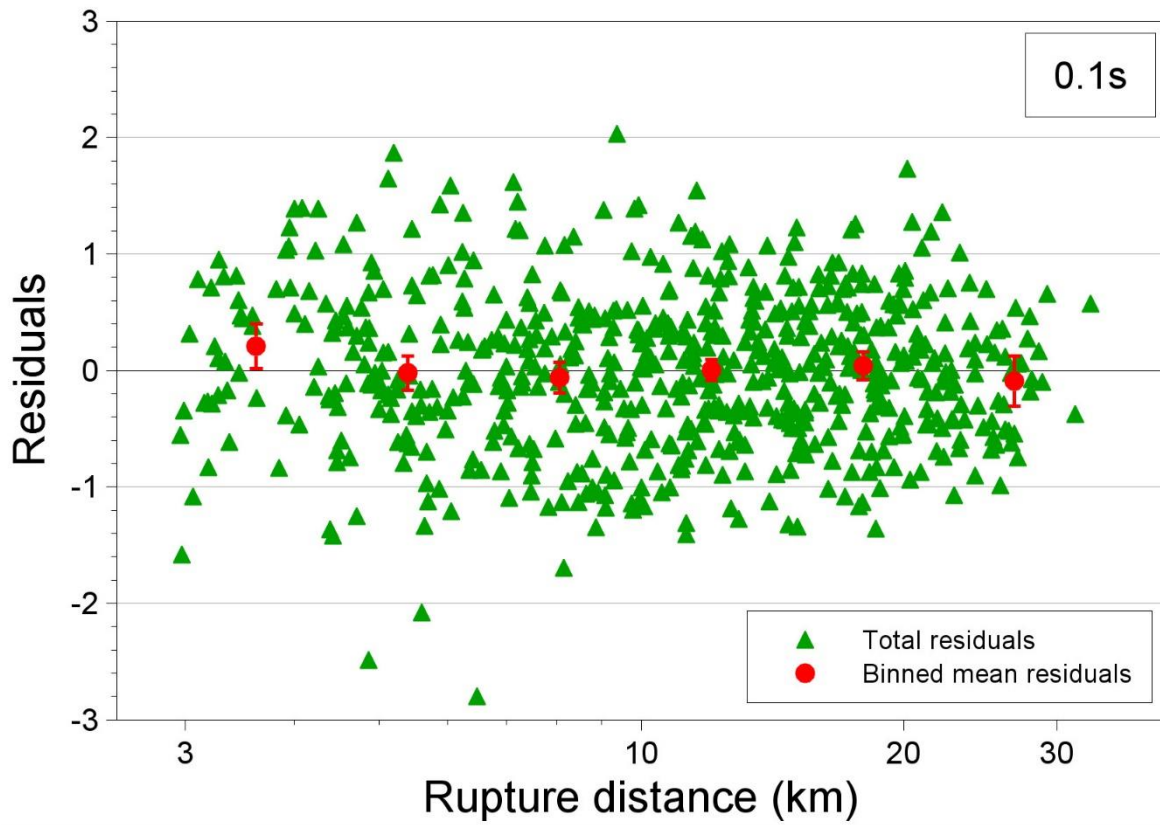


Figure 10.2. Same as Figure 10.1 but for the period of 0.1 s.

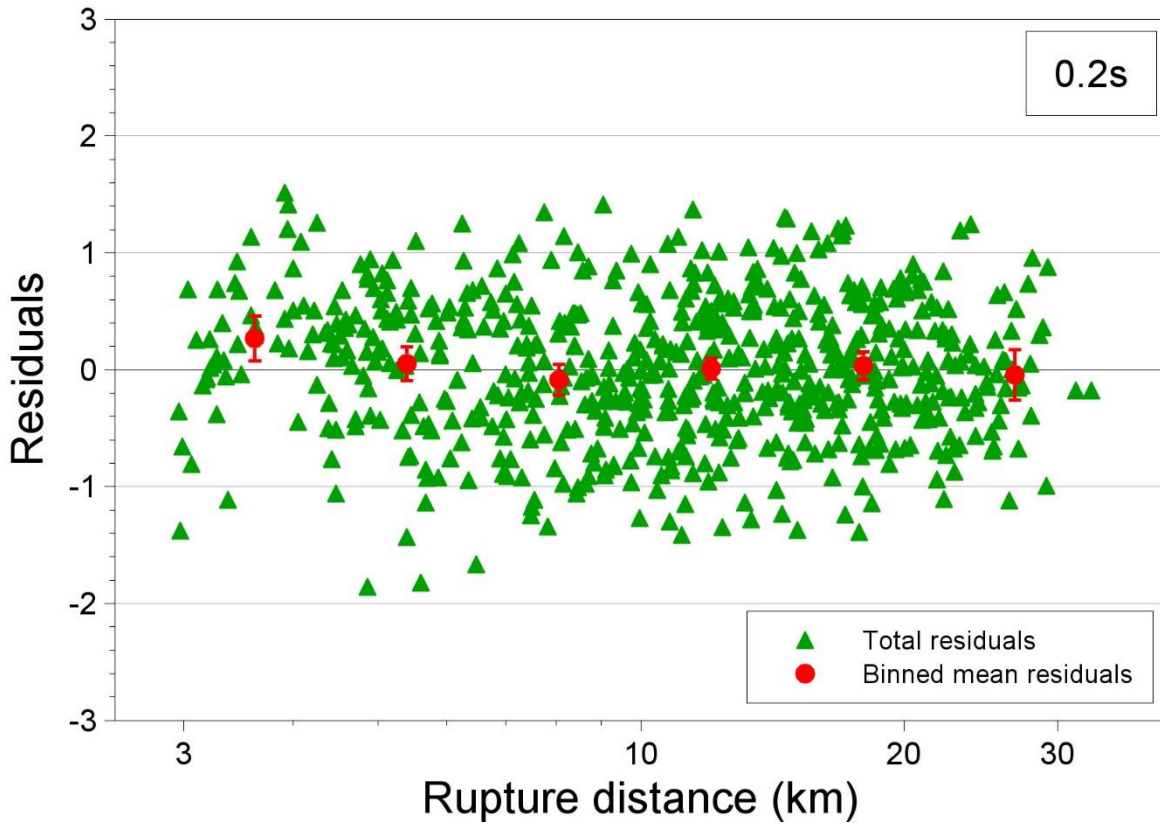


Figure 10.3. Same as Figure 10.1 but for the period of 0.2 s.

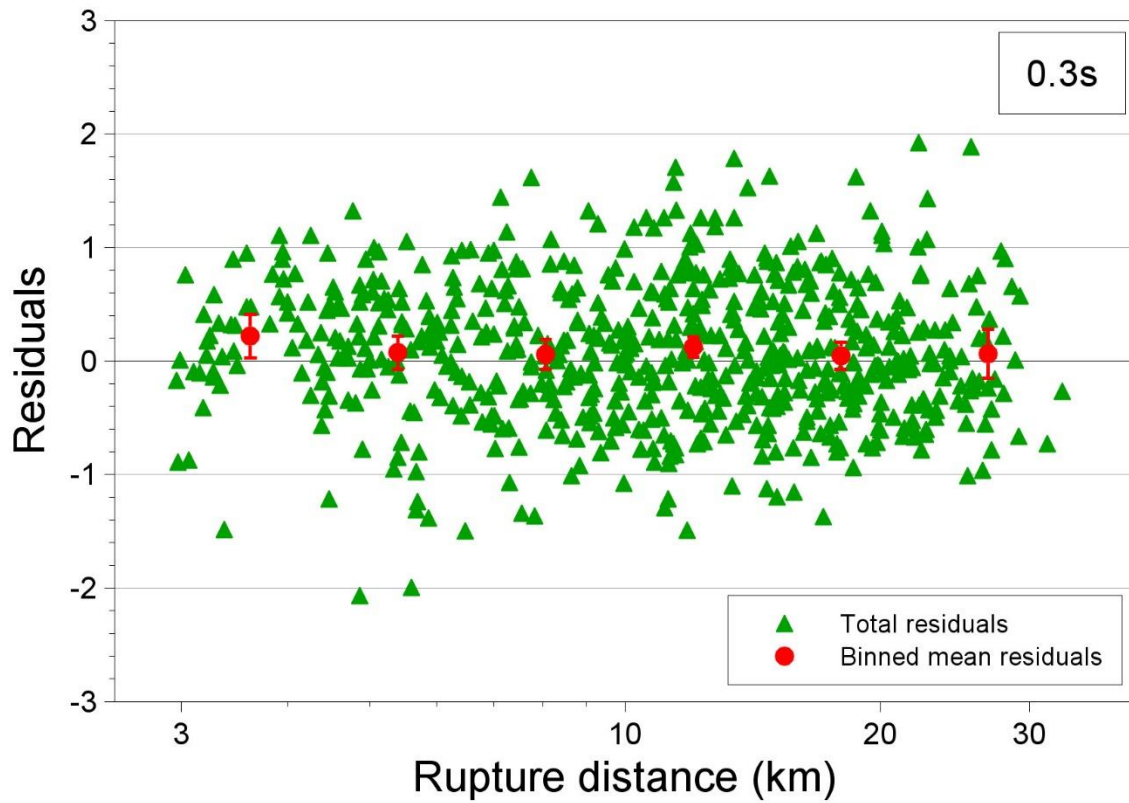


Figure 10.4. Same as Figure 10.1 but for the period of 0.3 s.

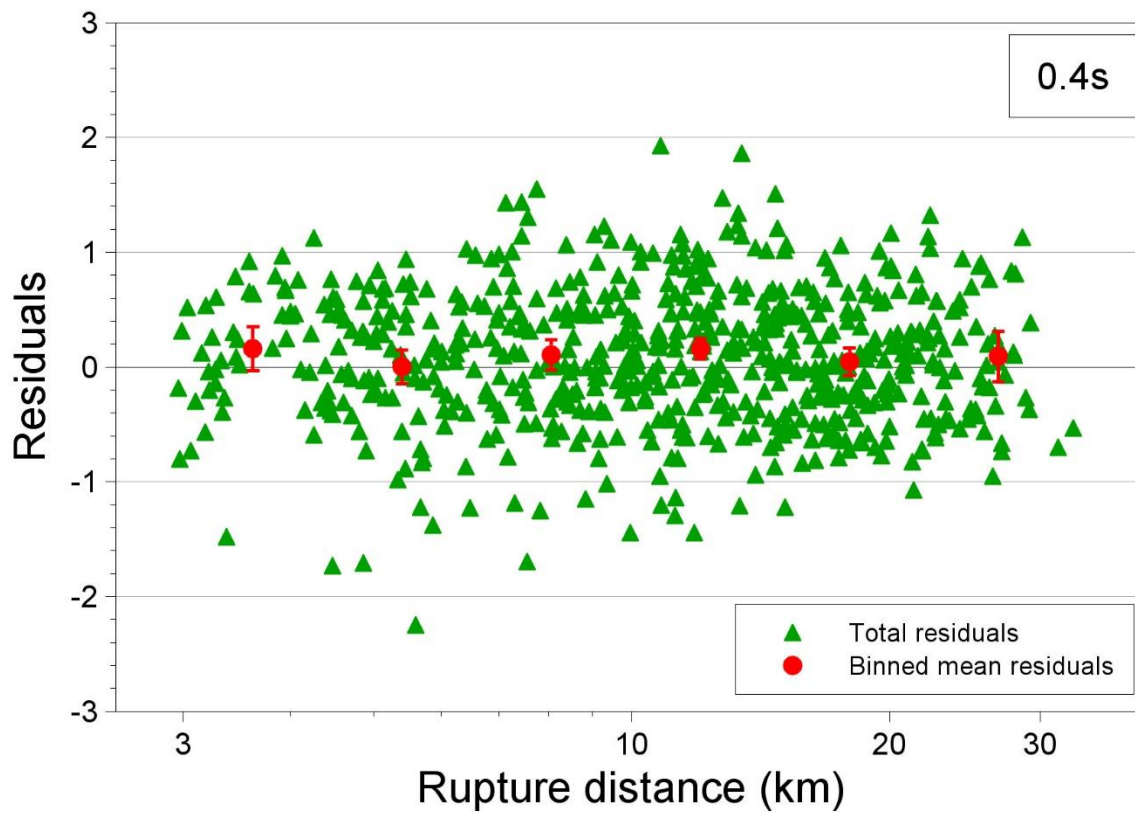


Figure 10.5. Same as Figure 10.1 but for the period of 0.4 s.

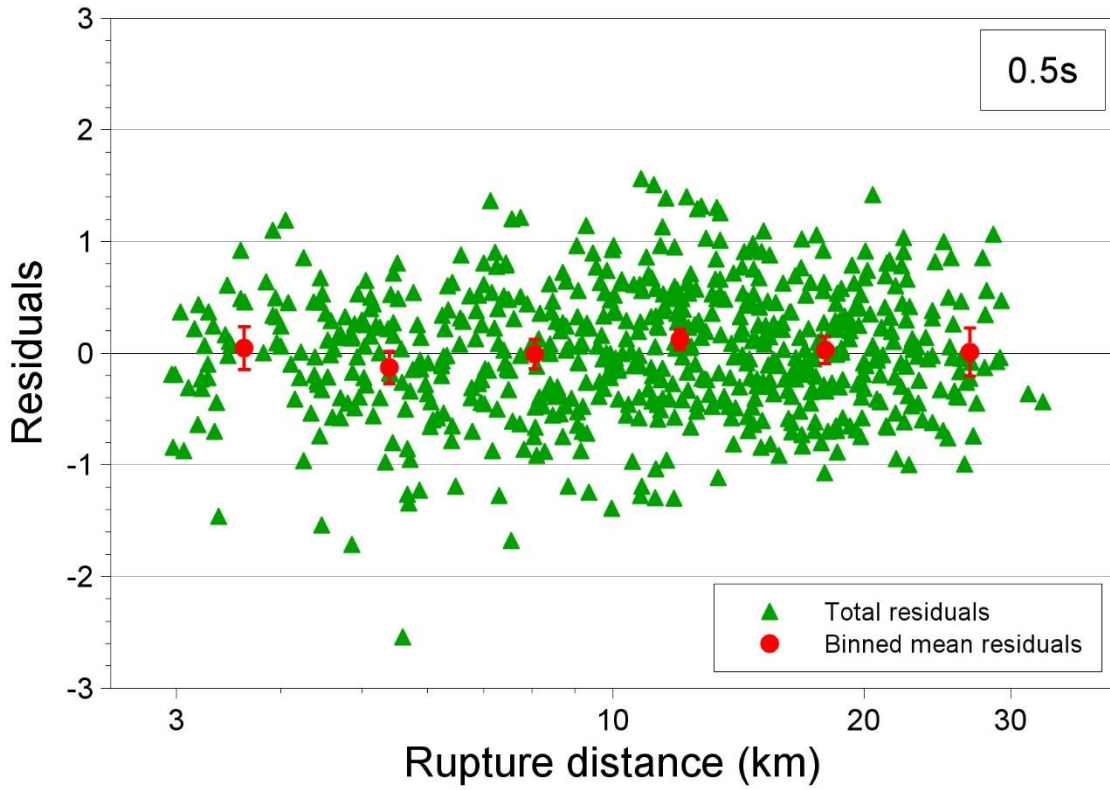


Figure 10.6. Same as Figure 10.1 but for the period of 0.5 s.

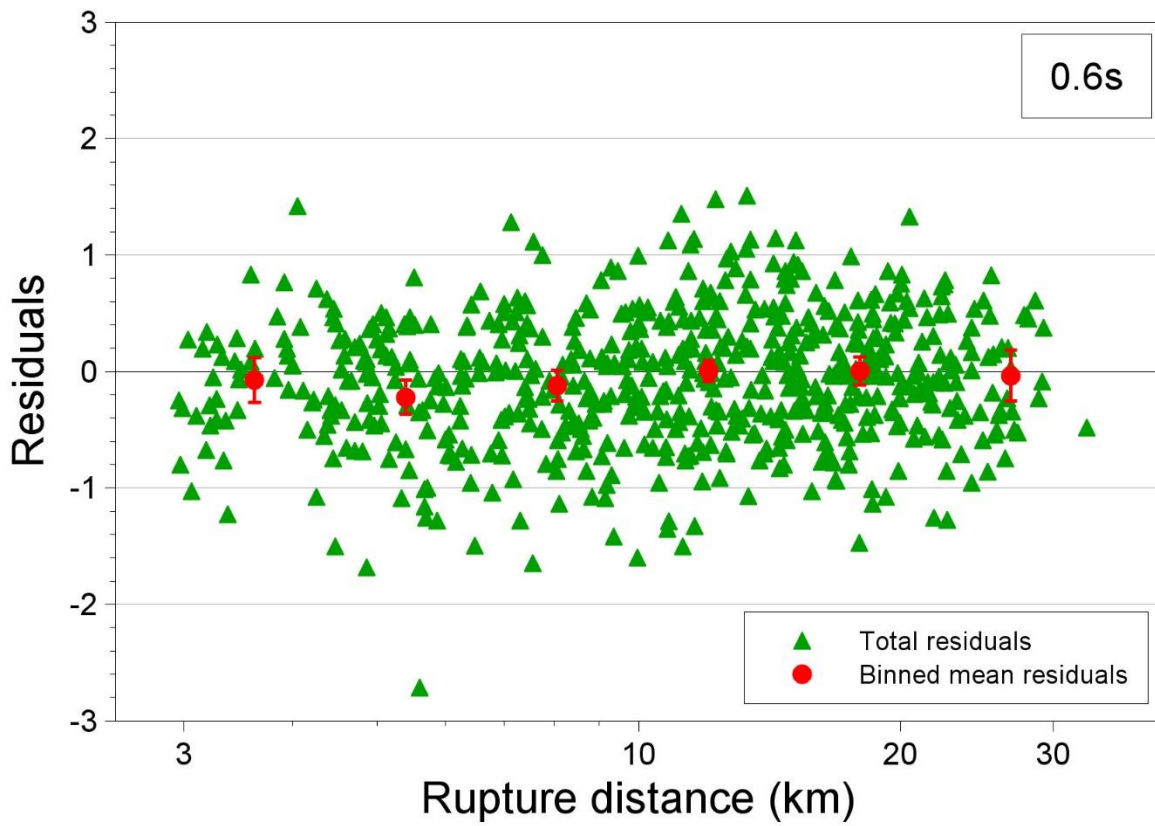


Figure 10.7. Same as Figure 10.1 but for the period of 0.6 s.

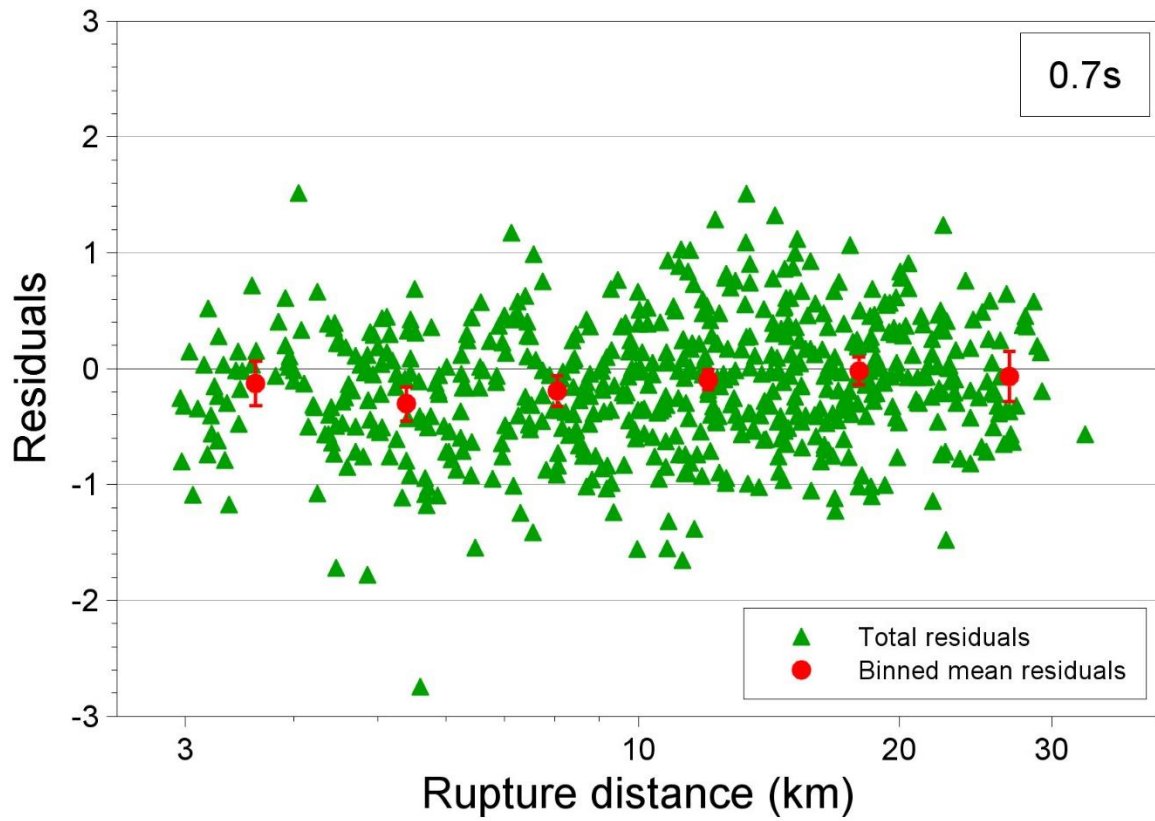


Figure 10.8. Same as Figure 10.1 but for the period of 0.7 s.

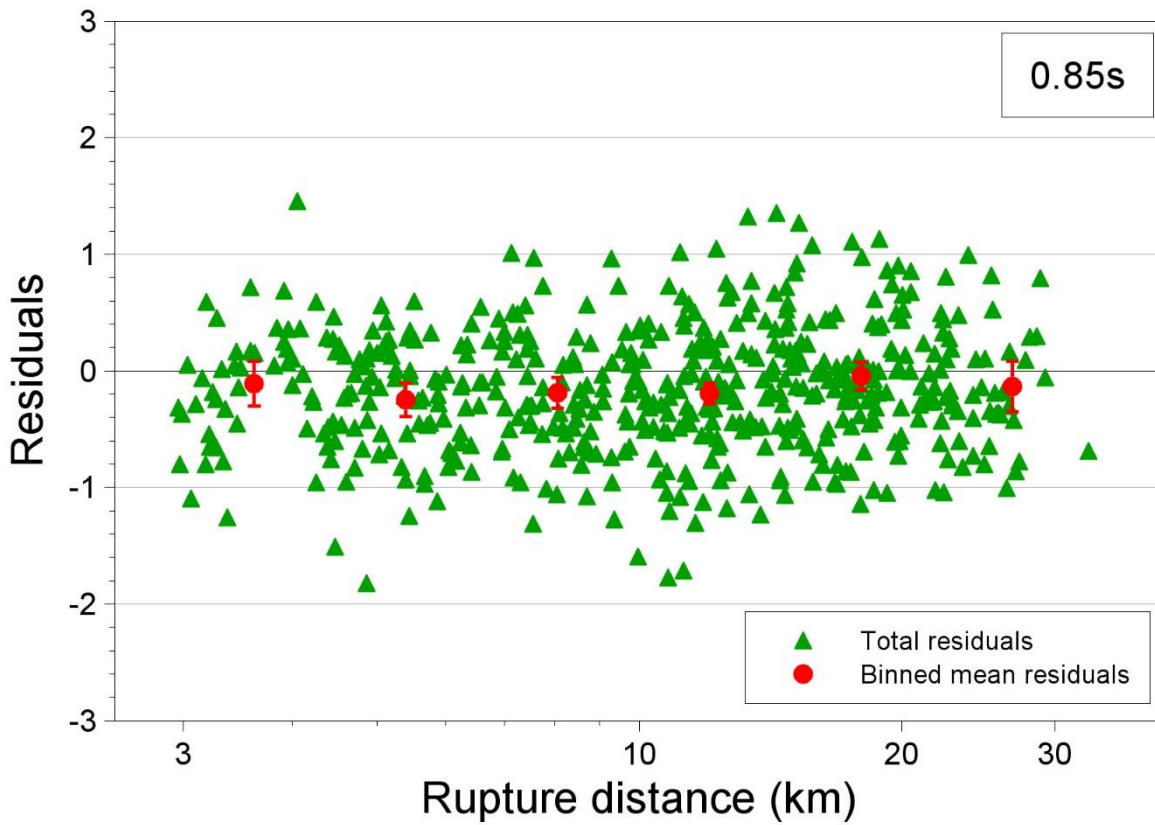


Figure 10.9. Same as Figure 10.1 but for the period of 0.85 s.

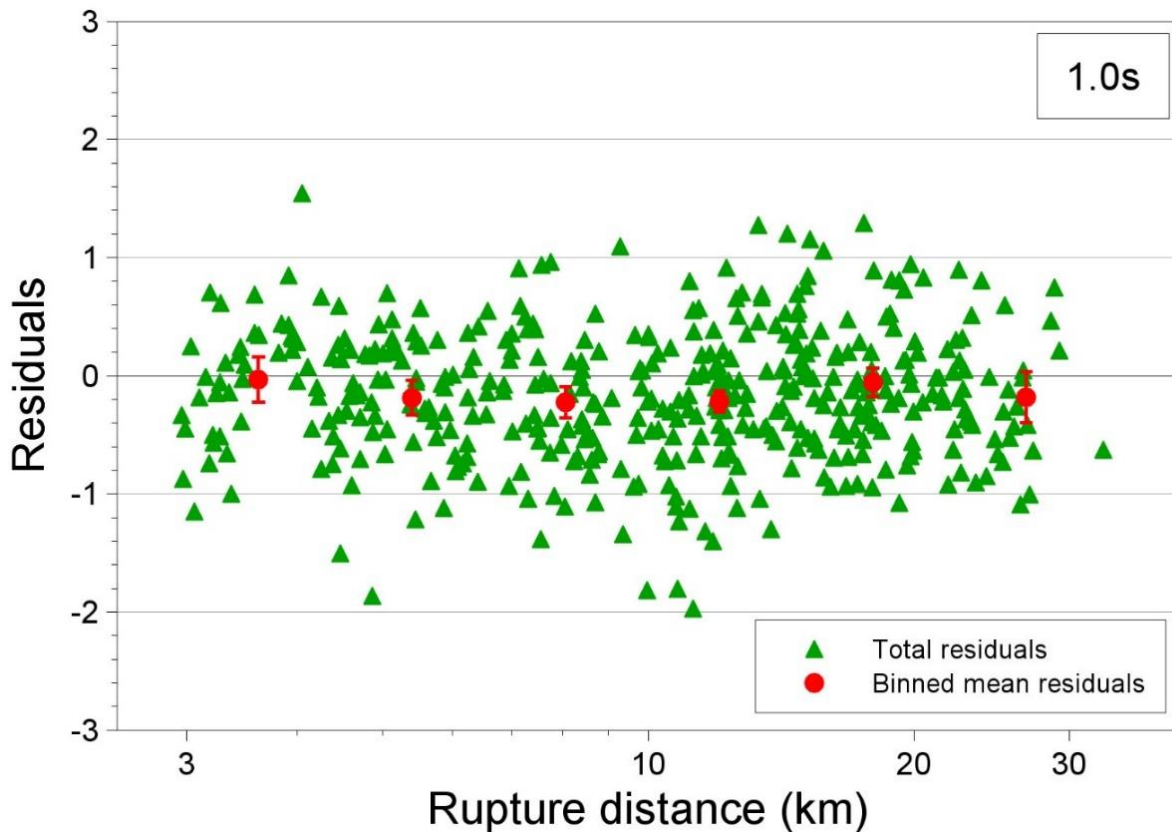


Figure 10.10. Same as Figure 10.1 but for the period of 2.0 s.

The underestimation of PGA values at the surface (Figure 10.1) is a perplexing feature of the V7 GMM that is worthy of some discussion. The same feature is observed at the NS_B horizon (Figures 6.21 and 6.22), so it is very unlikely to be attributable to the site response model. Indeed, the underestimation of PGA values, especially at short distances, feature has been present to some degree in all versions of the GMM (see Appendix II), regardless of the damping models that have been adopted. As can be appreciated from Figures 10.2 to 10.10, the fit of the model to the surface data at the other target periods is generally very good, with a very slight tendency towards slight overprediction at the longer periods. Plots of the total surface residuals with respect to the V5 and V6 GMMs are shown for the same 10 oscillator periods in Appendix II, from which it can be appreciated that the fit of the current model to the Groningen database is notably superior to that of any previous model. This is not to say that the underprediction of the observed PGA values is not an undesirable feature of the V7 model, but it is also important to bear in mind that the objective of the GMM is to provide estimates of the spectral accelerations over the full range of earthquake magnitudes considered in the hazard and risk calculations, informed by the field data and capturing the epistemic uncertainty that is inevitably associated with extrapolation to much larger magnitudes. The primary purpose of the GMM is not to reproduce the recorded ground motions, which are from earthquakes of magnitudes that generally exert very little influence on the hazard and risk estimates. The poor performance in terms of PGA predictions at small magnitudes does not necessarily mean that the

model is unreliable at the larger magnitudes that control the hazard and risk. In passing we also note that the upper branch of the V7 GMM predicts the surface PGA values quite well (Figure 10.11), although the underestimation at short distances continues. One possible explanation for the underestimation of PGA at very short distances might lie in the role of P-waves: although the full waveforms are considered in the calculation of the FAS that are inverted at the NS_B horizon, the simulations essentially model the radiation of S-waves. Wave focusing effects could also be a contributing factor.

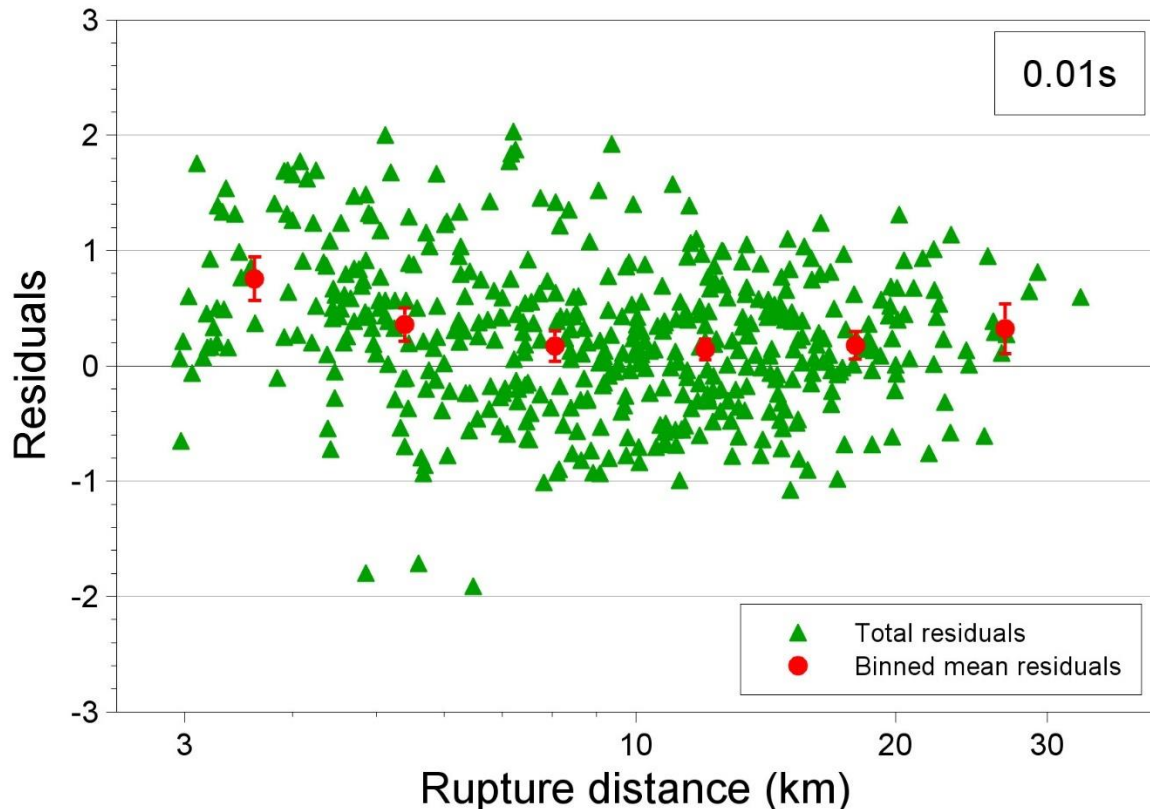


Figure 10.1. Total residuals of the spectral accelerations of the V7 database with respect to the median surface predictions of the upper branch model for the period of 0.01s; the red dots are bin means and the bars their associated 90 percentile confidence intervals.

The observation that the PGA values from the Groningen records are underpredicted initially prompted consideration of the possibility of simply removing the predictions for SA(0.01s) in the calculation of the average spectral acceleration used as input to the fragility functions. Figure 10.12 shows the pairs of values of average spectral acceleration for the Groningen ground-motion records (excluding any records with unusable ordinates at any of the 10 target periods) calculated using all 10 periods and also only using the other nine periods. The figure shows that the latter is a reasonable estimate of the former, but with a tendency to underestimate, on average, the fragility function input parameter by 5%.

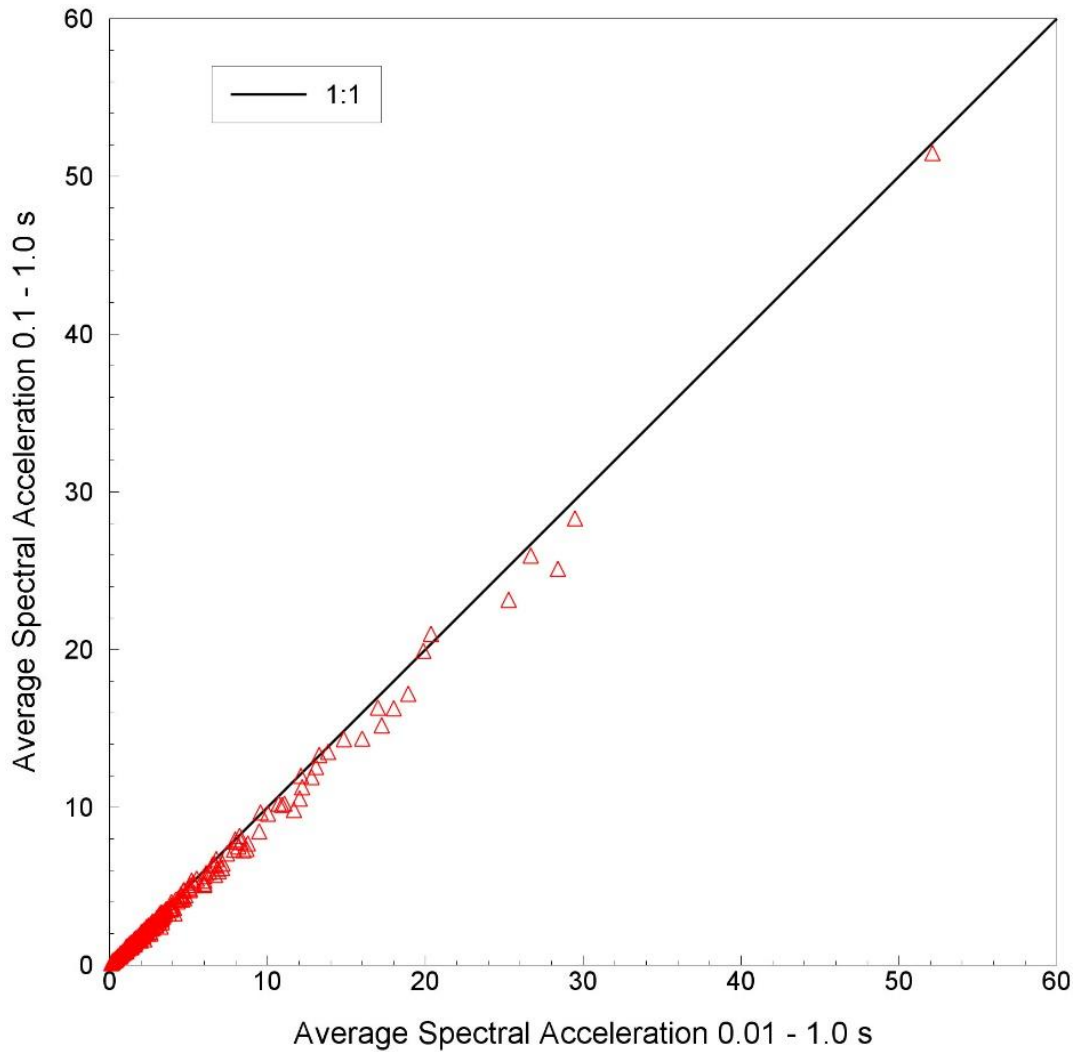


Figure 10.12. Average spectral accelerations of the Groningen horizontal ground motions calculated across 10 periods and calculated excluding SA(0.01s).

On the basis of these observations, one option would be to calculate the average spectral acceleration using the oscillator periods from 0.1 to 1.0 s (i.e., omitting PGA), and then apply an adjustment factor of 1.05. However, Figure 10.13 suggests that this would be highly conservative at greater distances and particularly so at larger magnitudes, the latter being the primary control on the hazard and risk estimates. Therefore, we do not recommend the application of such an approach, but it is acknowledged that the underestimation of PGA at small magnitudes will also lead to a modest underestimation of the average spectral acceleration in this magnitude range. The impact is unlikely to be very large and it is unknown whether there is a corresponding underestimation at the larger magnitudes that drive the risk estimates. The model for SA(0.01s) is also retained because of the insistence of some stakeholders in generating hazard maps in terms of PGA.

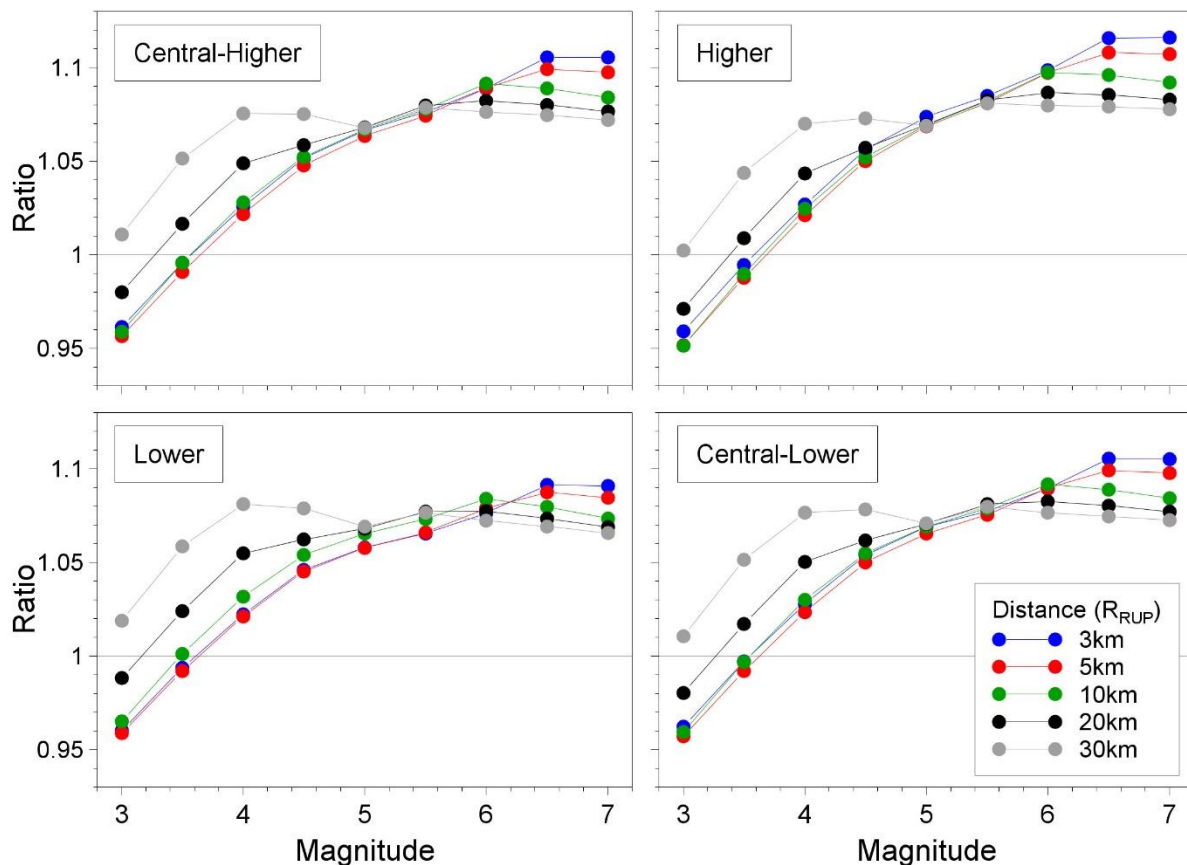


Figure 10.13. Ratios of predicted average spectral acceleration calculated using nine periods between 0.1 to 1.0 s to the value calculated also using the acceleration at 0.01 s. The spectral accelerations are the median predictions obtained from the four branches of the logic tree applied in site response zone 2207 (which has an average V_{S30} close to the field average), for multiple combinations of magnitude and distance.

As described in Section 3, there is a large database of records from the Groningen field’s Household Network that has not been used in the development of this model, as well as a small number of usable records from stations of the KNMI B- and G-networks that were also not used because the V_s profiles of those stations have not been measured. These records provide the opportunity to test the performance of the model against a local database to which it is applicable but not calibrated. The characteristics of this database are shown in Figure 10.14. Prior to 2016, the stations of the Household network operated with a triggering mechanism which allowed the generation of records only once a velocity threshold of 1 cm/s had been exceeded (Ntinalexis *et al.*, 2019). This led to the censoring of a large portion of the records the network would have generated during its operation between 2014 and 2016, which were irredeemably lost. At the same time, it also resulted in the impression that the motions recorded by the Household network were significantly larger than those of the KNMI networks during preliminary analyses of the data (Bommer *et al.*, 2015). Hence, this comparison only includes Household Network records from events 23 – 26, which occurred between the time that this issue was corrected in 2016 and the end of operation of the network in 2020. A total of 845 records from four earthquakes have

been used from the Household Network as well as 40 records from eight events from the G-network.

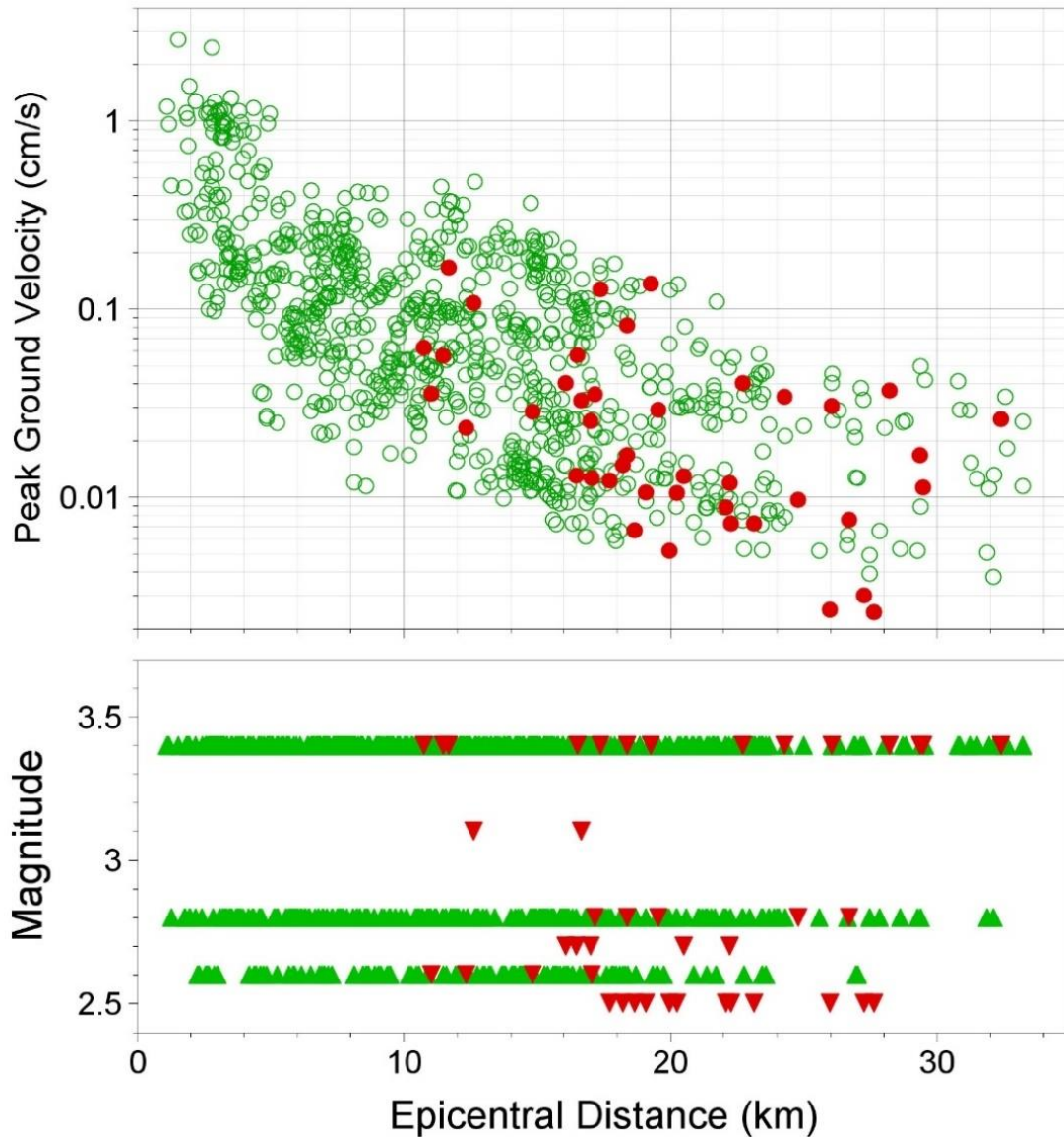


Figure 10.14. PGV- and magnitude-distance distribution of the 86 records included in the comparison.

Figures 10.15 to 10.24 present the residuals of the spectral accelerations of the records also with respect to the median surface predictions of the central-lower model for periods up to one second. The same observations made for Figures 10.1-10.13 can be made for these records as well, however with the overestimation of recorded motions in the longer periods being more prominent in this case.

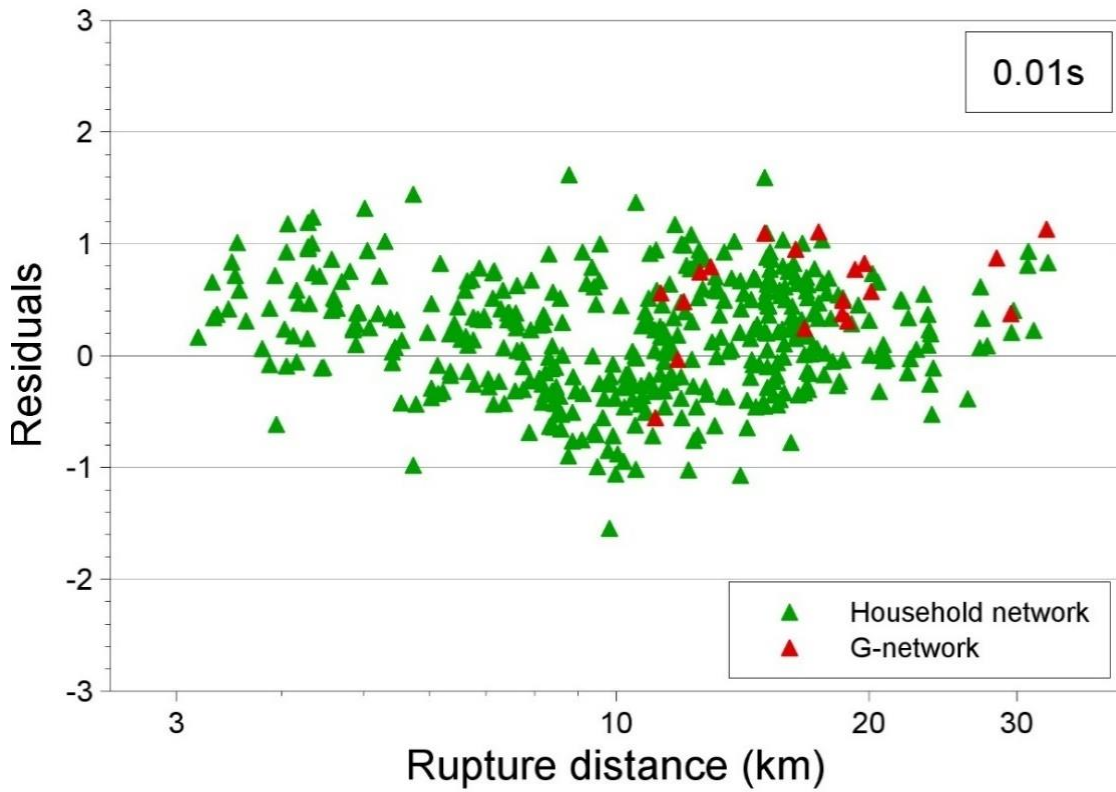


Figure 10.15. Total residuals of the spectral accelerations of the records with respect to the median surface predictions of the central-lower model for the period of 0.01 s.

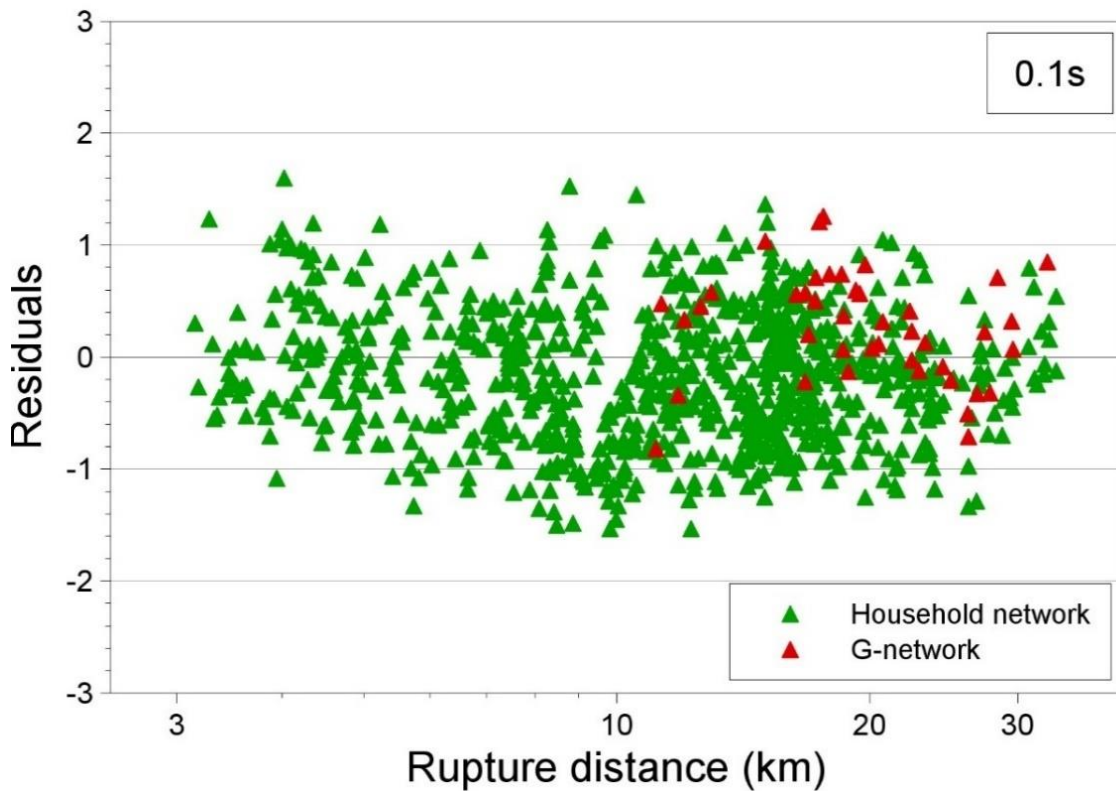


Figure 10.16. Total residuals of the spectral accelerations of the records with respect to the median surface predictions of the central-lower model for the period of 0.1 s.

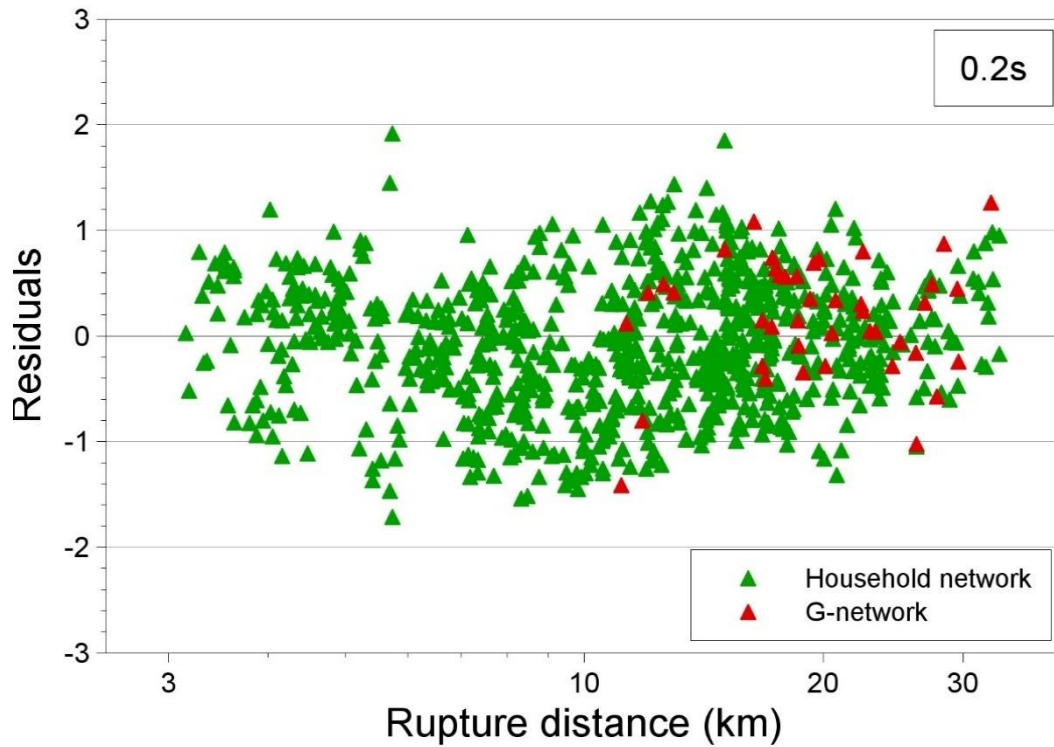


Figure 10.17. Total residuals of the spectral accelerations of the records with respect to the median surface predictions of the central-lower model for the period of 0.2 s.

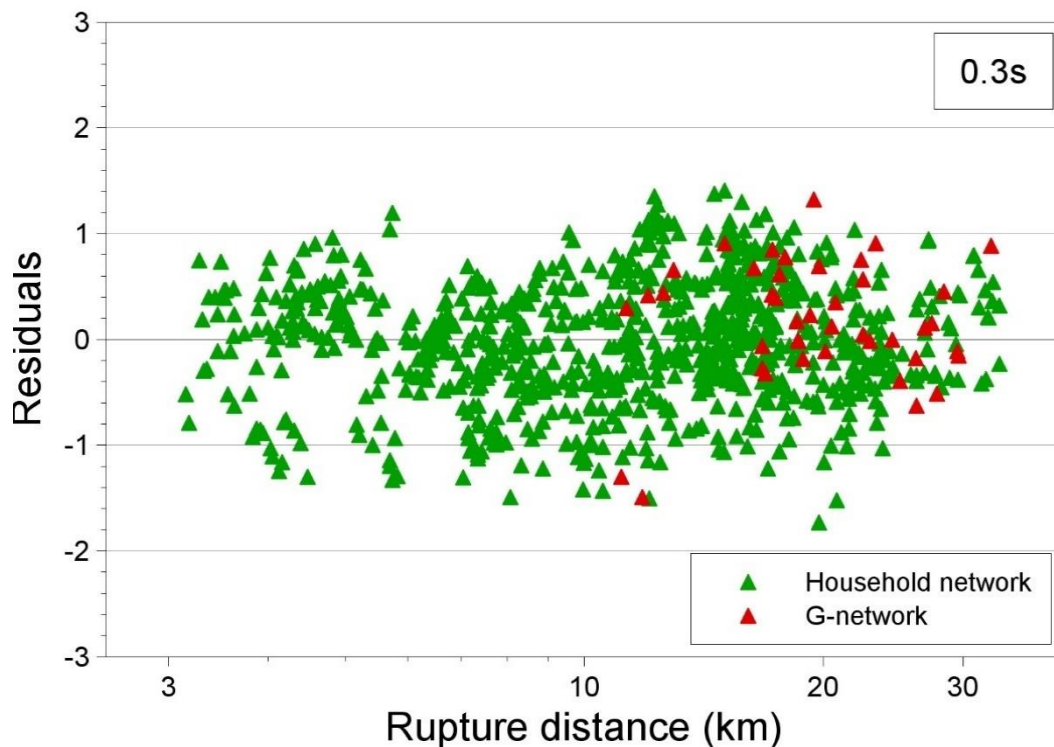


Figure 10.18. Total residuals of the spectral accelerations of the V7 database with respect to the median surface predictions of the central-lower model for the period of 0.3 s

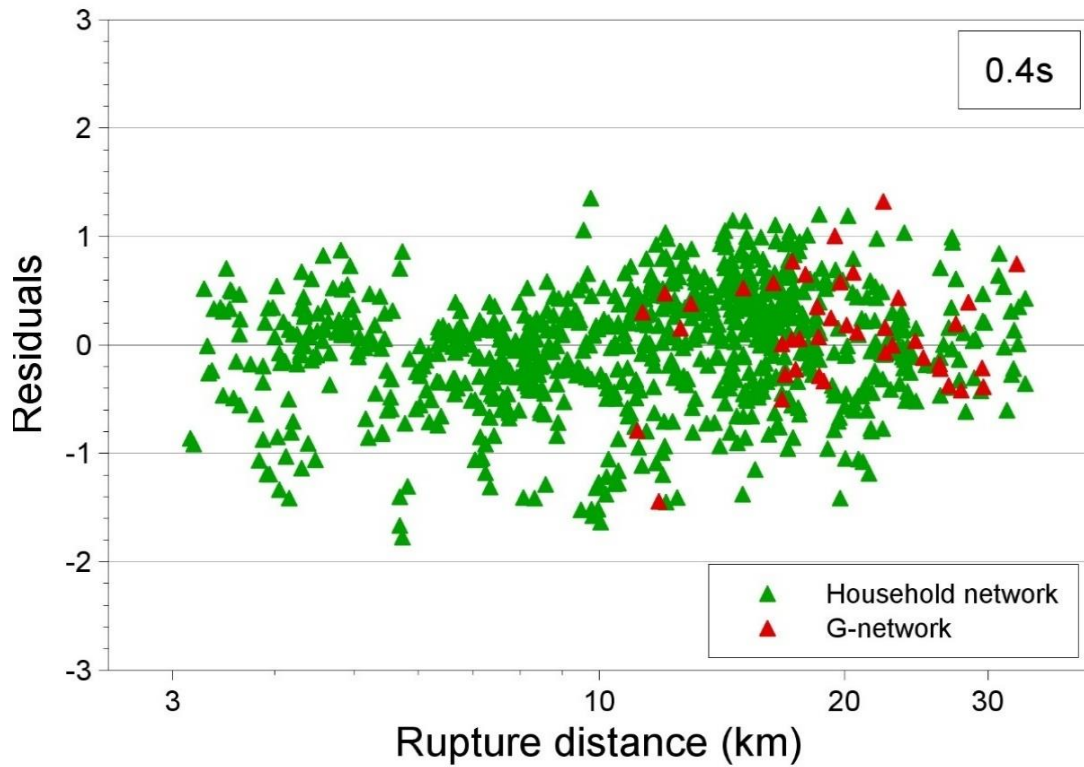


Figure 10.19. Total residuals of the spectral accelerations of the V7 database with respect to the median surface predictions of the central-lower model for the period of 0.4 s.

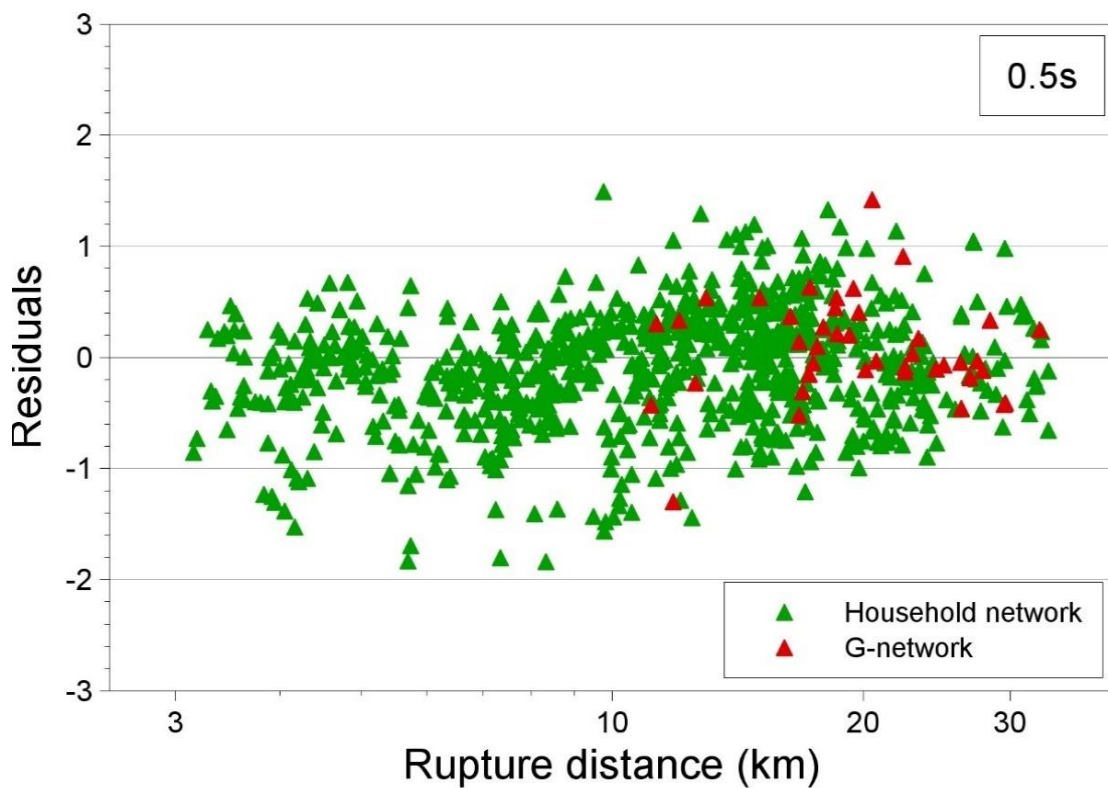


Figure 10.20. Total residuals of the spectral accelerations of the V7 database with respect to the median surface predictions of the central-lower model for the period of 0.5 s.

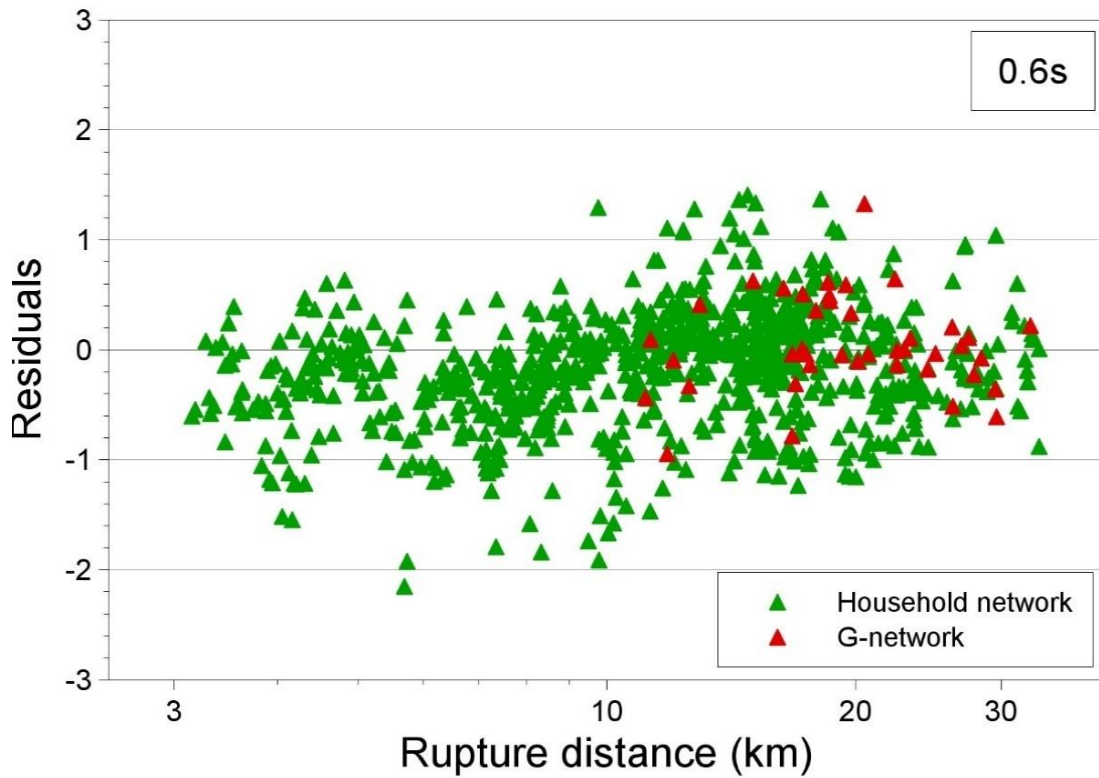


Figure 10.21. Total residuals of the spectral accelerations of the V7 database with respect to the median surface predictions of the central-lower model for the period of 0.6 s.

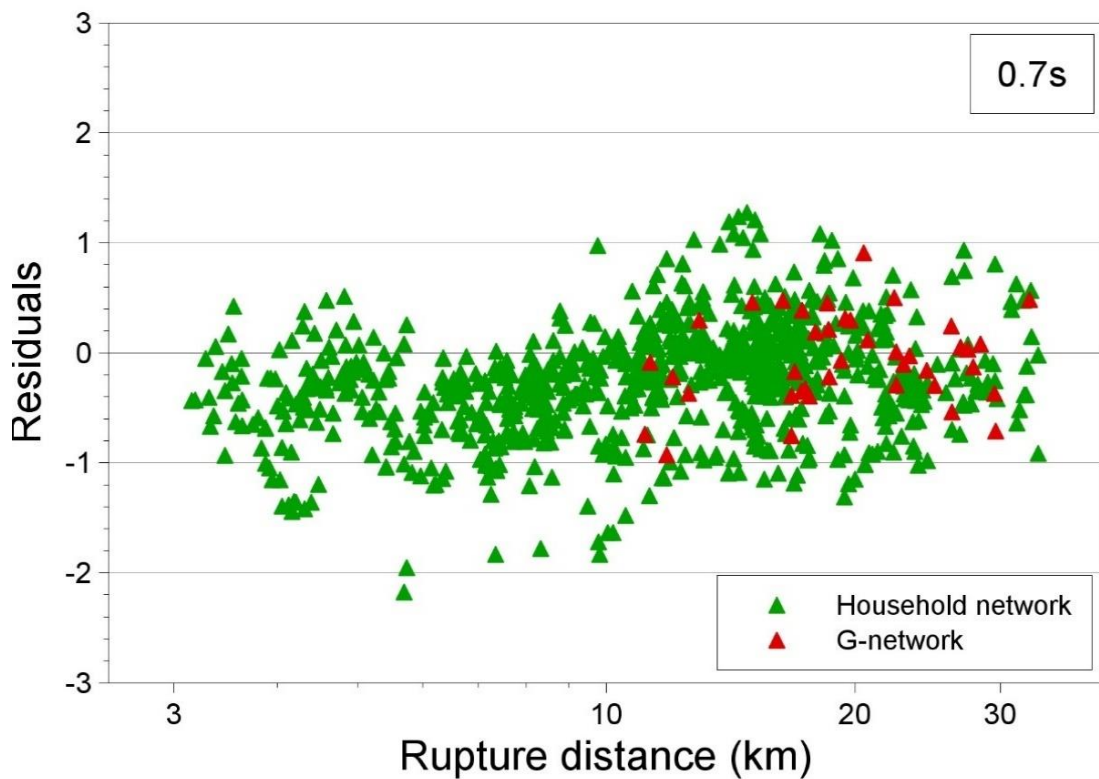


Figure 10.22. Total residuals of the spectral accelerations of the V7 database with respect to the median surface predictions of the central-lower model for the period of 0.7 s.

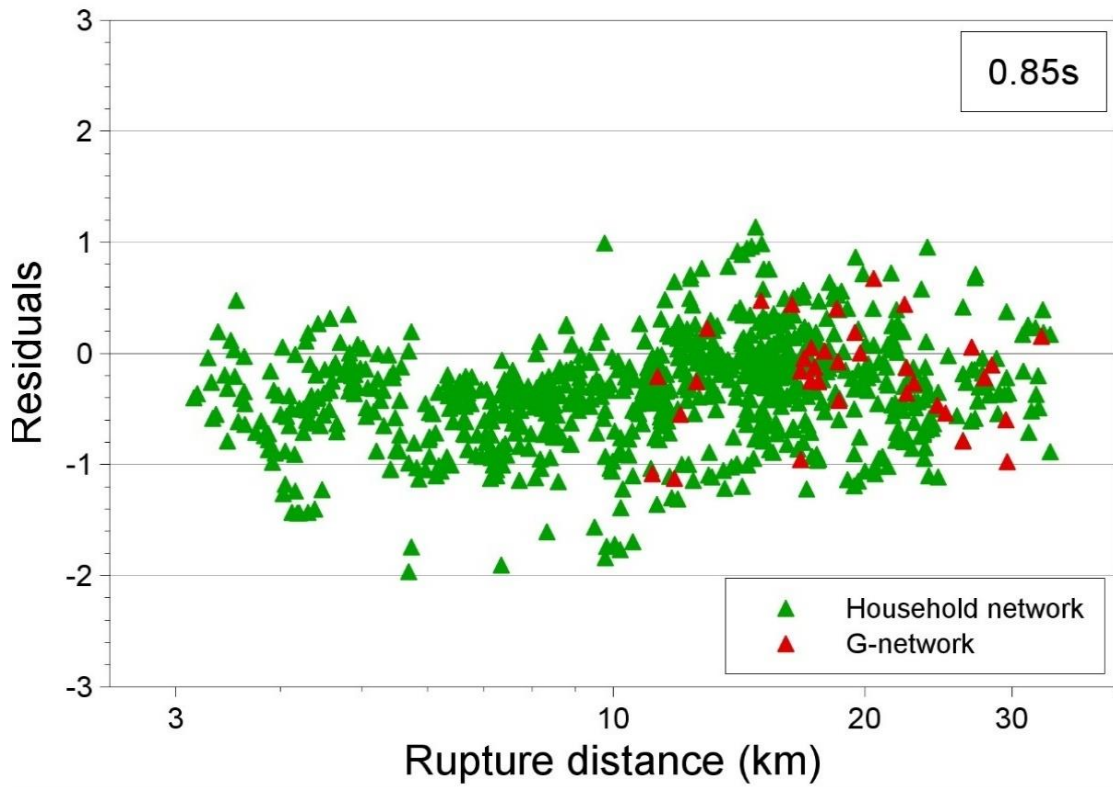


Figure 10.23. Total residuals of the spectral accelerations of the V7 database with respect to the median surface predictions of the central-lower model for the period of 0.85 s.

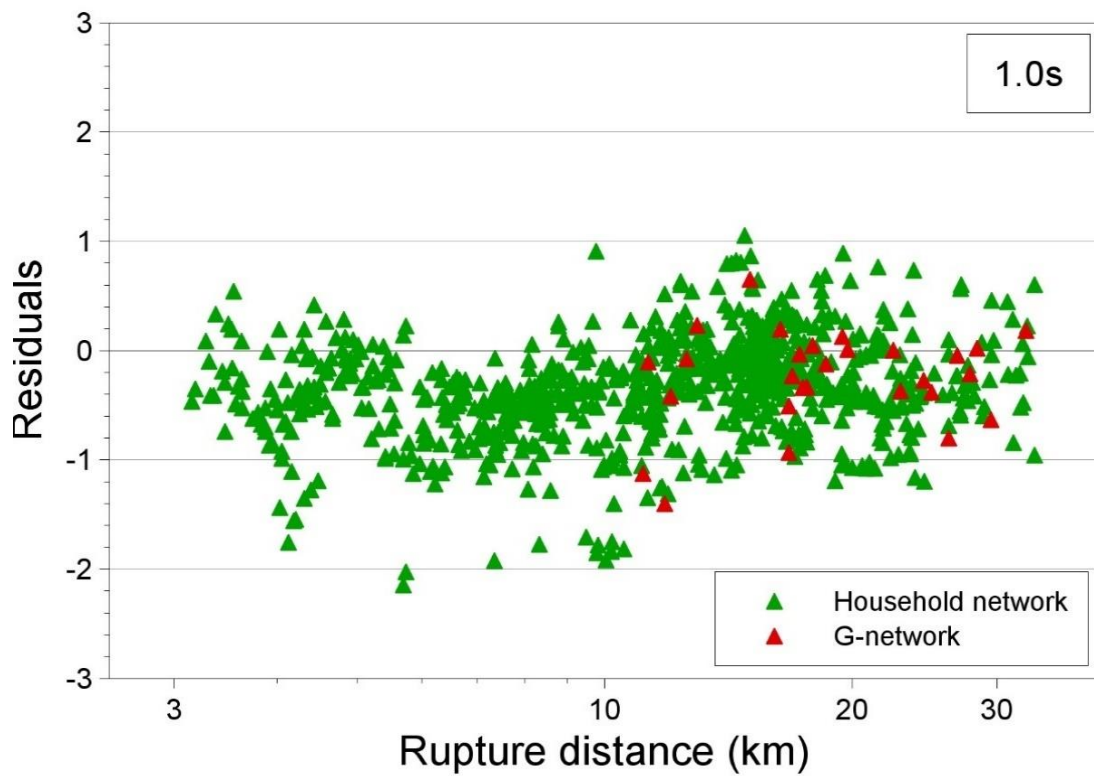


Figure 10.24. Total residuals of the spectral accelerations of the V7 database with respect to the median surface predictions of the central-lower model for the period of 1.0 s.

10.2. Comparison with V6 GMM

In this section, we present comparisons between the median predictions of the V6 and the V7 GMMs, for three zones which have been unaltered between iterations of the GMMs and have median V_{S30} values that cover the V_{S30} distribution of the field: zones 308, 604 and 1206. The comparisons are made at six distances (3, 5, 9, 17, 25 and 40 km) and six magnitude scenarios (4.0, 4.5, 5.0, 5.5, 6.0 and 7.0) and are shown in Figures 10.25 to 10.42. It should be noted that the difference in spectral shapes between the two models in the short-period range is due to the sparser period sampling chosen for V7, where all oscillator periods between 0.01s and 0.1s have been removed.

For the magnitude 4.0 scenario and the distance of 3 km, the spectral accelerations of the V6 GMM are higher than V7 at 0.01s, lower at 0.1s and then similar or slightly higher in longer periods. As the distance increases, the V7 predictions become smaller than those of the V6 GMM at all periods. The image observed at magnitude 4.0 for the distance of 3 km then applies to all distances for the magnitude 4.5 scenario.

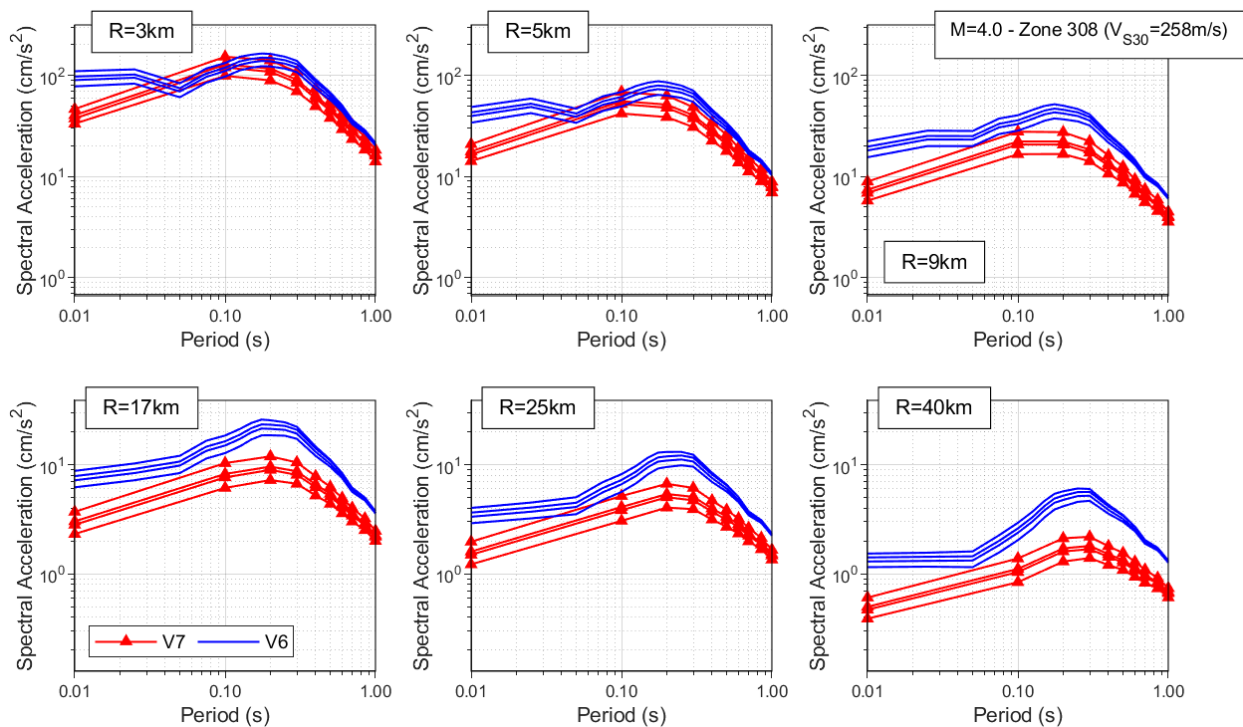


Figure 10.25. Comparison of the median spectral acceleration predictions of the V6 and V7 GMMs for M_L 4.0 and Zone 308.

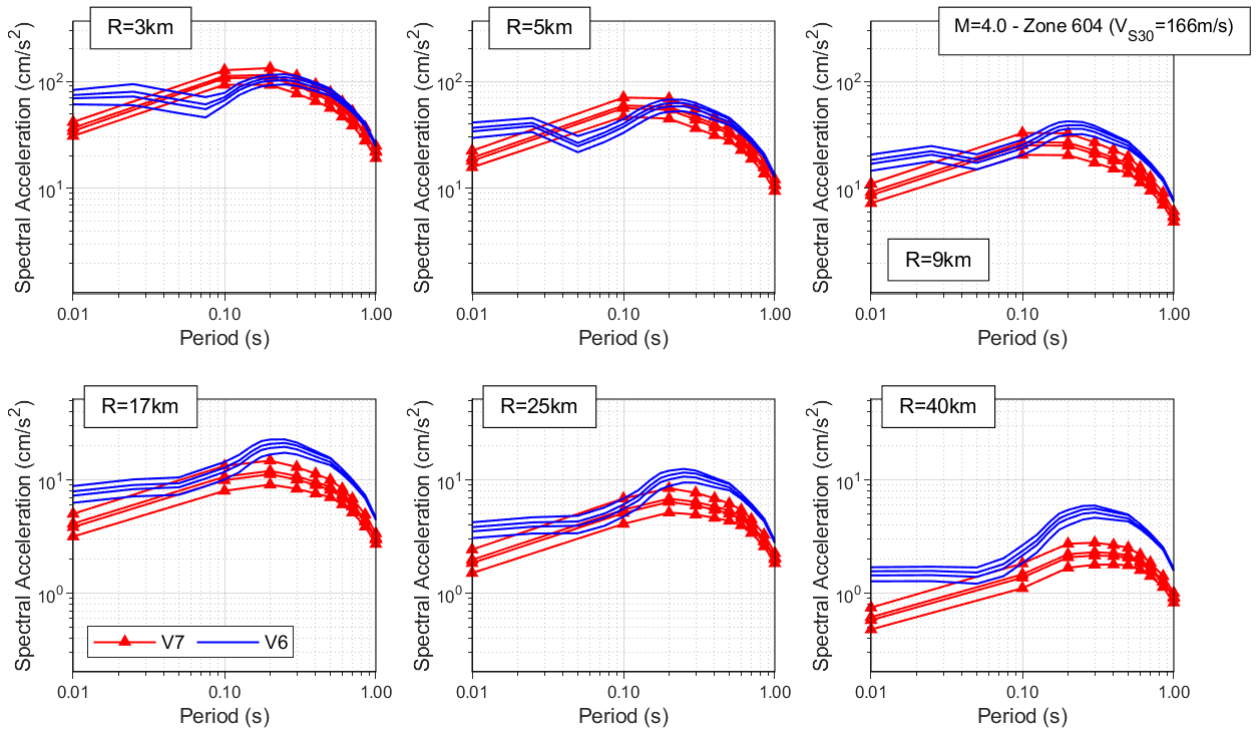


Figure 10.26. Comparison of the median spectral acceleration predictions of the V6 and V7 GMMs for M_L 4.0 and Zone 604.

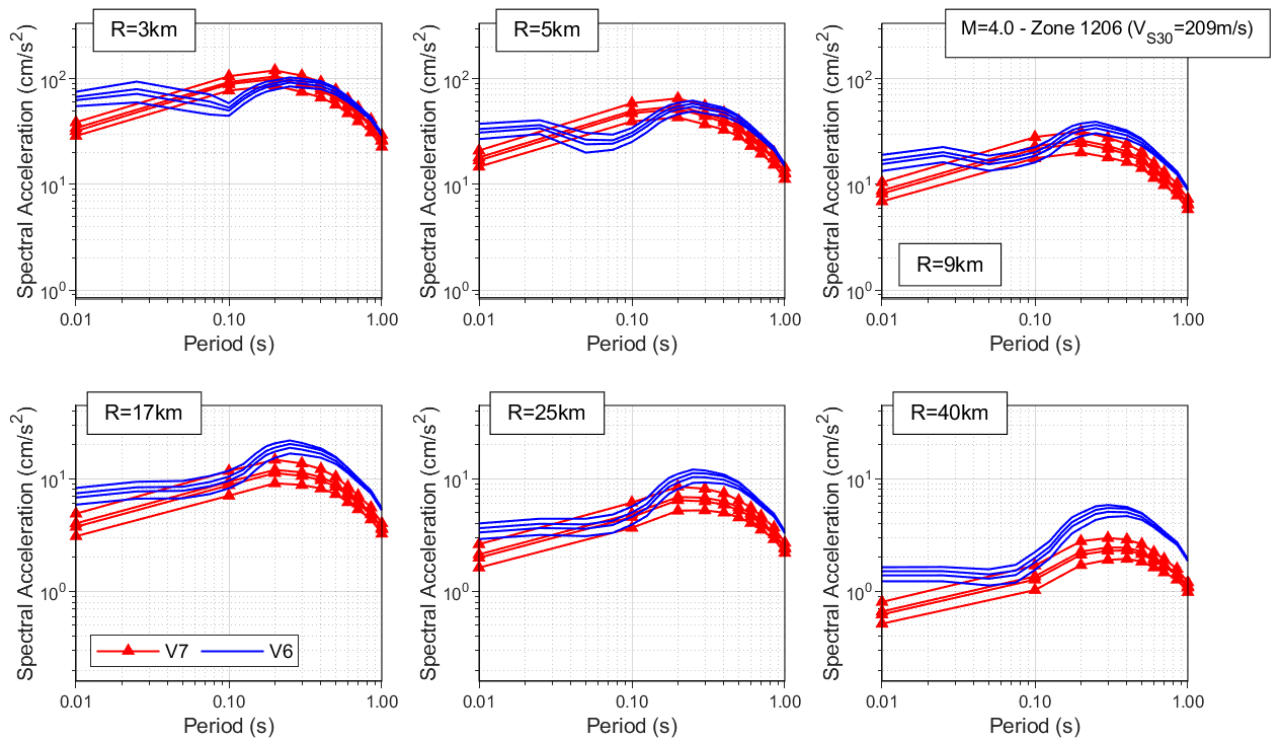


Figure 10.27. Comparison of the median spectral acceleration predictions of the V6 and V7 GMMs for M_L 4.0 and Zone 1206.

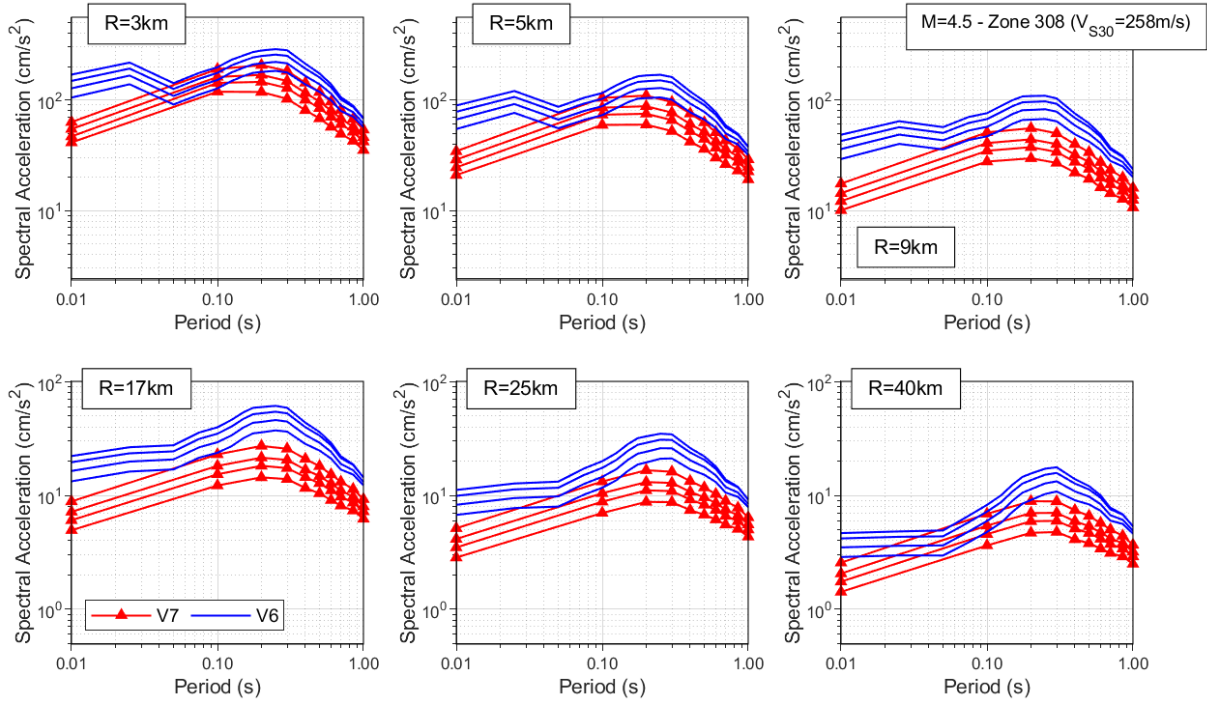


Figure 10.28. Comparison of the median spectral acceleration predictions of the V6 and V7 GMMs for M_L 4.5 and Zone 308.

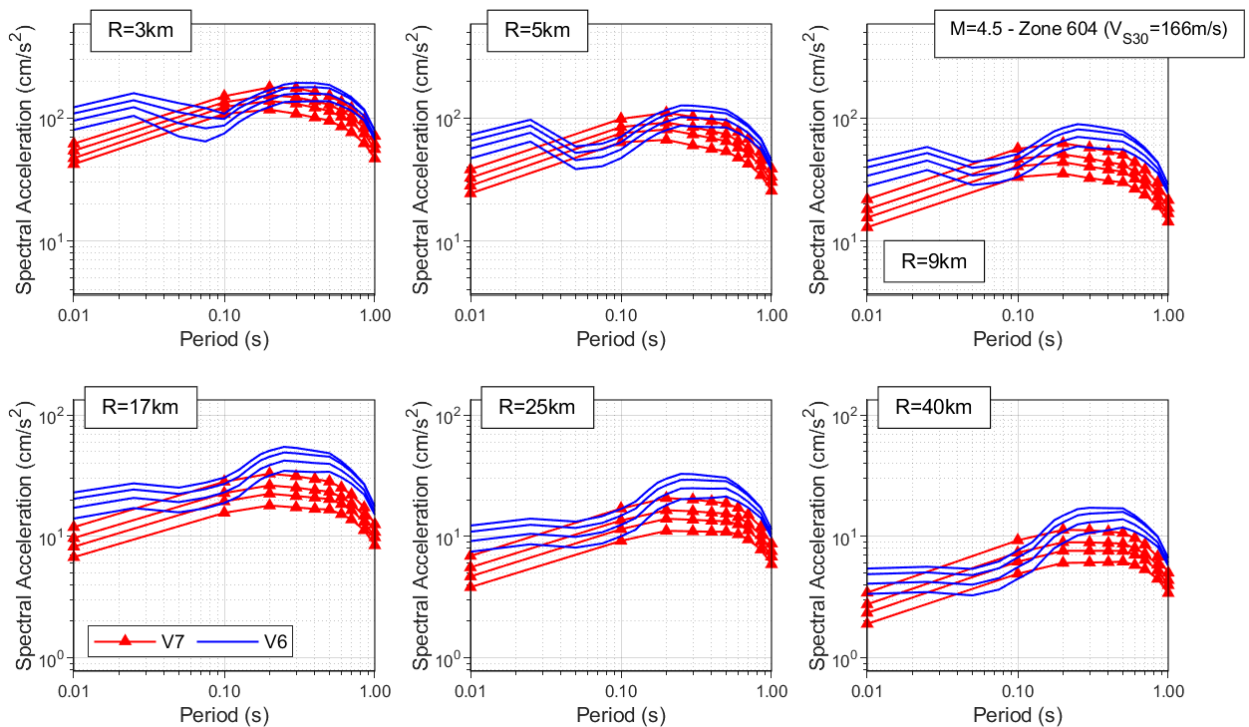


Figure 10.29. Comparison of the median spectral acceleration predictions of the V6 and V7 GMMs for M_L 4.5 and Zone 604.

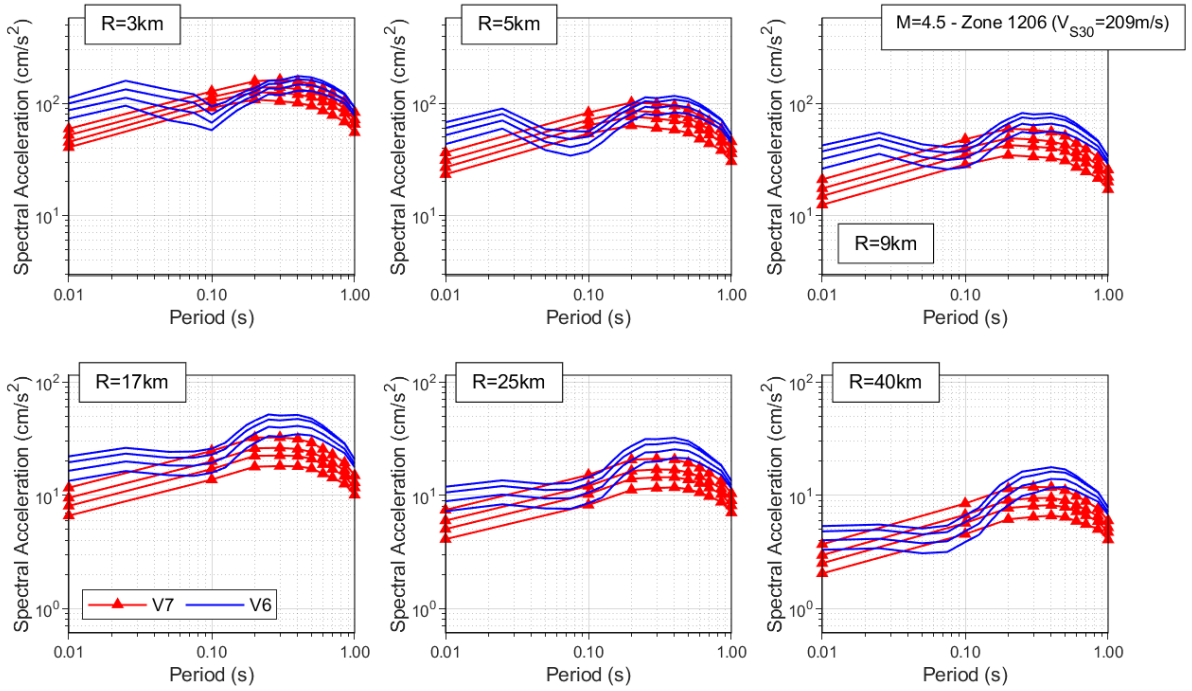


Figure 10.30. Comparison of the median spectral acceleration predictions of the V6 and V7 GMMs for M_L 4.5 and Zone 1206.

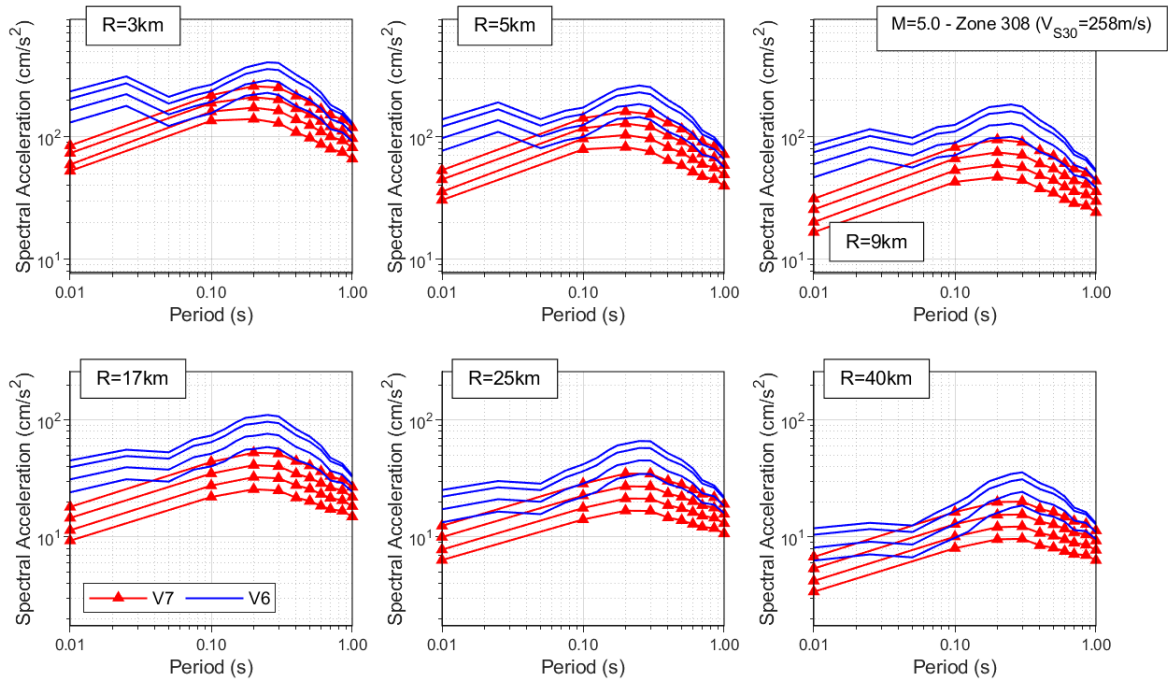


Figure 10.31. Comparison of the median spectral acceleration predictions of the V6 and V7 GMMs for M_L 5.0 and Zone 308.

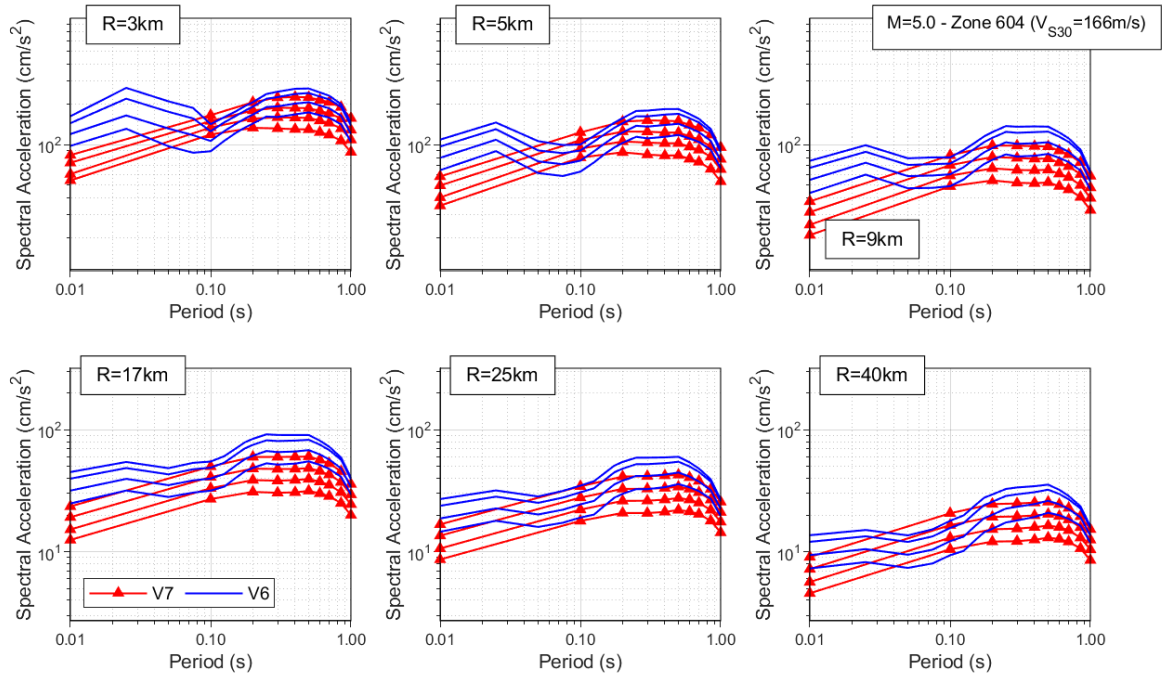


Figure 10.32. Comparison of the median spectral acceleration predictions of the V6 and V7 GMMs for M_L 5.0 and Zone 604.

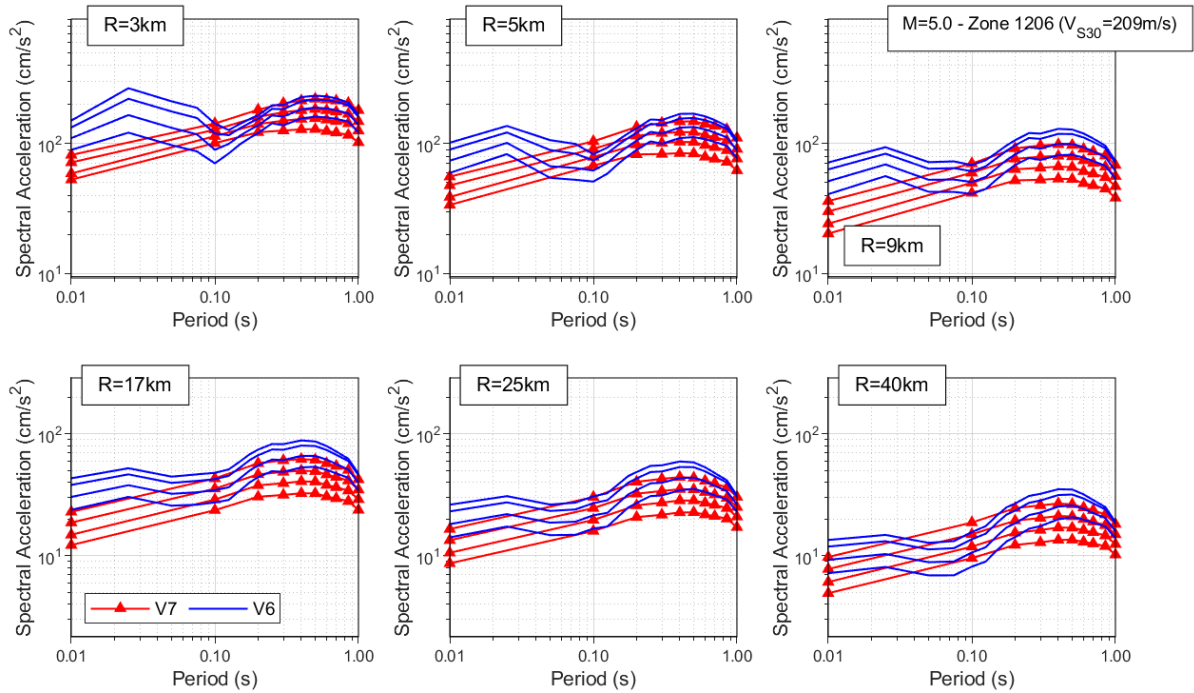


Figure 10.33. Comparison of the median spectral acceleration predictions of the V6 and V7 GMMs for M_L 5.0 and Zone 1206.

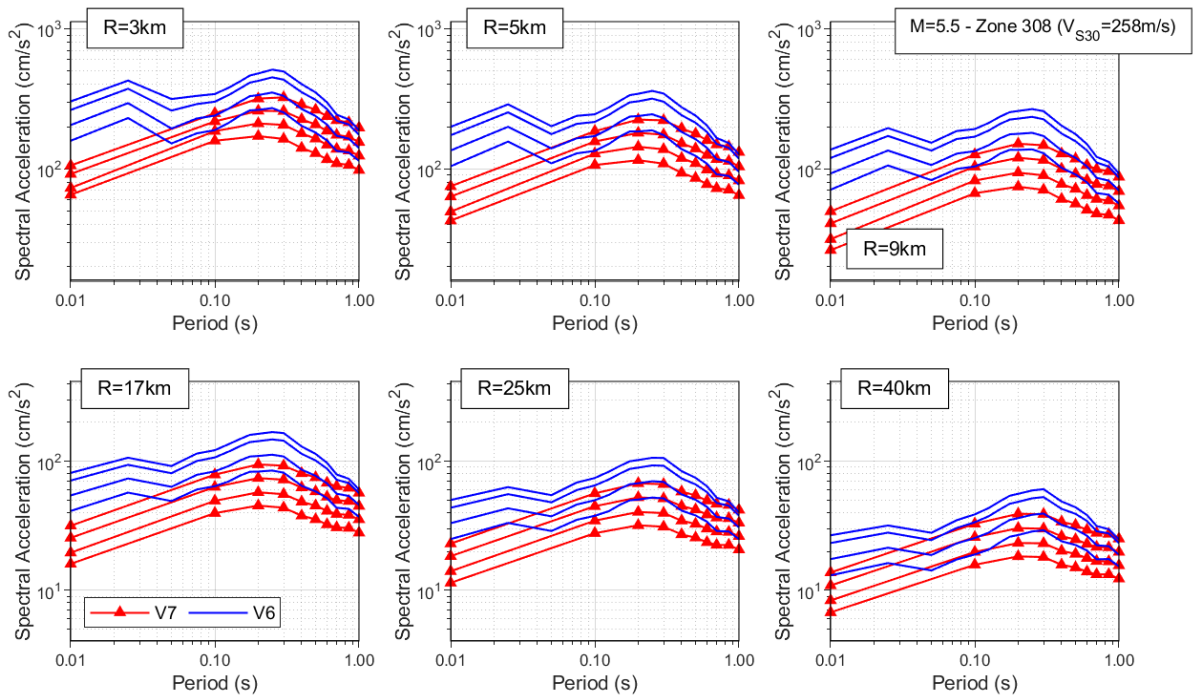


Figure 10.34. Comparison of the median spectral acceleration predictions of the V6 and V7 GMMs for M_L 5.5 and Zone 308.

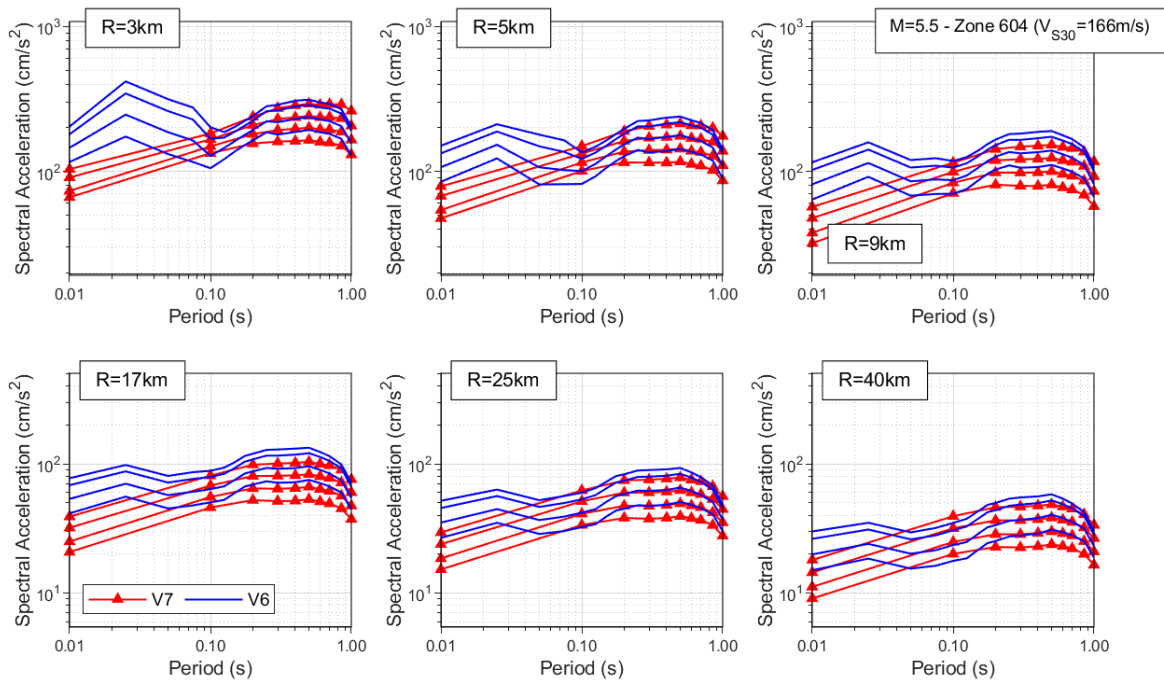


Figure 10.35. Comparison of the median spectral acceleration predictions of the V6 and V7 GMMs for M_L 5.5 and Zone 604.

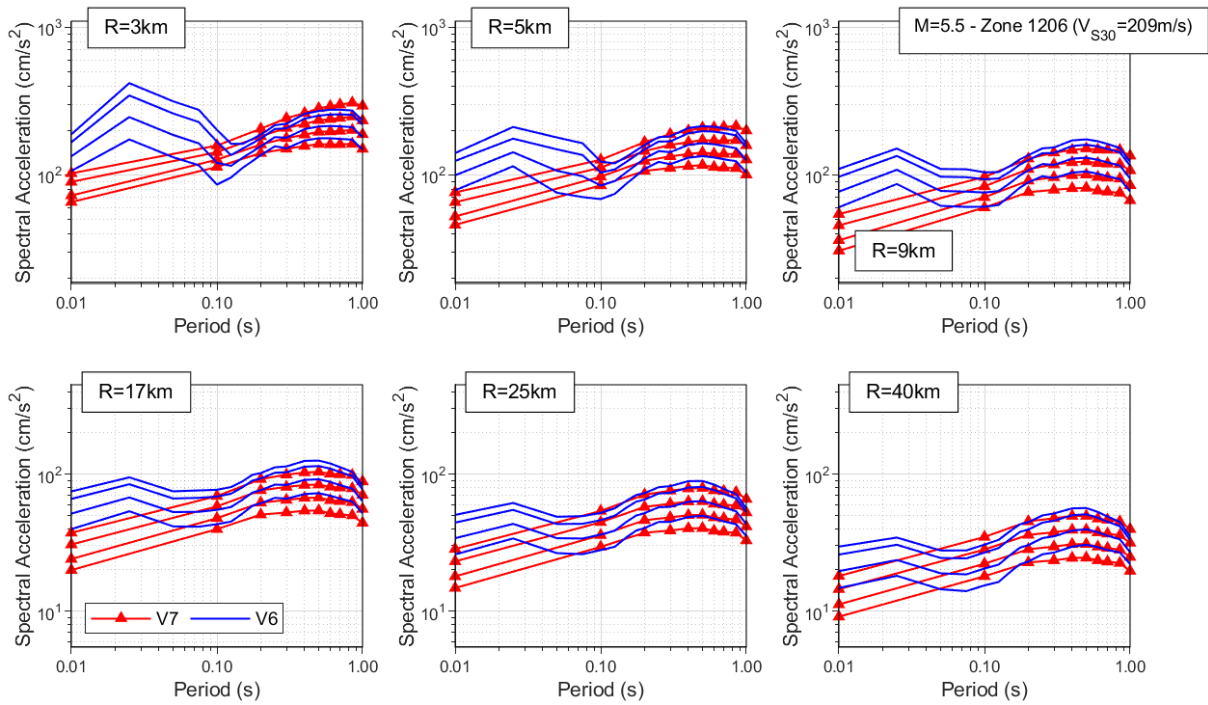


Figure 10.36. Comparison of the median spectral acceleration predictions of the V6 and V7 GMMs for M_L 5.5 and Zone 1206.

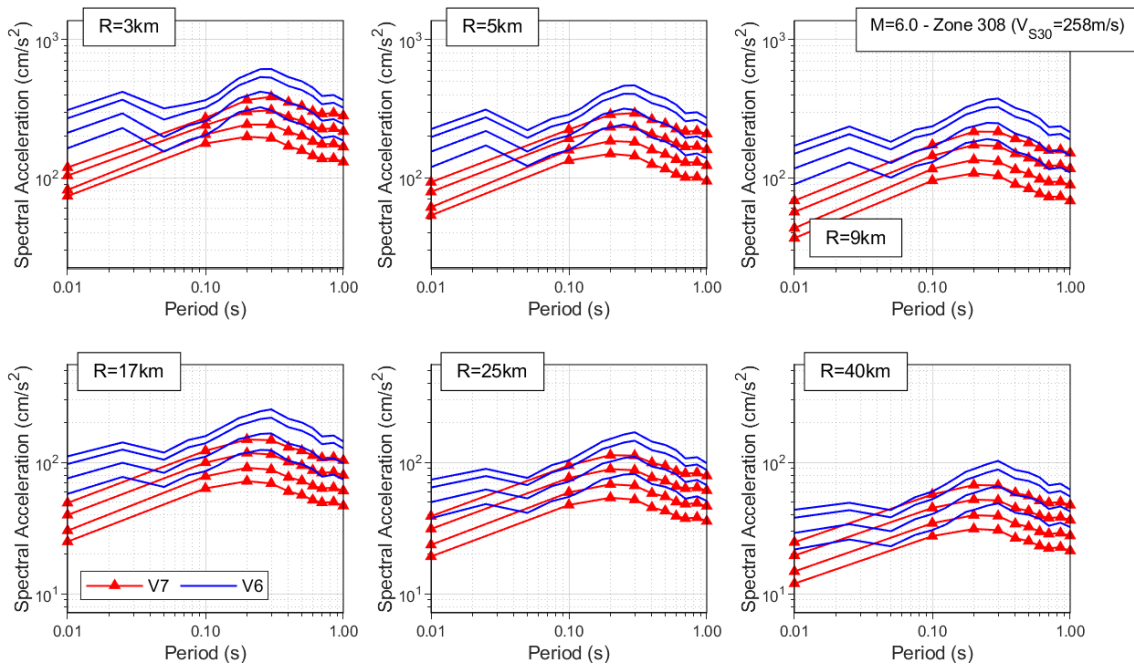


Figure 10.37. Comparison of the median spectral acceleration predictions of the V6 and V7 GMMs for M_L 6.0 and Zone 308.

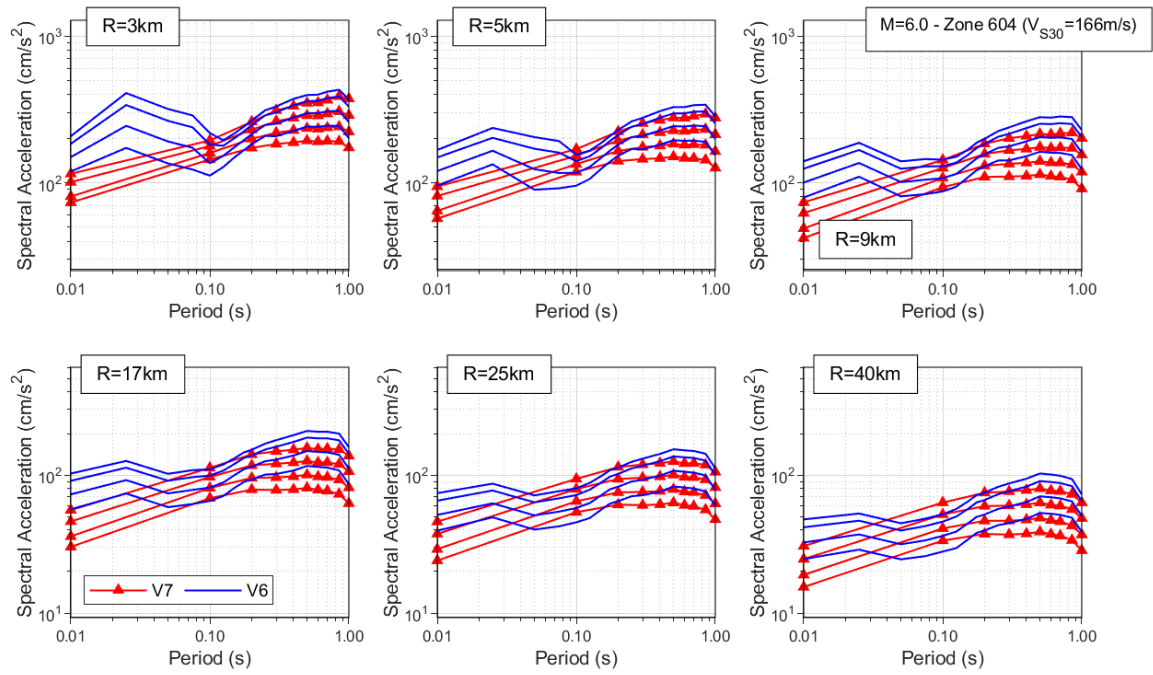


Figure 10.38. Comparison of the median spectral acceleration predictions of the V6 and V7 GMMs for M_L 6.0 and Zone 604.

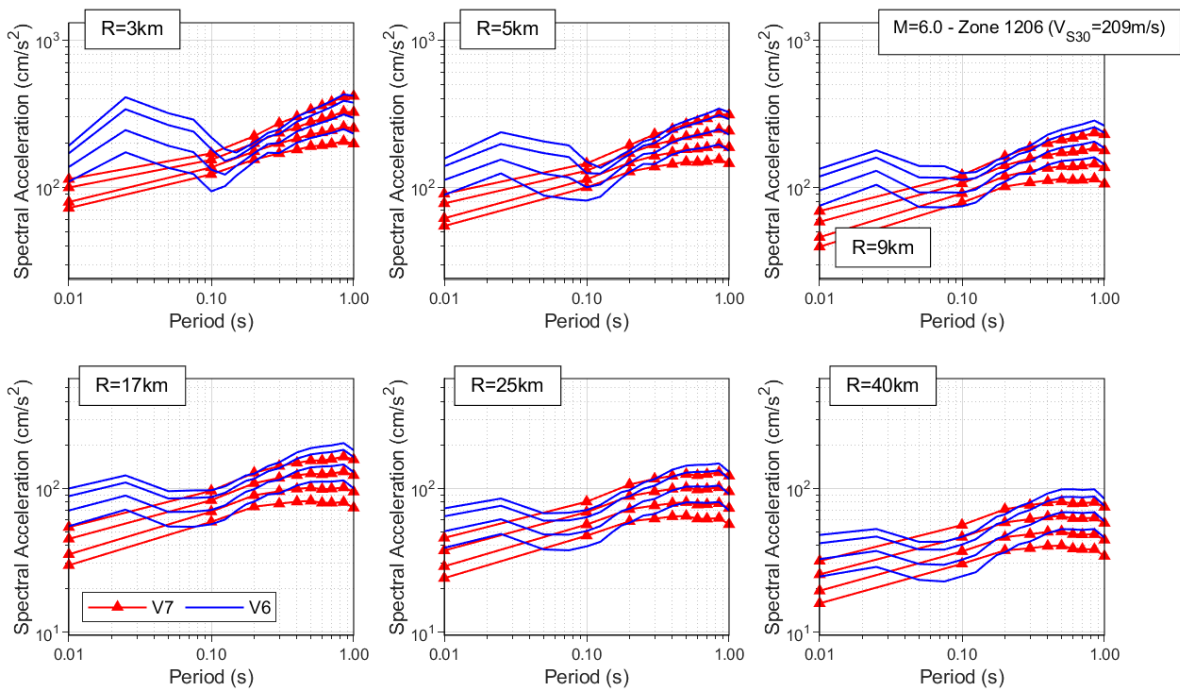


Figure 10.39. Comparison of the median spectral acceleration predictions of the V6 and V7 GMMs for M_L 6.0 and Zone 1206.

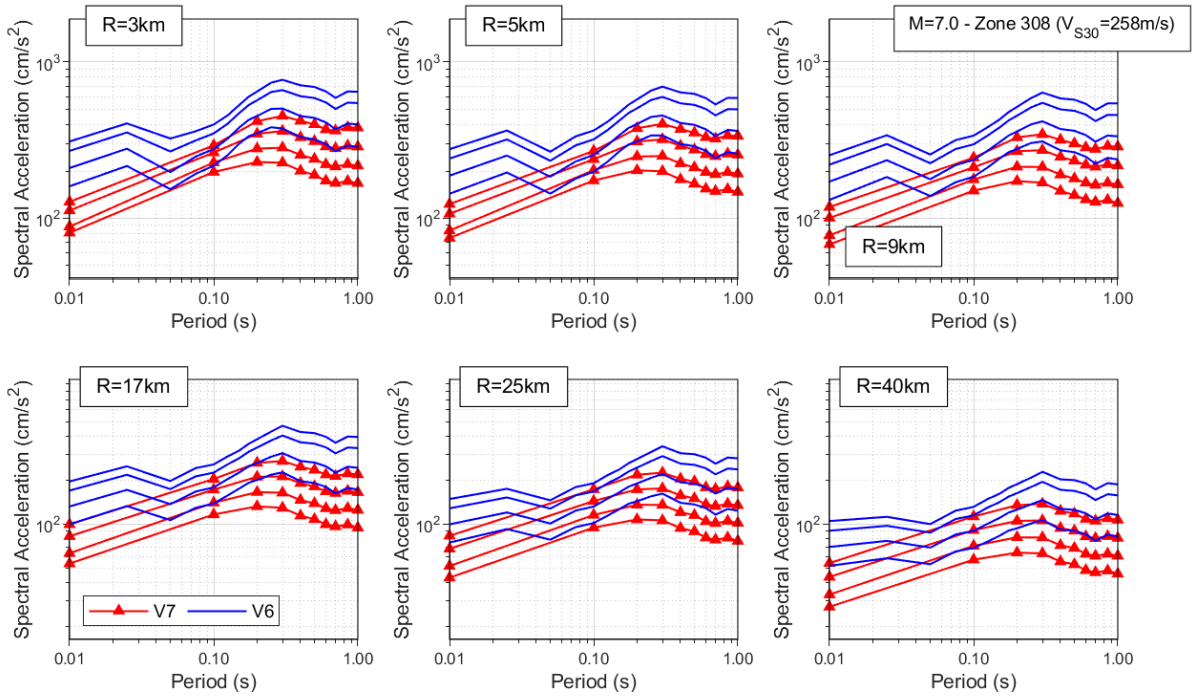


Figure 10.40. Comparison of the median spectral acceleration predictions of the V6 and V7 GMMs for M_L 7.0 and Zone 308.

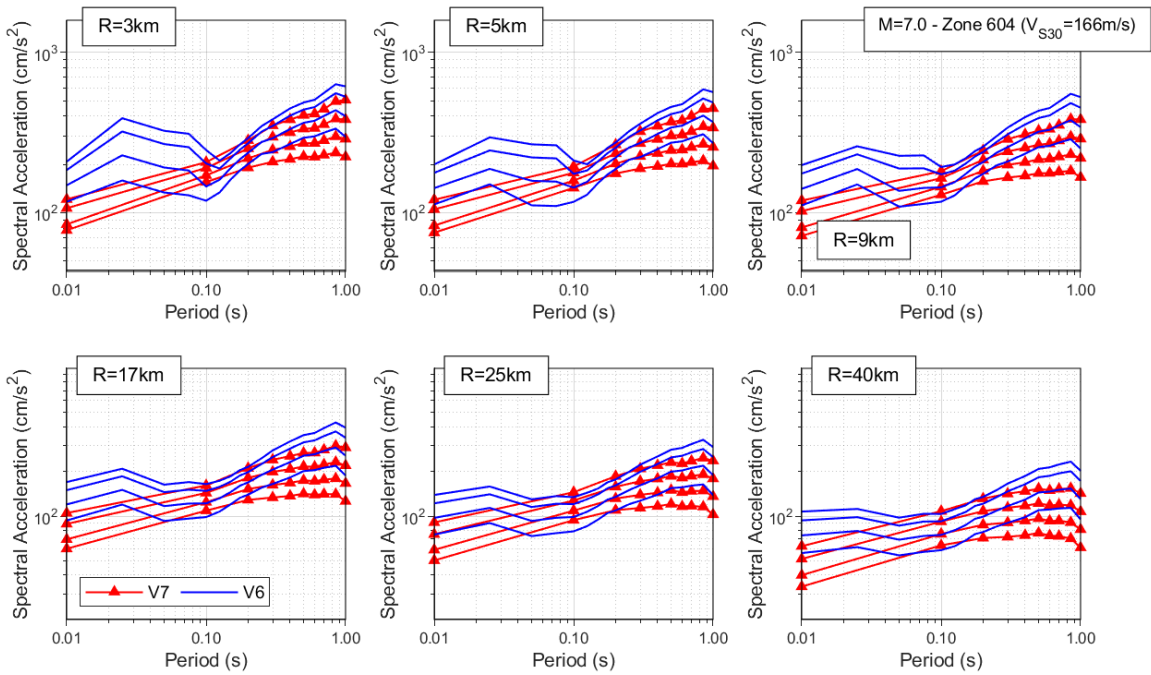


Figure 10.41. Comparison of the median spectral acceleration predictions of the V6 and V7 GMMs for M_L 7.0 and Zone 604.

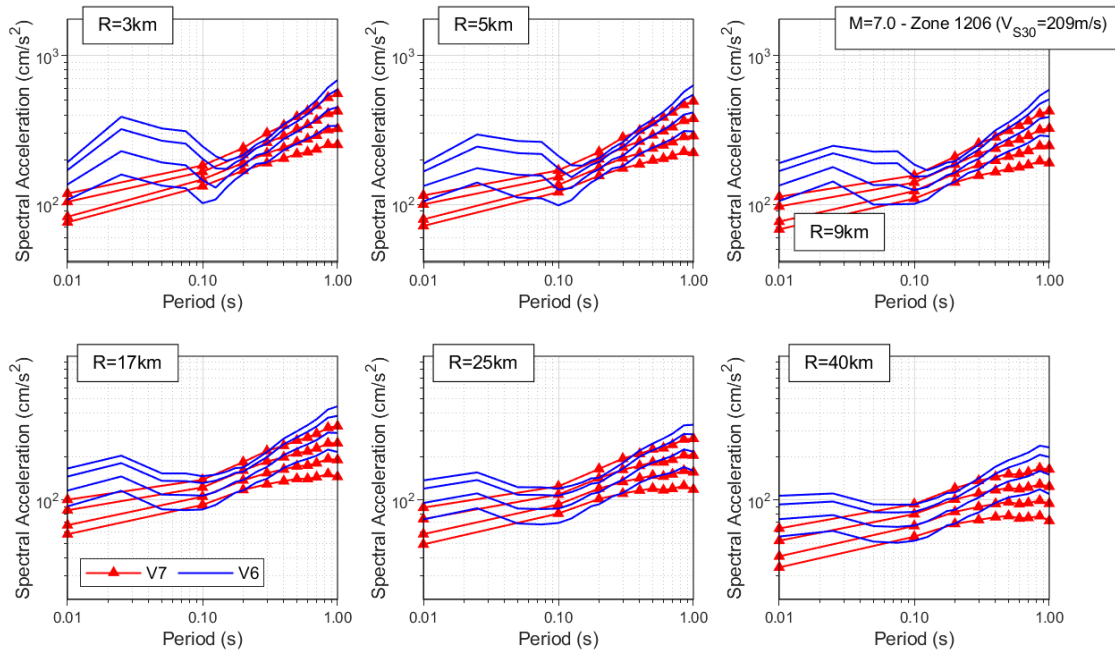


Figure 10.42. Comparison of the median spectral acceleration predictions of the V6 and V7 GMMs for M_L 7.0 and Zone 1206.

Generalised observations can be made, but we also note that the ratio between the V7 and V6 model predictions does appear to be zone-specific. Indeed, a dependence on the site conditions can be observed in the magnitude 5.0 scenario, with V6 and V7 predictions being very similar in the softest zone (604), similar but with the V6 values being slightly higher on average for the zone with a V_{S30} similar to the approximate field median which is 200m/s (zone 1206), and the V6 values being consistently higher for the zone with the highest V_{S30} among the three. Overall, however, the V7 median predictions are lower than those from the V6 model—except at 0.1 s where the latter results in a local dip in the response spectral shape—especially at larger magnitudes. To pinpoint the cause of this difference is not straightforward because there have been several important changes in the development of the V7 GMM relative to the derivation of the V6 model. These changes include the expansion of the ground-motion database and, possibly more importantly, the application of new record processing procedures and criteria for the selection of usable period ranges. Another very significant change is the modification of the low-strain damping model for the uppermost part of the site response columns, which influences both the high-frequency motions deconvolved to the NS_B horizon and the forward modelling through application of the AFs. In the inversions of the FAS at the NS_B horizon, there have been several modifications to the procedure, the most significant probably being the treatment of path Q and the use of ray tracing over a layered Q model.

The single most influential change, however, may be the calibration of the uppermost branch of the logic tree, which previously involved conservatively enveloping the predictions from tectonic GMPEs like the NGA-West2 models, over a broad range of

oscillator periods. For the V7 GMM, the focus was instead on matching the average spectral ordinate between 0.01 and 1.0 s, in order to be consistent with the application of the GMM in the risk analyses. In other words, the upper branch (which influences all the logic-tree branches at larger magnitudes) of the V6 GMM was deliberately conservative (see p.41 of Bommer *et al.*, 2019b); this is not the case for the V7 GMM and the somewhat lower predictions are therefore to be expected.

10.3. Comparison with predictions and epistemic uncertainty of other GMMs

The comparisons carried out between the V6 and V7 models in Figures 10.25-42 are repeated in Figures 10.43 to 10.60 between V7 and the NGA-West2 models (with the exception of the model of Idriss, 2003), for the same zones and magnitude-distance combinations. With the exception of short distances (3 and 5 kilometres) at magnitudes 4.0 and 4.5 and the longer periods ($T > 0.6$ s) at magnitudes below 6.0, the NGA-West2 median predictions are consistently higher than those of the V7 GMM. The predictions of the V6 GMM are also retained for reference.

Figures 10.61 to 10.68 present comparisons of the epistemic uncertainty in the V6, V7, and NGA-West2 models, with and without the addition of the values provided by the Al Atik & Youngs (2014) model.

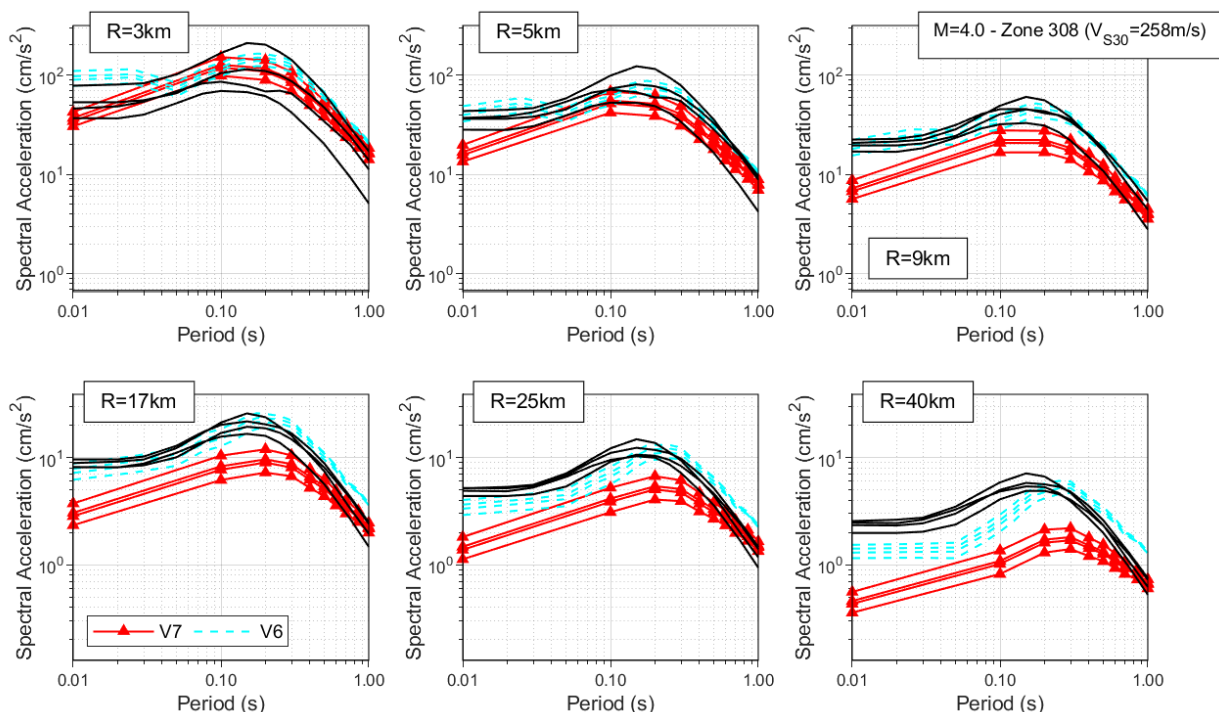


Figure 10.43. Comparison of the median spectral acceleration predictions of the V6, NGA-West2 and V7 GMMs for M_L 4.0 and Zone 308.

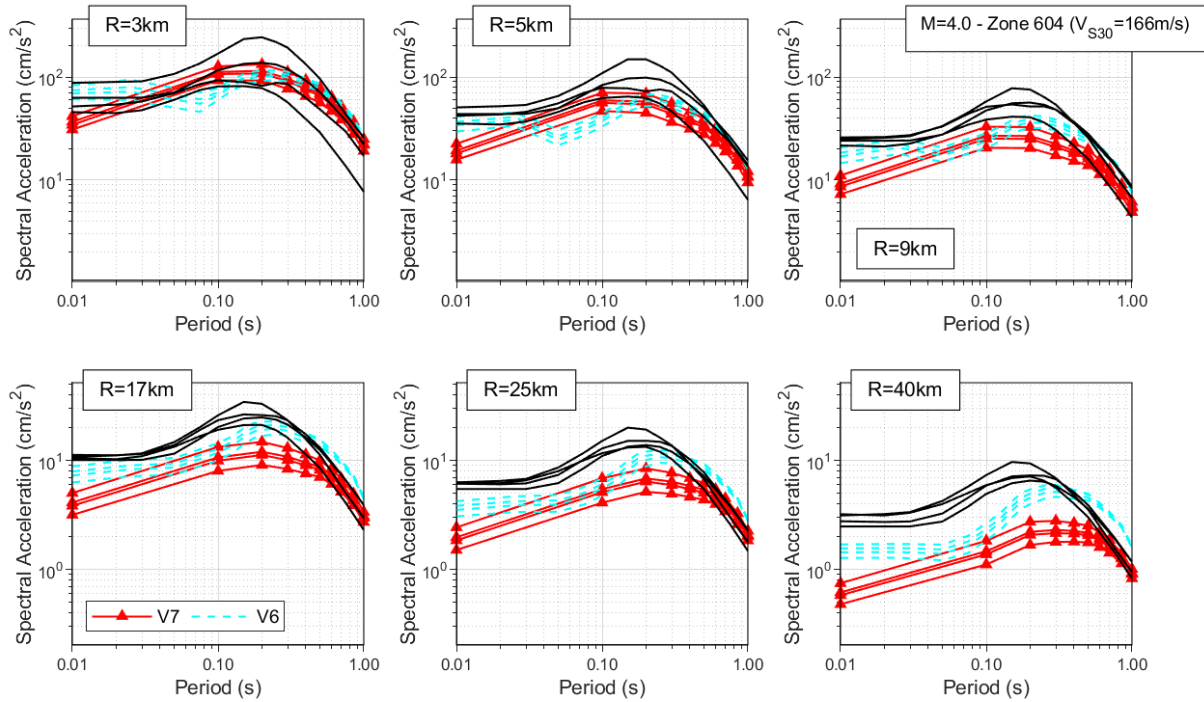


Figure 10.44. Comparison of the median spectral acceleration predictions of the V6, NGA-West2 and V7 GMMs for M_L 4.0 and Zone 604.

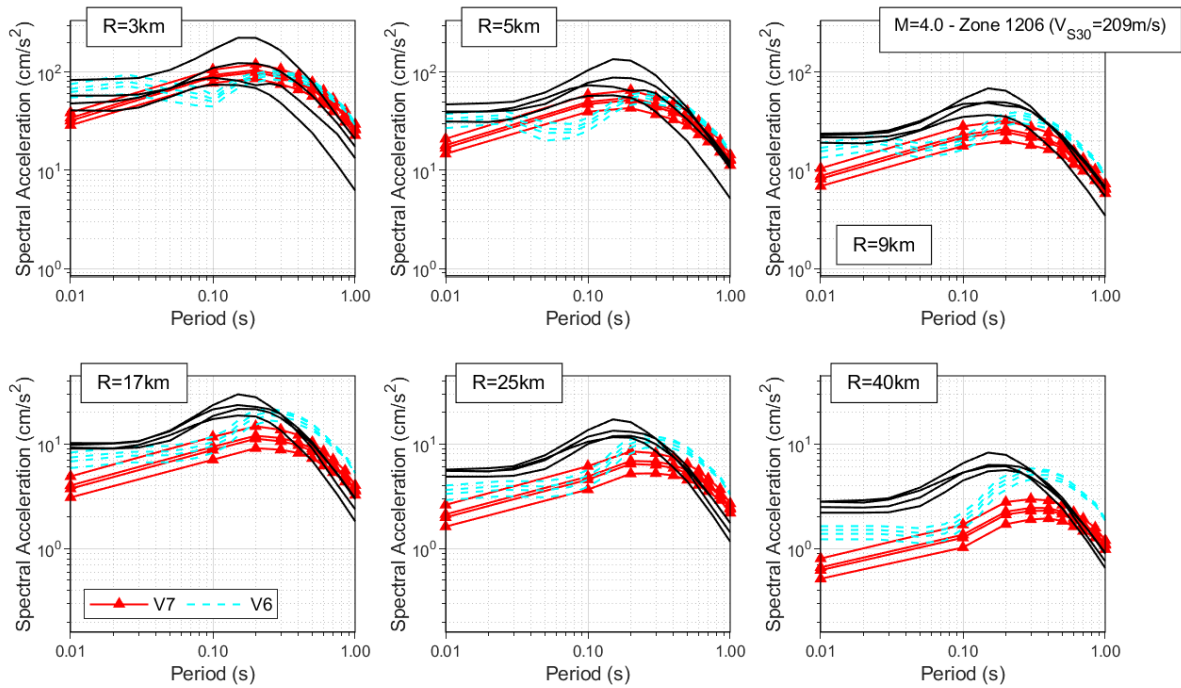


Figure 10.45. Comparison of the median spectral acceleration predictions of the V6, NGA-West2 and V7 GMMs for M_L 4.0 and Zone 1206.

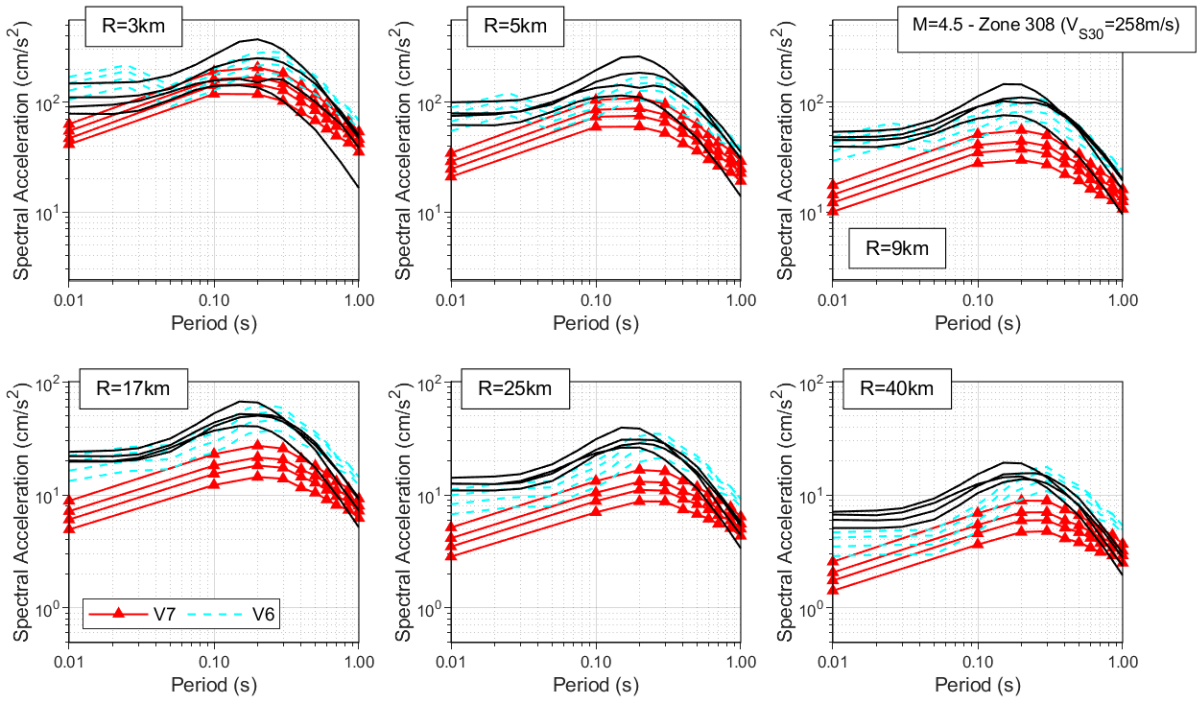


Figure 10.46. Comparison of the median spectral acceleration predictions of the V6, NGA-West2 and V7 GMMs for M_L 4.5 and Zone 308.

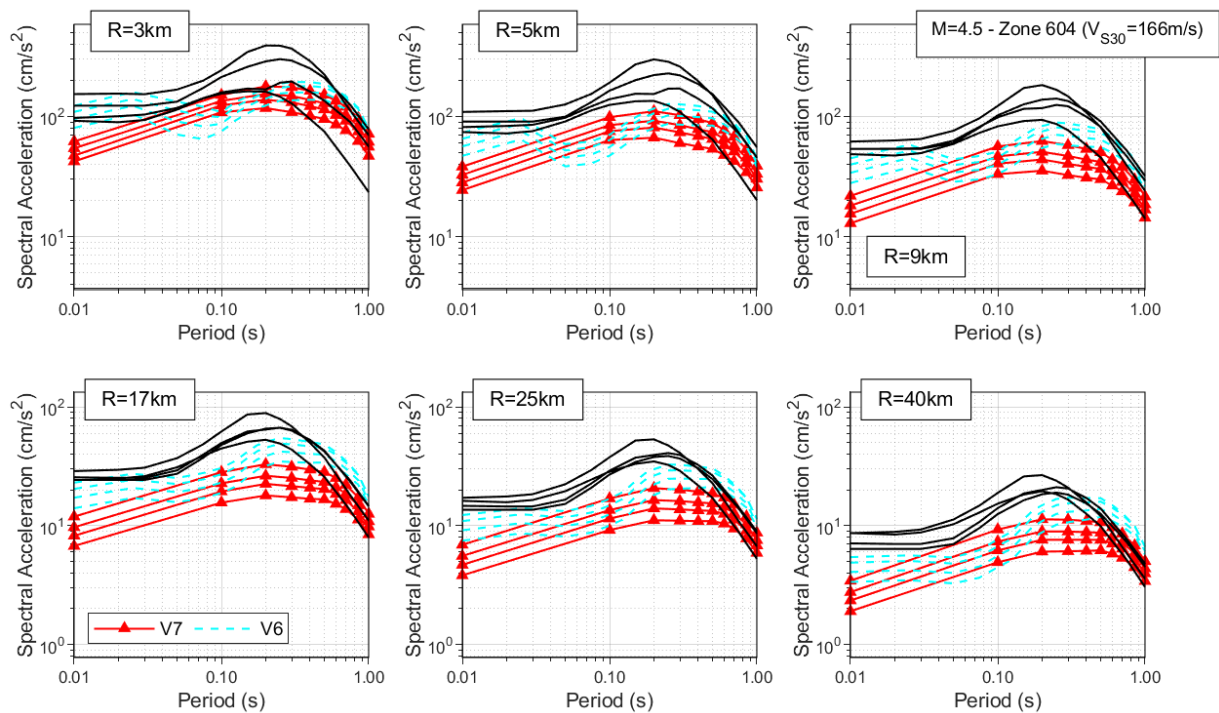


Figure 10.47. Comparison of the median spectral acceleration predictions of the V6, NGA-West2 and V7 GMMs for M_L 4.5 and Zone 604.

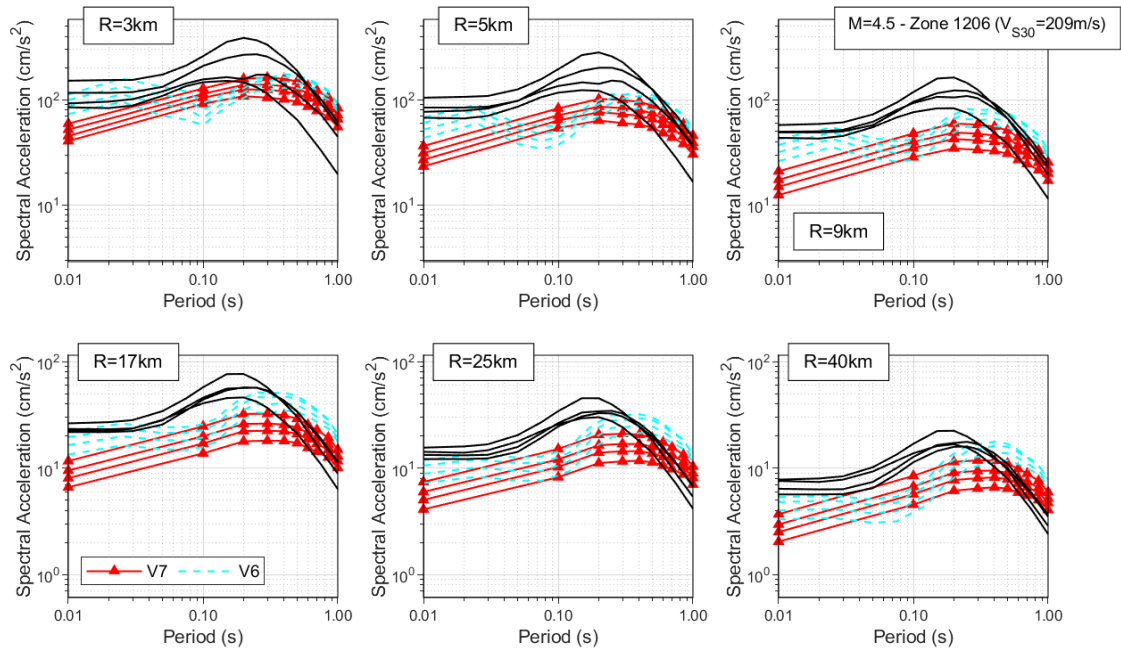


Figure 10.48. Comparison of the median spectral acceleration predictions of the V6, NGA-West2 and V7 GMMs for M_L 4.5 and Zone 1206.

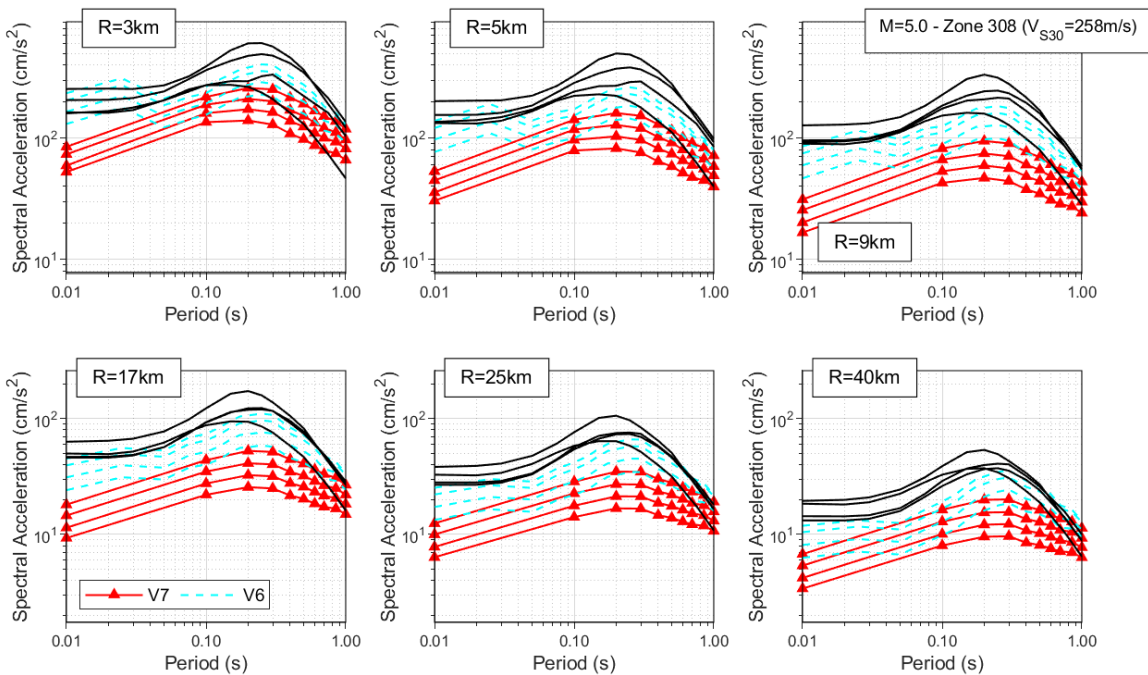


Figure 10.49. Comparison of the median spectral acceleration predictions of the V6, NGA-West2 and V7 GMMs for M_L 5.0 and Zone 308.

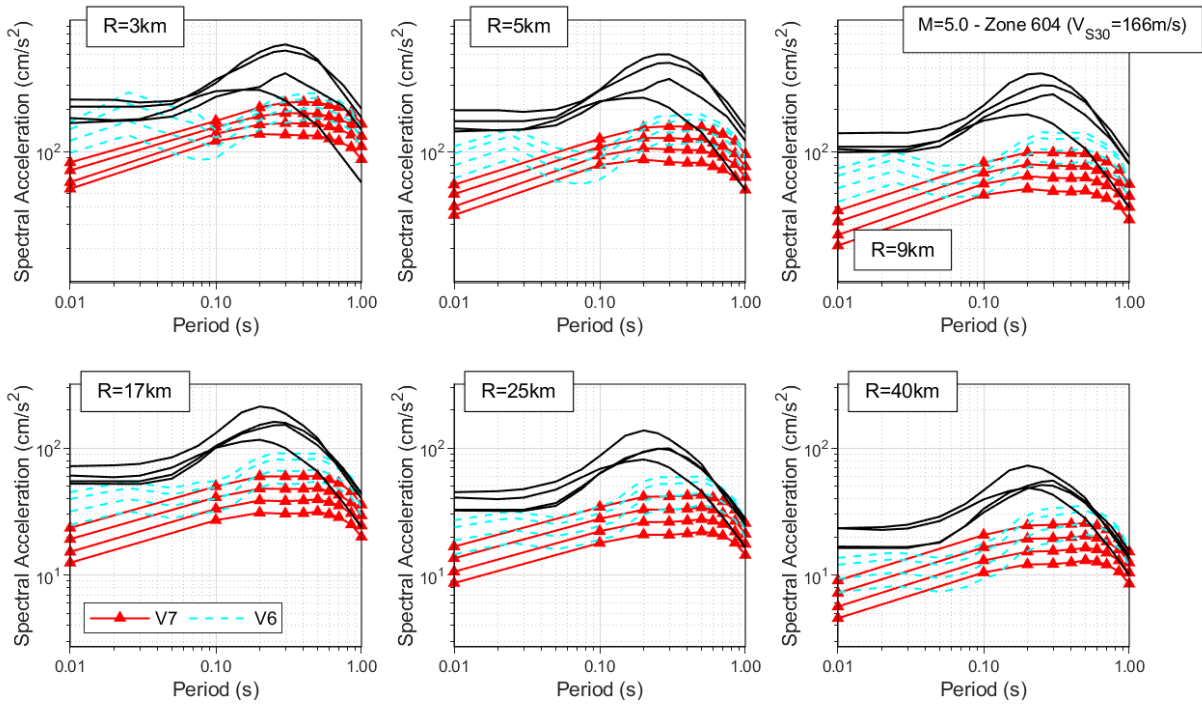


Figure 10.50. Comparison of the median spectral acceleration predictions of the V6, NGA-West2 and V7 GMMs for M_L 5.0 and Zone 604.

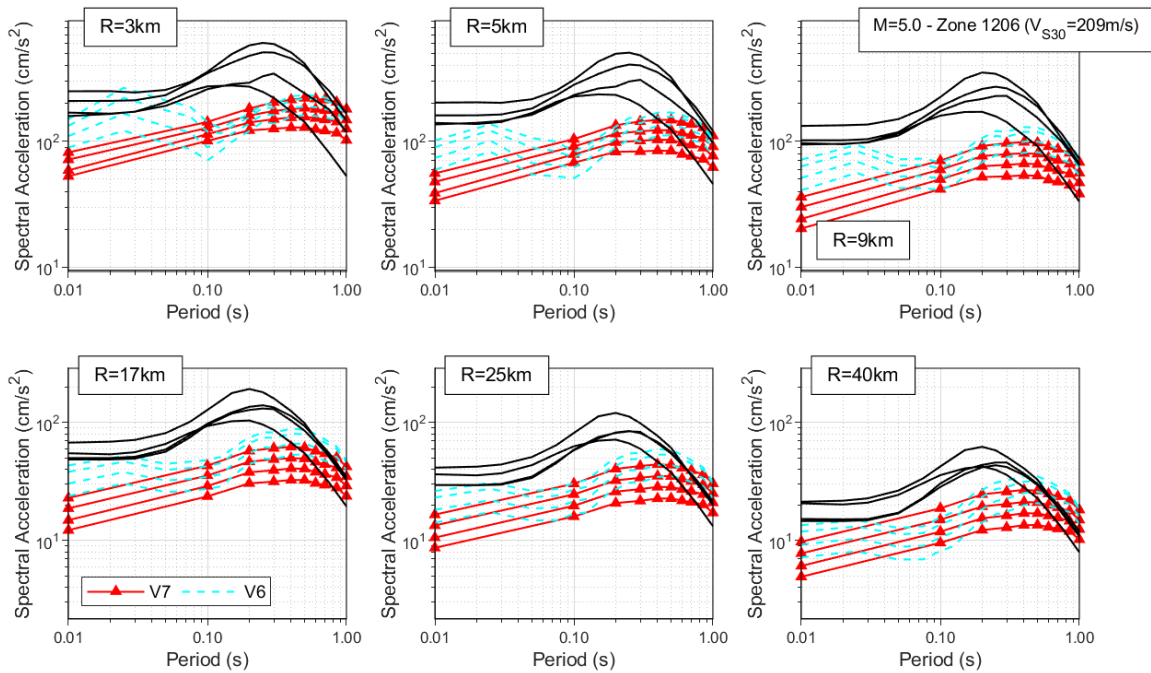


Figure 10.51. Comparison of the median spectral acceleration predictions of the V6, NGA-West2 and V7 GMMs for M_L 5.0 and Zone 1206.

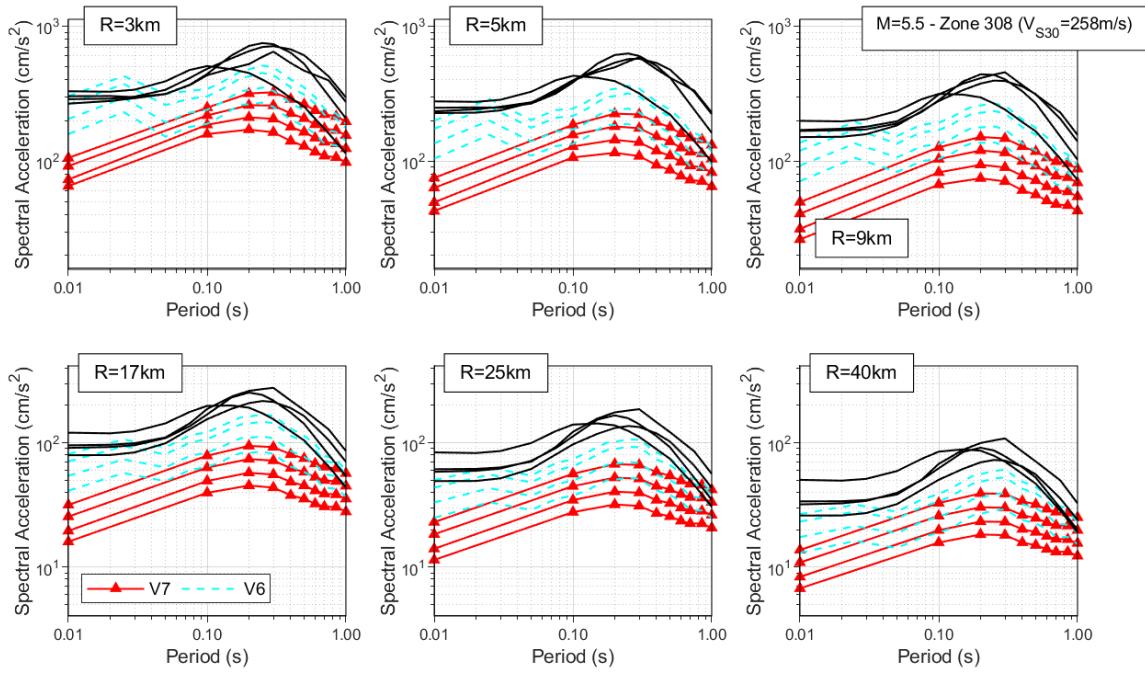


Figure 10.52. Comparison of the median spectral acceleration predictions of the V6, NGA-West2 and V7 GMMs for M_L 5.5 and Zone 308.

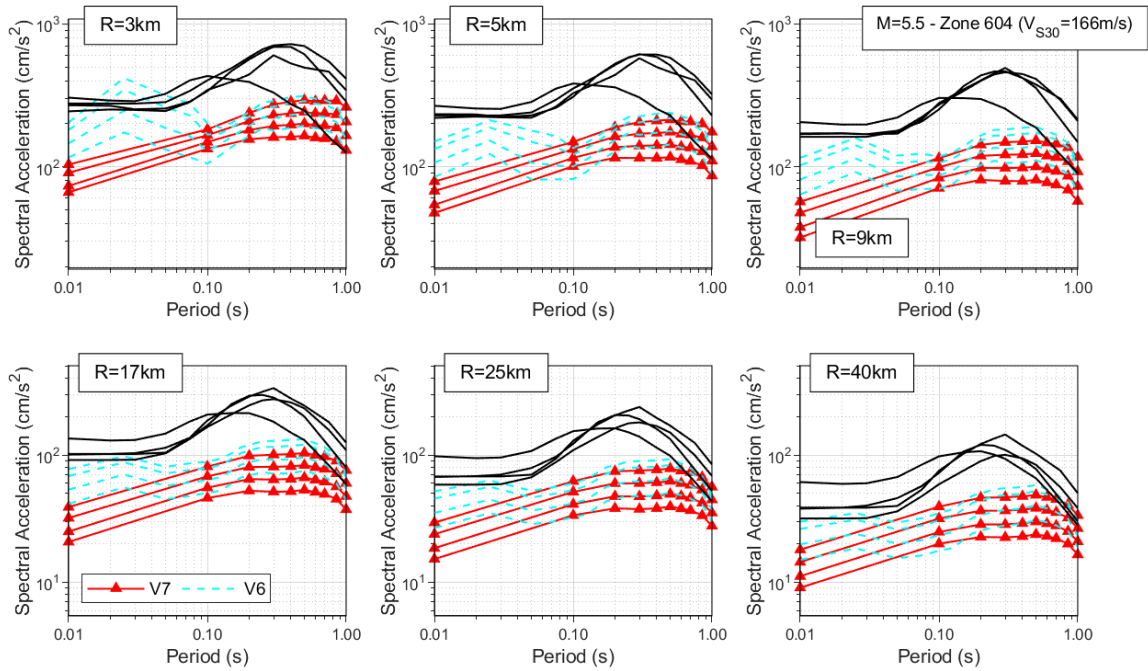


Figure 10.53. Comparison of the median spectral acceleration predictions of the V6, NGA-West2 and V7 GMMs for M_L 5.5 and Zone 604.

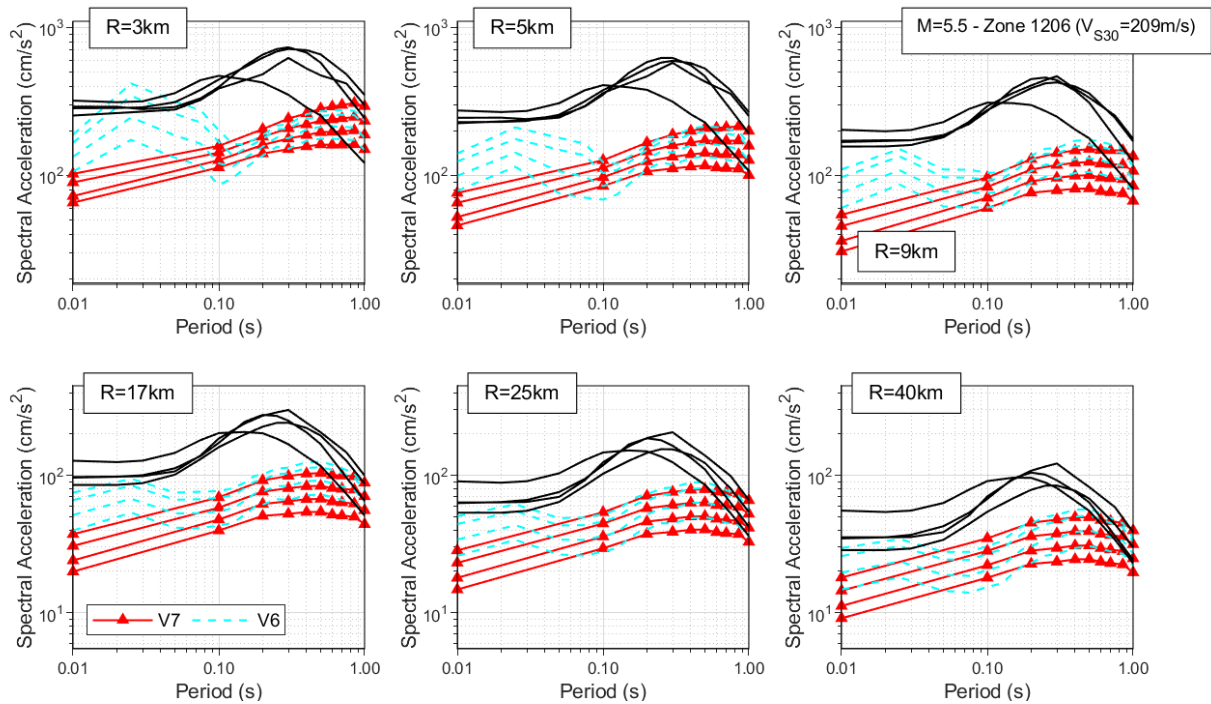


Figure 10.54. Comparison of the median spectral acceleration predictions of the V6, NGA-West2 and V7 GMMs for M_L 5.5 and Zone 1206.

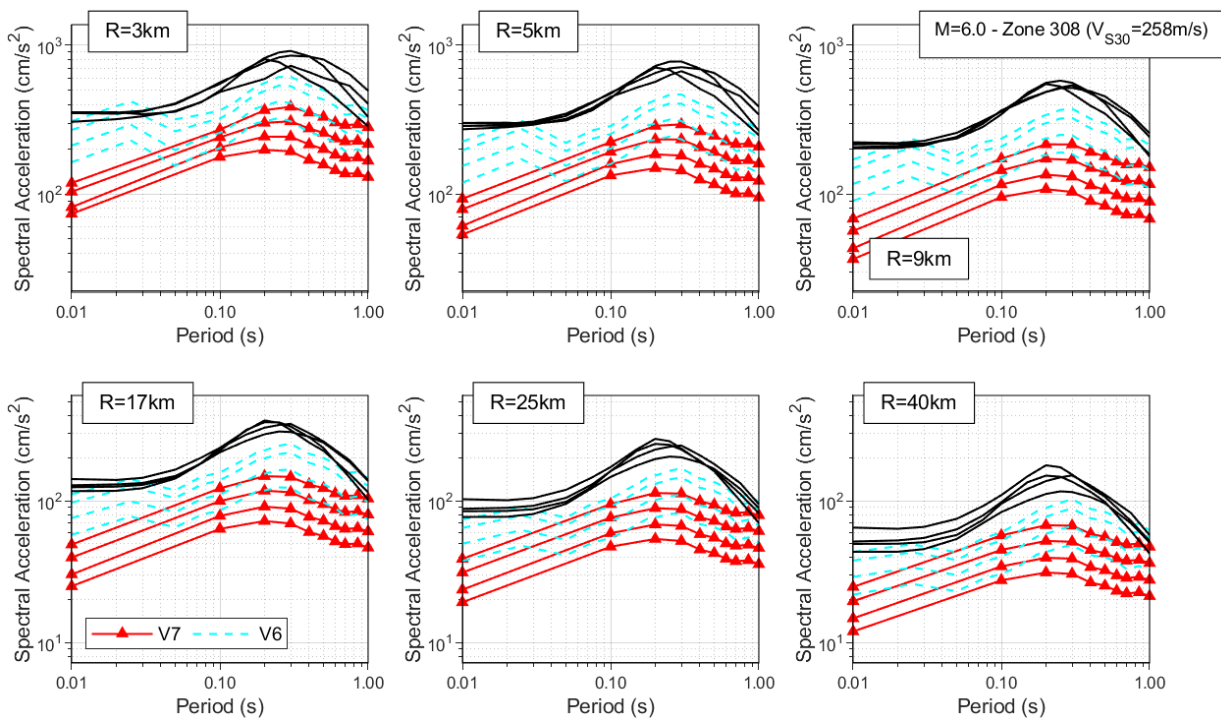


Figure 10.55. Comparison of the median spectral acceleration predictions of the V6, NGA-West2 and V7 GMMs for M_L 6.0 and Zone 308.

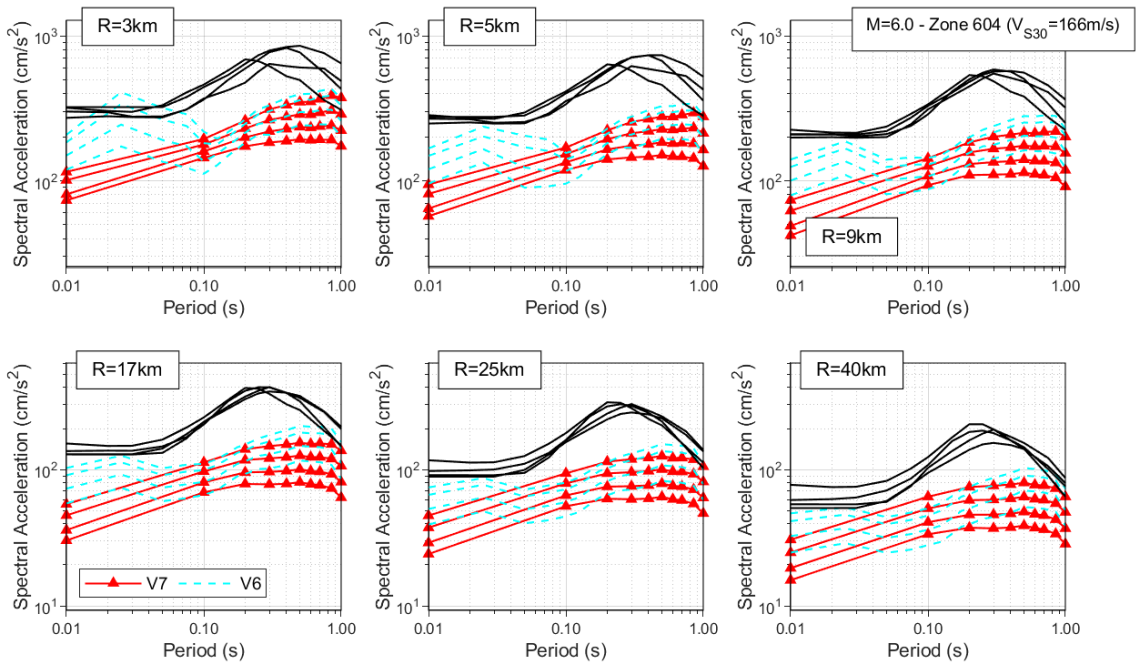


Figure 10.56. Comparison of the median spectral acceleration predictions of the V6, NGA-West2 and V7 GMMs for M_L 6.0 and Zone 604.

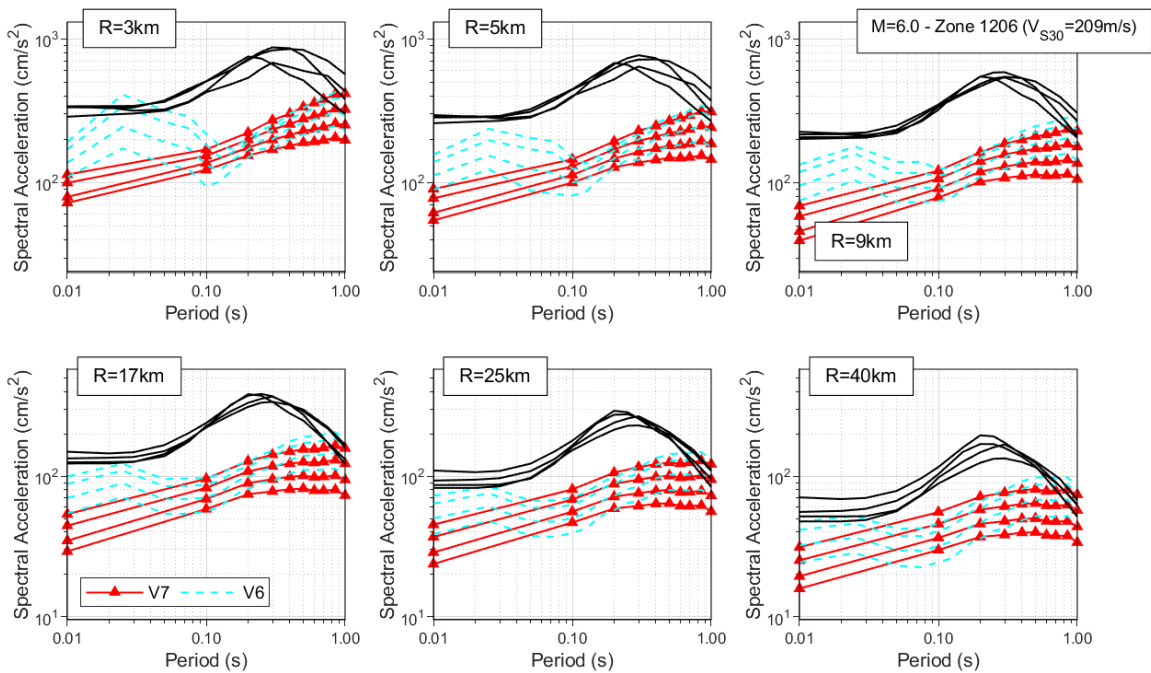


Figure 10.57. Comparison of the median spectral acceleration predictions of the V6, NGA-West2 and V7 GMMs for M_L 6.0 and Zone 1206.

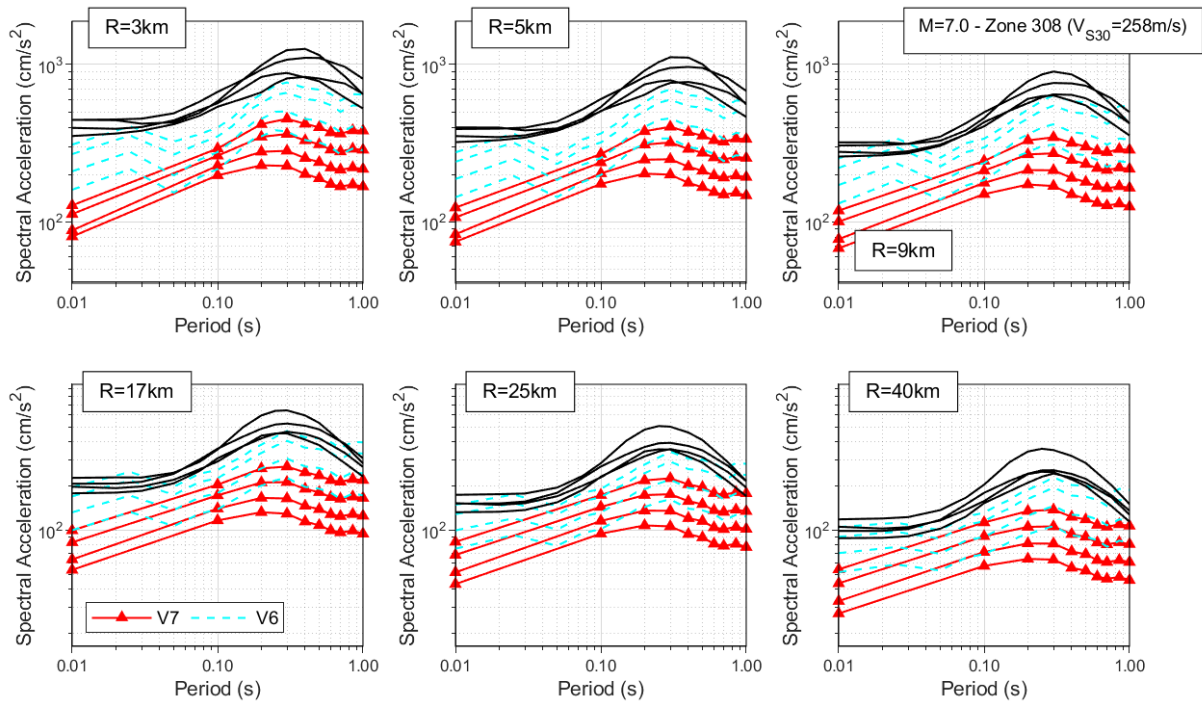


Figure 10.58. Comparison of the median spectral acceleration predictions of the V6, NGA-West2 and V7 GMMs for M_L 7.0 and Zone 308.

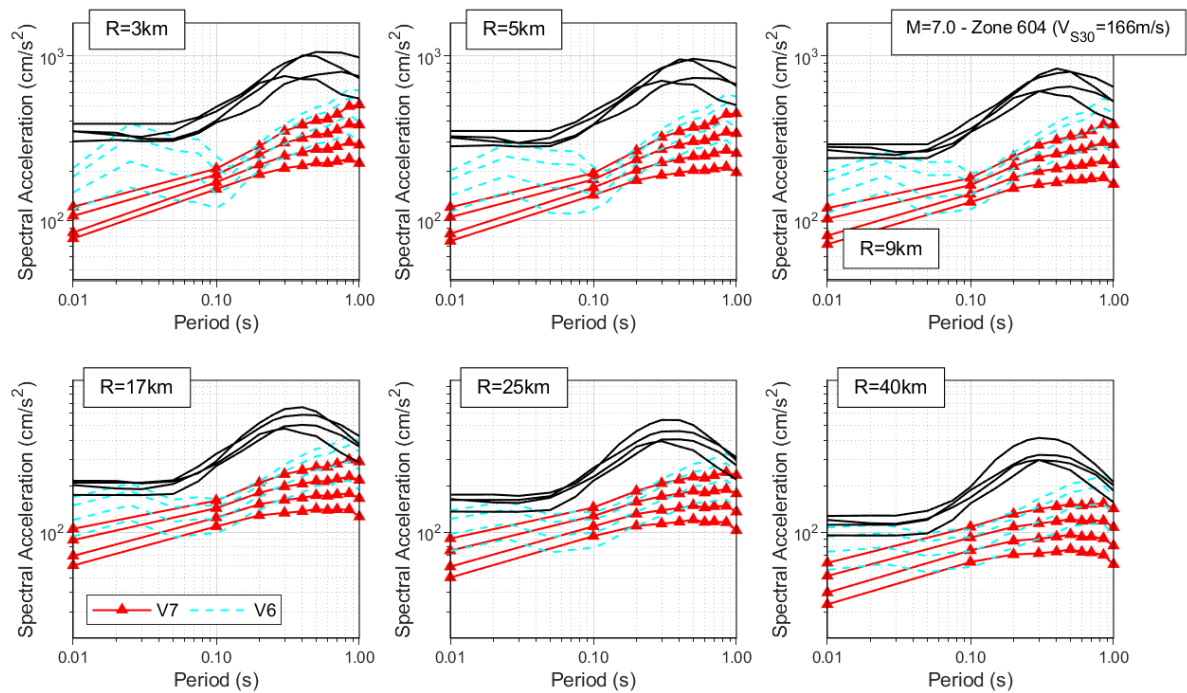


Figure 10.59. Comparison of the median spectral acceleration predictions of the V6, NGA-West2 and V7 GMMs for M_L 7.0 and Zone 604.

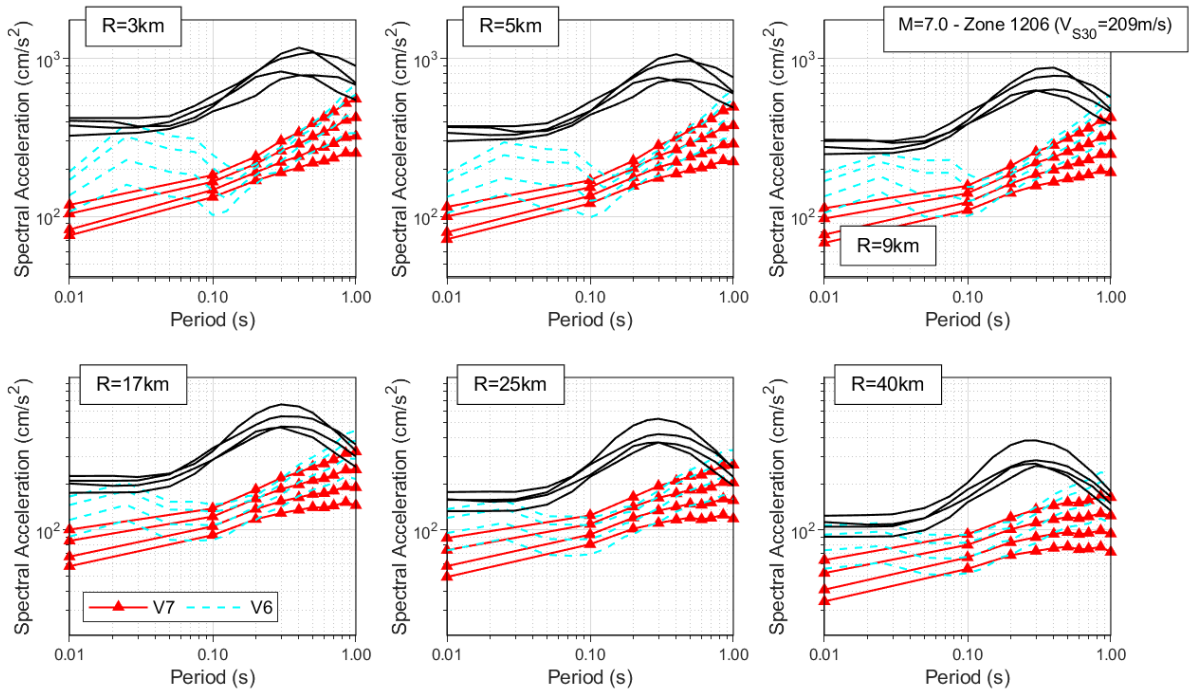


Figure 10.60. Comparison of the median spectral acceleration predictions of the V6, NGA-West2 and V7 GMMs for M_L 7.0 and Zone 1206.

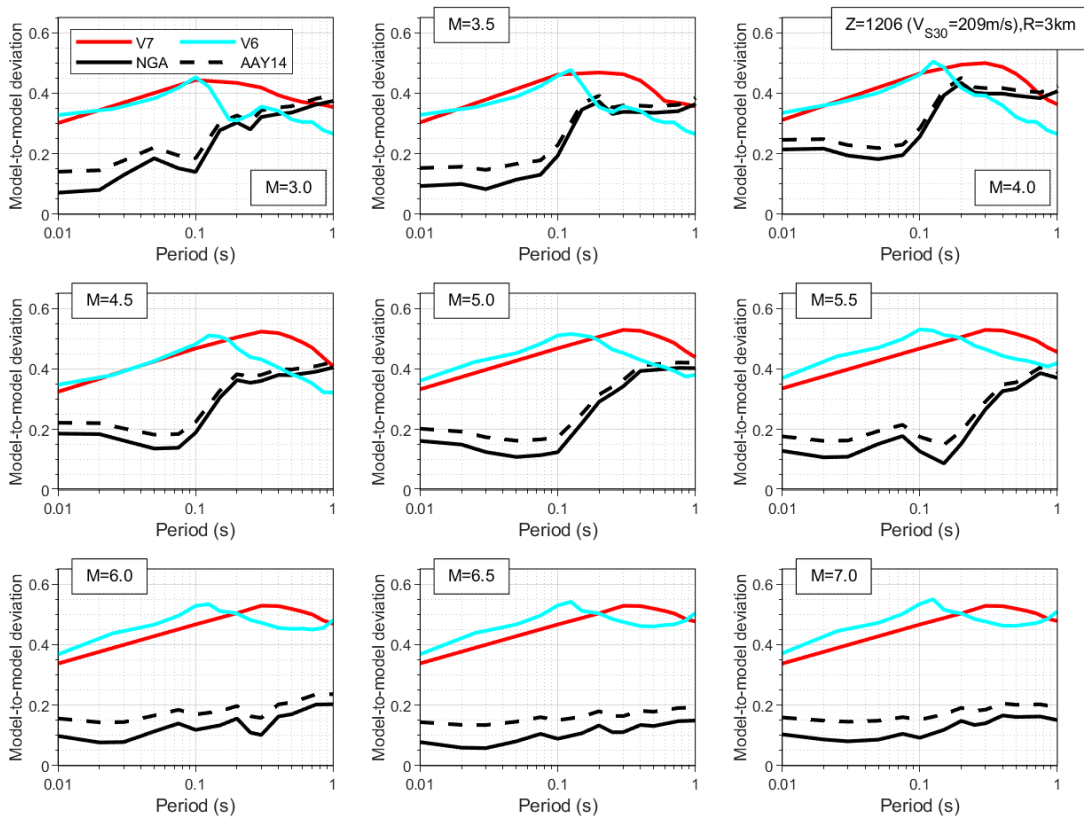


Figure 10.61. Comparison of the epistemic uncertainty in the V6, V7 and NGA-West2 models.

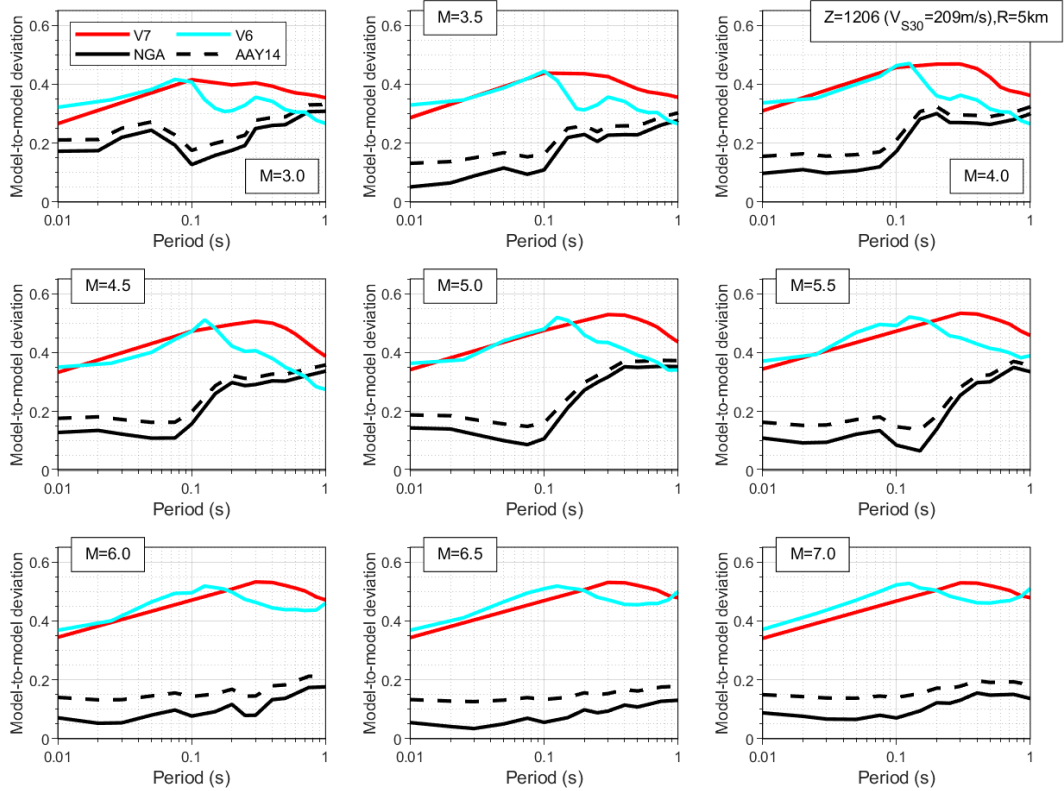


Figure 10.62. Comparison of the epistemic uncertainty in the V6, V7 and NGA-West2 models.

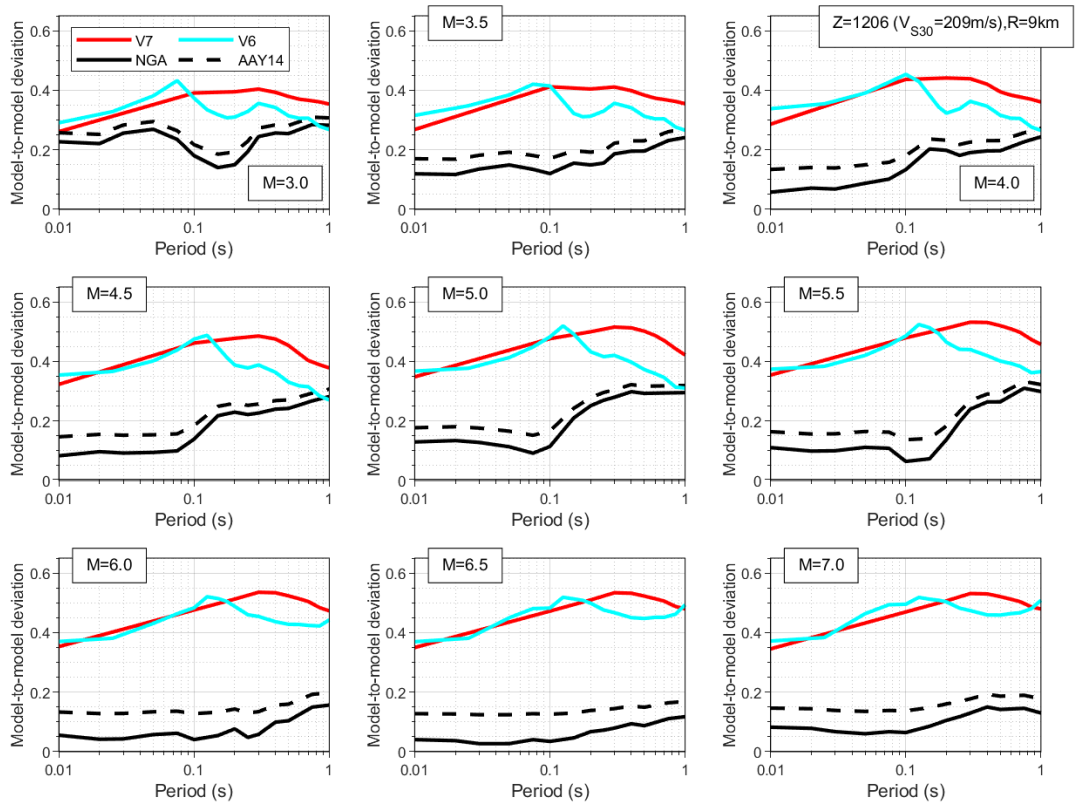


Figure 10.63. Comparison of the epistemic uncertainty in the V6, V7 and NGA-West2 models.

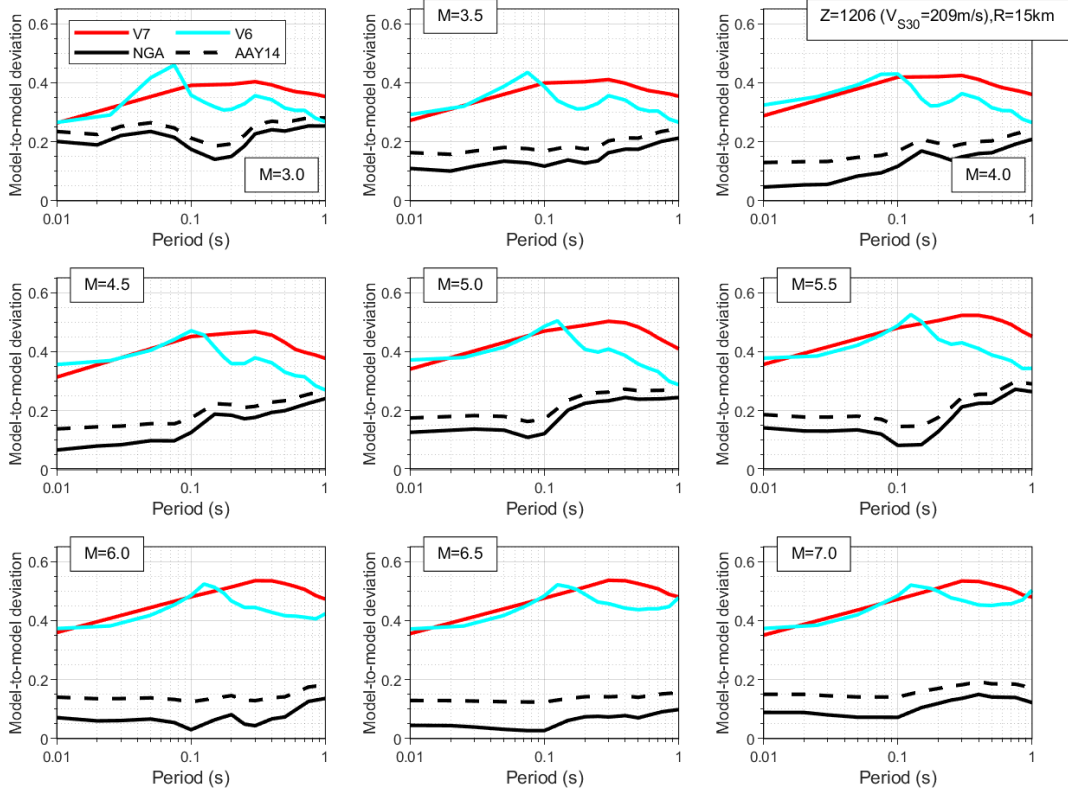


Figure 10.64. Comparison of the epistemic uncertainty in the V6, V7 and NGA-West2 models.

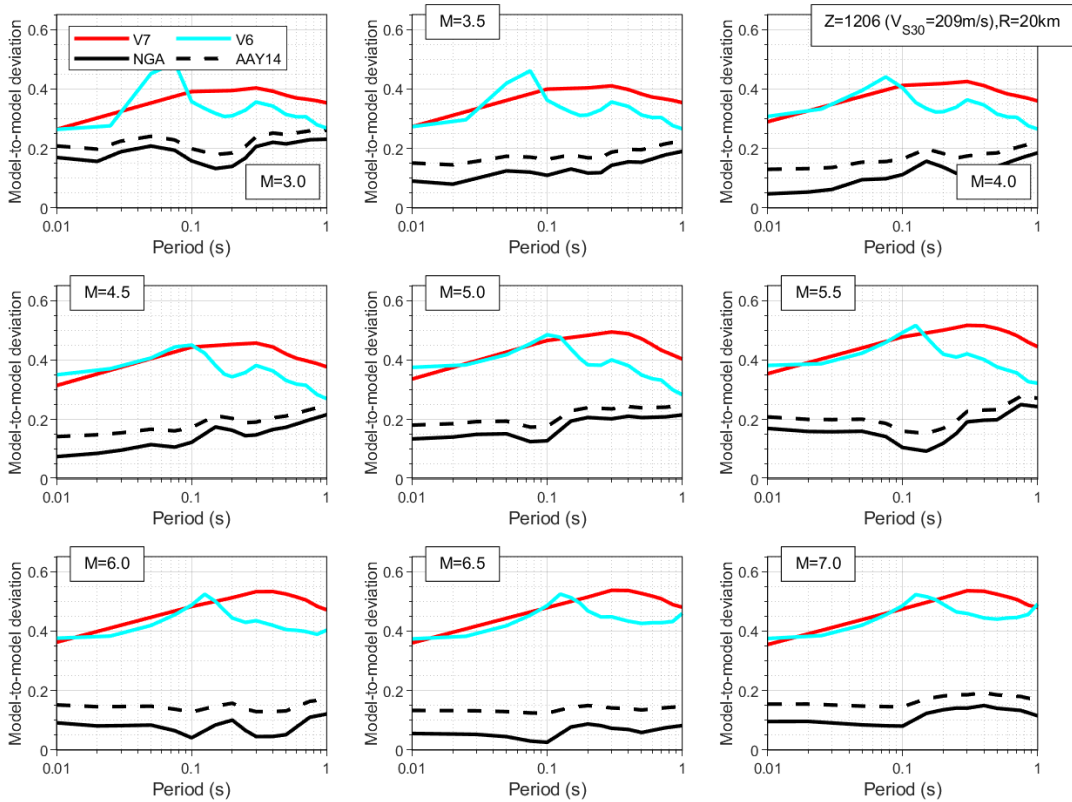


Figure 10.65. Comparison of the epistemic uncertainty in the V6, V7 and NGA-West2 models.

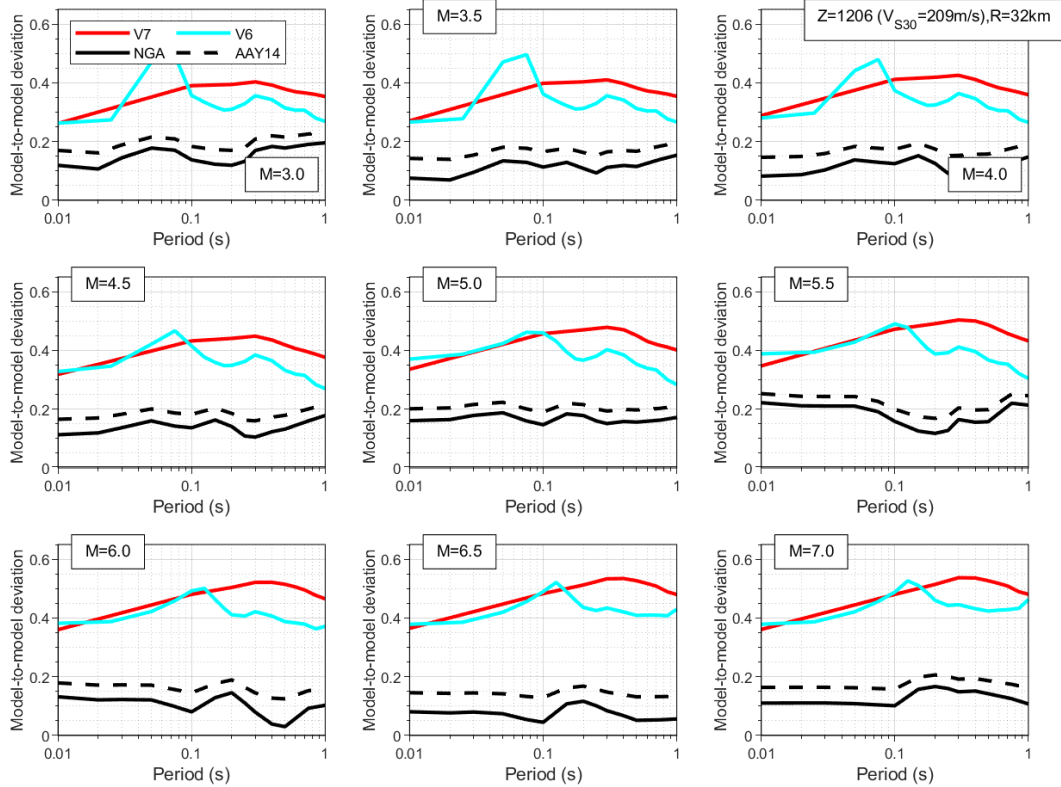


Figure 10.66. Comparison of the epistemic uncertainty in the V6, V7 and NGA-West2 models.

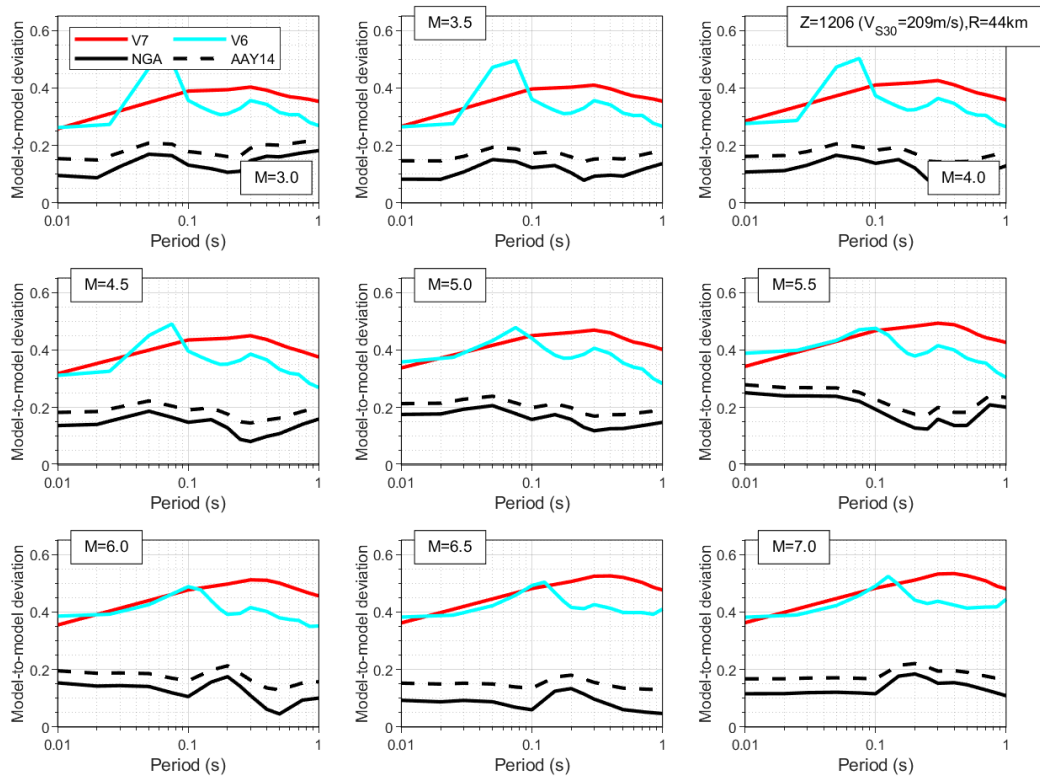


Figure 10.67. Comparison of the epistemic uncertainty in the V6, V7 and NGA-West2 models.

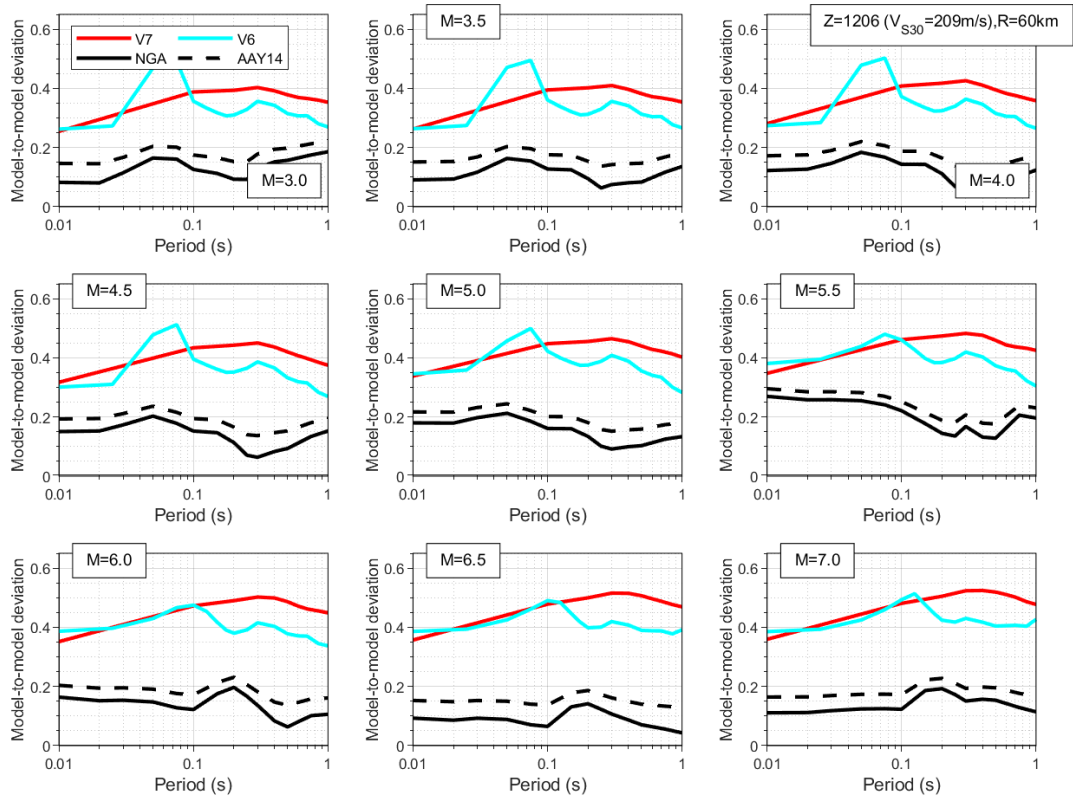


Figure 10.68. Comparison of the epistemic uncertainty in the V6, V7 and NGA-West2 models.

The comparisons in Figures 10.61 to 10.68 shown correspond to predictions only for zone 308, as the results for the other two zones are very similar. As can be observed, the epistemic uncertainty of the V7 GMM is similar to and, at the longer periods, smaller than that of the NGA-West 2 models for small magnitudes and shorter distances. These scenarios are well covered by the Groningen ground-motion database, but not as well covered in the NGA-West2 database. The epistemic uncertainty range in the V7 model increases with both magnitude and distance, becoming consistently larger than that of the NGA-West2 models at larger magnitudes and longer distances, scenarios well covered by the NGA-West2 database, but which correspond to extrapolation far beyond the data for the Groningen GMM. These observations lead us to conclude that there would appear to be adequate epistemic uncertainty captured in the V7 GMM.

11. CONCLUDING REMARKS

In this report we have presented a new ground-motion model (GMM) for the prediction of acceleration response spectra for induced and triggered earthquakes in the Groningen gas field. The V7 model presented in this report is the final outcome of work conducted over a period of about eight years and through multiple iterations. The work has benefitted enormously from ambitious data collection efforts that have included the installation of large networks of strong-motion recording instruments and extensive geotechnical investigations. The GMM development has also been enriched by interdisciplinary collaborations among many engineers and scientists, as well as by rigorous peer review by a panel of world-renowned experts.

The V7 model predicts 5% damped horizontal acceleration response spectra at oscillator periods between 0.01 and 1.5 seconds for magnitudes from M_L 2.5 to about 7.3 and rupture distances ranging from the epicentral location of Groningen earthquakes to distances of around 40 to 50 km. The predictions account for non-linear site amplification effects through a zonation map and associated frequency-dependent amplification factors. The model, therefore, cannot be applied outside the limits of the area defined for the hazard and risk study, namely the boundary of the gas field plus a 5 km buffer onshore. The GMM is defined in terms of a logic-tree that captures the epistemic uncertainty in the predictions, particularly at the larger magnitudes currently considered in the hazard and risk calculations.

The primary purpose of the GMM is to provide inputs to seismic risk calculations, for which the average response spectral acceleration over 10 periods from 0.01 to 1.0 second is the intensity metric used in the fragility functions. The model predicts the geometric mean horizontal component but for the risk calculations this is transformed to the arbitrary horizontal component through addition of the component-to-component variability. The model may also be employed for other applications, but users should be aware that the empirical constraint at periods greater than 1 second is limited due to the need to apply filters to remove long-period noise in the recordings. It should also be noted that the prediction of PGA—equivalent the spectral acceleration at 0.01 s—tend to be underestimated at short distances in the magnitude range of the data; this is not viewed as a major concern for application of the model in the risk calculations through the average spectral acceleration but should be borne in mind if the GMM is used to generate hazard estimates in terms of PGA. For predictions of PGV for earthquakes in the magnitude range of the observed earthquakes in Groningen, a separate empirical GMM has been developed and is presented in the report by Bommer *et al.* (2021b).

During the course of the model development, it became apparent that there are differences in the average short-period spectral accelerations from the two accelerograph networks operating in the field, with recordings from within buildings

(mostly houses) showing lower amplitudes on average. This effect, which appears to affect only some of the B-stations and does not seem to be related to the size of building, is not well understood. Analyses have shown that it is not the result of dynamic soil-structure interaction, but it may be due to layers of improved (pre-loaded and compressed prior to construction) soil directly below building foundations. The model has been derived using all recordings from both the B-network stations located in houses and the free-field G-network stations, since removal of the former would have seriously impoverished the database in terms of magnitude and distance distribution. Moreover, the model is intended for predicting motions experienced within Groningen buildings, and from this perspective the B-network recordings are clearly relevant.

The V7 GMM logic-tree has been shown to capture an appropriate range of epistemic uncertainty. The upper branch of the logic-tree is calibrated to match ground motions expected from tectonic earthquakes at the reference rock horizon, but the surface predictions at larger magnitudes differ from the response spectra predicted by tectonic GMMs both because of the different spectral shapes observed at the rock horizon and the site amplification effects associated with the unique near-surface profiles in Groningen. These differences vindicate the choice to develop a ground-motion model specifically for the region rather than to adopt GMMs developed for other regions.

The uncertainty associated with the ground-motion predictions for magnitudes much greater than 5 is inevitably large since this represents a large extrapolation beyond the limits of the data: the largest earthquake to have occurred in the field is still the 2012 M_L 3.6 Huizinge earthquake. The application of the GMM to magnitudes larger than 7 corresponds to a huge extrapolation beyond the data. We note that a second workshop to address the issue of the maximum magnitude for earthquakes in the Groningen field has been organised (originally for October 2021 but it will now take place in June 2022 due to the ongoing effects of the Covid-19 pandemic).

The V7 GMM is fit for purpose and can be used with confidence in the Groningen field within the magnitude and distance ranges for which it is calibrated. The model should, of course, be checked against new ground-motion recordings from any future earthquakes, although tests with recordings from a single earthquake cannot be conclusive due to the between-event variability. In the more immediate future, it is hoped that the model will also be 'tested' through implementation, and we welcome feedback from all and any users. Indeed, this final version of the report has been influenced not only by the detailed review by the international expert panel but also by feedback from NAM, KNMI and TNO teams implementing the model in their respective risk engines.

In the near future, we will publish a paper presenting the complete database of ground-motion, geotechnical and geophysical data used to derive the model and to make the entire database available for download by any interested group (Ntinalexis et al.,

2022). We would be delighted to see other researchers produce a superior model in the future since we have no illusions that the V7 GMM is in any sense a perfect model (if such a thing even exists). During the course of the model derivation through multiple iterations, there have been numerous criticisms of individual components of the model—the more constructive of which have sometimes influenced the GMM development—and there have been cases of alternative elements of the model being proposed, in isolation, by other groups. The real challenge is to build a complete model that is applicable to the full range of magnitudes and distances considered in the risk calculations, reflecting local conditions, and also appropriately capturing epistemic uncertainty. We would very much welcome efforts by others to generate new and better models that could replace the V7 GMM in its entirety. A more refined partitioning of epistemic uncertainty and aleatory variability, especially in the site response component of the model, is one particular aspect of the GMM that could be pursued by any party interested in providing a better model. However, until such models are developed, peer reviewed, and published, we believe that the V7 GMM is entirely suitable for its intended application of seismic risk calculations in the Groningen field and can be used with confidence.

12. References

- Abercrombie, R.E. & P.C. Leary (1993). Source parameters of small earthquakes recorded at 2.5 km depth, Cajon Pass, southern California: implications for earthquake scaling. *Geophysical Research Letters* **20**, 1511-1514.
- Abrahamson N.A., J.F. Schneider & J.C. Stepp (1991). Empirical spatial coherency functions for application to soil-structure interaction analyses. *Earthquake Spectra* **7**(1), 1-27.
- Abrahamson, N.A., W.J. Silva & R. Kamai (2014). Summary of the ASK14 ground motion relation for active crustal regions. *Earthquake Spectra* **30**(3), 2015-1055.
- Abrahamson, N.A. & R.R. Youngs (1992). A stable algorithm for regression analyses using the random effects model. *Bulletin of the Seismological Society of America* **82**(1), 505-510.
- Afacan, K.B., S. Yniesta, A. Shafee, J.P. Stewart & S.J. Brandenberg (2019). Total stress analysis of soft clay ground response in centrifuge models. *Journal of Geotechnical and Geoenvironmental Engineering* **145**(1), 04019061.
- Akkar, S. & J.J. Bommer (2006). Influence of long-period filter cut-off on elastic spectral displacements. *Earthquake Engineering & Structural Dynamics* **35**(9), 1145-1165.
- Akkar, S., M.A. Sandıkkaya & J.J. Bommer (2014). Empirical ground-motion models for point- and extended-source crustal earthquake scenarios in Europe and the Middle East. *Bulletin of Earthquake Engineering* **12**(1), 359-387. *Erratum: 12*(1), 389-390.
- Al Atik, L. (2015). *NGA-East: Ground-motion standard deviation models for central and eastern North America*. PEER Report No. 2015/07. Pacific Earthquake Engineering Research Center, University of California at Berkeley, 217 pp.
- Al Atik L. & R.R. Youngs (2014). Epistemic uncertainty for NGA-West2 models. *Earthquake Spectra* **30**(3), 1301-1318.
- Anderson, J.G. & S.E. Hough (1984). A model for the shape of the Fourier amplitude spectrum of acceleration at high frequencies. *Bulletin of the Seismological Society of America* **74**, 1969-1993.
- Atkinson, G.M. (1993). Note on ground motion parameters for Eastern North America: duration and H/V ratio. *Bulletin of the Seismological Society of America* **83**, 587-596.
- Atkinson, G. M. (2006). Single-station sigma. *Bulletin of the Seismological Society of America* **96**(2), 446-455.
- Bahrampouri, M. (2021). *Quantification of Uncertainties for Conducting Partially Non-Ergodic Probabilistic Seismic Hazard Analysis*. Ph.D. Dissertation, Virginia Tech, Blacksburg, Virginia, 166 pp.
- Bahrampouri, M., A. Rodriguez-Marek, & J.J. Bommer (2019). Mapping the uncertainty in modulus reduction and damping curves onto the uncertainty of site amplification functions. *Soil Dynamics and Earthquake Engineering* **126**, 105091.
- Bindi, D. & S.R. Kotha (2020). Spectral decomposition of the Engineering Strong Motion (ESM) flat file: Regional attenuation, source scaling and Arias stress drop. *Bulletin of Earthquake Engineering* **18**(6), 2581-2606.

- Bindi, D., M. Massa, L. Luzi, G. Ameri, E. Pacor, R. Puglia & P. Augliera (2014). Pan-European ground-motion prediction equations for the average horizontal component of PGA, PGV, and 5%-damped PSA at spectral periods up to 3.0 s using the RESORCE dataset. *Bulletin of Earthquake Engineering* **12**(1), 391-430.
- Bommer, J.J., B. Dost, B. Edwards, P.P. Kruiver, P. Meijer, M. Ntinalexis, A. Rodriguez-Marek, E. Ruigrok, J. Spetzler & P.J. Stafford (2018). *V5 Ground-Motion Model for the Groningen Field*. Revision 1, 14 March 2018, 299 pp.
- Bommer, J.J., B. Dost, B. Edwards, P.P. Kruiver, P. Meijer, M. Ntinalexis, A. Rodriguez-Marek & P.J. Stafford (2016). *Development of V3 GMPEs for response spectral accelerations and significant durations from induced earthquakes in the Groningen field*. Version 0, 8 July 2016, 476 pp.
- Bommer, J.J., B. Dost, B. Edwards, P.J. Stafford, J. van Elk, D. Doornhof & M. Ntinalexis (2016a). Developing an application-specific ground-motion model for induced seismicity. *Bulletin of the Seismological Society of America* **106**(1), 158-173.
- Bommer, J.J., B. Dost, B. Edwards, P.P. Kruiver, P. Meijers, M. Ntinalexis, B. Polidoro, A. Rodriguez-Marek & P.J. Stafford (2015). *Development of Version 2 GMPEs for response spectral accelerations and significant durations from induced earthquakes in the Groningen field*. Version 2, 29 October 2015, 515 pp.
- Bommer, J.J., B. Edwards, P.P. Kruiver, A. Rodriguez-Marek, P.J. Stafford, B. Dost, M. Ntinalexis, E. Ruigrok & J. Spetzler & (2019b). *V6 Ground-Motion Model for Induced Seismicity in the Groningen Gas Field*. Revision 1, 19 December 2019, 196 pp.
- Bommer, J. J. & M. Ntinalexis (2020). *A Preliminary Analysis of the Surface Ground-Motions Recorded During the Zijldijk ML 2.5 Earthquake of 2 May 2020*, 13 May 2020
- Bommer, J.J., P.J. Stafford, B. Edwards, B. Dost, E. van Dedem, A. Rodriguez-Marek, P. Kruiver, J. van Elk, D. Doornhof & M. Ntinalexis (2017). Framework for a ground-motion model for induced seismic hazard and risk analysis in the Groningen gas field, The Netherlands. *Earthquake Spectra* **33**(2), 481-498.
- Bommer, J.J., P. J. Stafford, J. E. Alarcón & S. Akkar (2007). The Influence of Magnitude Range on Empirical Ground-Motion Prediction. *Bulletin of the Seismological Society of America* **97**(6), 2152-2170.
- Bommer, J. J., P. J. Stafford & M. Ntinalexis (2019a). *Updated empirical GMPEs for PGV from Groningen earthquakes*, 10 March 2019
- Bommer, J. J., P. J. Stafford & M. Ntinalexis (2021a). *Empirical Equations for the Prediction of Peak Ground Velocity due to Induced Earthquakes in the Groningen Gas Field*, 1st June 2021.
- Bommer, J. J., P. J. Stafford & M. Ntinalexis (2021b). *Empirical Equations for the Prediction of Peak Ground Velocity due to Induced Earthquakes in the Groningen Gas Field*, 10 October 2021, 35 pp.
- Bommer, J.J. & J. van Elk (2017). Comment on “The maximum possible and maximum expected earthquake magnitude for production-induced earthquakes at the gas field in Groningen, The Netherlands” by Gert Zöller and Matthias Holschneider. *Bulletin of the Seismological Society of America* **107**(3), 1564-1567.

Boore, D.M. (2005). SMSIM – Fortran programs for simulating ground motions from earthquakes: Version 2.3—A revision of OFR 96-80. US Geological Survey Open-File Report 00-509, 55 pp.

Boore, D. M. (2009). Comparing stochastic point-source and finite-source ground-motion simulations: SMSIM and EXSIM. *Bulletin of the Seismological Society of America* **99**, 3202-3216.

Boore, D.M. & J. Boatwright (1984). Average body-wave radiation coefficients. *Bulletin of the Seismological Society of America* **74**, 1615-1621.

Boore, D.M., J.P. Stewart, E. Seyhan & G.M. Atkinson (2014). NGA-West2 equations for predicting PGA, PGV, and 5% damped PSA for shallow crustal earthquakes. *Earthquake Spectra* **30**(3).

Bosch, J.H.A., R. Harting & J.L. Gunnink (2014). *Lithologische karakterisering van de ondiepe ondergrond van Noord-Nederland (Topsysteem hoofdgebied 5)*. Geological Survey of the Netherlands TNO report 2014-R10680.

Boulanger, R.W., R. Arulnathan, L.F. Harder, R.A. Torres & M.W. Driller (1997). *Dynamic properties of Sherman Island peat*. Report UCD/CGM-97/01, Department of Civil & Environmental Engineering, University of California, Davis, California.

Bourne, S.J., S.J. Oates, J.J. Bommer, B. Dost, J. van Elk & D. Doornhof (2015). A Monte Carlo method for probabilistic hazard assessment of induced seismicity due to conventional natural gas production. *Bulletin of the Seismological Society of America* **105**(3), 1721-1738.

Brune, J.N. (1970). Tectonic stress and spectra of seismic shear waves from earthquakes. *Journal of Geophysical Research* **75**, 4997-5009. Correction (1971), **76**(20), 5002.

Cabas, A., Rodriguez-Marek, A., & Bonilla, L. F. (2017). Estimation of site-specific kappa (κ_0)-consistent damping values at KiK-net sites to assess the discrepancy between laboratory-based damping models and observed attenuation (of seismic waves) in the field. *Bulletin of the Seismological Society of America* **107**(5), 2258-2271.

Campbell, K.W. & Y. Bozorgnia (2014). NGA-West2 ground motion model for the average horizontal components of PGA, PGV, and 5%-damped elastic pseudo-acceleration response spectra. *Earthquake Spectra* **30**(3), 1087-1115.

Cavalieri, F., A.A. Correia & R. Pinho (2020). *Soil-structure-interaction analysis in support of Groningen B-stations verification effort*. Report Deliverable D-16, Mosayk, Italy, 52 pp.

Chiou, B.S.J. & R.R. Youngs (2014). Update of the Chiou and Youngs NGA model for the average horizontal component of peak ground motion and response spectra. *Earthquake Spectra* **30**(3), 1117-1153.

Cotton, F., R. Archuleta & M. Causse (2013). What is sigma of the stress drop? *Seismological Research Letters* **84**(1), 42-48.

Darendeli, M. (2001). *Development of a new family of normalized modulus reduction and material damping curves*. Ph.D. Thesis, Dept. of Civil Eng., University of Texas, Austin, TX.

Den Haan, E.J. & G.A.M. Kruse (2007). Characteristics and engineering properties of Dutch peats. *Proceedings of 2nd International Workshop on Characterisation and Engineering Properties of Natural Soils*, Singapore, Taylor & Francis, vol. 3, 2108-2133.

- Douglas, J. & D.M. Boore (2011). High-frequency filtering of strong-motion records. *Bulletin of Earthquake Engineering* **9**(2), 395-409.
- Dost, B., B. Edwards & J.J. Bommer (2018). The relationship between **M** and M_L – a review and application to induced seismicity in the Groningen gas field, the Netherlands. *Seismological Research Letters* **89**(3), 1062-1074.
- Dost, B., B. Edwards & J.J. Bommer (2019). *Erratum*: The relationship between **M** and M_L – a review and application to induced seismicity in the Groningen gas field, the Netherlands. *Seismological Research Letters* **90**(4), 1660-1662.
- Dost, B., E. Ruigrok & J. Spetzler (2017). Development of probabilistic seismic hazard assessment for the Groningen gas field. *Netherlands Journal of Geoscience* **96**(5), s235-s245.
- Dost, B., T. van Eck & H. Haak (2004). Scaling of peak ground acceleration and peak ground velocity recorded in the Netherlands. *Bolletino di Geofisica Teorica ed Applicata* **45**(3), 153-168.
- Edwards, B., D. Fäh, and D. Giardini (2011). Attenuation of seismic shear wave energy in Switzerland. *Geophysical Journal International* **185**(2), 967-984.
- Edwards, B. & M. Ntinalexis (2021). Usable bandwidth of weak-motion data: application to induced seismicity in the Groningen Gas Field, the Netherlands. *Journal of Seismology*, doi: 10.1007/s10950-021-10010-7.
- Edwards, B., B. Zurek, E. van Dedem, P.J. Stafford, S. Oates, J. van Elk, B. deMartin & J.J. Bommer (2019). Simulations for the development of a ground motion model for induced seismicity in the Groningen gas field, The Netherlands. *Bulletin of Earthquake Engineering*, **17**, 4441-4456.
- Eshelby, J. D. (1957). The determination of the elastic field of an ellipsoidal inclusion, and related problems. *Proceedings of the Royal Society of London: Series-A* **241**, 376-396.
- Fugro (2020a) Geotechnical Site Investigation Seismic CPT's KNMI G-stations Groningen. Report 1019-153172_21.KR01, 26 November 2019. Available from <https://www.nam.nl/feiten-en-cijfers/onderzoeksrapporten.html>
- Fugro (2020b) Seismic CPT's KNMI G-stations Groningen – Rapportage geotechnisch onderzoek Loppersum. Report 1320-171323, 14 July 2020. Available from <https://www.nam.nl/feiten-en-cijfers/onderzoeksrapporten.html>
- Fukushima, R., Nakahara, H., & Nishimura, T. (2016). Estimating S-wave attenuation in sediments by deconvolution analysis of KIK-net borehole seismograms. *Bulletin of the Seismological Society of America* **106**(2), 552–559.
- GeoPentech (2015). *Southwestern United States Ground Motion Characterization SSHAC Level 3 Technical Report Rev. 2.*, GeoPentech, March 2015.
- Goulet, C., Y. Bozorgnia, N. Abrahamson, N. Kuehn, L. Al Atik, R. Youngs, R. Graves & G. Atkinson (2018). *Central and Eastern North America Ground-Motion Characterization: NGA-East Final Report*. PEER Report 2018/08, Pacific Earthquake Engineering Research Center, University of California at Berkeley, December, 817 pp.

- Green, R.A., J.J. Bommer, P.J. Stafford, B.W. Maurer, P.P. Kruiver, B. Edwards, A. Rodriguez-Marek, G. de Lange, S.J. Oates, T. Storck, P.Omidi, S.J. Bourne & van Elk, J. (2020). Liquefaction hazard in the Groningen region of the Netherlands due to induced seismicity. *Journal of Geotechnical and Geoenvironmental Engineering*, **146**(8), 04020068.
- Haberland, C. & A. Rietbrock (2001). Attenuation tomography in the western central Andes: A detailed insight into the structure of a magmatic arc. *Journal of Geophysical Research: Solid Earth* **106**(B6), 11151-11167.
- Hanks, T.C. & H. Kanamori (1979). Moment magnitude scale. *Journal of Geophysical Research* **84**, 2348-2350.
- He, Y., Li, J., Tian, W., & Li, Z. (2021). Characterization of the near-surface shear wave attenuation in the Groningen gas field using borehole recording. *Geophysical Journal International* **226**(3), 2057-2072.
- Jagt, L., E. Ruigrok & H. Paulssen (2017). Relocation of clustered earthquakes in the Groningen gas field. *Netherlands Journal of Geosciences* **96**(5), s163-s173.
- Jayaram, N. & J.W. Baker (2009). Correlation model for spatially distributed ground-motion intensities. *Earthquake Engineering & Structural Dynamics* **38**(15), 1687-1708
- Kaklamanos, J., L.G. Baise, E.M. Thompson & L. Dorfmann (2015). Comparison of 1D linear, equivalent-linear, and nonlinear site response models at six KiK-net validation sites. *Soil Dynamics & Earthquake Engineering* **69**, 207-219.
- Kaklamanos, J., B.A. Bradley, E.H. Thompson & L.G. Baise (2013). Critical parameters affecting bias and variability in site-response analyses using Kik-net downhole array data. *Bulletin of the Seismological Society of America* **103**(3), 1733–1749.
- Kallioglou, P., T. Tika, G. Koninis, S. Papadopoulos & K. Pitilakis (2009). Shear modulus and damping ratio of organic soils. *Geotechnical and Geological Engineering* **27**(2), 217-235.
- Keefer, D. L., & S.E. Bodily (1983). Three-point approximations for continuous random variables. *Management Science* **29**(5), 595-609.
- Kim, B., Y.M.A. Hashash, J.P. Stewart, E.M. Rathje, J.A. Harmon, M.I. Musgrove, K.W. Campbell & W.J. Silva (2016). Relative differences between nonlinear and equivalent-linear 1D site response analyses. *Earthquake Spectra* **32**(3), 1845-1865.
- Kishida, T., R.W. Boulanger, N.A. Abrahamson, M.W. Driller & T.M. Wehling (2009a). Site effects for the Sacramento-San Joaquin delta. *Earthquake Spectra* **25**(2), 301-322.
- Kishida, T., R.W. Boulanger, N.A. Abrahamson, T.W. Wehling & M.W. Driller (2009b). Regression models for dynamic properties of highly organic soils. *Journal of Geotechnical and Geoenvironmental Engineering* **135**(4), 533-543.
- KNMI (1993). *Netherlands Seismic and Acoustic Network*. Royal Netherlands Meteorological Institute (KNMI). Other/Seismic Network. doi:10.21944/e970fd34-23b9-3411-b366-e4f72877d2c5
- Konno, K. & T. Ohmachi (1998). Ground-motion characteristics estimated from spectral ratio between horizontal and vertical components of microtremor. *Bulletin of the Seismological Society of America* **88**, 228–241.

Kottke, A.R. & E.M. Rathje (2008). *Technical Manual for Strata*. PEER Report 2008/10, Pacific Earthquake Engineering Research Center, University of California at Berkeley, February, 84 pp.

Kottke, A.R. & E.M. Rathje (2013). Comparisons of time series and random-vibration theory site-response methods. *Bulletin of the Seismological Society of America* **103**(3), 2111-2127.

Kraaijpoel, D. & B. Dost (2013). Implications of salt-related propagation and mode conversion effects on the analysis of induced seismicity. *Journal of Seismology* **17**(1), 95-107.

Kramer, S.L. (1996). *Dynamic response of peat*. Washington State Department of Transportation, Report WA-RD 412.2, November 1996, 55 pp.

Kramer S.L. (2000). Dynamic response of Mercer Slough peat. *Journal of Geotechnical and Geoenvironmental Engineering* **126**(6), 504-510.

Kruiver, PP, M Pefkos, E Meijles, G Aalbersberg, X Campman, W van der Veen, A Martin, K Asshoff, JJ Bommer, A Rodriguez-Marek, R Pinho, Hn Crowley, F Cavalieri, AA Correia, J van Elk (2021). Incorporating dwelling mounds into induced seismic risk analysis for the Groningen gas field in the Netherlands. *Accepted for publication in Bulletin of Earthquake Engineering*.

Kruiver PP, van Dedem E, Romijn R, de Lange G, Korff M, Stafleu J, Gunnink JL, Rodriguez-Marek A, Bommer JJ, van Elk J & Doornhof D (2017a) An integrated shear-wave velocity model for the Groningen gas field, The Netherlands. *Bulletin of Earthquake Engineering* **15** (9): 3555–3580.

Kruiver PP, Wiersma A, Kloosterman F, de Lange G, Korff M, Stafleu J, Busschers FS, Harting R, Gunnink JL, Green RA, van Elk J, Doornhof D (2017b) Characterisation of the Groningen subsurface for seismic hazard and risk modelling. *Netherlands Journal of Geosciences* **96**(5), S215-S233.

Kulhawy, F.H. & P.H. Mayne (1990). *Manual on estimating soil properties for foundation design*. Report EPRI-EL-6800, Electric Power Research Institute, Palo Alto, California.

Lefebvre, G., & D. LeBoeuf (1987). Rate effects and cyclic loading of sensitive clays. *Journal of Geotechnical Engineering* **113**(5), 476-489.

Lunne, T., P.K. Robertson, & J.J.M. Powell (1997). *Cone Penetration Testing in Geotechnical Practice*. EF Spon/Blackie Academic, Routledge Publishers, London, 312 pp.

Menq, F.Y. (2003). *Dynamic Properties of Sandy and Gravelly Soils*, PhD Thesis, Department of Civil Engineering, University of Texas, Austin, TX.

Mosayk (2019) *Calibration and verification of a nonlinear macro-element for SSI analysis in the Groningen region*. Report n. D14. Available from NAM platform: <http://www.nam.nl/feiten-en-cijfers/onderzoeksrapporten.html>

Motazedian, D. & G.M. Atkinson (2005). Stochastic finite-fault modelling based on a dynamic corner frequency. *Bulletin of the Seismological Society of America* **95**, 995-1010.

Nakata, N., & Snieder, R. (2012). Estimating near-surface shear wave velocities in Japan by applying seismic interferometry to KiK-net data. *Journal of Geophysical Research: Solid Earth*, 117(B1).

National Institute of Standards and Technology (2012), *Soil-Structure Interaction for Building Structures*, 13 September 2012, 292 pp.

- Noorlandt, R.P., P.P. Kruiver, M.P.E. de Kleine, M. Karaoulis, G. de Lange, A. Di Matteo, J. von Ketelhodt, E. Ruigrok, B. Edwards, A. Rodriguez-Marek, J.J. Bommer, J. van Elk & D. Doornhof (2018). Characterisation of ground-motion recording stations in the Groningen gas field. *Journal of Seismology* **22**(3), 605-623.
- Ntinalexis, M., J.J. Bommer, E. Ruigrok, B. Edwards, R. Pinho, B. Dost, A.A. Correia, J. Uilenreef, P.J. Stafford & J. van Elk (2019). Ground-motion networks in the Groningen field: usability and consistency of surface recordings. *Journal of Seismology* **23**(6), 1233-1253.
- Ntinalexis, M., P.P. Kruiver, J.J. Bommer, E. Ruigrok, A. Rodriguez-Marek, B. Edwards, R. Pinho, J. Spetzler, E. Obando Hernandez, M. Pefkos, M. Bahrampouri, B. Dost & J. van Elk (2022). A database of ground-motion recordings, site profiles, and amplification factors from the Groningen gas field in the Netherlands. *Submitted to Earthquake Spectra*.
- Phoon, K.K. & F.H. Kulhawy (1999). Evaluation of geotechnical property variability. *Canadian Geotechnical Journal* **36**(4), 625-639.
- Rathje, E.M. & M.C. Ozbey (2006). Site-specific validation of random vibration theory-based seismic site response analysis. *ASCE Journal of Geotechnical & Geoenvironmental Engineering* **132**(7), 911–922.
- Rijkers, R.H.B., D.J. Huisman, G. de Lange, J.P. Weijers, & N. Witmans-Parker (1998). *Inventarisatie geomechanische, geochemische en geohydrologische eigenschappen van Tertiaire kleipakketten - CAR Fase II*. TNO report NITG 98-90-B, 167 p.
- Robertson, P.K. (1990). Soil classification using the cone penetration test. *Canadian Geotechnical Journal* **27**(1), 151-158.
- Rodriguez-Marek, A., F. Cotton, N.A. Abrahamson, S. Akkar, L. Al Atik, B. Edwards, G.A. Montalva & H.M. Dawood (2013). A model for single-station standard deviation using data from various tectonic regions. *Bulletin of the Seismological Society of America* **103**(6), 3149-3163.
- Rodriguez-Marek, A., P.P. Kruiver, P. Meijers, J.J. Bommer, B. Dost, J. van Elk & D. Doornhof (2017). A regional site-response model for the Groningen gas field. *Bulletin of the Seismological Society of America* **107**(5), 2067-2077.
- Romijn., R. (2017) *Groningen Velocity Model 2017 – Groningen full elastic velocity model September 2017*. NAM report.
- Ruigrok, E., Rodriguez-Marek, A., Edwards, B., Kruiver, P.P., Dost, B. & Bommer, J.J. (2022). Estimation of damping profiles with seismic interferometry. *Accepted for publication in Geophysical Journal International*.
- Seed, H.B. & I.M. Idriss (1970). Analysis of ground motions at Union Bay, Seattle, during earthquakes and distant nuclear blasts. *Bulletin Seismological Society of America* **60**(1), 135-136.
- Skempton, A.W. & Henkel, D.J., 1953. The post-glacial clays of the Thames Estuary at Tilbury and Shellhaven. *Proceedings of 3rd International Conference on Soil Mechanics and Foundation Engineering, Zurich, Switzerland* 1: 302–308.

Sorensen, K. K., & N. Okkels (2013). Correlation between drained shear strength and plasticity index of undisturbed overconsolidated clays. *Proceedings of the 18th International Conference on Soil Mechanics and Geotechnical Engineering*, Paris, France, 423-428.

Spetzler, J. & B. Dost (2017). Hypocentre estimation of induced earthquakes in Groningen. *Geophysical Journal International* **209**(1), 453-465.

Stafford, P.J. (2021). Risk oriented earthquake hazard assessment: Influence of spatial discretisation and non-ergodic ground-motion models. *Advances in Assessment and Modeling of Earthquake Loss*, ed. S. Akkar et al., Springer, 169-187.

Stafford, P.J., Rodriguez-Marek, A., B. Edwards, P.P. Kruiver & J.J. Bommer (2017). Scenario dependence of linear site effect factors for short-period response spectral ordinates. *Bulletin of the Seismological Society of America* **107**(6), 2859-2872.

Stafford, P.J., B.D. Zurek, M. Ntinalexis & J.J. Bommer (2019). Extensions to the Groningen ground-motion model for seismic risk calculations: component-to-component variability and spatial correlation. *Bulletin of Earthquake Engineering* **17**, 4417-4439.

Stewart J.P. (2000). Variations between foundation-level and free-field earthquake ground motions. *Earthquake Spectra* **16**(2), 511-532.

Stewart, J. P., & K. Afshari (2021). Epistemic uncertainty in site response as derived from one-dimensional ground response analyses. *Journal of Geotechnical and Geoenvironmental Engineering* **147**(1), 04020146.

Stewart, J.P., K. Afshari & Y.M.A. Hashash (2014). *Guidelines for Performing Hazard-Consistent One-Dimensional Ground Response Analysis for Ground Motion Prediction*. PEER Report 2014/16, Pacific Earthquake Engineering Research Center, University of California, Berkeley, CA.

Stokoe, K. H., J.A. Bay, B.L. Rosenbald, S.K. Hwang & M.R. Twede (1994). *In situ seismic and dynamic laboratory measurements of geotechnical materials at Queensboro Bridge and Roosevelt Island*. Geotechnical Engineering Report GR 94-5, Civil Engineering Department, University of Texas at Austin, Texas.

Tao, Y., & E.M. Rathje (2020). The importance of distinguishing pseudoresonances and outcrop resonances in downhole array data. *Bulletin of the Seismological Society of America* **110**(1), 288-294.

Thurber, C. & D. Eberhart-Phillips (1999). Local earthquake tomography with flexible gridding. *Computers & Geosciences* **25**(7), 809-818.

Tokimatsu, K. & T. Sekiguchi (2006a). Effects of nonlinear dynamic soil properties on strong Motions at Ojiya K-Net and JMA Stations during 2004 Mid Niigata Prefecture earthquake. *Proceedings of the 8th U.S. National Conference on Earthquake Engineering*, San Francisco, California, USA, April 18-22.

Tokimatsu, K & T. Sekiguchi (2006b). Effects of nonlinear properties of surface soils on strong ground motions recorded in Ojiya during 2004 mid Niigata Prefecture earthquake. *Soils and Foundations* **46**(6), 765-775.

Tokimatsu, K. & T. Sekiguchi (2007). Effects of dynamic properties of peat on strong ground motions during 2004 Mid Niigata Prefecture earthquake. *Proceedings of 4th International Conference on Earthquake Geotechnical Engineering* June 25-28, Paper No. 1531.

Tonn, R. (1991). The determination of the seismic quality factor Q from VSP data: a comparison of different computational methods. *Geophysical Prospecting* **39**(1), 1–27.

van Essen, H. (2017). *Proevenverzameling Noorderzijlvest - Deelverzameling ten behoeve van dijkversterking Eemskanaal*. Deltares report 1220173-024-GEO-0071, 30 May 2017 (in Dutch).

Wapenaar, K., Draganov, D., Snieder, R., Campman, X., & Verdel, A. (2010). Tutorial on seismic interferometry: Part 1—Basic principles and applications. *Geophysics* **75**(5), 75A195-75A209.

Wehling, T.M., R.W. Boulanger, L.F. Harder & M.W. Driller (2001). *Dynamic Properties of Sherman Island Peat: Phase II Study*. Department of Civil & Environmental Engineering, College of Engineering, University of California at Davis. Report No. UCD/CGM-01/05, March 2001, 130 pp.

Wells, D.L. & K.J. Coppersmith (1994). New Empirical Relationships among Magnitude, Rupture Length, Rupture Width, Rupture Area, and Surface Displacement. *Bulletin of the Seismological Society of America* **84**(4), 974-1002.

Yee, E., J.P. Stewart & K. Tokimatsu (2013). Elastic and large-strain nonlinear seismic site response from analysis of vertical array recordings. *Journal of Geotechnical and Geoenvironmental Engineering*, **139**(10), 1789-1801.

Zalachoris, G. & E.M. Rathje (2015). Evaluation of one-dimensional site response techniques using borehole arrays. *Journal of Geotechnical and Geoenvironmental Engineering* **141**(12), 04015053-1-15.

Zwanenburg, C. (2005). *The influence of anisotropy on the consolidation behaviour of peat*. Ph.D thesis Delft University of Technology, October 2005.

Zwanenburg C, Konstadinou M, Meijers P, Goudarzy M, König D, Dyvik R, Carlton B, van Elk J, Doornhof D & Korff M (2020) Assessment of the dynamic properties of Holocene peat. *Journal of Geotechnical and Geoenvironmental Engineering* **146**(7), 04020049.

APPENDIX I

Geomechanical Look-Up Tables for Soil Properties

Table I.1. Codes for stratigraphic units

| Code | Formation - Member |
|-------------|---------------------------|
| AAOP | Anthropogenic |
| AP | Appelscha |
| BX | Boxtel |
| BXKO | Boxtel |
| BXSI1 | Boxtel - Singraven 1 |
| BXSI2 | Boxtel - Singraven 2 |
| BXWI | Boxtel - Wierden |
| DN | Drachten |
| DR | Drente |
| DRGI | Drente - Gieten |
| EE | Eem |
| NA | Naaldwijk |
| NASC | Naaldwijk - Schoorl |
| NAWA | Naaldwijk - Walcheren |
| NAWO | Naaldwijk - Wormer |
| NAZA | Naaldwijk - Zandvoort |
| NIBA | Nieuwkoop - Basal peat |
| NIGR | Nieuwkoop - Griendtsveen |
| NIHO | Nieuwkoop - Holland peat |
| NINB | Nieuwkoop - Nij Beets |
| PE | Peelo |
| UR | Urk |
| URTY | Urk - Tynje |

Table I.2. Groningen specific V_s relationships for V7 GMM

| Formation (see Table V.1) | Lithology | Depth dependence *) | # observations | Mean $\ln(V_s)$ | Standard deviation $\ln(V_s)$ | Coefficient of variance | Slope n | Intercept $\ln V_{s1}$ | Mean $\ln(\sigma'_0/\text{pa})$ | Sum of squares $\ln(\sigma'_0/\text{pa})$ | Variance regression | Variance velocity (not used) | Source **) | Remark |
|---------------------------|--------------------------------|---------------------|----------------|-----------------|-------------------------------|-------------------------|---------|------------------------|---------------------------------|---|---------------------|------------------------------|------------|---|
| AAOP | peat | 2 | 87 | 5.12 | 0.43 | 0.08 | -- | -- | -- | -- | -- | -- | 1 | All combined in one lithoclass - no depth dependence because of presence in shallow top only |
| AAOP | clay | 2 | 87 | 5.12 | 0.43 | 0.08 | -- | -- | -- | -- | -- | -- | 1 | All combined in one lithoclass - no depth dependence because of presence in shallow top only |
| AAOP | sandy clayey and clayey sand | 2 | 87 | 5.12 | 0.43 | 0.08 | -- | -- | -- | -- | -- | -- | 1 | All combined in one lithoclass - no depth dependence because of presence in shallow top only |
| AAOP | fine sand | 2 | 87 | 5.12 | 0.43 | 0.08 | -- | -- | -- | -- | -- | -- | 1 | All combined in one lithoclass - no depth dependence because of presence in shallow top only |
| AAOP | medium sand | 2 | 87 | 5.12 | 0.43 | 0.08 | -- | -- | -- | -- | -- | -- | 1 | All combined in one lithoclass - no depth dependence because of presence in shallow top only |
| AAOP | coarse sand, gravel and shells | 2 | 87 | 5.12 | 0.43 | 0.08 | -- | -- | -- | -- | -- | -- | 1 | All combined in one lithoclass - no depth dependence because of presence in shallow top only |
| AP | peat | 3 | 0 | -- | 0.27 | -- | 0.25 | 4.81 | -- | -- | -- | -- | 3 | n from clay literature - intercept consistent with NIBA - $\sigma \ln V_s$ increased to 0.27 for peat |
| AP | clay | 3 | 0 | -- | 0.20 | -- | 0.25 | 5.59 | -- | -- | -- | -- | 3 | n from clay literature - $V_s=350$ at average depth of 40 m below surface |
| AP | sandy clayey and clayey sand | 2 | 0 | 5.86 | 0.20 | 0.03 | -- | -- | -- | -- | -- | -- | 3 | Similar to EE so no depth dependence - different average $\ln V_s$ |
| AP | fine sand | 2 | 0 | 5.86 | 0.20 | 0.03 | -- | -- | -- | -- | -- | -- | 3 | Similar to EE so no depth dependence - different average $\ln V_s$ |
| AP | medium sand | 2 | 0 | 5.99 | 0.20 | 0.03 | -- | -- | -- | -- | -- | -- | 3 | Similar to EE so no depth dependence - different average $\ln V_s$ - Medium & coarse sand combined in one V_s class |
| AP | coarse sand, gravel and shells | 2 | 0 | 5.99 | 0.20 | 0.03 | -- | -- | -- | -- | -- | -- | 3 | Similar to EE so no depth dependence - Medium & coarse sand combined in one V_s class |

| Formation (see Table V.1) | Lithology | Depth dependence *) | # observations | Mean ln(Vs) | Standard deviation ln(Vs) | Coefficient of variance | Slope n | Intercept lnVs1 | Mean ln(σ_0' /pa) | Sum of squares ln(σ_0' /pa) | Variance regression | Variance velocity (not used) | Source **) | Remark |
|---------------------------|--------------------------------|---------------------|----------------|-------------|---------------------------|-------------------------|---------|-----------------|---------------------------|-------------------------------------|---------------------|------------------------------|------------|--|
| BX | peat | 3 | 0 | -- | 0.27 | -- | 0.25 | 4.81 | -- | -- | -- | -- | 3 | n from clay literature - intercept consistent with NIBA - σ lnVs increased to 0.27 for peat |
| BX | clay | 3 | 0 | -- | 0.20 | -- | 0.25 | 5.18 | -- | -- | -- | -- | 3 | n from clay literature (not enough data) - average Vs from 8 datapoints - in agreement with expert knowledge |
| BX | sandy clayey and clayey sand | 1 | 43 | -- | -- | -- | 0.20 | 5.38 | 0.10 | 5.67 | 0.04 | 0.04 | 1 | sufficient data from SCPT data set - depth dependence |
| BX | fine sand | 1 | 260 | -- | -- | -- | 0.11 | 5.51 | -0.06 | 64.41 | 0.05 | 0.05 | 1 | sufficient data from SCPT data set - depth dependence |
| BX | medium sand | 2 | 67 | 5.62 | 0.20 | 0.04 | -- | -- | -- | -- | -- | -- | 1 | No depth dependence in data - σ lnVs increased to 0.2 - Medium & coarse sand combined in one Vs class |
| BX | coarse sand, gravel and shells | 2 | 67 | 5.62 | 0.20 | 0.04 | -- | -- | -- | -- | -- | -- | 1 | No depth dependence in data - σ lnVs increased to 0.2 - Medium & coarse sand combined in one Vs class |
| BXKO | peat | 3 | 0 | -- | 0.27 | -- | 0.25 | 4.81 | -- | -- | -- | -- | 3 | n from clay literature - intercept consistent with NIBA - σ lnVs increased to 0.27 for peat |
| BXKO | clay | 3 | 0 | -- | 0.20 | -- | 0.25 | 5.18 | -- | -- | -- | -- | 3 | From BX |
| BXKO | sandy clayey and clayey sand | 1 | 43 | -- | -- | -- | 0.20 | 5.38 | 0.10 | 5.67 | 0.04 | 0.04 | 3 | From BX |
| BXKO | fine sand | 1 | 260 | -- | -- | -- | 0.11 | 5.51 | -0.06 | 64.41 | 0.05 | 0.05 | 3 | From BX |
| BXKO | medium sand | 2 | 0 | 5.62 | 0.20 | 0.04 | -- | -- | -- | -- | -- | -- | 3 | From BX - Medium & coarse sand combined in one Vs class |
| BXKO | coarse sand, gravel and shells | 2 | 0 | 5.62 | 0.20 | 0.04 | -- | -- | -- | -- | -- | -- | 3 | From BX - Medium & coarse sand combined in one Vs class |
| BXS11 | peat | 2 | 0 | 4.43 | 0.27 | 0.06 | -- | -- | -- | -- | -- | -- | 3 | From NIHO |
| BXS11 | clay | 2 | 0 | 4.44 | 0.27 | 0.06 | -- | -- | -- | -- | -- | -- | 3 | From NIHO |
| BXS11 | sandy clayey and clayey sand | 2 | 0 | 4.70 | 0.27 | 0.06 | -- | -- | -- | -- | -- | -- | 3 | From NIHO |
| BXS11 | fine sand | 2 | 0 | 4.93 | 0.27 | 0.05 | -- | -- | -- | -- | -- | -- | 3 | From NIHO - all sand combined in one Vs class |

| Formation (see Table V.1) | Lithology | Depth dependence *) | # observations | Mean ln(Vs) | Standard deviation ln(Vs) | Coefficient of variance | Slope n | Intercept lnV _{s1} | Mean ln(σ ₀ /pa) | Sum of squares ln(σ ₀ /pa) | Variance regression | Variance velocity (not used) | Source **) | Remark |
|---------------------------|--------------------------------|---------------------|----------------|-------------|---------------------------|-------------------------|---------|-----------------------------|-----------------------------|---------------------------------------|---------------------|------------------------------|------------|--|
| BXSI1 | medium sand | 2 | 0 | 4.93 | 0.27 | 0.05 | -- | -- | -- | -- | -- | -- | 3 | From NIHO - all sand combined in one Vs class |
| BXSI1 | coarse sand, gravel and shells | 2 | 0 | 4.93 | 0.27 | 0.05 | -- | -- | -- | -- | -- | -- | 3 | From NIHO - all sand combined in one Vs class |
| BXSI2 | peat | 3 | 0 | -- | 0.27 | -- | 0.25 | 4.81 | -- | -- | -- | -- | 3 | n from clay literature - intercept consistent with NIBA - σlnVs increased to 0.27 for peat |
| BXSI2 | clay | 3 | 0 | -- | 0.20 | -- | 0.25 | 5.18 | -- | -- | -- | -- | 3 | From BX |
| BXSI2 | sandy clayey and clayey sand | 1 | 43 | -- | -- | -- | 0.20 | 5.38 | 0.10 | 5.67 | 0.04 | 0.04 | 3 | From BX |
| BXSI2 | fine sand | 1 | 260 | -- | -- | -- | 0.11 | 5.51 | -0.06 | 64.41 | 0.05 | 0.05 | 3 | From BX |
| BXSI2 | medium sand | 2 | 0 | 5.62 | 0.20 | 0.04 | -- | -- | -- | -- | -- | -- | 3 | From BX - Medium & coarse sand combined in one Vs class |
| BXSI2 | coarse sand, gravel and shells | 2 | 0 | 5.62 | 0.20 | 0.04 | -- | -- | -- | -- | -- | -- | 3 | From BX - Medium & coarse sand combined in one Vs class |
| BXWI | peat | 3 | 0 | -- | 0.27 | -- | 0.25 | 4.81 | -- | -- | -- | -- | 3 | n from clay literature - intercept consistent with NIBA - σlnVs increased to 0.27 for peat |
| BXWI | clay | 3 | 0 | -- | 0.20 | -- | 0.25 | 5.18 | -- | -- | -- | -- | 3 | From BX |
| BXWI | sandy clayey and clayey sand | 1 | 43 | -- | -- | -- | 0.20 | 5.38 | 0.10 | 5.67 | 0.04 | 0.04 | 3 | From BX |
| BXWI | fine sand | 1 | 260 | -- | -- | -- | 0.11 | 5.51 | -0.06 | 64.41 | 0.05 | 0.05 | 3 | From BX |
| BXWI | medium sand | 2 | 0 | 5.62 | 0.20 | 0.04 | -- | -- | -- | -- | -- | -- | 3 | From BX - Medium & coarse sand combined in one Vs class |
| BXWI | coarse sand, gravel and shells | 2 | 0 | 5.62 | 0.20 | 0.04 | -- | -- | -- | -- | -- | -- | 3 | From BX - Medium & coarse sand combined in one Vs class |
| DN | peat | 3 | 0 | -- | 0.27 | -- | 0.25 | 4.81 | -- | -- | -- | -- | 3 | n from clay literature - intercept consistent with NIBA - σlnVs increased to 0.27 for peat |
| DN | clay | 3 | 0 | -- | 0.20 | -- | 0.25 | 4.99 | -- | -- | -- | -- | 3 | n from clay literature - Vs = 150 m/s at average depth of 15 m below surface |

| Formation (see Table V.1) | Lithology | Depth dependence *) | # observations | Mean ln(Vs) | Standard deviation ln(Vs) | Coefficient of variance | Slope n | Intercept lnVs1 | Mean ln(σ_0 /pa) | Sum of squares ln(σ_0 /pa) | Variance regression | Variance velocity (not used) | Source **) | Remark |
|---------------------------|--------------------------------|---------------------|----------------|-------------|---------------------------|-------------------------|---------|-----------------|--------------------------|------------------------------------|---------------------|------------------------------|------------|---|
| DN | sandy clayey and clayey sand | 3 | 0 | -- | 0.20 | -- | 0.25 | 5.40 | -- | -- | -- | -- | 3 | n from clay literature - Vs = 226 m/s at average depth of 15 m below surface |
| DN | fine sand | 2 | 0 | 5.87 | 0.20 | 0.03 | -- | -- | -- | -- | -- | -- | 2 | No depth dependence for sands |
| DN | medium sand | 2 | 0 | 6.11 | 0.20 | 0.03 | -- | -- | -- | -- | -- | -- | 3 | No depth dependence for sands - Medium & coarse sand combined in one Vs class |
| DN | coarse sand, gravel and shells | 2 | 0 | 6.11 | 0.20 | 0.03 | -- | -- | -- | -- | -- | -- | 3 | No depth dependence for sands - Medium & coarse sand combined in one Vs class |
| DR | peat | 2 | 0 | 5.43 | 0.27 | 0.05 | -- | -- | -- | -- | -- | -- | 3 | No depth dependence due to varying glacial conditions - σ lnVs increased to 0.27 for peat |
| DR | clay | 2 | 0 | 5.30 | 0.20 | 0.04 | -- | -- | -- | -- | -- | -- | 3 | No depth dependence due to varying glacial conditions |
| DR | sandy clayey and clayey sand | 2 | 0 | 5.35 | 0.20 | 0.04 | -- | -- | -- | -- | -- | -- | 3 | From DRGI - No depth dependence due to varying glacial conditions |
| DR | fine sand | 3 | 0 | -- | 0.20 | -- | 0.25 | 5.42 | -- | -- | -- | -- | 3 | n from Menq, not enough data, Vs = 285 m/s at average depth of 29 m below surface |
| DR | medium sand | 3 | 0 | -- | 0.20 | -- | 0.25 | 5.48 | -- | -- | -- | -- | 3 | n from Menq, not enough data, Vs = 300 m/s at average depth of 29 m below surface |
| DR | coarse sand, gravel and shells | 3 | 0 | -- | 0.20 | -- | 0.26 | 5.47 | -- | -- | -- | -- | 3 | n from Menq, not enough data, Vs = 300 m/s at average depth of 29 m below surface |
| DRGI | peat | 2 | 0 | 5.43 | 0.27 | 0.05 | -- | -- | -- | -- | -- | -- | 3 | No depth dependence due to varying glacial conditions - σ lnVs increased to 0.27 for peat |
| DRGI | clay | 2 | 0 | 5.30 | 0.20 | 0.03 | -- | -- | -- | -- | -- | -- | 3 | No depth dependence due to varying glacial conditions |
| DRGI | sandy clayey and clayey sand | 2 | 33 | 5.35 | 0.20 | 0.04 | -- | -- | -- | -- | -- | -- | 1 | No depth dependence in data - in agreement with to be expected due to varying glacial conditions - σ lnVs increased to 0.2 |
| DRGI | fine sand | 3 | 0 | -- | 0.20 | -- | 0.25 | 5.63 | -- | -- | -- | -- | 3 | n from Menq, not enough data, Vs = 285 m/s at average depth of 15 m below surface |

| Formation (see Table V.1) | Lithology | Depth dependence *) | # observations | Mean ln(Vs) | Standard deviation ln(Vs) | Coefficient of variance | Slope n | Intercept lnVs ₁ | Mean ln(σ ₀ /pa) | Sum of squares ln(σ ₀ /pa) | Variance regression | Variance velocity (not used) | Source **) | Remark |
|---------------------------|--------------------------------|---------------------|----------------|-------------|---------------------------|-------------------------|---------|-----------------------------|-----------------------------|---------------------------------------|---------------------|------------------------------|------------|---|
| DRGI | medium sand | 3 | 0 | -- | 0.20 | -- | 0.29 | 5.69 | -- | -- | -- | -- | 3 | n from Menq, not enough data, Vs = 300 m/s at average depth of 15 m below surface |
| DRGI | coarse sand, gravel and shells | 3 | 0 | -- | 0.20 | -- | 0.26 | 5.69 | -- | -- | -- | -- | 3 | n from Menq, not enough data, Vs = 300 m/s at average depth of 15 m below surface |
| EE | peat | 3 | 0 | -- | 0.27 | -- | 0.25 | 4.81 | -- | -- | -- | -- | 3 | n from clay literature - intercept consistent with NIBA - σlnVs increased to 0.27 for peat |
| EE | clay | 3 | 0 | -- | 0.20 | -- | 0.25 | 5.27 | -- | -- | -- | -- | 3 | n from clay literature - Vs = 225 m/s at average depth of 23 m below surface |
| EE | sandy clayey and clayey sand | 2 | 24 | 5.56 | 0.20 | 0.04 | -- | -- | -- | -- | -- | -- | 1 | No depth dependence according to data (lot of scatter) - σlnVs increased to 0.2 |
| EE | fine sand | 2 | 31 | 5.55 | 0.20 | 0.04 | -- | -- | -- | -- | -- | -- | 1 | No depth dependence for sand according to data - σlnVs increased to 0.2 |
| EE | medium sand | 2 | 7 | 5.59 | 0.20 | 0.04 | -- | -- | -- | -- | -- | -- | 1 | No depth dependence for sand according to data, average Vs based on 7 points = in good agreement with expert knowlegde - σlnVs increased to 0.2 - Medium & coarse sand combined in one Vs class |
| EE | coarse sand, gravel and shells | 2 | 7 | 5.59 | 0.20 | 0.04 | -- | -- | -- | -- | -- | -- | 1 | No depth dependence for sand according to data, average Vs based on 7 points = in good agreement with expert knowlegde - σlnVs increased to 0.2 - Medium & coarse sand combined in one Vs class |
| NA | peat | 2 | 0 | 4.43 | 0.27 | 0.06 | -- | -- | -- | -- | -- | -- | 3 | From NIHO, no depth dependence |
| NA | clay | 1 | 303 | -- | -- | -- | 0.18 | 4.91 | -1.20 | 107.49 | 0.11 | 0.11 | 1 | sufficient data from SCPT data set - depth dependence |
| NA | sandy clayey and clayey sand | 1 | 245 | -- | -- | -- | 0.28 | 5.25 | -0.98 | 59.65 | 0.07 | 0.06 | 1 | sufficient data from SCPT data set - depth dependence |
| NA | fine sand | 1 | 166 | -- | -- | -- | 0.36 | 5.51 | -0.78 | 34.05 | 0.10 | 0.10 | 1 | sufficient data from SCPT data set - depth dependence |
| NA | medium sand | 3 | 0 | -- | 0.20 | -- | 0.25 | 5.73 | -- | -- | -- | -- | 3 | n from Menq, Vs = 250 m/s at average depth of 8 m below surface |

| Formation (see Table V.1) | Lithology | Depth dependence *) | # observations | Mean ln(Vs) | Standard deviation ln(Vs) | Coefficient of variance | Slope n | Intercept lnVs1 | Mean ln(σ_0' /pa) | Sum of squares ln(σ_0' /pa) | Variance regression | Variance velocity (not used) | Source **) | Remark |
|---------------------------|--------------------------------|---------------------|----------------|-------------|---------------------------|-------------------------|---------|-----------------|---------------------------|-------------------------------------|---------------------|------------------------------|------------|---|
| NA | coarse sand, gravel and shells | 3 | 0 | -- | 0.20 | -- | 0.25 | 5.73 | -- | -- | -- | -- | 3 | n from Menq, Vs = 250 m/s at average depth of 8 m below surface |
| NASC | peat | 2 | 0 | 4.43 | 0.27 | 0.06 | -- | -- | -- | -- | -- | -- | 3 | From NIHO, no depth dependence |
| NASC | clay | 1 | 303 | -- | -- | -- | 0.18 | 4.91 | -1.20 | 107.49 | 0.11 | 0.11 | 3 | From NA |
| NASC | sandy clayey and clayey sand | 1 | 245 | -- | -- | -- | 0.28 | 5.25 | -0.98 | 59.65 | 0.07 | 0.06 | 3 | From NA |
| NASC | fine sand | 1 | 166 | -- | -- | -- | 0.36 | 5.51 | -0.78 | 34.05 | 0.10 | 0.10 | 3 | From NA |
| NASC | medium sand | 3 | 0 | -- | 0.20 | -- | 0.25 | 5.73 | -- | -- | -- | -- | 3 | From NA - Medium & coarse sand combined in one Vs class |
| NASC | coarse sand, gravel and shells | 3 | 0 | -- | 0.20 | -- | 0.25 | 5.73 | -- | -- | -- | -- | 3 | From NA - Medium & coarse sand combined in one Vs class |
| NAWA | peat | 2 | 0 | 4.43 | 0.27 | 0.06 | -- | -- | -- | -- | -- | -- | 3 | From NIHO, no depth dependence |
| NAWA | clay | 1 | 303 | -- | -- | -- | 0.18 | 4.91 | -1.20 | 107.49 | 0.11 | 0.11 | 3 | From NA |
| NAWA | sandy clayey and clayey sand | 1 | 245 | -- | -- | -- | 0.28 | 5.25 | -0.98 | 59.65 | 0.07 | 0.06 | 3 | From NA |
| NAWA | fine sand | 1 | 166 | -- | -- | -- | 0.36 | 5.51 | -0.78 | 34.05 | 0.10 | 0.10 | 3 | From NA |
| NAWA | medium sand | 3 | 0 | -- | 0.20 | -- | 0.25 | 5.73 | -- | -- | -- | -- | 3 | From NA - Medium & coarse sand combined in one Vs class |
| NAWA | coarse sand, gravel and shells | 3 | 0 | -- | 0.20 | -- | 0.25 | 5.73 | -- | -- | -- | -- | 3 | From NA - Medium & coarse sand combined in one Vs class |
| NAWO | peat | 2 | 0 | 4.43 | 0.27 | 0.06 | -- | -- | -- | -- | -- | -- | 3 | From NIHO, no depth dependence |
| NAWO | clay | 1 | 303 | -- | -- | -- | 0.18 | 4.91 | -1.20 | 107.49 | 0.11 | 0.11 | 3 | From NA |
| NAWO | sandy clayey and clayey sand | 1 | 245 | -- | -- | -- | 0.28 | 5.25 | -0.98 | 59.65 | 0.07 | 0.06 | 3 | From NA |
| NAWO | fine sand | 1 | 166 | -- | -- | -- | 0.36 | 5.51 | -0.78 | 34.05 | 0.10 | 0.10 | 3 | From NA |
| NAWO | medium sand | 3 | 0 | -- | 0.20 | -- | 0.25 | 5.73 | -- | -- | -- | -- | 3 | From NA - Medium & coarse sand combined in one Vs class |

| Formation (see Table V.1) | Lithology | Depth dependence *) | # observations | Mean ln(Vs) | Standard deviation ln(Vs) | Coefficient of variance | Slope n | Intercept lnVs ₁ | Mean ln(σ ₀ /pa) | Sum of squares ln(σ ₀ /pa) | Variance regression | Variance velocity (not used) | Source **) | Remark |
|---------------------------|--------------------------------|---------------------|----------------|-------------|---------------------------|-------------------------|---------|-----------------------------|-----------------------------|---------------------------------------|---------------------|------------------------------|------------|---|
| NAWO | coarse sand, gravel and shells | 3 | 0 | -- | 0.20 | -- | 0.25 | 5.73 | -- | -- | -- | -- | 3 | From NA - Medium & coarse sand combined in one Vs class |
| NAZA | peat | 2 | 0 | 4.43 | 0.27 | 0.06 | -- | -- | -- | -- | -- | -- | 3 | From NIHO, no depth dependence |
| NAZA | clay | 1 | 303 | -- | -- | -- | 0.18 | 4.91 | -1.20 | 107.49 | 0.11 | 0.11 | 3 | From NA |
| NAZA | sandy clayey and clayey sand | 1 | 245 | -- | -- | -- | 0.28 | 5.25 | -0.98 | 59.65 | 0.07 | 0.06 | 3 | From NA |
| NAZA | fine sand | 1 | 166 | -- | -- | -- | 0.36 | 5.51 | -0.78 | 34.05 | 0.10 | 0.10 | 3 | From NA |
| NAZA | medium sand | 3 | 0 | -- | 0.20 | -- | 0.25 | 5.73 | -- | -- | -- | -- | 3 | From NA - Medium & coarse sand combined in one Vs class |
| NAZA | coarse sand, gravel and shells | 3 | 0 | -- | 0.20 | -- | 0.25 | 5.73 | -- | -- | -- | -- | 3 | From NA - Medium & coarse sand combined in one Vs class |
| NIBA | peat | 1 | 22 | -- | -- | -- | 0.57 | 5.05 | -0.77 | 3.70 | 0.19 | 0.15 | 1 | sufficient data from SCPT data set - depth dependence |
| NIBA | clay | 3 | 0 | -- | 0.27 | -- | 0.25 | 4.95 | -- | -- | -- | -- | 3 | n from clay literature - Vs = 125 m/s at average depth of 10 m - σlnVs increased to 0.27 for peat |
| NIBA | sandy clayey and clayey sand | 3 | 0 | -- | 0.27 | -- | 0.25 | 5.14 | -- | -- | -- | -- | 3 | n from clay literature - Vs = 150 m/s at average depth of 10 m - σlnVs increased to 0.27 for peat |
| NIBA | fine sand | 3 | 0 | -- | 0.27 | -- | 0.25 | 5.14 | -- | -- | -- | -- | 3 | n from clay literature - Vs = 150 m/s at average depth of 10 m - σlnVs increased to 0.27 for peat |
| NIBA | medium sand | 3 | 0 | -- | 0.27 | -- | 0.25 | 5.14 | -- | -- | -- | -- | 3 | n from clay literature - Vs = 150 m/s at average depth of 10 m - σlnVs increased to 0.27 for peat |
| NIBA | coarse sand, gravel and shells | 3 | 0 | -- | 0.27 | -- | 0.25 | 5.14 | -- | -- | -- | -- | 3 | n from clay literature - Vs = 150 m/s at average depth of 10 m - σlnVs increased to 0.27 for peat |
| NIGR | peat | 2 | 0 | 4.43 | 0.27 | 0.06 | -- | -- | -- | -- | -- | -- | 3 | From NIHO |
| NIGR | clay | 2 | 0 | 4.44 | 0.27 | 0.06 | -- | -- | -- | -- | -- | -- | 3 | From NIHO |

| Formation (see Table V.1) | Lithology | Depth dependence *) | # observations | Mean ln(Vs) | Standard deviation ln(Vs) | Coefficient of variance | Slope n | Intercept lnVs1 | Mean ln(σ_0' /pa) | Sum of squares ln(σ_0' /pa) | Variance regression | Variance velocity (not used) | Source **) | Remark |
|---------------------------|--------------------------------|---------------------|----------------|-------------|---------------------------|-------------------------|---------|-----------------|---------------------------|-------------------------------------|---------------------|------------------------------|------------|--|
| NIGR | sandy clayey and clayey sand | 2 | 0 | 4.70 | 0.27 | 0.06 | -- | -- | -- | -- | -- | -- | 3 | From NIHO |
| NIGR | fine sand | 2 | 0 | 4.93 | 0.27 | 0.05 | -- | -- | -- | -- | -- | -- | 3 | From NIHO - all sand combined in one Vs class |
| NIGR | medium sand | 2 | 0 | 4.93 | 0.27 | 0.05 | -- | -- | -- | -- | -- | -- | 3 | From NIHO - all sand combined in one Vs class |
| NIGR | coarse sand, gravel and shells | 2 | 0 | 4.93 | 0.27 | 0.05 | -- | -- | -- | -- | -- | -- | 3 | From NIHO - all sand combined in one Vs class |
| NIHO | peat | 2 | 13 | 4.43 | 0.27 | 0.06 | -- | -- | -- | -- | -- | -- | 1 | No depth dependence in SCPT data - average Vs in agreement with expert knowledge |
| NIHO | clay | 2 | 0 | 4.44 | 0.27 | 0.06 | -- | -- | -- | -- | -- | -- | 3 | σ lnVs increased to 0.27 for peat |
| NIHO | sandy clayey and clayey sand | 2 | 0 | 4.70 | 0.27 | 0.06 | -- | -- | -- | -- | -- | -- | 3 | σ lnVs increased to 0.27 for peat |
| NIHO | fine sand | 2 | 0 | 4.93 | 0.27 | 0.05 | -- | -- | -- | -- | -- | -- | 3 | σ lnVs increased to 0.27 for peat - all sand in one combined Vs class |
| NIHO | medium sand | 2 | 0 | 4.93 | 0.27 | 0.05 | -- | -- | -- | -- | -- | -- | 3 | σ lnVs increased to 0.27 for peat - all sand in one combined Vs class |
| NIHO | coarse sand, gravel and shells | 2 | 0 | 4.93 | 0.27 | 0.05 | -- | -- | -- | -- | -- | -- | 3 | σ lnVs increased to 0.27 for peat - all sand in one combined Vs class |
| NINB | peat | 2 | 0 | 4.43 | 0.27 | 0.06 | -- | -- | -- | -- | -- | -- | 3 | From NIHO |
| NINB | clay | 2 | 0 | 4.44 | 0.27 | 0.06 | -- | -- | -- | -- | -- | -- | 3 | From NIHO |
| NINB | sandy clayey and clayey sand | 2 | 0 | 4.70 | 0.27 | 0.06 | -- | -- | -- | -- | -- | -- | 3 | From NIHO |
| NINB | fine sand | 2 | 0 | 4.93 | 0.27 | 0.05 | -- | -- | -- | -- | -- | -- | 3 | From NIHO - all sand combined in one Vs class |
| NINB | medium sand | 2 | 0 | 4.93 | 0.27 | 0.05 | -- | -- | -- | -- | -- | -- | 3 | From NIHO - all sand combined in one Vs class |

| Formation (see Table V.1) | Lithology | Depth dependence *) | # observations | Mean ln(Vs) | Standard deviation ln(Vs) | Coefficient of variance | Slope n | Intercept lnVs ₁ | Mean ln(σ ₀ /pa) | Sum of squares ln(σ ₀ /pa) | Variance regression | Variance velocity (not used) | Source **) | Remark |
|---------------------------|--------------------------------|---------------------|----------------|-------------|---------------------------|-------------------------|---------|-----------------------------|-----------------------------|---------------------------------------|---------------------|------------------------------|------------|---|
| NINB | coarse sand, gravel and shells | 2 | 0 | 4.93 | 0.27 | 0.05 | -- | -- | -- | -- | -- | -- | 3 | From NIHO - all sand combined in one Vs class |
| PE | peat | 3 | 0 | -- | 0.27 | -- | 0.25 | 4.81 | -- | -- | -- | -- | 3 | n from clay literature - intercept consistent with NIBA - σlnVs increased to 0.27 for peat |
| PE | clay | 1 | 455 | -- | -- | -- | 0.33 | 5.27 | 0.39 | 41.89 | 0.03 | 0.03 | 1 | sufficient data from SCPT data set - depth dependence |
| PE | sandy clayey and clayey sand | 1 | 41 | -- | -- | -- | 0.43 | 5.20 | 0.66 | 2.59 | 0.03 | 0.03 | 1 | sufficient data from SCPT data set - depth dependence |
| PE | fine sand | 1 | 222 | -- | -- | -- | 0.10 | 5.58 | 0.54 | 16.26 | 0.02 | 0.02 | 1 | sufficient data from SCPT data set - depth dependence |
| PE | medium sand | 1 | 72 | -- | -- | -- | 0.24 | 5.58 | 0.61 | 3.04 | 0.02 | 0.02 | 1 | sufficient data from SCPT data set - depth dependence - Medium & coarse sand combined in one Vs class |
| PE | coarse sand, gravel and shells | 1 | 72 | -- | -- | -- | 0.24 | 5.58 | 0.61 | 3.04 | 0.02 | 0.02 | 1 | sufficient data from SCPT data set - depth dependence - Medium & coarse sand combined in one Vs class |
| UR | peat | 3 | 0 | -- | 0.27 | -- | 0.25 | 4.81 | -- | -- | -- | -- | 3 | from URTY |
| UR | clay | 3 | 0 | -- | 0.20 | -- | 0.25 | 5.12 | -- | -- | -- | -- | 2 | from URTY |
| UR | sandy clayey and clayey sand | 3 | 0 | -- | 0.20 | -- | 0.25 | 5.27 | -- | -- | -- | -- | 3 | from URTY |
| UR | fine sand | 3 | 0 | -- | 0.20 | -- | 0.26 | 5.39 | -- | -- | -- | -- | 2 | from URTY |
| UR | medium sand | 3 | 0 | -- | 0.20 | -- | 0.26 | 5.39 | -- | -- | -- | -- | 3 | from URTY |
| UR | coarse sand, gravel and shells | 3 | 0 | -- | 0.20 | -- | 0.26 | 5.58 | -- | -- | -- | -- | 3 | from URTY |
| URTY | peat | 3 | 0 | -- | 0.27 | -- | 0.25 | 4.81 | -- | -- | -- | -- | 3 | n from clay literature - intercept consistent with NIBA - σlnVs increased to 0.27 for peat |
| URTY | clay | 3 | 0 | -- | 0.20 | -- | 0.25 | 5.12 | -- | -- | -- | -- | 3 | n from clay - Vs=190 m/s at average depth of 20 m |

| Formation (see Table V.1) | Lithology | Depth dependence *) | # observations | Mean ln(Vs) | Standard deviation ln(Vs) | Coefficient of variance | Slope n | Intercept lnVs1 | Mean ln(σ_0' /pa) | Sum of squares ln(σ_0' /pa) | Variance regression | Variance velocity (not used) | Source **) | Remark |
|---------------------------|--------------------------------|---------------------|----------------|-------------|---------------------------|-------------------------|---------|-----------------|---------------------------|-------------------------------------|---------------------|------------------------------|------------|--|
| URTY | sandy clayey and clayey sand | 3 | 0 | -- | 0.20 | -- | 0.25 | 5.27 | -- | -- | -- | -- | 3 | n from clay - Vs=220 m/s at average depth of 20 m |
| URTY | fine sand | 3 | 0 | -- | 0.20 | -- | 0.26 | 5.39 | -- | -- | -- | -- | 3 | n from Menq (not enough data in SCPT data set) - Vs=235 m/s at average depth of 20 m |
| URTY | medium sand | 3 | 0 | -- | 0.20 | -- | 0.26 | 5.39 | -- | -- | -- | -- | 3 | n from Menq (not enough data in SCPT data set) - Vs=250 m/s at average depth of 20 m |
| URTY | coarse sand, gravel and shells | 3 | 0 | -- | 0.20 | -- | 0.26 | 5.58 | -- | -- | -- | -- | 3 | n from Menq (not enough data in SCPT data set) - Vs=300 m/s at average depth of 20 m |

Notes on Table V.2:

*) Depth dependence:

1. Depth dependence according to Eq. (7.1) based on data.
2. No depth dependence for Vs.
3. Depth dependence according to Eq. (7.1) based on data based on literature and expert judgement.

***) Source:

1. SCPT data set
2. Wassing *et al.* (2003)
3. Expert estimate

Table I.3. Geomechanical parameters for organic deposits (peat). OCR = oler-consolidation ratio; Su = undrained shear strength. (see Table I.1 for codes of stratigraphic units).

| Strat. unit GeoTOP | Average unit weight wet (kN/m3) | Based on | Average OCR | Based on | Average Su (kPa) | Based on | K0 | Based on |
|-----------------------|--|------------------|-----------------------|---|---------------------|---------------------------------------|------|---|
| AAOP | 12 | Expert judgement | 2 | From NA | 22.2 | CPT dataset and adjusted Su = qnet/17 | 0.35 | Holocene peat |
| AP | 12 | Expert judgement | 4 | Value for Peelo at 30 m depth | 60 | Maximum value NIBA at ~ 20 m depth | 1.1 | Clay |
| BX | 11.4 | CPT dataset | $4.5+0.005*\sigma'v0$ | CPT dataset and Kulhawy&Mayne (1990), max=6 | $0.47*\sigma'v0+5$ | From NIBA | 1.1 | Clay |
| BXKO | 11.4 | CPT dataset | $4.5+0.005*\sigma'v0$ | CPT dataset and Kulhawy&Mayne (1990), max=6 | $0.47*\sigma'v0+5$ | From NIBA | 1.1 | Clay |
| BXSI1 | 10.8 | CPT dataset | 2 | From NA | $0.39*\sigma'v0+8$ | From NIHO | 0.5 | Clay |
| BXSI2 | 11.4 | CPT dataset | $4.5+0.005*\sigma'v0$ | CPT dataset and Kulhawy&Mayne (1990), max=6 | $0.47*\sigma'v0+5$ | From NIBA | 1.1 | Clay |
| BXWI | 11.4 | CPT dataset | $4.5+0.005*\sigma'v0$ | CPT dataset and Kulhawy&Mayne (1990), max=6 | $0.47*\sigma'v0+5$ | From NIBA | 1.1 | Clay |
| DN | 12 | Expert judgement | 4 | Value for Peelo at 30 m depth | 60 | Maximum value NIBA at ~ 20 m depth | 1.1 | Clay |
| DR | 12 | CPT dataset | $4.5+0.005*\sigma'v0$ | CPT dataset and Kulhawy&Mayne (1990), max=6 | 60 | Maximum value NIBA at ~ 20 m depth | 1.1 | Clay |
| DRGI | 12 | CPT dataset | $4.5+0.005*\sigma'v0$ | CPT dataset and Kulhawy&Mayne (1990), max=6 | 60 | Maximum value NIBA at ~ 20 m depth | 1.1 | Clay |
| EE | 11.4 | CPT dataset | $4.5+0.005*\sigma'v0$ | CPT dataset and Kulhawy&Mayne (1990), max=6 | $0.47*\sigma'v0+5$ | From NIBA | 1.1 | Clay |
| NA | 10.3 | CPT dataset | 2 | Median from CPT data set, based on Kulhawy&Mayne (1990) | $0.39*\sigma'v0+8$ | From NIHO | 0.35 | Holocene peat |
| NASC | 10.3 | CPT dataset | 2 | Median from CPT data set, based on Kulhawy&Mayne (1990) | $0.39*\sigma'v0+8$ | From NIHO | 0.35 | Holocene peat |
| NAWA | 10.3 | CPT dataset | 2 | Median from CPT data set, based on Kulhawy&Mayne (1990) | $0.39*\sigma'v0+8$ | From NIHO | 0.35 | Holocene peat |
| NAWO | 10.3 | CPT dataset | 2 | Median from CPT data set, based on Kulhawy&Mayne (1990) | $0.39*\sigma'v0+8$ | From NIHO | 0.35 | Holocene peat |
| NAZA | 10.3 | CPT dataset | 2 | Median from CPT data set, based on Kulhawy&Mayne (1990) | $0.39*\sigma'v0+8$ | From NIHO | 0.35 | Holocene peat |
| NIBA | 11.3 | CPT dataset | 2 | Median from CPT data set, based on Kulhawy&Mayne (1990) | $0.47*\sigma'v0+5$ | CPT dataset and adjusted Su = qnet/17 | 0.7 | NIBA special case k0=07 for all lithologies |
| NIGR | 10.8 | CPT dataset | 2 | Median from CPT data set, based on Kulhawy&Mayne (1990) | $0.39*\sigma'v0+8$ | From NIHO | 0.35 | Holocene peat |
| NIHO | 10.8 | CPT dataset | (1) | Median from CPT data set, based on Kulhawy&Mayne (1990) | $0.39*\sigma'v0+8$ | CPT dataset and adjusted Su = qnet/17 | 0.35 | Holocene peat |
| NINB | 10.8 | CPT dataset | 2 | Median from CPT data set, based on Kulhawy&Mayne (1990) | $0.39*\sigma'v0+8$ | From NIHO | 0.35 | Holocene peat |
| PE | 12 | Expert judgement | $6-0.005*\sigma'v0$ | CPT dataset larger set Kulhawy&Mayne (1990), min=4 | 60 | Maximum value NIBA at ~ 20 m depth | 1.1 | Clay |
| UR | 12 | Expert judgement | 4 | Value for Peelo at 30 m depth | 60 | Maximum value NIBA at ~ 20 m depth | 1.1 | Clay |
| URTY | 12 | Expert judgement | 4 | Value for Peelo at 30 m depth | 60 | Maximum value NIBA at ~ 20 m depth | 1.1 | Clay |

(1) MRD curves for NIHO peat based on Zwanenburg et al. (2020)

Table I.4. Geomechanical parameters for clays. Ip = plasticity index; OCR = overconsolidation ratio; Su = undrained shear strength. (see Table I.1 for codes of stratigraphic units)

| Strat. unit GeoTOP | Lith. class | Average unit weight wet (kN/m ³) | Based on | Ip | Based on | Average OCR | Based on | Average σ'_{v0u} (kPa) | Based on | K0 | Based on |
|-----------------------|----------------------------|--|-------------|----|---|-------------------------|---|-------------------------------|--|-----|-------------------------------------|
| AAOP | Clay | 13.9 | CPT dataset | 50 | From PE clay used for dike studies | 2 | From NA | 20 | CPT dataset and Lunne et al (1997) | 0.5 | Holocene clay |
| AAOP | Clayey sand and sandy clay | 16.8 | CPT dataset | 50 | From AAOP clay | 2 | From NA | 55 | CPT dataset and Lunne et al (1997) | 0.5 | Clay |
| AP | Clay | 17.6 | CPT dataset | 30 | Sorensen&Okkels (2013) | 4 | Value for Peelo at 30 m depth | $0.88\sigma'_{v0}+26$ | From PE | 1.1 | Depends on OCR for Pleistocene clay |
| AP | Clayey sand and sandy clay | 18.1 | CPT dataset | 30 | Sorensen&Okkels (2013) | 4 | Value for Peelo at 30 m depth | $0.60\sigma'_{v0}+55$ | From PE | 1.2 | Clay |
| BX | Clay | 14.4 | CPT dataset | 50 | Sorensen&Okkels (2013) & expert judgement | $4.5+0.005\sigma'_{v0}$ | CPT dataset and Kulhawy&Mayne (1990), max=6 | $1.15\sigma'_{v0}$ | CPT data σ'_{v0et} and Lunne et al (1997) | 1.1 | Depends on OCR for Pleistocene clay |
| BX | Clayey sand and sandy clay | 16.9 | CPT dataset | 50 | Sorensen&Okkels (2013) & expert judgement | $4.5+0.005\sigma'_{v0}$ | CPT dataset and Kulhawy&Mayne (1990), max=6 | $0.97\sigma'_{v0}+30$ | CPT dataset and Lunne et al (1997) | 1.1 | Clay |
| BXKO | Clay | 14.4 | CPT dataset | 50 | Sorensen&Okkels (2013) & expert judgement | $4.5+0.005\sigma'_{v0}$ | CPT dataset and Kulhawy&Mayne (1990), max=6 | $1.15\sigma'_{v0}$ | CPT dataset and Lunne et al (1997) | 1.1 | Depends on OCR for Pleistocene clay |
| BXKO | Clayey sand and sandy clay | 16.9 | CPT dataset | 50 | Sorensen&Okkels (2013) & expert judgement | $4.5+0.005\sigma'_{v0}$ | CPT dataset and Kulhawy&Mayne (1990), max=6 | $0.97\sigma'_{v0}+30$ | CPT dataset and Lunne et al (1997) | 1.1 | Clay |
| BXSI1 | Clay | 14.1 | CPT dataset | 50 | Sorensen&Okkels (2013) & expert judgement | 2 | From NA | $0.31\sigma'_{v0}+10$ | From NA | 0.5 | From NIHO |
| BXSI1 | Clayey sand and sandy clay | 16 | CPT dataset | 50 | Sorensen&Okkels (2013) & expert judgement | 2 | From NA | $0.49\sigma'_{v0}+44$ | From NA | 0.5 | Clay from NIHO |
| BXSI2 | Clay | 14.4 | CPT dataset | 50 | Sorensen&Okkels (2013) & expert judgement | $4.5+0.005\sigma'_{v0}$ | CPT dataset and Kulhawy&Mayne (1990), max=6 | $1.15\sigma'_{v0}$ | CPT dataset and Lunne et al (1997) | 1.1 | Depends on OCR for Pleistocene clay |
| BXSI2 | Clayey sand and sandy clay | 16.9 | CPT dataset | 50 | Sorensen&Okkels (2013) & expert judgement | $4.5+0.005\sigma'_{v0}$ | CPT dataset and Kulhawy&Mayne (1990), max=6 | $0.97\sigma'_{v0}+30$ | CPT dataset and Lunne et al (1997) | 1.1 | Clay |

| Strat. unit GeoTOP | Lith. class | Average unit weight wet (kN/m ³) | Based on | Ip | Based on | Average OCR | Based on | Average σ'_{v0u} (kPa) | Based on | K0 | Based on |
|-----------------------|----------------------------|--|-------------|----|---|--------------------------|--|----------------------------------|---|-----|-------------------------------------|
| BXWI | Clay | 14.4 | CPT dataset | 50 | Sorensen&Okkels (2013) & expert judgement | $4.5+0.005*\sigma'_{v0}$ | CPT dataset and Kulhawy&Mayne (1990), max=6 | $1.15*\sigma'_{v0}$ | CPT dataset and Lunne et al (1997) | 1.1 | Depends on OCR for Pleistocene clay |
| BXWI | Clayey sand and sandy clay | 16.9 | CPT dataset | 50 | Sorensen&Okkels (2013) & expert judgement | $4.5+0.005*\sigma'_{v0}$ | CPT dataset and Kulhawy&Mayne (1990), max=6 | $0.97*\sigma'_{v0}+30$ | CPT dataset and Lunne et al (1997) | 1.1 | Clay |
| DN | Clay | 17.6 | CPT dataset | 30 | Sorensen&Okkels (2013) | 4 | Value for Peelo at 30 m depth | $0.88*\sigma'_{v0}+26$ | From PE | 1.1 | Depends on OCR for Pleistocene clay |
| DN | Clayey sand and sandy clay | 18.1 | CPT dataset | 30 | Sorensen&Okkels (2013) | 4 | Value for Peelo at 30 m depth | $0.60*\sigma'_{v0}+55$ | From PE | 1.2 | Clay |
| DR | Clay | 14.7 | CPT dataset | 15 | Sorensen&Okkels (2013) | $4.5+0.005*\sigma'_{v0}$ | CPT dataset and Kulhawy&Mayne (1990), max=6 | $1.15*\sigma'_{v0}$ | CPT dataset and Lunne et al (1997) | 1.1 | Depends on OCR for Pleistocene clay |
| DR | Clayey sand and sandy clay | 16.7 | CPT dataset | 15 | Sorensen&Okkels (2013) | $4.5+0.005*\sigma'_{v0}$ | CPT dataset and Kulhawy&Mayne (1990), max=6 | $0.97*\sigma'_{v0}+30$ | CPT dataset and Lunne et al (1997) | 1.2 | Clay |
| DRGI | Clay | 14.7 | CPT dataset | 15 | Sorensen&Okkels (2013) | $4.5+0.005*\sigma'_{v0}$ | CPT dataset and Kulhawy&Mayne (1990), max=6 | $1.15*\sigma'_{v0}$ | CPT dataset and Lunne et al (1997) | 1.1 | Depends on OCR for Pleistocene clay |
| DRGI | Clayey sand and sandy clay | 16.7 | CPT dataset | 10 | TNO data | $4.5+0.005*\sigma'_{v0}$ | CPT dataset and Kulhawy&Mayne (1990), max=6 | $0.97*\sigma'_{v0}+30$ | CPT dataset and Lunne et al (1997) | 1.2 | Clay |
| EE | Clay | 14.4 | CPT dataset | 40 | TNO data | $4.5+0.005*\sigma'_{v0}$ | CPT dataset and Kulhawy&Mayne (1990), max=6 | $1.15*\sigma'_{v0}$ | CPT dataset and Lunne et al (1997) | 1.1 | Depends on OCR for Pleistocene clay |
| EE | Clayey sand and sandy clay | 17.2 | CPT dataset | 40 | From EE clay | $4.5+0.005*\sigma'_{v0}$ | CPT dataset and Kulhawy&Mayne (1990), max=6 | $0.97*\sigma'_{v0}+30$ | CPT dataset and Lunne et al (1997) | 1.3 | Clay |
| NA | Clay | 12.9 | CPT dataset | 30 | Skempton&Henkel (1953) and expert judgement | 2 | CPT dataset and Kulhawy&Mayne (1990), median value | $0.31*\sigma'_{v0}+10$ | CPT dataset for all NA and Lunne et al (1997) | 0.5 | Constant 0.5 for Holocene clay |
| NA | Clayey sand and sandy clay | 16.2 | CPT dataset | 30 | From NA clay | 2 | CPT dataset and Kulhawy&Mayne (1990), median value | $0.49*\sigma'_{v0}+44$ | CPT dataset for all NA and Lunne et al (1997) | 0.5 | Clay |

| Strat. unit GeoTOP | Lith. class | Average unit weight wet (kN/m3) | Based on | Ip | Based on | Average OCR | Based on | Average $\sigma'v0u$ (kPa) | Based on | K0 | Based on |
|-----------------------|-------------------------------|---|-------------|----|----------------|-------------|--|-------------------------------|---|-----|---|
| NASC | Clay | 12.9 | CPT dataset | 30 | From NA clay | 2 | CPT dataset and Kulhawy&Mayne (1990), median value | $0.31 \cdot \sigma'v0+10$ | CPT dataset for all NA and Lunne et al (1997) | 0.5 | Constant 0.5 for Holocene clay |
| NASC | Clayey sand and sandy clay | 16.2 | CPT dataset | 30 | From NA clay | 2 | CPT dataset and Kulhawy&Mayne (1990), median value | $0.49 \cdot \sigma'v0+44$ | CPT dataset for all NA and Lunne et al (1997) | 0.5 | Clay |
| NAWA | Clay | 12.9 | CPT dataset | 30 | From NA clay | 2 | CPT dataset and Kulhawy&Mayne (1990), median value | $0.31 \cdot \sigma'v0+10$ | CPT dataset for all NA and Lunne et al (1997) | 0.5 | Constant 0.5 for Holocene clay |
| NAWA | Clayey sand and sandy clay | 16.2 | CPT dataset | 30 | From NA clay | 2 | CPT dataset and Kulhawy&Mayne (1990), median value | $0.49 \cdot \sigma'v0+44$ | CPT dataset for all NA and Lunne et al (1997) | 0.5 | Clay |
| NAWO | Clay | 12.9 | CPT dataset | 30 | From NA clay | 2 | CPT dataset and Kulhawy&Mayne (1990), median value | $0.31 \cdot \sigma'v0+10$ | CPT dataset for all NA and Lunne et al (1997) | 0.5 | Constant 0.5 for Holocene clay |
| NAWO | Clayey sand and sandy clay | 16.2 | CPT dataset | 30 | From NA clay | 2 | CPT dataset and Kulhawy&Mayne (1990), median value | $0.49 \cdot \sigma'v0+44$ | CPT dataset for all NA and Lunne et al (1997) | 0.5 | Clay |
| NAZA | Clay | 12.9 | CPT dataset | 30 | From NA clay | 2 | CPT dataset and Kulhawy&Mayne (1990), median value | $0.31 \cdot \sigma'v0+10$ | CPT dataset for all NA and Lunne et al (1997) | 0.5 | Constant 0.5 for Holocene clay |
| NAZA | Clayey sand and sandy clay | 16.2 | CPT dataset | 30 | From NA clay | 2 | CPT dataset and Kulhawy&Mayne (1990), median value | $0.49 \cdot \sigma'v0+44$ | CPT dataset for all NA and Lunne et al (1997) | 0.5 | Clay |
| NIBA | Clay | 15 | CPT dataset | 50 | From NIHO clay | 2 | CPT dataset and Kulhawy&Mayne (1990), median value | $0.31 \cdot \sigma'v0+10$ | From NA | 0.7 | NIBA special case $k0=07$ for all lithologies |
| NIBA | Clayey sand and sandy clay | 17 | CPT dataset | 50 | From NIBA clay | 2 | CPT dataset and Kulhawy&Mayne (1990), median value | $0.49 \cdot \sigma'v0+44$ | From NA | 0.7 | NIBA special case $k0=07$ for all lithologies |
| NIGR | Clay | 14.1 | CPT dataset | 50 | From NIHO clay | 2 | CPT dataset and Kulhawy&Mayne (1990), median value | $0.31 \cdot \sigma'v0+10$ | From NA | 0.5 | Constant 0.5 for Holocene clay |
| NIGR | Clayey sand and sandy clay | 16 | CPT dataset | 50 | From NIHO clay | 2 | CPT dataset and Kulhawy&Mayne (1990), median value | $0.49 \cdot \sigma'v0+44$ | From NA | 0.5 | Clay |

| Strat. unit GeoTOP | Lith. class | Average unit weight wet (kN/m ³) | Based on | Ip | Based on | Average OCR | Based on | Average $\sigma'v0u$ (kPa) | Based on | K0 | Based on |
|-----------------------|----------------------------|--|------------------|----|---|-----------------------------|--|-------------------------------|--------------------|-----|--------------------------------------|
| NIHO | Clay | 14.1 | CPT dataset | 50 | Skempton&Henkel (1953) and expert judgement | 2 | CPT dataset and Kulhawy&Mayne (1990), median value | $0.31 \cdot \sigma'v0 + 10$ | From NA | 0.5 | Constant 0.5 for Holocene clay |
| NIHO | Clayey sand and sandy clay | 16 | CPT dataset | 50 | From NIHO clay | 2 | CPT dataset and Kulhawy&Mayne (1990), median value | $0.49 \cdot \sigma'v0 + 44$ | From NA | 0.5 | Clay |
| NINB | Clay | 14.1 | CPT dataset | 50 | From NIHO clay | 2 | CPT dataset and Kulhawy&Mayne (1990), median value | $0.31 \cdot \sigma'v0 + 10$ | From NA | 0.5 | Constant 0.5 for Holocene clay |
| NINB | Clayey sand and sandy clay | 16 | CPT dataset | 50 | From NIHO clay | 2 | CPT dataset and Kulhawy&Mayne (1990), median value | $0.49 \cdot \sigma'v0 + 44$ | From NA | 0.5 | Clay |
| PE | Clay | 17.6 | CPT dataset | 50 | Sorensen&Okkels (2013) and TNO data | $6 - 0.005 \cdot \sigma'v0$ | CPT dataset Kulhawy&Mayne (1990), min=4 | $0.88 \cdot \sigma'v0 + 26$ | CPT larger dataset | 1.1 | Depends on OCR for Pleistocene clay |
| PE | Clayey sand and sandy clay | 18.1 | CPT dataset | 30 | Sorensen&Okkels (2013) | $6 - 0.005 \cdot \sigma'v0$ | CPT dataset Kulhawy&Mayne (1990), min=4 | $0.60 \cdot \sigma'v0 + 55$ | CPT larger dataset | 1.2 | Clay |
| UR | Clay | 17.6 | CPT dataset | 30 | Sorensen&Okkels (2013) and TNO data | 4 | Value for Peelo at 30 m depth | $0.88 \cdot \sigma'v0 + 26$ | From PE | 1.1 | Depends on OCR for Pleistocene clay |
| UR | Clayey sand and sandy clay | 17.6 | CPT dataset | 30 | Sorensen&Okkels (2013) | 4 | Value for Peelo at 30 m depth | $0.60 \cdot \sigma'v0 + 55$ | From PE | 1.4 | Clay |
| URTY | Clay | 17.6 | CPT dataset | 30 | Sorensen&Okkels (2013) and TNO data | 4 | Value for Peelo at 30 m depth | $0.88 \cdot \sigma'v0 + 26$ | From PE | 1.1 | Depends on OCR for Pleistocene clay |
| URTY | Clayey sand and sandy clay | 17.6 | CPT dataset | 30 | Sorensen&Okkels (2013) | 4 | Value for Peelo at 30 m depth | $0.60 \cdot \sigma'v0 + 55$ | From PE | 1.4 | Clay |
| PZ | Clay (deep) | 21 | Expert judgement | 30 | Sorensen&Okkels (2013) | 2 | Expert judgement | $0.88 \cdot \sigma'v0 + 26$ | From PE | 1 | Uncertain for deep clay, assume K0=1 |
| PZWA | Clay (deep) | 21 | Expert judgement | 30 | Sorensen&Okkels (2013) | 2 | Expert judgement | $0.88 \cdot \sigma'v0 + 26$ | From PE | 1 | Uncertain for deep clay, assume K0=1 |
| NUOT | Clay (deep) | 21 | Expert judgement | 40 | Sorensen&Okkels (2013) and TNO-inventory Tertiary Clays | 2 | Expert judgement | $0.88 \cdot \sigma'v0 + 26$ | From PE | 1 | Uncertain for deep clay, assume K0=1 |

| Strat. unit GeoTOP | Lith. class | Average unit weight wet (kN/m ³) | Based on | Ip | Based on | Average OCR | Based on | Average σ'_{v0u} (kPa) | Based on | K0 | Based on |
|-----------------------|-----------------------|--|---------------------|----|---|-------------|------------------|----------------------------------|--|----|---|
| NUOT | Clayey sand (deep) | 21 | Expert judgement | 40 | Sorensen&Okkels (2013) and TNO- inventory Tertiary Clays | 2 | Expert judgement | 325 | Inferred from TNO inventory Tertiary clays | 1 | Uncertain for deep clay, assume K0=1 |
| NUBA | Clayey sand (deep) | 21 | Expert judgement | 40 | Sorensen&Okkels (2013) and TNO- inventory Tertiary Clays | 2 | Expert judgement | 325 | Inferred from TNO inventory Tertiary clays | 1 | Uncertain for deep clay, assume K0=1 |

Table I.5. Geomechanical parameters for sand. D50 = median grain size; Cu =coefficient of uniformity. (see Table I.1 for codes of stratigraphic units).

| Strat. unit GeoTOP | Lith. Class | Average unit weight wet (kN/m ³) | Based on | K0 | Based on | Whole sample D50 (mm) | Whole sample Median Cu | Based on |
|-----------------------|--------------------------------|--|------------------|-----|--------------------------|--------------------------|---------------------------|---|
| AAOP | Fine sand | 18.4 | CPT dataset | 0.5 | Holocene sand | 0.0803 | 5.53 | Rijkers et al. (1998) |
| AAOP | Medium sand | 21 | Expert judgement | 0.5 | Holocene sand | 0.18818 | 3.71 | Rijkers et al. (1998) |
| AAOP | Coarse sand, gravel and shells | 21 | Expert judgement | 0.5 | Holocene sand | 0.23233 | 12.34 | Rijkers et al. (1998) |
| AP | Fine sand | 19.6 | CPT dataset | 1 | Older than Holocene sand | 0.11474 | 1.86 | From PE |
| AP | Medium sand | 21 | Expert judgement | 1 | Older than Holocene sand | 0.19803 | 1.94 | From PE |
| AP | Coarse sand, gravel and shells | 21 | Expert judgement | 1 | Older than Holocene sand | 0.5283 | 7.14 | Estimate from deep drillings in Groningen |
| BX | Fine sand | 19.4 | CPT dataset | 1 | Older than Holocene sand | 0.11524 | 2.34 | Rijkers et al. (1998) |
| BX | Medium sand | 21 | Expert judgement | 1 | Older than Holocene sand | 0.19477 | 2.23 | Rijkers et al. (1998) |
| BX | Coarse sand, gravel and shells | 21 | Expert judgement | 1 | Older than Holocene sand | 0.36272 | 1.99 | Rijkers et al. (1998) |
| BXKO | Fine sand | 19.4 | CPT dataset | 1 | Older than Holocene sand | 0.11524 | 2.34 | From BX |
| BXKO | Medium sand | 21 | Expert judgement | 1 | Older than Holocene sand | 0.19477 | 2.23 | From BX |
| BXKO | Coarse sand, gravel and shells | 21 | Expert judgement | 1 | Older than Holocene sand | 0.36272 | 1.99 | From BX |
| BXSI1 | Fine sand | 18.8 | CPT dataset | 1 | Older than Holocene sand | 0.11399 | 2.03 | From NA |
| BXSI1 | Medium sand | 21 | Expert judgement | 1 | Older than Holocene sand | 0.18347 | 1.75 | From NA |
| BXSI1 | Coarse sand, gravel and shells | 21 | Expert judgement | 1 | Older than Holocene sand | 0.30837 | 1.74 | From NA |
| BXSI2 | Fine sand | 19.4 | CPT dataset | 1 | Older than Holocene sand | 0.11524 | 2.34 | From BX |
| BXSI2 | Medium sand | 21 | Expert judgement | 1 | Older than Holocene sand | 0.19477 | 2.23 | From BX |
| BXSI2 | Coarse sand, gravel and shells | 21 | Expert judgement | 1 | Older than Holocene sand | 0.36272 | 1.99 | From BX |
| BXWI | Fine sand | 19.4 | CPT dataset | 1 | Older than Holocene sand | 0.12113 | 1.94 | Rijkers et al. (1998) |
| BXWI | Medium sand | 21 | Expert judgement | 1 | Older than Holocene sand | 0.18135 | 2.44 | Rijkers et al. (1998) |
| BXWI | Coarse sand, gravel and shells | 21 | Expert judgement | 1 | Older than Holocene sand | 0.36272 | 1.99 | From BX |

| Strat. unit GeoTOP | Lith. Class | Average unit weight wet (kN/m ³) | Based on | K0 | Based on | Whole sample D50 (mm) | Whole sample Median Cu | Based on |
|-----------------------|--------------------------------|--|------------------|-----|--------------------------|--------------------------|---------------------------|------------------------------------|
| DN | Fine sand | 19.6 | CPT dataset | 1 | Older than Holocene sand | 0.13223 | 2.27 | Rijkers et al. (1998) |
| DN | Medium sand | 21 | Expert judgement | 1 | Older than Holocene sand | 0.19647 | 2.21 | Rijkers et al. (1998) |
| DN | Coarse sand, gravel and shells | 21 | Expert judgement | 1 | Older than Holocene sand | 0.33565 | 1.88 | Rijkers et al. (1998) |
| DR | Fine sand | 19.5 | CPT dataset | 1 | Older than Holocene sand | 0.13163 | 2.11 | From DRSC |
| DR | Medium sand | 20.6 | CPT dataset | 1 | Older than Holocene sand | 0.2387 | 1.86 | From DRSC |
| DR | Coarse sand, gravel and shells | 21 | Expert judgement | 1 | Older than Holocene sand | 0.38726 | 2.35 | From DRSC |
| DRGI | Fine sand | 19.5 | CPT dataset | 1 | Older than Holocene sand | 0.13163 | 2.11 | From DRSC |
| DRGI | Medium sand | 20.6 | CPT dataset | 1 | Older than Holocene sand | 0.1743 | 8.85 | Only medium sand known for DRGI |
| DRGI | Coarse sand, gravel and shells | 21 | Expert judgement | 1 | Older than Holocene sand | 0.38726 | 2.35 | From DRSC |
| EE | Fine sand | 19.4 | CPT dataset | 1 | Older than Holocene sand | 0.10824 | 1.76 | Rijkers et al. (1998) |
| EE | Medium sand | 21 | Expert judgement | 1 | Older than Holocene sand | 0.17146 | 2.57 | Rijkers et al. (1998) |
| EE | Coarse sand, gravel and shells | 21 | Expert judgement | 1 | Older than Holocene sand | 0.37613 | 2.88 | Rijkers et al. (1998) |
| NA | Fine sand | 18.8 | CPT dataset | 0.5 | Holocene sand | 0.11399 | 2.03 | Rijkers et al. (1998) |
| NA | Medium sand | 21 | Expert judgement | 0.5 | Holocene sand | 0.18347 | 1.75 | Rijkers et al. (1998) |
| NA | Coarse sand, gravel and shells | 21 | Expert judgement | 0.5 | Holocene sand | 0.30837 | 1.74 | Rijkers et al. (1998) |
| NASC | Fine sand | 18.8 | CPT dataset | 0.5 | Holocene sand | 0.11399 | 2.03 | From NA |
| NASC | Medium sand | 21 | Expert judgement | 0.5 | Holocene sand | 0.18347 | 1.75 | From NA |
| NASC | Coarse sand, gravel and shells | 21 | Expert judgement | 0.5 | Holocene sand | 0.30837 | 1.74 | From NA |
| NAWA | Fine sand | 18.8 | CPT dataset | 0.5 | Holocene sand | 0.11399 | 2.03 | From NA |
| NAWA | Medium sand | 21 | Expert judgement | 0.5 | Holocene sand | 0.18347 | 1.75 | From NA |
| NAWA | Coarse sand, gravel and shells | 21 | Expert judgement | 0.5 | Holocene sand | 0.30837 | 1.74 | From NA |
| NAWO | Fine sand | 18.8 | CPT dataset | 0.5 | Holocene sand | 0.11399 | 2.03 | From NA |
| NAWO | Medium sand | 21 | Expert judgement | 0.5 | Holocene sand | 0.18347 | 1.75 | From NA |
| NAWO | Coarse sand, gravel and shells | 21 | Expert judgement | 0.5 | Holocene sand | 0.30837 | 1.74 | From NA |

| Strat. unit GeoTOP | Lith. Class | Average unit weight wet (kN/m ³) | Based on | K0 | Based on | Whole sample D50 (mm) | Whole sample Median Cu | Based on |
|-----------------------|--------------------------------|--|------------------|-----|--|--------------------------|---------------------------|-----------------------|
| NAZA | Fine sand | 18.8 | CPT dataset | 0.5 | Holocene sand | 0.11399 | 2.03 | From NA |
| NAZA | Medium sand | 21 | Expert judgement | 0.5 | Holocene sand | 0.18347 | 1.75 | From NA |
| NAZA | Coarse sand, gravel and shells | 21 | Expert judgement | 0.5 | Holocene sand | 0.30837 | 1.74 | From NA |
| NIBA | Fine sand | 18.3 | CPT dataset | 0.7 | NIBA special case k0=07 for all lithologies | 0.11399 | 2.03 | From NA |
| NIBA | Medium sand | 20 | CPT dataset | 0.7 | NIBA special case k0=07 for all lithologies | 0.18347 | 1.75 | From NA |
| NIBA | Coarse sand, gravel and shells | 20 | CPT dataset | 0.7 | NIBA special case k0=07 for all lithologies | 0.30837 | 1.74 | From NA |
| NIGR | Fine sand | 18.8 | CPT dataset | 0.5 | Holocene sand | 0.11399 | 2.03 | From NA |
| NIGR | Medium sand | 21 | Expert judgement | 0.5 | Holocene sand | 0.18347 | 1.75 | From NA |
| NIGR | Coarse sand, gravel and shells | 21 | Expert judgement | 0.5 | Holocene sand | 0.30837 | 1.74 | From NA |
| NIHO | Fine sand | 18.8 | CPT dataset | 0.5 | Holocene sand | 0.11399 | 2.03 | From NA |
| NIHO | Medium sand | 21 | Expert judgement | 0.5 | Holocene sand | 0.18347 | 1.75 | From NA |
| NIHO | Coarse sand, gravel and shells | 21 | Expert judgement | 0.5 | Holocene sand | 0.30837 | 1.74 | From NA |
| NINB | Fine sand | 18.8 | CPT dataset | 0.5 | Holocene sand | 0.11399 | 2.03 | From NA |
| NINB | Medium sand | 21 | Expert judgement | 0.5 | Holocene sand | 0.18347 | 1.75 | From NA |
| NINB | Coarse sand, gravel and shells | 21 | Expert judgement | 0.5 | Holocene sand | 0.30837 | 1.74 | From NA |
| PE | Fine sand | 19.6 | CPT dataset | 1 | Older than Holocene sand | 0.11674 | 1.84 | Rijkers et al. (1998) |
| PE | Medium sand | 21 | Expert judgement | 1 | Older than Holocene sand | 0.19803 | 1.94 | Rijkers et al. (1998) |
| PE | Coarse sand, gravel and shells | 21 | Expert judgement | 1 | Older than Holocene sand | 0.46823 | 2.62 | Rijkers et al. (1998) |
| UR | Fine sand | 19.7 | CPT dataset | 1 | Older than Holocene sand | 0.11674 | 1.84 | Parameters from PE |
| UR | Medium sand | 21 | Expert judgement | 1 | Older than Holocene sand | 0.19803 | 1.94 | Parameters from PE |
| UR | Coarse sand, gravel and shells | 21 | Expert judgement | 1 | Older than Holocene sand | 0.46823 | 2.62 | Parameters from PE |
| URTY | Fine sand | 19.7 | CPT dataset | 1 | Older than Holocene sand | 0.11961 | 2.14 | Rijkers et al. (1998) |
| URTY | Medium sand | 21 | Expert judgement | 1 | Older than Holocene sand | 0.22028 | 2.04 | Rijkers et al. (1998) |
| URTY | Coarse sand, gravel and shells | 21 | Expert judgement | 1 | Older than Holocene sand | 0.43259 | 1.98 | Rijkers et al. (1998) |

| Strat. unit GeoTOP | Lith. Class | Average unit weight wet (kN/m ³) | Based on | K0 | Based on | Whole sample D50 (mm) | Whole sample Median Cu | Based on |
|-----------------------|-------------|--|------------------|----|--------------------------|--------------------------|---------------------------|---|
| PZWA | Sand (deep) | 21 | Expert judgement | 1 | Older than Holocene sand | 0.25 | 4.08 | Estimate from deep drillings in Groningen |
| NUOT | Sand (deep) | 21 | Expert judgement | 1 | Older than Holocene sand | 0.156 | 2.61 | Estimate from deep drillings in Groningen |
| Nttx | Sand (deep) | 21 | Expert judgement | 1 | Older than Holocene sand | 0.156 | 2.61 | Estimate from deep drillings in Groningen |

APPENDIX II

Total Surface Residuals for the V5 and V6 GMMs

On the following pages, plots are presented showing the total residuals of the recorded surface motions with respect to the V5 (upper frames) and V6 (lower frames) GMMs, plotted against distance. In each case, the red symbols show the mean residual in each (logarithmically spaced) distance bin and the bars indicate the 90% confidence interval on these means. The plots are shown for the 10 target periods of the V7 GMM.

